INDIRA GANDHI CENTRE FOR ATOMIC RESEARCH

2011

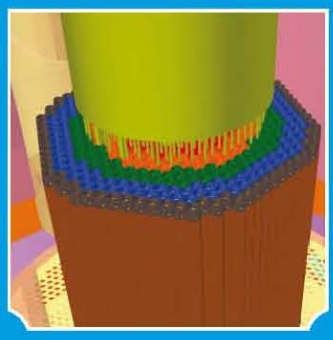

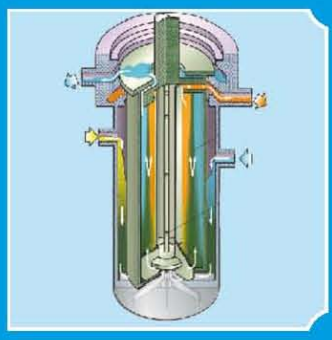

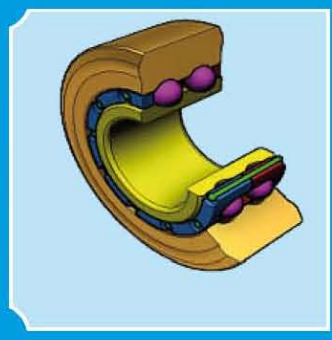

ANNUAL REPORT

Government of India
Department of Atomic Energy
Indira Gandhi Centre for
Atomic Research
Kalpakkam 603 102

IGCAR

2011

INDIRA GANDHI CENTRE FOR ATOMIC RESEARCH

ANNUAL REPORT

Government of India
Department of Atomic Energy
Indira Gandhi Centre for
Atomic Research
Kalpakkam 603 102

"Actions today mould our tomorrows"

- Indira Gandhi

".... The relative role of indigenous science & technology and foreign collaboration can be highlighted through an analogy. Indigenous science & technology plays the part of an engine in an aircraft, while foreign collaboration can play the part of a booster. A booster in the form of foreign collaboration can give a plane an assisted take-off, but it will be incapable of independent fight unless it is powered by engines of its own. If Indian industry is to take-off and be capable of independent fight, it must be powered by science & technology based in the country ..."

- Homi Jehangir Bhabha

"There is a totality about modernisation, and in order to gain confidence, we must experiment with our resources even at the risk of failure. There is a need for a constant interplay between basic sciences, technology, industrial practice and management, if economic progress is to result from the activity undertaken."

- Vikram Sarabhai

Editorial Committee

Address for Correspondence
Dr. P. R. Vasudeva Rao
Chairman, Editorial Committee
Director, Chemistry Group
Indira Gandhi Centre for Atomic Research
Kalpakkam - 603 102

Phone : +91-44-2748 0229 / 0222
Fax : +91-44-27480222 / 0065
Email : vasu@igcar.gov.in
dcg@igcar.gov.in
Website : www.igcar.gov.in

Published by:

Scientific Information Resource Division
Resources Management Group
Indira Gandhi Centre for Atomic Research
Kalpakkam - 603 102

CONTENTS

FRONT COVER

1. 3D model of in-vessel handling system
2. Schematic operation of annular centrifugal contactor
3. Fast Breeder Test Reactor
4. Roller bearing for IFTM transfer pot
5. Morphologies of ZnO nanostructures

BACK COVER

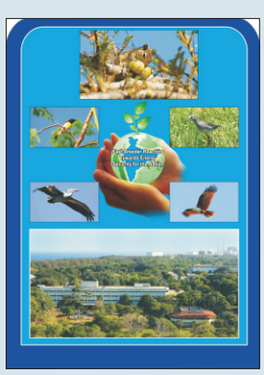

Flora and Fauna at IGCAR

Foreword

I am happy to share with you the Annual Report 2011. This report highlights the achievements of the Centre in diverse and interlinked fields within the ambit of Fast Reactor and associated Closed Fuel Cycle Technologies interlaced with research in basic sciences.

Fast Breeder Test Reactor, which is the flagship of our Centre, has completed 18th irradiation campaign and several subassemblies of the unique carbide fuel now achieved a burn-up of 155 GWd/t, which is an international benchmark. The performance of the sodium systems for the last 26 years has been excellent and the pumps have crossed 7,11,000 hours of cumulative continuous operation. The confidence in early detection of failed fuel subassembly, the only clad failure in FBTR so far, was well demonstrated. Life extension studies for FBTR have been completed and the residual life is assessed to be ten effective full power years. A beginning has been made to use FBTR for metal fuel irradiation by loading the pins of U-6%Zr sodium bonded design fabricated at IGCAR with modified 9Cr-1Mo cladding. The post irradiation examination of 37 pin PFBR MOX test subassembly with a burn-up of 112 GWd/t in FBTR is in the final stage of completion. Structure-property studies on irradiated 20% CW SS 316 clad and wrapper material and performance evaluation of an irradiated nickel reflector subassembly used in FBTR have been successfully completed. KAMINI continued to operate efficiently and is expected to play a crucial role in the development and validation of new types of neutron detectors in the future.

The year 2011 has seen considerable progress on the construction front of Prototype Fast Breeder Reactors, with integration of the roof slab with the main vessel. Evaluation of thermal design of top shield, performance qualification of inflatable seals, seismic qualification of components manufactured by various industries, design and development of special bearings, primary ramp, primary tilting mechanism for inclined fuel transfer machine, experimental investigation of inter-wrapper flow heat transfer, testing of transfer arm, shut down mechanisms, vibration studies in steam generator test facility, probabilistic safety analysis of internal events level-I and preparation of final safety report have been completed. The PFBR operator training simulator, instrumentation and control systems corresponding to safety critical, safety related and non nuclear safety systems have been developed. Development of In-Service Inspection (ISI) techniques for the reactor assembly components and addressing the safety issues related to sodium are in progress. Construction of the Demonstration Fuel Reprocessing Plant is in an advanced stage. Preliminary criticality and shielding calculations for the Fast Reactor Fuel Cycle facilities have been completed. The construction would commence upon obtaining the cabinet approval and financial sanction which is expected to be obtained this year.

Our Centre has also set its focus on basic research relating to development of newer materials and methodologies for adapting to reactor and fuel cycle applications. Studies on post-accidental heat removal, sodium fire, molten fuel coolant interaction and inertial impact behavior of fuel particles during severe accident scenario have been taken up. Design and analysis of welded grid plate, upgradation of design of instrumented irradiation capsule, development of novel devices and sensors, modeling and simulation studies towards the

development of robotic sampling systems are some of the areas where we have directed considerable effort. On the materials front, we have made considerable progress in the development of novel structural materials with improved properties, oxide dispersion strengthened ferritic alloys, reduced activation steel for fusion applications, A-TIG welding on austenitic stainless steel, nano hybrids/ nanostructures for sensor applications and alternate extractants.

We have been successful in augmenting the qualified manpower for our programmes through Training School, Homi Bhabha National Institute and encouraging collaborations with eminent academic institutes.

The services sector has contributed towards providing better amenities, infrastructure, safety, medical facilities and better environment. We would like to take our neighbourhood along with us in sharing our laurels and extending cooperation towards their betterment evenwhile educating them about the safety and necessity of our programmes.

I would like to compliment the editorial team steered by Dr.P.R.Vasudeva Rao and led by Dr. M. Sai Baba for bringing out this document traditionally with the same vigour and quality. I also appreciate colleagues from Scientific Information Resources Division, Shri Gaddam Pentaiah and Shri A. Rangarajan for their contributions and efforts.

With the conclusion of XI plan and commencement of XII plan, we have a very important phase ahead with new challenges with opportunities to better our performance and improve our stakes. I am confident that dedicated efforts with the support of colleagues and peers would reap rich rewards for the Centre and the organization.

(S. C. Chetal)
Director, IGCAR

Mission of IGCAR

- ★ *To conduct a broad based multidisciplinary programme of scientific research and advanced engineering development, directed towards the establishment of the technology of Sodium Cooled Fast Breeder Reactors (FBR) and associated fuel cycle facilities in the Country*
- ★ *The development and applications of new and improved materials, techniques, equipment and systems for FBRs and*
- ★ *To pursue basic research to achieve breakthroughs in fast reactor technology*

Vision

To be a Global Leader in Sodium cooled Fast Breeder Reactor and associated Fuel Cycle Technologies by 2020

Editorial

It is with great pleasure that the editorial committee presents you the Annual Report of Indira Gandhi Centre for Atomic Research for the year 2011. As in the previous years, the committee has taken all efforts to present a balanced picture of the activities of IGCAR in a variety of domains. The articles were also peer reviewed and put through multiple stages of editing and we hope that the report provides a comprehensive idea of IGCAR's strength and achievements in a readable manner.

The primary mission of IGCAR being R&D on the science and technology of fast reactors and the associated fuel cycle, it is but natural that major portion of the report reflects the progress with respect to FBTR, PFBR and future fast reactors, as well as the activities related to fast reactor fuel cycle. Chapter I illustrates that the FBTR operation has been robust and it continues to provide valuable inputs to the fast reactor proramme as a research tool. While all the essential R&D activities towards the PFBR construction had been completed earlier, some aspects of R&D programme in support of PFBR have continued in the current year also. The articles in Chapter II thus provide the results of R&D activities such as testing and evaluation of the thermal design of the PFBR top shield, examination of the MOX fuel discharged from reactor after irradiation to 112 GWd/t burn-up, sodium calibration of the eddy current flow meter, and commissioning of the PFBR training simulator. Chapter III relates to the R&D work being carried out at IGCAR towards future fast reactors including metal fuelled fast reactors. It is interesting to find that 21 articles on this subject appear in Chapter III. This is an indication of the increasing R&D on future reactors, aiming to enhance the safety and economics of fast reactor systems as well as to explore the metal fuelled reactors as a crucial next step in the Indian fast reactor programme. As part of the R&D on future fast reactors, one can see articles on welded grid plate development, setting up of unique facilities for studying safety aspects such as molten fuel–coolant interaction, etc. It is very significant that a few test fuel pins of U-Zr-Na bonded metallic fuel have been introduced in FBTR for test irradiation. The activities on CFBR (the next version of the MOX fuelled FBRs) and the metal fueled fast reactors are bound to increase in the coming years, with the tapering of efforts on PFBR. In Chapter IV, we see a variety of R&D efforts related to fast reactor fuel cycle and many achievements of high significance. The chapter includes studies on the PUREX processes for fast reactor fuel reprocessing as well as the molten salt electro refining process for the metallic fuels. Studies on red oil formation due to degradation of the PUREX solvent, development of the measurement systems for the assay of Pu in waste drums by passive neutron counting and engineering scale demonstration of the molten salt electrorefining of uranium are important examples. The 30 articles under the Chapter on Basic Research indicate the healthy content of basic research programmes at IGCAR- very essential for the sustained growth of R&D in the complex technology of fast reactors and for achieving breakthroughs. The variety of infrastructures that have been realized in the year 2011 for aiding the R&D programmes is also highlighted in Chapter VI. It is obvious from this chapter that the growth of infrastructure has been in line with the R&D requirements. Chapter VII portrays the comprehensive efforts at IGCAR towards human resource development and collaborations. The large number of special lectures and colloquia conducted at IGCAR and the visit of a number of dignitaries as well as awards and honours received by the colleagues are indicators of the dynamism and excellence prevailing in the centre.

The Editorial Committee is thankful to all the authors who have contributed interesting articles highlighting the above achievements. We welcome inputs from readers both with respect to the technical content as well as the quality of the publication.

I personally thank the members of the Editorial Committee and in particular, Dr. M. Sai Baba for their professional efforts to bring out a good report. I particularly thank Shri Gaddam Pentaiah and Shri A. Rangarajan of SIRD, for all their contributions that have helped us to expedite the publication. The Editorial Committee is indebted to Dr. Baldev Raj (former Director) and Shri S.C. Chetal, Director, IGCAR whose motivation and guidance have helped us to bring out the publication, maintaining a high standard.

(P. R. Vasudeva Rao)
Chairman, Editorial Committee
Director, Chemistry Group

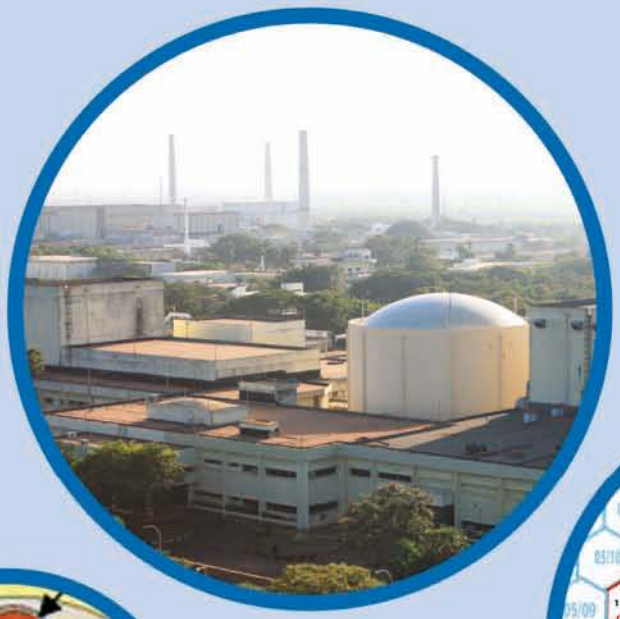

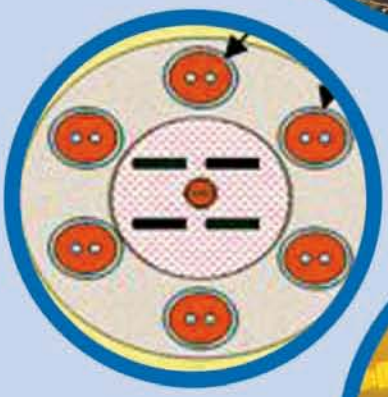

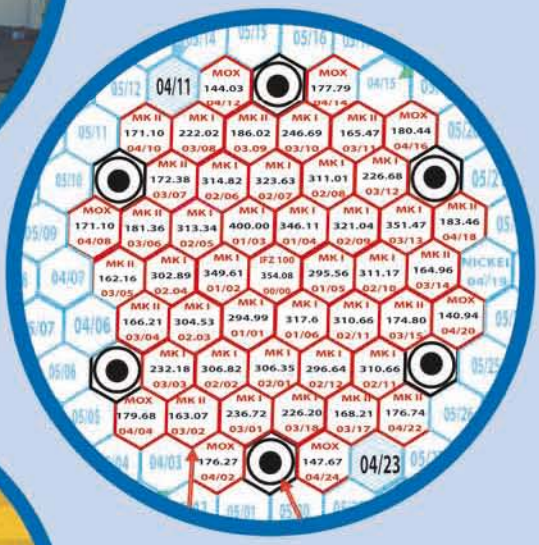

CHAPTER - I

Fast Breeder Test Reactor

I.1 Highlights of 17th and 18th Irradiation Campaigns

During 17th irradiation campaign, which started in December 2010, reactor underwent SCRAM on delayed neutron detector west signals on February 3, 2011. The delayed neutron detector counts in all the three channels crossed the SCRAM threshold of double the background value of 420 cps and contrast ratio between the west and east signals was found to be more than five. The clad rupture detection (CRD) monitors in cover gas showed large increase in activity, confirming the clad failure to be genuine. This is the first ever clad failure in the history of FBTR and the challenge of identifying the failed fuel was met successfully. Failed fuel localization set up was valved in to find out the age of the failed fuel subassembly. Based on the $^{85}Kr/^{88}Kr$ ratio, the failed subassembly was assessed to be a highly burnt subassembly (>100 GWd/t). Sodium sample was taken to assess the leaching of fuel and solid fission products (especially ^{131}I) in sodium and leaching was found to be negligible. After getting clearance from safety authorities, reactor was restarted and operated at 2.25 MWt to identify the failed subassembly. From the various tests including neutron flux tilting experiment, the subassembly at position 03/06 was identified to be the failed one. Only two reactor start ups with one fuel handling operation in between were required to successfully identify the failed subassembly. Later on, it was discharged and stored in the sealed container in the storage location outside the reactor.

The 18th irradiation campaign with a core of forty fuel subassemblies (27 MK-1, 13 MK-II & 8 MOX fuel) (Figure 1) was started on July 17, 2011. The initial part of the campaign was meant for collecting core temperature data for reconciling the outlet temperature anomalies observed at two locations (00/00 and 01/04). Both the locations have high burn-up subassembly. Based on the core temperature data, it was concluded that subassemblies are adequately cooled and one of the reasons for the temperature anomaly is flow area reduction due to clad swelling relative to wrapper with the increase in burn-up. Even though adequate margin exists between operating and allowable LHR value, it was decided to increase the core flow equivalent to flow reduction caused by reduction in flow area. Reactor operation was resumed in August 2011, after obtaining safety clearance for high power operation, power was raised

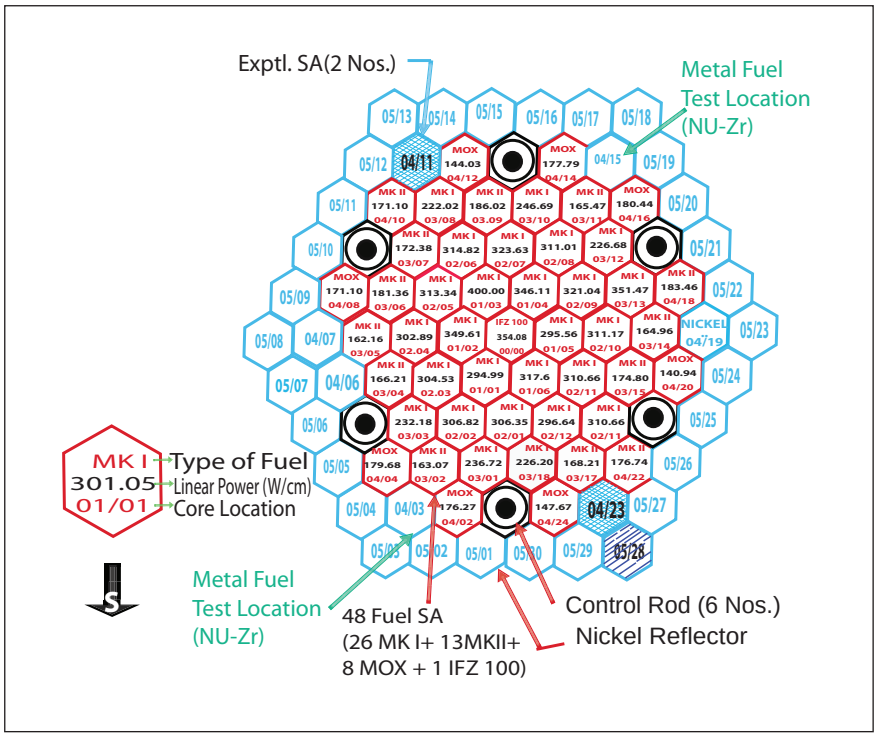

Fig. 1 Core configuration and LHR for the 18th irradiation campaign

Table 1: Reactor parameters during 17th &18th irradiation campaigns

Irradiation campaign	17th	18th
Reactor power MWt)	20	20.3
Turbine-generator power (MWe)	4.0	4.2
Reactor inlet temperature (K)	663	663
Reactor outlet temperature (K)	753	751
Central SA outlet temperature (K)	805	803
Duration of high power operation(hr)	577	840
Steam temperature (K)	733	723
Cumulative thermal energy developed (GWh)	10.99	15.55
Cumulative electrical energy developed (MU)	1.387	2.279

to 20.3 MWt in November 2011 with turbine-generator connected to grid producing 4.2 MWe. This is the highest power reached so far (Table 1).

An important step in the history of FBTR was the commencement of irradiation of metallic fuels for the future metallic fuelled fast reactors. Two special subassemblies, each containing three sodium bonded metallic fuel test pins (natural uranium + 6% Zr alloy) were loaded in the 4th ring in the reactor. Yttria capsule was loaded in a special subassembly (IFZ100) at core centre for production of strontium (^{89}Sr). During this campaign, high temperature fission chamber for PFBR was installed in experimental canal # 1 and tested up to a maximum power of 10 MWt. The test was repeated at an isothermal temperature of 673 K and up to a reactor power of 400 kWt. The detector was found to be responding as expected in both Pulse and Campbell modes on both the occasions and the detector output readings were found to be linear with power. Kalman filter based instrument meant for drop time measurement of DSRDM for PFBR was tested at low power. Steam generator safety valves were tested with live steam as a part of surveillance checking.

Major shut down activities carried out are installation of seismically qualified stands for station batteries, biennial surveillance of internal inspection of reactor vessel with reactor vessel in partially drained condition and reactor containment building leak test in “as- is- where -is” condition.

I.2 Life Extension Activities in FBTR

FBTR has completed twenty six years of successful operation this year. Based on the maintenance difficulties due to obsolescence of spares, several major components have been replaced for improvement in performance and life extension of FBTR. Some of the major activities carried out recently are discussed below.

Replacement of battery stands with seismically qualified stands

The control power supply system in FBTR consists of 24 , 48, 220 V DC and 220 V AC UPS systems. The battery banks, consisting of Plante type lead acid batteries, of all these systems are located in the battery room in the first floor of service building. The 24 V DC system is provided with 3x150 Ah battery banks each having 12 cells. The 48 V DC system has 2x645 Ah banks each consisting of 23 cells. The 220 V DC system has 2x100 Ah banks each consisting of 108 cells. The UPS system has two banks each of 645 Ah capacity and consisting of 110 cells.

These batteries were placed on free standing wooden stands. Replacement of all the wooden battery stands by seismically qualified mild steel stands was undertaken as a part of seismic retrofitting. In order to optimise the use of available space in the battery room, battery banks of 24 and 220 V DC were provided with single row double tier (SRDT) stands and UPS while 48 V DC battery banks were provided with single row single tier (SRST) stands.

In order to minimise the holes to be drilled in the floor for fixing the stands, ladder like channels (fabricated in-house) were anchored to the beams at equal intervals and at a few additional locations on the floor by using suitable Hilti bolts as recommended by Civil Engineering Group. The battery stands were assembled and bolted to the base structure. The cells are held in position by rubber beadings pasted on the inner-sides of the stand and spacers provided between adjacent cells.

The batteries in seismically qualified stand will be immune to any vibration or seismic activity and there will not be any acid spillage from the cells or damage to the cells.

Replacement of LT air circuit breakers

The LT switch gear in FBTR consists of emergency buses with diesel generator back up and non emergency buses. In all these switch gears there are altogether sixteen air circuit breakers (ACBs) of 2000 A capacity.

Maintenance of these breakers had become difficult due to obsolescence and non-availability of spares. Hence, all these breakers were replaced with state-of-the-art breakers of identical capacity as a part of life extension of FBTR.

Five breakers were replaced in 2001 with L&T make ACBs which could fit into the existing cradle in order to reduce down time. Replacement of all other breakers with the new model was taken up based on the performance of these breakers.

The breakers with additional features like anti pumping, trip free features and wiring changes to suit retrofitting. One breaker was tested at the manufacturer's premises. This was installed (Figure 1) and put into service. After the first breaker installation, some of the features which were not provided in the newly supplied breaker like additional micro switch, locking mechanism for breaker in isolated position and under voltage release were incorporated for the remaining breakers as well as for the breaker already installed. All the routine tests were carried out on all the breakers at manufacturer's premises.

As bus section isolation was required for installing new breakers, important loads were provided with alternate power supply. Each breaker installation was completed in one day with minimum disturbance to the loads connected to the bus section. The breakers were tested in test position and all the interlocks were ensured to be functioning satisfactorily and then put in service. In the emergency buses, load test was also carried out after the replacement to ensure proper functioning of the bus transfer logic. The panel doors to suit the front fascia of the new breakers were provided.

Upgradation of real time computer system

The central data processing system plays a critical role in protecting the reactor against events like plugging of fuel subassemblies, power excursions, etc. Central data processing system monitors many important signals like core thermocouples, control rod positions, steam generator leak detection signals, etc and initiates several direct safety actions. The central data processing system also monitors the various conditions required for reactor start-up, fuel-handling etc.

The functions of central data processing system were segregated, as per AERB D-25 safety guide, into safety-critical, safety-related and non-safety systems with independent computer systems. Development of hardware including the CPU cards and I/O cards, collectively known as ED-20 system, was done. The architecture was carefully chosen so that dedicated, real-time ED-20 based embedded systems carry out acquisition of all signals and implementation of various functions ensuring a very high reliability, by dedicated industrial computer based server computers. While replacing the systems, all analog signals, (around 600) were isolated with individual signal isolators. In 2004, Unipower-30 based SS-II system was replaced with three ED-20 based systems. The performance of the SS-II safety-critical, safety-related and non-safety systems during the 15th campaign was excellent. Based on the performance of the ED-20 based SS-II systems, the PDP11/84 based SS-I has now been replaced with three independent computer systems (Figure 2).

Many improvements were carried out in the new systems. New instrument panels were used so that hardware components like isolation amplifiers, CPU bin, signal interface modules etc, could be placed ergonomically facilitating optimal

Fig. 1 *New ACB*

cooling and easy maintenance. The older relay output cards, which were operating on ±12 V power supply drawn through the VME bus were replaced with modified cards operating on external, standard 24 V power supply. This eliminated the need for separate power supply for these cards and reduced the load on the VME bus.

In order to improve the accuracy and stability of measurements, isolation amplifiers with improved protective features and lower power consumption were developed with close interaction with industry. Most of the internal wiring and installation of components were carried out off-site in order to expedite in-situ works with minimum disturbance at site.

Integrity of all input and output signal wiring was validated by in-house developed test software, which expedited commissioning. An independent check on wiring and termination was carried out as part of hardware quality assurance.

Fig. 2 *ED-20 based sub-system I of central data processing system*

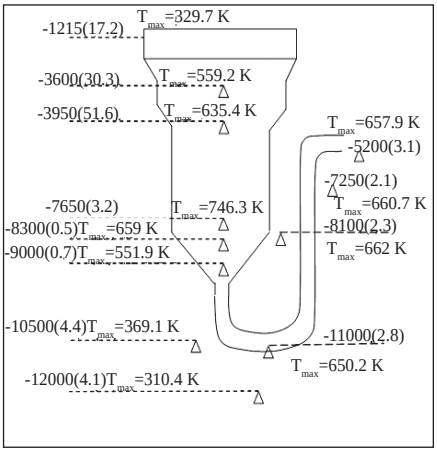

Fig. 3 Temperature distribution in reactor vessel at 18 MWt power

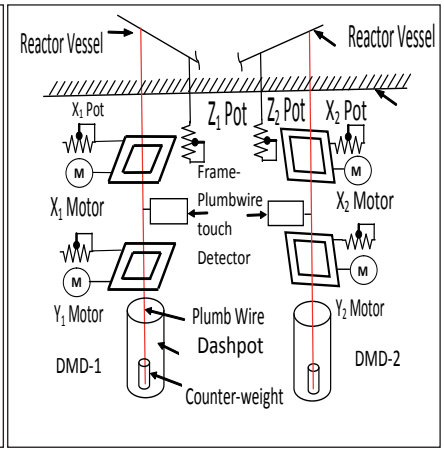

Fig. 4 Displacement measuring device assembly at the bottom of the reactor vessel

Since the software developed for SS-II based systems were well proven and had undergone rigorous quality control including independent Verification and Validation (V&V), review by committee constituted by SARCOP and independent functional testing, the software for the new systems, with modifications arising out of new hardware was re-used. All modifications were subjected to independent V&V. Several features have been incorporated to ensure reliable operation of the computer system.

Each ED-20 based embedded system is connected to an operator console and will respond to relevant commands only. Confirmation of commands is required to prevent inadvertent operations. A comprehensive configuration management policy has been evolved to oversee software modifications that may arise in future.

Various functions implemented in the new SS-I have been completely checked in the field independently. The automatic switch-over from SS-I to SS-II when SS-I fails was simulated and found to be smooth and seamless. Hence, both the sub-systems of central data processing system are now available for the plant to ensure smooth and safe operation of FBTR.

Replacement of existing PLC based controller with embedded system based controller for measuring displacement of reactor vessel of FBTR

The reactor vessel houses all the subassemblies and the control rod outer sheath supported on a grid-plate which inturn is welded to the reactor vessel. The control rods are gripped by the drive mechanisms. The non-uniform azimuthal temperature difference at different elevations of the reactor vessel when the reactor is in power causes the reactor vessel to tilt, disturbing the alignment between the control rods and their outer sheaths. Figure 3 shows the temperature distribution in reactor vessel at a reactor power of 18 MWt.

Displacement measuring device assemblies (Figure 4) have been provided at two locations viz 45º and 315º, measured with respect to sodium inlet pipe axis. Position of the reactor vessel is represented by a plumb-wire suspended from the reactor vessel at the grid-plate level. A rectangular metallic frame is moved along the axis by an AC synchronous motor until it touches the plumb wire. The frame is connected to a potentiometer slider, whose body is fixed to a mechanically rigid platform. The distance traveled by the frame to establish contact with the plumb wire, with respect to the initial position, is a measure of the displacement of the reactor vessel in that axis. Expansion in X_2 and Y_2 direction may also change in temperature of the reactor vessel at the grid-plate level and are to be measured and discounted from the net displacement in those axes, since as such they do not affect control rod movement.

The existing PLC-controller had failed and could not be rectified for want of spares. A new embedded-system based controller has been developed, installed and commissioned at FBTR. With this, position of the plumb-wire of each displacement measuring device mechanism is detected and the final displacement for each axis is displayed and the tilt of the reactor vessel can be deduced during power campaigns.

VME bus based embedded hardware was chosen for designing the displacement measuring device controller which acquires the potentiometric signals, frame and plumb-wire touch signals and the temperature of the grid-plate. The displacement measuring device controller controls the rotation of the frame motors. A simple dumb-terminal is used to display the acquired readings as well as the final displacement. Compensation for temperature changes in X_2 and Y_2 directions is provided in the embedded system. The controller can be run in auto and manual modes. In auto mode, the complete measurement is automated. The manual mode helps in maintenance.

I.3 Successful Identification of Failed Fuel Subassembly in FBTR

During 17th irradiation campaign, on February 3, 2011 at 05.05 hours, when reactor was operating at 18 MWt, reactor underwent SCRAM on delayed neutron detector west signals. All three delayed neutron detector channels of west loop crossed the SCRAM threshold of double the background value of 420 cps (Figure 1a and 1b). There was also increase in east delayed neutron detector signal up to alarm threshold. The increase in cover gas reject circuit activity monitors was of the order of around 250 times the background value (Figure 2). Reactor cover gas sample also showed large increase in fusion product nobel gases concentrations.

Particulate activity monitors at 0 & -2.81 m level in reactor containment building crossed the alarm threshold. Gross βγ activity in reactor containment building had gone up to 16460 Bq/m³ (background 268 Bq/m³). Exhaust activity monitors increased to 3000 from 230 cps. Exhaust gas sample showed traces of radioisotopes of krypton and xenon along with ^{41}Ar. Gamma spectral analysis of sample showed the presence of short lived daughter product of fusion product nobel gases, ^{88}Rb and ^{138}Cs. Spectral analysis of spot gas sample collected from reactor containment building showed presence of radioisotopes of xenon, krypton and ^{41}Ar. General background in reactor containment building was only 0.5 mR/h. Area gamma monitors located at reactor containment building showed an increase of around 0.15 mR/h.

The contrast ratio (west delayed neutron detector signal/east delayed neutron detector signal) during the reactor SCRAM was observed to be more than 4.5 and the probable position of failed fuel subassembly was inferred to be in the 3rd or 2nd ring of west side.

Hence it was inferred that any one of the highly burnt subassemblies located in the west side of 3rd ring locations could have failed as there is no subassembly with burn-up above 100 GWd/t present in the second ring. For the subassemblies in 03/01 located in north – south axis of 3rd ring, the expected contrast ratio is similar to the central subassemblies (around one) and hence it was less likely to have failed than the remaining high burnt subassemblies.

After confirming that the iodine activity in sodium is less than 0.2 µCi/gm, reactor was restarted at a sodium temperature of 523 K and power was raised in steps up to 2.25 MWt (10% of target power) by closely monitoring the delayed neutron detector count rates in clad rupture detection circuit and in argon monitor signals. SCRAM on delayed neutron detector counts was inhibited during the experiment. After measuring the DND counts accurately, the contrast ratio was observed to be 4.3.

During the reactor operation with failed fuel subassemblies in the core, the counts in east and west DND per MWt had gone up to 8.4 and 20.5 cps, respectively from the background counts 5.8 and 9.5 cps (Figure 3). This contrast ratio pointed out suspicion more

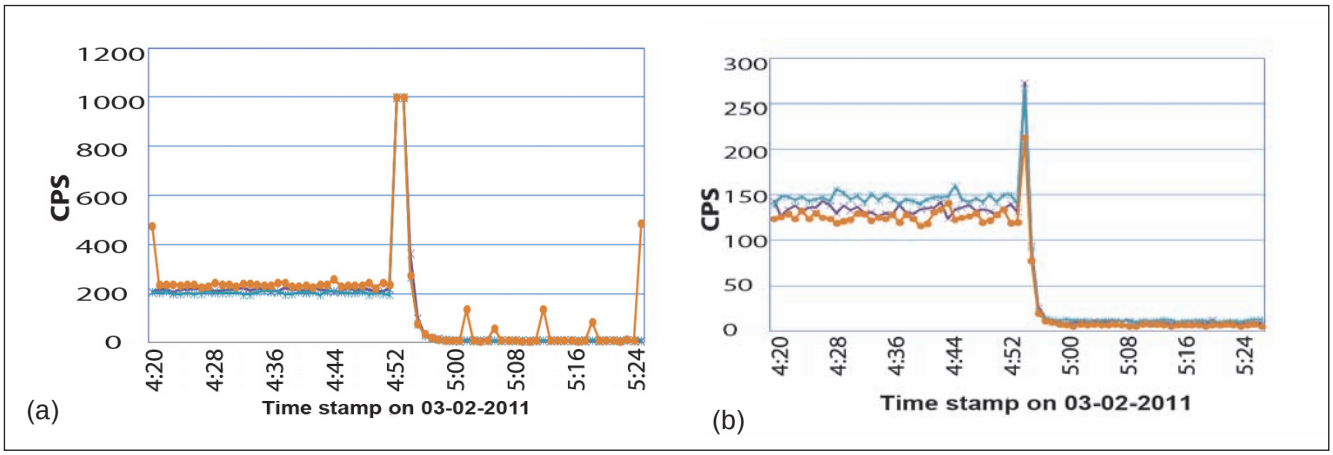

Fig. 1 *(a) West and (b) East delayed neutron detector signals during the incident*

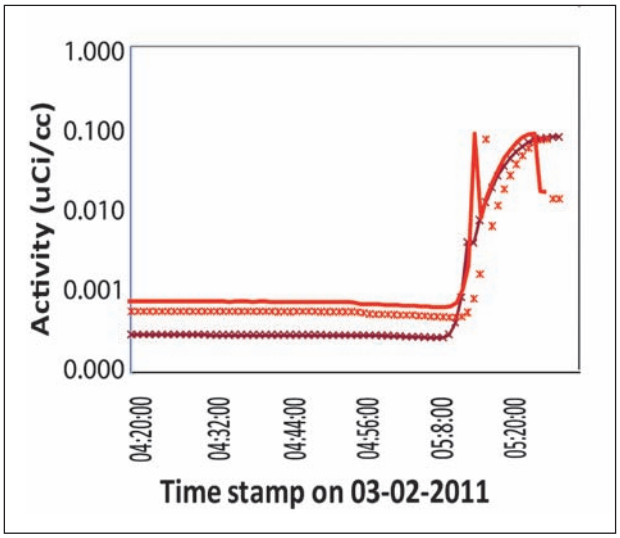

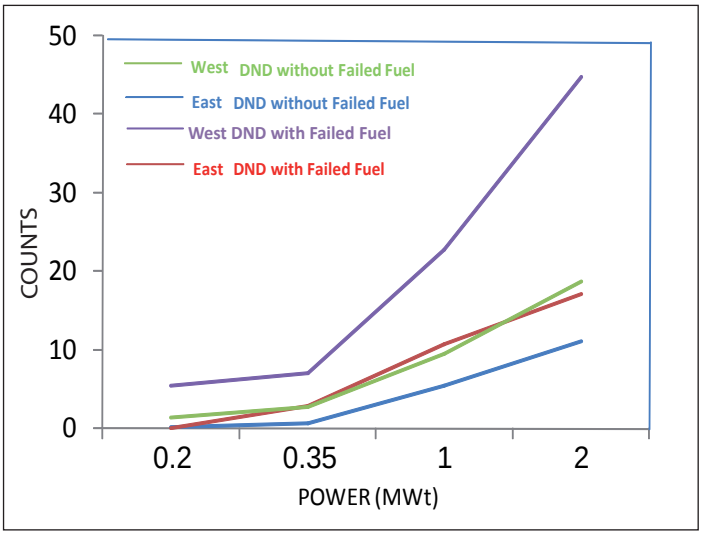

Fig. 2 *Increase in covergas activity during the incident*

Fig. 3 *DND counts as a function of power*

on subassembly at 03/06 location as the earlier experiments with displacement measuring device experimental subassemblies at locations along east-west central line had shown high contrast ratios. The location 03/06, though not on the east-west line, is next to the locations 03/05 and 02/04 locations on the central east-west line. No increase in fission product activity in cover gas was observed during the reactor operation at 2 MWt. This could be due to the fact that all the fission gases accumulated in the fuel pin would have got released after the clad rupture incident and short duration of operation at 2 MWt for the experiment. In order to cross check the region of failed fuel subassembly, neutron flux tilting experiment was carried out with reactor operating at 2 MWt. For this, control rods B and C (near to the suspected subassemblies) were operated between 25 and 405 mm from the bank critical height maintaining the reactor power constant by adjusting the other control rods. The increased total counts observed with control rod C at the top indicated the failed fuel subassemblies as the one in core position 03/06. There was no change in the counts when control rod B or D at the top position which ruled out the possibility of subassemblies in positions 03/03 and 03/08 as the failed ones.

Fuel handling operations were carried out to change the core configuration and to confirm the failed fuel subassemblies as indicated below:

• MKI subassemblies from 03/06 were transferred to storage location as this was the main suspect.

• Fuel subassemblies between core positions 03/03 and 03/16 were swapped.

• The location 03/06 was filled by shifting fuel subassemblies from 4th ring which in turn was filled by a reflector subassemblies.

With suspected subassemblies in the storage location, reactor was started and operated at 2 MWt. No increase in Displacement measuring device signal was noticed. For further confirmation, reactor power was raised up to 10 MWt and operated for two hours. Before raising the reactor power, the thresholds for delayed neutron detectors SCRAM was set corresponding to 10 MWt and inhibition on delayed neutron detectors SCRAM was lifted. There was no increase in DND counts and fission product activity in cover gas above the normal background. Gamma and air activity level in reactor containment building was found to be equal to background. Stack activity monitors also indicated the activity levels corresponding to the 10 MWt reactor power and fission products were not detected. This confirmed the failed subassembly was located in 03/06 location in core. The failed subassembly in the core was identified to be a highly burnt subassembly having a burn-up of 148 GWd/t.

Primary sodium sample had less than below detectable limits of ^{131}I activity and Pu content.

The total stack activity release was much less than the permitted value. The failed subassembly was identified and reactor operation could be resumed in a very short time. Later on the subassembly was discharged and stored in the storage location outside the reactor in a sealed container.

I.4 Calibration of FBTR Secondary Flow Meter Using Noise Analysis Technique

In Fast Breeder Reactors, permanent magnet flow meters (PMFM) are used extensively to measure the liquid sodium flow rate. The performance of these flow meters may degrade with respect to time due to aging process. This degradation can result in change in sensitivity. Hence, it is desirable to calibrate the permanent magnet flow meters at periodic time intervals. However, it is very difficult to remove the permanent magnet flow meters from the sodium circuits and calibrate it under actual flow conditions in sodium. Noise analysis technique, using cross correlation analysis, for in-situ calibration of permanent magnet flow meters was developed and FBTR secondary flow meter has been calibrated.

Cross correlation is a signal processing technique that measures the degree of the similarity between two waveforms. In the case of permanent magnet flow meters, the time delay between the upstream and downstream electrode output, say x(t) and y(t) respectively, is calculated using the cross correlation technique.

$$Rxy(\tau) = \frac{1}{T}\int_{0}^{T} x(t)y(t+\tau)dt$$

where T is the integration time and Rxy(τ) is obtained by shifting the y(t) along the time axis and calculating the integral of the product of x(t) and y(t) at each position.

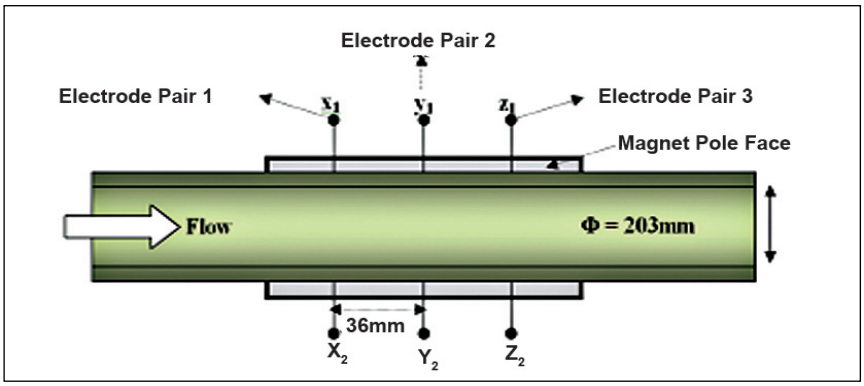

Fig. 1 *Permanent magnet flow meter configuration*

FBTR secondary sodium loop flow meters are provided with three pairs of electrodes as shown in Figure 1. The axial distance between electrode pairs is 36 mm. The voltage fluctuations from the two pairs of electrodes of the permanent magnet flow meters are acquired for estimating the cross correlation function. The sodium flow through the flow meter is changed from 85 to 180 m^3/h during the experiment. The mean value (DC) of the voltage output was removed by filtering the signal using a band pass filter. Cross correlation analysis is done using LabVIEW software and the normalized cross correlation function is obtained from the average of ten measurements. The time delay and the distance between electrodes are taken as the inputs for determining the velocity of the sodium, which is used for the calculation of sodium flow through the pipe. Figure 2 shows a typical time signal recorded from the permanent magnet flow meters and Figure 3 shows the cross-correlation plot. Two permanent magnet flow meters in fast breeder test reactor (secondary) was calibrated using the noise analysis technique and the calibration curve for DNa 600 is shown in Figure 4. The deviation of the flow rate estimated using cross correlation technique is found to be within ±5%. Cross correlation technique is found to be promising for in-situ calibration of permanent magnet flow meters in FBRs.

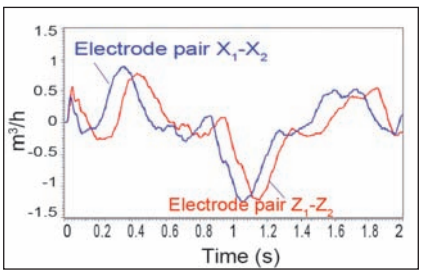

Fig. 2 *Time signal from permanent magnet flow meters*

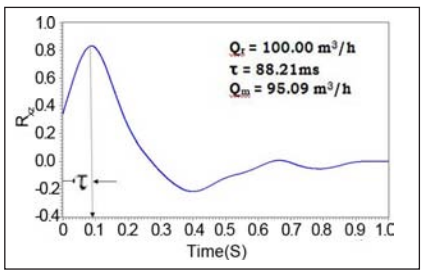

Fig. 3 *Cross correlation plot*

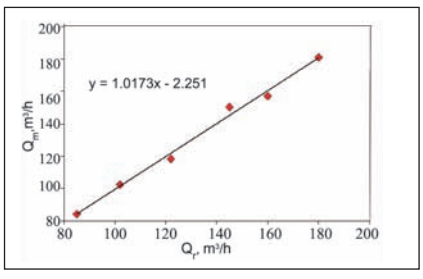

Fig. 4 *Calibration plot of DNa 600*

I.5 Metrological Inspection and NDE of PFBR MOX Experimental Fuel Subassembly Irradiated in FBTR

Postirradiation examination (PIE) of the PFBR MOX experimental fuel subassembly irradiated in FBTR has been taken up. The 37 pin MOX test fuel subassembly has undergone a peak burn-up of 112 GWd/t, the D9 clad and wrapper material has attained a maximum displacement damage of 60 dpa. The performance assessment of MOX, the D9 clad and wrapper material will provide valuable feedback to the designers. Here the results of dimensional measurements of the fuel subassembly and various non-destructive examinations (NDE) carried out so far on the fuel pins are presented in brief.

Dimensional measurements were aimed at determining the extent of deformations of the fuel subassembly including the head-to-foot misalignment and increase in the width-across-flats and corner-to-corner distance. A head-to-foot misalignment of 1.8 mm was noticed in the subassembly. The increase in width-across-flats in the hexagonal sheath was found to be varying along the length of the fuel subassembly and was peaking in the centre region at 0.4 mm as compared to the dimension at the ends of the fuel subassembly. Maximum increase in the corner-to-corner distance was found to be 0.31 mm. Figure 1 shows the variation in the width-across-flat in the hexagonal sheath as measured in three different orientations. The length of fuel subassembly was found to be 1661.9 mm indicating no significant increase. After dismantling the fuel subassembly by laser and retrieval of the fuel pin bundle from the wrapper, fuel pin numbers were identified and ten fuel pins were selected for detailed examinations. Length of the pins measured using an LVDT based measurement bench indicated increase in length varying from 0.07 to 0.59 mm. A new remotely operated fuel pin profilometer that can handle both 5.31 and 6.6 mm diameter pins was used for acquiring the diameter at various locations. A typical plot of variation in diameter along the length of

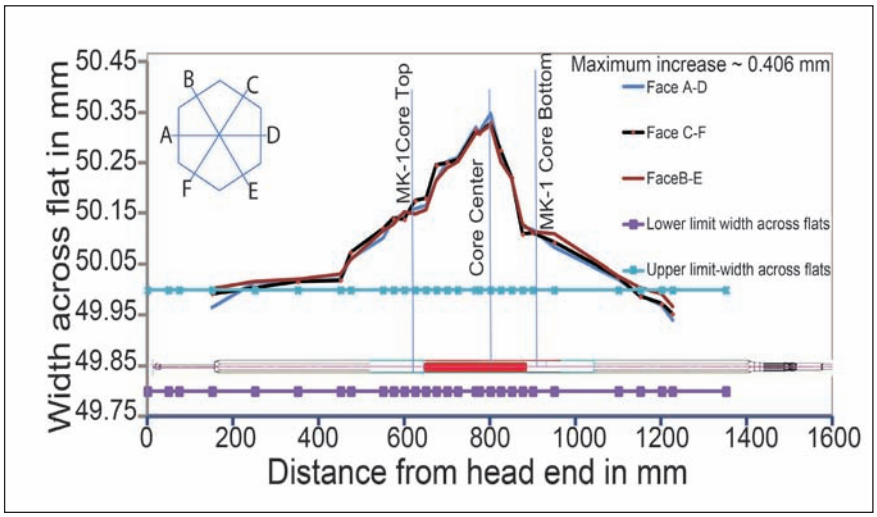

Fig. 1 *Variation of width-across-flats along the length of FSA*

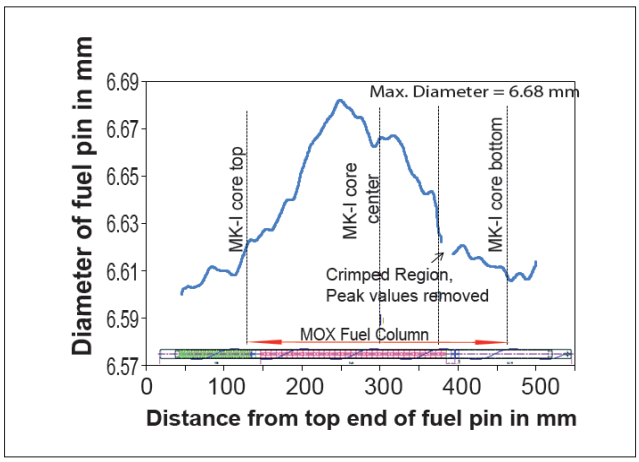

Fig. 2 *Typical variation of diameter along the length of a fuel pin*

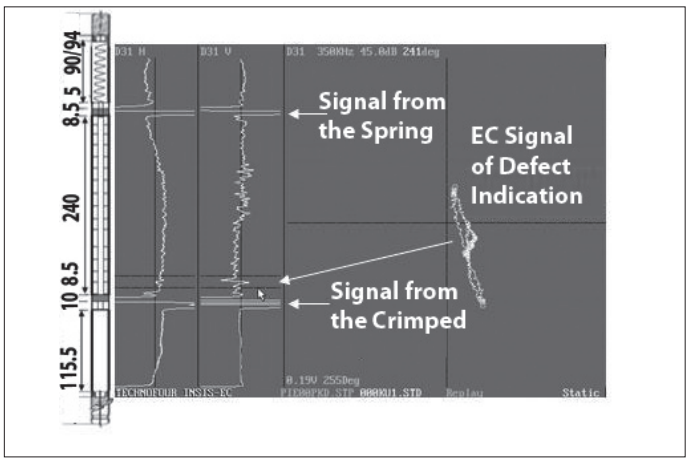

Fig. 3 *Eddy current signals from a typical fuel pin and that of an indication near the crimped region*

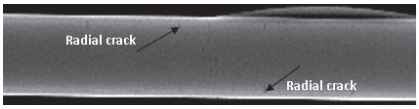

Fig. 4 Digitised radiographic image of the spring side fuel column of the MOX fuel pin

Fig. 5 Neutron radiographic image showing portion of (a) Unirradiated and (b) Irradiated MOX fuel pin

Fig. 6 Neutron radiographic image indicating annular hole in the fuel column

an irradiated fuel pin is shown in Figure 2. Maximum increase in diameter observed among the selected pins was 0.09 mm.

Eddy current examination was performed on ten irradiated fuel pins using differential encircling probe operating at 350 kHz. The impedance plane and time domain eddy current signals of a typical fuel pin is shown in Figure 3. In all the fuel pins, high amplitude eddy current indications were observed from the crimped (middle plug) and spring support disc regions. A series of localised eddy current indications (amplitude > reference defect of 0.3 mm dia. hole) were observed between 150 and 225 mm of the fuel column, measured from the crimped region. When compared with the reference defect signal amplitude, these indications appear to be originating from the inner side of the fuel pin.

X-radiography of the fuel pins was carried out using a 420 kV industrial X-ray unit. Optimal voltages of 360 and 390 kV were employed to get the desired indications including stack length and annular hole. In some fuel pins, radial cracks were observed in the pellets. Pellet-to-clad gap, pellet-to-pellet gap etc. were also observed at a few locations. Figure 4 shows the digitized X-radiography image of the spring side fuel column of a fuel pin.

Neutron radiography was carried out using the KAMINI reactor. Indirect transfer technique using dysprosium foil and track etch technique using cellulose nitrate film were employed to obtain neutron radiography images of the irradiated fuel pins. The foils/films were kept in close contact with a five pin cassette to increase sharpness. Reactor power, exposure time and film processing parameters were optimized to obtain good results. The important features/information available from the neutron radiography images are integrity of fuel pellets, fuel stack length, pellet dimensions, central hole, pellet-pellet gap and shape changes of the pellets. Figures 5 and 6 show the neutron radiography images. There is no indication for the presence of chipped fuel particles or deposits in the plenum region. Inter pellet gaps are clearly visible in most of the fuel pins.

Axial gamma scanning was carried out on three fuel pins. Axial profile of fission products (Figure 7) clearly revealed migration and deposition of ^{137}Cs at the ends of fuel column/insulation pellet interface. Axial profile of ^{106}Ru indicates localised peaks in the bottom region of fuel column, which may be a consequence of migration and segregation of metallic fission product precipitates.

Metrological examinations carried out so far on the hex-can and fuel pins indicate moderate increase in dimensions of D9 clad and wrapper at 60 dpa. Swelling rate of MOX fuel is found to be very low as indicated by various complementary NDE techniques. Further destructive examination such as fission gas analysis, metallography and tensile testing of clad and wrapper specimen will give comprehensive data leading to an in-depth understanding of irradiation behaviour of PFBR MOX experimental fuel subassembly.

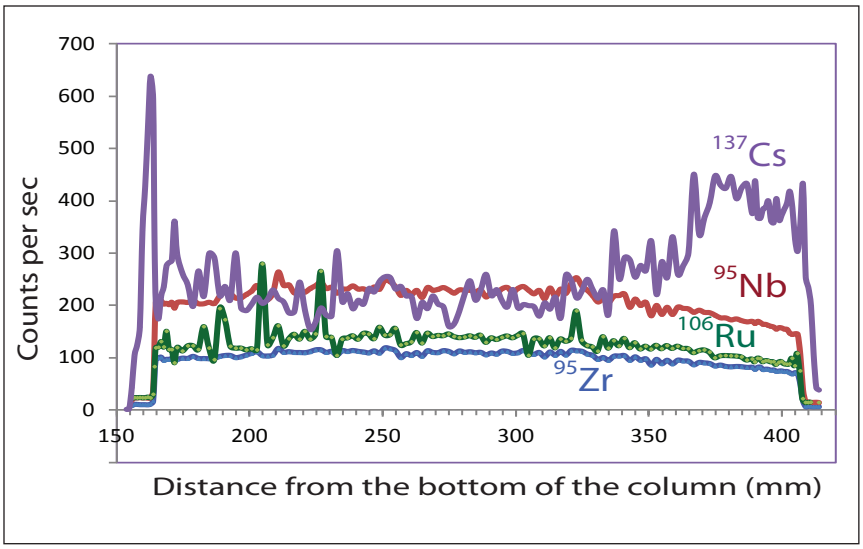

Fig. 7 Axial distribution of fission products in a typical fuel pin

I.6 Post-Irradiation Examinations of FBTR Nickel Reflector Subassembly

The nickel reflector sub assemblies used in FBTR have a fluence limit of 1.14×10^{23} n/cm^2. One nickel reflector subassembly was discharged from the FBTR core after reaching a fluence level of 1.09×10^{23} n/cm^2 and taken up for post irradiation examinations (PIE) in the hot cells of radio metallurgy laboratory. The examinations were intended to assess the extent of swelling of the nickel blocks. Excessive swelling in the axial and radial directions can lead to mechanical interaction between the nickel blocks and the wrapper.

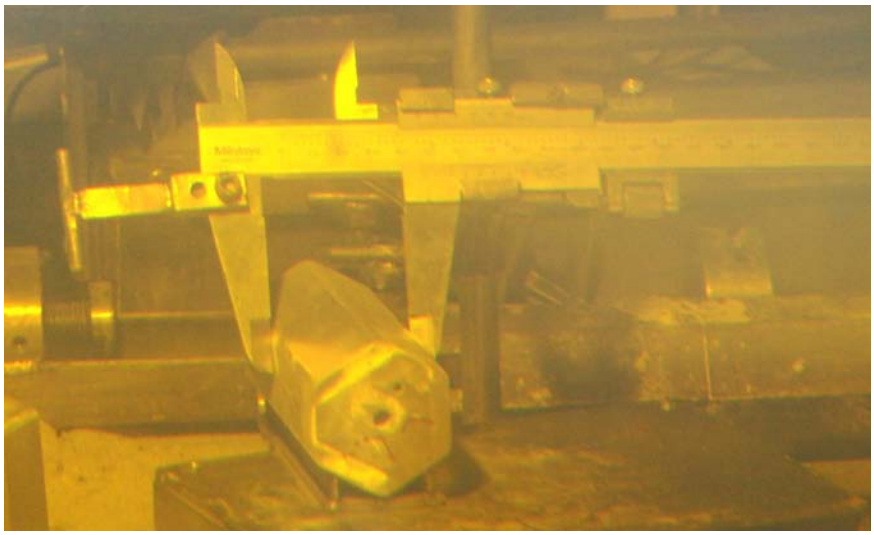

Fig. 1 *Dimensional measurement of the nickel blocks*

Non-destructive examinations such as neutron radiography and gamma autoradiography were carried out to examine the internals of the nickel subassembly and to assess the compression of the collapsible tube and the spacing between the hexagonal wrapper and the nickel blocks. Dimensional measurements were done on the hexagonal wrapper and the nickel blocks (Figure 1) after dismantling the subassembly using laser cutting torch and retrieving the nickel blocks from the wrapper. Volume and density measurements (Figure 2) were employed to estimate the irradiation induced swelling of the nickel blocks.

Neutron radiographic (NR) images (Figure 3) indicated that the collapsible tube had undergone compressive deformation due to axial expansion of the nickel blocks, which is of the order of 7 mm. This was confirmed by gamma autoradiography of the head portion of the subassembly. The collapsible tube is designed to accommodate maximum expansion of 18 mm in the axial direction. On dismantling, it was noticed that the interior annular space had minimal residual sodium making the retrieval of the nickel blocks less difficult, as compared to the extraction of B_4C pellets from the control rod.

Dimensional measurements on the nickel blocks revealed that the radial gap between the blocks and the hexagonal wrapper has reduced from 3 to 2 mm. Density measurements indicate that the maximum volumetric swelling is of the order 3.6%. This correlates well with the dimensional measurements.

Thus, the present PIE results indicate that adequate margins are available for accommodating radial and axial expansion of the nickel reflector subassemblies present in the FBTR core before life-limiting mechanical interaction between the nickel blocks and the wrapper begins.

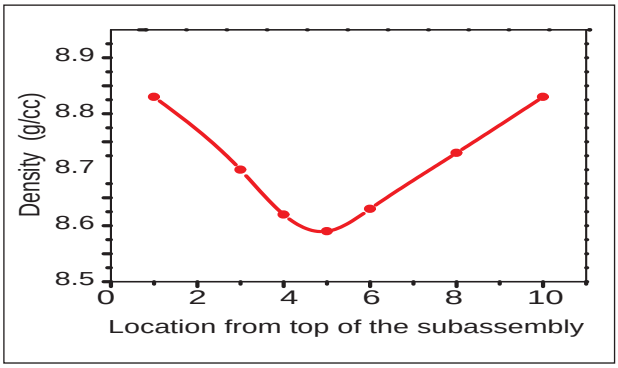

Fig. 2 *Density variation in the irradiated nickel blocks (Pre-irradiation density of nickel block – 8.9 g/cc)*

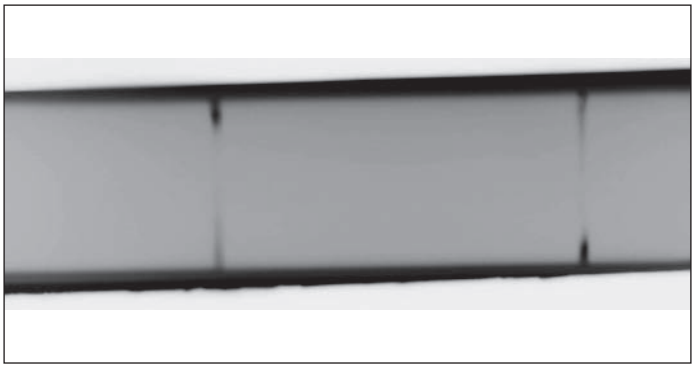

Fig. 3 *Neutron radiograph showing the nickel blocks inside the subassembly*

I.7 Fractographic Examination of Mechanically Tested Irradiated Clad Specimens

Some of the mixed carbide fuel pins of FBTR have achieved a maximum burn-up of 165 GWd/t. Correspondingly, the 20% cold worked austenitic stainless steel (316 SS) which is used as the clad and wrapper material in FBTR has undergone a peak displacement damage of 83 dpa. Fast neutron irradiation leads to degradation of mechanical properties in the core structural materials. Remote mechanical testing carried out on the clad specimens from FBTR fuel pins had indicated significant reduction in ductility and strength especially at high dpa levels. The degradation in mechanical properties is closely linked to the deformation and fracture behaviour associated with microstructural changes which are revealed by fractographic examination.

Examination of the fracture surface of the tensile tested clad specimens was taken up using scanning electron microscope for correlation of the mechanical properties with the fracture mode. Specimens for fracture surface examination were extracted from the broken portions of the tensile tested clad specimens of various displacement damage doses, using diamond wafer wheel cutting machine.

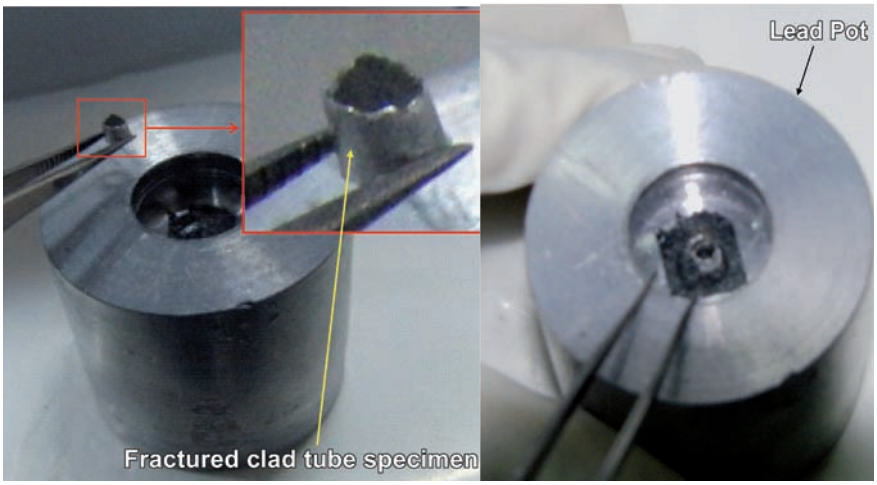

Fig. 1 *Fracture specimen inside the special lead pot*

Fracture surface samples for exaltation were extracted from tensile tested specimens of irradiated clad tubes corresponding to dpa levels of 13, 56 and 83. Yield strengths measured for these samples were 532, 543 and 465 MPa respectively while the corresponding residual ductilities were found to be 8, 3 and 3%

Fig. 2 *Specimen being loaded in the SEM*

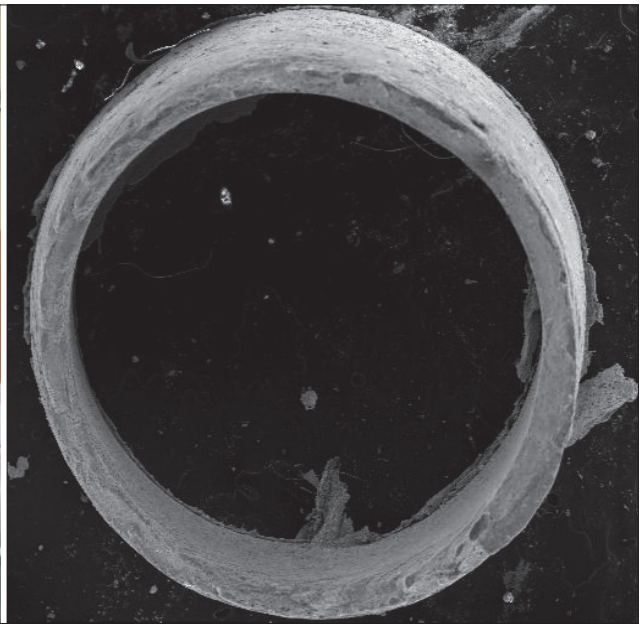

Fig. 3 *Low magnification SEM image of fracture specimen*

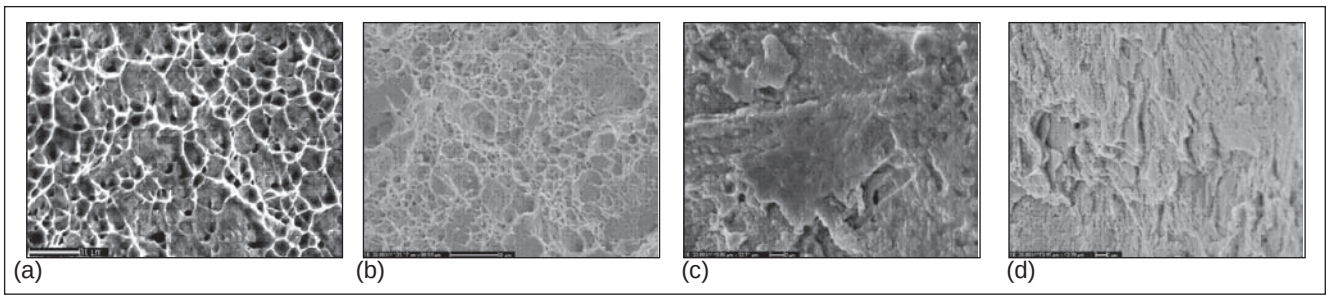

Fig. 4 *SEM images of the fracture specimens at different dpa levels (a) Unirradiated (b) 13 dpa (c) 56 dpa (d) 83 dpa*

respectively. The samples were transferred to a glove box and decontaminated to reduce the transferrable contamination after which the dose rate was measured to be of the order of 170 mR/h. The specimens were transferred from the glove box and sputter coated with gold. Specimens were then transferred to the SEM laboratory in a special lead pot (Figure 1), and loaded inside the specimen chamber (Figure 2) of the SEM.

Low magnification image of a typical fracture surface is shown in Figure 3. Examination of clad specimen exposed to 13 dpa (Figure 4b) showed features similar to that of un-irradiated cladding (Figure 4a). Fracture mode was found to be ductile with numerous dimples on the fracture surface.

Examination of 56 dpa specimen (Figure 4c) showed mixed mode of fracture with predominantly brittle fracture. Faceted surfaces typical of channel fracture reported in irradiated austenitic stainless steel were observed. In contrast, fractography of 83 dpa specimen (Figure 4d) showed completely brittle faceted surfaces. No indication of ductile fracture was found in the 83 dpa specimen.

The above observations correlate well with the measured tensile properties of the irradiated clad at different dpa levels.

I.8 A New Instrumented Irradiation Capsule to Achieve Constant Irradiation Temperature

A new version of instrumented irradiation capsule has been designed and developed for irradiation of structural material specimens in FBTR. This capsule is provided with thermocouples and heating coils to measure and control the temperature of specimens during irradiation. The irradiation capsule will enable raising the temperature of structural material specimens kept in it to the temperature above the reactor sodium temperature and maintain this temperature as constant during the period of irradiation, irrespective of reactor power level (full power to shutdown condition). An out-of-pile version of this instrumented capsule has been fabricated and tested in an electrical furnace successfully to validate the design concepts.

In this instrumented irradiation capsule, six numbers of twin core heating coils with diameter 1.6 mm are placed at the peripheral locations of the irradiation capsule at equal intervals, as shown in Figure 1. The overall diameter of the irradiation capsule is 18 mm. The heating coils are inserted into six small size tubes joined to the top portion of the irradiation capsule in a leak tight manner by laser welding. The specimens are kept at the central portion of the irradiation capsule surrounded by sodium. There is an annular gas-gap layer at the external boundary of the irradiation capsule in which mixture of helium and argon gas is filled up to provide a thermal barrier and thereby to raise the temperature of specimens above the ambient sodium temperature. Three thermocouples are attached to measure the temperatures at the top, centre and bottom regions of the sodium filled central portion to measure and control the temperature of the specimens through the use of heating coils.

During irradiation in FBTR, the temperature of the specimens rises by attenuation of neutrons and gamma rays in the specimens and surrounding materials. The specimen temperature varies during the period of irradiation due to change in the reactor power conditions (full power to shutdown state), and can be measured by the thermocouples provided in the irradiation capsule. If it is desired to have an isothermal temperature in the specimens, say

848 K, irrespective of the reactor power, it is possible to maintain this temperature by supplying required electrical power to the heating coils. The temperature of the specimens can be maintained within a small range (± 1 K) of the set temperature during the period of irradiation by varying the current through the heating coil. The heating coils and the output of the thermocouple indicating the temperature at the middle region of the irradiation capsule are connected to a temperature controller and thyristor. The temperature controller senses any decrease/ increase from the set temperature and the temperature is brought back to the target value by adjusting the current to the heating coils.

An experimental capsule was fabricated to carry out out-of-pile validation test in an electrical furnace.

Drilling of six deep 250/300 mm holes of 2 mm diameter on the periphery of the irradiation capsule of overall diameter 18 mm was found to be challenging. Since deep drilling facility of required size was not available, deep holes were drilled in three pieces each of about 85 mm length which were joined together to form a length of 250 mm in leak tight manner by GTAW / laser welding processes. The welding was carried out without affecting the drilled holes.

Capillary tubes closed and welded with tiny end plugs at one end were inserted into the deep holes and welded to the top portion of the capsule by laser welding.

Similarly, three capillary tubes with inner diameter of 1.2 mm and closed at one end were welded at the central region of the irradiation capsule to insert the thermocouples (to perform as thermowells). These thermowells were terminated at top, middle and bottom portions of the specimen region to measure the temperatures at the respective regions.

Specimens were kept in the central region of the capsule, sodium was filled around the specimens in a glove box for efficient heat transfer purpose, and the filling path was sealed.

Helium was filled in the annular space (radial width - 0.5 mm) at the periphery of the experimental capsule to act as a heat barrier and the helium filling passage was sealed.

The fabricated experimental capsule (Figure 2) was installed in a vertical furnace and heater coils were connected to a power source to supply controlled current to them. The thermocouples of the capsule were connected to a data acquisition system. The temperature of the furnace was raised to 473 K and the heating coils inserted in the capsule were energized. By increasing the current to the heater coils, a temperature of upto 888 K was achieved in the specimens kept in the central region of irradiation capsule while the furnace temperature was maintained at 473 K. It was also found that the specimen temperature was maintained at the set temperature within ±1 K consistently irrespective of the furnace temperature. This experiment clearly demonstrates that it is possible to attain a higher temperature in the specimens kept in an irradiation capsule and to maintain it at all states of reactor operation.

Further work such as shielding against radiation in the top portion of the capsule, method of routing of thermocouples and heating coils from reactor containment building to reactor core etc. will be carried out to develop the components required to adopt this instrumented capsule in FBTR.

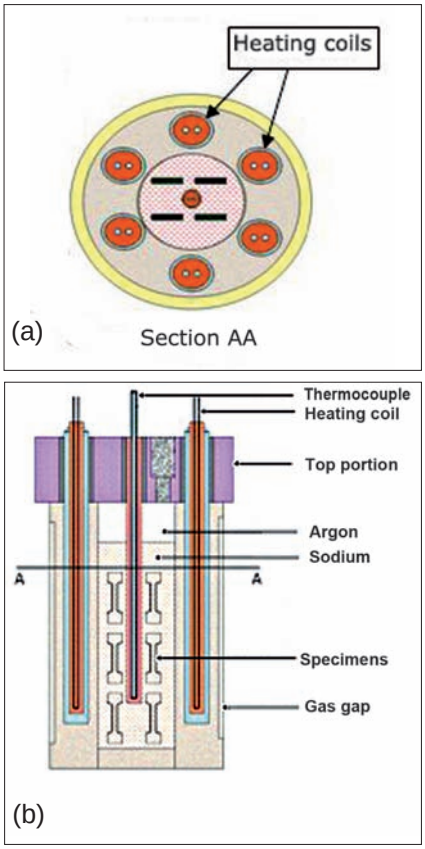

Fig. 1 *(a) Sectional and (b) Schematic view of instrumented irradiation capsule*

Fig. 2 *Fabricated capsule with attachment of thermocouples*

I.9 Fabrication of Sodium Bonded Metallic Test Fuel Pin with U-6Zr in T91 Clad Tube for Test Irradiation in FBTR

It is proposed to introduce metallic fuels in future fast reactors in India to achieve enhanced breeding necessary to meet the enhanced energy demands. Since, experience in fabrication and irradiation of metallic alloy fuel does not exist in the country, it is imperative to generate fabrication and irradiation experience before launching commercial FBRs with metallic alloy fuel. While development of metallic fuel slug of suitable composition has been initiated at BARC, development of technology for fabrication of sodium bonded fuel pins followed by irradiation has been taken up at IGCAR. The activities taken up are a) end plug (both bottom and top) welding and qualification, b) sodium wire extrusion and transfer into clad tube, c) loading and settling of fuel slug and blanket, d) establishing sodium bonding of fuel pin, e) pin qualification by non-destructive techniques.

For fabrication of the metallic fuel pins, a negative pressure argon atmosphere glove box train consisting of double and single module glove boxes along with automatic pressure control, independent gas recirculation and gas purification has been set up. This facility also contains common header lines with gas manifolds for argon, helium and argon-hydrogen gases and emergency evacuation system as shown in Figure 1. The facilities provided inside the glove boxes are shown as inserts. In addition, a stand-alone positive pressure argon atmosphere glove box with automatic pressure control, gas recirculation and gas purification systems has been set

Fig. 1 *Argon atmosphere negative pressure glove box train with various facilities*

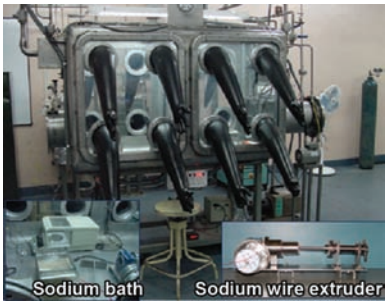

Fig. 2 *Sodium handling glove box with argon atmosphere*

up for sodium wire extrusion and transfer into clad tube is shown in Figure 2. The sodium extruder and sodium bath are shown as inserts.

Qualified U-6Zr fuel slugs and T91 clad tube received from BARC and NFC respectively were used for fabrication of fuel pin.

The following are the fabrication procedures followed for sodium bonded metallic test fuel pins in the facility.

1. Welding of bottom end cap to clad tube (both T91) by pulsed arc welding and qualification of the weld by HLT, X-radiography and metallography.

2. Sodium wire extrusion and transfer into the one end closed clad tube inside sodium handling box without mouth contamination.

3. Blanket/fuel slug loading into clad tube using levitation method to prevent mouth contamination.

4. Blanket/fuel slug settling inside clad tube by heating to 423 K in a furnace with facility to vibrate the clad tube containing the fuel slug.

5. Welding of fuel pin with internals, by pulsed TIG process, inside argon atmosphere glove box followed by qualification by HLT, X-radiography and metallography.

6. Establishing sodium bonding between fuel slug and clad by heating to 823 K in a furnace with vibrating facility for 60 min with fuel pin jump frequency of 10 mm.

7. Metrology of fuel pin followed by measurement of sodium level above fuel slug by X-radiography.

Six numbers of sodium bonded metallic fuel pins were fabricated and qualified. Figure 3 shows the internals of the fuel pins by X-radiography. Two irradiation capsules each containing three fuel pins were fabricated and incorporated in the form of special subassemblies and loaded in the fourth ring of FBTR for irradiation studies.

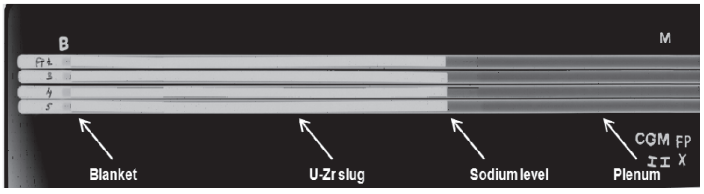

Fig. 3 *X-radiography of the sodium bonded metallic test fuel pins fabricated for FBTR test irradiation*

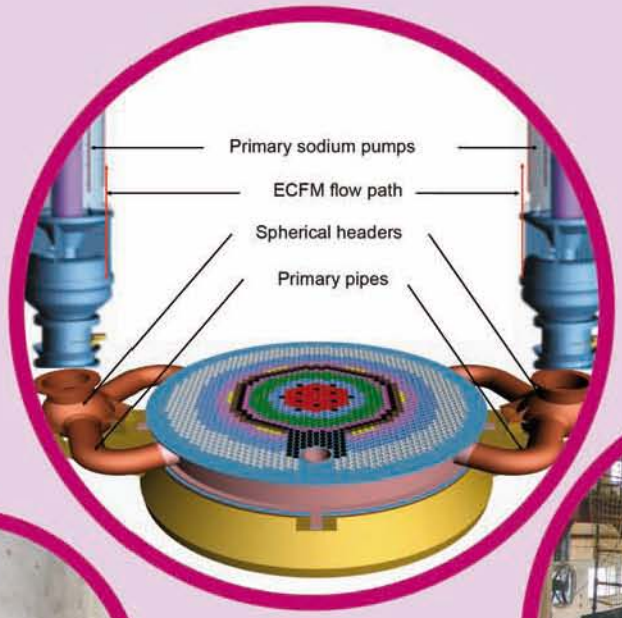

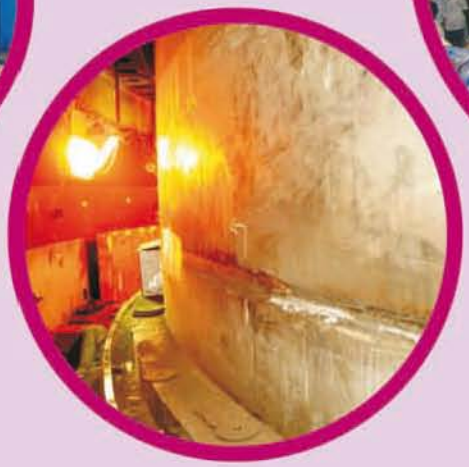

CHAPTER - II

Prototype Fast Breeder Reactor

II.1 Construction Status of Prototype Fast Breeder Reactor

The civil structural works for nuclear island connected building has been completed and the roof of reactor containment building has also been concreted. The construction of peripheral buildings surrounding nuclear island connected building, namely service water pump house, horton sphere, ventilation stack, diesel generator building and service building have been completed.

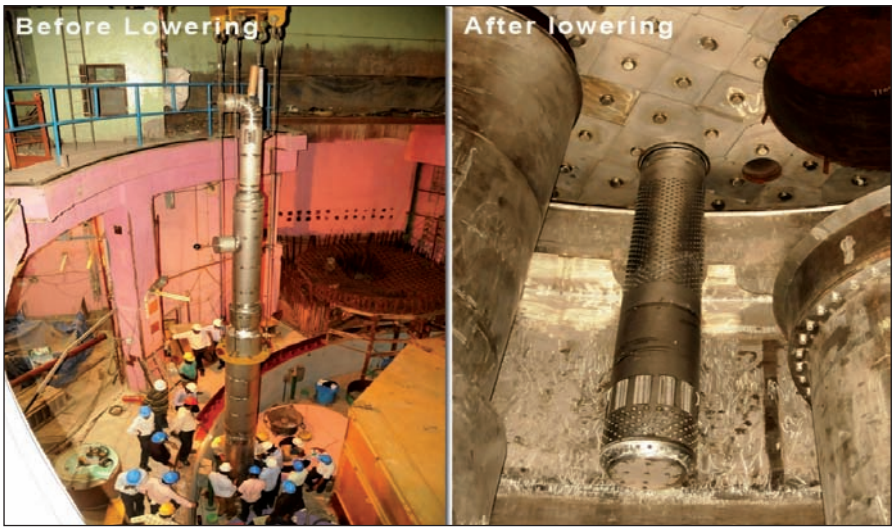

Fig. 1 *Erection of decay heat exchangers through roof slab penetration*

The erection of major large diameter critical reactor components like safety vessel, main vessel along with core catcher and core support structure, thermal baffle, grid plate integrated with primary pipe and inner vessel have been erected inside the reactor vault in the previous year. Subsequent to the erection of roof slab which forms as a top cover of the reactor vault, welding of the roof slab with reactor main vessel has been completed in this year which required extensive mock-up and qualification exercises to be taken up to avoid distortion during welding.

Erection of top mounted reactor equipments above roof slab commenced (Figure 1). Two decay heat exchangers Type B and one Hot pool level (Figure 2) detectors have been erected in the roof slab penetrations. Erection of outer B_4C subassemblies (Figure 3) on the Grid plate commenced and 14 numbers. have been completed till date.

Erection of long components commenced and entire 4 nos. of steam generator (Figure 4) required for one loop commissioning has been erected in steam generator building-1. Heavy duty crawler crane configuration has been changed to reach steam generator building-2 and 2 out of 4 steam generators have been erected till date.

Raw water reservoir has been commissioned and filling of water in reservoir has been completed. Further raw water has been transferred from reservoir to De-mineralized plant through pump house and one stream of de-mineralized plant (Figure 5) has been commissioned successfully. Pre-commissioning works for other auxiliary service system are under progress.

The electrical and instrumentation systems are in advance stage of commissioning. Commissioning of 230 kV gas insulated switch yard(Figure 6) has been completed. All the thirteen bays of switch yard and associated station transformer (ST), generator transformer (GT) and SCADA supervisory

Fig. 2 *Erection of hot pool level detector inside inner vessel*

Fig. 3 *Erection of outer B_4C subassemblies*

Fig. 4 *Four steam generators in steam generator building-1*

Fig. 5 *Commissioning of de-mineralized plant*

protection system had been fully commissioned through MAPS tie line. 230 kV double circuit line from BHAVINI switchyard to Sirucheri has been energized.

Class IV 6.6kV boards with associated Cable to Bus duct Transition Panel and 6.6 kV bus ducts were commissioned. Pre-commissioning works are under progress for energisation of class-III 6.6 kV boards. 220 V DC battery charging commenced and is in progress.

All main control room, back-up control room and handling control room panels have been erected in control building.

Turbine building has reached its final top elevation and roof concreting has been completed. Turbine building EOT crane erection has been completed and is in operation. Condenser erection commenced and the erection of condenser hot well bottom plate has been completed. Erection of various auxiliary equipments like heaters, tanks and debris-filter also has been completed. All pre-requisite works have been completed for erection of Stator.

Indian boiler regulation (IBR) clearance has been obtained for erection of pressure parts of auxiliary boiler and erection commenced.

In sea water pump house all columns have been raised up to roof level. Erection of large diameter buried piping has been completed and erection of auxiliary sea water pumps is in progress.

Manufacture of major components like Secondary sodium pumps, Steam generators, Intermediate Heat exchangers, Sodium to Sodium heat exchangers, Liquid honing machine, 280/85T EOT Crane for Reactor containment building, EOT cranes for Diesel generator Building and Fuel Building have been completed & delivered to site.

Pre-commissioning of various conventional system equipments like compressors and air receivers for compressed air generation system, air handling units and chillers for air conditioning and ventilation system are under progress.

Power and control cable laying works in nuclear island control building (Figure 7) is under progress. Conduit laying for tele-communication cables, plant annunciation cables, fire detection system in nuclear island connected building are nearing completion.

Fig. 6 *Commissioning of switchyard*

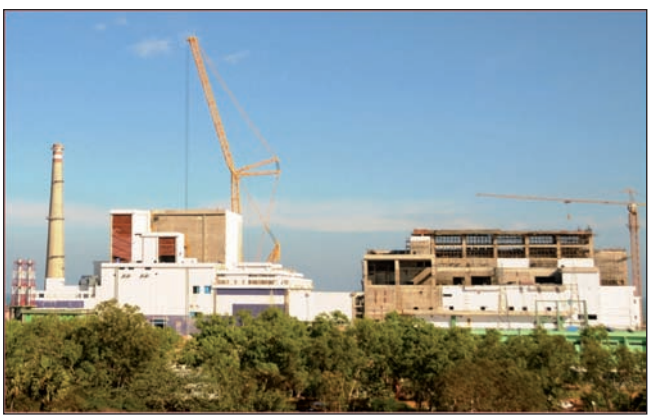

Fig. 7 *Overall view of nuclear island connected building*

II.2 Challenges and Achievements of Integration of Main Vessel and Roof Slab

Prototype Fast Breeder Reactor (PFBR) is in an advanced stage of construction. The major reactor assembly components such as safety vessel and main vessel along with core catcher, core support structure, grid plate, primary pipes, inner vessel and thermal baffles have been erected inside the reactor vault and the roof slab which is a part of top shield has been mounted over the vault.

Since the top shield supports all the components which enter the main vessel, the vertical distance between the support flanges in roof slab and the corresponding components within the main vessel, their relative locations and orientations are critical design requirements to be met. Stringent erection tolerances have been specified to ensure satisfactory functioning of various components, safe reactor operation, proper fuel handling, in-service inspection etc. and to prevent any mechanical interaction between the interfacing components during various operating conditions of the reactor. The in-situ circumferential weld joint between roof slab and main vessel is the most critical joint in achieving the required dimensions and tolerances which have far reaching implications in ensuring the safe and satisfactory operation of the reactor.

The following are the critical parameters that are to be monitored and achieved within the design limits after in-situ welding:

- Horizontality of grid plate
- Alignment of axes of large rotatable plug support flange in roof slab and grid plate
- Distance between large rotatable plug support flange in roof slab and top of grid plate
- Distance between top of thermal baffle and top of grid plate
- Alignment between ex-vessel transfer port (EVTP) and in-vessel transfer port (IVTP) through primary ramp & tilting mechanism
- Alignment of the stand pipes of intermedia heat exchanger in inner vessel and the corresponding openings in roof slab.

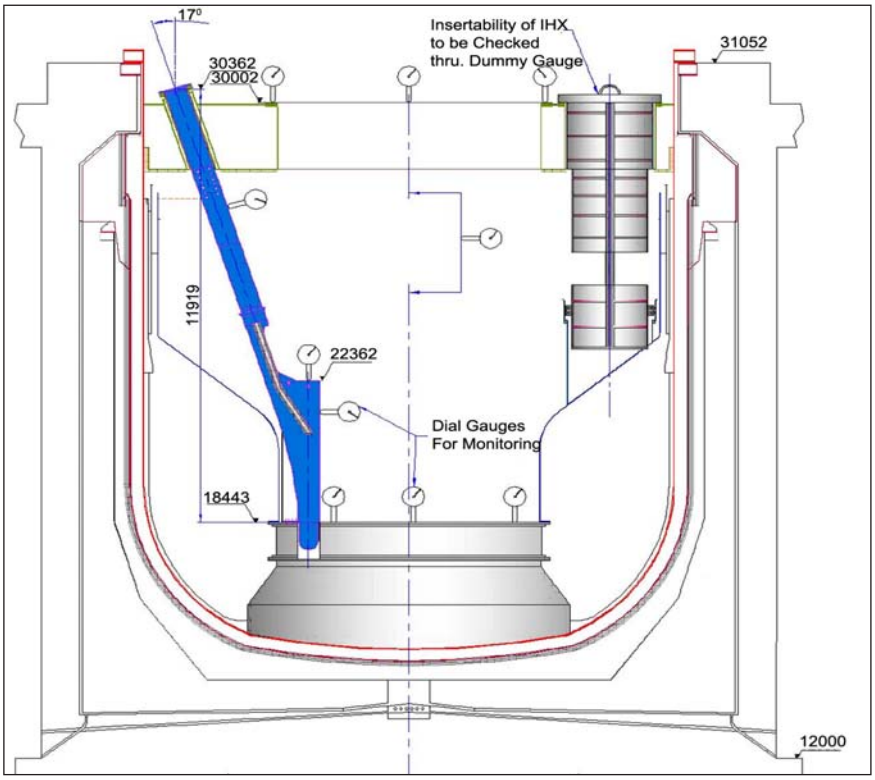

***Fig. 1** Schematic of main vessel and roof slab*

The radial mismatch at the weld region between the bottom end of roof slab and top end of main vessel (Figure 1) necessitated the development of novel toolings and methodologies for corrective actions.

Considering the importance of the joint, the implications of the process of integration of roof slab and main vessel on the safety and economic aspects, the challenges posed such as limited access, space constraints, heavy duty handling (~500 t) combined with precise requirements on positioning of main vessel along with its internals while making this long in-situ weld joint (over 40 m), a full scale mock-up of integration was planned and successfully completed within a short period to facilitate the availability of feedback, tooling, techniques and welders to be used while execution of the job at PFBR site.

Apart from this, mock-up activities were also carried out as part of

Fig. 2 *Roof slab to main vessel weld joint (a) Outside view (b) Inside view*

complete qualification of weld as per codal requirements and the procedures to be followed for distortion control and integration strategies, simulating all the space constraints.

Several rounds of extensive brain storming sessions involving designers, erection, quality assurance and industry teams were conducted to ensure seamless assessment and integration of activities and to resolve the day-to-day issues that arose during execution of the integration. Detailed systematic inspection and assessment at every stage of integration were carried out to closely monitor and control the evolution of all the critical dimensional relations and tolerances during the progress of welding activity. To ensure repeatability of inspections carried out, two independent inspection agencies were involved. The effect of the welding activities were assessed at the end of each day and based on this, appropriate sequence of welding to be followed on the next day was judiciously planned, documented and executed to meet all the specified requirements on completion of integration.

With all the sustained, dedicated efforts and co-ordination of design, construction, quality assurance and industry teams all through the entire course of integration of roof slab and main vessel right from the planning stage, the job was successfully completed meeting all the design, functional and safety objectives related to this critical and challenging in-situ weld joint (Figures 2a and 2b).

With this in-situ welding, all the major activities related to erection and integration of the large size permanent and static components of reactor assembly are successfully completed.

II.3 Testing and Evaluation of Thermal Design of PFBR Top Shield

In Prototype Fast Breeder Reactor (PFBR), top shield consisting of roof slab, large rotatable plug, small rotatable plug and control plug, receives heat from hot pool sodium and loses heat by (i) partial removal through internal cooling system (ii) heat removal by vault cooling system after complex heat exchange through main vessel, safety vessel, safety vessel insulation, reactor vault liner and (iii) heat loss from its top surface. There are conflicting requirements of temperature limits for materials such as steel, concrete, neutron detectors, cables etc. Maintaining the temperature and temperature difference across the top shield is important to limit the thermal bowing of the top shield in order to limit the slope at primary sodium pumps (PSP) and IHX locations. Thus, thermal design of the top shield is a complex process, which needs detailed theoretical and experimental investigations. Similarly, there are conflicting requirements of temperature limits to be maintained at different locations in control plug. The temperature distribution estimated by numerical analyses needs to be validated through detailed experiments.

Towards this, an experimental facility (Figure 1) has been conceived, constructed and commissioned. The primary objectives of the facility are:

- To validate the thermal design of top shield
- Assessment of effectiveness of jet type cooling system provided inside top shield
- Study of temperature distribution in main vessel - roof slab dissimilar metal weld junction considering the multi-modal exchange of heat through main vessel, safety vessel, wire mesh insulation and liner to the reactor vault under various operating conditions
- Effectiveness of wire mesh insulation in obtaining gradual temperature distribution in the upper portion of main vessel within annulus and inhibiting setting-up of convection currents within the annulus
- Effectiveness of the location of anti-convection barrier between main vessel and safety vessel
- Heat flux to reactor vault cooling system
- Thermal management of control plug, considering heat removal from the upper mechanism box
- Effectiveness of thermal shield provided below top shield
- Thermal loading during loss of cooling
- Understanding natural convection in the annular gaps at interface of LRP & SRP

Salient features of the facility

1. Reactor vault of ϕ9.5 m and 6.7 m height comprising two concrete walls with 50 mm thick insulation in between them, vault cooling coils embedded within the concrete, liner on its inner surface and support embedment for roof slab and safety vessel.
2. Heater plate embedded with electrical heaters (~150 kW) to simulate the heat flux from sodium pool to top shield.
3. Roof slab of ϕ6 m x 1.8 m height with its jet cooling system, step on outer periphery, dissimilar metal weld, wire mesh insulation in step region and cylindrical support shell support as in PFBR.
4. Main vessel of ϕ6 m x 2.7 m in SS304L welded to roof slab outer shell.
5. Safety vessel (SS 304L / IS 2062 Gr. B) along with its thermal insulation.
6. Anti-convection barrier in the space between main vessel and safety vessel.
7. 1:1 scale SRP (IS: 2062 Gr. B) supported on roof slab with annular gap geometry similar to LRP-SRP gap along with cooling of the shells similar to that of PFBR.
8. Control plug including its mechanism box of size similar to that of PFBR with suitable simulation of components housed in it.
9. SS 304 wire mesh of 14 screen size filled within the annulus between roof slab and main vessel to a density of ~1400 kg/m^3.
10. Top shield air cooling system and vault water cooling system.
11. More than 900 thermocouples embedded within the facility to record the temperature distribution.
12. State-of-art data acquisition system to record all the temperature readings simultaneously.

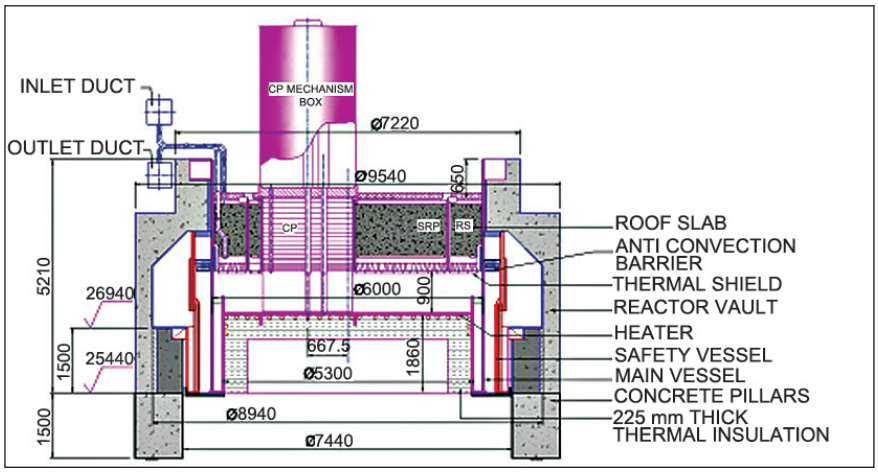

***Fig. 1** Integrated top shield model*

***Fig. 2** Overall view of facility*

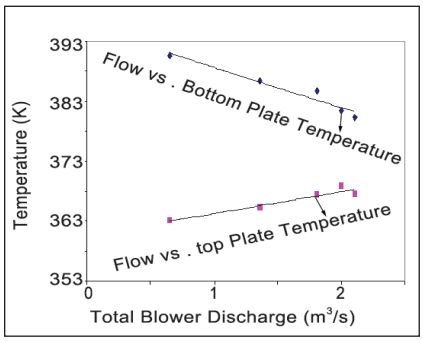

Fig. 3 *Evolution of roof slab bottom plate & top plate temperature with respect to blower discharge*

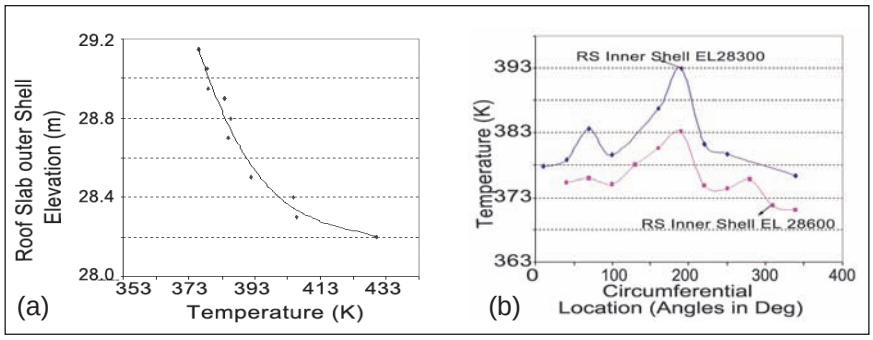

Fig. 4 *Temperature distribution along (a) Outer (b) Inner shell of roof slab*

Validation Studies

Following validation studies were carried out.

Normal operation simulation: In this mode, the total heat flux from heater plate to top shield is simulated as that in reactor, which is estimated to be 1100 W/m^2. The emissivity of the plate provided over the heater plate is experimentally measured to be 0.3 and the surface temperature of heater plate to provide the above heat flux is estimated to be 723 K. Under this condition, temperature distribution at the following locations were recorded and analysed.

Roof slab/small rotatable plug bottom plate temperature distribution to validate the effectiveness of jet cooling.

Temperature gradient across top plate and bottom plate in roof slab and small rotatable plug.

Temperature distribution in the annulus between roof slab, small rotatable plug and small rotatable plug & control plug.

Temperature distribution in the main vessel shell, particularly in the portion corresponding to cover gas region in reactor and up to dissimilar weld in roof slab. This will also validate the effectiveness of wire mesh insulation provided in the annulus between roof slab and main vessel.

Fuel handling operation simulation: In this mode, the heat transfer from sodium pool to top shield is estimated to be 1/10th of that during normal operation. Accordingly, the heater plate temperature is expected to be 453 to 473 K. Under this condition also, temperature distribution at all the locations will be recorded.

Other experiment conducted to asses the loss of cooling to the top shield for the heater plate temperature simulating normal operation condition as well as fuel handling condition.

Some of the important results from the studies carried out at the facility are:

(i) Evolution of roof slab bottom plate temperature as well as thermal gradient across roof slab with respect to cooling. Understanding of these phenomena is very essential to demonstrate the effectiveness of jet cooling system provided for maintaining the temperature of top shield in PFBR. From the plot (Figure 3), it is seen that the average roof slab bottom plate temperature of 390.6 K at 30% of blower discharge is reduced to 380.3 K at 98% of blower discharge. During this time, the thermal gradient is reduced from 27.5 to 12.8 degree. This indicates that the jet cooling is effective in regulating the roof slab bottom plate temperature within 393 K as well as the thermal gradient across roof slab within 20 degree.

(ii) The temperature distribution along the roof slab outer shell in the main vessel-roof slab annulus region was extracted and plotted in Figure 4a for an average heater plate temperature of 573 K. From the results, it is seen that in the presence of wire mesh insulation, the thermal gradient along the outer shell in the annular portion is gradual.

(iii) Understanding the temperature distribution (Figure 4b) along inner shell of roof slab is very important to understand the cellular convection phenomenon expected to occur in the narrow annular gaps, the amount of heat transferred to the component and the structural implications of non-uniform distribution. The temperature measurements were carried out at two elevations i.e., at 100 and 400 mm from bottom plate for an average heater plate temperature of 573 K. For an annular gap diameter of 4.1 m with gap varying from 16 to 30 mm, three loops of cellular convection occur with one more prominent.

The planned experiments with integrated top shield test facility are in progress. Analysis of preliminary results from the extracted temperature data has validated important design features like jet cooling, provision of wire mesh in the roof slab - main vessel annuls, presence of cellular convection loops etc.

II.4 Lessons Learnt from Manufacturing and Erection Experiences of PFBR Components for Future Sodium Cooled Fast Reactors

The construction of 500 MWe Prototype Fast Breeder Reactor (PFBR) will be completed in this year. Beyond PFBR, department is planning to build six 500 MWe Sodium cooled Fast Reactors (SFR) adopting twin unit concept. The first twin unit (2x500 MWe) would be constructed at Kalpakkam near PFBR. The capital cost of these twin units as well as construction time should be reduced significantly for the commercial exploitation. To achieve this, many features have been identified and are being studied. One of the essential steps is incorporation of lessons learnt during manufacturing and erection of PFBR components. Robust strategy was adopted for PFBR towards successful manufacture and erection of reactor assembly components. Technology development prior to start of construction and formation of standing task forces involving IGCAR-BHAVINI for manufacture and erection of components, which are functioning effectively since September 2006 are the key factors for the success.

Three components, viz. grid plate, roof slab and fuel handling systems are having impact on the project schedule, in turn motivating us to opt for alternate design concepts. The manufacturing challenges of grid plate mainly originated from large number of sleeves resulting in higher self weight and hard facing of large diameter sleeves. Machining of large diameter plates and shell assembly to the required tight tolerances on dimensions, hard facing with nickel based cobalt free

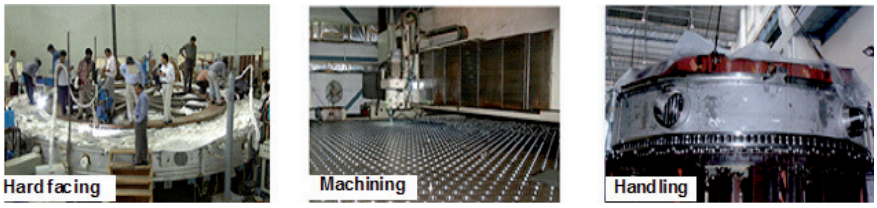

Fig.1 *Manufacturing stages of grid plate*

hard facing material on continuous, large diameter (6.7 meter) annular tracks, heat treatment of large austenitic stainless steel parts at 1323 K with controlled rates of cooling and heating together with control on temperature gradient across the parts, complex assembly of a large number of parts (~14900) meeting the important requirements on verticality of sleeve assemblies and delicate handling and transportation are truly challenging activities in the manufacturing technology (Figure 1).

In case of roof slab, complex manufacturing process, especially welding between the shell and stiffeners caused lamellar tearing problems and extensive testing time (Figure 2). Inclined fuel transfer machine, multiple repairs, heavy weight and testing strategy resulted in long manufacturing and testing time.

It is also worth to note some general lessons learnt. Technology development prior to start of construction is essential for long delivery components. The important outcome of technology development exercise undertaken for PFBR components are brought out comprehensively. Judicious choice of tolerances, number and location of welds and inspections has to be made. Robust criteria need to be applied for the acceptance of manufacturing deviations and material compositions. Indigenous materials should be used after qualifications of manufacturing process of direct relevance apart from routine standards. Manufacturing drawings should be finalized after discussions with prospective industries giving due considerations to economy. Subsequently, the revision of manufacturing drawings should be minimised in particular with respect to materials and tolerances. Single industry for manufacture of permanent components of reactor assembly will certainly help to minimise the integration problems and also to respect the schedule. In case industry needs technical supports, decisions should be

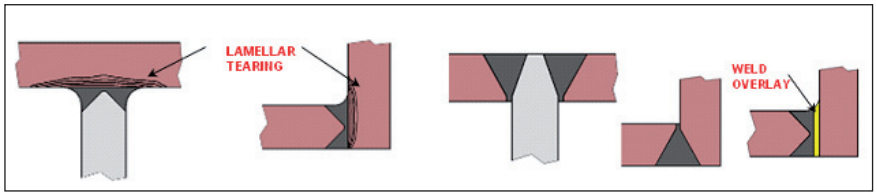

Fig. 2 *Lamellar tearing at 'T' & 'L' joints in roof slab and solutions*

taken quickly based on scientific input giving due considerations to international experience.

Computer simulations were extensively used based on 3-D virtual models for establishing erection sequences. Based on these a document has been made to give guidelines for industries and erection agencies. Handling scheme structures were designed, developed and tested in novel ways to achieve minimum material, no weld attachments and minimum assembly time. Many useful mockup trials ideal for training of crane operations were carried out and confidence gained before going for safety vessel handling. It is worth to bring out here two typical full scale mockups built and employed at IGCAR for the successful erection of safety vessel (Figure 3) and welding of roof slab hanging shell and main vessel (Figure 4). Further a full scale mockup has been built for visualizing the complicated layout of top shield components (Figure 5). to ensure the availability of space and access for adding and removing complementary shield blocks at any time and smooth operation of trailing cables without any entanglement during rotation of plugs. Computer simulations and mockup trials helped to ensure good access for critical welds, to establish techniques and tools for the mismatch correction procedure and methodology, appropriate welding sequence to minimize distortions.

Fig. 3 *Mockup trials for the successful erection of safety vessel*

Erection sequences and handling systems should be finalized after detailed discussions with the use of advanced computer software techniques. Care should be taken so that there is no revision of erection sequences and handling systems and handling schemes. Judicious choice of construction sequences of civil, mechanical and electrical systems is essential for the success. There is a need for optimum number and sizes of site assembly shops. Possibility should be studied to manufacture the entire reactor assembly components as a factory-made single package items. One possible strategy is schematically explained in the sketch (Figure 6). As per this, the reactor assembly components and civil construction of reactor vault along with safety vessel are constructed in parallel in matching time schedule so that the reactor assembly can be erected without time delay. Subsequently, other reactor internals kept ready in site assembly shop can be introduced. Towards achieving this, it is essential to motivate the prospective industries to participate as consortium attracting them high business opportunities in a long run.

From the rich experience gained through the manufacture and erection of reactor assembly components of PFBR, important guidelines and approaches were derived. These will be very useful for the success of future SFRs, planned by the department. It is estimated that by adopting these, reduce the construction time.

Fig. 4 *Mockup trials for the successful erection of safety vessel*

Fig. 5 *Full scale top shield layout mockup*

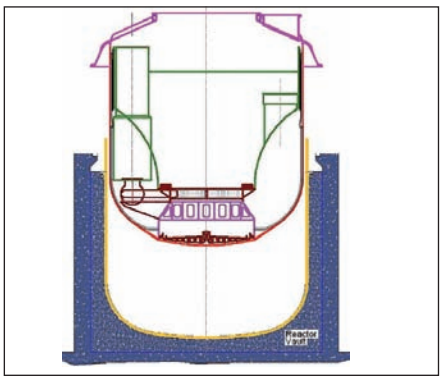

Fig. 6 *A proposal for manufacture and erection of reactor assembly of future sodium cooled fast reactors*

II.5 Seismic Qualification of Large Stem Sodium Valve

The extended stem frozen seal valve is used in the primary sodium fill and drain circuit (PSFDC) system inside reactor containment building (RCB). The valve is located in Cell no: 21 of reactor containment building and is operated from outside with the help of an extended stem (4.98 meter long) which is mounted on the pipeline and penetrates through and thus supported at the reactor containment building wall. The stem is also supported at two locations to the roof. The weight of the valve is 271 kg and with extension it is 385 kg. The valve and the stem will experience different differential support excitation, which calls for the qualification of the valve by creating multi support excitation effect.

Qualification of the valve is done on the shake table in Structural Mechanics Laboratory. The qualification procedure is based on the IEEE recommended practice for seismic qualification of class-IE equipment for nuclear power generating station (IEEE-344-1987)

Description of the test facility

A 10 tonne capacity shake table test facility has been installed at Structural Mechanics Laboratory for the seismic related R&D activities and seismic qualification of FBR components.

The vibration test platform/table is a box type structure of 3 x 3 x 0.5 m. The facility has three actuators for the movement in two horizontal direction (X and Y axes) and three actuators for the movement in vertical direction (Z axis). The actuators are driven by hydraulic power and precisely controlled by the servo-valves to produce the simultaneous and independent motions with six degrees of freedom. Maximum permissible distance of center of gravity of specimen from table top is two meters. The maximum displacement, velocity and acceleration the table can be operated at ± 100 mm, 0.3 m/s and 1.5 m/s^2 respectively. The shake table operates in the frequency range of 0.1 – 50 Hz.

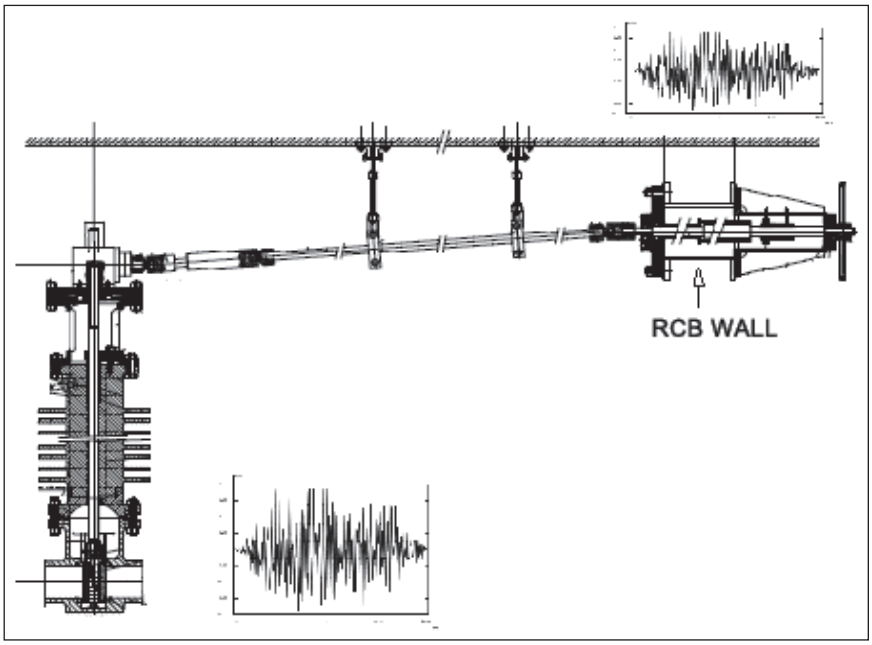

Fig. 1 *Loading details of large stem sodium valve*

The required response spectrum (RRS) is the spectrum corresponding to the location of the valve in the RCB. Spectrum compatible time histories are generated such that the test response spectrum (TRS) envelopes the RRS for the frequency range of interest as per IEEE criteria.

Design of support structure

The valve assembly shown in Figure 1 is a multiple support structure. The specially designed support structure creates the multi-support effect between the valve and the extended stem. The design of the structure is such that its fundamental frequency falls in the peak region of the response spectrum (between 8 to 12 Hz) without compromising the rigidity. This is achieved by increasing the mass of the structure by filling the lead shots in the hollow region support column and placing an additional box filled with lead at the top of the support column.

The support structure is analyzed using Cast 3M software and the natural frequencies are verified with hand calculation. The designed support structure has first mode at a frequency of 8.67 Hz. This corresponds to the frequency band of 8-12 Hz required for the structure. The weight of the support structure is two tonnes; this respects the decoupling criteria for the valve. The overhang truss is rigidly designed to meet the requirement of the structure.

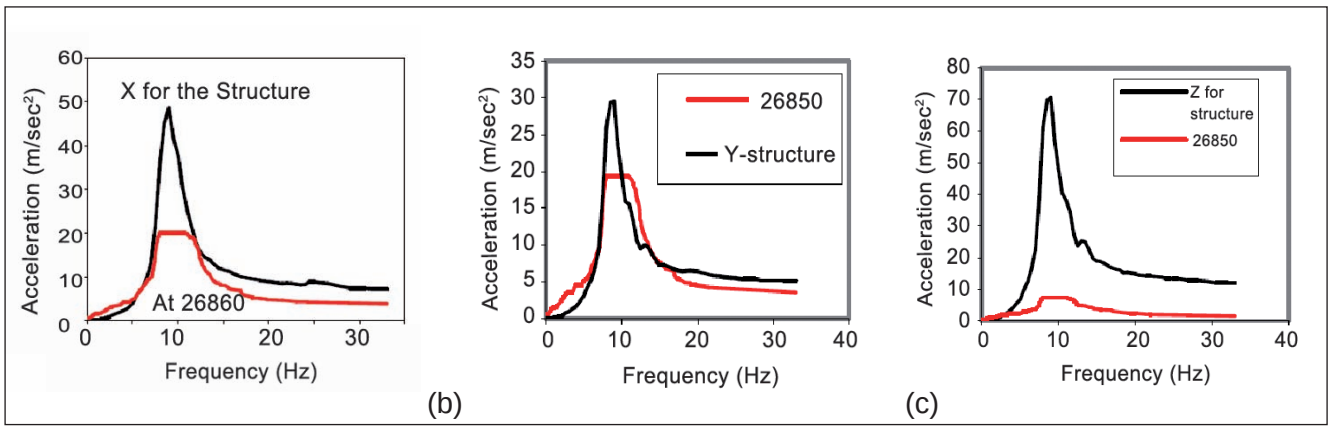

Fig. 2 *Response spectrum and floor response spectra at the highest location (a) X direction (b) Y direction (c) Z direction (vertical)*

The mounting of the valve is made by attaching two pipes to the valve flange which is in turn welded to two stiffened plates. The connecting rod along with the rotating wheel is mounted on the over hanging beam of the support structure with rod supports and welded plates.

Qualification by analysis (support structure)

Time history analysis of the support structure is done with the base excitation. The response spectrum obtained from the time history analysis is compared with the floor response spectra at the corresponding location of valve support (Figure 2).

Qualification by experiment (support structure)

The qualification test setup is mounted on the shake table as shown in Figure 3. The procedure for the qualification of the support structure is given as:

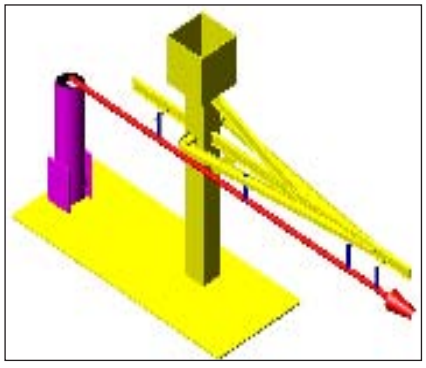

Fig. 3 *Qualification setup layout*

Perform frequency sweep test in X,Y and Z directions to assess the natural frequencies of the structure in the respective directions.

Perform the operational basis earthquake test on the structure and compare the frequency at the highest location and supporting point.

The procedure for qualification of the valve is given in Table 1.

The qualification experiments were conducted and the large stem sodium valve was qualified for OBE and SSE loading. The response spectra and frequency of the support structure obtained in analysis was compared with experiment and was found comparable.

Table 1: Qualification of valve

Sl.No	Procedure	
1	Check for the leak from the valve before the test	
2	Perform sine sweep tests in X, Y and Z directions for getting the dynamic characteristics of the valve	
3	Perform the operational basis earthquake test (5 times) using simulated support excitations	
	3.1	Check for mechanical interaction
	3.2	Check displacements vertical, and horizontal (X and Y)
	3.3	Check torsional and bending strains
	3.4	Check leak during test
4	Check for any damage or dislocation. Check the operation of the valve by rotating the hand wheel after the test is performed	
5	Perform the safe shutdown earthquake test (1 time) using simulated support excitations. Checks are performed as per 3.1 to 3.4	
6	Check for any damage or dislocation. Check the operation of the valve by rotating the hand wheel	
7	Check for leak till one hour after test	

II.6 Design and Development of Special Bearings for Inclined Fuel Transfer Machine

Inclined fuel transfer machine (IFTM) is a critical machine used for the ex-vessel transfer of subassemblies during refuelling. In IFTM, the subassembly is transferred in a sodium filled pot called transfer pot (TP) from in-vessel transfer position on the grid plate to ex-vessel transfer position located inside fuel building. The transfer pot is hoisted up and down using dual welded link chains attached to the pot. The transfer pot movement is achieved using rollers rolling over three rails (one guide rail at bottom and two tilting rails at sides) fixed inside primary/secondary ramp, primary/secondary tilting mechanism, and rotating shielded leg. Two side rollers, four bottom guide rollers and three top guide rollers are attached to the transfer pot for its guided movement along the guide/tilting rails. Smooth movement of transfer pot is required to ensure uninterupted fuel handling and to avoid stuck up of spent subassemblies having high decay heat.

In the original design of transfer pot, guide/tilting rollers were mounted on journal bearings between the roller ID and their mounting shafts with large diametral clearence (800 µm) provided from considerations of smooth rotation inside liquid sodium. Sliding surfaces on the rollers and shafts were provided with a wear resistant coating of colmonoy-5. Lubrication was not provided for the journal due to requirement of working inside sodium. During functional testing of transfer pot in air at the manufacturers works, jerky movement of transfer pot was observed due to high friction on the sliding surfaces of rollers and pins. High noise was also noticed during the movement of transfer pot along with seizure of the rollers. Detailed analysis revealed that high friction and noise were due to high contact stress generated between the bearing and the journal. High contact stress exceeding the threshold galling stress from skew and edge loading of rollers due to large diameteral clearances provided, resulted in severe wear and ultimately seizure. Since the rollers are required to be guided during their motion, it was not possible to avoid lateral force and susequent edge loading on the rollers due to cocking of the same. This necessitated improvement in the design of bearings for tilting/guide rollers of transfer pot. It was decided to replace the journal bearing with roller bearing (Figure 1a and 1b) which can take radial as well as thrust loads together with reduced friction as compared to journal bearing.

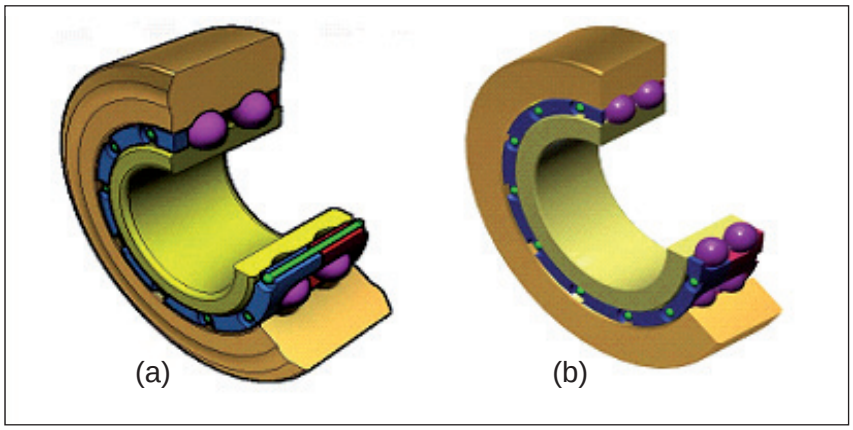

Fig. 1 *(a) Guide and (b) Tilting roller bearings for IFTM transfer pot*

Based on the kinematics analysis of the roller/rail system, radial, axial and moment loads on the bearings during normal and extreme conditions of travel were estimated. Since it was not possible to accommodate bearings in pair to take moment loading due to limited available axial space, double row deep groove ball bearing was selected for both guide and tilting rollers. Available radial space was also limited due to the restriction on the internal dimensions of the ramp and rails on which transfer pot moves. It was not possible to accommodate roller bearing having the required load carrying capability within the available radial space of the roller. Design of rollers was changed to track roller type bearing, the outer race of the same acts as the rolling surface.

Dimensional stability and metal softening are the primary concern for rolling bearings operating at high temperature. The satisfactory operation of bearings at elevated temperature also depends on whether the chosen lubricant will retain its lubricating properties and whether the materials of the seals, cage etc. are suitable. No such lubrication effect can be expected from liquid sodium. Since the bearing has to operate inside main vessel, use of any lubricating oil is prohibited. Martensitic stainless steel 440C was

chosen for the races and balls of the bearing because of its high hot hardness, compatibility with liquid sodium and argon atmosphere, operating experience with similar components in other reactors and also due to the experience gained in the manufacture of 440C bearings by Indian industries. Material of cage is selected as SS304 because of its vast experience in FBR applications. Since it was not possible to select a commercially available track roller type double row deep groove ball bearing in 440C material, satisfying the design requirements, the same was designed in-house and manufactured by M/s MTAR Technologies, Hyderabad as per the detailed manufacturing drawings. Boundary dimensions of these bearings are made equivalent to 4207A (guide roller bearing) and 4210A (tilting roller bearing). Static and dynamic load rating of these bearings are estimated by derating the catalogue values based on the hot hardness and the lubrication effects for the design life of nearly one million revolutions. Since these bearings are operating at high temperature and in liquid sodium environment, selection of radial internal clearance is very important to avoid seizure of the rolling elements due to temperature variation.

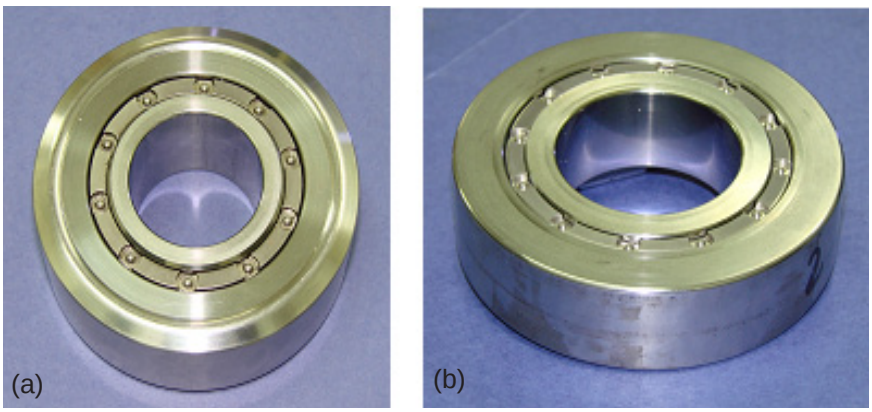

Fig. 2 *Actual bearings manufactured for IFTM transfer pot (a) Guide and (b) Tilting*

Sufficient radial clearance was provided based on the estimation of differential thermal movements of races and rolling elements with due consideration for rapid cooling of outer ring with respect to the inner ring during conditions of temperature changes. In order to utilize the full load carrying capability of the bearing, the inner rings are designed to provide satisfactory interference fit during the operation at high temperature still maintaining transition fit at room temperature.

Bearing rings after rough machining were solution annealed at 1303 K followed by oil quenching. Subzero treatment at 193-203 K was done immediately after quenching to increase the formation of martensite. These components were further tempered at 523 K to achieve a finished hardness of 57 HRC. All finish machined rings were fluorescent magnetic particle tested for crack detection to ensure that they were defect free. Finished balls were 100% inspected for size, grade, form and surface texture. These balls were also subjected to triple axis radiographic inspection. After assembly of bearing, radial and axial internal clearances were verified for conformity.

After successful manufacturing (Figure 2), these bearings were mounted on the transfer pot and the air testing of primary side of IFTM for 50 cycles was completed successfully. Movement of the transfer pot was very smooth and noise free. Preparations are underway for sodium testing at large components test rig.

II.7 Internal Events Level-1 Probabilistic Safety Analysis

Internal events Level-1 probabilistic safety analysis study for PFBR was completed and its objective is to present an integrated safety picture of the design aspects within the probabilistic framework. In addition, identification of dominant core damage categories and identifying components, systems and structures for risk minimisation effort are part of the objective. The scope of the analysis is limited to internal initiating events, excluding internal fire, flood, load falls and projectiles. The study consists of several steps, starting with system analysis, and detailed modeling of event progression logic through a combination of event trees and fault trees, data analysis, common cause failure evaluation, human error analysis, quantification, sensitivity and uncertainty analysis. The fault trees capture the logical structure of safety systems, while event trees spell out the possible paths taken, as any initiator progresses towards a safe or unsafe state.

Systems analysis and reliability assessment

The important safety systems in PFBR are given in Table 1. Safety grade decay heat removal system is a passive decay heat removal system (category D passive system as per IAEA classification) with four thermo siphon loops transporting heat from hot pool to atmospheric air. Each loop has a heat removal capacity of 8 MW at a hot pool temperature of 820 K. In addition various other systems like emergency diesel generator system, safety related service water system etc. were considered for this analysis. Totally eight systems were identified which have safety and safety support functions and the list of systems along with their unavailability are given in Table I. Detailed fault tree modeling of these systems were carried out. As an example, top segment of the fault tree for the operation grade decay heat removal system reliability assessment is shown in Figure 1. While modeling each system the support systems were also modeled along with required human error probability assessments for critical operation or maintenance interventions.

Table 1: System analysis results

Sl.No	System	Unavailability
1	Shutdown system (global fault / local fault)	$3.2 / 3.3 \times 10^{-8}$
2	Operation grade decay heat removal system (OGDHRS)	3.0×10^{-2}
3	Safety grade decay heat removal system (SGDHRS) (calculated for a mission time of 720 h)	1.0×10^{-7}
4	Class III power supply system - 6.6 kV bus section level	2.5×10^{-6}
5	Safety related service water system (SRSWS)	4.85×10^{-4}
6	Class I power supply system - 48 V division level	1.2×10^{-6}
7	Class II power supply system	9.0×10^{-7}
8	Compressed air system (calculated for a mission time of 24 h)	6.0×10^{-5}

Event analysis and event tree development

All initiating events whose frequency of occurrence is > 1×10^{-6}/ ry were considered for this analysis. These events are grouped into 15 event groups. Wherever possible the initiating event frequency was calculated based on detailed modeling of individual systems as in the case of roof slab cooling system and biological shield cooling system. For all other events frequency of initiating events are based on operating experience with PHWRs, FBTR and worldwide experience.

For each of the initiating event groups identified, event trees were developed. The fault trees developed for each of the safety systems were connected to the event trees. The primary system is common to both operation and safety grade decay heat removal systems. The primary system was modeled separately in the event tree and unavailability values of operation and safety grade decay heat removal systems excluding primary system were used in event tree. Since safety grade decay heat removal system is a passive decay heat removal system, its functional failure probability was calculated as a function of number of loops available and these values are used in event tree. As an example, event tree for primary sodium pump trip, which includes the functional failure of safety grade decay heat removal system is shown in Figure 2.

Depending on the event sequence progression the end states of the event tree branches can be either safe or any one of the core damage categories namely few pin failures, subassembly failure and whole core accident.

The core damage categories core damage 1 and core damage 2 appear in local loss of flow event trees. There are two event trees

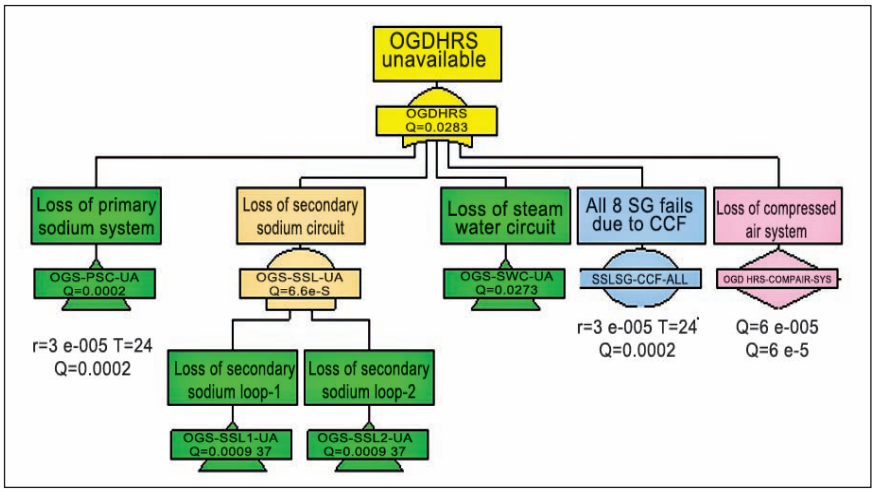

Fig. 1 *Part of fault tree for operation grade decay heat removal system*

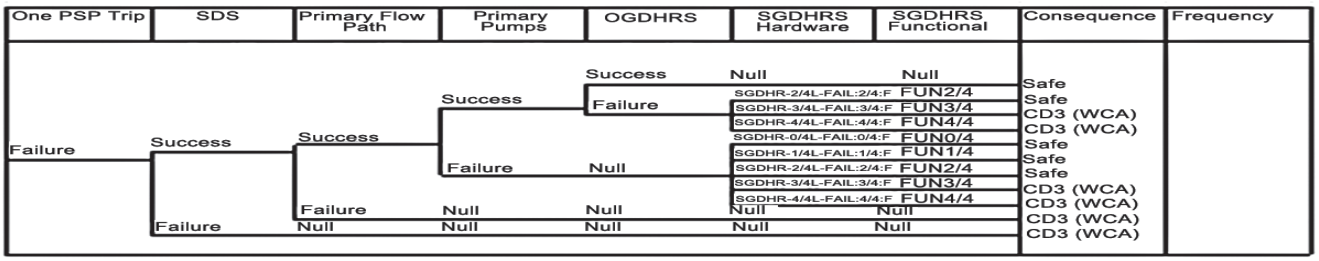

Fig. 2 *Typical event tree with functional failures included as branches for primary sodium pump trip event*

in local loss of flow with initiating events adventitious pin failures and other events that can lead to blockage in the subassembly.

The estimated core damage frequency (CDF) of PFBR is less than $1.0x10^{-6}$ per year and is comparable in magnitude, to those available in literature for EBR-II ($1.6x10^{-6}$), CRBR ($3.7x10^{-6}$) and SNR-300 ($2x10^{-6}$). Figure 3 gives the contribution to the core damage frequency from different initiating event groups. It shows that the loss of steam water system (LSWS) is the dominant contributor to CDF. The loss of offsite power (PSS1) is the next major contributor. The contribution from local loss of flow (LLF) is ~6%. Many conservative assumptions have been made in the above analysis, for example, in the LSWS event tree one of the decay heat removal systems namely operation grade decay heat removal system is considered unavailable. Common cause failure and human error analyses were also part of the study.

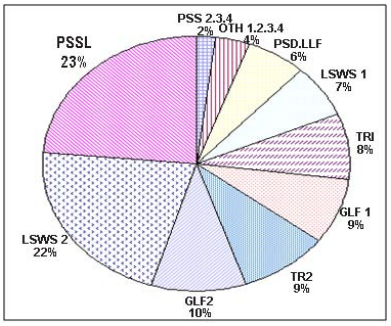

Fig. 3 *CDF contribution from different initiating event groups*

II.8 Manufacture of Scale Model of PFBR - Inner Vessel for Thermal Hydraulics and Vibration Analysis

Prototype Fast Breeder Reactor inner vessel 1/4th scale model (Figure 1) was fabricated using SS304 material for thermal hydraulic and vibration studies. The overall size of the model is Ø3500 mm OD X 3000 mm height. It consists of top shell with ring flange, truncated cone with intermediate heat exchanger stand pipes & pump stand and bottom shell with ring flange. The top and bottom shells of thickness 5 and 8 mm respectively were rolled and welded using GTAW process.

The truncated cone was fabricated from SS 304 plate of 10 mm thick with six equal segments. The segments were formed in press brake machine and long seams were welded. The bottom and top ring flanges were precisely machined and achieved the geometrical tolerances. The flanges were welded with the shells using GTAW process. Special fixtures were designed, fabricated, low heat input and segmental weld techniques were adopted to minimize the distortion.

The truncated cone has two purification pipe at an angle of 0° & 180°, four intermediate heat exchanger stand pipes at 46°, 134°, 226° & 314° and two pump stands at 90° & 270° with respect to centre axis. The pipes were assembled with the vessel in correct orientation and welded. After completion of fabrication, the inner vessel model was subjected to chemical cleaning pickling and passivation surface treatment. With the expertise and adoption of best methodology at different stages, the test vessel was manufactured successfully to ensure its functionality meeting the requirements of ASME Section VIII div I.

Fig. 1 *PFBR inner vessel 1/4th scale model*

II.9 Manufacture of Large Size Test Vessel for Testing PFBR- Transfer Arm in Sodium

The large size test vessel (TV-5) was manufactured to test the PFBR - transfer arm. The overall size of TV-5 is 2200 mm OD X 13500 mm height. It consists of various subassemblies namely main vessel with tori-spherical dish end, grid plate assembly and shielding assembly. The material of construction is SS316LN. The tori-spherical dished end was fabricated using progressive forming technique and subsequently annealed. The main shell (Figure 1) was fabricated with six segments. Special fixture was designed, fabricated and used during welding and fabrication. Also, low heat input and segmental welding techniques were used to minimize distortion and achieved the geometrical tolerances.

Fig. 1 *Main shell of test vessel*

The inner shielding shell of size 1476 mm OD x 1735 mm height was fabricated with 8 mm thickness SS316LN plate with ring flange and elliptical opening at the top. Forty nine baffle plates (Figures 2a and 2b) of Dia 1500 x 2 mm thickness with elliptical opening were fabricated using profile laser cutting machine and it was assembled using tie-rods and connecting pipes with the machined main vessel flange of Dia 2200 x 100 mm thickness.

The grid plate assembly (Figure 3) consists of grid plate at the top and supporting flange at the bottom of size Dia 1650 x 33 mm thickness. Seven grid plate sleeves with inner diameter 104 mm having satellite-6 hardfacing was carried out using plasma arc transformer process. The dimensional tolerance of sleeves was achieved within 50 microns. The finish machined grid plate sleeves were assembled with top and bottom flanges using special nuts and tie rods and achieved the flatness within 0.5 mm. The entire assembly was assembled on the supports inside the main vessel at the lower end.

The main vessel was assembled with top flange and subjected to pneumatic test at 3 bar. Helium leak test under vacuum was carrried out and achieved leak tightedness was within 1 x 10^{-8} std cc/sec.The large size TV-5, shielding assembly and grid plate assembly were fabricated meeting the requirements.

Fig. 2 *(a) and (b) Baffle plate assembly*

Fig. 3 *Grid plate assembly*

II.10 Sodium Calibration of Eddy Current Flow Meter for PFBR Primary Sodium Pump

Primary system of Prototype Fast Breeder Reactor (PFBR) consists of two vertical centrifugal pumps operating in parallel to maintain sodium flow through the core. The primary sodium pumps take suction from the cold pool and discharge to a spherical header from which the flow enters the reactor grid plate (Figure 1). The flow through the reactor core is controlled by varying the pump speed and is measured using eddy current flow meter, which is located in the pump bypass line, from pump discharge to suction.

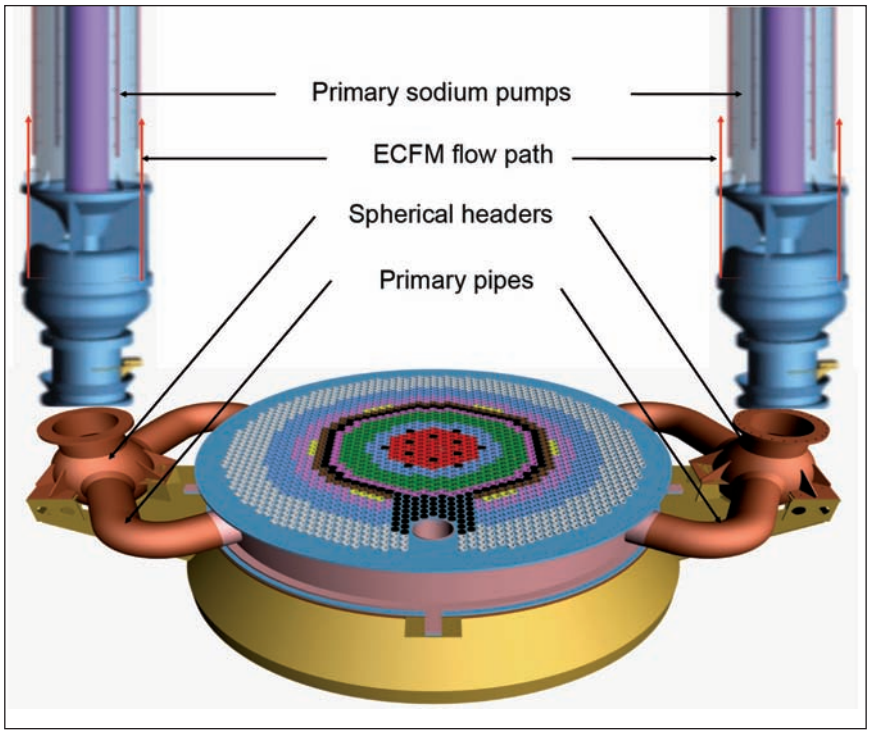

Fig. 1 *Schematic of primary sodium pump*

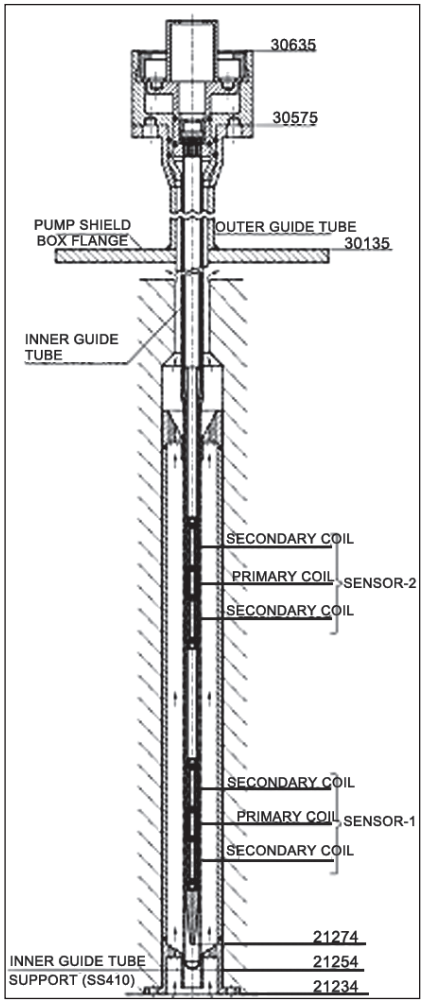

Fig. 2 *Schematic of eddy current flow meter*

Each flow meter consists of two sensors and there are two such flow meters in each pump 180° apart. A part of the sodium flow delivered by the primary pump flows through the eddy current flow meter (Figure 1). The flow sensor consists of three coils wound on a former made of pure iron. The primary coil is excited with a constant current source at constant frequency. The two secondary coils are wound symmetrically on either side of the primary coil on the same core. When sodium is in motion, motion voltage is produced in both the secondary coils in addition to transformer voltage. This motion voltage is subtractive to transformer voltage in upstream coil and additive to transformer voltage in downstream coil. As a result of this the voltages induced in the two secondaries differ from each other and this difference is proportional to the sodium velocity.

A prototype probe was made and calibrated in sodium for different temperatures and flow rates. Based on the testing experience eight probes were machined and fabricated for the primary sodium pumps in PFBR. Figure 2 shows the schematic of the eddy current flow meter for primary sodium pumps. All the eight probes were calibrated in sodium in 500 kW loop. A permanent magnet flow meter is used as the reference for calibration. Optimum current, optimum frequency, output curves, accuracy and linearity for each probe were established by calibrating probes in sodium for a temperature range of 473 to 673 K and for flow range upto 40 m^3/h. Accuracy of the flow meter was calculated to be ± 2% for flow velocities above 1 m/s.

II.11 Qualification Testing of Primary Ramp and Primary Tilting Mechanism of Inclined Fuel Transfer Machine in Air

Inclined fuel transfer machine (IFTM) of PFBR transfers spent subassemblies from In vessel transfer position (IVTP) located in the reactor core to ex-vessel transfer position (EVTP) located in fuel building and fresh subassemblies in reverse direction.

Primary side of IFTM, located in the reactor containment building mainly consists of primary ramp (PR), primary tilting mechanism (PTM), primary gate valve, shield plug, PR liner, bellows and interconnecting piece. Secondary side of inclined fuel transfer machine, located in the fuel building consists of secondary gate valve, secondary ramp and secondary tilting mechanism. Rotatable shield leg of inclined fuel transfer machine is supported on the rotary support table located over the roof slab. Interconnection between primary side and secondary side is achieved by rotation of the rotary support table along with rotatable shield leg over a slewing ring. Transfer of the subassemblies is carried out in a sodium filled pot to ensure removal of the decay heat of the spent fuel subassemblies. Hoisting and controlled lowering of the transfer position is achieved by hoisting mechanism provided at the top of rotatable shield leg. Transfer of transfer position takes place with an inclination of 17º to vertical. The primary and secondary tilting mechanism serves to tilt transfer position from vertical to 17/23º inclination. The transfer position moves on the rollers over rails provided on both the sides. For the smooth movement of transfer position, rollers are provided with ball bearings. Manufacturing of inclined fuel transfer machine is at an advanced stage at the manufacture site.

Manufacturing and testing strategy of the inclined fuel transfer machine involves two stages. In stage-1 PR and PTM are manufactured ahead of other inclined fuel transfer machine components, tested and assembled in the reactor matching with the sequence of reactor assembly components. In stage-2, integral testing of the machine shall be carried out along with additional primary ramp and tilting mechanism.

Manufacture and shop floor testing of primary ramp/tilting mechanism was completed. Presently primary ramp/primary tilting mechanism is assembled in test vessel-2 (Figure 1) of large component test rig located in Engg Hall-III for the performance test which involves testing in air at ambient condition and then in sodium simulating reactor conditions. Primary ramp and tilting mechanism test assembly consists of grid plate, PR-liner, transfer position, gate valve, ramp extension piece and hoisting mechanism with support structure. Total height of the test setup is 20 meter and weighs 30 tones which make assembly a challenging task. During assembly alignments of the rails, inclination of PR and angle difference between primary ramp and primary tilting mechanism are obtained well within the allowable limits. Hoisting and lowering of the transfer position is carried out through a control console. For safe operation, control logics and safety interlocks are incorporated in the control console.

Fig. 1 *Primary ramp and tilting mechanism test assembly*

Stipulated requirement of fifty cycles of air testing have been carried out successfully. Required torque for raising and lowering of the transfer position are within the limits. No rubbing marks or scoring marks are observed on the rollers of transfer position and rails of primary ramp and primary tilting mechanism. Over all movement of the transfer position on the rails is smooth. This has given confidence in the performance of the machine. Preparatory works for sodium is under progress.

II.12 Experimental Investigation of Inter Wrapper Flow Heat Transfer Using a Slab Model of PFBR Cores

Safety grade decay heat removal (SGDHR) system is a natural circulation based decay heat removal system available in PFBR. inter wrapper flow (IWF) is one of the important flow path for core cooling during safety grade decay heat removal. Experimental studies were conducted to understand and estimate the contribution of heat transfer by flow through the inter wrapper spaces (IWS). Since the inter wrapper spaces are of 3- 4 mm size, larger size of the model was necessary in achieving the detailed geometric modelling in core region. Hence a 1:1 scaled slab model of reactor core and hot pool was selected for this study.

All geometrical features those are important to influence the inter wrapper flow, have been considered in this model. The schematic and actual model are shown in Figure 1 & 2. Only fuel and blanket zone subassembiles were simulated in 1:1 scale of prototype subassembly. Pressure drop was simulated with Euler number criteria. DHX heat removal is modelled by direct injection of cold water in the hot pool. The height of the liquid column above core has been maintained as in the reactor. To facilitate flow visualization viewing windows are provided in the model. Heater power was calculated based on Richardson number (Ri Number) similitude and rod type heaters were used for decay heat simulation. Thermocouples along with the data acquisition system (DAS) were employed for temperature measurement inside the model at various locations.

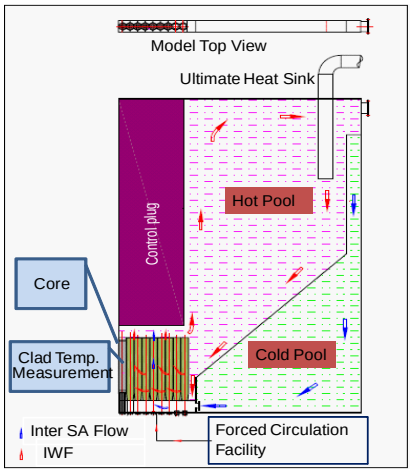

Fig. 1 *Slab model schematic for inter wrapper flow studies*

Fig. 2 *Experimentel slab model for inter wrapper flow studies*

Flow visualization studies have been conducted by dye injection. Flow mapping was achieved by 2D particle image velocimetry recording.

The model was filled with the water and decay heat was simulated by core heaters and DHX heat removal was simulated by cold water injection. This experimental procedure was continued until steady state temperature is achieved in the model. Initially dye was injected in the bottom region of the inter wrapper spaces above the top grid plate. It is observed that within a short time, dye started appearing at the core outlet. Visual observation of dye particles tracing the flow path demonstrated the presence of inter wrapper flow during heat removal. Radial flow was also witnessed in the bottom conical portion of the subassemblies. Dye injection of the dye inside the subassembly through respective ports showed the presence of flow through subassemblies. It was possible to visualise a plume of the hot water coming out of the subassembly and inter wrapper spaces. These results prove the presence of inter wrapper flow due to onset of natural convection.

Experimental test runs were carried out under different conditions. Studies were conducted for different cold water injection rate and at different overflow height of the model. Steady state hot pool temperature is found to be lower with higher cold water injection rate i.e. with higher stratification in hot pool. In addition to this, particle image velocimetry measurements were also recorded at the outlet of fuel subassembly. Velocity profile obtained at the outlet of the subassembly is used for estimation of flow rate through subassembly which in turn is used for estimation of heat removal by flow through subassembly. Approximate contribution of the inter wrapper flow in core heat removal is estimated to be 25 % as per particle image velocimetry measurements.

II.13 Testing of DSRDM Electromagnet in Thermal Shock Test Facility

Diverse safety rod drive mechanism (DSRDM) is one of the two independent, diverse systems employed in PFBR to shutdown the reactor in the event of abnormal conditions. The electromagnet of DSRDM holds the DSR poised for insertion into the core during normal operation of the reactor. The electromagnet is immersed in hot sodium pool and is partially inside the DSRDM subassembly. It is designed for the lifetime of 40 years. The electromagnet is subjected to thermal cycling during various transients such as reactor start up, power variations and most importantly during reactor SCRAM. The electromagnet assembly as shown in Figure 1 contains dissimilar weld joints and thermal cycling, mainly the thermal shocks during reactor SCRAM, can cause failure of these critical welds due to thermal fatigue. Demonstration of the soundness of the welds under all design basis loadings is an important step towards ensuring a reliable design. In view of this, the electromagnet is tested in thermal shock test facility to check its structural integrity against simulated thermal shocks.

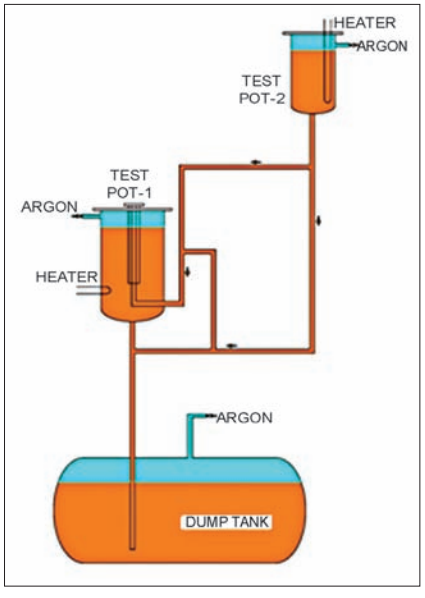

Fig. 2 *Schematic of thermal shock test facility*

Thermal shock test facility was constructed to test vital reactor components for thermal shock loading and commissioned. The maximum operating temperature of the facility is 908 K. The flow rates and temperatures can be adjusted to simulate the anticipated thermal shock rates to which the components may be subjected to inside the reactor during transient conditions. The material of construction of the facility is SS316LN/SS316L.

The schematic of thermal shock test facility is shown in Figure 2. The main components of the facility are test pot-1, test pot-2, sodium storage tank, argon cover gas system and the connected piping. The electromagnet to be tested is located in test pot -1. Test pot -2 is sized and located at a sufficiently higher elevation with respect to test pot -1 so that the sodium flow rate variation with change in level in test pot -2 is within acceptable limits. In this facility maximum flow rate of 20 m^3/hr (approx.) can be achieved under gravity flow and 90 m^3/hr by applying differential pressure.

The instrumentation and control provided in the facility enables measurement of parameters such as sodium flow, sodium levels in various test pots, sodium temperature, metal temperature, and cover gas pressure. Surface & immersion heaters are provided to attain the required temperatures.

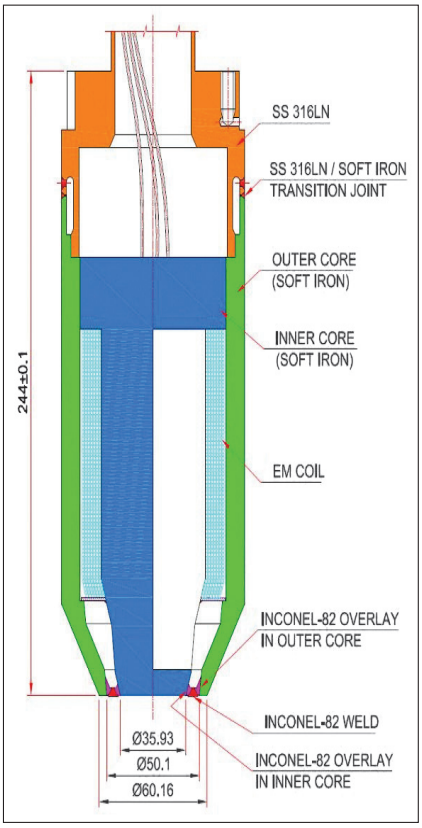

Fig. 1 *Sketch of electromagnet*

The facility is provided with a number of safety features such as sodium leak detectors at all critical locations, leak collection trays, sodium ionization detector to detect leaks, safety relief valves to guard against over pressurisation of cover gas system, safe shutdown in the event of emergencies such as sodium leak, power failure etc.

The expected number of thermal shocks on the electromagnet during reactor design life of 40 years is around 752 cycles based on number of reactor SCRAM. Based on the ASME, B&PV Code Section III requirement for a full scale component testing, the electromagnet shall be subjected to 3460 cycles simulating the reactor scram condition. During SCRAM, the temperature of sodium at the

outlet of DSR subassembly, where electromagnet is located, reduces from 773 to 673 K at a peak shock rate of 5.2 K/s.

After introducing the electromagnet in test pot -1 through the nozzle provided in top flange of test pot -1, the following test procedure is followed. Test pot -1 and test pot -2 are filled with sodium and sodium temperatures are raised to 773 to 673 K respectively. Then test pot -1 sodium is drained into dump tank followed by allowing test pot-2 sodium to impinge on electromagnet through interconnecting piping, thus creating the required thermal shock. This completes one thermal shock cycle.

SS sheathed chromel-alumel thermocouples of 0.5 mm outside diameter are fixed directly on the outer diameter of electromagnet as shown in Figure 3, to enable

Fig. 3 *Electromagnet with thermocouples fixed on it*

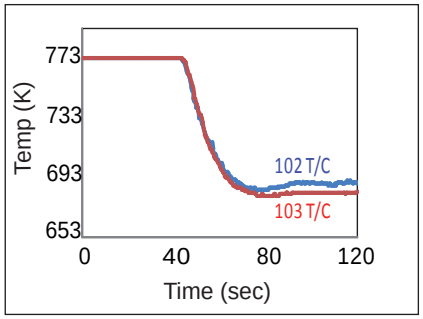

Fig. 4 *Temperature evolution during thermal shock*

direct measurement of the shock rate. The temperature readings of thermocouples are recorded using HP data logger with scan time of 200 ms. A typical temperature evolution is shown in Figure 4. The healthiness of the electromagnet is monitored using current decay method after every 10 shocks. In this method, the decay characteristics of electromagnet current are recorded and any sodium leak into the electromagnet will be detected through broadening of the decay curve. Upon completion of 360 thermal shock cycles, the electromagnet was taken out of test pot -1 for inspection. Surface and volumetric examination of the electromagnet was carried out after sodium cleaning. Both DP and UT has revealed no indication of cracks anywhere on the electromagnet including the weld regions. Subsequently, further testing of electromagnet was taken up. So far 725 shocks have been completed.

II.14 Full Power Operation and Flow Induced Vibration Studies in Steam Generator Test Facility

Steam generator test facility is being operated at different power levels up to the rated power and various experiments were carried out successfully. Steam generator test facility was operated continuously for 28 days during August-September 2011 at the rated power of 5.5 MWt demonstrating the endurance and robustness of the design of the sodium heated once-through steam generator for Indian fast breeder reactors. This test has also validated the excellence in manufacturing and quality assurance of the steam generator.

The 5.5 MWt capacity steam generator of the test facility has 19 tubes similar to 547 tube steam generator of PFBR with 157 MWt capacity. Heat transfer length of each tube is 23 meter. Support system of tube bundles is similar in both the steam generators.

Flow induced vibration testing of steam generator tubes were carried out. The steam generator tubes were subjected to cross flow of the liquid sodium at the inlet, expansion bend and outlet regions, making it susceptible to flow induced vibration. The main flow induced vibration mechanisms are turbulence, vortex shedding and fluid-elastic instability. The tube-support system of steam generator is designed against vibrations due to vortex shedding and instability phenomenon. However, the

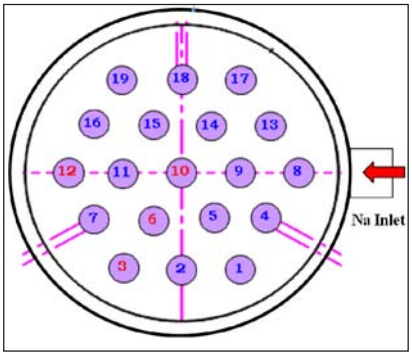

Fig. 1 *Steam generator tube layout*

turbulence will be present in various ranges of shell side flow and the vibration due to this mechanism will be the predominant one. Flow induced vibration studies have been carried out on steam generator tubes to assess the amplitude and frequency of vibration for different shell side flow conditions.

Measurements were carried out in four steam generator tubes (Tube No-3, 6, 10 and 12) and the layout is shown in Figure 1. In each tube, measurements were carried out at 38 different locations covering six spans above the bend region and three spans below the bend region. In each span measurements were carried out at five locations including two tube support regions. Bi-axial accelerometer is used for the measurement. The vibration signals are acquired for various shell side sodium flow conditions. The output of the accelerometer was connected to the charge converter module, galvanic isolation module and the amplified signal was recorded in multi channel FFT analyzer. Figure 2 shows typical vibration spectra recorded from the steam generator tube. Sodium flow in the shell side was varied from 20 to 100% of the rated flow for maximum steam generator power level. The measurement was carried out at a sodium temperature of 553 K and the tube side was filled with nitrogen.

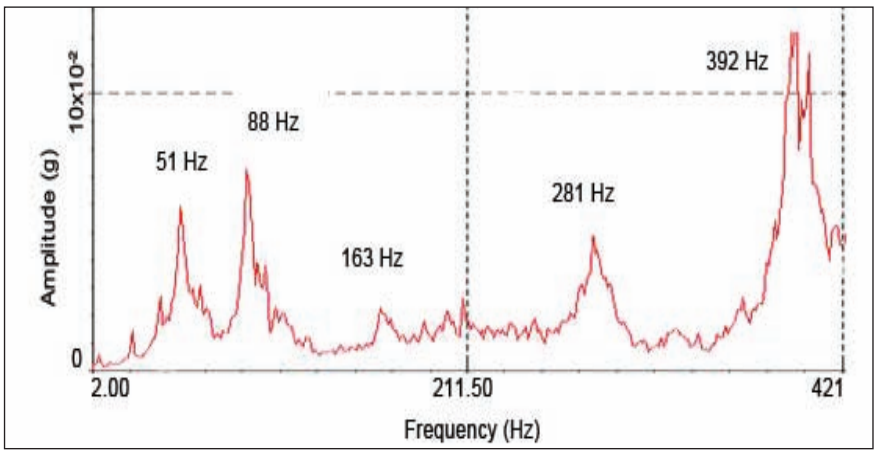

Fig. 2 *Typical vibration spectra*

The maximum amplitude of vibration is observed in the first span in all the tubes and this is due to the effect of sodium cross flow at this location. The amplitude of vibration was less in the outlet region compared to the inlet region. The resultant amplitude of vibration measured is 0.12 g and the maximum amplitude of displacement calculated is 110 microns. The resulting bending stress is much lower than the endurance limit of the material. The design of steam generator support system is found to be safe against flow induced vibration.

II.15 Demonstration of PFBR Under Sodium Ultrasonic Scanner Performance by Water Experiments

Under sodium ultrasonic scanner (USUSS) has been developed for use in PFBR during reactor shutdown. The ultrasound in the fast breeder reactor has been utilized for two operations. The first operation is to detect any fuel subassembly projecting from its original location and also to check the decoupling of ARDMs before rotation of plugs for fuel handling. Another operation is to locate the tops of the core subassemblies located directly underneath the scanner for the safe positioning of the scanner inside the reactor. To establish the methodology for the detection of subassembly protrusion and decoupling of ARDMs, various experiments were carried out in water.

Methodology for the detection of subassembly protrusion

In PFBR two methods are envisaged for finding the presence of an object in the 100 mm gap between subassemblies top and lattice plate. Depending on the orientation of the projected subassembly with respect to the transducer, echo may or may not be received by the transducer. Receiving the echo directly from the projected object is called direct imaging and other one is indirect imaging using shadowing effect of protruded object on blocking subassemblies. The blocking subassemblies are the B_4C shielding subassemblies projected by 100 mm above

the normal subassemblies top elevation and located in the last row of the core. In the later technique there is a change in the echo pattern received from the blocking subassembly due to the protruding object. In order to study the shadowing effect, a sector of PFBR core configuration was simulated in a ten meter water tank as shown in Figure 1 and various experiments were carried out in water with cylinders of different diameter placed in the last row. Figure 2 shows the reduction in the echo amplitude from B_4C shielding subassemblies projected by 100 mm above the normal subassembly top elevation for the protrusion of subassembly by 50 mm for various distances from the transducer. From the experimental results, it was decided to have 130 mm diameter and 100 mm long attachments to the last row of B_4C shielding subassemblies.

Imaging experiments with ARDMs

For PFBR, it is necessary to ensure that no control & safety rod drive mechanism (CSRDM) or diverse safety rod drive mechanism (DSRDM) or control and safety rod (CSR) is protruded in the above core plenum before starting the fuel handling operation. To study the feasibility of direct ultrasonic imaging of CSRDM/DSRDM and CSR, experiments were carried out in water using in house developed personnel computer based automatic scanning system.

The simulated object of CSRDM, DSRDM and CSR was imaged ultrasonically at possible orientations and the echo was obtained from the object.

The DSRDM is having a rectangular slot and conical portion of 36 mm.

Fig. 1 *Experimental setup with simulated core configuration of mock up subassemblies heads in the 10 m water tank*

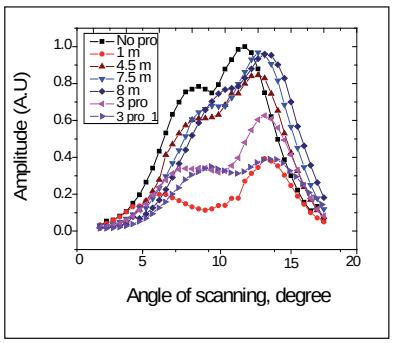

Fig. 2 *Echo amplitude reduction from the shielding subassemblies for various protrusion distances*

The cylindrical portion of DSRDM without the rectangular slot reflects very strong echo compared to DSRDM with the rectangular slot. The echo is not received from conical portion of 36 mm. However, as the conical portion is at the extreme end of the DSRDM, it will not hinder the fuel handling operation even if it is protruded from top.

In the case of CSRDM, the cylindrical portion gives a very good image provided the slot of the CSRDM is not in the direct view of the ultrasonic transducer. The conical portion of 53.8 mm does not give back echo irrespective of the position of the slot. The position of CSRDM & DSRDM can also be measured using potentiometer as well as synchros. Ultrasonic imaging will provide alternative option in determining the positions ensuring redundancy in measurements and thus increasing safety.

The CSR consists of cylindrical portion at both the ends with 84 mm conical portion at the centre. The experiment shows that conical portion does not give back echo but the cylindrical portion of both ends gives back sufficient echo. Therefore CSR can be ultrasonically imaged using direct imaging technique in all possible conditions.

Testing of ultrasonic transducer against gamma radiation

In-house developed high temperature ultrasonic transducers which can work upto 453 K in liquid sodium are used in the under sodium ultrasonic scanner. These transducers should withstand the neutron and gamma radiation in the reactor during the scanner operation. Gamma flux in the reactor during fuel handling will be $1.2x10^5$ rad/hour. Irradiation experiments on the ultrasonic transducer were carried out in the gamma chamber. The radiation level at the center of the gamma chamber is $3x10^5$ rad/hour. Considering the transducer life as five years, the transducer was exposed to the radiation level of $3x10^5$ rad/hour in the gamma chamber for 40 days.

The transducer was exposed to a cumulative radiation of $2.88x10^9$ rads in forty days. A scan wave form shows that the echo amplitude remains almost same throughout the experiment indicating the performance of the transducer was not changed due to irradiation. The insulation resistance (IR) value of the mineral insulated (MI) cable of the transducer was found to be increased with the duration of gamma radiation.

II.16 Radiometry and Gammatography Testing of Various Shielding Components

Proper shield design, its fabrication and installation play an important role in controlling radiation exposures to operating staff and public. Shields are in variety of forms, shapes and sizes. The most commonly used shielding materials are concrete and lead. Lead shields are fabricated by pouring lead in steel shells of desired size and shape. Due to the relatively large contraction of lead on cooling, porosities, cavities and blow-holes may be formed. Poor bonding of lead with the steel structure would also result in loss of shielding. In addition, internal structural details such as rod and stiffeners might impair uniform lead flow. Many shielding components are made by filling lead shots. Non uniformity of lead shot filling and setting down would result in shielding loss. Thus it is necessary to ensure the integrity of the shield structure using appropriate nondestructive testing.

Here the state of the art Gammatography (radiometry) method based on the gamma ray spectrometry, is used in which the exit surface of the shield structure is scanned for the uncolloided flux using NaI(Tl) scintillation detector.

The selectivity and high sensitivity of the detector enables reduction of required source strengths by more than an order of magnitude. The advantages are that the normal background in the range of interest is practically negligible and the interference from scattered radiation is totally avoided. The method has been used for testing lead thicknesses varying from few tens of mm to about 250 mm and detects loss in shielding integrity down to 2% of thickness.

Earlier a NaI(Tl) detector based gamma ray spectrometer with single channel analyzer and counter timer was being used. With the advent of handheld gamma ray spectrometer with connectivity to laptops field testing has been made simpler. Many of the PFBR shielding componets have been tested for their shielding integrity, uniformity of concrete pouring and lead shot filling using radiometry. Shielding mock-ups have been tested and qualified prior to making of actual shieldings.

Sodium condenser shielding arrangement

The lead shielding for PFBR sodium condenser arrangement is a lead poured structure. It is having ID of 1580 mm and OD of 1980 mm with 180 mm lead thickness. The shielding structure of 5000 mm height is made up of four rings kept one over other. Two semicircular parts make each ring. The rings have penetrations for sodium pipe lines at different places. If one uses conventional radiometery for testing the integrity of lead pouring, the streaming dose rates would completely mask any small lead loss in shielding thickness. Hence it was tested using gammatography technique (Figure 1).

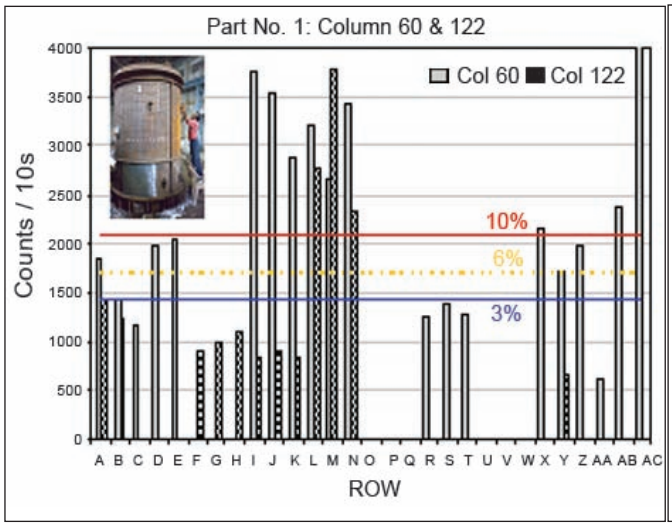

Fig. 1 *Sodium condenser shielding*

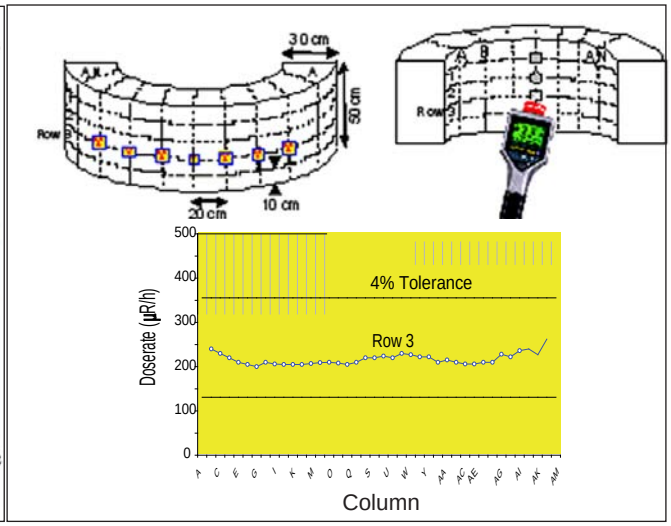

Fig. 2 *Radiometry results of IFTM cast steel blocks*

IFTM shielding (cast steel block & cast iron rings)

The IFTM cast steel block was semicircular in shape with inner radius 2270 mm, outer radius 2570 mm, height 500 mm and steel thickness 300 mm. Radiometry testing (Figure 2) of the IFTM cast steel block revealed that the reduction in steel thickness is well within the 4% of designed steel thickness of 300 mm.

The dimensions of the cast iron rings are 1700 mm OD, 800 mm ID and 850 mm height. All the shield structures were made of cast iron with density 7.2 g/cm^3. A ^{60}Co source of 120 GBq (3.245 Ci) was used for the testing. Conventional 'Radiometry' testing on IFTM shield structures viz., a) six numbers of cast iron rings, b) flange and c) cast iron block was carried out.

The radiometry testing (Figure 3) indicated that the shielding integrity of all the six numbers of cast iron rings, flange and cast iron block is found to be satisfactory and their thicknesses are found to be within 6% tolerance values.

Lead poured and lead shot filled shielding blocks

Lead blocks (PbSb5 GR: IS1654) of Cat-IV liquid effluent tank in FB of dimensions 250 mm by 250 mm and 100 mm thick with three numbers of 'tees' embedded inside each block (two on one side and one on the opposite side) with grooves and with density of 11.2 g/cm^3 as per the design were radiometry tested using a ^{60}Co source of 9.2 MBq strength. The radiometry testing (Figure 4) revealed that the reduction in lead thickness, if any, is within 3% tolerance of designed thickness at all locations in the blocks that were tested and the density of lead is also as per the specifications.

Fig. 5 *Lead shots filled PI flask shell mockup*

The Gammatography technique was employed to evaluate the shielding integrity of mockup of PI flask shell representing a sector (Figure 5). In the form of 50x 50 mm grid, a total of 80 locations in the mockup were tested using handheld spectrometer. The effectiveness of packing density of lead shots was found to be within 6% tolerance at around 90% of locations. In the remaining locations it varied upto 10%.

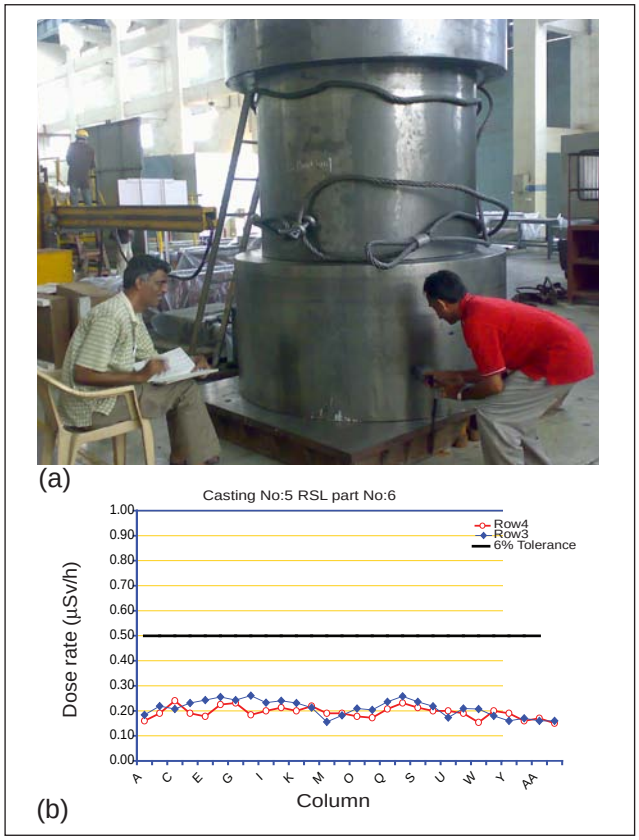

Fig. 3 *(a) IFTM cast iron shielding rings and (b) Radiometry test results*

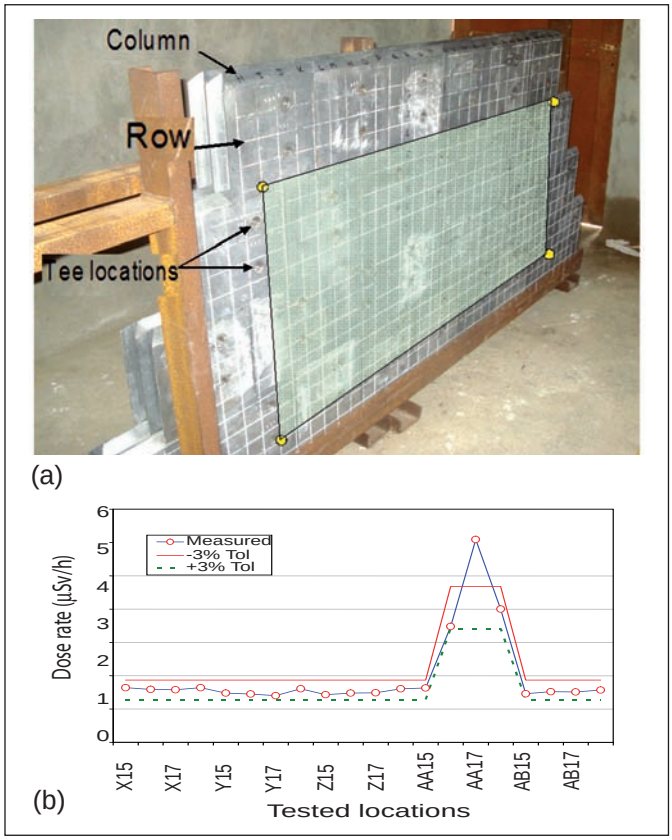

Fig. 4 *(a) Lead poured shielding blocks (b) Test results*

II.17 Calibration and Testing of Electrochemical Hydrogen Meters

Ten numbers of electrochemical hydrogen meters (ECHMs) are to be installed in PFBR for steam leak detection. These sensors were fabricated, assembled, calibrated and tested in Chemistry Group. The associated electronic units for the sensor were designed in-house and fabricated by ECIL. These instruments were qualified for PFBR application by subjecting them to the prescribed EMI/EMC tests and the environmental tests. Calibration and testing are carried out in bench top sodium loops (~10 kg sodium inventory), in which hydrogen concentrations could be precisely controlled using a mini cold trap section of the loop. The outputs of the sensors are continuously monitored at the operating temperature of 723 K and various tests simulating plant conditions are also carried out. The laboratory testing involves (i) calibration of electrochemical hydrogen meters along with the electronics module, (ii) simulation of plant conditions such as large decrease in sodium temperature, line heater failure, etc. and (iii) response of electrochemical hydrogen meters for meter temperature variations.

(i) Calibration

The electrochemical hydrogen sensor uses the principle of a concentration cell and can be used to measure the hydrogen pressures. The cell is represented as:

p_{H_2} (sample) // electrolyte // p_{H_2} (reference)

The expression relating the output of the sensor E(V), with hydrogen concentration in sodium, C_H are given in Table 1.

The sensors are tested and calibrated in the mini sodium loop (shown in Figure 1) that is set up for this purpose. In each loop, the meter section can accommodate six sensors and twelve sensors are calibrated simultaneously in two such loops. In the calibration set up, the temperatures of the cold trap and the sensors are well defined and controlled. Hydrogen concentration in the sodium loop is determined from the solubility of hydrogen at each cold trap temperature, which is well established and reported in the literature.

This procedure ensures calibration with absolute hydrogen

Fig. 1 *Testing of ECHMs in hexamini bench-top sodium loop*

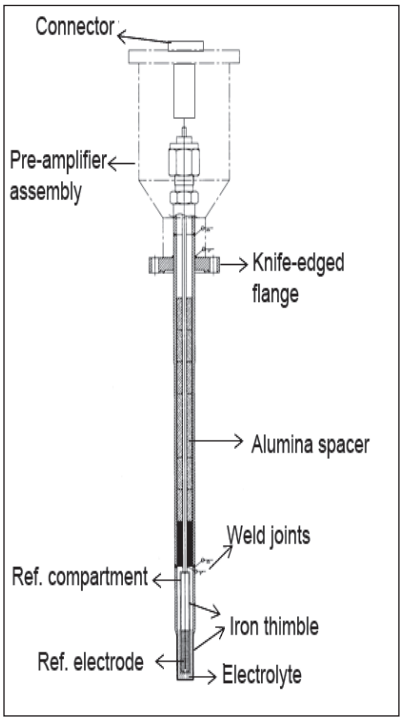

Fig. 2 *Schematic of electrochemical hydrogen meter*

Table 1: Relation between the potential and hydrogen concentration

For the cell is p_{H_2} (sample) // electrolyte //p_{H_2} (reference). The relation between the potential and the concentration hydrogen is given by

$$E(V) = \frac{RT_S}{2F} \times \left[\ln(p_{H_2}{}^{reference}) - 2\ln C_H + 2\ln k\right]$$

where, k is the Siverts' constant for Na-H system and p_{H_2} (reference) is a constant at the meter operating temperature, T_S. Rearranging the terms, the C_H can be expressed in the simplified form as

$$C_H = \exp\left(\frac{E(V) - A}{B}\right)$$

where A and B are system constants, which are determined during the calibration of the sensor T_S, 723 K

concentration in sodium. For different C_H, the corresponding E (V) is measured.

A signal conditioning preamplifier is placed close to the sensor within the meter assembly as shown schematically in Figure 2.

The linearity of amplified sensor output with gain 100, E_{amp}, (E_{amp}= 100*E (V)) with respect to logarithm of hydrogen concentration in sodium (C_H) is verified during the calibration from 50 to 500 ppb to determine the calibration constants A and B. These constants are then entered into the microcontroller of the electrochemical hydrogen meters display unit. By measuring the E_{amp} accurately, the ECHMs display unit calculates the unknown hydrogen concentration (ppm) in sodium and the same is displayed in units of 'ppb' in digital panel meter of the ECHMs display unit. The same analog output (calibrated in ppb) is available for recording/logging purposes from the rear panel of the ECHMs display unit. Typical calibration graphs of three meters are shown in Figure 3.

Simulation of plant conditions along with calibration, each meter is also tested at conditions simulating plant operational situations such as large decrease in sodium temperature arising from line heater failure or sodium dumping etc. These tests are done in order to determine the duration for restoration of meter signal for plant availability under such conditions. The duration for restoration of meter signal was typically ~20 hours for long term (24 hours at low temperature) and ~2 hours for short term (5 hours at low temperature cycle tests between 723 and 423 K.

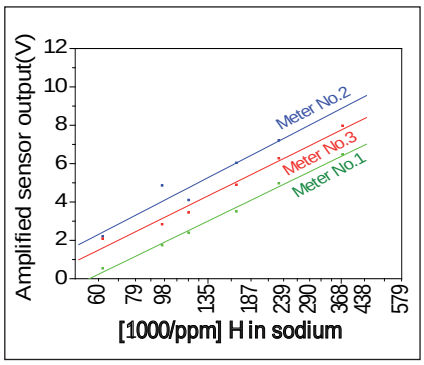

Fig. 3 *Typical calibration graph for three meters assembled for PFBR*

Temperature coefficient of each sensor is determined by changing the meter temperature from 703 to 743 K in steps of 10 degrees and recording the meter output at a fixed hydrogen level in the loop. The temperature coefficient of the sensor is found to be ~0.1 V/ K (E_{amp}).

II.18 Advanced Methodology in Fabrication of Hydrogen in Sodium Detector (HSD)

Liquid sodium is used as the coolant in the primary/secondary loop and steam is used in the tertiary loop for power generation in liquid metal fast breeder reactors. The liquid sodium in the secondary loop is separated from high pressure steam in the tertiary loop by thin walled steel tubes at the steam generator. Development of any defects in steel tubes during reactor operation would lead to a major accident. To prevent such an event, it is essential to detect steam leak into sodium at its inception. In the case of occurrence of such an event with sodium temperature > 673 K, the hydrogen and sodium hydroxide produced in the sodium-water reaction would completely dissolve in sodium. This would cause an increase in hydrogen level concentration in sodium. The hydrogen sensor designed and fabricated indigenously is used for online detection of such failures at its inception.

As this sensor is a critical component of the safety system of reactor, a stringent manufacturing procedure was followed to achieve the required dimensional and geometrical tolerances. The sensor is fabricated out of special materials like pure iron and stainless steel. A special automated welding process called orbital welding process was utilized to manufacture the sensor. A systematic procedure was developed and established for machining of the components, dissimilar welding of thin walled iron thimble with austenitic stainless steel pipe sleeve, maintaining dimensional tolerances and weld quality.

A schematic diagram of the hydrogen in sodium detector (HSD) which is a electrochemical based hydrogen meter (ECHM) is shown in Figure 1. It consists of four parts, namely, ECHM-hood, ECHM-probe, ECHM-housing and reference electrode. The critical features of ECHM-probe and ECHM-housing are as follows:

ECHM-probe

The subassembly is made out of five components namely SS threaded adaptor, pipe sleeve, pure iron thimble, high vacuum flange and cap nut. A typical sketch of ECHM-probe is shown in Figure 1b.

This part of the sensor was made by manual TIG welding process in the past, but, the desired weld quality could not be achieved consistently. Hence, orbital welding process, which is an automated and autogenous TIG welding process, was employed. In this process, the work piece is held stationary in a weld fixture and the tungsten electrode with shielding gas nozzle rotates around the work piece to form a weld joint. An orbital welding system consists of a power source, weld head and a weld fixture.

The power source provides the arc, drives the weld head and shields gas nozzle around the weld joint. The most commonly used weld heads are enclosed weld head and open arc wire feed weld head. Enclosed weld heads provide an inert atmosphere chamber surrounding the weld joint and open arc weld heads are used for thick wall applications (>3.5 mm) with filler wire feeder. Conventionally this process is used for welding of standard tubes and pipes. But, we have made special fixtures to deploy the orbital welding system for manufacture of the sensor.

ECHM-Housing (Figure 2)

There are many critical requirements in machining of components and fabrication of subassemblies of ECHM-housing like (i) machining of a 210 mm long finned pipe sleeve to a straightness tolerance of 0.2 mm and with a surface finish 0.2 µm, (ii) machining of pulled out nozzles and (iii) Eccentric drilling of 45 holes of 2 mm diameter with a pitch of

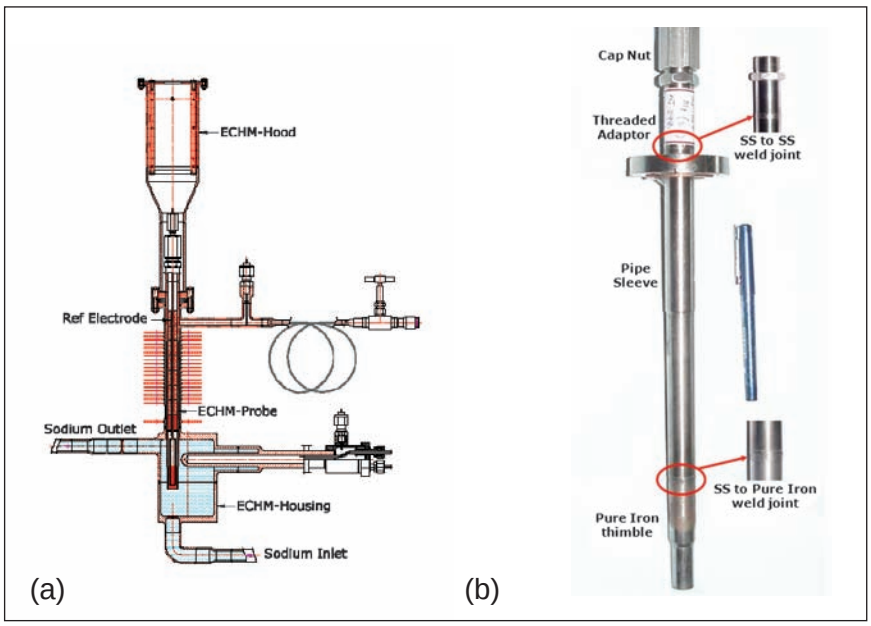

Fig. 1 *(a) Hydrogen in sodium detector (b) Electrochemical hydrogen meter probe*

2.5 mm in X & Y Plane. All the butt weld joints were qualified by 100% liquid penetrant examination and 100% X-radiography. The whole assembly was subjected to helium leak testing under pressure and the leak rate was found to be within the acceptable limit of 1 x10^{-7} pa. l / s.

The challenges faced and the experience gained during various stages of fabrication, largely due to intricate shape and miniature in size, in meeting the desired quality are useful towards optimisation and improving the design of the detector for future reactors.

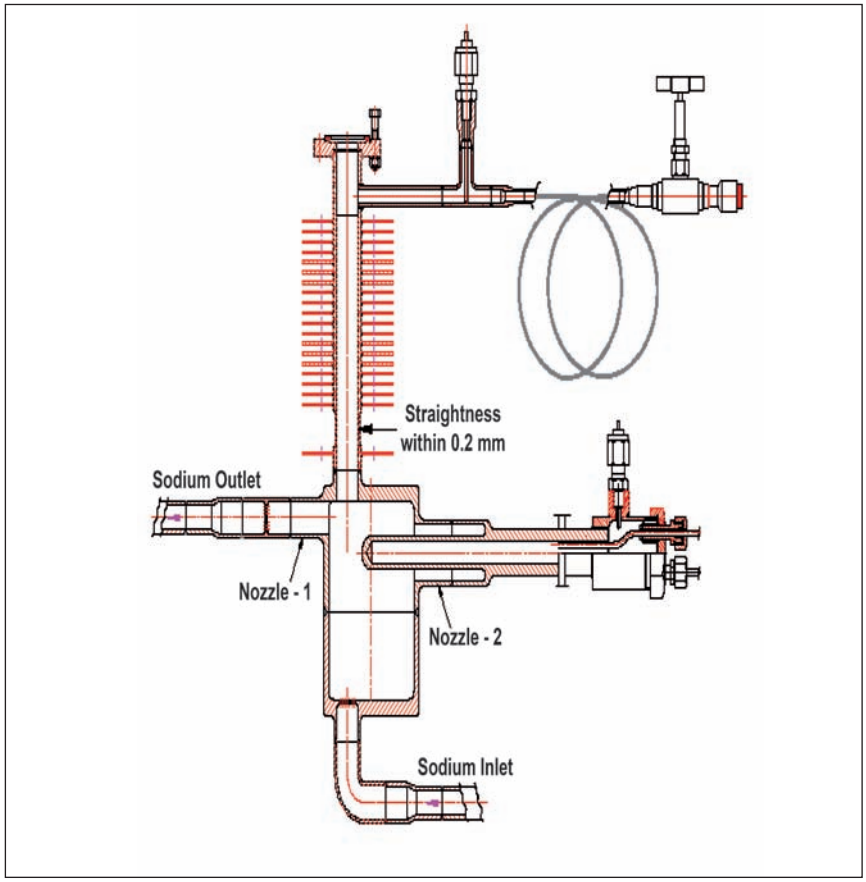

Fig. 2 *Electrochemical hydrogen meter housing*

II.19 An Absolute Method for Assessment of Alignment of Under-Sodium Ultrasonic Scanner

A procedure has been developed for detection of fuel subassembly protrusion using under-sodium ultrasonic scanner (USUSS) in PFBR based on the drop in reflection amplitude from peripheral subassemblies in case of protrusion. For unambiguous analysis of the reflected signals from the peripheral subassemblies, it is required to know the orientation of ultrasonic transducers in the USUSS with respect to horizontal plane. For this purpose retro-reflector (Figure 1) is designed to serve as a reference target. It reflects the ultrasonic energy parallel to the incident beam. Thus, high intensity reflections are obtained even in case of misalignment of the transducer and the target.

In order to develop the methodology for measuring the misalignment of the transducer, experiments were carried out using an in-house developed C-scan imaging system. Figure 2 shows typical amplitude and time of flight based C-scan images of the retro reflector obtained by scanning a 1 MHz transducer at about 300 mm away from the reflector.

The studies with various misalignments of the transducer indicated that the minimum in the time of flight based C-scan always appears when the transducer is in the same horizontal plane as the vertex of the retro-reflector (Figure 2), as shown schematically in Figure 3. In this configuration, the shortest time path always corresponds to the closest distance between the center of the transducer and the vertex of the target, irrespective of the misalignment of the transducer.

However, the amplitude maximum occurs at the vertical location where the central beam of the transducer is aligned in the direction of the vertex of the target (position *b* in Figure 3). The vertical locations corresponding to the minimum in the time of flight based C-scan and the maximum in the amplitude based C-scan coincide (Figure 2), only when the transducer is aligned horizontally. For better visualization, the profile of the target is superimposed on the C-scan images in Figure 2.

This distinction in the behaviour of time of flight minimum and amplitude maximum provides

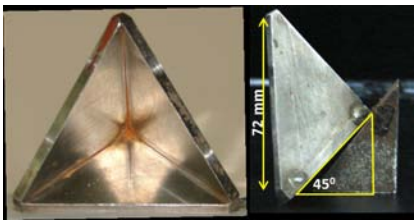

Fig. 1 *The retro-reflector target showing its optimized orientation*

a means to estimate the misalignment. For example, if the transducer is misaligned upwards as shown in Figure 3, the maximum amplitude will be obtained when the transducer is at location *b*, whereas the minimum in the time of flight will occur when the transducer is at the vertical location *a***.** By knowing the vertical distance between the two locations *ab*, the misalignment of the transducer θ can be measured. The target offers maximum area for retro-reflection to the ultrasonic beam when the plane of its opening is perpendicular to the horizontal plane. In this position the base plate of the target will be approximately 35° with reference to the horizontal. However, the sections of the face plane of the target are asymmetrically placed on either side of the horizontal

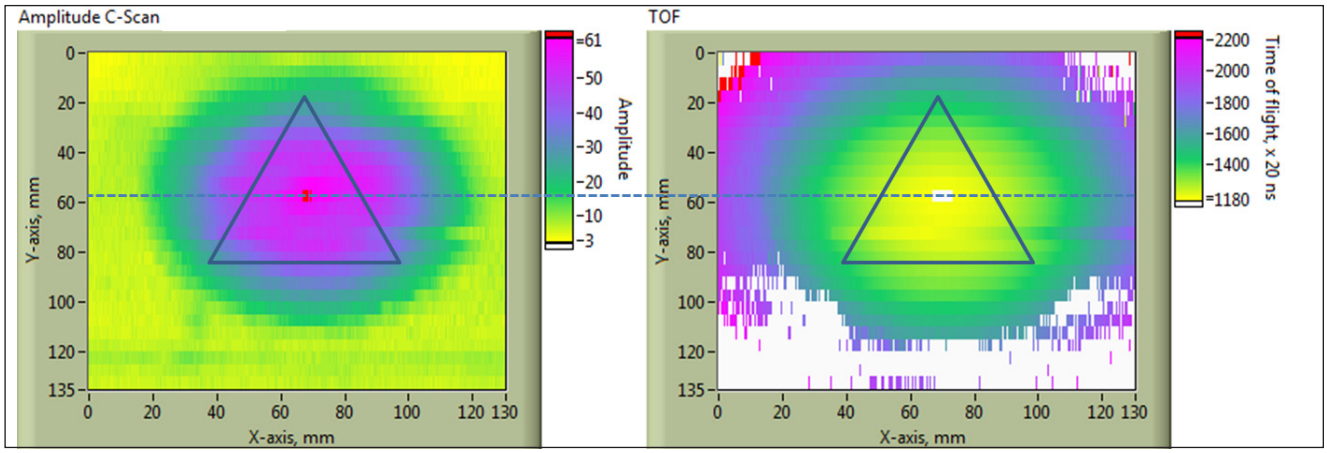

Fig. 2 *Amplitude and time of flight (TOF) based c-scans of the retro-reflector with the base at 45^0 orientation*

along vertex. As a result, the upward misalignment that can be measured is less than the downward misalignment. In order to make measurable misalignments nearly equal on either side of the horizontal, various angles (>35^o) of the base plate were studied. Distortion was observed in the retro-reflected beam when the angle is greater than 47^o. Based on these observations, the orientation of the target was optimized at 45^o (Figure 1).

The validity of the above described methodology is also demonstrated in a 5 meter diameter water tank using a θ-Z scanner system. The retro-reflector was kept with 45^o orientation at a distance of about four meter from the transducer. The angle of the transducer (θ) was first aligned by maximizing the reflection from the retro-reflector. The ultrasonic B-scan images were then acquired by scanning the transducer for 130 mm in the vertical (Z-) direction with the transducer in 0° and 0.6^o upwards misalignment conditions. As the scanner has control only for two axes (θ and Z), the vertical tilt was introduced by placing shims

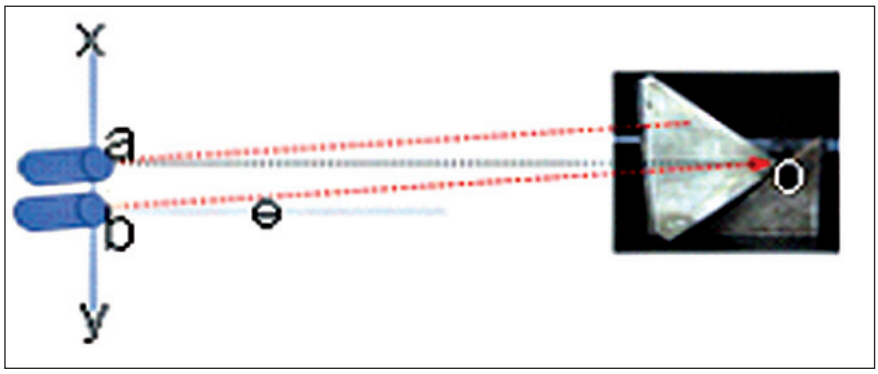

Fig. 3 *Schematic drawing the transducer locations corresponding to (a) The minimum time of flight and (b) The maximum amplitude for an upward transducer misalignment*

of appropriate thickness under the front side of the transducer. Figure 4 shows the B-scan images generated by acquiring 65 A-scans at 2 mm intervals along the centerline of the retro-reflector with 0^o and 0.6^o transducer orientations. The B-scan images in Figures 4(b) and 4(d) are expanded in time scale to resolve the individual cycles of the reflections from the retro-reflector. It can be seen in Figure 4(b) that the time of flight minimum occurs at 38 mm, whereas the amplitude maximum (marked in red) occurs at 58 mm, as shown by the cursors at the two positions. The distance of 20 mm (58 - 38 mm) at 4 m corresponds to 0.3° downwards tilt (Figure 3). This indicates that the original position of the transducer was about 0.3° downwards tilted.

On tilting the transducer through 0.6^o, the maximum amplitude location moved downwards to 0 mm position, whereas, the position corresponding to the minimum TOF is still the same at 38 mm. The distance of 38 mm (38 to 0 mm) at four meter corresponds to 0.6° upward tilt.

This demonstrated the validity of the approach for measuring the misalignment. The present methodology for assessment of alignment of under-sodium ultrasonic scanner is an absolute method and no prior reference/ calibration is needed.

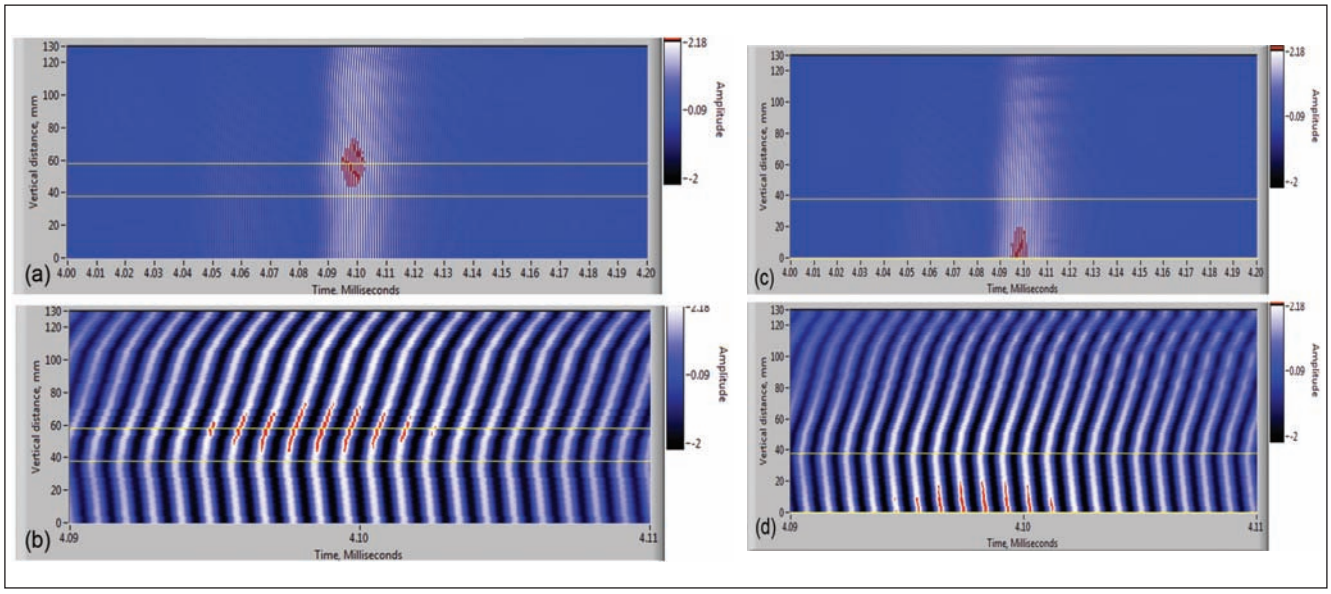

Fig. 4 *B-scan image generated by acquiring 65 A-scans at 2 mm intervals along the centre line of the retro-reflector with (a-b) 0° transducer orientation and (c-d) 0.6° transducer orientation*

II.20 Commissioning of PFBR Training Simulator at BHAVINI

Preparatory work for the migration of first version of PFBR operator training simulator was started in 2010 at BHAVINI. As we all know that a full scope replica operator training simulator is being developed with the main role players being engineers from Computer Division as a development team and the design experts from Nuclear Safety Engineering Group and Reactor Engineering Group as the simulated process model evaluation team. The simulated process models that are developed tested and validated at our Centre need to be ported to PFBR training simulator at BHAVINI for further testing and approval. Before porting the models, one has to ensure that the hardware setup for simulator control room is ready in all aspects i.e. with all the control panels and operator consoles installed and commissioned. The commissioning activities that are carried out at BHAVINI with the help of the Commissioning Group towards achieving the target are reported here.

The layout of PFBR Training Simulator which is located at Training Centre, BHAVINI consists of simulator main control room (MCR) located at the centre, server room, LCC room, backup control room (BCR) and handling control room (HCR) located on either side of the main control room (MCR), the shift charge engineers room and instructor station located in front of main control room (Figure 1).

The hardware architecture of PFBR training simulator at BHAVINI includes, control panels, consoles, simulator servers, instructor station, virtual panels, field terminal device, network & ethernet switches, power supply distribution board, LCC Panels, large video display panel, BCR panels, HCR panels and display stations. All the components are networked using ethernet switches for signal flow between them. In principle, it follows the data highway mechanism adapted in the real plant and the signal segregation is done as per the Safety Classification of reactor systems like safety critical -1, 2 (SC1 & SC2) and non nuclear system (NNS). The simulated plant signals are communicated through I/O computers to the control panels and control consoles.

Commissioning work at BHAVINI started with physical checking of control panels, consoles, backup control room and handling control room panels (Figures 2,3 and 4). Task force meetings were held periodically to review the status of commissioning work, jointly by IGCAR and BHAVINI engineers. As a first step the availability of power supply to all the panels in the simulator control room was ensured. A check list was prepared to check the hardware and software systems of the simulator in a systematic manner. The hardware panel checking was carried out for each panel with respect to alarm inscription, display of parameters, controls etc. as per the approved drawings. The simulator server and standby server were commissioned by loading and testing UNIX operating system & simulation

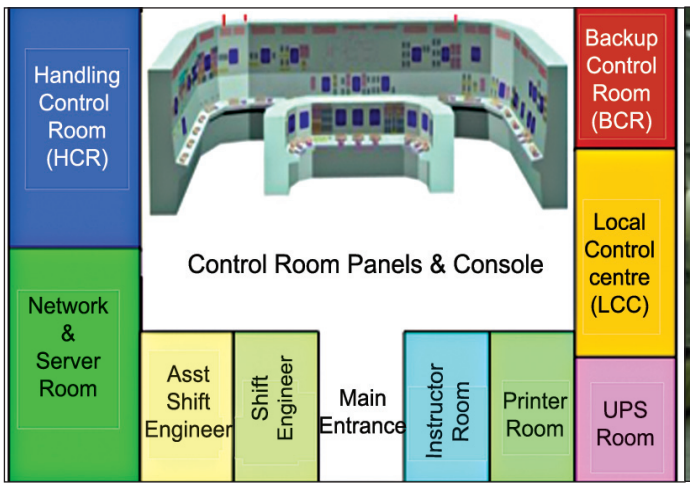

Fig. 1 *BHAVINI simulator layout*

Fig. 2 *BHAVINI simulator main control room*

tool. All the display stations were loaded with client module in order to display the simulated parameters and the flow sheet mimics. Network connectivity was checked thoroughly for appropriate signal communication between simulator, control panels, consoles, display stations, and instruction station. All the panel alarm windows, lamp indications and meters were checked for healthiness. Before proceeding for steady state testing, off line and on line I/O signal testing was carried out. The panel meter readings were checked for correctness and configured with appropriate units.

Migration of developed process models was carried out based on the experience gained on simulator development platform at IGCAR. A migration procedure has also been established for reconfiguration of the developed modules at a later stage. Latest version of the software module was ported to BHAVINI and interfaced with the hardware panels. The large display panel was configured by displaying the simulator mimic diagrams. Backup control room was commissioned following the same procedure.

External logic codes were developed wherever necessary for panel annunciation like system faulty, component tripped on fault; system temperature low and system pressure high etc.

Porting of core temperature monitoring system model was carried out successfully. The display station on operator console was configured to display the 2D core temperature distribution system for monitoring purpose.

Fig. 3 *Handling control room*

Integrated testing was carried out for all process models i.e. neutronics, primary and secondary sodium system, safety grade decay heat removal system, steam water and electrical systems. All the process models were tested for steady state and transient conditions. All the process parameters were recorded and checked with the design data and a test report was prepared by capturing the profiles. The steady state profiles were checked for various system parameters like neutronic/thermal power, primary sodium inlet and outlet temperature, steam generator inlet/outlet temperature/ pressure/ enthalpy, hot well level, deaerator level, pressure, temperature, LPH/ HPH inlet and outlet temperature/ flow, heater levels, generator/ bus / battery voltage /power/ current etc were checked and recorded.

After completing the steady state testing, system transients were simulated and the dynamic behavior of the process models were tested and analyzed. The profiles of various process parameters like power, reactivity, flow, temperature, pressure, level etc were recorded for each transient for analysis purpose. The transients tested include neutronics system - inadvertent withdrawal of one control rod, primary sodium system - one primary sodium pump trip/seizure, primary pipe rupture, intermediate heat exchanger sleeve valve closure, secondary sodium system - one SSP trip, steam water system - one/both CWP trip, one/both CEP trip, one/ both BFP trip, turbine trip, electrical system-generator trip, station black out, class-IV failure and grid failure.

Fig. 4 *Backup control room*

II.21 Influence of Sodium on the Properties of Structural Materials

In PFBR, (SS316 LN) and modified 9Cr-1Mo steel (P91) are used as the materials of construction for intermediate heat exchanger and steam generator respectively. The compatibility of these materials with liquid sodium is of utmost importance for the safe operation of the reactor. At high temperatures, liquid sodium in contact with these steels can transport alloying elements such as nickel, chromium, molybdenum and carbon. Transport of carbon causes the steels to either carburize or decarburize depending on the relative carbon activities in steels and sodium at the relevant temperatures. Selective leaching of nickel causes modification of the surface layer, resulting in material degradation. To assess the long term integrity and performance of structural materials in flowing high temperature liquid sodium, there is a need to evaluate the mechanical properties in sodium.

Effect of sodium exposure on microstructure and mechanical properties of SS316 LN and P91

A bi-metallic (BIM) sodium loop was designed and constructed, which simulates the secondary circuit of PFBR with respect to sodium velocity, temperature gradient, material sequence and area ratios. The changes in SS316 LN and P91 were investigated after 30000 h of exposure at 798 K in bi-metallic loop.

Microstructures of type 316LN stainless steel are shown in Figure 1. The matrix of the sodium exposed material had a sensitized microstructure; it also showed a degraded layer of about 10 µm depth (Figure 1(c)). The degraded layer was confirmed to be ferrite by GIXRD analysis. Tempered martensitic microstructure with abundant precipitates along prior austenite and martensitic lath boundaries were observed in normalized and tempered (NT) condition of modified 9Cr-1Mo steel (Figure 2(a)). An increase in the density of carbides was observed in thermally aged (Figure 2(b)) and sodium exposed materials (Figure 2(c)).

Analysis of the cross-section of the sodium exposed SS316 LN specimen using EDAX technique showed depletion of nickel and chromium at the surface (Figure 3). Concentration of nickel at 2 µm distance was about 4 wt.% which reached the matrix concentration at the depth of ~25 µm. Similar trend was observed for chromium also. At around 30 µm depth, chromium level reached the original concentration of the matrix (Figure 3).

Microhardness of sodium exposed SS316 LN specimens was found to decrease as compared to thermally aged specimens. Hardness for thermally aged condition was around 200 VHN, whereas for sodium exposed material, the hardness values gradually decreased from around 480 VHN at the surface due to carburization and at about 100 µm, attained the matrix hardness. Similar trend was observed for modified 9Cr-1Mo steel, but the decrease in hardness was not significant.

Results of tensile and impact tests are tabulated in Table 1. In the case of SS316 LN, changes in yield strength (YS) and ultimate tensile strength (UTS) due to sodium exposure were not significantly different from those for thermal ageing. However, the sodium exposed steel showed a decrease in ductility as compared to mill-annealed and thermally aged specimens. The changes observed in yield strength, ultimate tensile strength and ductility of P91 steel due to sodium exposure were only marginal. Impact energy values for sodium exposed 316LN SS was lower compared to that for mill-annealed and thermally aged material. Decrease in impact energy was noticed for sodium exposed as well as thermally aged P91 compared to that for NT(normalized and tempered). Change in impact

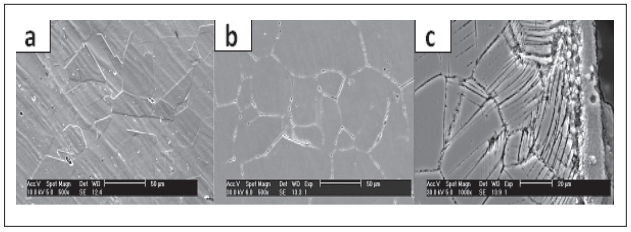

Fig. 1 *Micrographs of SS316 LN: (a) Mill-annealed, (b) Thermally aged and (c) Sodium exposed*

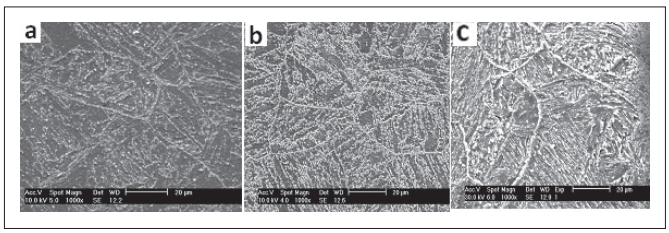

Fig. 2 *Micrographs of P91 steel (a) Mill-annealed, (b)Thermally aged and (c) Sodium exposed*

Table 1:Tensile and impact data for 316LN SS and P91				
Material condition	YS (MPa)	UTS (MPa)	TE(%)	C_v(J)
316 LN SS annealed	324	627	66	144
316 LN SS: aged	303	577	61	143
316 LN SS:Na-exposed	373	576	24	123
P91:N&T	510	629	20	99
P91: aged	443	602	18	45
P91:Na-exposed	446	636	22	48

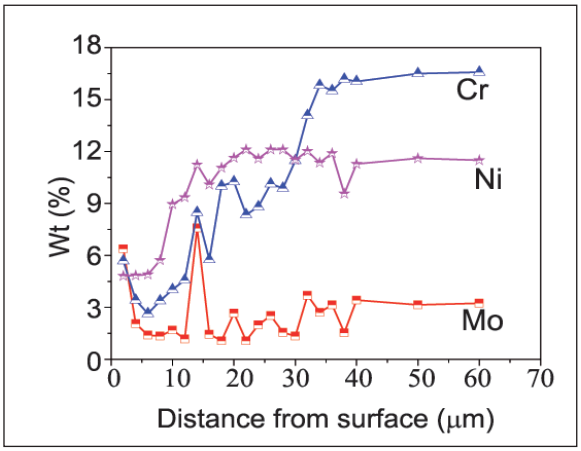

Fig. 3 *Composition profile show depletion of Cr and Ni in SS316 LN exposed to sodium at 798 K*

energy between thermally aged and sodium exposed materials was insignificant.

Creep properties of SS316 LN in flowing sodium

The influence of flowing sodium on creep deformation and rupture behaviour of 316L(N) austenitic stainless steel has been investigated at 873 K over a stress range of 235 – 305 MPa, in the creep test loop of in-sodium test facility. Velocity of the liquid sodium across the creep specimen was maintained at 2.5 m/sec. Oxygen content of the flowing sodium was maintained at less than 3 ppm by continuously passing the liquid sodium through a cold trap. The creep test results are compared with those obtained from testing in air environment. The steady state creep rate of the material was found not to influence appreciably by the testing environments. The time to onset of tertiary stage of creep deformation was delayed in flowing sodium over that in air. The creep-rupture lives of the material increased in sodium environment over that in air, which became more pronounced at lower applied stresses (Figure 4). The increase in rupture life of the material in flowing sodium was accompanied by an increase in rupture ductility (Figure 5). The creep damage on specimen surface as well as inside the specimen was less in specimen tested in sodium. SEM fractographic investigation revealed predominantly transgranular dimple failure for the specimen tested in sodium, whereas predominantly intergranular creep failure was observed in the air tested specimens. Almost no oxidation was observed in the creep tested specimens in the sodium environment. Absence of oxidation and less creep damage cavitation extended the secondary state in liquid sodium tests and led to increase in creep rupture life and ductility of the material as compared to that in air.

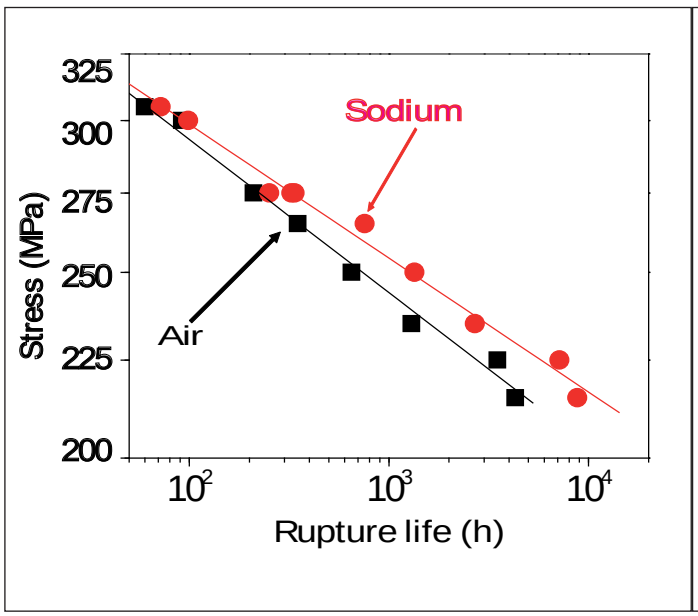

Fig. 4 *Comparison of creep rupture life of type SS316 LN in flowing sodium and in air environment at 873 K*

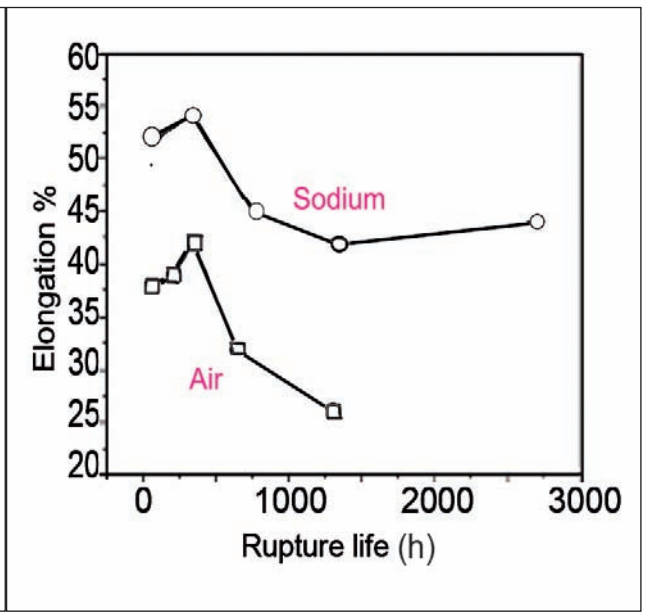

Fig. 5 *Comparison of creep rupture ductility of type SS316 LN in flowing sodium and in air environment at 873 K*

II.22 3D Modeling and Animation of PFBR Fuel Handling System at Advanced Visualization Centre

The fuel handling operations of the PFBR will be performed off line i.e. with the reactor in shutdown condition. The operators performing the fuel handling operations in the PFBR have to be certified during every fuel handling cycle. Hence it becomes an utmost necessity to ensure that the operators are equipped with sufficient on hand experience and knowledge about the system before they engage in the fuel handling activities of the actual reactor.

This can be achieved with the help of 3D advanced visualization centre featuring 3D passive high definition stereoscopic projection, powerful graphics workstation and multipoint audio system to give a fully immersed experience to the user.

PFBR fuel handling system is classified into ex-vessel handling and in-vessel handling, each of them is further sub divided into fresh subassembly fuel handling and spent subassembly fuel handling systems.

The various sub systems in the fresh subassembly fuel handling are transport cask, transfer chamber, transfer chamber carriage, storage bay, inspection facility, preheating facility, cell transfer machine, transfer gripper, entry port and nitrogen filling facility.

The various sub systems in spent subassembly fuel handling are washing facility, under water trolley, storage racks, transport cask and storage bay transfer machine. The systems in in-vessel handling are reactor assembly main components, transfer arm and inclined fuel transfer machine (IFTM).

Three dimensional CAD models of all the above mentioned systems were created part by part with 1:1 scale dimensions and then assembled together to form the complete system. In the case of systems with higher complexity the assembly was done in multiple stages. All the models of the systems were arranged in a schematic arrangement according to their operational role in the sequence of fuel handling operation. This was preferred over the actual arrangement of the systems in order to provide maximum visibility to all the systems.

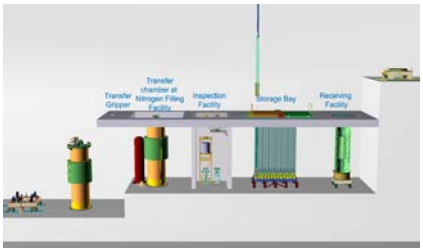

Fig. 1 *3D model of fresh subassembly handling system of PFBR*

Once 3D models and assemblies were created, animation sequences were applied to the models so as to show the working of the systems during the fuel handling operation.

The animation for fresh fuel handling starts from transport cask and ends with loading of fresh subassembly in in-vessel transfer port using inclined fuel transfer machine (Figure 1). This is followed by the animation of the in-vessel handling which shows the operation of transfer arm, rotation of large and small rotatable plugs (Figure 2). Then animations of spent fuel handling systems for spent and failed subassembly has been made separately. For spent subassembly handling, animation will start from ex-vessel transfer port (EVTP) up to loading in storage racks (Figure 3). Subassembly can get failed either inside the core or

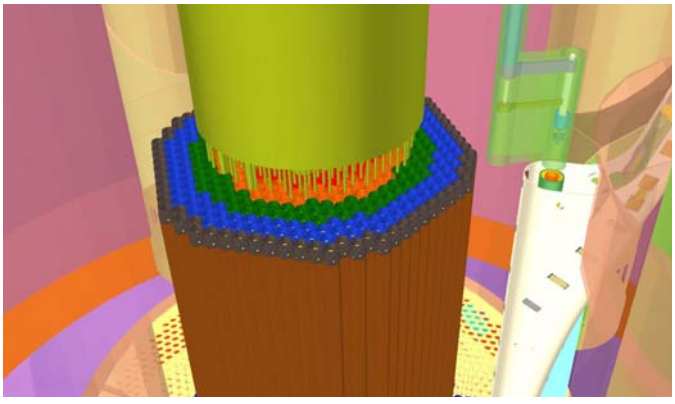

Fig. 2 *3D model of in-vessel handling system*

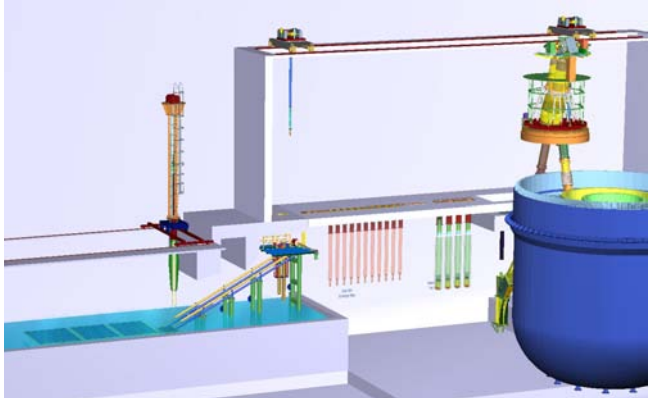

Fig. 3 *3D model of spent subassembly handling system*

during its transfer from the core to the washing facility. In the case of handling of subassembly which gets failed during transit, the same would be identified at washing facility. Then animation sequence will show loading of failed subassembly in a water filled container vessel till it is transferred to storage racks.

Once the animations were created, the models and animations were exported to advanced visualization centre. Here rendering elements such as cameras for generating viewpoints, lights for providing illumination to the scene, 3D and 2D text frames for indicating details and scripting for sequencing, applying behaviour on the 3D objects, cameras, lights, text frames would be carried out.

Special features were rendered in the animation sequence like a) movement of rope in cell transfer machine to raise and lower the gripper assembly b) movement of weights connected to linear variable differential transducer in inspection facility c) blowing of air for flow test of fresh subassembly at inspection facility d) creation of vacuum in transfer chamber at nitrogen filling facility e) surface heating of subassembly at pre-heating facility f) Modeling of water pool at under water trolley and storage racks of spent subassembly handling system.

Mechanical sounds like movement of transport cask on rails, opening and closing of locking mechanism of storage bay, blowing of air in flow test of fresh subassembly fuel handling system was added to create a better immersion into the virtual environment.

An audio narration explaining the fuel handling systems and operations being performed runs in synchronization with the animation. This enhances the depth of the visualization by providing a better understanding of the system to the operators as they are viewing the animation and listening to the narration simultaneously.

The duration of the entire animation sequence is about 70 minutes. Due to the enormous complexity of the systems, the 3D model of the system contains more than 20 million polygons and it will be twice for 3D visualization. Hence various graphics optimization techniques like polygonal approximation for complex shapes, hidden surface removal, disable refraction of light, view volume generation using clipping algorithms were used to render the visualization in the desired resolution.

II.23 Development of Obstacle Avoidance Algorithm for PFBR Steam Generator Tube Inspection Using SCARA Robot

PFBR has eight steam generators for converting the water to steam to run the turbines. In the secondary loop, sodium is used in the shell side and the water is allowed to pass through 547 tubes from a bottom header to the top header in the steam generator. The steam generator has an overall tube length in the order of 23 meters. In-service inspection (ISI) is mandatory for the maintenance of the integrity of the water tubes as the secondary sodium and water are separated by these tubes. Remote field eddy current testing (RFECT) envisaged for the tube inspection requires RFECT probes to be deployed to all the 547 tubes through its full length to assess the integrity by measuring for wall thinning or any defects. Since the 547 tubes open out at both the top and bottom domes, a selective compliant articulated robotic arm (SCARA) is designed to locate distinctly all these holes for the probes to be inserted. The SCARA is inserted through the top man hole at an angle of 60°. The approach from the bottom man hole will lead to the restriction of inserting RFECT probes through the holes from the bottom as orifices are inserted into every hole at the bottom tube sheet location.

During manufacturing or later, any tubes to be isolated (due to the problems in the welding of the tubes to the support or if the tube does not qualify for its purpose of use) are plugged. The tube plug heads project out 10 mm above the tube sheet surface. Though it has been accounted in the design of

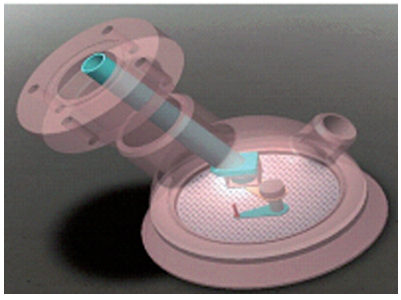

Fig. 1 *Steam generator top dome*

Table 1: Remote Handling Protocol operation	
1	Mathematical modeling of the tube sheet hole array
2	Read initial position of the SCARA arms
3	Find the inverse kinematic solution (IKE) to the destination hole to be inspected
4	Compute the sweep area of the shoulder arm and the elbow arm
5	Check if the obstacle (plug) falls in the sweep area
6	Create a detour point and travel to that point and proceed to the destination avoiding obstacle
7	Continuously monitor shortest distance of the obstacle from shoulder and elbow links

the SCARA to have this clearance, in order to ensure safe use, the robotic device is designed to have the obstacle avoidance algorithm to avoid any contacts of the SCARA shoulder or elbow arm with the plug heads.

Figure 1 shows the top dome with the SCARA arm. Vector based obstacle avoidance algorithm has been developed in house. The protocol of operation is given in Table 1.

The vector approach is representing a vector of magnitude arm length along the arm and another vector from the joint to the circular plug head (circle) centre. The dot product gives the projected length on the arm vector and a normal vector is computed which is directed towards the obstacle centre from the arm which is the shortest distance of the arm from the obstacle centre. It is also ensured that the arm width and the plug diameter are accounted to check for the interference.

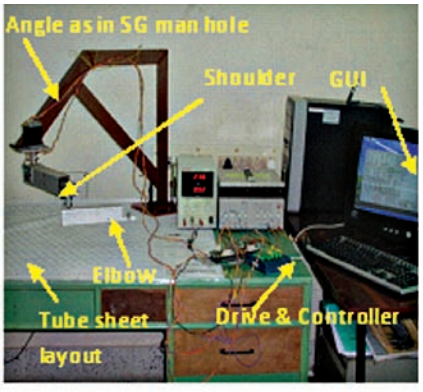

Fig. 3 *SCARA mock-up facility*

The mathematical model of the tube array and the inverse kinematic solution for a two axis serial robotic arm have been completed through the Visual Basic (VB) and the front end graphics developed to represent the tube sheet with the holes and the obstacle. The Visual Basic front end has the provision to look for the user input through the mouse click on the hole to be inspected. Figure 2 shows the obstacle avoidance of the SCARA. The obstacle avoidance algorithm has been checked visually by the graphical representation and a mock up facility representing the SCARA is developed as shown in Figure 3 for testing the algorithm.

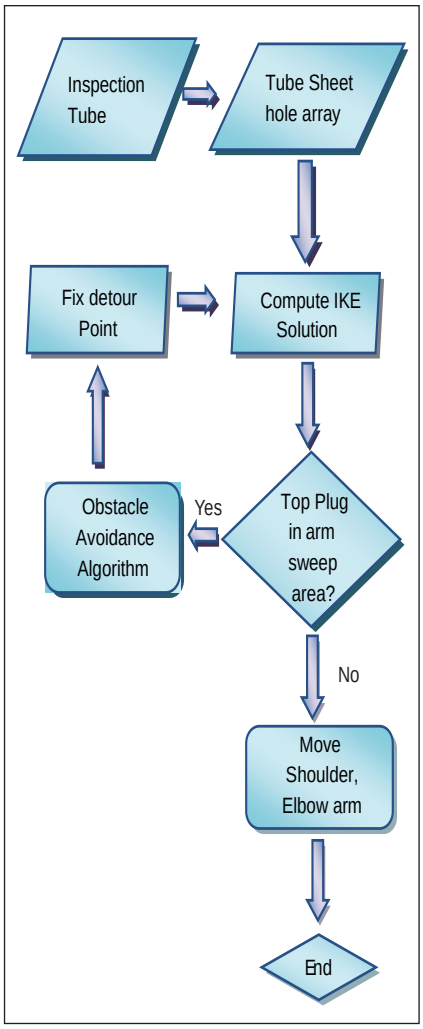

Fig. 2 *Obstacle avoidance abstraction layer*

This vector method of implementation of the obstacle avoidance of SCARA for the SG ISI application helps reduce the inspection time and also ensures safety even when the inspections are performed by less trained or untrained personnel as the system has its own detour path avoiding any obstacle which are generally the plug heads. The abstraction layer of obstacle avoidance is shown in Figure 2. This avoids the requirement of continuous guidance from the user to move the arms based on other visual or sensor inputs. However, sensors and other visual inputs shall assist the user to only visually monitor the negotiation of the obstacles by the SCARA arms which are totally automatic.

II.24 Development of Genetic Algorithm based Optimization Model for Condenser

Genetic Algorithm (GA) is a powerful and broadly applicable stochastic search and optimization tool based on Darwinian Theory of biological evolution. During the last three decades, Genetic Algorithms found its growing applications in various fields like industrial engineering, computing, data mining, image processing, pattern recognition, signal processing etc. Choice of optimum design parameters for condenser of a power plant from among a large number of technically viable combinations is a complex task. This is primarily due to the conflicting nature of the economic implications of the different system parameters for maximizing the capitalized profit. The main objective of this work is to develop a Real-parameter Genetic Algorithm model to find the optimum design parameters for the circulating water system of PFBR. The results arrived are validated with the conventional mathematical programming based reference study.

The circulating water system of PFBR consists of steam surface condenser (single pass shell and tube heat exchanger), circulating water pumps and drives, intake, pump house, piping/ducts, seal well, outfall structure etc. Cooling is by using sea water in a once-through mode. The parameters that are selected as design candidates for this study are condenser flow rate (Q), outer diameter of condenser tube (d_o), condenser tube length (l) and water velocity inside tube (v). The range of feasible values for each of the parameters along with the optimum design parameters from the reference study are given in Table 1.

Table 1: Range of parameter values

Parameter	Symbol (Unit)	Min	Max	Optimum
Condenser flow rate	Q (m^3/hr)	96000	105000	98000-99000
Outer diameter of condenser tube	d_o (mm)	22.225	25.400	25.4
Condenser tube length	L (m)	13.00	16.00	14-16
Water velocity inside tube	V (m/s)	2.1	2.7	2.1

For a specified sea water temperature regime and known relationship between the condenser back pressure and turbine output for the cycle, our aim is to find the optimum values for the above parameters that would provide highest capitalized profit. The environmental regulation stipulates that the temperature range (r) of the CWS should not exceed 7 degree. Another constraint which is recommended by heat exchanger institute is the terminal temperature difference (TTD) for the condenser should be greater than 2.78 degree. Considering the above factors and boundary conditions, we arrive at a mathematical formulation of the given problem on which the GA can be applied as:

Max(Capitalized profit)=$f(Q,l,d_o,v)$
Such that, r<7 degree and TTD > 2.78 degree.

A Real-parameter Genetic Algorithm model has been formulated in C language with Q, l, d_o and v parameters encoded as chromosomes. Roulette-Wheel method with Elitism is applied for selection. The other genetic operators considered and compared are arithmetic crossover and non-uniform mutation. The Genetic Algorithm modeling scheme is given in Table 2.

The methodology used for performance calculation can be

Table 2: Genetic Operators, methods and values used

Parameter	Values
Encoding	Real number
Chromosome size	4
Population size	100
Crossover probability	0.8
Mutation probability	0.01
Maximum no. of generations	1000
Elitism fitness value	785800

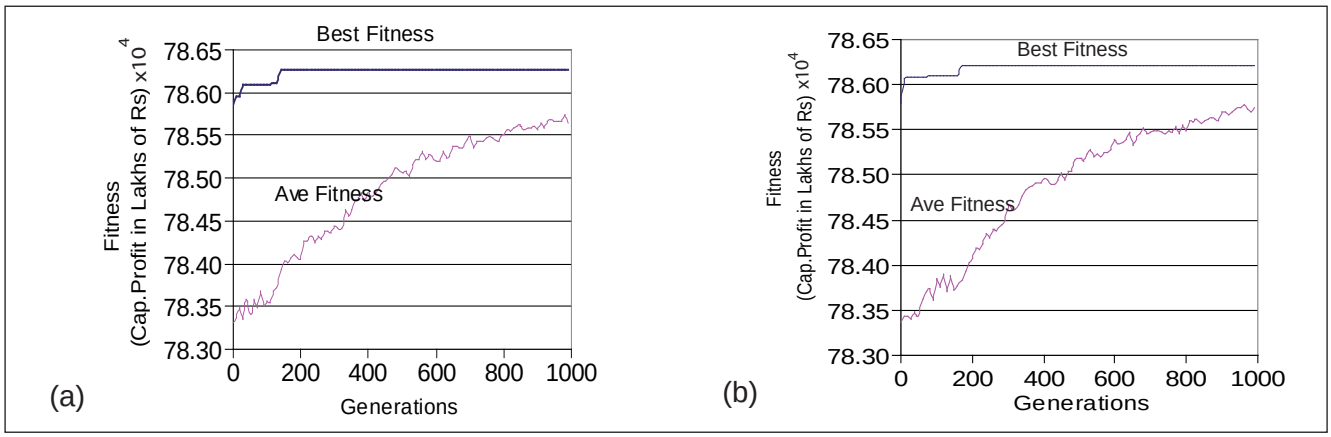

Fig. 1 *Genetic algorithm performance for the study (a) Trial run 1 and (b) Ttrial run 2*

described as follows. For the selected chromosome, the performance of the circulating water system is evaluated for a given cooling water temperature based on the thermodynamic relationship between the condenser backpressure and turbine output. The calculation takes in to account the correction factors for the tube diameter, inlet sea water temperature, tube material, gauge factor and tube cleanliness. The term "performance" means calculation of the saturation temperature and corresponding pressure of the condensing steam at the turbine exhaust and hence the power generated and corresponding revenue earned. During the above performance calculation, if the solution violates constraints regarding condenser inlet-outlet temperature range and terminal temperature difference, then the performance calculation is repeated by replacing the gene values with new set of values. If we get viable solution candidates from performance calculation, then we go for the capitalized profit calculation for each solution set based on the arrived performance.

The results obtained by the ten trial runs of the final genetic algorithm implementation with the given Genetic Algorithm parameter values (refer Table 2) are furnished. Here all economic figures including profit are in lakhs of rupees. The results confirm with the optimum design parameter values obtained from the reference study (refer Table 1) and hence the results are validated. The evolution of best fitness and average fitness values for two trial runs are shown in Figures 1a and 1b which shows the behavior of the algorithm is proper.

A study on the influence of chromosome elements on economic figures of circulating water system has been made which shows that the chromosomes have a direct impact on the cost of the system. However, their impact on the capitalized revenue is only marginal. Hence, the profit variation is dependent on the total cost of the system as illustrated in Figure 2.

We have taken a complex problem related to fast reactor steam condenser optimization and found out different system parameters for maximizing the capitalized profit. The study shows the feasibility of applying Genetic Algorithm in diverse design optimization problems pertaining to nuclear reactors.

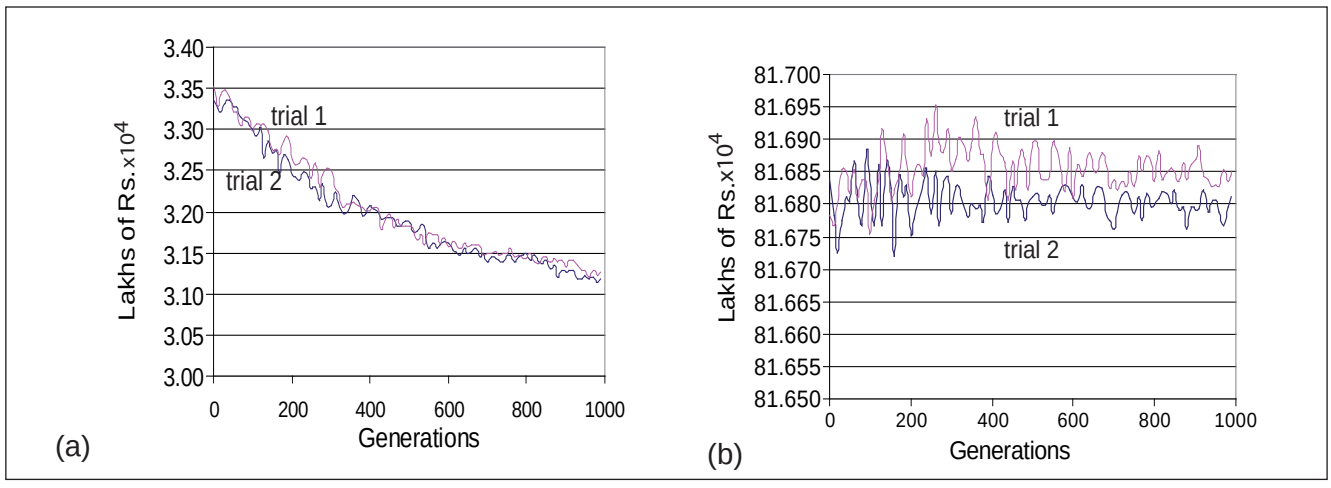

Fig. 2 *Evolution profile for cost and revenue (a) Total cost (b) Capitalized revenue*

II.25 Safety Critical Pump Speed Measurement Electronics

In PFBR, the heat produced in the core due to fission reaction is extracted by circulating liquid sodium as coolant. Two pumps are used in the primary circuit for this purpose. The seizure of any one of the pump causes sudden reduction in the flow of coolant through the core thus reducing the heat extracted from the core. This leads to increase in the temperature of the clad and fuel. In order to prevent the temperature from reaching the design safety limits, protection to the plant is provided by selecting primary pump speed as a SCRAM parameter. Safety action is initiated when speed falls below 560 rpm. Further, pump seizure is classified as category-3 event and the time available to initiate trip is 330 ms. To achieve high availability of reactor and reliability of the system, triple modular redundancy (TMR) was employed. Each pump is independently provided with a toothed wheel, three variable reluctance sensors (VRS) for sensing the speed and associated electronics channels for measuring the speed and initiating safety action. The sensor provides a signal whose frequency and amplitude are proportional to speed. Frequency based measurement was selected against amplitude based measurement, so that periodic calibration is eliminated. The block diagram of the system is shown in Figure 1. The electronics channel for each pump is located in the reactor containment building local control centre. As frequency measurement method involves counting the signal for a fixed time, in order to achieve the response time requirement, the incoming frequency was first doubled and time staggered counters were used to measure the speed. By this method, a response time of 110 ms was achieved with a measurement accuracy of 2 rpm, which is well below the available time meeting the requirement. The channel was designed in modular way for ease of maintanance. In a single 6U subrack, channels for both the pumps were housed. The speed measurement logic was implemented in programmable logic device to reduce the interconnections to enhance the reliability. Failsafe features were incorporated into the design against failure of clock, gate pulse generator, corruption of setpoints and malfunction of power supply. On-demand testability was also provided for surveillance. The electronic channel has successfully undergone environmental qualification as per IS-9000 standard.

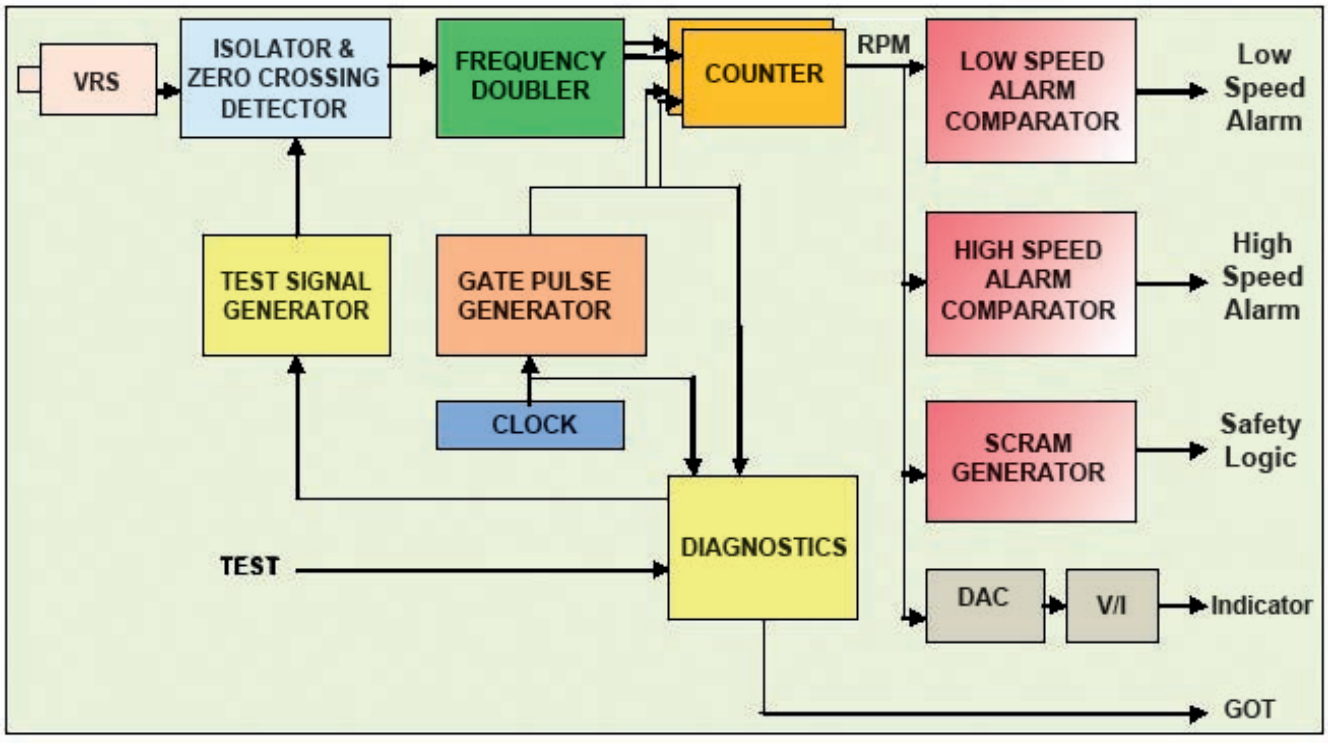

Fig. 1 *Block diagram of the system*

II.26 Seismic Qualification of Safety Logic Systems

PFBR is provided with two independent fast acting shutdown systems to initiate safety action against various design basis events. For shutdown systems-1, safety logic with fine impulse test system (SLFIT) is used and for shutdown systems-2, pulse coded safety logic system (PCSL) is used. The safety logic systems are responsible for initiating safety action after performing 2/3 voting of triplicated SCRAM parameters. The safety logic systems are categorized as safety critical systems. The systems need to undergo stringent qualification tests, before being deployed in the reactor.

As part of the qualification testing, they have undergone EMI/EMC testing, environmental qualification esting and seismic qualification testing. In PFBR, both the SLS are deployed at the local control centre of control building which is at 25 m elevation. Floor response spectra at the floor of local control centre is drawn with reference to 2% & 5% damping for operating basis earthquake (OBE) and 4% & 5% damping for safe shutdown earthquake. Peak ground acceleration. values for shutdown earthquake and operating basis earthquake with reference to the floor response spectra are shown in Table-1. The peak ground acceleration limit for which, a nuclear power plant is required to remain functional and safe, during and after the vibratory ground motion, caused by the earthquake is called operating basis earthquake. The earthquake that produces the maximum vibratory ground motion for which certain structures, systems and components are designed to remain functional is called safe shutdown earthquake.

For qualification of safety logic systems, each system has undergone seismic tests at Structural Mechanics Lab in a box type shake table of dimension 3 x 3 x 0 .5 m. The safety logic systems were mounted on the shake table, simulating the actual mounting condition of the panel in the power plant by welding the panel to a rigid metal frame of 20 mm base plate. The plate is bolted to shake table using M12 bolts. Figure 1 and Figure 2 show SLFIT and PCSL mounted on the shake table.

Table 1: Peak ground acceleration for OBE and SSE

Description	Peak ground acceleration(g)		
	X	Y	Z
OBE	0.078	0.078	0.052
SSE	0.156	0.156	0.104

Fig. 1 PCSL system at shake table

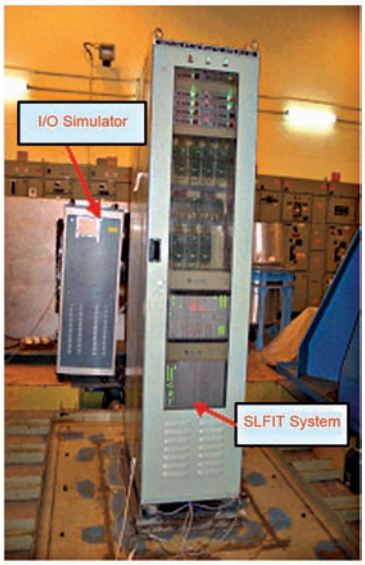

Fig. 2 SLFIT system on shake table

Seismic qualifications of the panels were carried out as per IEEE-344-1987 criteria. Accelerometers are mounted at the top of the cabinet to check the response amplification. Strain gauges are pasted at the corner block locations to capture the strain developed during the seismic excitations. Target required response spectrum (RRS) and achieved RRS are shown in Figure 3 for operating basis earthquake and shutdown earthquake for X, Y and Z direction.

Detailed performance evaluation tests were carried out before they are subjected to the seismic qualification test. The systems were kept in “Power ON” condition during the seismic test. The systems were tested for five numbers of operating basis earthquake and one number of Shutdown Earthquake as

stipulated by IEEE guidelines. During the tests, observations were carried out for proper functioning. Detailed performance evaluation tests were carried out after seismic experiments by measuring various parameters. Visual inspection was carried out after seismic tests, to check any permanent deformation, dislocation, breakage, major crack and loosening of components/ equipments from their original mounting.

Thus, structural integrity and functional requirements of safety logic systems were demonstrated by shake table experiments in energized condition.

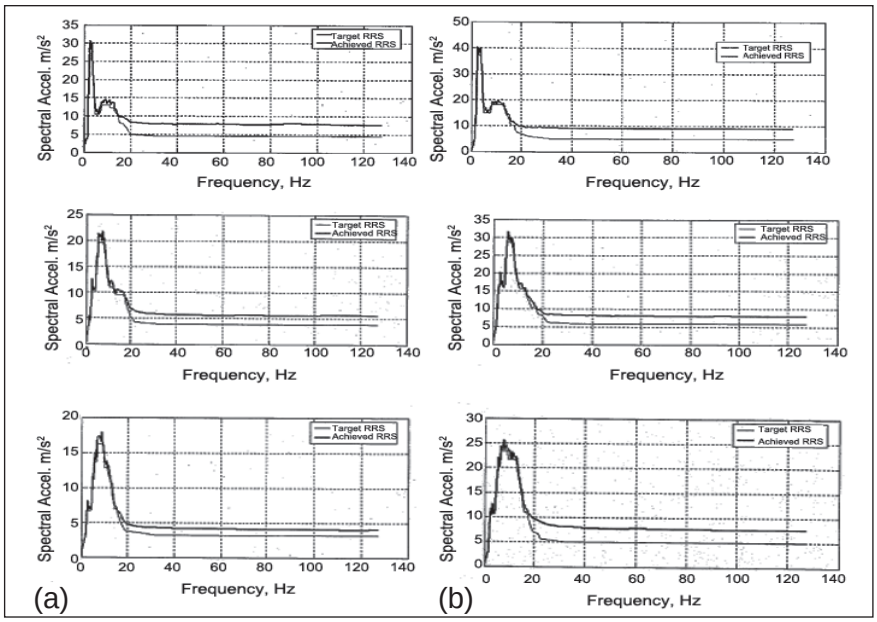

Fig. 3 *Floor response spectra at X,Y&Z direction (a) Operating basis earthquake (b) Safe shutdown earthquake*

II.27 Real Time Computer Based Core Temperature Monitoring System

As the power density is very high in fast reactors, it is essential to continuosly monitor the core cooling. It is carried out to ensure that clad hot spot and fuel temperature do not reach their design limits. In this regard, core temperature monitoring system (CTMS) is provided to detect the plugging of the fuel subassemblies (FSA) and initiate safety action. As large number of fuel subassemblies outlet temperatures (211 numbers) are to be monitored and calculations are to be performed to detect plugging, the use of a computer becomes necessary. Hence, a real time computer (RTC) system based on Versa Modular European (VME) bus platform was employed for this purpose in triple modular redundancy (TMR) configuration. It is the only safety critical system in PFBR employing processor and software. As software is called upon to perform safety function, its reliability is of paramount importance. Hence, the software was modelled using safety critical application development environment (SCADE), which helps in verification of safety properties and error free code generation. The block diagram of the system is shown in Figure 1. Each fuel subassembly outlet temperature was monitored using two thermocouples (TC). The thermocouple signals are terminated on signal conditioner modules (SCM) located in the reactor containment building (RCB) local control centre (LCC), which performs cold junction compensation, isolation and provides current loop output. The signals are then triplicated in the

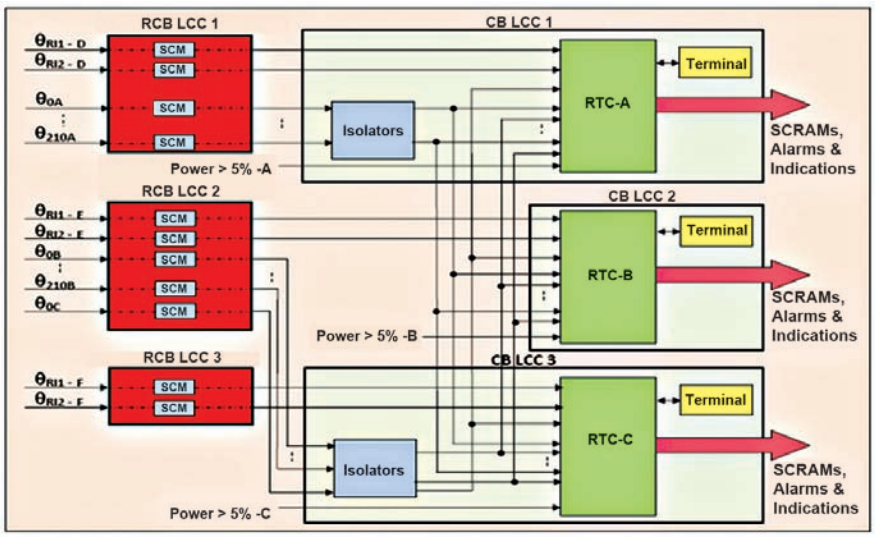

Fig. 1 *Block diagram of the system*

control building (CB) local control centre for achieving triple modular redundancy, isolated and distributed to three independent RTCs, which are also present in control building local control centre. The software, which runs periodically every second, performs acquisition of thermocouples signals, linearization and validation of the temperature readings. Further, reactor inlet temperature (θ_{RI}), mean core outlet temperature (θ_M), mean core temperature gradient ($\Delta\theta_M$) was computed to determine plugging of the fuel subassemblies and initiate safety action. The hardware and software were designed based on AERB guidelines SG D-25 and the system software has undergone extensive independent verification and validation.

A typical representative configuration of real time computer system has successfully undergone environmental qualification as per IS-9000, EMI/EMC qualification as per IEC-61000 and Seismic qualification as per IEEE-344 standards.

II.28 Real Time Computer Based Control Systems for Shutdown Mechanisms

The shut down systems of PFBR namely control and safety rod drive mechanism (CSRDM) and diverse safety rod drive mechanism (DSRDM) are controlled by VME bus based real time computer systems. These control systems are classified as SC2 systems, which have a fault tolerant architecture achieved through redundancy.

Each control and safety rod (CSR) is handled by a separate driving mechanism and driven by a 3 phase induction motor. The shaft of the motor is attached to a screw-nut mechanism and an electromagnet coil is attached to the nut. Gripper operating rod passes through the translation tube and the lower end of the mobile assembly goes inside the top hollow portion of control and safety rod and gripper opens out to hold control and safety rod. The total travel of the mobile assembly is 1085 mm. Under normal conditions, the electromagnet of the mechanism is in energized condition and it holds the mobile assembly with gripper holding the control and safety rod. When the control system drives the induction motor, the control and safety rod moves up and down. During SCRAM, the electromagnet is de-energised and the mobile assembly along with control and safety rod falls due to gravity. Before starting the fuel-handling operations, control and safety rod is deposited inside the core by closing the gripper finger and the mechanism is lifted and parked at the top for sufficient clearance, with the help of lifting plate. Each control and safety rod drive mechanism is provided with potentiometer and synchro control transmitter to indicate the positions of mobile assembly and electromagnet respectively and three load cells to indicate the weight of the mechanism.

Three diverse safety rod are located in the reactor core and each DSR is handled by a separate mechanism. It is driven by a three phase induction motor. The mobile assembly has got an electromagnet at its bottom. During normal reactor operations, the electromagnet is energized and with diverse safety rod, it is parked at the top. During SCRAM, the electromagnet is de-energised and diverse safety rod falls due to gravity. During fuel-handling operations, EM is de-energised, diverse safety rod is deposited inside the core and mobile assembly is parked at the top by locking the support rods. Each mechanism is provided with potentiometer to indicate the position of mobile assembly and three load cells to indicate the weight of the mobile assembly with or without diverse safety rod.

The functions of I&C are to facilitate remote operation of control and safety rod drive mechanism & DSRDMs from control room, ensure safety of the reactor by imposing interlocks in raise and lower operations for power control and reactivity-worth check, measure drop time of control and safety rod, check the healthiness of drive motors and giving alarms, provide the status to other systems like reactor protection systems, startup systems etc. and to administratively control the sequence of operations before startup of reactor and fuel-handling operations. The reliability and availability of the control system is achieved by having redundancy in system design and also in sensors level.

The control system consists of dual redundant real time computers with

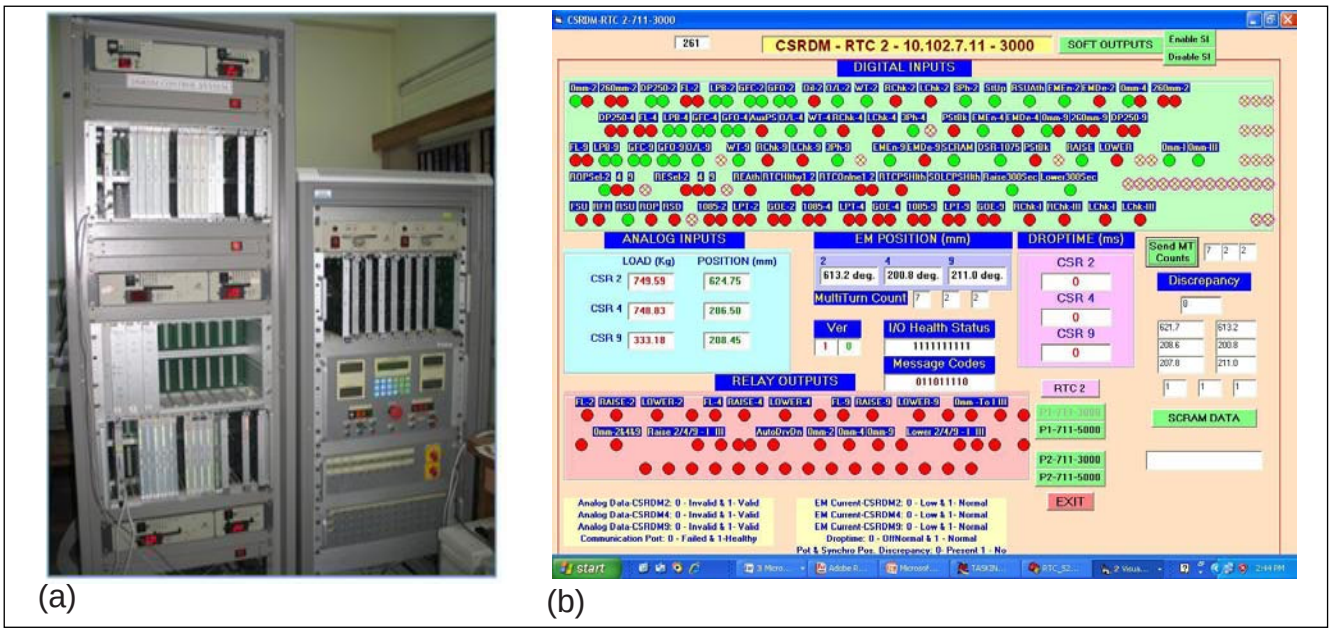

Fig. 1 *Control system (a) Test setup and (b) Display station interface*

MC68020 processor based CPU card, digital, analog and synchro input cards, relay and opto output cards. The healthiness of real time computers are monitored by a switchover logic system, which routes the outputs of healthy system to the plant. The real time computer systems are qualified for environmental tests as per IS 9000, EMI-EMC tests as per IEC 61000 and CISPR, seismic tests as per IEEE 344 and drop and topple tests as per IS 9000.

For developing the application software, software development methodology is followed as per AERB/SG/D-25 guidelines. It starts with system requirements specification (as per IEEE 1233), software requirements specification (as per IEEE 830), software design description (as per IEEE 1016), software coding (as per MISRA C guidelines), software unit and integrated testing along with the system hardware by preparing the detailed test cases and verification and validation by an independent verification and validation committee. Computer aided software engineering (CASE) tools are also used throughout the software life cycle. The specifications are prepared using DOORS and traceability was obtained with the previous phase of the development. The control logic of the systems are developed using a SCADE (safety critical application development environment) suite, in which requirements are modeled and simulated. Then model test coverage analysis is done to explore the model thoroughly and design is verified using formal verification technique. When the model design is verified for correctness, the certified code generator of the suite generates the code in 'C' language. This code along with the manual code is loaded in EPROM of the real time computer and executed.

The application software for control and safety rod drive mechanism and diverse safety rod drive mechanism were developed and tested thoroughly by feeding digital and analog inputs from signal simulator and synchro control transmitter inputs from synchros. The relay outputs from real time computers were observed in the fascia of the cards. In addition, the inputs, outputs and alarm messages are sent through ethernet communication using TCP/IP protocol to three destinations. These data were captured in a GUI display station and tested for correctness. The general control system test setup and display station interface are shown in Figure1.

The hardware integration testing functional testing (FT-1) for twin cabinets of DSRDM control system was conducted, then subjected to hundred hours burn-in test followed by FT-2. Then the application software fused in EPROM was tested by IV&V team with the test cases generated by feeding digital and analog inputs from a field signal simulator to both the real time computers. The performance of each real time computer was observed in GUI and fascia of the systems. The switchover of real time computers was tested by simulating the required conditions. The end limits of the mechanism were simulated and processing of interrupts by real time computers to stop the mechanisms movement were also checked. After testing, the cabinets were subjected to burn-in test for sixty eight hours, during which system functioning was found to be satisfactory.

II.29 Quantitative Accelerated Life Testing of Field Programmable Gate Array

For PFBR I&C systems, field programmable gate arrays (FPGA) are extensively used to implement digital logics such as VME bus interface logic, control logic and sequencing logic etc. A field programmable gate arrays consists of an array of programmable logic modules and a programmable interconnecting area. They are considered for their robust features such as high gate density, performance, speed etc.

To enhance the system reliability, field programmable gate arrays with high mean time between failure values (as per manufacturer's specification) are selected. Further to improve reliability, good practices are followed at device level and board level. Since these devices are reliable as per the manufacturer's specification, they were used in R&D facilities like Fast Breeder Test Reactor and augmented boron enrichment plant as test beds. However, in order to use PLDs in commercial nuclear power plant (in PFBR), it is vital to know about their performance in critical applications. The availability of required data is limited, other than for space applications. So, quantitative accelerated life tests for the field programmable gate arrays were proposed, to get required data for accelerated life data analysis. This analysis method uses life data obtained under accelerated conditions to extrapolate an estimated probability density function for the product under normal use conditions. Accelerated life tests are conducted on products to understand their failure modes and life characteristics. The products are subjected to enhanced stresses in order to force the products to fail early than they would normally, under use conditions. This process reduces test time. Though accelerated tests are new entrants in reliability engineering, they are gaining acceptance in the industry.

For the quantitative accelerated life tests (temperature as stress parameter), an antifuse technology based field programmable gate array is selected. The tests were carried at the Centre for Reliability, Chennai. Since it is a destructive test involving time and cost, failures other than field programmable gate array are avoided by exclusive field programmable gate array design and PCB design. For field programmable gate array, a testable stress design with good logic utilization and good interconnecting complexity was designed. Further a pair of test boards (Testboard-1 and Test board-2) was developed. During quantitative accelerated life tests, the field programmable gate arrays was kept in a test chamber and exposed to multiple stress levels in step fashion.

Table 1: Results (FPGA's MTBF value at 60% confidence level is 8,771,920 hours)

Stress Level (ºC)	Sample size	Test duration (hours)	No. of failures
100	4	361	0
150	4	1060	0
180	4	1152	1

The test boards with minimal neighbouring circuitry were designed considering the test chamber and test conditions. Test

Fig. 1 Complete ALT setup

Fig. 2 Test boards inside chamber

board-1 was kept inside the test chamber with field programmable gate arrays and test board-2 kept outside the chamber to receive field programmable gate arrays status. To avoid failures other than the field programmable gate arrays, which is industrial grade, military grade neighbouring circuitry on testboard-1, was used. Even the PCB was designed as per Mil-Prf-55110G-Group B. Test board-1 consisted of only power supply connector, a crystal oscillator for clock and a buffer to drive the signals outside the chamber. Test board-2 consisted of reset circuitry and test points. Finally the signals were connected to a monitoring device. The complete test set up is shown in Figure 1. Field programmable gate array boards inside the chamber are shown in Figure 2. For each stress level, 4 numbers of field programmable gate array devices are exposed. For acceleration of failure mechanisms associated with electronic components the Arrenhius method of modeling the effects of temperature was used. The estimation of the distribution of the failures of the products was calculated using an exponential Chi-Squared distribution as per the procedure laid down in MIL-HDBK-781A. The results are reported in Table 1.

II.30 Environmental Qualification Test Facility for I&C Systems

Environmental qualification is essential to determine the ability of electronic systems to withstand and function under operating environmental conditions of high temperature and humidity. PFBR I&C systems are to be qualified for environmental test as per IS 9000 standard. Environmental qualification includes dry cold, dry heat, temperature cycling and damp heat tests. These environmental tests are to be conducted for every system.

An environmental test facility has been setup (Figure 1) for the electronic systems in which the temperature and humidity can be controlled as per the requirements. The test space volume of the chamber is 600 litters and maximum load of 80 Kg is possible. Two test shelves are available inside the chamber and both can be combined or separated depending on the requirements. Provision is provided to run the cable in and out of the chamber for monitoring purpose without affecting the inside chamber environment. The temperature of the chamber can be controlled from 228 to 453 K with an accuracy of ± 0.1 to ± 0.5 K. Heating can be done 4 K/ min and cooling with 3 K/ min. Demineralised water is used to control the humidity and the chamber is having reservoir capacity of 20 litres for DM water. To maintain a constant temperature of 313 K and 92 % Rh, two litres of DM water are consumed per day. The humidity fluctuation can be maintained ±1 to ± 3 % Rh inside the chamber.

This chamber has a programmable option of storing upto 100 profiles. Hence different test profiles as per standard can be programmed and required profile may be selected while starting the test. A personal computer interface is provided to upload the real time profile data for documentation and post-test analysis.

As per PFBR I&C environmental test requirement standard, for dry cold test, temperature has to be varied from 288 to 298 K (Figure 2a) for the system under test and test has to be carried out in power OFF condition. Performance is verified in nodal points by switching ON the system. Total time required to complete the test is six hours and twenty minutes.

For dry heat cycle test, temperature has to be varied from 298 to 328 K in steps and humidity maintained below 50% Rh (Figure 2b) and test has to be carried out in power ON condition. Performance verification has to be done in nodal points.

Fig. 1 *Environmental chamber*

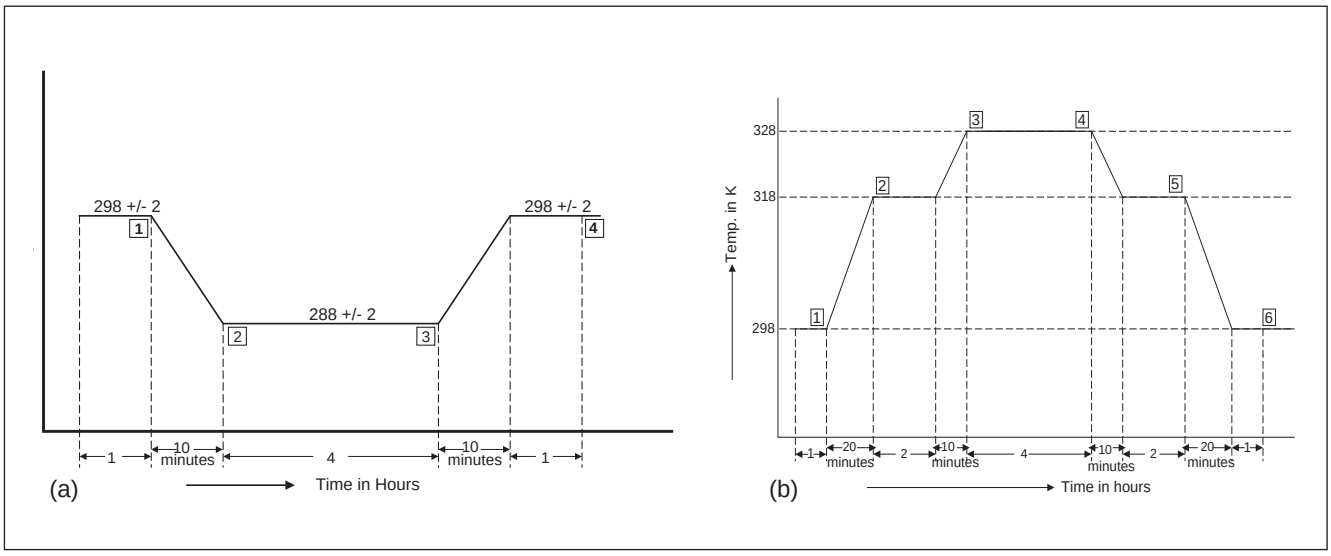

Fig. 2 (*a) Dry cold test and (b) Dry heat test*

Total time required to complete the test is 11 hours.

For temperature cycle test, temperature has to be varied from 288 to 328 K and humidity maintained below 50% Rh (Figure 3a) and test has to be carried out in power OFF condition. Performance verification has to be done in nodal points. Two cycles have to be carried out and fourteen hours and forty minutes is required to complete the test.

For damp heat cycle test, temperature has to be maintained from 298 to 313 K and humidity maintained above 80% Rh and 95% Rh (Figure 3b) and test has to be carried out in power OFF condition. Performance verification has to be done in nodal points. Two cycles have to be carried out and forty eight hours is required to complete the test hours.

Several PFBR I&C systems like real time computer system, remote terminal unit system, pump speed electronics and central subassembly temperature monitoring system were tested successfully using this chamber for environmental qualification. Systems under development also are environmentally qualified using this chamber. This facility is not only helping to successfully conduct the environmental qualification of I&C systems, but also saving enormous time and cost.

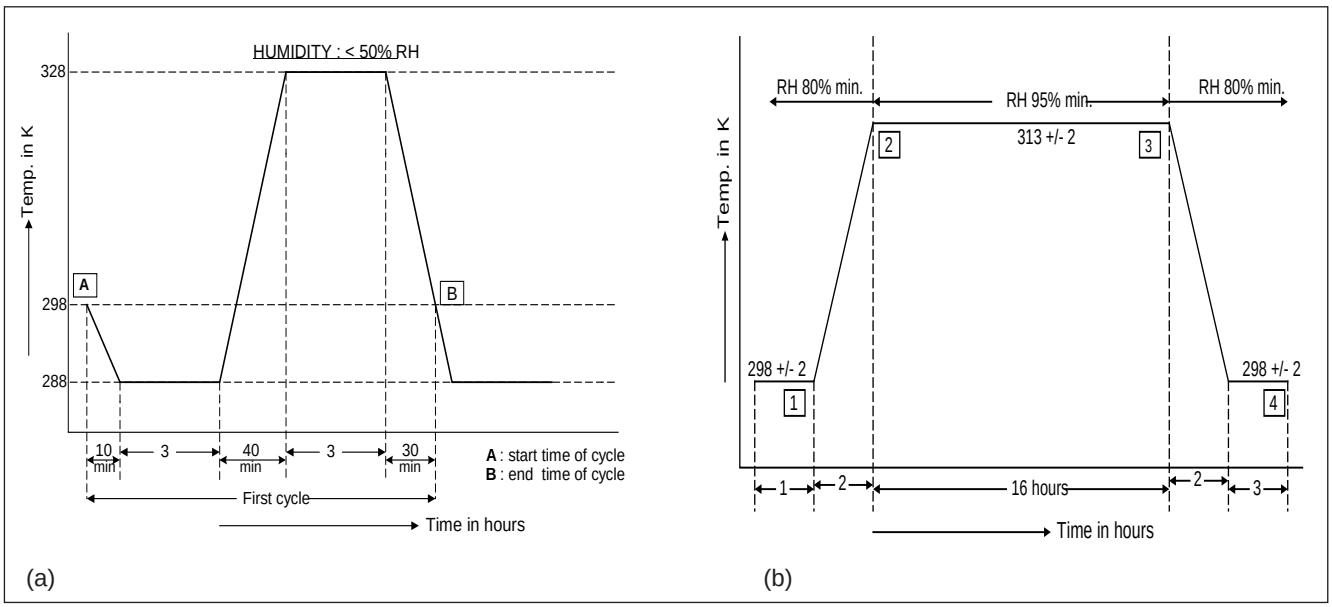

Fig. 3 *(a) Temperature cycle test and (b) Damp heat test*

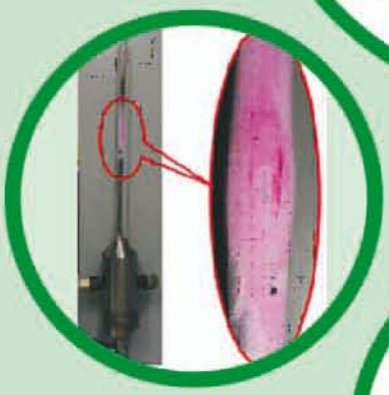

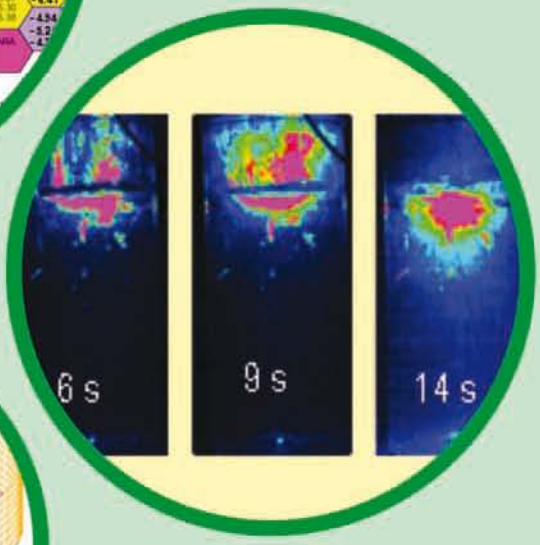

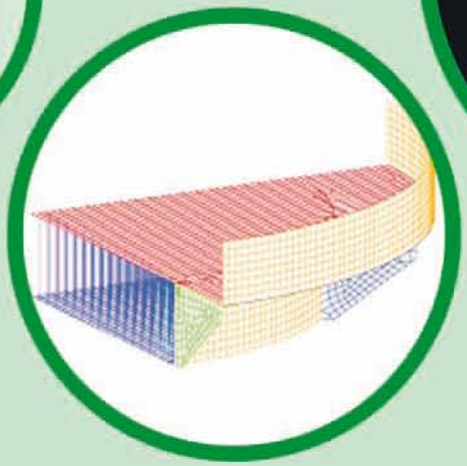

CHAPTER - III

Research & Development for FBRs

III.1 Design and Safety Studies on Metallic Fuelled Fast Breeder Reactor

Physics design of a 1000 MWe metallic fuelled fast breeder reactor is made for studying the static and transient characteristics.

Figure 1 gives the core configuration of a 1000 MWe metallic fuelled fast breeder reactor. The core is divided into three enrichment zones, to achieve power flattening. There are 247 fuel subassemblies (SAs) in these three cores viz., core-1 with 79, core-2 with 96 and core-3 with 72 subassemblies respectively. There are 271 pin per subassembly in the core. Core inlet and outlet temperatures are 638/827 K. There are 18 control safety rods and 6 diverse safety rods, making a total of 24 absorber rods. Natural B_4C absorber rods are expected to meet the reactivity requirements. Metal fuel with both 10 and 6% Zr content have been tested in the past, the latter was chosen, because of its higher breeding capacity.

Metal fuel has better thermo-physical properties such as high density and high thermal conductivity. Liquid sodium bond gap material increases the conductance and reduces the thermal time constant. With metal fuel Doppler reactivity swing is small between the zero power and nominal power due to hard neutron. Higher breeding ratio and low burn-up loss brings down excess reactivity and lowers control requirements. Required control rod worth is almost half of oxide core, thus making uncontrolled withdrawal accident significantly less severe.

Un-protected loss of flow analysis of 1000 MWe (2632 MWt) MFBR (U-Pu-6% Zr) reactor was carried out to verify its passive shutdown capability. Feedback reactivities from axial fuel expansion, radial expansion of the core, clad and coolant expansion, Doppler feedback due to broadening of resonances, spacer pad expansion and coolant voiding were considered.

Scenario of pump flow coast down (possibly initiated by power failure) with all the shut down rods unavailable was considered for the transient analyses. The coolant flow was assumed to be coasting with a flow halving time of eight seconds. After the initiation of flow reduction, the reactor becomes sub-critical and the power decreases continuously. Working of natural convection based safety grade decay heat removal system was also considered. The overall feedback and net reactivity is negative throughout the un-protected loss of flow analysis and even after the power reduces to natural convection based safety grade decay heat removal system level as shown in Figure 2.

Studies showed that even if the sodium worth is reduced to 80% by design (i.e 5.8 to 4.6 $), the reactor goes to a safe shutdown state and also considering 20% uncertainties on core radial expansion and sodium void feedback. Alternatively, increasing flow halving time (15 seconds instead of 8 seconds) without the above design change was analysed and it ensures the safety of 1000 MWe reactor.

Construction of a test reactor with metallic fuel is also envisaged to provide full-scale testing of fuel subassemblies planned for the

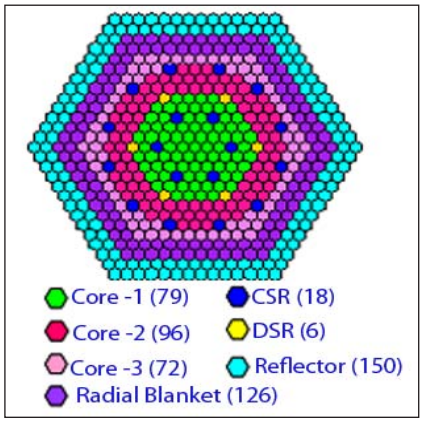

Fig. 1 *Core map of 1000 MWe FBR*

1000 MWe commercial power reactor. Physics design studies have been carried out to arrive at a core configuration for this experimental facility. The aim of this study was to find out minimum power of the core to meet the requirements of safety as well as full-scale demonstration. In addition, fuel sustainability was also a consideration in the design.

Two types of metallic fuel pins, viz. a sodium bonded ternary (U-Pu-6%Zr) alloy and a mechanically bonded binary (U-Pu) alloy with 125 µm thickness zirconium liner, were considered. A 320 MWt self-sustaining breeder metal core was recommended for the test facility.

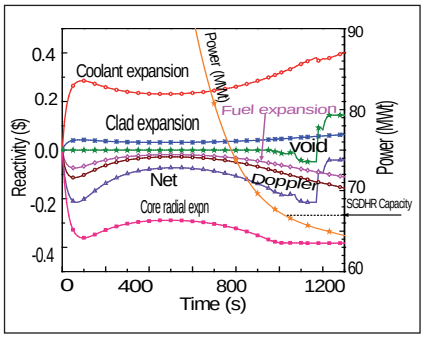

Fig. 2 *Feedback reactivity of 1000 MWe un-protected loss of flow analysis with conservative decay heat estimation*

III.2 Comparative Study of Phenix Absorber Rod Withdrawal End-of-Life Analysis Using FARCOB and ERANOS 2.1

Absorber rod withdrawal end-of- life experiments carried out in the French Fast Reactor Phenix during June 2009 was analyzed in our Centre, as a part of IAEA coordinated research project (CRP) on “control rod withdrawal and sodium natural circulation tests performed during the PHENIX end-of-life experiments”. The end-of-life core of Phenix reactor has 6 main control rods and one emergency control rod. The emergency control rod is located at the center of the core and it is always placed outside the core during reactor operation. The absorber rod material is 48% enriched boron carbide.

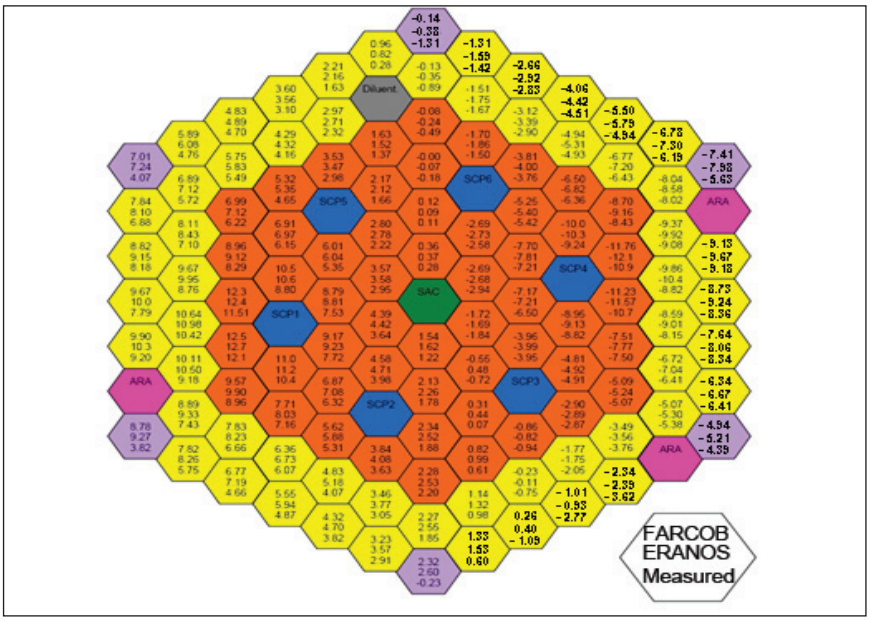

Fig. 1 *Comparison of computed and measured sodium heating deviation (%) with respect to the reference state for step-2*

Before performing this test, the worths of control rod-1 and control rod-4 were measured at low power (~50 kWt). Later on, the reactor was made critical around 340 MWt with uniform elevation of all main absorber rods (reference state). Then, the control rod-1 and control rod-4 were moved by reactivity balance method to achieve three critical core states (called as step-1, step-2 and step-3) with distorted radial power distributions. Table 1 gives the control rod positions, sodium inlet and outlet temperature and reactor power for the critical steady-state configurations involved in this test. All these critical core configurations have been simulated both by FARCOB developed at IGCAR and ERANOS 2.1 (European) systems and the results computed were compared with the measured values. The parameters estimated were criticality for four core states, absorber rod worth, and the deviation of subassembly sodium heating deviation in a critical state with respect to the reference core. It can be seen from Table 2 that both these codes predict well the criticality for all the four critical core states. The FARCOB under predicts criticality by ~55 pcm whereas ERANOS 2.1 over predicts criticality by ~300 pcm. The accuracy in the prediction of criticality is closely related to the errors associated with the neutron cross sections, geometrical modeling of core and the calculation method. Both these code systems use 3-D neutron diffusion theory for criticality calculations.

Table 1: Global parameters of various critical core states

Confi-guration	Power (MWt)	Sodium temperature (K)		Control rod position (mm)					
		Inlet	Outlet	1st	2nd	3rd	4th	5th	6th
Refe-rence	335.4	646.5	795.7	558.3*	557.4	558.0	557.4	557.4	557.6
Step 1	337.0	646.8	796.8	608.5	608.6	606.6	340.8	608.5	607.8
Step 2	338.7	646.8	797.3	848.4	567.7	571.0	340.6	566.3	573.5
Step 3	336.3	646.5	795.2	848.4	523.6	523.4	523.4	523.5	523.5

*These positions are given at full power state .
The origin is taken at 5 mm below core bottom.

The total measured worth for control rod-1 and control rod-4 are 1258 and 1238 pcm, respectively. A close agreement between the measured and calculated worth is observed. Maximum difference in the worth prediction between ERANOS and FARCOB is only 34 pcm. Maximum deviation in the measured power change or sodium heating deviation (with respect to the reference state) due to absorber rod movement is for step-2 and it

is -10.94% in fuel subassemblies around main control rod-4, whereas it is 12.71% in subassemblies around main control rod-1 (Figure 1). A close agreement is noted in prediction of this quantity for all the configurations with the measured values.

This benchmark exercise has provided an experimental validation of FARCOB code system against Phenix reactor for criticality, absorber rod worth and radial power distribution. This is the first experimental validation of tilt in the radial power distribution due to control rod movement at full power. It also enabled the benchmarking of calculation procedures and code systems being used at our Center for applications to oxide fueled sodium cooled fast power reactors. A good agreement is obtained in the prediction of experimental results both by FARCOB and ERANOS 2.1 code systems.

Table 2: Multiplication factor and core reactivity for critical core states

Configu-ration	K-eff		Reactivity (pcm)	
	FAR COB	ERA NOS	FAR COB	ERA NOS
Refe-rence State	0.99937	1.00213	-63	213
Step 1	0.99945	1.00359	-55	358
Step 2	0.99955	1.00305	-45	304
Step 3	0.99944	1.00306	-56	305

III.3 Design and Analysis of Welded Grid Plate for Future FBRs

The grid plate of Commercial Fast Breeder Reactor (CFBR) is a large safety related structure which supports the entire core subassemblies and inner vessel. It is made of two plates inter connected by a cylindrical intermediate shell. The bottom plate and shell are of equal outer diameter and that of top plate is larger with the excess portion hanging over the shell. To lower the stresses and deflection, stiffeners are provided between the shell outer surface and over hanging portion of top plate. The portion of top plate, which is inside the shell, and bottom plate are perforated in exactly similar triangular array and the corresponding holes will be in vertical alignment in assembled structure. Sleeves connecting these holes hold the subassemblies and also give grillage reinforcement to the grid plate. The intermediate shell along with top and bottom plate forms a space called 'inlet plenum', which contains the pressurized inlet sodium. The main functions of grid plate are (i) to support the core subassemblies and inner vessel and to allow insertion and withdrawal of subassemblies, (ii) to maintain the verticality of the subassemblies so as to ensure the smooth operation of the fuel handling and control and safety rod drive mechanism (CSRDM) and diverse safety rod drive mechanism (DSRDM) and (iii) to serve as plenum to distribute the coolant (sodium) flow to subassemblies through sleeves. Since it holds the active core, which is radioactive, it is categorized as safety class-1. Further, the grid plate is not accessible once reactor becomes critical. Some of the features of CFBR grid plate have been improved, compared to PFBR grid plate, for enhancing economy and safety as described in Table 1.

Input data

The material of grid plate is SS316 LN to enhance the resistance against the radiation damage. The normal operating temperature of grid plate is 670 K. The allowable stress, S_m, is 98 MPa. The schematic of mechanical load in the operating condition is shown in Figure 1.

The grid plate is supported at the lower end of intermediate shell and bottom as shown in Figure 2.

Design criteria

As per functional limit of grid plate, the maximum deflection of the grid

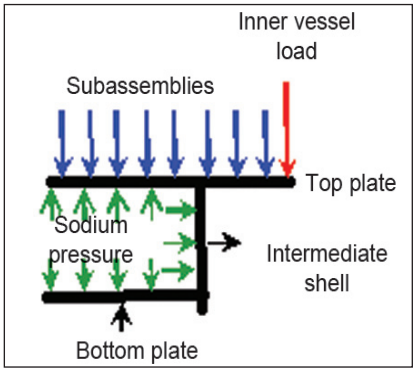

Fig. 1 *Loading details of CFBR grid plate*

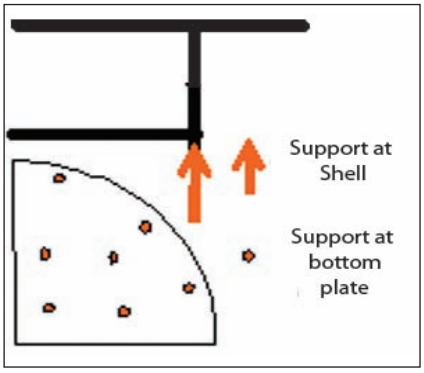

Fig. 2 *Boundary condition details of grid plate*

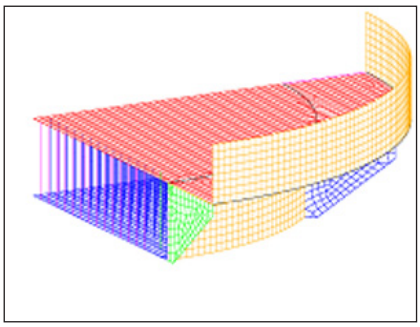

Fig. 3 Finite element model of 90º symmetric sector of grid plate

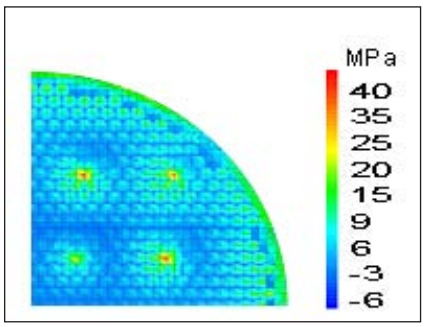

Fig. 4 Von mises stress intensity (P_m+P_b) of top plate (perforated region) under mechanical loading

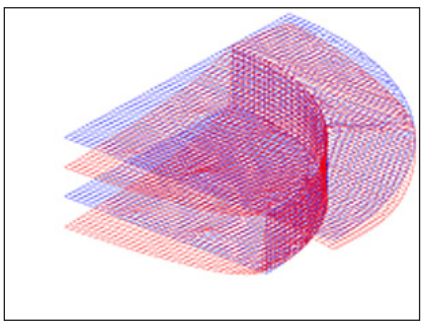

Fig. 5 Deformation of over all grid plate under mechanical loading

plate is limited up to 3 mm. The maximum slope at the control safety rod and diverse safety rod location is $5.0x10^{-4}$ radian to ensure their proper insertion. The maximum slope at the subassemblies location is $7.5x10^{-4}$ radian to ensure the proper fuel handling operation. Design check, for stress limit, for grid plate is carried out as per RCC-MR 2007 procedure for class-1 component.

Parametric study to optimize the diameter of intermediate shell

For finalizing the major dimension, like diameter of intermediate shell, a parametric study has been carried out by varying the diameter of shell and keeping the thickness of top plate and thickness of shell as 40 mm. The weight of subassembly on the top plate of grid plate, up to the shell, is counter balanced by weight of inner vessel and the subassemblies, out side of shell. The aim of parametric study are: (i) to arrive at the bending stress optimum at the junction of top plate and shell and (ii) to optimize the deflection at the centre and periphery of top plate. The top plate and shell are modeled using axisymmetric thin shell elements in CAST-3M FE software, developed by CEA, France. It gives a rough idea of shell diameter (~4.6 m) for technology development purpose.

Table 1: CFBR grid plate

Sl. No	Features
1	Reduction of sleeves: Sleeves, with hole, are provided only for the subassemblies that require force cooling and spikes are provided for the rest of the subassemblies
2	Reduction of diameter of intermediate shell
3	Comfort layout of eight primary pipes
4	Reduction of height of intermediate shell from 1000 to 685 mm
5	Welded joints: Due to welded joints the flange of grid plate, inner vessel and core support structure, high strength bolting material is not required. Moreover, there will be no undesirable leakage of sodium
6	Stiffeners are provided between outer surface of intermediate shell and lower surface of over hanging portion of top plate to strengthen the overhanging portion of top plate, which optimizes the stress and deflection
7	Cost saving: The net weight reduction of CFBR grid plate is ~55% as compared to that of PFBR grid plate, with an estimated cost saving of 30%

Parametric study to optimize the thickness of top plate and bottom plate

For detailed analysis, a 90º symmetric sector, of grid plate including sleeves, stiffeners and a small portion of inner vessel and core support structure, has been modelled with three/four nodded thin shell element for top plate, bottom plate and intermediate shell and beam element for sleeves as shown in Figure 3. The top plate (up to the intermediate shell) and bottom plate of grid plate are treated as perforated plates and modeled as equivalent solid plates with modified elastic constants given by ASME code section-III, Div-1, APPENDICES (Article A-8000) and corrected for $t/p \leq 2$. The ratio of modified Young modulus of elasticity and Young modulus of elasticity (E^*/E) is 0.09. The modified Poisson's ratio (ν^*) is 0.43.

The thickness of top and bottom plate varied as 30, 40 and 50 mm keeping the thickness of shell and stiffeners as 40 mm. The primary stress intensities in various parts of grid plate has been extracted; the top plate stress contour is shown in Figure 4.

Slope and deflections

The slopes at each sub-assemblies point are extracted, for top plate, bottom plate and shell thicknesses

as 40 mm. The overall deflection of grid plate is shown in Figure 5.

The maximum slope at diverse safety rod and control safety rod and subassembly locations is $1.2x10^{-4}$ radian. The maximum slope at subassemblies is $4.5x10^{-4}$ radian. The deflection at the periphery of top plate is found to be 1.5 mm.

Stress analysis for the mechanical load (sodium pressure load, inner vessel load, subassemblies load and self weight of grid plate) shows that with increase in thickness of top plate and bottom plate, a significant decrease of primary stress intensities, P_m and (P_m+P_b), is seen in top plate, bottom plate and shell but no significant change in that of stiffener. The increase in thickness of stiffeners does not affect the stresses in top and bottom plates. However, the stress in stiffener decreases and that in shell increases due to increase in rigidity of stiffeners. The P_m and (P_m+P_b) values in shell are 38 and 93 MPa against the allowable limit of 98 and 147 MPa respectively as per RCC-MR. The margin in stress may be absorbed by eight openings on the shell for the primary pipe entry. For a stiffener thickness of 40 mm, the values of P_m and (P_m+P_b) are 100 MPa against the allowable limit of 98 MPa. The P_m and (P_m+P_b) values in top plate, thickness as 40 mm, are 23 and 72 MPa respectively. The margin may be used against seismic excitation load, during earthquake. Similarly for the bottom plate, for thickness of 40 mm, the values of P_m and P_m+P_b is 38 MPa.

The maximum slope at CSR and diverse safety rod location is $1.2x10^{-4}$ radian that is less than allowable limit of $5.0x10^{-4}$ radian. The maximum slope in subassemblies is $4.5x10^{-4}$ radian against the allowable limit of $7.5x10^{-4}$ radian. Here change in thickness of stiffener is not affecting the slope of subassemblies.

III.4 Assessment of Design Safety Limits for Fuel Cladding Based on Benchmark Tests

The spacing of PFBR fuel rods is such that adjacent rods straining by 6% will touch each other; the key question is thus whether strains of this magnitude or greater can occur in practice in adjacent rods at the same level in the assembly. If adjacent pins balloon at the same axial level (coherent ballooning) they may touch each other impeding a proper flow of the coolant. Thus, the associated question is how coolability is affected by large strains leading to progressive blockage of the coolant sub-channels.

The design safety limits (DSL) for fuel pins are given based on the rupture of the fuel clad. The coolability, has to be validated in specific cases. The reason for conducting out-of-pile tests with single fuel pin at high temperature and high pressure is that ballooning takes place in the beginning of cycle, at low levels of irradiation when the material is ductile. With increasing irradiation levels, the material becomes brittle and the concern will be rupture, not ballooning.

An experimental facility has been indigenously developed to simulate the various category events. High sensitivity X-ray radiography method is used to measure the deformation of the specimen. The details of these experimental activities have been presented in this report.

In PFBR, the core temperature may rise locally due to loss of flow accident, primary sodium pump trip, seizure or rupture, sodium voids, or any kind of loss of heat removal from the fuel pin. At this condition the clad tube can suddenly undergo large circumferential deformation. This type of behavior of fuel clad tube is reported as ballooning. Materials like polymers, rubber etc. generally exhibit this behavior. This phenomenon is also seen in metals at high temperatures.

If the temperature is high enough, the cladding can even burst releasing the fission product gases into the coolant. The most serious result from clad ballooning is that it may cause blockage of the flow channels and result in a permanent restriction of the coolant flow. A coolant flow restriction results in an increase in the cladding and fuel temperatures resulting in severe fuel damage. Figure 1 shows the flow obstruction and fuel damage caused due to ballooning.

It is also observed that the unirradiated fuel pins fail after ballooning late in the transient when the cladding temperature is high. The failure of the cladding in these

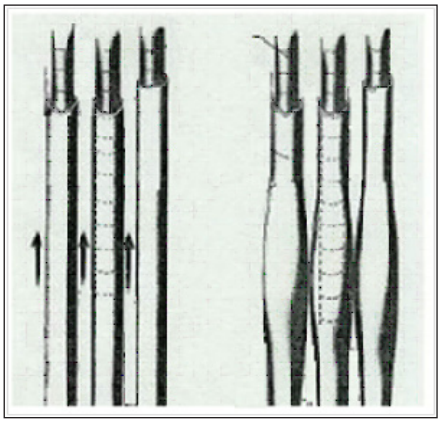

Fig. 1 Clad ballooning obstructing flow

Fig. 2 Experimental set-up

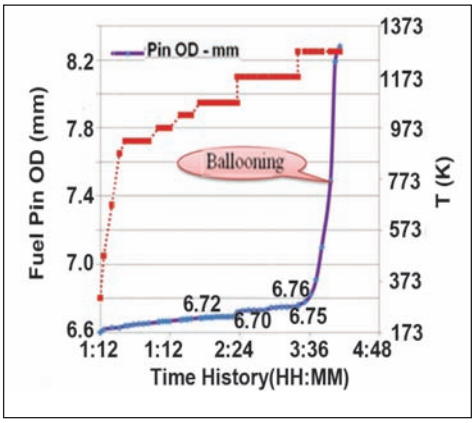

Fig. 3 Material behavior at 100 bar

tests was ductile, and it was a burst opening. The used fuel fails early in the transient with brittle fracture which was a longitudinal crack.

Experimental investigations

A high temperature clad tube test facility (HTCTTF) has been indigenously developed to study the behavior of clad tube material under various operating conditions. The test facility includes a stainless steel pressure vessel, D9 clad tube and electric furnace held together by the stand. The experimental set up is shown in Figure 2.

The clad tube is 320 mm long and 6.6 mm in diameter, with a thickness of 0.45 mm and is welded to the pressure chamber. It is filled with argon gas at high pressure, to simulate the fission gas pressure. The closed tube under internal pressure facilitates biaxial state of stress in the clad tube. The furnace is positioned such that a length of 50 mm of the fuel pin is heated to the maximum temperature and the heat transfer to the weld is negligible. High intensity X-ray system is deployed to measure the deformation of the clad tube inside the furnace at the desired time interval.

Ballooning experiment

An experiment has been conducted at 100 bars internal pressure, and the temperature is raised in stages. It is held for some time at each temperature. This is done to find the temperature range at which ballooning is likely to take place. X-ray images are taken periodically. Based on proper image processing, the change in dimensions of the tube has been measured (Figure 3). It is observed that the fuel clad keeps deforming slowly with increase in temperature and time. Sudden bulging, i.e., ballooning of the pin is observed around 1273 K and rupture takes place after 40 minutes at 1273 K. The failure of the cladding in this unirradiated test is ductile and it is a burst opening.

Experiment conducted to verify category 1 limit

The temperature of the furnace is raised to 1243 K and held for 4 hours. It is observed that the diameter of the fuel pin at the end of 4 hours is 6.74 mm. It can be observed that ballooning has not started up to 4 hours. In the design, up to 6% of clad dilation is allowed during the life time of the fuel pin, which is 2 years at 973 K and 60 bars pressure. It is found from the experiment that 2.1% dilation takes place up to twice the time it is kept in the reactor. Figure 5 shows the sudden ballooning. Rupture has taken place 10 minutes after ballooning.

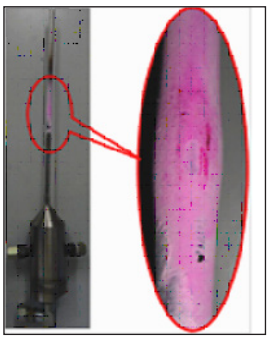

Fig. 4 Ballooned clad

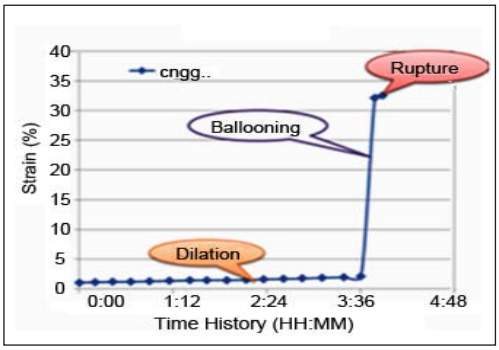

Fig. 5 After ballooning at 1243 K and 60 bar

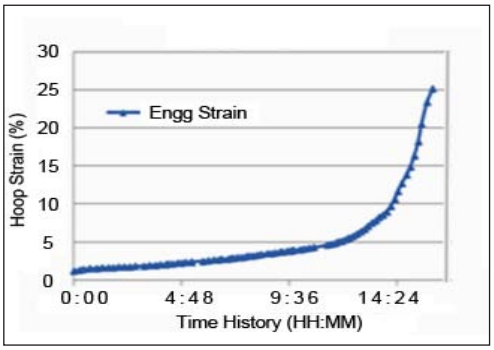

Fig. 6 Creep curve at 1223 K and 100 bar

Experiment conducted at 1223 K and 100 bars pressure

Another experiment has been conducted to obtain the multiaxial creep curve at 1223 K and 100 bars pressure and to study the ballooning behavior. Figure 6 shows the creep curve at 1223 K and 100 bars pressure. It is observed that the strain at the end of 16 hours is 25%.

Conclusions

Based on limited tests carried out at high temperature, a few new and interesting results have been obtained on rapid deformation behavior of fuel claddings. The tests exhibit phenomenon of ballooning at the beginning of life of the core. Creep curves at high temperatures for the structural material (D9) have been obtained. The whole deformation properties obtained at various time intervals provide important data for the development of constitutive models for the material. Further, tests are in progress to identify the zones where either clad would rupture or clad would undergo ballooning. This information adds new insight into mechanics of deformation and failure of structures at high temperature.

III.5 Challenges and Achievements in Molten Fuel Coolant Interaction Studies

The sodium fuel interaction facility (SOFI) has been commissioned to carryout molten fuel coolant interaction (MFCI) experiments, with prime objective to study fragmentation process and morphological characteristics of generated debris bed. Data obtained will also help in development and validation of mathematical model towards post accident heat removal (PAHR) assessment. Experiments are planned in phases using uranium fuel in both metal and oxide forms, starting from notional melt mass of ~1 to 20 kg in future. The experimental setup comprises an induction melting system with release mechanism on top of the sodium interaction vessel. This interaction vessel contains filter basket with model core catcher inside and is connected to dump vessel housed in a pit. The sodium system is shown in Figure 1. Required quantity of sodium is loaded in interaction vessel and heated up to 673 K before carrying out the experiment.

The predetermined fuel charge is loaded in crucible and inductively heated to targeted drop temperature, before being released into the interaction vessel. After the interaction process, sodium is cooled to 473 K and drained to dump vessel through filter basket kept inside, which along with the catcher plate helps in retaining all the fragmented debris.

Successful commissioning and operation of such sophisticated facility demands several innovative design features to be incorporated to meet challenges like melting of charge, simultaneous cooling of induction power supply with transformer and coil, ensuring integrity of crucible, melt hold and release, isolation of melt crucible from sodium vessel, remote operation of various fast acting mechanisms, non contact high temperature measurement, insulated melt guide path and remote handling of filter basket with debris. A few of such incorporated systems have been detailed here. For the first phase experiments with melt mass upto 1 kg, induction heating system is installed with separate cooling circuits for power supply, transformer and coil. Thermo fluid named as Therminol-59 has been selected as cooling medium. For safe melting of charge, cold crucible methodology has been adopted where the ceramic crucible is casted with embedded cooling tubes. Both inert gas and oil cooling options are provided for cooling of crucible during heating, to retain integrity. The fuel mass is encapsulated in steel cladding and loaded inside

Fig. 1 *Experimental set-up*

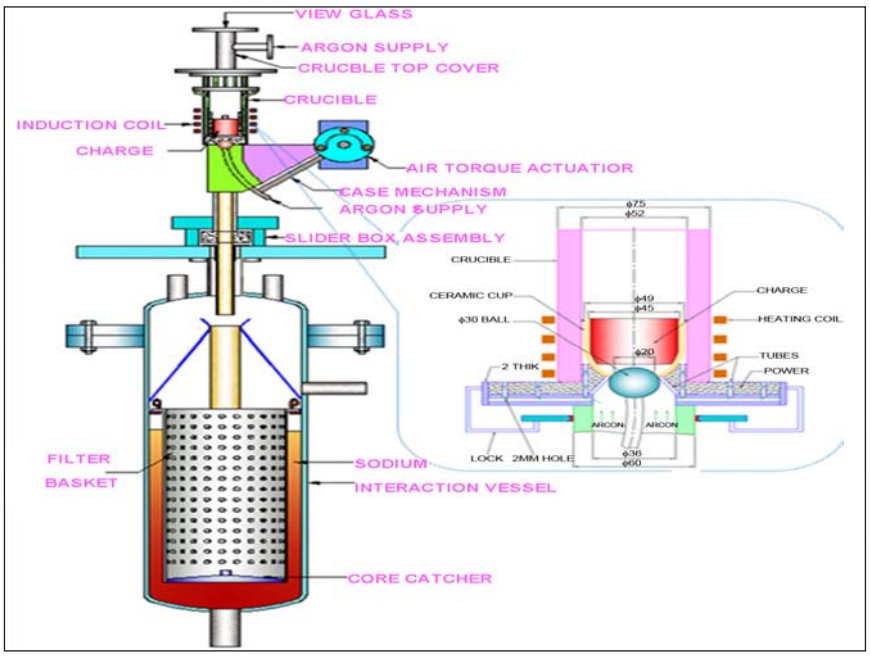

Fig. 2 *Swing and slider valves*

Fig. 3 *Crucible with coil and valves*

the crucible. Inert atmosphere is maintained for the charge throughout, starting from heating inside the crucible to releasing into interaction vessel. Melt guide tube has been internally lined with ceramic wall to handle the high temperature melt flow. Dedicated instrumentation such as two color pyrometer to measure melt temperature, fast response thermocouples on melt release path, online temperature monitoring for sodium system, oil and water circuits are deployed in the facility. Entire melting system is enclosed in a small chamber and provided with nitrogen cooling along with venting through HEPA filter. Isolation of melt crucible from sodium vessel and controlled release of melt mass is accomplished using combination of two innovative automated valves in sequence as shown in Figure 2 and 3. The swing valve just below the crucible helps in retaining the melt at targeted temperature and releasing to the guide tube, on command from control room. Separate inert gas flow system is attached to the valve plunger and base for cooling as well as to maintain inertness. Slider valve above the interaction vessel, isolates the melt system from sodium vapor during heating and just opens up for a short time for melt release, allowing the flow of melt through guide tube. Synchronization of operation for both the valves are very important for successful melt release into the interaction vessel. A rail mounted, low speed geared motor integrated carriage trolley is installed on the top to facilitate post campaign removal and reloading of filter basket with catcher plate, kept inside interaction vessel. This helps in smooth handling of debris bed on catcher plate after sodium draining.

At the commissioning stage, one campaign was carried out to ensure smooth operation of the systems. Uranium (60 g) encapsulated in steel clad (500 g) was inductively heated upto 1873 K and released into sodium (35 kg) at 473 K, with an interaction height of 700 mm. After experiment, sodium was successfully drained to bottom drain vessel through filter, retaining the fragmented debris on catcher plate undisturbed for investigation. The debris bed formed on catcher plate is shown in Figure 4, which was retrieved after thorough sodium cleaning of the internals. No noticeable pressure rise was observed during the interaction and the collected debris was found to be well fragmented and evenly dispersed all along the catcher plate. Experiments are planned both in metal and oxide of uranium, in the present facility and finally higher inventory campaigns will be carried out in newly designed setup in future.

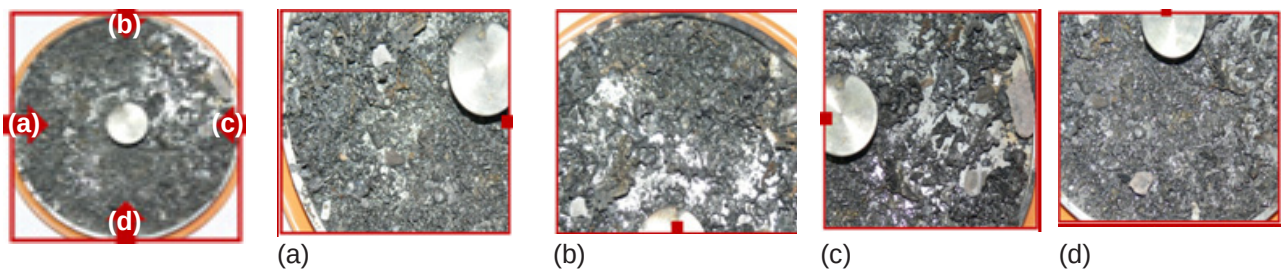

Fig. 4 *Uranium metal+stainless steel debris collected on catcher plate*

III.6 Numerical Simulation of Single Sodium Droplet Burning and its Implication on Containment Design

Analysis of sodium fire events upon its accidental leakage from the heat transport systems of sodium fast reactors (SFR) is important in order to evaluate its consequences such as burning rate of sodium, formation of the aerosols, and temperature and pressure rise in the reactor system cells. Reactor containment building (RCB) which encloses the primary sodium system is the final barrier for radioactivity release into the atmosphere and this has to be designed to withstand the consequences of the anticipated severe accident scenario. During core disruptive accident, primary sodium from the reactor vessel is ejected into the RCB through various leak paths in the roof slab, and resultant temperature and pressure rise due to this sodium fire forms the design basis of the RCB.

In the event of leakage into the atmosphere, sodium burns in two main modes namely, spray fire and pool fire depending on the leakage conditions. Among these two modes, spray fire is generally considered to be more severe in terms of the resultant thermal and pressure transients since it involves droplet form burning, which provides more surface area for combustion. Sodium spray fire involves various concurrent complex transport processes but essentially its characteristics are influenced by the ignition and combustion behaviour of individual droplets making the spray. Hence, the single sodium droplet combustion has been studied.

Sodium droplet combustion takes place in two stages namely, pre-ignition stage during which the surface oxidation prevails followed by the vapor phase combustion. Of these two stages, sodium droplet combustion predominantly occurs in vapor phase, and it is the major phase in terms of duration (i.e., with respect to the droplet life time), whereas, the surface oxidation plays an important role in the ignition of sodium, and decides the droplet to attain its vapor phase combustion.

Numerical studies have been carried out to understand the ignition and combustion behaviour of sodium droplet in convective environments under different initial conditions.

Pre-ignition stage combustion

During pre-ignition stage, the oxidation reaction occurs at the droplet surface due to very low vapor pressure of sodium at its initial temperature (even at 773 K, the vapor pressure is 5 mm of Hg only). Generally, the reaction heat generated from this surface oxidation process can be easily transferred to the droplet surface due to high thermal conductivity of liquid sodium. Owing to this, within a small transient period there is a rapid increase in the droplet surface temperature, and it can reach very close to the boiling point of sodium (1156 K). This result in vast evaporation of the droplet and hence further combustion takes place in vapor phase. The time required to raise the temperature of the sodium droplet from its initial temperature to the ignition temperature is called ignition delay time, and it has been estimated by considering energy balance at the droplet surface in terms of rate of heat generation from the surface oxidation reaction and rate of heat loss to the ambient. The rate of heat generation depends on the reaction rate at the droplet surface, and it has been evaluated from the temperature-dependent surface oxidation reaction considering the formation of sodium monoxide alone. The reaction rate parameters,

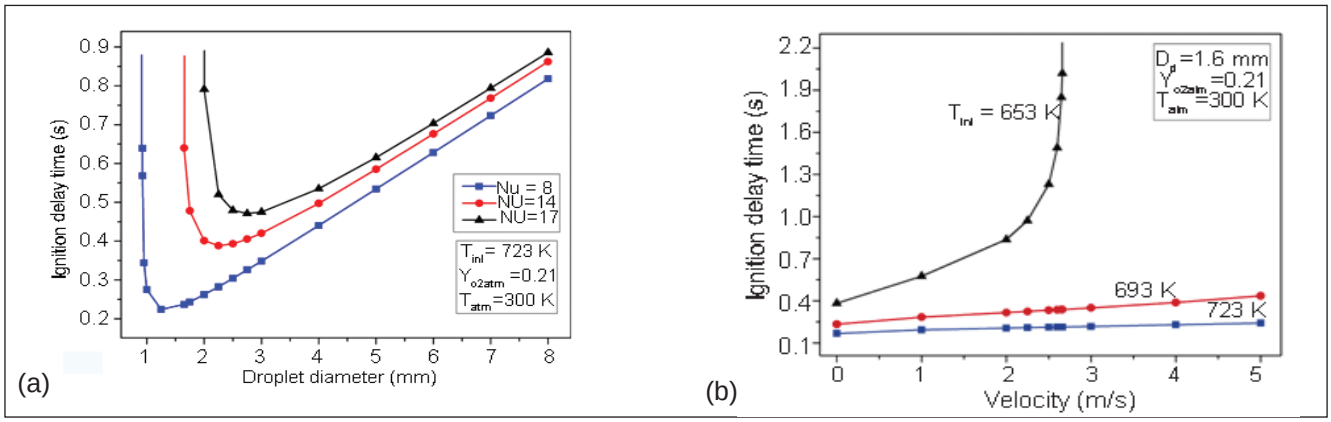

Fig. 1 *Variation of ignition delay time with (a) Droplet diameter and (b) Relative velocity*

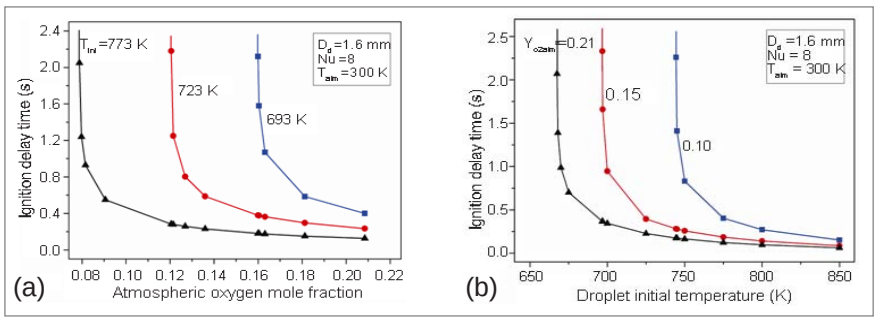

Fig. 2 Variation of ignition delay time with (a) Atmospheric oxygen mole fraction and (b) Droplet initial temperature

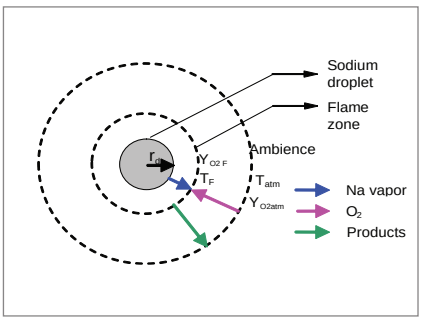

Fig. 3 Schematic of burning sodium droplet

i.e. activation energy and frequency factor, were taken from the published experimental results available in the literature. The heat loss rate has been estimated from the well-known Ranz-Marshell correlation. Ignition delay times were evaluated numerically for different ranges of values to the main parameters (i.e. droplet initial temperature, its diameter, relative velocity and atmospheric oxygen concentration) that can affect the ignition of the sodium droplet.

The ignition delay time is found to increase with the increase in droplet size and relative velocity due to increase in heat loss rate from the droplet surface (Figures 1a and 1b). With the increase in droplet initial temperature and atmospheric oxygen concentration, the surface reaction rate increases and hence the ignition delay time decreases (Figure 2a and 2b). The steep increase in ignition delay time implies the ignitability limit of sodium droplet under given conditions.

Vapor phase combustion

The steady-state vapor phase combustion of the sodium droplet has been analyzed based on the spherico- symmetric model shown in the Figure 3.

The burning rate of sodium droplet is obtained based on the rate of oxygen diffusion to the flame zone along with heat balance and chemical equilibrium consideration for the formation of sodium monoxide. The rate of oxygen diffusion to the burning zone has been estimated from the modified Frossling correlation. The heat balance at the flame zone is obtained by equating the rate of combustion heat generation to the heat transfer rate to the ambience (by convection and radiation). The convection heat transfer coefficient between the droplet and ambience has been estimated using the Ranz-Marshell correlation.

The burning rate of sodium droplet has been evaluated numerically for various initial and convective conditions. With the increase in droplet velocity or decrease in droplet size, the mass transfer coefficient increases appreciably and hence the droplet burning rate increases (Figures 4a and 4b). As the oxygen concentration in the atmosphere reduces the burning rate decreases due to the reduction in oxygen mass transfer rate. The maximum flame temperature estimated is below the decomposition temperature of sodium monoxide (2220 K), and it decreases as the oxygen concentration in the ambience is reduced (Figure 4c). The burning rate reduces drastically when the oxygen concentration falls below 5 mole%, which was observed experimentally too. Below this oxygen concentration level, the vapor phase combustion is no longer valid since the estimated flame temperature approaches the boiling point of sodium.

The numerical results obtained from this analysis have been compared with the experimental results available in the literature and found to be satisfactory. The developed sodium droplet combustion models will be employed in the analysis of different sodium spray fire scenarios.

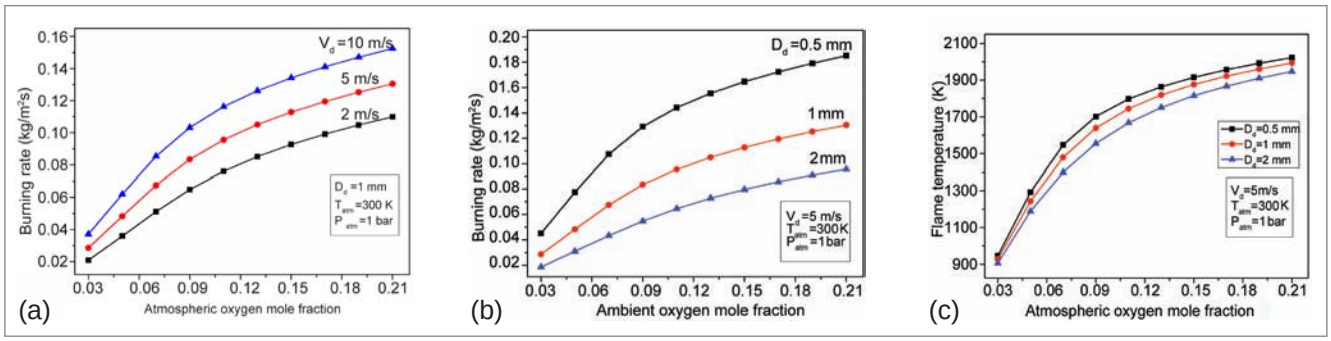

Fig. 4 Effect of droplet velocity on (a) Burning rate, (b) Size on burning rate and (c) Ambient oxygen concentration on flame temperature

III.7 Establishing Scaling Laws for Experimental Studies on Post-accident Heat Removal in Fast Reactors

The fast reactor design includes the core catcher, an in-vessel debris retention device. This device also serves as a barrier to prevent settling of debris on the main vessel (Figure 1) and thereby keeping its maximum temperature within acceptable limits.

The pool thermal hydraulics inside a fast reactor is very complex with core catcher dissipating its heat to decay heat exchangers by natural convection through the degraded core. Hence, suitable experiments are essential to assess the heat removal capacity of the core catcher. Apart from estimating the heat removal capacity of core catcher by computational studies, it is essential to demonstrate it experimentally. Unfortunately, it is very difficult to perform experiments in sodium pool of large size. This is mainly due to fact that the sodium is opaque and is unsuitable for any type of flow visualization, sodium experiments have to be performed at elevated temperature due to its high freezing point and sodium also reacts violently with air and water.

On the other hand, there are lot of incentives to perform experiment in water, on geometrically similar models. Due to the vast difference between the Prandtl numbers of water and sodium, it is difficult to transpose thermal results of water to sodium conditions in the reactor. To enable this transposability, a novel combined experimental cum computational study has been performed. The experimental model has been numerically simulated by 2-D Computational Fluid Dynamics (CFD) studies towards validating the

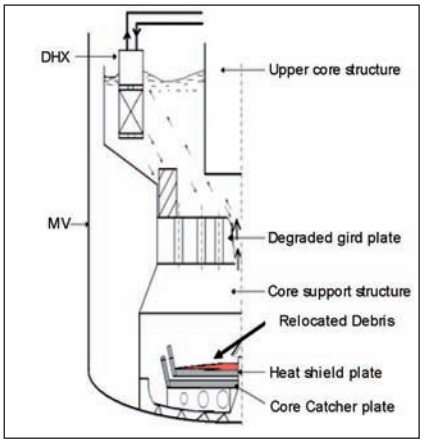

Fig. 1 *Typical representation of settled core debris*

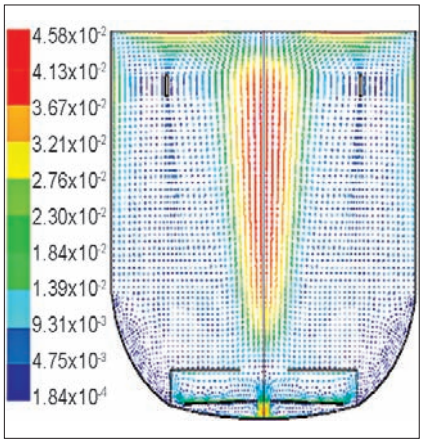

Fig. 2 *Velocity vectors at 48 hours*

CFD code. Following this, the CFD model has been used for sodium conditions in a 1:4 model of primary system. The mathematical model comprises the continuity, RANS and energy equations with *k*-ε turbulence closure model. By comparing the results of water and sodium conditions, the factor that accounts for change of fluid is established. Then, a scaling relationship is proposed for transposability of water model results to reactor condition.

The initial conditions used as no slip at solid surfaces and temperature of 304.5 K every where . Symmetric boundary conditions are imposed on the vertical axis. No slip boundary conditions are used for the entire solid-fluid interface. Side wall of the vessel is assumed to be convective boundary on the insulation. A uniform volumetric heat source is specified in the heat shield plate volume to simulate decay power from the heat generating debris. The convective boundary condition at top surface of water pool is updated as solution progresses with the evaporative heat loss as in case of the experimental vessel. The Boussinesq approximation is assumed to hold good for both the fluids.

The conservation equations of mass, momentum and energy along with the equations for turbulent kinetic energy and its dissipation rate are numerically solved by finite volume method. Pressure-velocity coupling in the above equations is resolved by the PISO algorithm. The first order UPWIND scheme is used to combine the convective and diffusive fluxes in the transport equations.

The computed velocity vectors after 48 hours are given in Figure 2. The results clearly show the establishment of natural circulation in the cavity.

The numerical analysis clearly indicates that there is inward and outward flows through the chimney, which aid the natural convection. The figure clearly depicts inception and growth of plume with time. It is also observed that the magnitude of maximum velocity decreases with time because temperature is penetrated not only in axial direction

but also in lateral direction. It is clear from these figures that the width of band of velocity vector in axial direction increases with time but the overall maximum velocity magnitude decreases.

The scaling law is developed to extrapolate the result of 1:4 scale water model results to the actual reactor condition where sodium is the coolant. Numerical analysis has been done for sodium and water for identical temperature differences (ΔT) between the source and sink. Nusselt number for both the cases is found out using distinct heat transfer characteristics in both the fluids.

$$Q_p = F \times S \times \frac{k_p}{k_m} \times \frac{\Delta T_p}{\Delta T_m} \times Q_m$$

The value of F, which is the ratio of Nusselt numbers in sodium and water, is found to be 0.112. k is the thermal conductivity of the fluid. The subscripts p and m denote the prototype and model respectively. The heat transfer rate (Q) in the actual experimental core catcher is found to be 30.1 kW for ΔT of 47 K. Using the scaling relationship developed and heat removal capacity achieved in a 1:4 scale experimental core catcher, the heat removal capacity of PFBR core catcher has been estimated as a function of temperature difference between core catcher and decay heat exchanger. It has been established that the total instantaneous blockage of a fuel subassembly leading to a decay heat load corresponding to melting of seven subassemblies can be very well accommodated on core catcher with enormous margin.

III.8 Studies on Sodium Cable Fire

In Prototype Fast Breeder Reactor (PFBR), top shield above reactor, houses power and control cables laid in cable trays for transmission of electrical power to various electrical equipments installed on the roof slab. The cables used are flame retardant low smoke type in which insulation material is cross linked polyethylene (XLPE) and the sheath is flame retardant low smoke Polyvinylchloride (PVC). In case of core disruptive accident, which is a very low probability incident, around 350 kg of sodium may be pushed out from reactor pool to the top shield as per the analysis. The high temperature liquid sodium coming out of reactor vessel may catch fire which may lead to secondary cable fire also. The sodium fire and cable fire will increase pressure and temperature in the reactor containment building. The sodium-cable interaction and resultant fire may damage the cable insulation resulting in loss of power and control supply to the equipment. Sodium cable fire studies were carried out to understand the extent of damage to the cable.

The experimental facility consists of a stainless steel vessel, stainless steel "U" tube and quartz glass chamber. Figure 1 shows the experimental facility along with a test sample cable mounted inside the quartz chamber. Both ends of the cable are brought out of the glass chamber for electrical connection and measurement of insulation resistance of the cable. About six gram of sodium is taken in the stainless steel vessel and heated to 773 K. The facility has a control valve which permits injection of liquid sodium inside glass chamber. The stainless stee vessel is pressurized to 41 KPa by operating gas solenoid valve. When sodium control valve is opened, liquid sodium ejects out through "U" tube/nozzle as spray into the quartz glass chamber. The sodium droplets sprayed at 773 K catches fire creating spray fire scenario by interacting with available oxygen inside the quartz glass chamber. Sodium spray fire impinges on test cable kept above nozzle. Sodium spray fire impinging on cable will cause damage to cable due to primary and secondary fire. The extent of damage to the cable is estimated by measuring the insulation resistance of the cable before and after sodium fire impingement. As a thumb rule, a cable can be used in service as long as its insulation resistance is more than 1 Mega Ohm. Extensive damage of the cable due to fire may cause electrical shorting indicated by stopping of a glowing lamp connected through this cable.

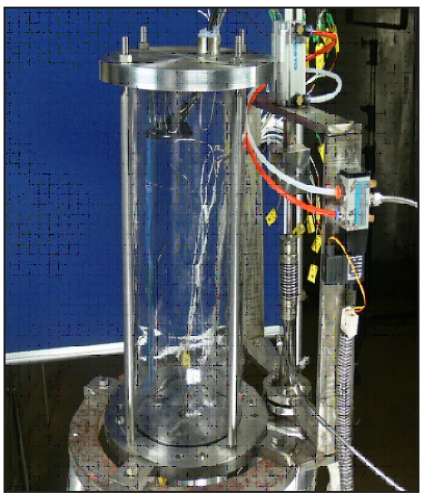

Fig. 1 *Experimental set-up*

Flame retardant low smoke cables used in our experiments (Figure 2a) are 1100 voltage grade, copper conductor, each core cross linked polyethylene insulated, flame retardant low smoke PVC overall inner and outer sheathed conforming to IS 7098.

The damaged flame retardant low smoke cable after impinging sodium fire followed by secondary cable fire is shown in Figure 2b.

One of the objectives of this study is to evaluate the pressure build up and temperature rise in the chamber during cable fire following sodium fire. In case of sodium-PVC cable fire, the maximum air temperature was measured to be 383 K and corresponding pressure build up was 127 KPa (Figure 3). Experiment was repeated with FRLS cable and it was observed that the maximum air temperature was as low as 345 K with pressure build up of 118 KPa (Figure 4).

It was observed that the insulation resistance values decreased from 11 to 2.2 G Ohm for PVC cable and 56.2 to 22 G Ohm for flame retardant low smoke cable during the impingement of sodium spray fire.

The sodium – cable fire scenario was recorded using high speed camera (Figure 5a) and Infra Red camera (Figure 5b). Sodium combustion occurs within 500 ms whereas cable fire continues for about 20 seconds. The self extinguishment of cable fire is due to oxygen depletion inside the quartz chamber, as indicated by on-line measurement of oxygen concentration. Oxygen concentration was found to be 17% g sodium- PVC cable fire whereas only 18.5% in case of flame retardant low smoke cable fire (Figure 6). This indicates the fire retardancy associated with flame retardant low smoke cables.

The sodium-cable fire residue was analyzed using various analytical techniques such as Mass spectrometry, Fourier Transform Infra Red (FTIR) spectroscopy and Nuclear Magnetic Resonance (NMR) spectroscopy. It was observed that the residue consists of 2.5% sodium chloride which indicates that the chlorine gas released during the cable fire reacts with sodium to form sodium chloride.

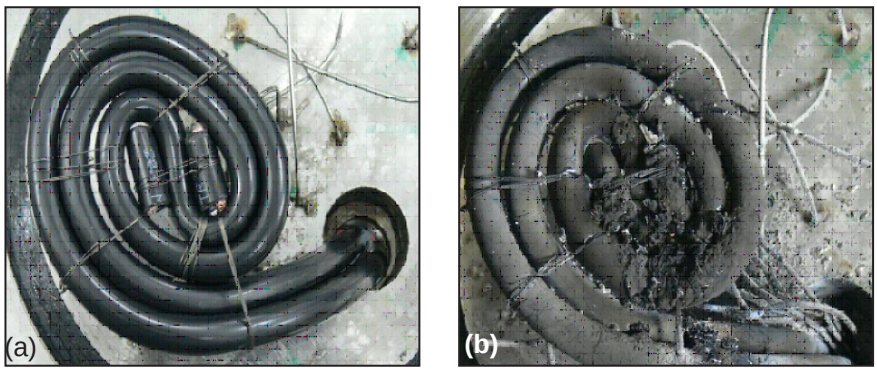

Fig. 2 *Flame retardant low smoke test cable (a) Before and (b) After impinging sodium fire*

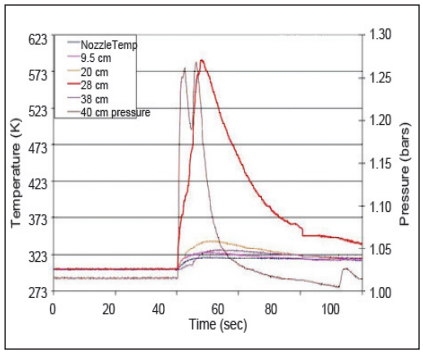

Fig. 3 *Pressure and temperature rise during sodium-PVC cable fire*

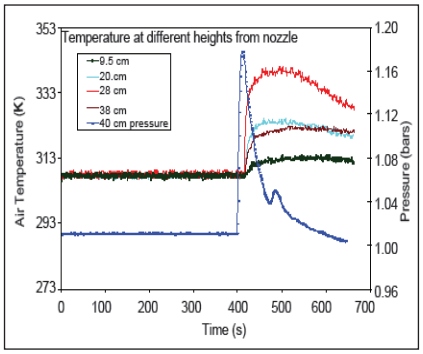

Fig. 4 *Pressure and temperature rise during sodium-FRLS cable fire*

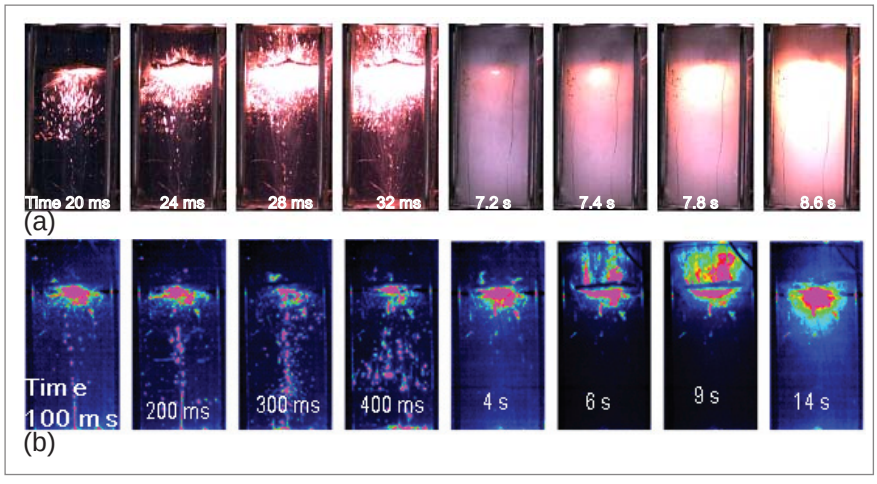

Fig. 5 *(a) Optical image and (b) Infra red image of sodium fire scenario*

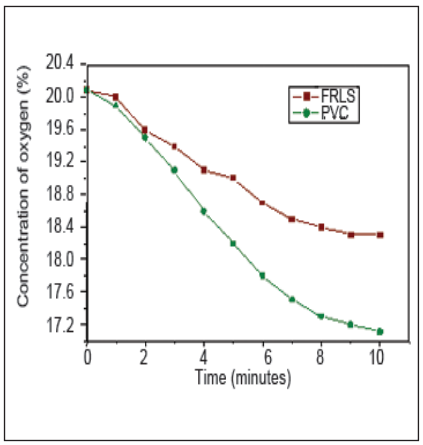

Fig. 6 *Oxygen depletion during sodium-cable fire*

III.9 Inertial Impaction Behaviour of Fuel Particles during Severe Accident Scenario in Sodium Cooled Fast Reactor

In the highly unlikely event of energetic core disruptive accidents in sodium cooled fast reactor (SFR), melting and relocation of a part of fuel inventory takes place, which may lead to recriticality and nuclear excursion followed by the formation of a high pressure, high temperature zone, which can be termed as fuel vapour bubble. This fuel vapour bubble, which is not in equilibrium with its surrounding, performs mechanical work on the primary containment. It further rises to the cover gas space due to its buoyance resulting in the radioactive material transport, which could ultimately contribute to the in-containment radiological source term. In relation to this, a computer code PTRACK has been developed to estimate the fraction of fuel particles absorbed by the sodium pool, which are present initially inside the rapidly expanding and oscillating fuel vapour bubble, by tracking the trajectory of the particles. The equations of motion for the fluid and particle are modeled in 1-D and adiabatic process (expansion and compression) is considered to model the behavior of fuel vapour bubble and cover gas region. Liquid sodium coolant is assumed to be incompressible and the particle momentum equation (PME) is solved numerically to predict the particle trajectory inside the expanding bubble. A particle is assumed to be removed permanently from the fuel vapour bubble once it crosses the coolant-vapour interface. The retention capability of sodium pool is quantified by particle absorption fraction (fraction of particles which are present initially inside the fuel vapour bubble and absorbed by the sodium pool), using Lagrangian approach. Finite number of particles is assumed to be uniformly distributed throughout the bubble and trajectory of each particle is evaluated to estimate the particle absorption fraction.

The PTRACK code predictions have been validated against published benchmark experiments. Subsequently, a parametric analysis has been carried out to evaluate particle trajectories corresponding to the pool type sodium cooled fast reactor geometry, with initial fuel vapour bubble pressures of 1, 2 and 4 MPa and for different particle diameters ranging from 3 to 500 microns. 20 particles are assumed to be distributed uniformly inside the bubble. Generally, the duration of fuel vapour bubble expansion process is in the order of few hundred milliseconds for the sodium fast reactor geometry considered and hence the present analysis has been carried out for the duration of 500 ms. The evaluated oscillation of bubble-coolant interface and associated particle trajectories for uniform diameters 10 and 100 micron using PTRACK code with an initial bubble pressure of 4 MPa are shown in Figures 1a & b respectively. The variation of particle absorption fraction with particle diameter is shown in Figure 2 for the initial pressure of 1, 2 and 4 MPa. From this study, it has been observed that during fuel vapour bubble expansion, fuel particles are effectively removed from the bubble due to the inertial impaction behavior over a wide range of particle diameter and initial pressure. Particles of diameter ranging from 50 to 200 micron are completely removed from the bubble for an initial pressure of 4 MPa due to the inertial impaction phenomenon and for diameters outside this range (i.e. on either sides), the particle absorption fraction decreases monotonically. Also, for a given diameter, particle absorption fraction decreases with decreasing initial pressure.

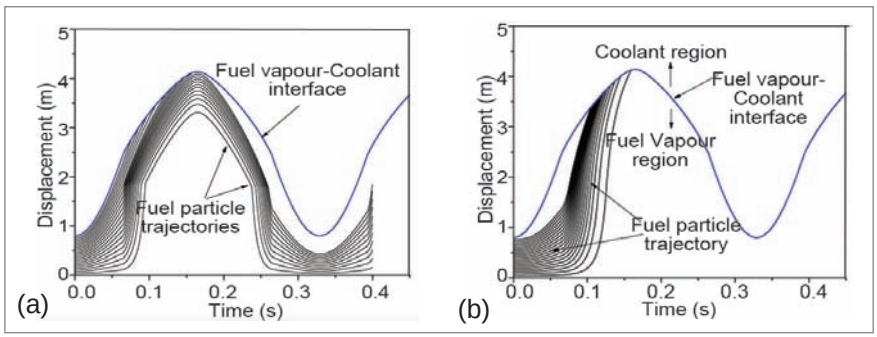

Fig. 1 Trajectories of coolant interface and fuel particles for initial pressure of 4 MPa and particle diameter (a) 10 micron and (b) 100 micron

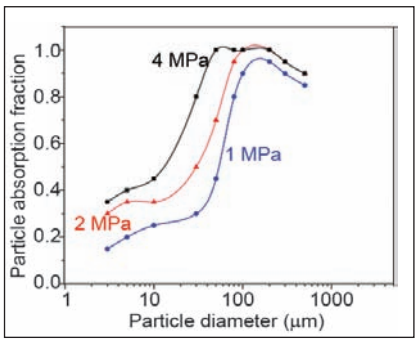

Fig. 2 Particle diameter vs particle absorption fraction

III.10 Development of Core Temperature Probe with Three Thermocouples

In PFBR, temperature at the outlets of all fuel subassemblies and inlet of the core are measured using thermocouple for monitoring the adequacy of core cooling. These temperature signals are used for monitoring adequacy of core cooling level and protecting the reactor against design basis event. These thermocouples are also used for detection of plugging of fuel subassemblies.

Thermocouple probes with two thermocouples are used for monitoring the fuel subassembly sodium outlet temperature. The probes are installed in thermowell. One thermowell is provided above each fuel subassembly and 30 blanket subassemblies. Figure 1 shows a thermocouple probe and location of the thermowells in the control plug.

Signal from each thermocouple is sent to three dedicated real time computers for further processing. Each computer generates SCRAM signal when the parameter exceeds their respective thresholds.

SCRAM signals from the three real time computers are fed to 2/3 logic of shutdown system. Since the three real time computer shares the thermocouple signals, total independency is lost. To provide totally independent monitoring system, three thermocouples are required for each subassembly. Presently, for PFBR application, thermocouple probes with two thermocouples are imported. Feasibility of providing three thermocouples without changing the dimension of the thermocouple probe was studied. Gripper assembly

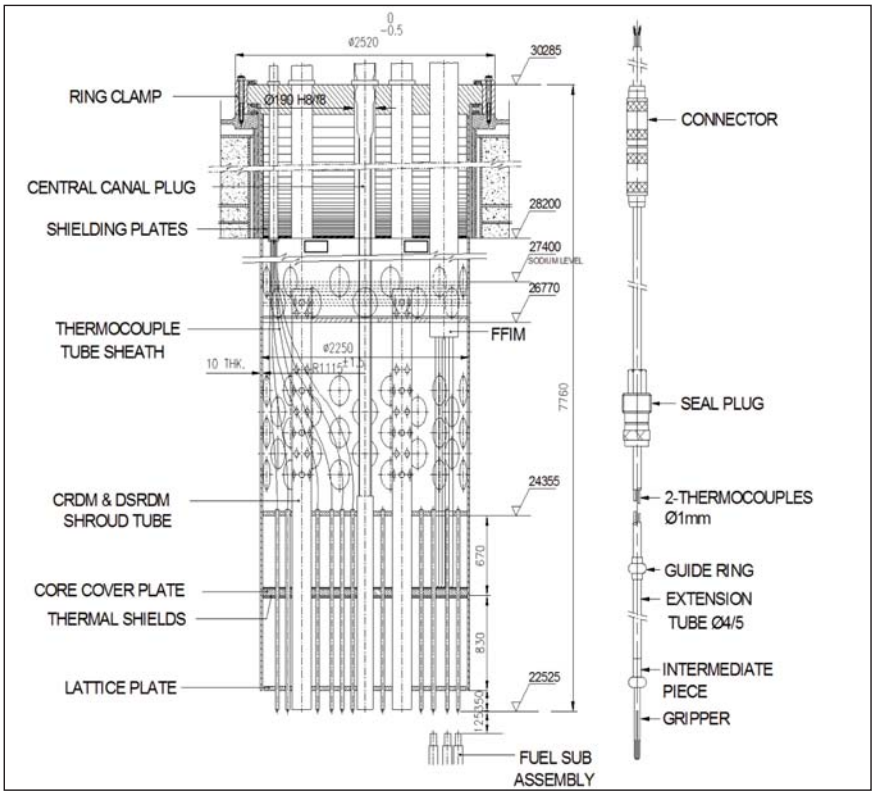

Fig. 1 *Core thermocouple probe*

which requires modification was machined to ensure that it can accommodate three thermocouples without losing its strength. It was decided to develop the thermocouple probe indigenously. A small scale industry was identified to take up manufacturing. Initially, a probe similar to that used in PFBR was fabricated with shorter length. Subsequently two meter length thermocouple probe with three thermocouples were fabricated.

After establishing the capability of the industry to take up the fabrication, probe with a length of 10 m and three thermocouples which can be used in future FBRs were fabricated. Thermocouple gripper assembly is shown in Figure 2 for three thermocouples. Insertion test was carried out with the tube sheath of similar bending radius of PFBR tube sheath. It was observed that insertion is very smooth and no damage was found on thermocouple tip. Further thermocouple probe performance was checked in FRTG SILVERINA loop up to 823 K and it was found that maximum deviation among the thermocouple in the probe was 1.2 K. Hence it is concluded that the probe design with three thermocouples is suitable for utilizing in future fast breeder reactors.

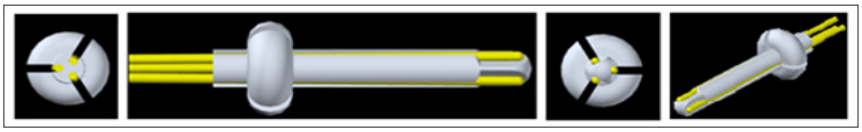

Fig. 2 *Gripper assembly for three thermocouples*

III.11 Permanent Test Facility for Neutron Detectors at KAMINI

KAMINI reactor is a unique U^{233} fuelled, light water moderated, natural convection cooled and beryllium oxide reflected research reactor with a rated thermal power of 30 kWt. Over the years, KAMINI has been utilized for a variety of purposes, ranging from activation analyses, shielding experiments to neutron radiography of fuel pins of FBTR and pyro-devices used in ISRO satellite launch vehicles.

KAMINI has now become the favored destination for testing several types of nuclear flux detectors. For low-flux range up to 10^3 n/cm^{2}s, neutron sources are available and in-situ testing in a reactor is not required. Start-up range detectors like boron coated counters (BCC) and fission counters (FC) can be tested with this kind of sources. Other detectors, which are subject to larger flux while in service, like Ionization chambers and also low-sensitivity detectors like SPND (Self Powered Neutron Detector), require higher neutron flux to validate their design/manufacturing process. High gamma activity present in such neutron sources necessitates heavy shielding, which makes it difficult to handle such sources. Consequently, testing detectors with such high-flux neutron sources is a cumbersome process and KAMINI reactor plays a very useful role to overcome this difficulty. Good neutron flux upto $1x10^{11}$ n/cm^{2}s combined with a maximum gamma field up to 10^5 R/h simulating the actual detector environment, ease-of-handling detectors for installation and removing, versatile reactor start-up procedures have made the KAMINI reactor a unique test bed for testing neutron detectors.

***Fig. 1** Shield plug for detector testing*

Recently, a permanent test facility consisting of two aluminum dry- tubes have been installed at KAMINI, close to the core. These dry-tubes have been provided with shield-plugs at the top to prevent radiation streaming and hooks for easy handling. The shield-plugs were designed by BARC based on the radiation survey conducted at KAMINI and were successfully fabricated at IGCAR. The shield plugs have alternate layers of polythene and lead for effective shielding of both neutron as well as gamma field, and are further augmented with a layer of steel (Figure 1).

In order to ensure that the presence of the dry-tubes do not affect the reactor environment, a number of studies were conducted after installing them, including the effect of their presence on the these test-tubes, on the existing neutronic channels, radiation levels at different points, structural stability of the reactor vessel due to the additional load etc; their marginal effect on the nuclear power read by the existing neutronic channels were suitably compensated in the electronics. With this, the test-facility is ready for receiving new detectors for testing.

It is also planned to test prototype high temperature fission chambers of PFBR in KAMINI reactor by placing it in a specially fabricated leak-proof test assembly. Since the maximum temperature of KAMINI reactor water is around 305 K, electrical heaters have been provided inside the test assembly to raise the temperature of the detector to the required level of 843 K. Sufficient insulation is provided around the detector to maintain outer surface of test assembly at the pool temperature. With these new facilities, KAMINI is expected to play a crucial role in the development and validation of new types of neutron detectors in the near future.

III.12 Hydrogen Management During Regeneration of Model Cold Trap

The hydrogen and oxygen levels in the sodium circuits of fast reactors are maintained within acceptable limits by cold trap. It works on the principle of precipitation of oxide/hydride of sodium on wire mesh column when the temperature is reduced below the saturation concentration. Over long period of operation, the cold trap gets saturated with hydride and oxide resulting in the reduction in sodium flow and consequent loss of efficiency. The cold trap, then, needs to be regenerated for further use. Regeneration of secondary cold trap with high hydride loading is carried out by thermal decomposition of the precipitated sodium hydride accompanied by large hydrogen release.

Large quantity of hydrogen (100 kg or 1000 m^3) is expected to be released during regeneration of PFBR cold trap. Safe management of released hydrogen is a challenge. Quantitative estimation of the hydrogen released can help in the estimation of the extent of regeneration of cold trap and hence, improvement in trap efficiency.

A newly designed model cold trap was tested to determine the trapping capacity for sodium hydride. Regeneration of this cold trap was carried out in order to estimate and correlate the amount of hydrogen released during regeneration to the sodium hydride trapped. This process was carried out by vacuum decomposition technique. A proton exchange membrane fuel cell based hydrogen management system was integrated to the cold trap regeneration setup for the first time for safe removal and accounting of hydrogen released during regeneration. The hydrogen management system consists of an electrochemical burner involving fuel cell assembly optimised for hydrogen removal from a gaseous stream. The electrochemical burner can safely remove hydrogen from the gaseous stream by electrochemical oxidation. Unlike a catalyst recombination set-up, the reactive gases do not come into direct contact in a fuel cell type electrochemical burner. The concentration of hydrogen, even in an inert gas mixture, can be brought down well below the lower explosion limit (LEL) value whereas a catalyst based recombination system needs air or oxygen in stochiometric amount or more in the gaseous medium containing hydrogen. In the electrochemical burner, hydrogen does not come into direct chemical contact with oxygen and is separated by the proton conducting electrolyte. A schematic of the fuel cell based electrochemical burner is shown in Figure 1. Being an electrochemical device, the burner can operate in close loop with a feed back from the hydrogen sensor monitoring the concentration of hydrogen in the process stream. Since hydrogen is converted to water, which can be recovered, the burner can be of utility in the recovery of deuterium or tritium.

The schematic diagram of the hydrogen management system is shown in Figure 2. The burner consists of a modified fuel cell stack of optimal power, a load box for controlling the load drawn from the fuel cell stack, hydrogen sensors for monitoring the concentrations

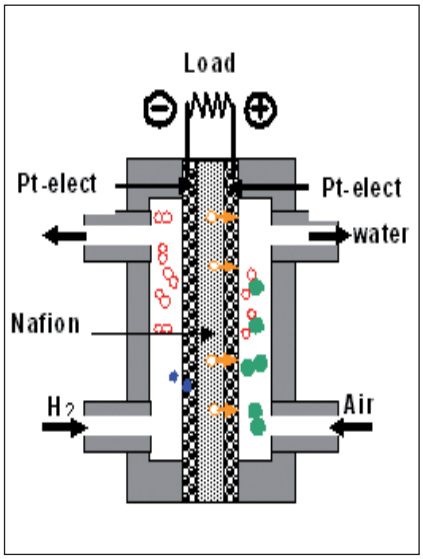

Fig. 1 *Schematic of fuel cell for electrochemical burner*

of hydrogen at the inlet and outlet of the stack and close loop instrumentation for regulating the load on the load box with respect to maximum set-value of concentration. The limit of hydrogen handling capability of the system is decided by the power of the fuel cell stack. Hydrogen is converted to water by electrochemical oxidation and is collected at the outlet of fuel cell.

Simulation studies were carried out in laboratory prior to incorporating hydrogen management system in the cold trap regeneration facility. The setup for simulation study consisted of a chamber of volume similar to that of model cold trap (approx 50 litres) with provision for evacuation of the chamber, filling with known amount of hydrogen and delivering hydrogen to fuel cell. The fuel cell used was of 1 kW power. The system was capable of safely handling up to a flow rate of 10 l/m of hydrogen. The chamber was evacuated and filled with known amount of hydrogen

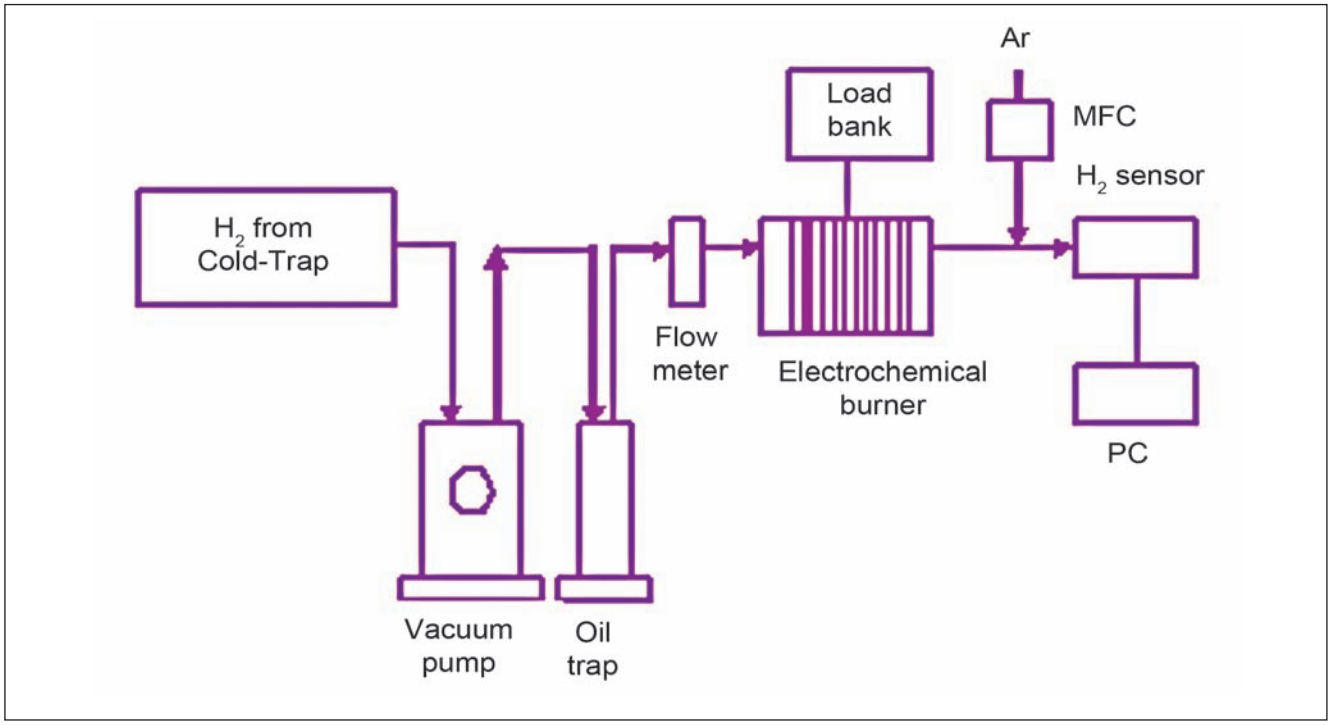

Fig. 2 *Schematic of experimental set-up for cold trap regeneration*

using mass flow controller and subsequently pumped to the fuel cell component of electrochemical burner. The flow rate during delivery of hydrogen was measured. Hydrogen was electrochemically oxidised to water by fuel cell reaction. Hydrogen sensor was used to monitor hydrogen at the outlet of electrochemical burner. The current produced during the electrochemical oxidation was measured using the load box. The electronic load box was also used to regulate the load from the fuel cell. Both hydrogen sensor output and current produced due to the oxidation of hydrogen by electrochemical burner were logged in the computer and used for the estimation of hydrogen passed and hence, its efficiency of removal. The hydrogen removal efficiency was found to be 97% indicating the suitability of the method for hydrogen removal during regeneration of model cold trap.

After simulation studies, the hydrogen management system was incorporated in the cold trap regeneration facility at FRTG. The hydrogen released was estimated in real time by the hydrogen management system as shown in Figure 3. About 300 liters of hydrogen was released during regeneration of model cold trap. Residual hydrogen was monitored at the outlet of the fuel cell using hydrogen sensor and was observed to be below 0.5%. The electrochemical conversion of hydrogen to water occurs in real time and hence, any accumulation of hydrogen was avoided. Since hydrogen release occurs due to the decomposition of sodium hydride, progress of regeneration of cold trap could also be monitored in real time. The regeneration campaign using electrochemical burner demonstrated the utility of the hydrogen management system for safe management and accounting of hydrogen.

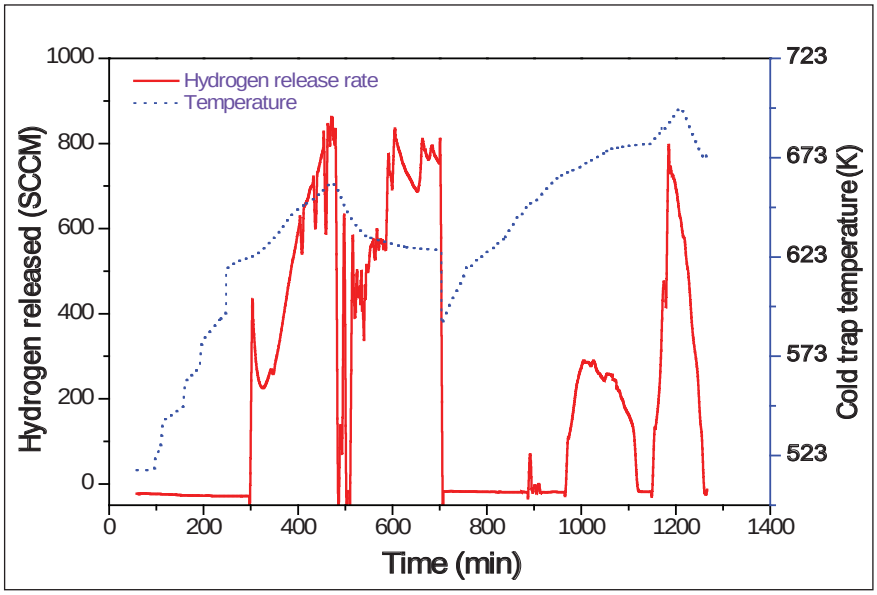

Fig. 3 *Hydrogen release during model cold-trap regeneration*

III.13 Process Disturbance Analyzer

Process disturbance analyzer is a specialized system for detecting, recording and analyzing disturbances occurring in a nuclear power plant. It is used to monitor some important parameters that enables post event analysis of the plant, leading to safe operation of the reactor. Some critical analog and digital signals from circuit breakers, power supply, variable speed drive etc., are fast varying in nature. These shall be monitored at a faster rate and checked for the cause of the disturbance/event (when an analog signal crosses a set-point or status of digital signal changes or combination of both is defined as the disturbance/ event).

The first subsystem is a fast data acquisition system, in which the signals from the field are connected after signal conditioning and isolation. Maximum of 60 analog and 30 digital channels are connected to this system. FDAS consists of Motorola MC 68020 based CPU card, 2 analog input cards and one digital input card The system scans all analog and digital channels at every 100 milli second.

The second sub system is a process computer system having connectivity with the fast data acquisition system through Ethernet ports. Event detection and storage software is continuously running on the process disturbance analyzer_ process computer system. It is online module and it detects events and records them. It stores data for 5 minutes prior to the event and for 5 minutes later to the event in the hard-disk as shown in Figure 1. Event information is sent from PDA_PCS to process computer of DDCS as and when needed.

PDA_PCS sends Health Event packet to process computer of DDCS for every 10 minutes. In case of user triggered event (UTE) as shown in Figure 2, past 10 minutes data will be stored as a file and latest 50 such files shall be maintained in hard disk. Event data are stored in two hard disks for mirroring. Trend chart for any four analog signals and diagnostic status of FDAS are displayed on the PDA_PCS screen as shown in Figure 3.

The latest 50 event files are available in hard disk for analysis. This analysis can be done on any other computer by offline analysis module.

This offline module shows the selected channels for the selected period of time as trend chart and tabular form with the resolution of 100 milli second for the predefined event.

Parameters of all analog and digital signals can be edited by authorized users with the offline edit channel database module. This software can run on PDA_PCS only when online module is not running.

- Process disturbance analyzer is required to know the primary “event” causing the shutdown of the reactor so that the problem can be rectified and started with minimum downtime.
- To improve the availability of the plant.
- Process disturbance analyzer is used for detecting, recording and analyzing the disturbances/ event occurring in nuclear power plant.
- The event recorded by process disturbance analyzer is used to find out the initiating event and consequences in other signal because of the initiating event. The knowledge gained by this analysis will be used to avoid such incidents in future.

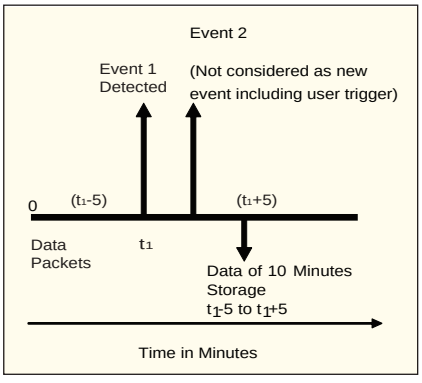

Fig. 1 Event detection

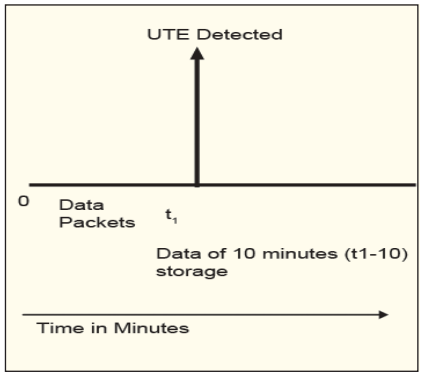

Fig. 2 User triggered event

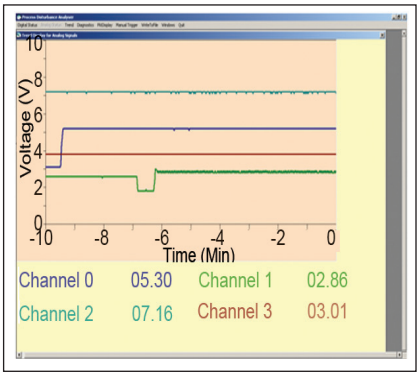

Fig. 3 Trend chart

III.14 Design & Development of Soft-Core Processor Based Remote Terminal Units for Fast Breeder Reactor

Remote terminal units (RTUs) are single board, microcontroller based real time remote data acquisition & control systems that are used in safety related and non-nuclear safety I&C systems of fast breeder reactors, to acquire various analog/digital signals received from different sensors such as surface thermocouple, leak detector and limit switches and send digitized data packets over Ethernet to the nearest local control centre (LCC) and generate control outputs in the form of potential free contacts during all states of the reactor operation. RTUs are deployed at various locations on the plant, closer to the field sensors, thereby reducing long cabling which in turn helps in reducing noise pickup by routing cables. RTUs are designed to operate in extreme field conditions in various reactor buildings.

Brief description of soft-core processor based RTU Design

With the advent of higher logic gate density field programmable gate array (FPGA), it is possible to implement soft-core processor in mature FPGA technology. In this design a soft-core processor i.e. TSK51 from Altium, is used in place of conventional microcontroller and remaining logic gates are coded in VHDL, hence replacing all the digital ICs present on board by a single FPGA. This has enabled us to overcome the problems of obsolescence of components, dependability on third party vendors, and embargo issues for Indian nuclear establishments along with added advantage of improved reliability, reduced power consumption and reduced cost which is also being proved.

A soft-core processor is a microprocessor fully described in hardware description language (HDL), which can be synthesized to a FPGA. TSK51 is the IP core of an 8 bit microcontroller, provided by Altium, which executes all ASM51 instructions and can be downloaded to any technology i.e. either Flash or SRAM based FPGAs from many vendors like Xilnx, Altera, Actel & Lattice etc. These soft-core processors combine the flexibility of software with the power of a parallelized design. Their greatest strength lies in the high level of integration they offer, making true system-on-chip (SoC) design possible, while maintaining the ease of use that conventional processor offer. The design of RTU is broadly divided into digital logic section and input/output (I/O) section.

The idea of implementing soft-core processor with other glue logic coded in VHDL and downloaded into a FPGA device. Rigorous test has been carried out on this core and for the last four years, there had been no deviation from its functionalities. Altium designer tool was particularly chosen as it provides complete electronic product development environment starting from FPGA based design, Schematic capture, PCB design, Embedded software development for soft-core processors, mixed signal simulation, signal integrity analysis and FPGA system implementation & debugging. For FPGA design validation, a test setup using Xilinx Spartan-3 FPGA present on Altium's NanoBoard and interfaced with external RAM & other peripherals present over piggyback board, and an application software was developed and tested as shown in Figure 1.

Design of 16-ch digital input and 16-ch relay output

A 16-ch digital input & 16-ch relay output RTU board was designed using FPGA device XC3S400-4PQ208C based on the resource utilization of logic gates present on NanoBoard FPGA, which was obtained during design validation. All digital inputs are optically isolated and accept 24 V DC as logic high & 0 V as logic low. All relay outputs are potential free contact types which can carry 500A at 24 V DC. These outputs can be configured as NO/NC using jumper selection. PCB layout routing was done in six layers as per the guideline, to minimize EMI/EMC issues, crosstalk and various other noises. PCB fabrication and component assembling was done through external agency. The assembled

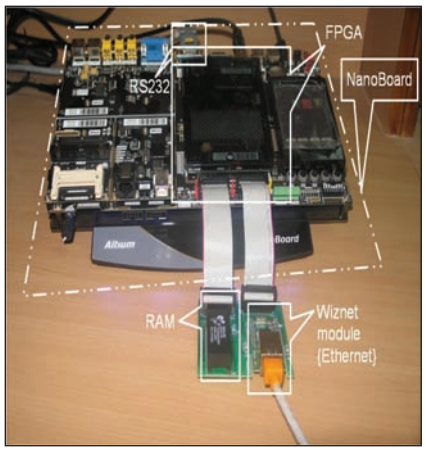

Fig. 1 *Test setup for validation of FPGA design*

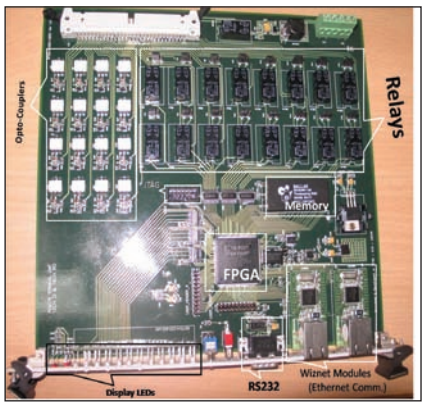

Fig. 2 *Assembled board*

board (Figure 2) was tested as per design specification. The on board FPGA was programmed and application software for testing the design was developed using tasking cross compiler and downloaded into the softcore through the JTAG connections using soft JTAG Nexus protocol.

The test program acquires digital inputs, energizes relay contacts and sends the data over reliable TCP/IP communication through Wiznet Modules (Hardwired TCP/IP stack).

Board reliability & power consumption calculation

The board reliability calculation was done using RELEX software as per MIL-HDBK-217-F standard. For the Spartan 3 FPGA device, failure rate of 22 FITs was considered for calculation. A significant change in MTBF was noticed compared with earlier version of RTU board with discrete components illustrated in the Table 1.

The RTU board operates at 5 V DC and the power consumption was calculated for both types of RTU boards as illustrated in Table 2.

The significant improvement in terms of reliability, component density and power consumption using soft-core processor based RTU design proves to be the preferred choice for future FBRs.

Table 1: Reliability calculation for two different types of RTU Boards

	FPGA Based RTU	Discrete component based RTU
Failure Rate	2.049141 failures/ million hours	3.064774 failures/ million hours
MTBF	488009.33 hours	326288.40 hours
Relia-bility	0.999795	0.999694

Table 2: Power consumption calculation for two different types of RTU Boards

	FPGA Based RTU	Discrete component based RTU
Current	500 mA	650 mA
Power	2.5 W	3.25 W

III.15 Impingement Wastage Studies on Steam Generator Tube Materials

Sodium heated steam generators (SG) are one of the key components of fast breeder reactors (FBR). Sodium, which is flowing in the shell side at moderate pressure, is separated from water/steam flowing in the tube side at 17.2 MPa, by a single walled tube. An accidental leakage of water/steam into sodium side will cause sodium water reaction. The principal effect of a small steam/water leak (0.05 –10 g/s), is 'damage of a single adjacent tube', which is usually designated as impingement wastage. Once a tube develops a small leak, minutes or even seconds are sufficient to puncture its adjacent tube, causing a secondary leak, which will be much higher than the original one. Sodium Water Reaction Test Facility (SOWART) was constructed to study various aspects of sodium-water reaction phenomenon. This test facility is equipped with both hydrogen in sodium detectors and hydrogen in argon detectors. The steam system can produce super heated steam of 17.2 MPa, 753 K. Leak simulators of modified 9Cr1Mo/Ni having a calibrated pinhole leak, were used for injecting steam into sodium. A

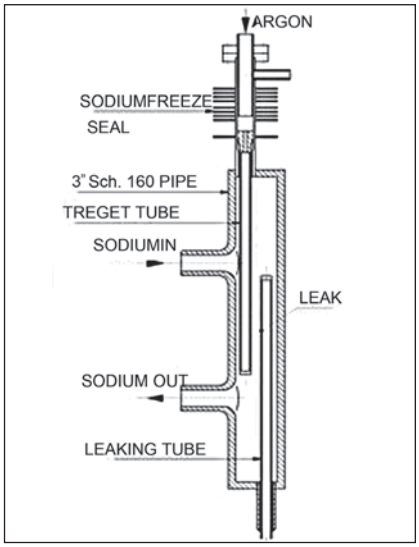

Fig. 1 *Impingement wastage test section*

target tube of modified 9Cr1Mo is fixed into the Impingement Wastage Test Section (IWTS) (Figure 1) from top in such a way that the reaction jet from the leaking tube hits on the target tube and produces wastage on its surface. The time of penetration is taken as the span from the time of response of acoustic sensor to the time of response of pressure transmitter indicating falling of argon pressure in target tube. It is found that wastage rate is increasing with steam leak rate as expected. At lower sodium temperature 703 K, relative wastage resistance of modified 9Cr1Mo is found to be higher when compared to wastage resistance at higher sodium temperature, 773 K.

In most of the literatures, the average relative resistance of 9Cr–1Mo with respect to 2.25Cr–1Mo steel is reported to be 1.2-1.5. In all of our experiments, a relative wastage resistance, of 1.96 and above could be obtained even at higher leak rates (> 700 mg/s). The wastage which had occurred on some target tubes is shown in Figure 2.

Fig. 2 *Wastage on target tube in sodium at (a) 773 K and (b) 703 K*

III.16 Sodium Testing of Core Thermocouple Probe with Three Thermocouples

In FBTR and PFBR, thermocouple probe with two thermocouples are used for monitoring the temperature of sodium at the outlet of fuel subassembly. The safety actions are initiated in FBTR on 2/2 logic. In PFBR, the thermocouple signals are multiplied into three signals and connected to three real time computers (RTCs) for processing and to initiate safety actions under various transients. The protection system functions on 2/2 logic at thermocouple level and on 2/3 logic at RTC level. In order to provide complete independency between redundant safety channels, three independent sensors are required. Hence, the feasibility of providing three thermocouples in the thermocouple probe was explored. Two probes with three thermocouples were fabricated indigenously in coordination with REG and tested in sodium loop in FRTG

Experiment and observations

An experiment was conducted in SILVERINA loop for performance study of the probes at various sodium temperatures (473 K to 823 K in steps of 50 K). The thermocouple probe of 10 meter length with three K-type 1 mm diameter thermocouples is shown in Figure 1a. A reference thermocouple of 1 mm dia, has been fixed on the outer side of the probe extending up to the test thermocouples position for comparison of the response of the thermocouple outputs. Figure 1b is the closer view of tip of thermocouple probe. The test pot-3 along with thermocouple probe test set-up is shown in Figure 2.

After allowing 30 minutes for stabilization at each temperature, the output data of all thermocouples at each temperature was collected while raising as well as lowering the temperature. The temperature data of the probe thermocouples were analyzed and compared with the reference thermocouple. The temperature data of the probe thermocouples were analyzed and compared with the reference thermocouple.

The maximum deviations observed for thermocouples of probe-1 and probe-2 were 1.52 K and 2.44 K. The deviation is found to be less at high temperature (823 K) compared to that at low temperature (473 K). Temperature profiles at 473 and 823 K are shown in Figure 3a and

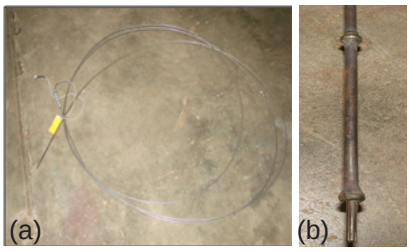

Fig. 1 *(a) Thermocouples of 10 m length and (b) Closer view of probe tip*

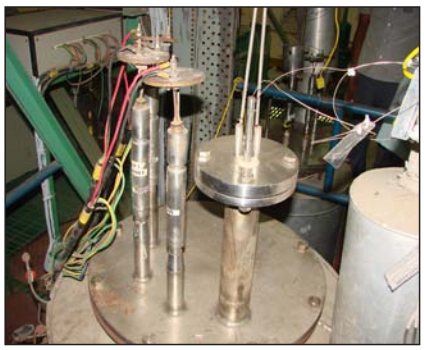

Fig. 2 Test pot with thermocouple probe test setup

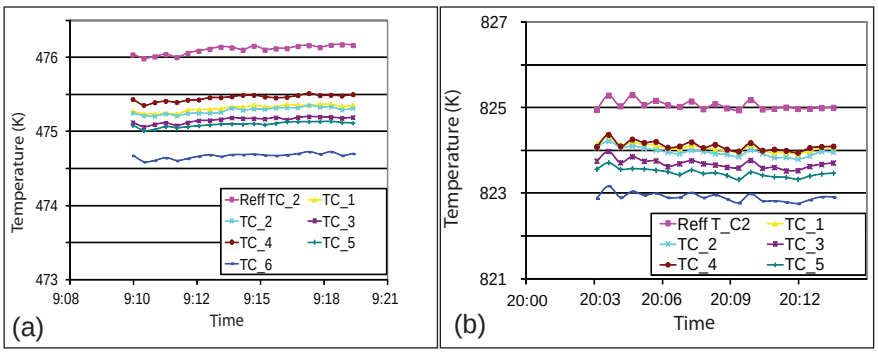

Fig. 3 Temperature profile at (a) 473 K and (b) 823 K

3b. During the calibration of the probes, maximum deviations among the thermocouples of probe-1 and probe-2 were 1.0 and 1.2 K. After installing the probes in the pocket in test pot-3 and testing, the maximum deviations among the thermocouples of probe-1 and probe-2 were 0.43 and 1.23 K.

The main challenge is in providing the three thermocouples of 1mm dia in the same pocket size which is meant for two thermocouples without affecting the performance. Further testing is planned to conclude the suitability of thermocouples probe for reactor use.

III.17 High Temperature Operation of INSOT Creep Loop for Long Term Creep Experiments

The creep loop of in-sodium test facility (INSOT) is meant for study and evaluation of the creep rupture properties of PFBR component materials in dynamic sodium. The creep loop has been operated at high temperatures of 873 K in five test campaigns from 2006.

The creep loop has been in operation at 873 K from October 2010 and fifth test campaign of creep experiments have been completed successfully in November 2011 after the last experiment reached 9612 hours. This is the longest test campaign in the creep loop history and is a milestone event. The creep loop was previously operated in several test campaigns for conducting creep rupture tests in different stress levels on SS316 LN material specimens at 873 K. The effective implementation of regular preventive maintenance and surveillance checks on various level, leak and control logic channels has helped in the safe operation of the loop.

In-sodium creep experiments

Four numbers of creep experiments at 873 K on SS316 LN material in test sections TS-2A, TS-2B, TS-3A and TS-3B were started in fifth test campaign and all experiments have been completed. A maximum of four creep tests can be conducted simultaneously in the loop. The test parameters and test results of the creep experiments of fifth test campaign are shown in Table-1.

The purity of the loop sodium was maintained consistently at reactor grade by continuous online purification. The cold point temperature of the cold trap was maintained at 393 ± 5 K. The plugging runs were taken weekly to monitor the oxygen content and oxygen level was maintained less than 2 ppm. The function of entire system was in perfect harmony to achieve an uninterrupted long term high temperature operation.

The performance of main components (Figure 1) such as

Table 1: Creep test - parameters and results of SS316 LN at 873 K

Test section	Stress (MPa)	Elongation (mm)	Duration (hours)
2A	215	9.159	8800
2B	215	11.356	9612
3A	225	9.50	7160
3B	225	11.403	7807

heat exchangers, immersion heaters, electromagnetic pumps, cold trap and programmable logic controller (PLC) based SCADA instrumentation system has been excellent and this is the key factor in ensuring loop availability. The sodium flow velocity around the test specimen was maintained at 2.5 m/sec. So far 16 nos. of creep experiments at 873 K have been completed. Creep experiment conducted in this campaign in test section-2B is the longest test duration (9612 hours) in the history of creep loop high temperature operation at 873 K. The overall experience in operating the sodium loop at high temperature for the above material testing is significant and excellent.

Fig. 1 *View of INSOT loop*

III.18 Enrichment of Boron to 91% in ^{10}B Isotope by Ion Exchange Chromatography

Boron enrichment plant was setup for developing the technology for production of boron enriched in ^{10}B isotope to 65% using ion exchange chromatography to meet the control rods requirement for Prototype Fast Breeder Reactor (PFBR). Resin with particle size of 0.3-1.2 mm (termed as normal resin) was used in Boron Enrichment Plant. This plant was operated to achieve the enrichment to 65% in ^{10}B. It had taken four years to get 65% enrichment. This technology has been successfully developed and transferred to HWB, Manuguru for commercial production.

Augmented boron enrichment plant has been setup using fine resin with particle size range in 75 to 150 micron (termed as fine resin) with an aim to decrease the equilibration time and also to produce boron enriched in ^{10}B isotope to 91% required for fast breeder test reactor. Figure 1 shows a view of Augmented boron enrichment plant. The plant has two streams each having five process ion exchange columns charged with fine resin. The plant is operated in cascade mode. The borate band was developed by transferring enriched boric acid containing approx 50% ^{10}B as feed material drawn from boron enrichment plant. The developed borate band was displaced using 0.1 N hydrochloric acid. The exhausted resin is regenerated externally in a separate regeneration column after transferring the exhausted resin hydraulically. The plant is in continuous operation. By using fine resin, the enrichment level of 65% in ^{10}B, which is the requirement of control rod material for PFBR, was reached in one year of operation. The technology of using fine resin has also been transferred to HWP, Manuguru for commercial production.

Augmented boron enrichment facility has now produced boric acid enriched to 91% in ^{10}B. The solution of enriched boric acid produced is being converted to solid boric acid powder.

The operation of the plant has given confidence that using fine resin, the plant can be operated with manageable pressure drop in columns and regeneration can be executed externally. Also all the more important is that enrichment could be achieved faster compared to process ion exchange columns charged with conventional resin.

Using this fine resin technology, equilibration time for 65% enrichment is reduced to one year from 4 years (using resin with particle size in 0.3 -1.2 mm range at boron enrichment plant). The enrichment in ^{10}B isotope to 91% has been achieved in augmented boron enrichment plant and this technology is successfully demonstrated for the first time.

Fig. 1 *Augmented boron enrichment plant*

III.19 A Scheme for Classification of Eddy Current Images from Sodium Bonded Stainless Steel Clad Tubes

One important aspect during structural integrity assessment of engineering components using NDE techniques is reliable detection of defects. Among various NDE techniques, eddy current technique is widely used for detection and sizing of defects in components made of metallic materials. While high-speed non-contact automated testing of components for reliable detection of defects is a clear advantage, the eddy current technique suffers difficulties for defect detection when there is a combined influence of several disturbing variables at one probe location. Reliable detection of voids, e.g. in sodium bonded metallic fuel pins, demands the use of multi-frequency eddy current data and novel signal and image processing approaches.

An inversion scheme has been developed for classification of eddy current images of voids in sodium annulus and defects in stainless steel clad of the metallic fuel pin. The scheme consists of two major steps; i) Principle component (Eigen value) analysis based feature extraction from eddy current images of expected defects in sodium and clad layers and unit length normalization of the features and ii) training using competitive learning neural network with cosine similarity (CLCS) method.

For generating training dataset, CIVA numerical modeling software was used. This is benchmarked software based on semi-analytical methods using dyadic Greens functions approach. A total of

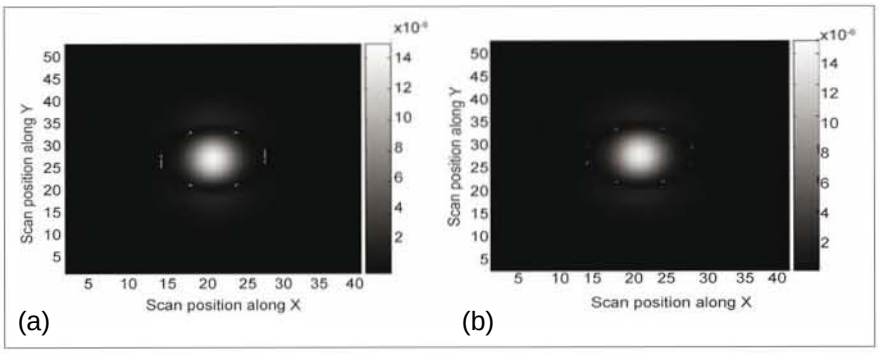

Fig. 1 *Model predicted images of (a) Defect in clad and (b) Void in sodium annulus at 300 kHz*

108 eddy current images (training dataset) from 300 and 600 kHz, have been predicted. Figure 1 shows the eddy current images of parallelepiped type defects of size 1.5x1.5x0.1 mm (length, width, depth) in clad and sodium layers at 300 kHz.

Competitive learning neural network with cosine similarity algorithm is efficient in terms of speed and accuracy where cosine similarity is used as a distance metric. For optimizing the number of dominant Eigen values and the frequencies, a leave one out cross validation strategy was followed. Based on this, two dominant Eigen values at 300 and 600 kHz were chosen as inputs to this algorithm. Figure 2 shows the dominant Eigen values of 600 kHz, in unit length normalized hypersphere. The directionality of the dataset corresponding to simulated defects in sodium and clad layers enables competitive learning neural network with cosine similarity algorithm to efficiently identify the layers in which the detected defects are located.

In order to assess the robustness of the proposed inversion scheme, evaluation was carried out using voids and defects of same as well as different shapes (elliptical) and of slightly different size, located in different layers. A classification accuracy of 90% was observed for the latter case and 100% classification was observed for the former case. Thus, the inversion scheme based on competitive learning with cosine similarity algorithm is able to reliably classify defects in sodium as well as in stainless steel clad layers of the metallic fuel pins. The scheme has been found to be robust to classify even the defects not used for training of the scheme.

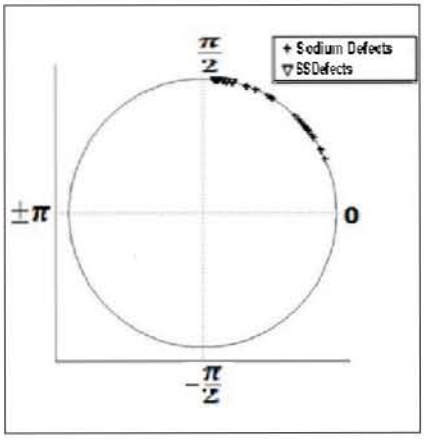

Fig. 2 *Eigen values at 600 kHz in unit normalized hypershpere*

III.20 Restitution of Parent High-Temperature Austenite Grain Orientation from Transformation Products in 9Cr-1Mo Steel

The 9Cr-1Mo ferritic steels and their variants are used as structural materials for generation and transport of steam in power plants. Owing to their excellent void swelling resistance in irradiation environment, they are also being envisaged as a core structural material for fast reactors. It is used in 'Normalized & Tempered' condition to obtain good mechanical properties. During normalizing, the high temperature austenite (γ) grains undergo a displacive mode of transformation to form several crystallites of martensite (α'), with a complex sub-structure morphology consisting of laths, blocks and packets. On tempering, the excess carbon atoms from α' diffuse out to form carbide precipitates, and the sub-structure morphology of ferrite (α) grains is largely retained. Prior-γ grain size and boundaries can influence the steel properties, and thus assessment of crystallographic orientation of γ grains becomes significant.

As the high-temperature γ phase is completely transformed, its crystallographic orientation cannot be directly evaluated by microtexture measurement using SEM-EBSD (Scanning Electron Microscopy-Electron Back Scattered Diffraction) technique at room temperature. However, the γ→α' transformation in low-carbon steels is known to obey K-S (Kurdjumov-Sachs) Orientation relationship: (111)γ//(011)α & [10-1]γ//[11-1]α, which can be used for restitution of parent γ grain orientation from the microtexture data of its α product crystallites.

Figure 1 shows the EBSD crystal orientation map of a typical tempered martensite structure and a selected prior-γ grain. The orientation/Euler angles data of α from each of the indexed pixel point within the prior-γ grain was selected for restitution analysis. Euler angles sets were converted to orientation matrices ***O***, for making further calculations. The K-S relation can be written as a matrix equation, and the ***O***γ can in principle be obtained from ***O***α. However, due to crystal symmetry, a single γ grain can result in 24 distinct product α orientations referred as variants. Similarly, a given α crystal could arise from 24 possible parent γ orientations, and thus γ cannot be uniquely found using K-S relation from a single α product. All the 24 possible γ orientations were back calculated for each of the α data points, and the Figure 2(a) shows the resultant orientation distribution ***n(g)*** plot in Euler angle domain. The common solution results in a sharp peak in the Euler space, which was used to identify the most possible γ orientation. The 23 other unlikely γ orientation were then discarded, and the resultant orientation distribution function ***f(g)*** of the predicted parent

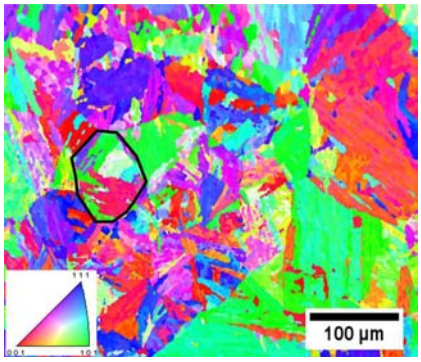

Fig. 1 *EBSD crystal orientation map of tempered martensite in 9Cr-1Mo steel, and selection of a single prior-γ grain*

γ grain is illustrated in Figure 2(b). The mean orientation of parent γ grain was estimated using the Quaternion averaging method. The deviation or misorientation angle of the individual orientations from the mean orientation was calculated, and Figure 3(a-b) show its distributions. The Euler angle values of the selected γ-grain was thus calculated to be ϕ_1=238°, Φ=38°, ϕ_2=36°, with the average angular deviation of 3°. The methodology was thus useful in predicting the high-temperature γ grain orientation, and the K-S relationship is seen to be reasonably obeyed in the system.

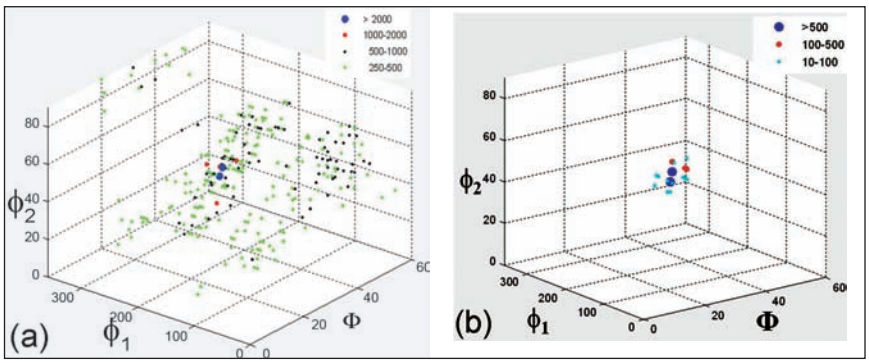

Fig. 2 *Euler angle distribution of calculated prior-austenite orientation: (a) n(g) for possible γ solution and (b) f(g) for the predicted γ*

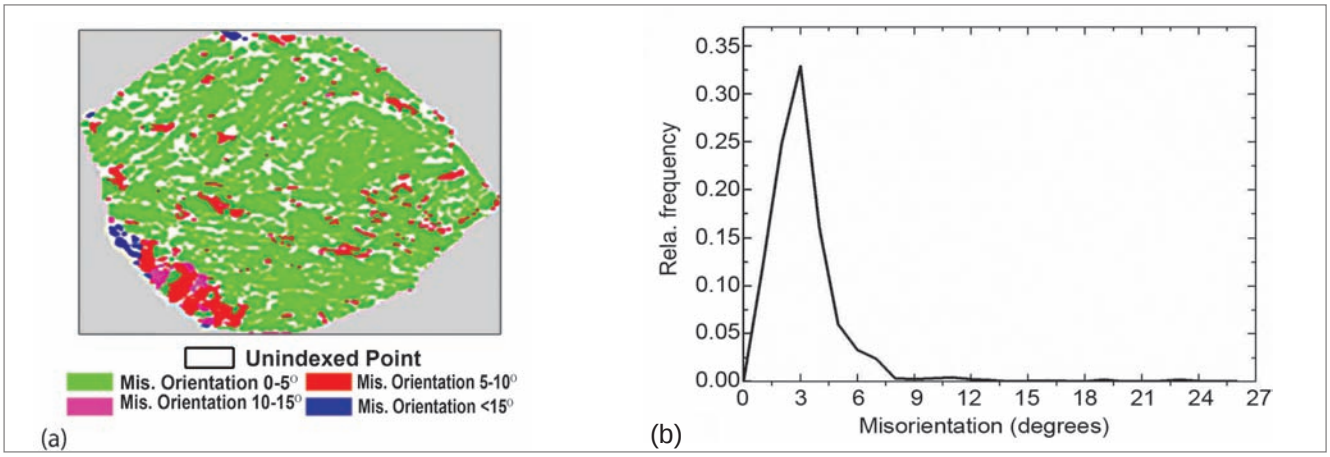

Fig. 3 *Misorientation angle spread about the mean calculated orientation of austenite displayed as (a) Spatial distribution and (b) Frequency distribution*

III.21 A New Relationship for Constitutive Analysis of Hot Deformation in Modified 9Cr–1Mo (P91) Steel

The simulation of metal forming processes using finite element analysis relies on accurate knowledge of hot deformation behavior described in terms of suitable constitutive equation that adequately correlates flow stress, strain, strain rate and temperature. The power–law description between flow stress and strain rate is suitable at low stresses/strain rates, while the exponential relationship is valid at high stresses/strain rates. The most widely accepted constitutive equation in the hot working domain is the Garofalo hyperbolic–sine expression with Arrhenius term which relates flow stress (σ), strain rate ($\dot{\varepsilon}$) and temperature (T), and is given as

$$\dot{\varepsilon} = A_g [\sinh(\alpha_g \sigma)]^{n_g} \exp(-Q/RT)$$

where Q is the apparent activation energy, A_g, n_g and α_g are constants, and this relation is valid for the entire strain rate/stress regime as it reduces to power–law at low stresses (valid for $\alpha_g\sigma < 0.8$) and exponential at higher stress limits (applicable for $\alpha_g\sigma > 1.2$).

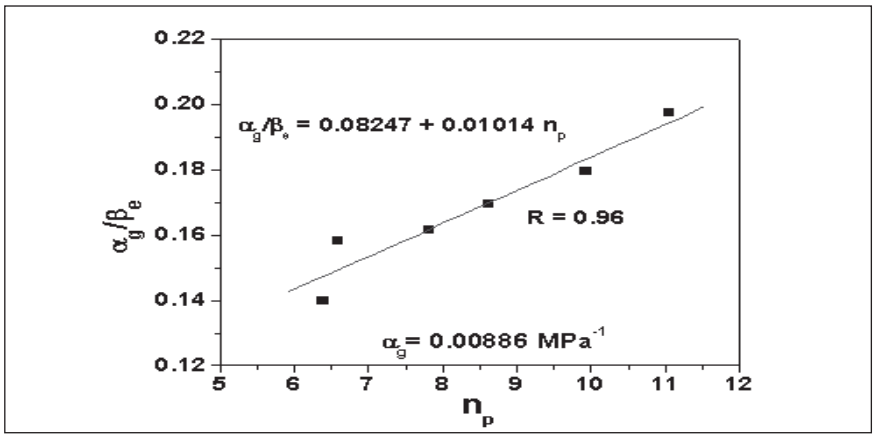

Fig. 1 *Linear dependence between (α_g/β_e) and n_p at strain = 0.15*

The determination of stress multiplier (α) is most crucial for constitutive analysis in hot working. Unlike creep conditions, the situation during hot deformation is different where strain rate is imposed and the flow stress data is force fitted by plotting ln($\dot{\varepsilon}$) Vs. ln [sinh($\alpha_g\sigma$)] and the adjustable stress multiplier α_g (MPa^{-1}) is iterated that brings ($\alpha_g\sigma$) into the correct range yielding parallel linear lines (with slope as n_g) for different temperatures. This is because the plots between $\dot{\varepsilon}$ and σ do not reveal the distinct deviation as observed for creep data. Therefore the stress exponent n_p ($\dot{\varepsilon} \propto \sigma^{np}$) and β_e ($\dot{\varepsilon} \propto \exp(\beta_e \sigma)$) obtained correspond to those for the entire stress/strain rate range. If the stress multiplier is determined as $\alpha = \beta_e/n_p$, then this α is designated as α_{ER} (i.e. $\alpha_{ER} = \beta_e/n_p$), where the subscript 'ER' indicates that it is determined by fitting the power and the exponential laws for the entire strain rate range. Whereas, those determined by force fitting the Garofalo equation are designated as α_g and n_g.

This study aims at addressing an important question whether any

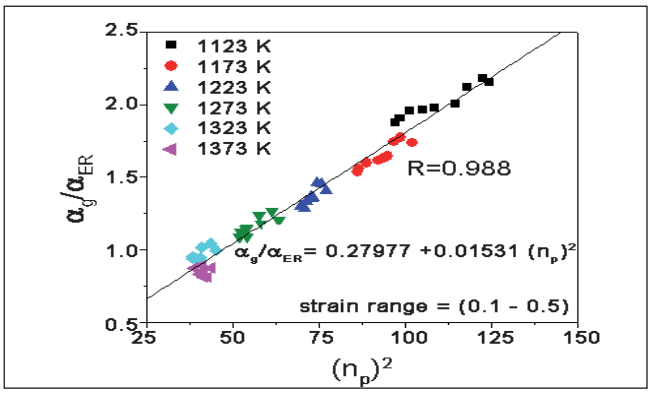

Fig. 2 *Proposed relationship between α_g and α_{ER} for P91 steel*

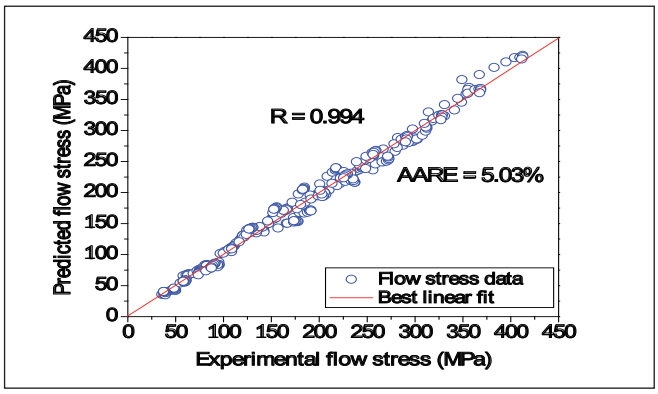

Fig. 3 *Correlation between the predicted and experimental flow stresses for the strain range 0.1-0.5 over the entire strain rate and temperature for P91 steel*

relationship exists between the two stress multipliers, viz. α_g and α_{ER}. This is useful, because evaluating the adjustable α_g by the iteration method involves considerable computational time and α_g can be evaluated by knowing α_{ER} which is much easier to be determined. A new relationship is proposed between α_g and α_{ER} in terms of n_p for the data obtained from hot compression tests on modified 9Cr-1Mo (P91) steel over wide ranges of strain rates (0.001-100 s^{-1}) and temperatures (1123-1373 K). Using the α_g values calculated following the proposed relationship, the other constitutive parameters n_g, Q and $\ln A_g$ were determined at various strains. On incorporating the strain dependence of these parameters, prediction of flow curves was performed following the Garofalo equation.

The flow stress data obtained at different strains (0.1-0.5 at steps of 0.05) were analysed to determine α_{ER}. Towards this, n_p and β_e were evaluated at different strains and the values of n_p and β_e were determined as reciprocal of slopes of lines in the plots ln (σ) vs. ln ($\dot{\varepsilon}$) and σ vs. ln ($\dot{\varepsilon}$), respectively at different temperatures. For calculating α_{ER}, the respective values of n_p and β_e obtained at different temperatures (1123-1373 K, at intervals of 50 K) were used and α_{ER} at each temperature was obtained as $\alpha_{ER} = \beta_e/n_p$ thus giving the average value of α_{ER} at respective strains. Though the average value of n_p = 8.398 at strain = 0.15, it was noticed that n_p decreases from 11.058 to 6.388 with increasing temperature from 1123 to 1373 K. The analysis also revealed that the same trend was observed for the variation of (α_g/β_e) with temperature, i.e. (α_g/β_e) was found to decrease from 0.1973 to 0.1397 with increase in temperature from 1123 to 1373 K; α_g = 0.00886 MPa^{-1} at strain = 0.15. This suggested that (α_g/β_e) would increase with increase in n_p and such a plot is shown in Figure 1, typically for strain = 0.15 which reveals that $(\alpha_g/\beta_e) \propto n_p$. Similar behavior was noticed at all strains for the strain range 0.1-0.5 at steps of 0.05. From the definition of $\alpha_{ER} = \beta_e/n_p$, it follows that $(\alpha_g/\beta_e) = \alpha_g/(\alpha_{ER} \times n_p) \propto n_p$. Therefore, (α_g/α_{ER}) would show a linear dependence with $(n_p)^2$. The (α_g/α_{ER}) was calculated at various strains (0.1-0.5, steps of 0.05) for different temperatures (1123-1373 K, 50 K interval). The plot of (α_g/α_{ER}) vs. $(n_p)^2$ is shown in Figure 2 which clearly demonstrates that the data could be described by linear relationship. Hence, the new relationship between the stress multipliers α_g and α_{ER} for the modified 9Cr-1Mo (P91) steel can be proposed as

$$\frac{\alpha_g^{\varepsilon}}{\alpha_{ER}^{\varepsilon}} = 0.27977 + 0.01531\left(n_p^{\varepsilon}\right)^2$$

where, the superscript ε indicates the strain dependence. An important implication of the above proposed relationship is that knowing α_{ER} and n_p at each strain, α_g values can be easily determined. After calculating α_g, following the Garofalo equation, the other constitutive parameters such as n_g, Q and $\ln A_g$ were evaluated.

On incorporating the strain dependence of constitutive parameters (α_g, n_g, Q and $\ln A_g$), flow stresses were predicted for the investigated strain rate range (0.001-100 s^{-1}) and temperature range (1123-1373 K at intervals of 50 K) successfully. The analysis of standard statistical parameters determined for the prediction of flow stress in entire ranges of strain, strain rate and temperature (Figure 3) revealed that the correlation coefficient, R = 0.994 and average absolute relative error, $AARE$ = 5.03%. Thus it can be concluded that α_g and in turn the other constitutive parameters (n_g, Q and $\ln A_g$) obtained based on the proposed relationship between the stress multipliers α_g and α_{ER} can be employed for predicting the flow behaviour of modified 9Cr-1Mo (P91) steel in the investigated strain rate–temperature domain.

III.22 Thermo-mechanical Fatigue Behaviour and Type IV Cracking Resistance of Modified 9Cr-1Mo Steel

The studies on thermo-mechanical fatigue and creep behaviour of modified 9Cr-1Mo steel (P91) and the role of boron and heat treatment temperature in improving creep resistance of P91 weldment are reported here.

Thermomechanical fatigue behaviour

The heat exchanger components of liquid metal cooled fast breeder reactors (LMFBRs) undergo thermally induced strain cycling during startup and shutdown or during variation in the operating conditions. The thermal fluctuations in the coolant lead to the development of thermal gradient from the surface to core of the component across the wall thickness. Such thermal gradients occurring cyclically during operation result in thermo mechanical fatigue (TMF). In-phase (IP) TMF represents combined thermal and mechanical cycling with tensile strain and peak temperature coinciding, while out-of-phase (OP) TMF is characterised by tensile strain and the minimum temperature occurring together. In-phase and out-of-phase thermomechanical fatigue tests were carried out on P91 with normalized (1313 K/1h) and tempered (1033 K/1h) microstructure, under mechanical strain control mode employing a constant strain amplitude of ±0.4%. The liquid sodium enters the shell side of the steam generator at 798 K and leaves at 628 K while the water enters the tube side at 508 K and leaves the bundle as steam at 766 K. Hence, different temperature ranges from 573 to 923 K were employed for the tests which were carried out in air environment on tubular specimens, using a constant strain rate of $1.2\times 10^{-4}\ s^{-1}$. A constant temperature interval (ΔT) of 200 degree was used for all tests. Isothermal low cycle fatigue (IF) tests were also performed at the maximum temperatures (T_{max}) of TMF cycling on identical specimens, employing the same strain amplitude and strain rate. The cyclic stress response behaviour of the alloy was characterized by continuous softening under all testing conditions. The life variation was seen to follow the sequence: IF < OP TMF < IP TMF. However, the difference in lives narrowed down with an increase in the T_{max} of TMF and test temperature of IF cycling, as shown in Figure 1. The lower lives observed under OP TMF in comparison with IP cycling was attributed to a combined influence of oxide cracking and a higher tensile hysteresis energy in the former. Cyclic life under IP TMF was observed to reduce more drastically compared to OP cycling with an increase in T_{max}, owing to the increasing prominence of dynamic recovery effects coupled with creep deformation. IF cycling at the T_{max} resulted in a greater substructural recovery, as presented in Figure 2a, compared to that produced by TMF cycling (Figure 2b), and as a consequence, the former led to lower lives compared to both the IP and OP TMF. Dynamic strain ageing associated with serrated flow was observed as the deformation temperature under TMF cycling traversed the regime of 573 to 673 K. The study showed that the traditional practice of high temperature component design with low cycle fatigue data based on the expected T_{max} is generally conservative for the P91 steel. However, the degree of conservativeness showed a diminishing trend with increasing T_{max}, as seen in Figure 1.

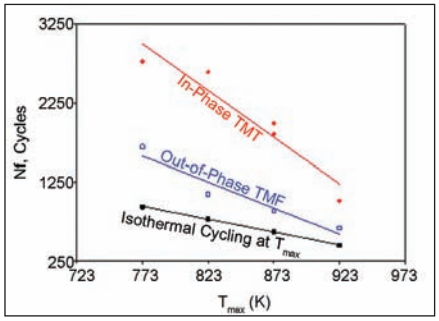

Fig. 1 *A comparative plot of the cyclic lives obtained under TMF (IP, OP) and IF cycling at T_{max}*

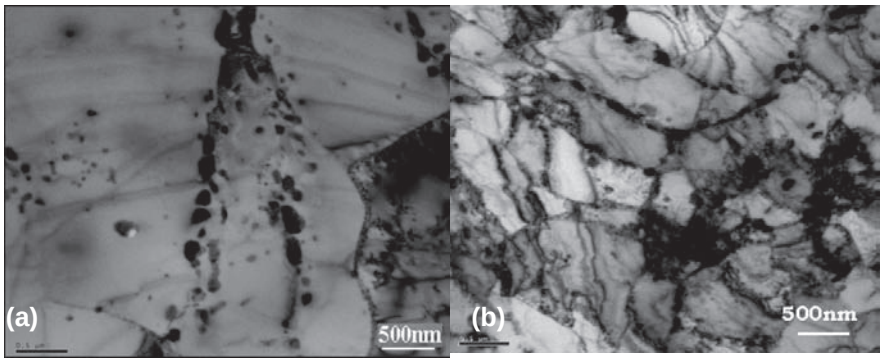

Fig. 2 *(a) Enhanced recovery observed under IF cycling at 773 K (b) Transformed tempered martensitic lath structure formed under OP TMF, 573-773 K*

Improvement in type IV cracking resistance by boron addition and heat treatment

Thermal cycling generates a highly inhomogeneous microstructure in the heat-affected zone (HAZ) of P91 welds, and a consequent gradient in mechanical properties across the joint. The localised creep damage and failure of weld joints in HAZ (Type IV cracking) is a concern. Controlled addition of boron is one of the methods being tried to minimize this.

Two heats of P91, one without boron, designated as P91 and the other with controlled addition (0.01 wt.%) of boron with very low nitrogen, designated as P91B and their welds were used to assess the benefits of B on resistance to type IV cracking. Normalizing at two temperatures, 1323 and 1423 K followed by tempering at 1033 K for three hours were chosen. These are designated as P91L, P91H, P91BL and P91BH (L for normalizing at 1323 K and H for 1423 K). Manual metal arc welds were prepared with these base metals using modified 9Cr-1Mo steel electrodes and subjected to post weld heat treatment. These are designated similar to the base metal used, suffixed with CW for cross weld.

Microstructures of all steels consisted of tempered lath martensite, with precipitates decorating the lath, block, packet and prior austenite grain boundaries. Decrease in hardness values from coarse grained HAZ to intercritical (IC) HAZ in P91BL-CW and P91BH_CW is gradual compared to that for P91L_CW and P91H_CW, suggesting the combined effects of boron addition and higher normalising temperature on the hardness variations between

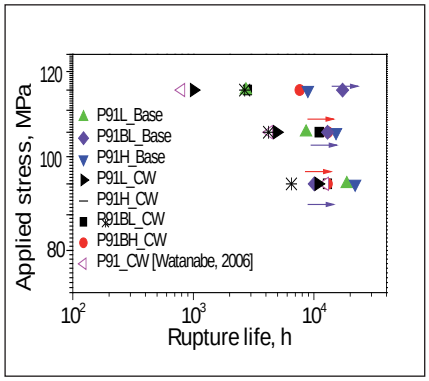

Fig. 3 *Applied stress vs rupture life for base metal and weldment*

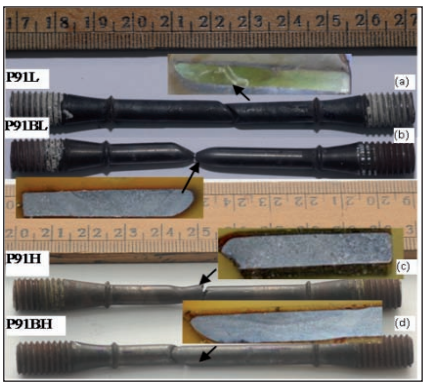

Fig. 4 *Cross weld specimens creep tested at 873 K and 120 MPa*

different regions of the welds. On the other hand, normalising temperatures had only marginal effect on hardness variations across P91L_CW and P91H_CW.

The yield and tensile strengths of P91L and P91BL are nearly same, while yield strength of P91H is higher compared to P91BH. All cross weld tensile specimens had failed outside the HAZ close to the base metal interface. Tensile tested specimens of P91L_CW and P91H_CW show necking at HAZ/ base metal interface on both sides of the weld. On the other hand, only one necking, at the location of failure was observed in P91BL_ CW and P91BH_CW, indicating the role of boron in strengthening the microstructures of HAZs.

Creep tests were carried out at 873 K and 80, 100 and 120 MPa. The rupture life of P91BL (test still in progress) is seven times higher than P91L and two times higher than P91H (Figure 3). Also, rupture life of P91H is higher than that of P91L, by a factor of four at 120 MPa which decreases with decreasing stress level. (Some of the tests are still in progress; P91BH has just crossed 500 hours). Significant improvement in rupture life of P91BH_CW over P91BL_CW is evident. The creep tested specimens of the weldments are shown in Figure 4. P91L_CW and P91H_CW had failed at ~2.2-2.5 mm from the weld interface parallel to the weld groove angle (Figures 4(a) and (c)) in the ICHAZ; with decreasing stress, the failure location did not change. Even though, P91BL-CW had failed at a distance of 3.7 mm from the weld interface (Figure 4 (b)) parallel to the weld groove angle, high ductility was evident at failure location. On the other hand, Figure 4(c) shows typical brittle failure in the weld metal and ductile failure in the ICHAZ of P91BH.

Higher rupture life as well as lower creep rate of P91BL_CW and P91BH_CW in comparison with P91L_CW and P91H_CW, are attributed to an increase in resistance against recovery in the transient creep stage, delay in recovery at lath and prior austenite grain boundaries and increase in resistance against creep cavity nucleation. Higher creep rupture life of P91BH_CW is due to better utilisation of boron at higher normalising temperature, since more precipitates dissolve and the alloying elements are distributed uniformly in the material. During tempering, fine precipitates form more uniformly thus stabilizing the lath boundaries and making the material more resistant to creep deformation.

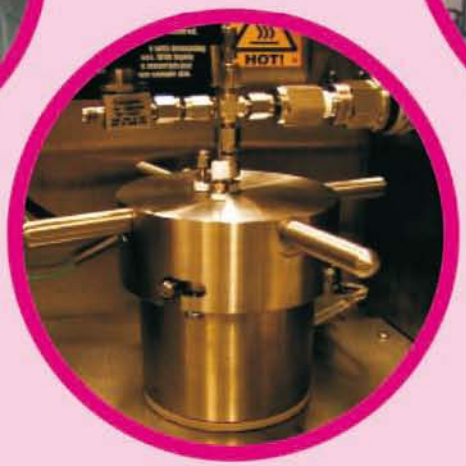

CHAPTER - IV

Fuel Cycle

IV.1 Fast Reactor Fuel Cycle Facility

Detailed design of the fast reactor fuel cycle facility (FRFCF) to close the fuel cycle of prototype fast breeder reactor (PFBR) is in progress. The work is being piloted by Indira Gandhi Centre for Atomic Research (IGCAR) with technical support from Bhabha Atomic Research Centre (BARC) and Nuclear Fuel Complex (NFC). A preparatory project for development of site infrastructure and engineering of FRFCF is nearing completion. Approval of Atomic Energy Regulatory Board (AERB) for the site of FRFCF has been obtained. Basic infrastructure like approach roads, construction, power supply system, workshop, storage and construction office space has been created at the site to reduce the lead time required to commence the construction work once the financial sanction for FRFCF project is available. Review of the preliminary safety analysis report by project design safety committee for FRFCF and specialist working groups is in progress. Detailed project report for FRFCF has been prepared and project proposal has been submitted for obtaining financial sanction. Approval of Atomic Energy Commission (AEC) for the proposal has been obtained. The proposal is being processed for approval by the Cabinet. Construction work on the project will commence during the year 2012. The perspective view of the fast reactor fuel cycle facility is given in Figure 1.

Fig. 1 *Perspective view of the fast reactor fuel cycle facility*

IV.2 Thermo-chemical Studies on TBP-HNO_3 System of Relevance to Fuel Reprocessing

Tri n-butyl phosphate (TBP) diluted with aliphatic hydrocarbons like n-dodecane (n-DD), odourless kerosene, etc. is being used as solvent for recovering uranium and plutonium from the spent fuel in nuclear fuel reprocessing plants employing PUREX process. Eventhough, TBP has several merits the solubility of TBP in aqueous streams as well as inadvertent entrainments in aqueous streams during evaporation results in the formation of the so called “red oil” which leads to violent run-away reactions and has caused accidents in various plants in the past. The thermo-chemical and kinetic studies on the thermal decomposition behaviour of TBP-nitric acid system available in literature are limited.

Results of the studies carried out on thermal decomposition of TBP-nitric acid systems are reported here. An adiabatic calorimeter as shown in Figure 1, capable of measuring temperature and pressure excursions due to accelerated reactions and operating with a container that can withstand the harsh decomposition conditions and corrosive degradation products, was used for the study. The systems studied include, TBP, nitric acid solvated TBP with and without

Fig. 1 *Photograph of calorimeter*

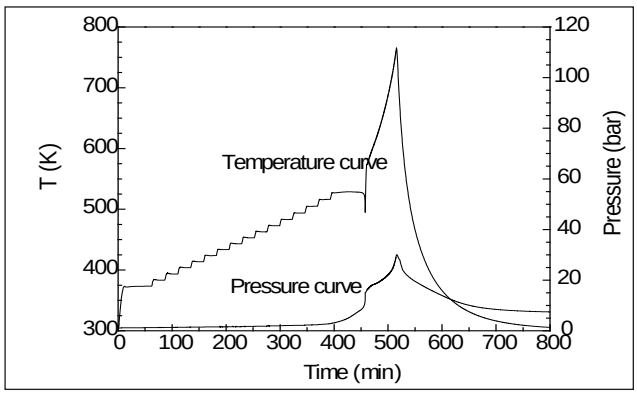

Fig. 2 Experimental data obtained for the decomposition of neat TBP

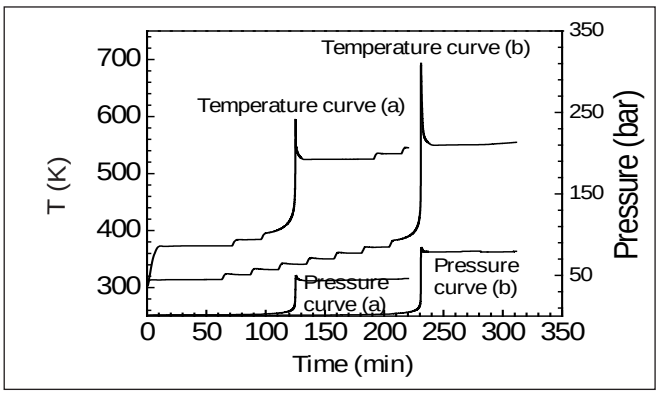

Fig. 3 Thermal behaviour of acid-solvates (a) TBP 1.1HNO_3 (b) TBP 2.4HNO_3

the presence of additives such as uranyl nitrate, sodium nitrate and sodium nitrite, solutions of 1.1 M TBP in n-DD and n-octane in either homogeneous single phase or two phase mixtures.

Neat TBP was equilibrated with 8 and 15.6 M nitric acid and the organic phase was separated and used for calorimetric studies. The stoichiometry of the organic phase was found to be TBP·1.1HNO_3 and TBP·2.4HNO_3 respectively by titration with sodium hydroxide. Solutions of 1.1 M TBP in n-DD and n-octane prepared by equilibrating with 8 and 15.6 M nitric acid were used for calorimetric measurements. The 1.1 M TBP in n-DD system formed "third phase" and in this case the heavier acid-solvate phase and the lighter diluent rich phase were together used for the decomposition studies. Uranyl nitrate, sodium nitrate and sodium nitrite were used as aditives and their effect on the decomposition of the above systems was studied.

Experiments were conducted in air and in closed conditions. About 2 ml aliquote of the desired liquid sample with or without salt was loaded in the test cell and assembled in the containment vessel of the calorimeter with thermocouple placed in direct contact. The cell was heated from room temperature to the decomposition temperature of the sample or to 773 K (the maximum limit of the calorimeter) in steps of 10 K in heat-wait-search mode.

The thermal decomposition of neat TBP is shown in Figure 2. The temperature curve exhibits no exothermic event upto 528 K indicating the thermal stability of TBP up to this temperature. An endo-thermic peak observed at 528 K is due to boiling of TBP beyond which, an exothermic event was observed possibly due to the decomposition of TBP vapour.

Thermal decomposition behaviour of the acid-solvates TBP·1.1HNO_3 and TBP·2.4HNO_3 is shown in Figure 3. These acid solvates start decomposing, at 393 and 384 K, respectively and produce non-condensable gaseous products such as N_2O, CO_2 and CO leaving behind a blackish solid residue on decomposition. These reactions were found to be exothermic with high increase in temperature and pressure as seen in Figure 3. The present investigations showed that the decomposition of acid solvates, TBP·1.1HNO_3 and TBP·2.4HNO_3 cause a temperature rise of 113 and 174 K and a pressure rise of 26 and 45 bar/g of the acid solvate, respectively under the conditions of the experiments, in the calorimetric vessel of 10 ml volume with a sample volume of 2 ml.

The enthalpy changes for the decomposition of acid solvates TBP·1.1HNO_3 and TBP·2.4HNO_3 derived using Equation.1 were found to be -495.8±10.9 and 1115.5±8.2 kJ·mol^{-1}, respectively.

$$\Delta H_r = C_p \times \Delta T_{ad} \times \Phi \qquad (1)$$

where ΔH_r is the enthalpy change of the reaction, C_p the heat capacity of the reactant, ΔT_{ad} the adiabatic temperature rise, and Φ, the phi-factor. The phi-factor is defined by the following expression.

$$\Phi = 1 + \frac{(mC_P)_C}{(mC_P)_S} \qquad (2)$$

where $(mC_P)_C$ and $(mC_P)_S$ are the thermal masses of the container and sample, respectively.

The rate constant for an exothermic reaction can be obtained by the following expression.

$$k = \frac{dT}{dt} \Big/ (T_f - T_i)\left(\frac{T_f - T}{T_f - T_i}\right)^n \qquad (3)$$

where k is the rate constant, n is the order of reaction, dT/dt is the rate of temperature rise, and T_i, T_f and T are the temperatures at initial, final and time t of the exothermic region.

The decomposition of acid-solvates followed first order kinetics. The rate constant k, for the decomposition of the acid-solvates was calculated using Equation 3 from the

calorimetric data and plotted as a function of reciprocal temperature in Figure 4.

The activation energy and the pre-exponential factor derived from the slope and intercept were found to be 108.8±3.7, 103.5±1.4 kJ·mol^{-1} and 6.1×10^{10} and 5.6×10^{9} s^{-1}, respectively for the decomposition of TBP·1.1HNO_3 and TBP·2.4HNO_3. The decomposition pattern of TBP indicates an interesting behaviour depending on the nitric acid stoichiometry. Presence of metal nitrites or nitrates did not have any influence on the onset temperature of decomposition of the acid-solvate. However, their presence increases the activation energy for the decomposition reaction, thus increasing the stability of the system. The solution of 1.1 M TBP in n-DD or n-octane did not exhibit any accelerated decomposition whereas the solutions of 1.1 M TBP in n-DD equilibrated with 8 and 15.6 M HNO_3 exhibited lower excursions in temperature and pressure due to the lower concentration of TBP and nitric acid present in these systems.

The heat capacities (C_p), of neat TBP and the acid-solvates, TBP·1.1HNO_3 and TBP·2.4HNO_3 were measured at constant pressure using a heat flux type differential scanning calorimeter (DSC) in the temperature range 305-340 K. About 20 µl of samples were sealed in aluminium pans of 40 µl capacity for DSC measurements. A hole was made in the lid of the pan to carry out the heat capacity measurements at constant pressure. The values obtained at 305 K for the neat TBP, acid-solvates TBP·1.1HNO_3 and TBP·2.4HNO_3 were 1.8, 1.76 and 1.63 J·K^{-1}·g^{-1}, respectively. The heat capacities of acid-solvates at 393 and 384 K calculated by extrapolation were found to be 2.17 and 3.1 J·K^{-1}·g^{-1}, respectively. These values were used for deriving the decomposition enthalpy of the acid solvates.

The results clearly confirm that a mixture of concentrated (15.6 M) nitric acid and neat TBP can cause run-away reactions when subjected to temperatures of 362 K and above in contrast to the value of 403 K reported in the literature for safe operation. Possibly, the mixture forms “red oil” insitu, resulting in thermal excursion. The present investigation shows that the decomposition reaction is highly exothermic and formation of non-condensable gaseous products during decomposition are responsible for increase in pressure and can lead to possible damage of the containment vessels.

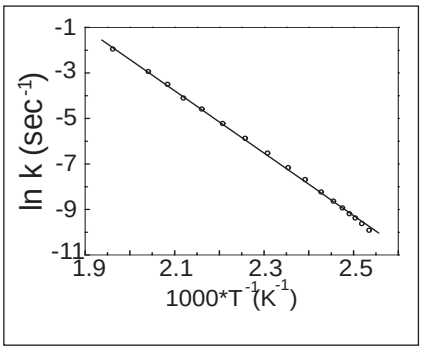

Fig. 4 *Arrhenius plot for the acid-solvate TBP.1.1HNO_3*

IV.3 Demonstration of Feasibility of Using Tri-Iso-Amyl Phosphate as an Alternate Extractant to Tri-n-Butyl Phosphate in Fast Reactor Fuel Reprocessing

Third phase formation in the extraction of Pu(IV) by Tri-*n*-butyl phosphate (TBP) is of serious concern in fast reactor fuel reprocessing. One of the options to tackle this situation in fast reactor fuel reprocessing is to employ an extractant with lesser third phase formation tendency and its extraction and stripping behaviour should be similar to that of TBP. Earlier studies carried out in our laboratory have shown that Tri-*iso*-amyl phosphate (TiAP) is a potential extractant for fast reactor fuel reprocessing. It has high capacity to load tetravalent metal ions such as Pu(IV) and Th(IV) without third phase formation and its extraction and stripping behaviour is also comparable to that of TBP. Preliminary studies also indicate that its radiation stability is at par with that of TBP and its aqueous solubility is less than that of TBP.

A mixer-settler facility was set up and commissioned in our laboratory for performing continuous solvent extraction runs to evaluate the feasibility of using TiAP as an alternate extractant to TBP in fast reactor fuel reprocessing. This facility (Figure 1) comprising an ejector mixer-settler unit and metering pumps is housed in a double-module glove box with several safety features. The mixer-

settler installed is a 16 stage equipment and is fabricated from a monolithic polypropylene block with a hold up volume of ~640 ml.

A pulse amplitude of 100 – 150 mm in the pulse probe (id = 6 mm) and a pulse frequency of 30 cycles/min were maintained in all mixer-settler runs. Duration of each run was about 7 – 9 hours. Outlet organic and aqueous streams were collected from 1st and 16th settlers, respectively. In all the runs, organic and aqueous stage samples (5 – 10 ml) were collected from all settlers after the attainment of steady state. All the stage samples were taken out of the glove box by bag out operation for analysis. Concentrations of nitric acid and metal ions in the organic and aqueous samples were estimated by using suitable analytical methods.

The performance of the equipment with respect to mixing and separation characteristics, hydrodynamic behaviour and the overall mass balance was tested by carrying out inactive runs for the extraction of nitric acid with 1.1 M TiAP/NPH-4 M HNO_3 system followed by a strip run using 1.1 M TiAP loaded with 0.824 M HNO_3-0.01 M HNO_3 system. Results revealed that extraction and stripping of nitric acid take place with good mass balance. Overall performance of the system during these runs was also found to be satisfactory.

Subsequently, the facility was used for flow sheet development studies with conditions simulating the PUREX process for fast reactor fuel reprocessing. The basic flow sheet for the extraction and stripping of U(VI) and Pu(IV) comprises three runs. First run is for the extraction of uranium and plutonium and the other two runs are for the stripping of extracted metal ions using nitric acid solutions with appropriate concentrations and flow rates.

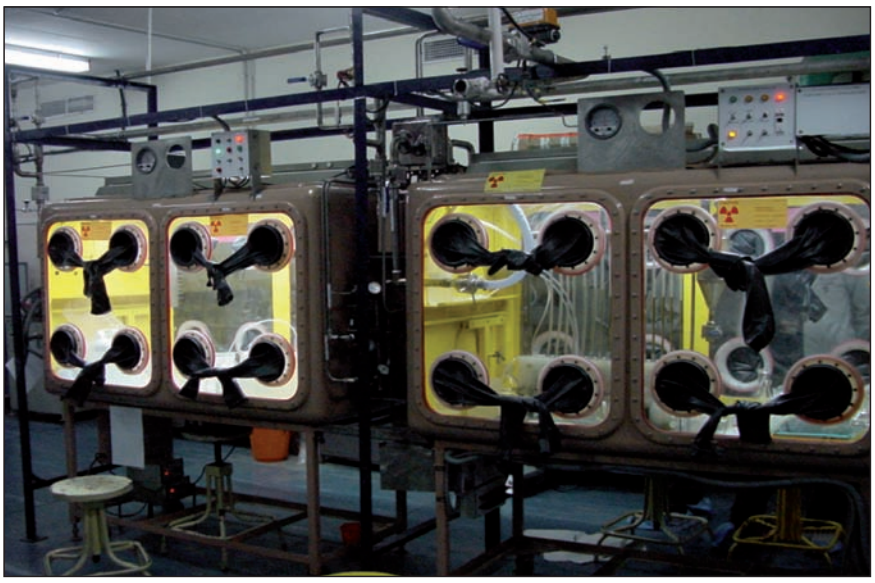

Fig. 1 *Mixer-settler facility for flow sheet development studies*

The first run composed of 10 stages for extraction and 6 stages for scrubbing. Though feed solution was free from any fission product, organic phase was scrubbed to generate an extraction profile for TiAP system under extraction-scrub conditions. The overall performance was found to be good except some minor problem of flooding. The stage profile data indicated that only 3 to 4 stages (Stage No. 7 –10) are required for the extraction of uranium and plutonium and their concentration decreases towards 16th stage where raffinate leaves the extractor bank. The results indicated that U(VI) and Pu(IV) were extracted by 1.1 M TiAP/NPH from the above feed solution with negligible loss of heavy metals into the raffinate stream. After keeping the TiAP solution loaded with Pu and U for about 48 hours, strip Run I was carried out. The data generated from this run indicated that more than 99.99% of Pu(IV) along with a fraction of U(VI) was stripped from the loaded organic with two different nitric acid solutions (4 M and 0.01 M HNO_3). The remaining fraction of U(VI) retained in the organic outlet stream of the strip Run I was stripped during strip Run II with a small loss of U(VI) in the lean organic stream (~0.16 mg U/ml) using 0.067 M HNO_3 as strippant. The data revealed that the recovery of uranium was around 99.8%.

In general, reasonably good trend for the distribution of nitric acid and actinides in the organic and aqueous phases has been obtained for the active runs. Results also indicated good mass balance for all active runs. The results showed the feasibility of using TiAP as an extractant in fast reactor fuel reprocessing. However, additional experiments with respect to the degradation aspects of TiAP, solvent recycling, measurement of decontamination factors achievable in TiAP system etc. need to be carried out in a comprehensive manner before its deployment in a plant.

IV.4 Development of Analytical Systems for the Reprocessing of Fast Reactor Fuels

The high radioactive samples generated during the reprocessing of FBTR fuels with a burn-up up to 155 GWd/t are analysed inside the CORAL itself since they require an alpha tight containment and shielded enclosure to reduce the beta and gamma activities. The samples are analysed mainly for free acidity, uranium and plutonium concentrations as well as alpha, beta and gamma activities. The concentration of uranium and plutonium are determined after extracting them into TOPO/xylene using either a vortex shaker or a simple advanced extraction set up with air-purging method (Figure 1). A remote titration set up is used to estimate the free acidity. The aliquoting of the sample for these analyses is carried out by using a remote aliquoting system as shown in Figure 2.

For the determination of the alpha, beta and gamma activities, the samples are transported to active analytical laboratory from the hot cell through a pneumatic conveyor line after suitable dilution.

Third phase formation studies

Electrical conductivity based sensors are being developed for the detection of the formation of third phase. As the solvent extraction chemistry of U^{4+} with 30% TBP from nitric acid medium is similar to that of Pu^{4+}, simulation studies were carried out for the detection of third phase by extracting U^{4+} from nitric acid medium by 30% TBP at different A/O (aqueous to organic) ratios. The results indicated that the conductivity of the third phase is about two orders of magnitude higher than the conductivity of the lean organic phase and saturated phase. The higher conductivity of third phase is explained based on the principle of inverse micelles formation. Variation of conductivity is plotted as a function of A/O ratio in Figure 3.

Detailed studies were carried out to find out the species responsible for the increased conductivity in the third phase and the probable mechanism. The charged micelles formed from the reverse micelle

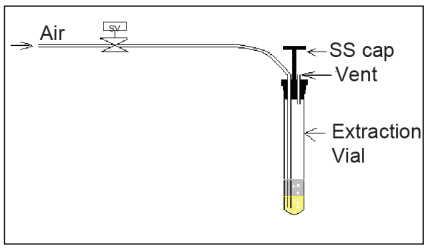

Fig. 1 *Remote TOPO extraction setup using air-purging method*

of TBP-HNO_3 complex in the low dielectric constant medium may be responsible for increasing the electrical conductivity in third phase. The formation of aggregates in the TBP-HNO_3 complex was confirmed from the Z number studies.

Uranium in the product solution is conventionally analysed by modified Davis Gray method. As this method generates large volume of sulphate bearing waste, a mini potentiometric cell is deployed to estimate uranium. Using this mini cell set up, the volume of analytical waste generated could be reduced by six times. Analysis of uranium is in the range 0.8-2.4 mg with the precision of 0.3% (higher aliquot volume < 200 mg)

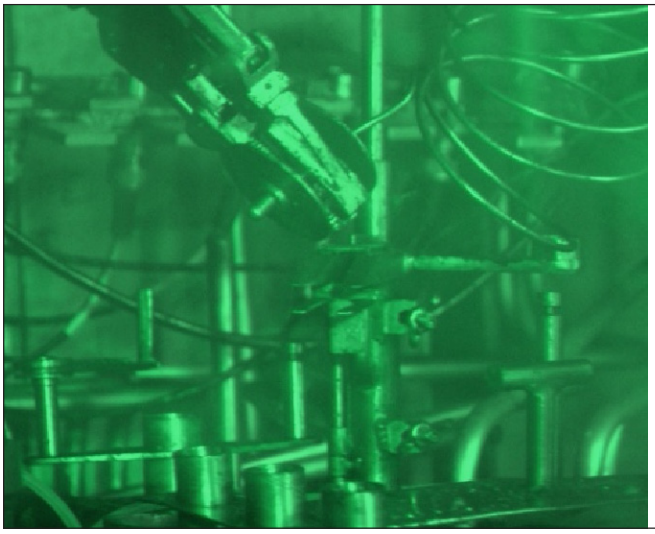

Fig. 2 *Remote aliquoting system*

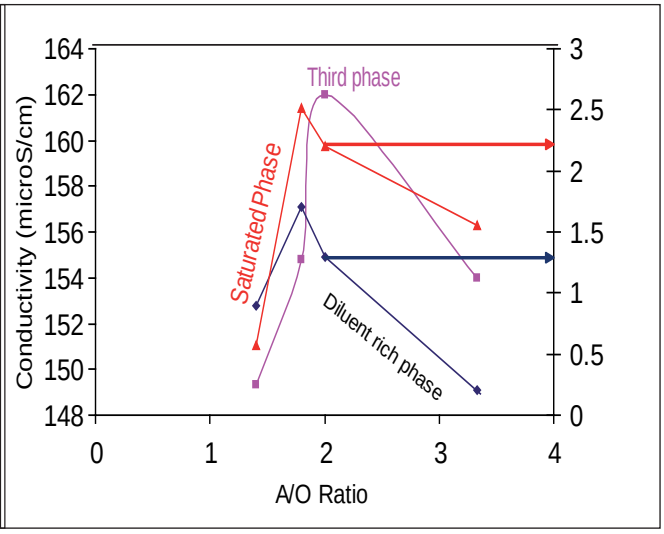

Fig. 3 *Variation in conductivity as a function of A/O ratio*

and bias 0.6%. Simultaneous determination of plutonium and uranium concentrations could be accomplished by a in-house developed fibre optic aided spectrophotometric method. Plutonium analysis is carried out at 660 nm to mitigate the interference of uranium.

Uranium is estimated at 422 nm after correcting for plutonium interference using the formulae

[Pu] (g/l) = (Absorbance at 660 - 690) x 12.45

[U] (g/l) = (Absorbance at 422 –0.113[Pu]) x 23.8

The concentration of U and Pu can be determined by simply adjusting the acidity of the solution and measuring the absorbance remotely using fibre optic sepctrophotometer without generating any analytical waste. The analysed sample can be sent back to process streams directly without any treatment. Procedures have also been standardized to monitor the concentration of plutonium in all the streams of CORAL (both on-line and in-cell) by varying the path length of the dip probes and wave length maximum on the basis of the nature of sample.

A method was developed to determine the concentrations of uranium in process organic samples (loaded and lean organics) using surfactants like tri block co-polymers for zero production of analytical organic (alcoholic) waste. The procedure for the spectrophotometric determination of U(VI) with 4-(2-pyridylazo) resorcinol (PAR) was modified to avoid the corrosive reagents sodium fluoride and tartaric acid.

Large quantities of uranous (U^{4+})/ hydrazine leading to high metal content are required in the conventional partitioning cycle in the PUREX process. One of the salt free partitioning agents, aceto-hydroxamic acid was synthesized and characterized by IR, NMR and UV visible spectrophotometric techniques. Its applicability in the separation and purification of U and Pu was demonstrated in batch mode.

PuO_2 powder obtained after re-conversion is assayed in order to determine the Pu content and the metallic and non metallic impurities present in PuO_2. For this purpose, PuO_2 is usually dissolved in nitric acid and hydrogen fluoride mixture. The presence of fluoride ions in the plutonium solution enhances the corrosion of stainless steel equipment during its storage. Hence, an alternate method is being developed for the dissolution of PuO_2 without using HF. It is reported that dissolution of PuO_2 in HNO_3 is catalyzed by either a strong oxidizing agent or a reducing agent for tetravalent Pu. Hence, systematic studies have been carried out for the dissolution of PuO_2 in nitric acid in the presence of uranous as reducing agent without using HF.

IV.5 Development of Radioanalytical Method for In-vitro Monitoring of Plutonium in Urine Matrix

Estimation of Pu at mBq levels in urine provides an indirect assessment of internal dose received by radiation workers. The rate of Pu excretion in the urine decreases so markedly with time after intake and concomitantly the Derived Investigation Level (DIL) for Pu in urine also decreases. Inhalation is the most likely route of occupational exposure to Pu. The DIL values for acute intake of ^{239}Pu due to compounds like plutonium nitrate, plutonium oxalate and plutonium hydroxide are 8.1 and 4.0 mBq for urine samples collected on second and third day of exposure respectively after intake. Moreover, the concentration of Pu excretes in each void of urine sample is variable. Hence, 24-hour urine sample is collected from radiation workers and the entire sample is processed to minimize the uncertainty in the dose

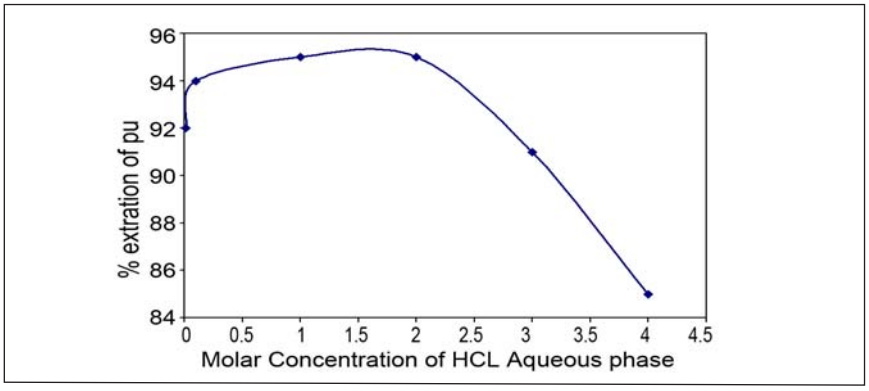

Fig.1 *Percent extraction of Plutonium into PC88A extractant based on molar concentration of aqueous phase*

assessment. The present solvent extraction method is simple, less expensive and Pu is extracted into 2-ethyl hexyl phosphonic acid mono-2-ethyl hexyl ester (PC-88A) dissolved in toluene.

In order to optimize the acidity of aqueous phase at different molar concentration of HCl, a known amount of ^{239}Pu (114.8 mBq) was spiked in each 25 ml of aqueous phase of varying molar concentration of the above said acid from 0.001 M to 4 M. The percent extraction of ^{239}Pu into PC-88A increases as the molar concentration of the aqueous phase increases up to 2 M HCl and then decreases to 85% when the concentration of the acid is 4 M as shown in Figure 1. Thus, after optimizing the solvent extraction scheme using PC-88A as extractant, it was applied to urine matrix to extract Pu. This scheme essentially consists of three steps viz: (a) pre concentration (b) solvent extraction separation and (c) alpha spectrometric estimation. Plutonium in urine is excreted in the form of plutonium citrate metabolized complex. It is not possible to separate the radionuclides of interest in the metabolized form from urine matrix. Therefore, before proceeding to co-precipitation technique, the sample was wet oxidized with the mixture of HNO_3-H_2O_2 mixture. This treatment breaks metabolic complexes of plutonium and other actinides (if present) in urine and keeps them in defined ionic state. The amount of plutonium present in urine matrix is not sufficient to precipitate as insoluble compound. Hence, plutonium in urine is pre concentrated by co-precipitation technique. plutonium was co-precipitated with calcium oxalate. Here, plutonium is preconcentrated through isomorphous replacement mechanisam. Pu^{4+} is quantitatively co-precipitated with $Ca_2C_2O_4$ from wet oxidized urine matrix with pH adjusted from 3 to 6.

To separate Ca, Mg and other ions carried out by oxalate precipitation, first the oxalate ion was destroyed by treatment with perchloric acid. Pu in +4 state is extracted into 0.01 M PC-88A (2-ethyl hexyl phosphonic acid mono-2-ethylhexyl ester) dissolved in toluene from optimized 2M HCl aqueous phase. Plutonium is stripped into 5% oxalic acid solution and is evaporated with HNO_3-$HClO_4$ mixture to destroy oxalate ions.

Plutonium present in the eluate was electrodeposited in ammonium oxalate medium on a stainless steel planchette, at 0.6 Amp for 3 hours and sample was counted for 20000 seconds in an alpha spectrometer which contains passivated implanted planar silicon (PIPS) detector with an active area of 450 mm^2. Full width half maximum (FWHM) for ^{242}Pu tracer is 93.5 keV and for ^{239}Pu is 78.5 keV when source to detector distance is 10 mm which are important for low level estimation of plutonium.

The radioanalytical method for plutonium developed reduces the analysis time to four days compared to seven days taken by the conventional anion exchange method. It is less expensive and quite useful for the 'special' and 'routine' monitoring of plutonium in urine samples.

IV.6 Studies on the Development of Pyrochemical Reprocessing

An engineering scale inactive demonstration facility for carrying out pyro process studies on uranium alloys at 2 kg scale was commissioned. A single pin chopper, electrorefiner and cathode processor are housed inside the facility. After attaining a high purity of argon inside the facility (20 vppm each of moisture and oxygen), electrorefining was carried out at 773 K with 1 kg of uranium metal contained in a perforated basket as the anode and a solid metal rod as the cathode. Prior to the experiment, 13 kg of LiCl-KCl was purified by chlorination at 723 K. The purified salt was loaded with $CdCl_2$ and equilibrated with uranium metal to get LiCl-KCl salt containing 5.5 wt % UCl_3 which served as the electrolyte. Dendritic deposit of uranium occluded with salt (Figure 1) was collected and scrapped. The deposit was loaded in the cathode processor (Figure 2). The cathode processor has a distillation set up made of graphite vessels kept inside a double walled vacuum chamber which is heated to 1223 K for distilling off the salt. The residual uranium was heated to ~1473 K for melting and consolidation into an ingot as shown in Figure 3. Heating was done using an induction heater of 40 kW capacity, positioned outside the containment box and the coils are

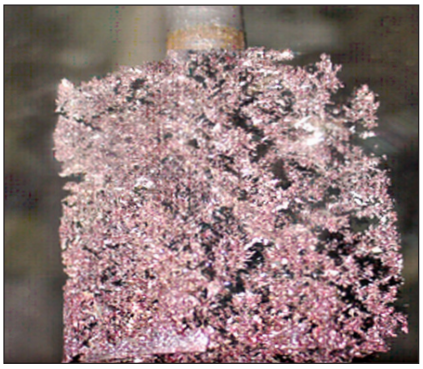

Fig. 1 *Uranium metal deposit on solid cathode covered with salt*

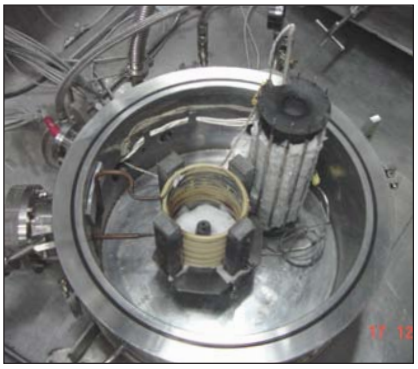

Fig. 2 *Inner view of the cathode processor*

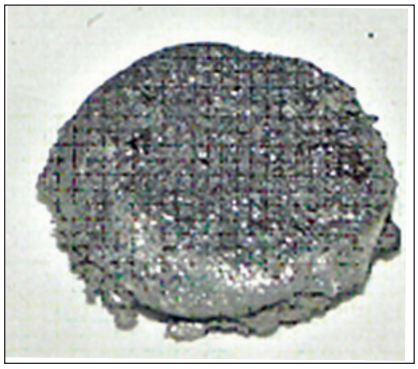

Fig. 3 *Uranium metal ingot*

taken inside the chamber through leak tight connections. To enable vision aided remote operation of the equipment, cameras have been installed inside the containment box and inside the distillation chamber. In the electrorefining process, use of solid cathode enables selective deposition of uranium whereas on liquid cadmium cathode all the actinides and minor actinides along with some amount of lanthanides are co-deposited. However, aluminium cathode shows better selectivity for actinides than lanthanides. For a better understanding of the electrorefining process using liquid cadmium and solid aluminium as cathodes, it is necessary to have complete knowledge of the thermochemical properties of the actinide and lanthanide chlorides and their electrochemical behaviour on inert cathode and reactive cadmium and aluminium cathodes. Hence, the electrode reaction at the salt -metal interface in UCl_3-LiCl-KCl, $LaCl_3$-LiCl-KCl and $NdCl_3$-LiCl-KCl eutectic melts was investigated over the temperature range 698 - 798 K at an inert electrode, liquid cadmium and solid aluminium electrodes using transient electrochemical techniques. Underpotential deposition of uranium, neodymium and lanthanum took place on cadmium and aluminium electrodes due to the formation of their respective stable intermetallic compounds, UCd_{11}, $NdCd_{11}$, $LaCd_{11}$, UAl_4, Nd_3Al_{11} and La_3Al_{11} as seen in Figure 4. The apparent standard electrode potential of La(III)/La(Al) was estimated in the temperature range 698-798 K from the cyclic voltammograms using Ag/Agcl reference electrode. The Gibbs energy of formation of the intermetallic compound La_3Al_{11}, activity of lanthanum in aluminium, the excess Gibbs energy and the activity coefficient of lanthanum in aluminium were estimated from the open circuit potential measurement (Figure 5). SEM-EDX and XRD analysis of the deposit showed the formation of the intermetallic compound La_3Al_{11}.

Electrolytic reduction of lanthanide and actinide halides to the respective metals in chloride as well as fluoride melts is of interest for the production of these metals. Reduction behaviour of lanthanide fluorides in fluoride melts is also of interest in the reprocessing of the fluoride fuels of molten salt breeder reactors (MSBR). Electrochemical redox behaviour of Ce(III) ion in LiF-CaF_2 eutectic was studied at 1093 K using tungsten (inert) and nickel (reactive) as working electrodes and platinum as quasi-reference electrode by various electrochemical transient techniques viz. cyclic voltammetry, squarewave voltammetry and chronopotentiometry. It was deduced that reduction of Ce(III) to Ce metal occurs by a single step, three electron transfer. Diffusion coefficient of Ce(III) ion was determined from CV, semi-integral analysis and CP. Electrochemical studies in the presence of Ni electrode showed the formation of the inter-metallic compounds $CeNi_5$ and Ce_2Ni_7 which were characterized by powder X-Ray Diffraction and SEM-EDAX analysis.

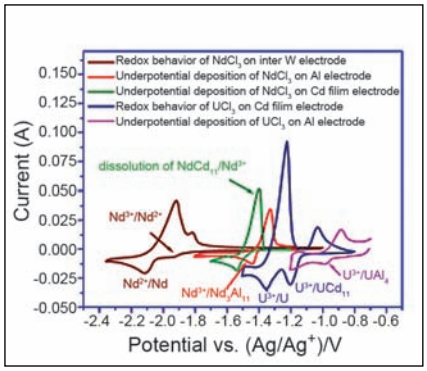

Fig. 4 *Cyclic voltammograms for UCl_3-LiCl-KCl and $NdCl_3$-LiCl-KCl melt on W, Cd and Al electrodes at 723 K*

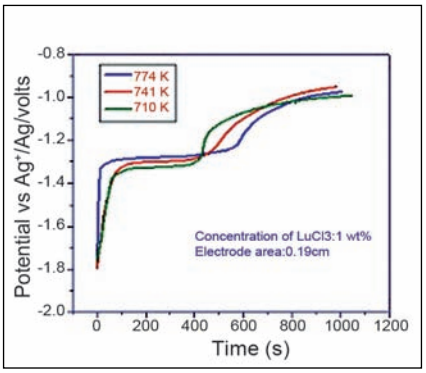

Fig. 5 *Open circuit potential after depositing lanthanum on aluminium electrode*

IV.7 Modeling and Simulation of Fixed Bed Adsorber for the Adsorption of Di-Butyl Phosphate on Activated Alumina

PUREX process using 30% TBP in n-paraffin hydrocarbon (NPH) or n-dodecane is employed in nuclear fuel reprocessing for the extraction of uranium and plutonium from spent fuel. In this process the solvent is being contacted with highly radioactive aqueous solutions which results in the hydrolytic as well as radiolytic damage to the solvent. The most significant parameter which affects the solvent extraction process is the quality of the solvent. The presence of the degradation products in the solvent can lead to problems such as formation of interfacial cruds, retention of uranium and plutonium in organic phase, increased phase separation time and poor extraction efficiency. So the solvent has to be purified before recycling. Vacuum distillation is the commonly used method for the removal of solvent degraded products from the used solvent. An alternate method, adsorption using solid sorbents such as silica gel, bauxite and activated alumina has also been reported in the literature. Activated alumina has the potential to adsorb various organic and inorganic substances and it can be easily regenerated and reused. It is widely used as an adsorbent because it is highly porous in nature and has high surface area.

The feasibility of solvent purification by adsorption using activated alumina as adsorbent was investigated. Towards this study, adsorption equilibrium characteristics and breakthrough behaviour of di-butyl phosphate (DBP) on activated alumina have been carried out.

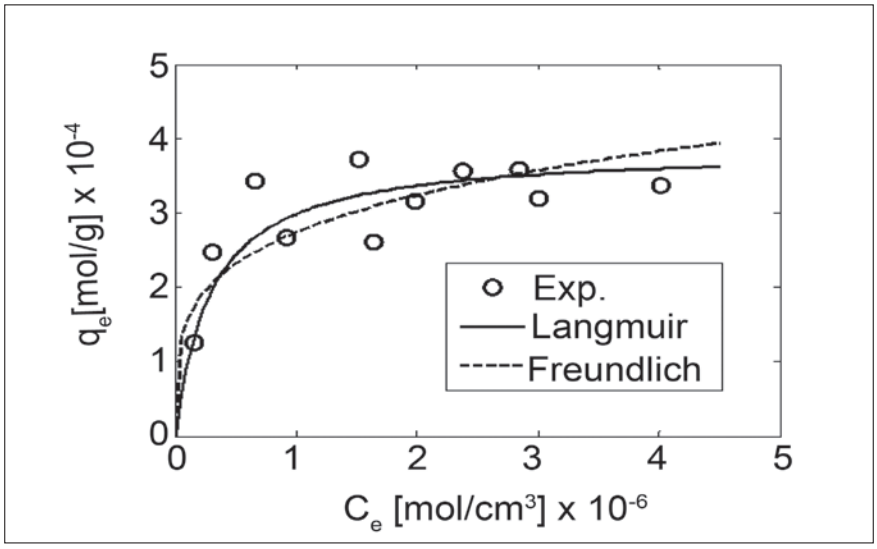

Fig. 1 *Equilibrium data of DBP on activated alumina*

The major concern in the design of adsorption column is the prediction of breakthrough time for a given flow rate and concentration of impurities. The concentration vs. time curve for fluid leaving the adsorption column is called breakthrough curve. The size and shape of the breakthrough curve are very important in determining the length of an adsorption bed because the steepness of the breakthrough curve decides the extent to which the capacity of an adsorbent bed can be utilized. Developing a model will help to generate the breakthrough curves for different experimental conditions without carrying out experiments. A model for fixed bed adsorber for the adsorption of DBP on activated alumina is developed and it is based on material balance, adsorption equilibrium relationships, boundary conditions and initial conditions.

Adsorption isotherm model

Equilibrium data for DBP-alumina system were generated and the experimental data obtained were fitted into Langmuir and Freundlich adsorption isotherms. Comparison of the fitted models with experimental data is shown in Figure 1. The experimental data were found to fit well with Langmuir adsorption isotherm which can be expressed as

$$\frac{q}{qm} = \frac{Kc}{1+Kc} \qquad (1)$$

where q is the concentration of DBP in the adsorbent, q_m is the maximum adsorption capacity, c is the concentration of adsorbate in solution and K is the adsorption equilibrium constant.

Fixed bed model

Neglecting the axial dispersion, the mass balance equation for the solute for a section of the bed in a column can be written as

$$\varepsilon dZ\frac{\partial C}{\partial t}+(1-\varepsilon)dZ\frac{\partial q}{\partial t}= \quad (2)$$
$$uC-u(C+dC)$$

or

$$\frac{\partial c}{\partial t}+\frac{(1-\varepsilon)}{\varepsilon}\frac{\partial q}{\partial t}+u\frac{\partial c}{\partial z}=0 \quad (3)$$

and

$$\frac{\partial q}{\partial t}=k(q^{*}-q) \quad (4)$$

Here, c is the concentration of adsorbate in solution, q is the concentration of adsorbate in the bed, q* is the equilibrium concentration of adsorbate in the bed, Z is the length of the bed, ε is the porosity of the bed, k is the mass transfer coefficient and u is the superficial velocity. Substituting the rate from equation (4) and upon rearranging, equation (3) becomes

$$\frac{\partial c}{\partial t}=-\frac{(1-\varepsilon)}{\varepsilon}k(q^{*}-q)-u\frac{\partial c}{\partial z} \quad (5)$$

The partial differential equations obtained for mass balance can econverted to dimensionless form using the equilibrium relationship as shown below

$$\frac{\partial \phi}{\partial t}=-u\frac{\partial \phi}{\partial z}- \quad (6)$$
$$\frac{(1-\phi)}{\varepsilon}kK(\phi-\psi)$$

$$\frac{\partial \psi}{\partial t}=k(\phi-\psi) \quad (7)$$

where

$$\phi=\frac{c}{c_F} \quad \text{and} \quad \psi=\frac{q}{q_F^{*}}$$

These dimensionless partial differential equations are converted to a set of ordinary differential equations in independent variables by method of lines. Discretised equations for N grid points along the length of the bed can be written as follows

$$\frac{d\phi_i}{dt}=-u\left(\frac{\Delta\phi}{\Delta Z}\right)_i- \quad (8)$$
$$\left(\frac{1-\varepsilon}{\varepsilon}\right)kK(\phi_i-\psi_i)$$

and

$$\frac{d\psi_i}{dt}=k(\phi_i-\psi_i) \quad (9)$$

where i = 1 to N.

Equations (8 and 9) along with equilibrium isotherm equation (1) were solved numerically by using variable order method in order to get concentration profile of solute in the fixed bed as well as breakthrough curve. The appropriate initial conditions and boundary conditions for solving the equations are as follows:

Initial conditions: $\phi = \psi = 0$

Boundary condition: $\phi = 1$ (0, t)

Comparison of the experimental breakthrough and that obtained by solving model equations is shown in Figure 2.

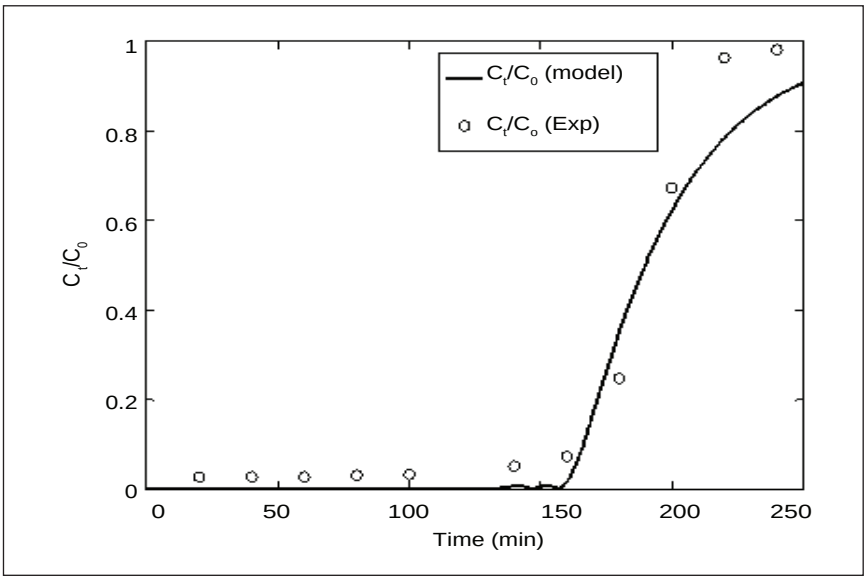

Fig. 2 *Comparison of the experimental and predicted breakthrough curves*

The saturation capacity of the bed was calculated from experimental data on breakthrough curve by the following equation

$$q_m=\frac{QC_o}{m}\int_0^{t_e}(1-\frac{C_t}{C_o})dt \quad (10)$$

where q_m is the adsorption capacity, Q is the volumetric flow rate, m is the mass of the bed, C_o is the feed concentration, C_t is the concentration of the exit fluid at time t and t_e is the bed exhaustion time.

The model predictions were found to fit the experimental data fairly well. The agreement among the experimental and predicted data indicated that the adsorption of DBP on activated alumina could be simulated by the proposed model. The saturation capacity of bed was estimated from the experimental data and it was found to be 42.71 mg of DBP per gram of activated alumina. Breakthrough curves at different flow rates and concentrations are being computed.

IV.8 Extraction Behaviour of Ruthenium with Tributyl Phosphate and n-Paraffin Hydrocarbon

Ruthenium is one of the major fission products (FPs) produced in the fission of plutonium. The complex behaviour of ruthenium in the reprocessing of spent fuels poses problems not only in the solvent extraction step, but has significant effect in the denitration and waste treatment processes also. During the dissolution of irradiated Pu-rich fuel in nitric acid, ruthenium passes into solution mainly in the form of various nitrato, nitro and nitrato-nitro complexes of ruthenium nitrosyl ion, $Ru(NO)^{3+}$. They are complexed with hydroxo and aqua ligands. Extractability of different nitrato or nitro complexes of ruthenium nitrosyl ions varies and therefore, the equilibrium between the species is critical for the decontamination of uranium and plutonium from ruthenium. Among the ruthenium complexes, the trinitrato complexes are the most extractable in TBP. Mixed nitrato-nitro species are more extractable than nitro compounds. The extent of extractability of some of these ruthenium species, primarily trinitrato complexes from nitric acid solutions is responsible for the ruthenium contamination of the products in the PUREX process. Ruthenium tetroxide, in the highest oxidation state is volatile even at room temperature. In the process of concentrating highly radioactive aqueous waste, ruthenium is oxidized partially to volatile tetroxide by nitric acid and escapes to the vapour phase. In the presence of cerium(IV) nitrate, quantitative oxidation of ruthenium to ruthenium tetroxide is favoured, which is extractable in paraffin oil. Hence, the extraction behaviour of ruthenium nitrate in 4 M nitric acid and ruthenium along with other simulated fission product elements (the concentrations of which correspond to those for FBTR fuel irradiated for 100 GWd/t and 1 year cooled) in 4 M nitric acid was determined with 30% TBP/n-paraffin hydrocarbon (NPH) as the organic extractant. 5 ml of ruthenium bearing HNO_3 solution (aqueous) and 5 ml of organic (30% TBP) were equilibrated in a vortex mixer for 5 minutes. Samples taken from the aqueous phase before and after extraction were analysed for ruthenium by spectrophotometry and ICP-OES and the concentration of ruthenium extracted into organic phase was estimated. The effect of 0.04 M Ce(IV) nitrate as the oxidising agent in the solvent extraction behaviour of ruthenium was evaluated. The ruthenium bearing solutions were also equilibrated separately with equal volume of pure normal paraffin hydrocarbon with and without Ce(IV) for the purpose of determining the efficiency of normal paraffin hydrocarbon in removing ruthenium from the simulated high level liquid waste (HLLW). The distribution coefficient of ruthenium, D_{Ru} in 30% TBP/ normal paraffin hydrocarbon system and the percentage recovery of ruthenium by normal paraffin hydrocarbon with and without Ce(IV) are given in Table 1. As only nitro and nitrato complexes of nitrosyl ruthenium in HNO_3 medium are extracted into 30% TBP/NPH, the D_{Ru} values determined for the extraction of pure $Ru(NO_3)_3$ and that in the presence of FP elements in the aqueous solutions by the organic were found to be insignificant. In the presence of 0.04 M Ce(IV) ions, ruthenium in the aqueous solution is oxidized to RuO_4 vapour. When the aqueous phase was equilibrated with the organic and allowed to settle after the addition of Ce(IV), the top organic layer was found to prevent the escape of RuO_4 vapour into the atmosphere. The trapped RuO_4 vapour in the organic got reduced and formed a black interface between the aqueous and organic phases. Analysis of the interface layer by powder XRD after drying confirmed the presence of RuO_2. Hence, on account of the oxidation of ruthenium by Ce(IV), the D_{Ru} values calculated based on the

Table 1: Distribution of Ru into 30% TBP and recovery of Ru by NPH

Aqueous Solution	Oxidizing agent	D_{Ru} in 30% TBP	Recovery (%) of Ru by NPH
Ru-nitrate	Nil	0.034	9.20
Ru-nitrate	0.04 M Ce(IV)	1.062	81.0
Simulated HLLW	Nil	0.011	2.30
Simulated HLLW	0.04 M Ce(IV)	1.119	96.10

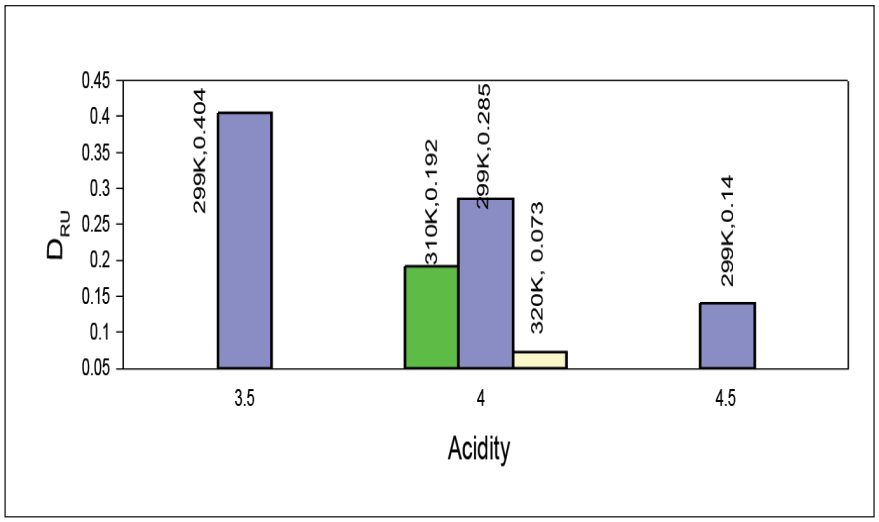

Fig. 1 *D_{Ru} at different acidities and temperatures*

Table 2: Effect of $NaNO_2$ on the distribution coefficient of Ru

$[NaNO_2]$/ (M)	D_{Ru}	
	Ru-nitrosyl nitrate	Ru in simulated HLLW
0.0	0.046	0.126
0.4	0.206	0.367
0.8	0.184	0.331
1.2	0.270	0.331
1.6	0.313	0.376
2.0	0.340	0.464

analysis of ruthenium content by ICP-OES in the aqueous phase after extraction were found to be high. Table 1 shows that the behaviour of ruthenium was similar with NPH also in the presence of Ce(IV). In a simulated dissolver solution, the distribution coefficient of ruthenium was determined to be 0.023 without Ce(IV) nitrate, 0.248 with Ce(IV) ions at ambient temperature and 0.345 with Ce(IV) at 333 K. One of the reagents proposed in the literature to suppress the extraction of $Ru(NO)^{3+}$ is sodium nitrite. As $NaNO_2$ is commonly used to adjust the valency of plutonium to Pu(IV) for its extraction into the organic phase, the effect of $NaNO_2$ on the extraction of ruthenium into the extractant 30% TBP/NPH at different concentrations of nitric acid and temperatures was studied. Two sets of experiments were conducted; (a) with pure ruthenium in HNO_3 (in the form of nitrosyl nitrate) and (b) ruthenium along with simulated fission products in HNO_3. Calculated quantities of $NaNO_2$ ranging from 0.4, 0.8, 1.2, 1.6 and 2.0 M were added to known concentration of the aqueous solutions (a), (b) and equilibrated with the organic.

Effect of temperature on the extraction of ruthenium (as nitrosyl nitrate) was evaluated by carrying out equilibration experiments without $NaNO_2$ and with 0.4 M $NaNO_2$ at 306 and 316 K in 4 M nitric acid. Dependence of feed acidity on the extraction of ruthenium into the organic phase was ascertained by conducting equilibration and extraction with aqueous feed whose acidity was adjusted to 3.5, 4.0 and 4.5 M nitric acid.

The D_{Ru} values calculated and listed in Table 2 for the acidity 4 M at 299 K in the presence of varying amounts of $NaNO_2$ revealed that addition of $NaNO_2$ enhances the extraction of ruthenium. The D_{Ru} values derived for the simulated FP solution were found to be higher than those for pure ruthenium nitrosyl ions (as evident from Table 2) due to the effect of metal ions in favouring the formation of nitrato complexes. For the nitric acid (aqueous) concentrations 4.5, 4.0 and 3.5 M, D_{Ru} values derived from the analysis by spectrophotometry were 0.140, 0.285 and 0.404 respectively for the extraction of pure ruthenium nitrosyl nitrate solution without $NaNO_2$. At 299 K the distribution coefficient of ruthenium nitrosyl nitrate was found to be 0.282 and the corresponding values derived at 310 and 320 K were 0.192 and 0.073 respectively. As the rate of hydrolysis of the trinitrato complex of ruthenium for the formation of di- and mononitrato complexes is proportional to temperature, the D_{Ru} values were found to decrease with increase in temperature. The effect of acidity and temperature on the extraction of ruthenium from pure nitrosyl nitrate solution is shown in the histograms in Figure 1.

This study revealed that addition of excess of $NaNO_2$ in the conditioning stage will enhance the distribution coefficient of ruthenium. Factors like experimental equilibration time (contact time), ageing of the aqueous in nitric acid, impurities or hydrolysis products of solvents and diluents, incomplete separation of different ruthenium complexes and incorrect identification of their structures are reported to affect the distribution of ruthenium. To resolve these issues, systematic extraction experiments require to be conducted for estimating the dependence of ageing time and contact time on D_{Ru} as well as for quantifying the fraction of nitrato, nitro and nitrato-nitro complexes of ruthenium.

To minimize the overall extractability of ruthenium, concentrations of HNO_3, HNO_2 and the solvent, temperature, contact time and the chemical nature of the aqueous solution should be adjusted.

IV.9 CFD Simulation of Flow Inside Annular Centrifugal Contactor

Annular centrifugal extractor (ACE) finds wide applications in chemical process industries and nuclear fuel reprocessing involving liquid-liquid extractions. It offers various advantages over conventional mixer-settlers which include low residence time, low hold up and high mass transfer rates. The design principle of annular centrifugal extractor is based on Taylor-Couette flow. It consists of a stationary outer cylinder, concentric to which is a rotating inner cylinder. The annular gap between the two cylinders is kept as minimum and it serves as the mixing chamber. The inner cylinder is rotated at a high speed and its motion is quantified by a dimensionless number known as Taylor number (Ta), which is the ratio of centrifugal force to the viscous force. At low speed of rotation, flow is purely circumferential and occurs at Ta <1708 and is called as circular Couette flow (CCF). When Ta exceeds the critical value, Ta_{Cr}=1708), the centrifugal instability gives rise to Taylor vortex flow. In Taylor vortex flow a sequence of counter rotating vortices stacked along the annulus occurs, which is a characteristic feature of this flow. At high Taylor numbers (Ta > 1000 Ta_{Cr}) the flow becomes turbulent and is called as turbulent Taylor vortex flow. Above this point, the vortex boundaries become difficult to discern.

The outer stationary bowl contains two tangential feed inlets (more dense phase inlet and less dense phase inlet) indicated by arrows in Figure 1, through which the two immiscible liquid phases enter inside the annulus. The stationary cylinder having a stationary bottom plate with radial vanes, helps to create fine dispersion in the annular space by monitoring the flow to the rotor. The spinning inner cylinder (rotor) exerts high shear owing to high power consumption in the range 20-500 kW/m^3 on the two fluids. As a result, fine dispersion forms create high interfacial area for liquid-liquid extraction. The phase dispersion is guided by the radial vanes located at the stationary bottom plate and enters inside the rotor through an orifice. The rotor also acts as a pump and suctions the fine dispersion and gets deflected towards the rotor wall with the help of horizontal baffles. The hollow rotor with deflector plate is divided into four vertical chambers formed by the four vertical vanes and baffles attached to the wall. Once the mixed phase is entrapped in the vertical chamber by the guidance of deflector plate, it is rapidly accelerated to the rotor speed. Owing to the pumping action inside the rotor, the liquid continues to rise upward and experiences centrifugal settling because of the elevated ‘g’ and the coexistence of phases of different densities in the mixed phase. As a result, the light phase is thrown inward (towards the centre) and the heavy phase is thrown towards the wall. Phase separation occurs based on the centrifugal force and each phase is collected separately.

Two phase flow inside a Taylor-Couette device is of special interest to researchers owing to its applications and the inherent complexities. Many experimental as well as numerical studies have been performed to investigate the flow instabilities. Most of the work concentrates on the measurement of gross mass transfer parameters such as mass transfer coefficient, effective interfacial area, dispersed phase hold up, etc. These investigations have resulted in many empirical correlations which have been extensively used in practice.

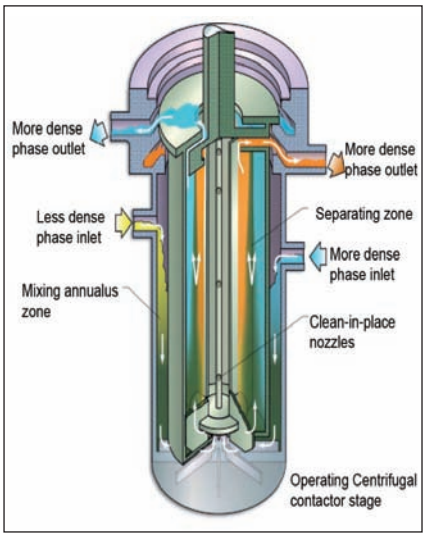

Fig. 1 *Schematic operation of annular centrifugal contactor*

The objective of this work is to understand the behaviour of annular centrifugal contactor with respect to the system constraints and to provide insight for guiding the scale up strategies for the design of the contactor. Three dimensional single phase, unsteady and turbulent flow simulation was carried out in the annular and rotor region of annular centrifugal extractor 250 mm using computational fluid dynamics. The model geometry is meshed by using unstructured tetrahedral grids with average grid size 0.01 m. Pressure inlet and velocity inlet boundary conditions are used for flow inlets and rotating wall boundary condition is implemented at the inner cylinder. Figure 2a represents the vector plot of flow field in the annular zone. It is observed that the fluid rotates with higher azimuthal velocity near the inner cylinder. This is attributed to the shear exerted by the inner rotor of the annular contactor.

Figures 2b and 2c show the contour plot of axial and radial component of velocity in a cross section in the annular mixing zone and stationary bottom region of the contactor. The interior is coloured with the tangential velocity, maximum at the inner cylinder and is zero at outer wall. It is observed that the flow of fluid is predominated by the movement of a series of Taylor vortices within the annulus. Formation of Taylor vortices leads to centrifugal instability of flow inside the contactor.

Figure 3a shows the vector plot of the flow field in the settling zone (inside rotor) of the contactor. It is observed that the liquid rises up to the settling zone with high axial velocity and enters inside the vertical chamber separated by the radial vanes in the rotor zone of annular centrifugal contactor. Further it rises up through a helical path and comes out through the tangential outlet. Figures 3b and 3c show the contour plots of axial and radial component of velocity inisde the rotor zone of the contactor. The interior of rotor is coloured with tangential velocity. Since it rotates with very high speed, the tangential velocity is maximum at the rotor wall, gradually increases in the radial direction and is zero at the centre. The contour of axial

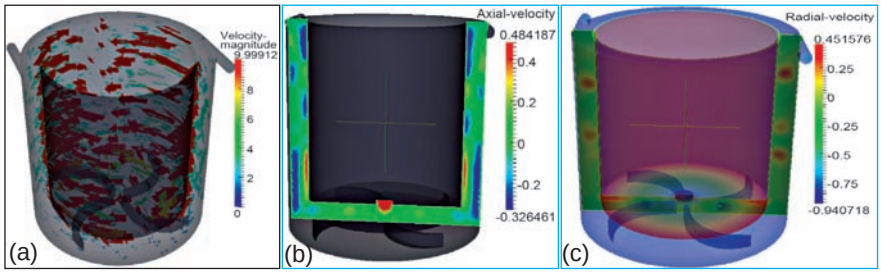

Fig. 2 *(a) Velocity vectors of flow inside (b) Contour of axial velocity over x-plane and (c) Contour of radial velocity over x-plane in the annular zone of contactor*

velocity shows the high accelerated flow against gravity at the inlet, the radial vanes and at the outlet. This is attributed to the forced vortex flow behaviour of fluid in the settling zone of the contactor.

This study has demonstrated the onset of centrifugal instability in the annular zone feature of CE-250 mm as well as the dynamics of flow inside the rotor attached with vertical vanes. The flow in the annular zone is attributed to mixing and flow inside the rotor is attributed to the settling zone of contactor. This study brings out the complete transparency of fluid mechanics associated with the complex geometry of annular centrifugal extractor and predicts the fluid properties and design variable with reasonable accuracy in the interior region of it. Further, detailed hydrodynamics study inside the contactor with respect to system constraints and operational parameters will provide input data for effective and sustainable design of annular centrifugal contactor for full potential in both pilot and plant scale process.

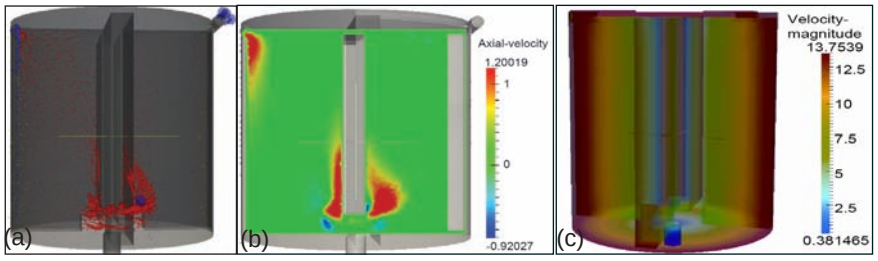

Fig. 3 *(a) Velocity vectors of flow inside (b) Contour of axial velocity over x-plan and (c) Contour of radial velocity at x-plane in rotor zone of contactor*

IV.10 Synthesis of Red-Oil from Alternate PUREX Solvent - 36%TiAP/n-Dodecane Mixture

Red-oil is a mixture of non-specific composition consisting of extractant, it's degradation products, nitrated solvent and unidentified red-coloured nitro-organics. Tri-iso amyl phosphate is a promising alternate solvent for PUREX process. Since TiAP has much lower aqueous solubility as compared to TBP, it will not lead to the formation of red-oil readily. An attempt was made to synthesize and determine the properties of TiAP/red-oil.

Synthesis of red-oil from TiAP

Details of the experimental runs for the synthesis of red-oil from TiAP are listed in Table 1. 40 ml of acid and 8 ml of TiAP were used in the experiments. The results indicated

Table 1: Feed conditions for red-oil synthesis from TiAP(36%)		
Run	[Acid]/M	Colour of the organic phase
1	0.02	Off white
2	2	Light yellow
3	4	Reddish orange

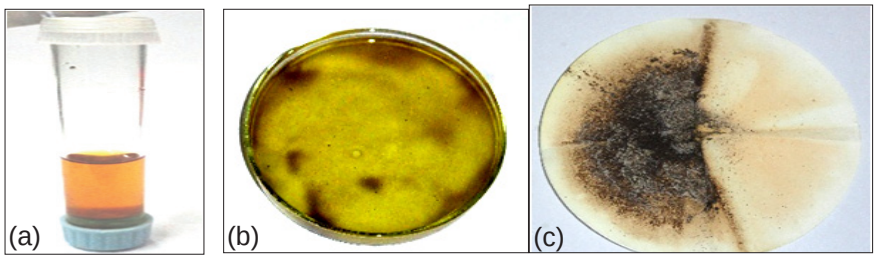

Fig. 1 *(a) Red oil prepared from TiAP (b) Jelly like material floating over organic phase and (c) Carbon particles on the filter paper after filtration*

that the rate of decomposition of TiAP solution is low at lower range of acidity but at higher acidity viz. 4 M, appreciable decomposition took place in the temperature range 403 - 1408 K. From the colour of the organic mixture as shown in Figure 1a, the compounds present were assumed to be nitrosoamines (R_2-N-N=O), azo compounds (R-N=N-R') and nitroso compounds (R-N=O). To determine the composition of the orange organic phase and to find out whether the phase was energetic to cause runaway reactions in the heating vessels, it was subjected to instrumental analyses. During partial nitration, jelly like emulsion was found floating over the aqueous phase as shown in Figure 1b. As the acidity went on increasing, intense orange colour of the organic phase was observed, indicating rigorous degradation of TiAP under moderate acidic condition and more nitration of diluent. With the formation of red-oil, some black particles were also seen (Figure 1c). The carbon particles accumulated owing to the charring of diluent were filtered off and the red-oil formed in the process was separated and characterized.

Measurement of density

Density of the synthesized TiAP red-oil was determined to be 0.882 g/ml. The lower density of TiAP/ red-oil, observed in this case, is due to the lower density of the decomposition products and the absence of extracted heavy metals.

Gas analysis

Gas-chromatographic analysis of the product gases indicated the presence of water vapour, CO_2, H_2, hydrocarbons, O_2 and N_2 as listed in Table 2. Individual hydrocarbons (may be saturated or unsaturated) could not be detected. As the amyl group contains five carbon atoms, the hydrocarbons formed would be in the range C_1 to C_5. Presence of NO_x gas was evident from the colour of the gas, but could not be quantified. Interference from other nitro and nitroso compounds was suspected. Nitrogen was found to be in the atmospheric range and the slightly lower decrease in oxygen than the atmospheric level could be attributed to the oxidation reactions that would have occurred in the reactor. Presence of hydrocarbons and hydrogen are a matter of concern as they are highly flammable. Especially, the amount of hydrogen generated in the range of 3600 ppm from 8 ml of 36% TiAP in a 1000 ml reactor is a matter of grave concern.

FT-IR studies

The peaks at 2922.89 cm^{-1} and 2859.01 cm^{-1} in the FT-IR absorbance spectra studies indicated the presencem of methylene group ($–CH_2$) asymmetry flex vibration. The peak at 1726.75 cm^{-1} represented the presence of aldehyde and conjugating effect with ketone. Absorption at 1551.97 cm^{-1} was attributed to the asymmetric N=O stretch present in primary, secondary or tertiary nitro group. The peak at 1461 cm^{-1} was ascribed to alkyl methylene group. Peak at 1377.51 cm^{-1} corresponded to either (C–H) bending vibration or the aliphatic nitro compounds like iso amyl nitrate and such type of compounds. Peak at 1269.17 cm^{-1} was ascribed to carboxylic acid. Peaks at 1078.51, 1057.19 and 1039.39 cm^{-1} represented primary alcohols. These alcohols could be iso-amyl alcohol, iso-butyl alcohol or iso-propyl alcohol. The peak at 1002.99 cm^{-1} was due to the presence of esters which might have been generated by reactions with alcohols and the acids present in the system.

Table 2: Gas Chromatographic analysis of the product gases generated				
S.No	Components	Columns used	Detector used	Concentration
1	H_2O Vapour	Porapak-Q	TCD	23,700 ppm
2	NO_x	Porapak-R	ECD	BDL*
3	CO	Porapak-N	FID-Methanator	BDL
4	CO_2	Porapak-N	FID-Methanator	300 ppm
5	H_2	Molecular Sieve 5A	TCD	3600 ppm
6	Hydrocarbon	SE- 30 20%	FID	18 ppm
*Interference suspected. BDL- below detectable limit.				

IV.11 Operation of Nitric Acid Loop and Modeling of the Corrosion Process of Type 304L Stainless Steel

A 400 litre capacity 6 N nitric acid loop was designed, constructed and operated for evaluating the corrosion performance of candidate materials over long operating periods under reprocessing plant simulated conditions (Figure 1). Corrosion rates of AISI type SS 304 L samples in different metallurgical conditions, namely, solution annealed, sensitized and welded conditions (used in DFRP), along with indigenous nitric acid grade (NAG) SS 304L (from M/s MIDHANI) were evaluated in this loop in flowing nitric acid at different temperatures (313, 333, 353 K, boiling and vapour phase). The instrumentation, electrical and mechanical systems of the nitric acid loop were checked for proper functionality periodically before each campaign. Charging of nitric acid into the loop and loading of samples were carried out before the start of the campaigns. Operation of nitric acid loop for 10000 hour has been completed with eleven different campaigns. At the end of the campaign, samples from each sample holder were removed and checked for weight loss, and morphological changes. Also, non-destructive examination of these samples by eddy current and ultrasonic methods, and chemical analysis of the loop acid were carried out. In-service inspection of the loop components at selected locations was carried out by ultrasonic methods during shutdown period of some of the campaigns.

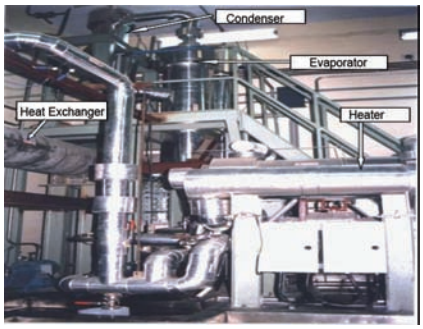

Fig. 1 *Nitric acid loop*

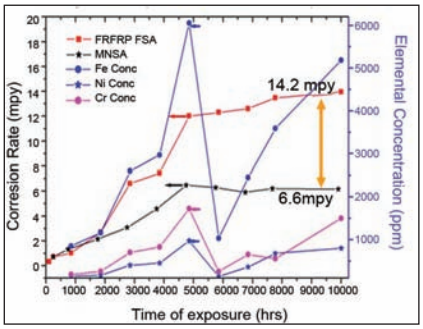

Fig. 2 *Corrosion rates of SS 304 L and NAG SS 304 L samples exposed to boiling 6 N HNO_3*

The average corrosion rate in boiling nitric acid was 14.2 mpy for the DFRP SS 304 L specimens compared to 6.6 mpy for the MIDHANI NAG SS 304 L specimens after 10000 hour of exposure (Figure 2). The corrosion rates were calculated to be 0.02, 0.06 and 0.75 mpy at temperatures 313, 333 and 353 K respectively. Significant increase in the quantity of the elements was noticed in the acid in the loop (with Fe ~5186 ppm, Cr ~1502 ppm and Ni ~800 ppm) after final campaign. Direct correlation was observed between the corrosion rates and the corrosion product concentration in the acid of the loop. Morphological examination indicated that the corrosion takes place by intergranular mode, and the severity of the intergranular attack increased with campaign duration. Further, the NDE examination showed matching thickness loss with the corrosion rate obtained. The in-service inspection of the nitric acid loop at critical weld joints, pipe bends and other vulnerable zones showed significant wall thickness loss in most of the locations. Maximum loss in wall thickness was observed at the vapour-phase regions. The cold-leg regions exhibited negligible loss in wall thickness. Anomaly of wall thickness increase observed in some regions can be attributed to deposition of elements dissolved in nitric acid.

An artificial neural network (ANN) model for the corrosion process was developed, using the large data bank obtained for 10000 hour of exposure of the samples. The modeling results are given in Table 1. The model predicted that the average thickness loss up to 50% thickness would provide typical life of 6 years for 3 mm thick and 11 years for a 5 mm thick component; however, for NAG SS 304 L, the life would be more than double that of conventional SS 304 L.

Table 1: Life time prediction results from the corrosion process model developed

Material	Cr-Ni-C (%)	Typical Thickness, (mm)	Predicted life, (years)
SS 304L	18-8-0.03	3	6
		5	11
NAG SS 304L	18-12-0.012	3	12 ½
		5	23 ½

IV.12 Development of Rotary Semi-Continuous Dissolver for Fast Reactor Fuel Reprocessing Plants

Dissolution of the fast reactor spent fuel at plant scale is the most critical process among the head end reprocessing steps. Conventional batch type dissolver systems are not conducive for plant scale reprocessing of fast reactor fuels. Therefore, a semi-continuous dissolver system with the following merits is designed.

- The system is critically safe in geometric design.
- Operation of the system and remote maintenance are very simple.
- The system can be easily automated in remote environment.
- As the system has independent rotary drum to contain the fuel pin bits, dissimilar metal joints can be avoided.
- The dissolver system with different operating conditions in each stage can tackle the problem of corrosion of materials in a better way than the conventional batch dissolver.
- The system with continuous movement of spent fuel bits will improve the dissolution rate and effectively reduce the total process time.
- Better handling of nitric acid fumes and off-gases.

The continuous dissolver system is a rotary segmented drum with oblique cone type ducts at the centre with perforated plate and mechanical drive system. When the drum rotates in forward direction, the bits from the bottom of the stage will be lifted up on the plate and again thrown back to the stage as the plate rotates at the top. This type of tumbling of fuel pin bits will enhance the dissolution. Rotation in the reverse direction will transfer the same fuel pin bits to the next stage through oblique duct cone. The system is essentially a counter current process and hot nitric acid will flow in opposite direction from the opposite end. As the process continues, the fuel pin bits keep on dissolving and finally empty hulls will be discharged to the rinsing portion of the dissolver system. After rinsing in a similar type of rotary drum, the hulls are discharged to the hull drum for further processing.

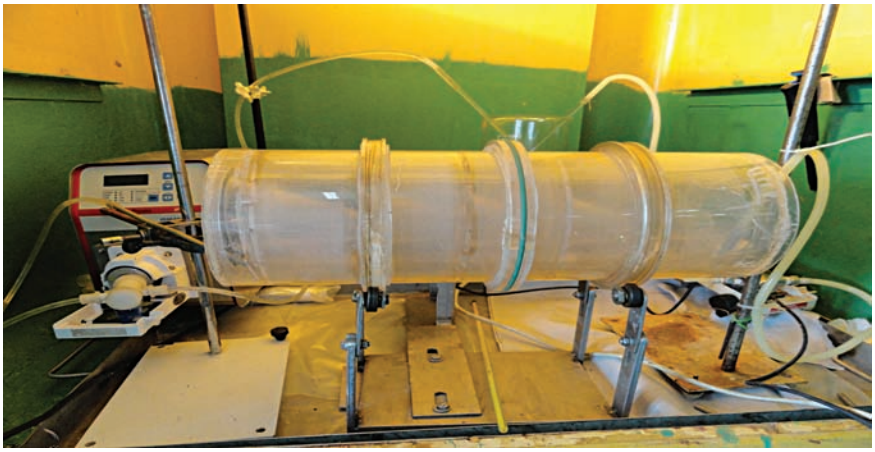

Fig. 1 *Dissolution of UO_2 pellet with simulated clad in nitric acid in the prototype rotary dissolver*

Though the equipment is simple in design and operation, various parameters affect the optimization of the system. They are optimum cone angle, stage length, stage volume, feeding and discharge of fuel pin bits as well as nitric acid, effective handling of off-gases and nitric acid fumes, operation and maintenance of the dissolver drive as well as supporting rolling mechanism, material of construction for the dissolver and supporting structure. A set of prototype models were developed, starting from 150 to 660 mm ID for the purpose of determining the effect of these parameters as well as to optimize the design to plant scale. It should be noted that while design of physical parameters is crucial, the kinetics of dissolution of spent fuel in the continuous dissolver also plays a vital role in the design. For validation, a set of experiments were carried out to study the effect of tumbling on the dissolution rate and kinetics of dissolution. Unirradiated UO_2 pellets equivalent to PHWR fuel were dissolved in a prototype continuous dissolver system at various temperatures from 333 to 363 K in 8 N HNO_3. Figure 1 shows the experimental set up for the dissolution studies. During the dissolution, inter pellet collisions were observed to play a significant role in enhancing the dissolution in the continuous dissolver system.

IV.13 Development of Robotic Sampling System for the analytical cell of Demonstration FBR Fuel Reprocessing Plant (DFRP)

Automated sampling and analysis of process solution in FBR fuel reprocessing plants is a step towards plant automation from unit level automation. An attempt has been made to develop a remote sampling system for DFRP analytical cell shown in Figure 1. Manufacture, assembly and testing of robotic sampling system has been completed and the system has been installed in the mock-up facility of remote handling section for rigorous trials before it is qualified for installation in DFRP. The entire sampling system is made in many modules which enable easy maintenance of various modules using master slave manupulators (MSM) and in-cell crane remotely.

The DFRP analytical cell has two compartments namely, upper and lower for sampling and analysis of process solutions respectively. The analytical cell is vertically mirrored side by side and the automation covers the whole cell. Of the sixty sampling points provided in the sampling cell to collect samples from various process pipe lines, twenty are accessible to both master slave manupulators as well as sample handling robot and the remaining only to sample handling robot. Most of the cell volume is occupied by the sampling lines from various process pipelines into the sampling cell posing one of the prime constraints.

The robotic sampling system consists of modules namely, sample handling robot (Figure 2), capping / decapping robot (CDR) and pipette robot (PPR). A Cartesian configuration has been chosen for

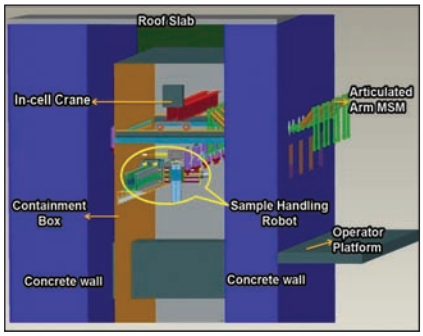

Fig. 1 *CAD model of analytical cell*

Fig. 2 *Photograph of sample handling robot installed in mock-up facility*

the sample handling robot with X, Y, and Z axes to cover 6000 x 700 x 400 mm. Additionally, a rotational axis (θ about Z-axis) with two redundant Y-axes are attached to θ-axis, which gives extended reach along Y-axis as well as precise motion to reach the target position with two grippers. The X-axis rail, a critical component of the sample handling robot is a long translation stage with double rails supported on custom-designed girders made of SS 304 for rigidity and precise motion. Counterweights are provided to offset the cantilever effects of Y-axis translation stage with two grippers.

Salient design feature of the sample handling robot is that remote assembly and disassembly is possible for maintenance of all axes using the in-cell crane and master slave manupulators provided in the sampling cell. The gripper can handle a payload of 50 N. The function of sample handling robot is to collect empty sample bottle from the user-defined location on the storage rack kept inside the cell and transport it to the pre-defined sampling station and collect samples and replace in the user defined storage location. The sample is collected by piercing the bottle using the forward Z-axis travel and retrieval by reverse travel of Z-axis. The sampled bottle can subsequently be transported to the analytical cell by using in-cell crane facility as and when required.

Challenges in the development of sample handling robot

Sample handling robot plays the major role since it has to cover all the 60 sampling stations in the cluttered environment, where the process pipelines and vent pot are present. Despite the precaution taken in design, choice of material, electrical actuators and other associated hardware, the working environment in the cell warrants remote maintenance for the whole system since the components need to function in a highly radioactive environment in the presence of acid fumes.

Stepper motors are chosen in place of servo motors for all the axes to avoid feedback devices. Stepper motors are superior in open loop control and are simple for control and operation. However, it may fail in the long run due to the environment. Hence, all the actuators are attached to the

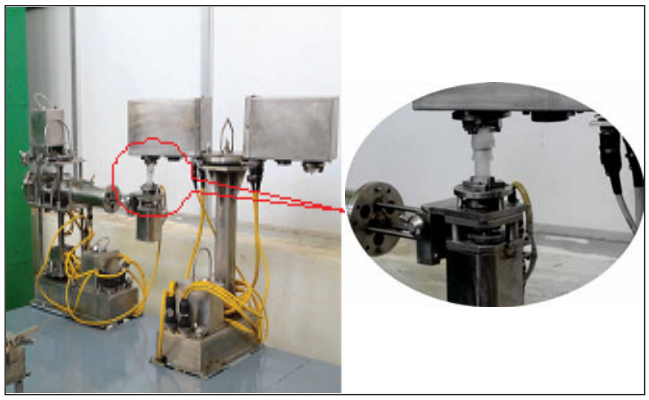

Fig. 3 *Photograph showing capper / de-capper*

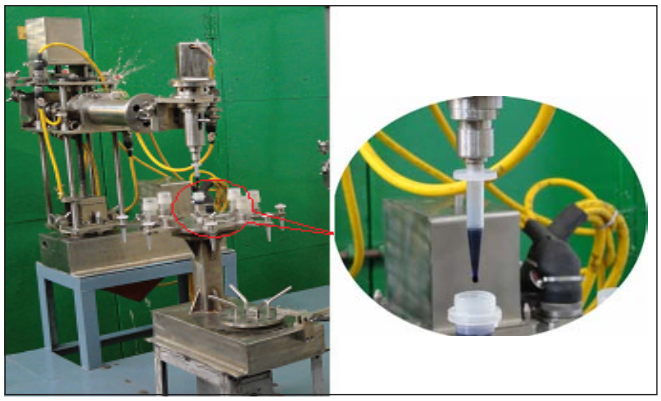

Fig. 4 *Photograph showing pipette robot in action*

respective mechanisms as modules which can be remotely removed and replaced along with its electrical connectors. To maintain modularity for all the actuators, as high as six interface connectors are provided. This has posed another challenge of remotely aligning the electrical connectors without exerting load on to the mating connector. All the stepper motors have been tested successfully after doing mock-up remote assembly.

Use of limit switches was inevitable to initialize the system and monitor its travel. It is achieved by using the hermetically sealed limit switches enclosed in a separate module which can be remotely removed and replaced using master slave manupulators along with its electrical connectors without losing its connectivity.

All the load bearing surfaces which are subject to wear and tear are made of SS410 with hard chrome plating. All the cables used inside the cell are radiation resistant. The connectors used inside the cell are made of SS304 and are of push/pull type for remote operation. Cable drag chain is of radiation tolerant and fire retardant type.

Lower compartment of the analytical cell is the region, where analytical operations such as collecting sample (100-1500 µl) and dispensing it in analytical stations, cleaning and disposing of waste are carried out. These operations are done by CDR and PPR with the assistance of master slave manupulators. CDR (Figure 3) is a cylindrical robot made in two major modules namely bottle handling module and cap handling module. Bottle handling module assists in transporting the filled sample to capping / decapping module. Cap handling module has two identical cap handling units placed 180° apart, facilitating dual purpose of reduced cycle time and redundancy. Each cap handling unit is capable of handling both inner and outer caps.

The pipette robot is also a cylindrical robot (Figure 4) similar to bottle handling module of capping / decapping robot with the pipette head attached to it in place of bottle gripper. Payload capacity of Pipette Robot at fully extended condition is 20 N. Both capping / decapping robot and pipette robot have a base rotation (θ) of ± 330°, vertical (z) travel of 0 - 200 mm, radial (r) travel of 150 mm and pipetting range of 100 to 1500 µl.

The complete sampling system is controlled by PLC based system. Dedicated application-specific software has been developed with complete security features having three layer administrative privilege and system operation/configuration rights and safety interlocks. Status monitoring and control screen has been provided to monitor the erroneous operations/operator violations which are simultaneously logged in the database for review. The sampling operations can be executed through human machine interface (HMI). The operations have lead-through teaching facility as well as auto mode execution, where provision is made to ensure execution of instruction only on receiving operator's acknowledgment. This feature facilitates the operator to correct any over shoot or under shoot during sampling. Each operation and sample movements are logged on to the back-end database which can be used later for analysis, report generation, etc.

Tests

Preliminary mock-up trials have shown that the accuracy and repeatability of the system is well within the design limits. Trials on the sampling operation, pipetting, capping/decapping and remote assembly/disassembly of the modules of the system are underway and this exercise would be highly beneficial in making such systems for Fast reactor fuel cycle facility.

IV.14 Assay of Plutonium in Waste Drum Based on Passive Neutron Counting Technique

Assay of plutonium in drums containing solid waste generated from the reprocessing plant is carried out using neutron counting technique. Since the surface dose of the drum is high, gamma spectrometry cannot be used. Solid wastes from the reprocessing plant typically contain ^{238}Pu, ^{239}Pu, ^{240}Pu, ^{241}Pu and ^{242}Pu isotopes. The emission rate of spontaneous fission neutrons is high for even-even isotopes of plutonium, namely ^{238}Pu, ^{240}Pu and ^{242}Pu. Passive neutron assay systems correlate the neutrons emitted in any sample owing to spontaneous fission of the even-even plutonium isotopes to the amount of plutonium present by utilizing the isotopic composition of the sample. Interference of ^{242}Cm is not observed because its presence is insignificant due to the very short half life of 185 days. The neutron emission rate due to spontaneous fission of Pu is given in Table 1. The system consists of eight ^{3}He detectors embedded in HDPE moderating medium to ensure adequate thermalization of the neutrons. The detectors are arranged in a semi-circular shape which encircles half of the drum containing the waste to be assayed. Figure 1 gives a view of the system and Figure 2 shows the schematic arrangement of the detectors. Output of the detectors is received in two channels which comprise 4 detectors each. In order to use the system in the reasonably high gamma field, 25 mm lead sheet is placed in the front side of the detector. All the detectors are identical with an active length of 900 mm and diameter of 50 mm. They are filled with the gaseous mixture 75% ^{3}He and 25% Kr at 3 bar pressure. Each detector has a sensitivity of 130 cps/nv and a gamma tolerance of about 5 mSv/h.

Table 1: Neutron emission from Pu isotopes

Nuclide	Neutrons emitted/g of Pu
^{238}Pu	2.590×10^{3}
^{240}Pu	1.020×10^{3}
^{242}Pu	1.720×10^{3}
^{242}Cm	2.10×10^{7}
^{244}Cm	1.08×10^{7}

Table 2: Effect of matrix on the counts obtained

Matrix	Counts/1000 seconds
Bare drum (air)	2594 ± 60
Surgical gloves	2617 ± 94
Shoe covers	2854 ±136
Metals	2929 ± 345

Calibration of the system was carried out by keeping a plutonium source (product from the campaigns) of known weight and isotopic composition at the centre of the drum. The counting time interval was fixed as 1000 seconds and the count values were recorded. In view of the nature of the intended application – assay of solid waste – the total plutonium quantity was varied from 70 milli gram to 5 gram.

The calibration graph obtained is shown in Figure 3. The graph reveals linear response in the range used and hence, Figure 3 can be used as the calibration graph for Pu in the waste. Since the solid waste to be assayed is expected to be either metallic (SS pieces, equipment, etc.) or non-metallic (papers, shoe covers, neoprene gauntlets and surgical gloves) components, the effect of the matrix on the counts obtained using a 1 g standard plutonium source was investigated. The results listed

Fig. 1 Drum monitoring system

Fig. 2 Detector arrangement

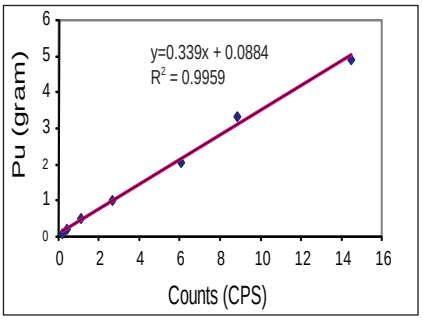

Fig. 3 Calibration curve for different quantities of Pu

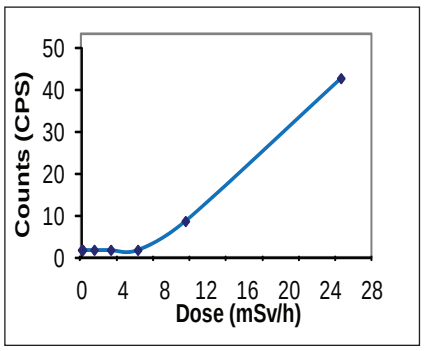

Fig. 4 *Effect of γ radiation on the counts*

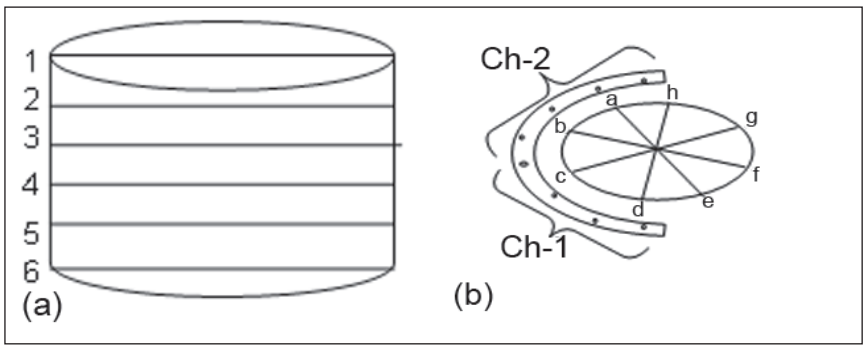

Fig. 5 *(a) Vertical divisions and (b) Radial divisions*

in Table 2 were used as reference for the quantification of plutonium in different waste matrices.

As ^{3}He detectors cannot operate at high gamma field, the effect of external gamma radiation was determined using a ^{137}Cs source (up to 5.4 mSv/h) and a ^{60}Co source (> 5 mSv/h) along with the 1 g standard plutonium source for measuring the counts on surgical gloves as the matrix. The dose at the surface of the system facing the drum was recorded using a wide range area gamma monitor. The effect of external gamma radiation on the measurement shown in Figure 4 indicates that there is no significant increase in the counts up to 5.4 mSv/h. This value may go up since the actual waste contains mainly ^{137}Cs and not ^{60}Co and they have different energies.

It is expected that the distribution of plutonium and other nuclides in the wastes would not be homogeneous and hence, the error due to this effect has to be determined. The method used to determine the error is as follows: plutonium (1 g) in a waste bag was used as the source for determining the error. The waste drum was divided into six segments (denoted as segment 1, 2,....,6) along the vertical axis as shown in Figure 5a and into eight zones along the circumference as shown in Figure 5b. The sample was positioned at different heights in each zone e.g. at positions a1, a2,...,a6 as well as b1 ,c1, d1,.....,f6, g6, h6 so that all possible locations within the drum were covered. The sample was also positioned along the centre line of the drum. In each case, the sample was counted thrice for a time period of 1000 second each time. Overall average value was calculated from the counts obtained from the above said positions and the percentage of error was computed based on the average value. The waste drum is capable of being rotated around its axis. The drum was rotated and counted at 0º (no rotation), 45º (8 rotations; 1 set of value), 90º (4 rotations; 2 sets of value) and 180º (2 rotations; 4 sets of value) and the calculated error

Table 3: Overall error estimated for different positions of the drum

Position	Range of error (#Set of values and hence no range)			
	0º	45º	90º	180º
1	(-) 52 to +39	-10 #	(-) 12 to (-8)	(-) 17 to (-) 5
2	(-) 48 to +47	-1 #	(-) 3 to +1	(-) 7 to +6
3	(-) 43 to +68	11 #	+12 to +11	+8 to +13
4	(-) 39 to +66	12 #	+12 to +13	+10 to +15
5	(-) 40 to +60	5 #	+7 to+ 3	0 to +10
6	(-) 51 to +15	-18 #	(-) 19 to (-)17	(-) 20 to (-) 16
Overall error	(-) 52 to 68	(-) 18 to 12	(-) 19 to 13	(-) 20 to 15

Table 4: Assay of waste bags (*Estimated from individual bag measurements; #Drum with all the bags)

Nature of the waste	Bags	Surface dose (mSv/h)	Estimated Pu/g
Booting and PVC hose	13	35	6.25* (10.24)#
Booting and PVC hose	20	26	10.1* (13.18)#
Metal waste	26	23	8.46* (9.98)#

is given in Table 3. From these data it is evident that 180º rotation of the drum is sufficient since the error did not reduce drastically beyond this.

Waste bags from plutonium reconversion step were analysed by this system and the data accrued are given in Table 4. From these data it is confirmed that when the β,γ activity on the surface of the drum exceeds 23 mSv/h, the total quantity of plutonium in the individual bags differ from the amount of plutonium estimated when the drum is filled with all the bags. Hence, it is concluded that assay can be possible only up to 20 mSv/h dose rate at the surface of the drum. The minimum detectable limit was found to be 35 mg plutonium (FBTR Mark I carbide grade).

IV.15 Thermo-physical Characterization of Simulated Glass, Ceramic and Glass-Ceramic Waste Forms

Glass, ceramic and glass-ceramic matrices are under development as radwaste disposal matrices. For example, iron phosphate glass, synroc and monazite are being investigated as candidate materials for the immobilization of high-level radioactive waste (HLW) from aqueous reprocessing, and glass bonded sodalite and chlorapatite (both glass-ceramics) for the high-level radioactive waste from pyrometallurgical reprocessing of irradiated nuclear fuels. In all cases, the strategy is to synthesize the waste forms in the laboratory using a simulated waste composition, and study their physico-chemical properties. Table 1 shows a typical fast reactor high-level radioactive waste simulated for these experiments. The long-term performance of the fabricated waste forms are dictated by several critical parameters such as the thermophysical properties of the materials. The results of enthalpy increment and heat capacity measurements on some simulated waste forms, viz., iron phosphate glass (IPG), monazite and barium chlorapatite are discussed in this work.

Heat capacity measurements were carried out on iron phosphate glass and its waste form using differential scanning calorimeter in the temperature of 320 to 700 K. The molar heat capacity data of iron phosphate glass waste form are found to be similar to that of iron phosphate glass. From the heat capacity data, enthalpy increment of iron phosphate glass and its waste form were evaluated. Enthalpy increment data were experimentally determined by using a home built drop calorimeter of the isoperibol type. Synthetic sapphire was used as the reference standard. In a typical measurement, the sample or the reference was placed in a furnace and equilibrated at the desired temperature and then dropped into the calorimeter vessel maintained at 298 K. The change in temperature as a function of time was continuously monitored using thermopile detector and the signal logged into the computer. From the area under these curves for the standard and sample and using the enthalpy increment data for the reference standard, the enthalpy increment of the sample was derived. At each temperature, standard and sample were dropped alternatively several times and the average value of the area was used for the calculation. Experimentally determined enthalpy increment data showed excellent agreement with the evaluated enthalpy increment data (Figure 1). The

Table 1: Simulated high-level radioactive waste composition from FBTR fuel

HLW Oxide	Wt.%	HLW Oxide	Wt.%
Ag_2O	0.73	TiO_2	0.10
BaO	3.75	NiO	0.77
CdO	0.33	Fe_2O_3	2.78
Ce_2O_3	6.27	Eu_2O_3 (Eu+Am)	1.54
Cs_2O	10.41	Gd_2O_3 (Gd+Pm+ Np+Cm)	0.84
Cr_2O_3	0.38	Nd_2O_3	9.66
La_2O_3	3.42	PdO	6.86
MoO_3 (Mo+Tc)	14.73	Pr_6O_{11}	3.45
MnO_2	0.15	Rh_2O_3	2.99
Rb_2O	0.49	RuO_2	9.97
SnO_2	0.41	Sm_2O_3	2.73
SrO	1.19	TeO_2	1.38
ZrO_2	8.49	Y_2O_3	0.73
U_3O_8 (U+Pu)	5.47		
Total		100.00	

measurements thus indicate that the thermal behaviour of iron phosphate glass is not altered by the presence of 20 wt. % simulated fast reactor waste.

Monazite, a mixed rare-earth orthophosphate, is a natural mineral known to exist for billions of years. It possesses excellent chemical and radiation stability. The advantage of monazite as the ceramic host is that it is single phase and accommodates all the elements of the high-level radioactive waste in its crystal lattice. It is particularly suitable for rare-earths and actinide wastes which constitute a major portion of the HLW. The enthalpy increments were measured in the temperature range 373 to 1023 K using the drop calorimeter. The enthalpy increments of $CePO_4$ and $CePO_4$ with 10 wt.% simulated high-level radioactive waste are given in Figure 2 and it can be seen that the enthalpy of the simulated waste loaded $CePO_4$ and bare $CePO_4$ are nearly the same. The enthalpy data on $CePO_4$ also agree very well with the data reported in the literature. The experimental data for $CePO_4$ and $CePO_4$ with 10 wt.% simulated high-level radioactive waste could be fitted to the equations given in the Table 2.

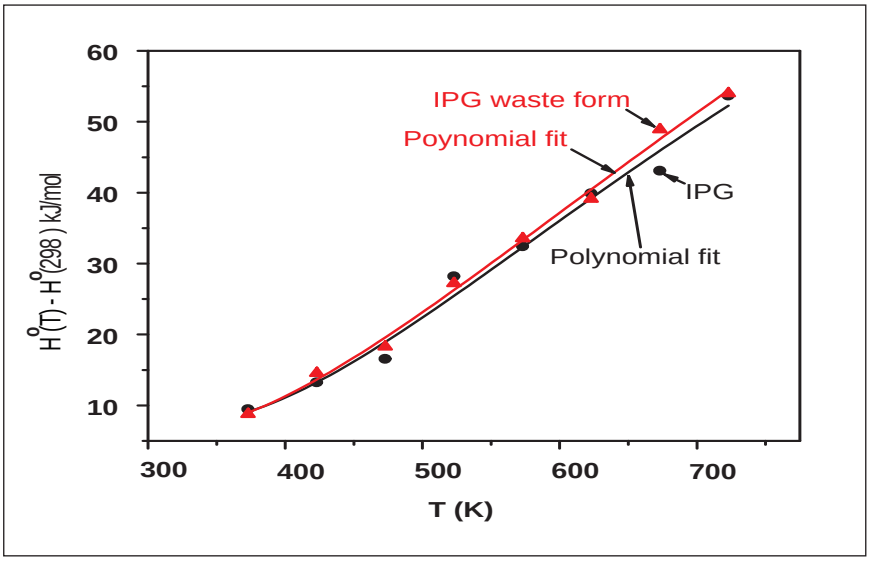

Fig. 1 *Enthalpy increment data of iron phosphate glass and it's waste form*

Table 2: Fitting data				
Composition	$H^o_T - H^o_{298} = -A+BT+CT^2+D/T$ (T=298-1023K)			
	A	B	C	D
$CePO_4$	56.10	1.23×10^{-1}	1.23×10^{-1}	5.04×10^{3}
$CePO_4$ with 10 wt.% simulated HLW	54.62	1.20×10^{-1}	2×10^{-5}	5.16×10^{3}

Alkali metal chlorapatites are candidate matrices for the chloride-containing high-level radioactive waste from pyrometallurgical reprocessing. They are natural minerals, and can immobilize halides and important radioactive elements such as Sr, Cs, and Tc in the crystal structure. The waste form efficacy can be improved by converting the ceramic material into a glass-ceramic by bonding with a suitable glass formulation. Figure 3 shows the results of C_p measurements (by differential scanning calorimetry) on barium chlorapatite and a related composition containing some cesium at the barium site.

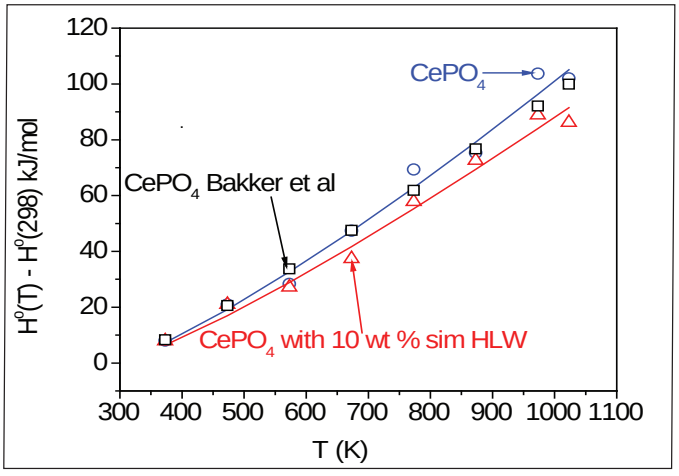

Fig. 2 *Enthalpy of $CePO_4$ and $CePO_4$ with 10 wt.% simulated HLW*

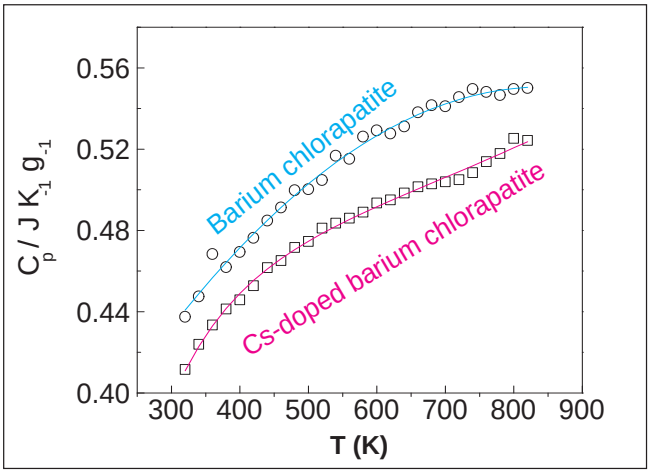

Fig. 3 *Heat capacity data of barium chlorapatite and Cs-doped barium chlorapatite*

IV.16 Solidus and Liquidus Measurements on U-Zr System

The solidus temperature of U-Pu-Zr alloy - fuel for fast reactor, is an important input parameter for the fuel design in order to estimate the maximum operating temperature. Experimental determination of the solidus temperature is often rendered difficult owing to the chemical incompatibility of the molten alloy and the container material. Hence, an experimental system based on thermo-optometry, viz., the "spot technique", has been developed in-house, vis-à-vis techniques for the fabrication of chemically compatible ceramic crucibles. A photograph showing this experimental system is presented in Figure 1. The "spot technique" was originally devised by Ackermann and Raugh and has been extended to temperatures below incandescence (1073 K) by the work carried out in our laboratory ("illuminated spot technique"). As part of our experimental endeavour to measure the solidus and liquidus in the relevant sub-binaries of the ternary system U-Pu-Zr, measurements on U-Zr system have been initiated. As a first step, solidus and liquidus in the system U-Zr were redetermined over the entire range of composition.

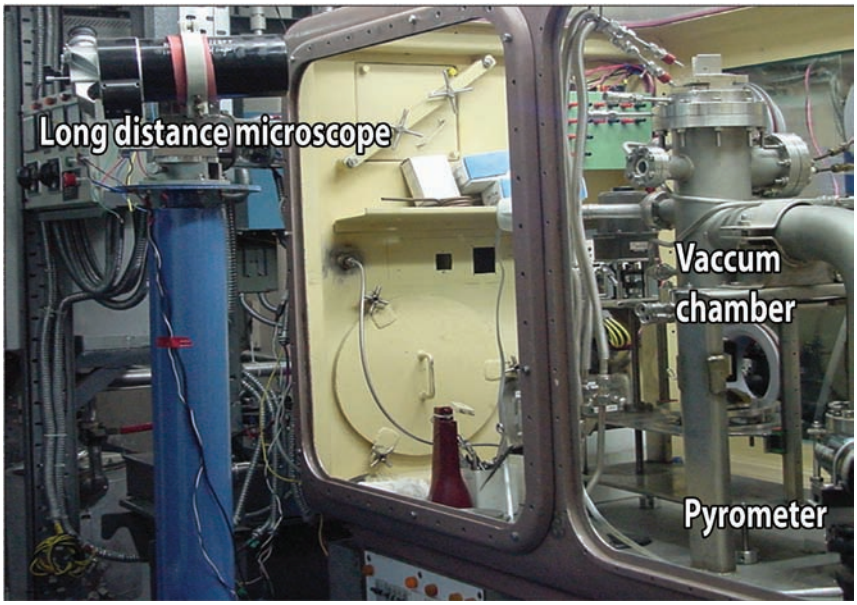

Fig. 1 *Experimental system for "spot-technique" measurement*

Figure 2 is a composite depiction of the experimental data obtained in this study along with the values reported in the literature. The values obtained in the present work are in reasonable agreement with the assessed values. This is the first investigation wherein the solidus and liquidus of the U-Zr system over the entire range of composition has been determined by using a single technique. In order to validate the experimental system as well as procedure, rigorous calibration runs were carried out. The temperature measurement was validated by measuring the melting temperatures of pure gold, copper, nickel, platinum and zirconium. These values agreed well with the reference values within 5 K. Extreme care was taken in the preparation of the alloys by arc melting for preserving the overall composition of the alloys. Alloys that showed difference in weight after the arc melting were rejected. In order to further ascertain the exact chemical composition, an analytical procedure has been evolved.

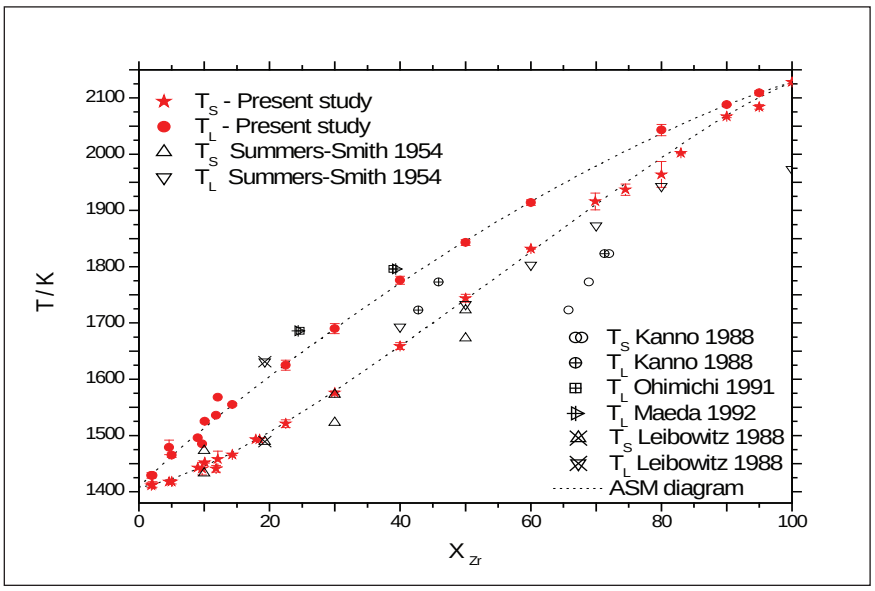

Fig. 2 *Experimental data on solidus and liquidus temperatures – literature and this study on the U-Zr system*

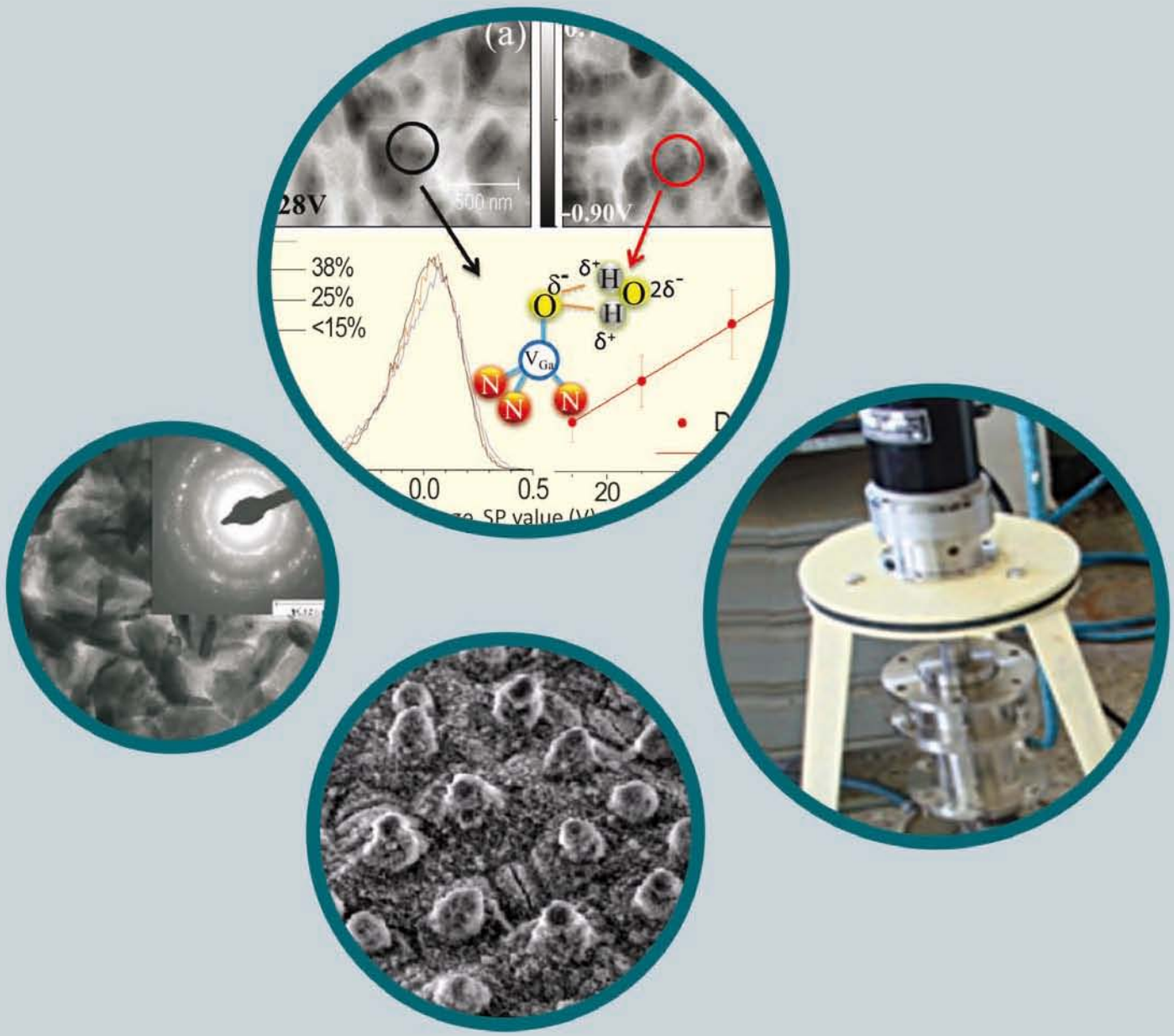

CHAPTER - V

Basic Research

V.1 First Raman Spectrum of Uranium Measured Using a Sub-SERS Technique

Technologically important actinide metals such as uranium and plutonium have not been investigated using Raman spectroscopy due to poor signal intensities.

Here, we report Raman measurement on uranium by a novel SERS(surface enhanced Raman scattering) technique. At ambient conditions uranium has orthorhombic structure with two atoms per primitive cell. Group theoretical considerations show that three Raman active modes (A_g+B_{1g}+B_{3g}) are expected to be present in this α-uranium. Lattice dynamical calculations and inelastic neutron scattering measurements have shown the presence of zone center optical modes at 80, 100 and 120 cm^{-1}, but there are no reports of Raman spectra of uranium in the literature.

Natural uranium metal discs of about 5 mm diameter and 1 mm thickness were used in this study. The discs were ground and polished with emery papers of gradually finer mesh, finally with 1 μm diamond paste. Even though mirror finish was obtained the sample had a large number of surface scratches as could be seen under optical and scanning electron microscopes. A high throughput Renishaw micro-Raman spectrometer (model Invia) was employed to record the spectra using the 514, 785 and 325 nm laser excitations.

Unpolished discs exhibited Raman bands characteristic of UO_2 and oxidized UO_2 at 450 and 580 cm^{-1} respectively (Figure 1a, spectrum (i)) that disappeared upon polishing the metal to a silvery mirror finish (Figure 1a, spectrum (ii)). In the frequency region below 150 cm^{-1} down to 50 cm^{-1}, however, a number of sharp Raman bands characteristic of the rotational modes of N_2 and O_2 are obtained. They are due the molecules from the ambient air adhering to the metal surface. This is in the same wave number region in which uranium Raman bands are expected. Thus it becomes a non-trivial problem to detect the Raman spectra of uranium metal.

A layer of gold was coated on the sample to see if surface enhanced Raman scattering effect could be invoked from the proximity of gold of a few nanometers thickness.

Gold layers of 5 and 15 nm thickness were deposited by pulsed laser deposition and thermal evaporation respectively on two different, polished discs of uranium.

Laser excitation of dark scratch lines and pits on the samples gave rise to Raman spectra expected of uranium metal (Figure 1(a)) spectrum (iii) and (Figure 1(b)). Spectra were recorded at many such points on from both samples. Well resolved Raman bands about 82 (B_{1g}), 108 (A_g) and 126 cm^{-1} (B_{3g}) were obtained. All sharp bands of N_2 and O_2 disappeared, indicating that the adhesion of N_2 and O_2 to gold surface is quite low. Several bands of different uranium oxides such as UO_2 and UO_{2+x} were observed in the extended range of wave numbers up to 800 cm^{-1} (Figure 1a, spectrum (iii)). Laser excitation of smooth golden

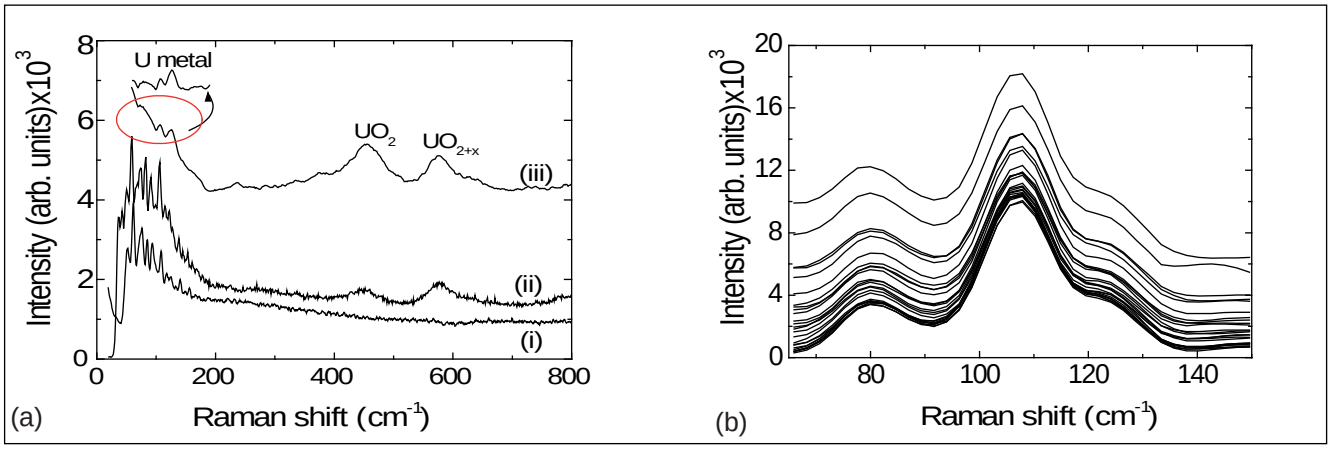

Fig.1 *(a) Raman spectra of uranium discs, (i) Unpolished, (ii) Freshly polished and (iii) 15 nm gold coated; (b) Raman spectra (background subtracted) of uranium disc coated with 5 nm gold film using 785 nm laser excitation*

yellow surface however did not result in uranium spectra.

The current understanding of SERS is that it arises mainly due to the excitation of localized surface plasmons of the sensitive metal (such as gold or silver); when the surface plasmon frequency is in close resonance with the exciting laser frequency, there is a large increase in the local electromagnetic field that polarizes the adsorbed molecules.

Electrical conductivity of uranium is an order of magnitude less than that of gold, but being a good conductor it cannot support surface plasmons of gold. It is envisaged that the thin uranium oxide layer that forms rapidly and naturally on the polished surface before gold coating serves to localize the surface plasmons. This oxide layer is akin to the ~2 nm SiO_2 or Al_2O_3 shell on 55 nm gold particles in the SHINERS (Shell-isolated nanoparticle-enhanced Raman spectroscopy) technique. Sharp edges of gold in the scratch lines act like nanorods with a range of aspect ratios. When these edges are excited by the 514 or 785 nm laser we have a SERS effect that enhances the Raman signal from uranium oxides and the metal itself. This is thus a 'sub-SERS effect' since we are looking at the SERS effect on uranium metal that is under the gold layer. The optical absorption spectrum of gold nanorods has two maxima, one about 520 nm and the other around 700 – 1050 nm for nanorods of different aspect ratios; aspect ratio of about 4 is expected to exhibit a maximum about 785 nm. Hence laser excitation at 514 and 785 nm can be expected to give rise to SERS spectra. 325 nm laser excitation did not result in Raman bands of uranium, consistent with the fact that the absorption spectrum of gold nanorods has no peak around this wavelength. The current technique is simple to implement involving only deposition of a thin film of gold on the surface oxidized metal. It is surmised that sub-SERS effect would be useful to study other metals and materials with low Raman scattering cross section.

V.2 Ultra Low Friction Engineering TiC/a-C-H Composite Coating

Modern engineering applications demand development of hard coatings with improved wear resistance combined with low friction and high toughness attributes. Isotropic nanocomposite coatings of TiC consisting of crystalline phase embedded into an amorphous matrix constitute a multifunctional coating architecture due to its high hardness, fracture toughness, wear resistance and low friction. The increase in carbide content results in a drop of friction coefficient from 0.7 to 0.45, the latter value is typically in the range for TiC coatings.

In the present study, we have synthesized TiC/a-C nanocomposite coatings by CH_4 gas carburization of titanium specimen and investigated their tribological properties with an aim to obtain ultra- low coefficient of friction. Ninety minutes of exposure yielded surface modified over-layers having thicknesses 18, 23 and 43 µm at temperatures of 1323, 1423 and 1523 K,

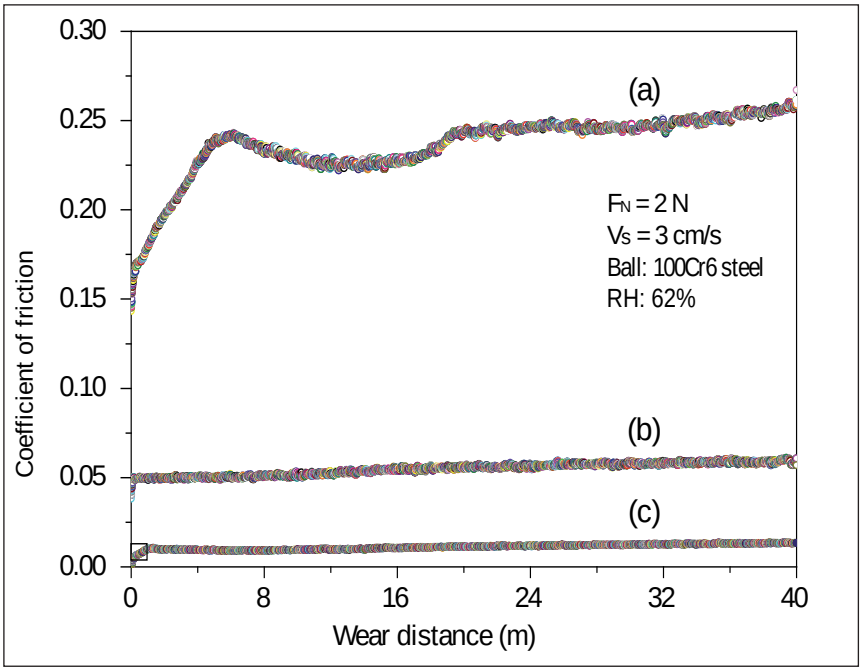

Fig. 1 *Coefficient of friction of coatings synthesized at (a) 1323, (b) 1423 and (c) 1523 K*

respectively. Linear eciprocating mode of tribological tests were performed using a micro-tribometer. A spherical steel ball (100Cr6 SS) of Ø6 mm with a surface roughness of 0.06 µm was used as a sliding body to measure the value of coefficient of friction where normal load and sliding speed were kept constant as 2 N and 3 cm/s, respectively. Tests were performed in ambient (dry and unlubricated) condition with a relative humidity of 62%.

TiC/a-C nanocomposite coatings were characterized by X-ray diffraction. The analysis revealed that at lower synthesis temperature, the Ti concentration is higher compared to ones obtained at higher synthesis temperature.

At low synthesis temperature of 1323 K, the average coefficient of friction is found to be comparatively high (~0.2) and at 1423 K, it is reduced to 0.045 and remains almost steady as shown in curve (a) and (b) of Figure 1. At higher synthesis temperature of 1523 K, the coefficient of friction is found to be extremely low (0.006) and remains stable as seen from the curve (c) of Figure 1.

Micro-hardness measurements on the composite coatings showed a pronounced dependence on TiC crystallinity, morphology and phase composition. The maximum value of hardness corresponding to TiC with crystallite size of 60 nm is observed at synthesis temperature of 1523 K. Hardness decreases with decrease in crystallite size to 58 and 54 nm at 1423 and 1323 K, respectively. Micro-hardness values are found to be 24.4, 20 and 16.5 GPa with wear rate 1.3×10^{-9}, 4.5×10^{-8} and 2×10^{-7} mm^3/Nm at synthesis temperature of 1523, 1423 and 1323 K, respectively. It is known that hardness of graphite is low and it can increase with disordering that result from the network of 3D carbon atoms. In our case, we find that an ordered graphite structure depict high hardness. This may be explained by considering the contribution of embedded crystalline TiC phase into a-C network. The excessive a-C matrix prevents the build up of intercrystalline incoherent strains and reduces the resistance to plastic deformation. At high processing temperature, crystallinity of TiC phase is found to be higher. In addition, at high temperature, coating density is higher and micro- homogeneity of surface is improved. These factors contribute to improvement in wear resistance and fracture toughness. Preponderant graphitic structure with considerably reduced disorder provide enhanced lubricity that allows easy sliding yielding an ultra- low friction regime. A reduced ID/IG ratio in Raman spectra signifies decrease in disorder associated with sp^2- like graphitic phase which brings about such a low friction value. Basically low friction of carbon based composite coatings is postulated to result from either rehybridization, or passivation of dangling σ-bonds formed during sliding. Rehybridization to ordered sp^2- bonding is reasonable because graphite is the thermodynamically stable form of carbon at room temperature and ambient pressure and is lubricious due to its layered lattice architecture. Rehybridization may also involve the formation of lubricious amorphous sp^2- containing carbon. Excess amount of hydrogen present in the coating material prevent the formation of dangling σ-bonds. Residual π- electron and σ-covalent bonds can form the double carbon C=C bonding which has higher bond energy than single C–H bonding. The double bond of C=C causes stronger interaction which yields larger friction. Excess amount of hydrogen present in the material passivates the formation of double C=C bonds. Intercalation of hydrogen and water molecules between the layered lattice structures of graphitic plane can also bring down friction value. In this case, molecules between the layered lattices transform sliding to rolling motion of friction. Ordered structure of graphitic lattice induces higher degree of rolling motion of intercalated molecules. Disorder lattice structures of carbon atoms disrupt the motion of molecules and hence larger dissipation of frictional energy occurs. Higher density of intercalated atoms and molecules can also disrupt the motion due to steric hindrance among each other. Such scenario transforms rolling to sliding motion. Composite coatings having free titanium atoms can have higher adhesive strength. Higher amount of TiC also leads to higher friction. Increased amount of a-C leads to higher hardness and lower dissipation of frictional force whereas a-C:H can have ultra-low friction and improved ductility. This ductility improves the fracture toughness. Hydrogen can passivate the interaction of dangling σ- bonds which leads to surface inertness. If a-C-H is embedded with TiC crystallite, the composite can have higher hardness with enhanced wear resistance properties and in addition, a-C-H environment can provide super low friction regime. Higher amount of free hydrogen in composite materials acts as a reservoir to provide consistent lubricity which otherwise can get eliminated due to repetitive sliding.

V.3 Superconductivity in Ru-Substituted $BaFe_{2-x}Ru_xAs_2$ Single Crystals : Critical Property Investigations

Superconductivity in the Fe based arsenides has been the subject of intense investigation in the last three years. There are several classes of systems in which superconductivity has been observed; of these the two layer systems based on alkaline earth (A) viz. AFe_2As_2 termed 122, compounds are well studied on account of availability of clean single crystals. $BaFe_2As_2$, a prototypical member of the 122 FeAs based layered compounds has a coupled structural (T_S) and antiferromagnetic (T_N) transition at ~140 K. We have demonstrated the occurrence of superconductivity by the isoelectronic Ru substitution at Fe site, in polycrystalline $BaFe_2As_2$ and had indicated a phase diagram. Crystals of Ru doped $BaFe_2As_2$ typically 1x1 mm are shown in left panel of Figure 1. XRD patterns of the powdered crystals show phase pure $BaFe_2As_2$ type structure with tetragonal (I4/mmm) symmetry, without any impurity phases. The lattice parameters, determined from the XRD data show a slight increase of 'a' axis and decrease of 'c' axis with increase in Ru concentrations (right panel of Figure 1). Figure 2 shows the variation of normalized resistivity

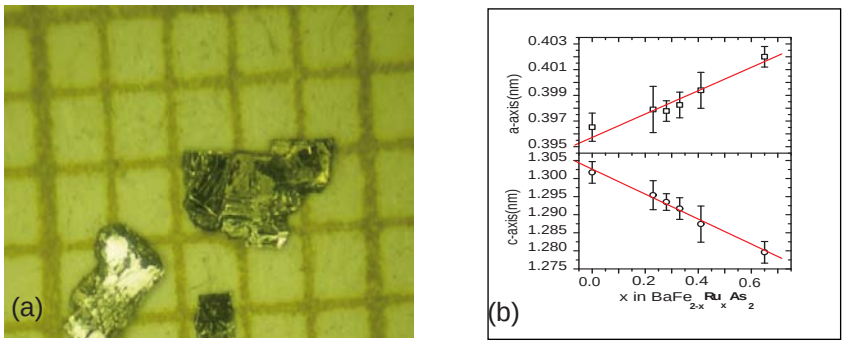

Fig. 1 *(a) Photographs of Ru doped single crystals (b) Variation of a and c lattice parameters with Ru substitution*

with temperature for the Ru doped crystals with different fractions. The pristine sample shows a sudden fall in the resistivity associated with the structural/magnetic transitions at T_S/T_N ~ 139 K. With the increase of Ru concentration T_S/T_N decreases, and the sharp fall in resistivity at T_S/T_N is preceded by a broad hump like feature. For the highest Ru doped sample, resistivity varies monotonically with temperature, showing no anomalies due to these transitions. Figure 3 shows the phase diagram of the $BaFe_{2-x}Ru_xAs_2$ obtained from the resistivity data. The system shows a suppression of the structural (T_S)/magnetic (T_N) transition and evolution of superconducting transition (T_C) with Ru content 'x'. With increasing Ru content, the value of T_S/T_N initially falls roughly by 3-5 K per atomic percentage of Ru. The lower temperature extrapolation of the T_S/T_N curve suggests that ~28% of Ru substitution fully suppresses the T_S/T_N to zero. Superconductivity starts at Ru concentration of around 15% and T_C onset passes through a dome/plateau like region around the regime where structural/ magnetic transitions are suppressed completely. The highest T_C was 20 K for a Ru fraction of x=0.65. The resistivity measurement as a function of temperature was carried out at different magnetic fields in the magnetoresistance cryostat. A systematic shift in the onset temperature seen in Figure 4 was used to estimate the upper critical field, H_{C2}, for H parallel and H perpendicular to c axis. The ratio of

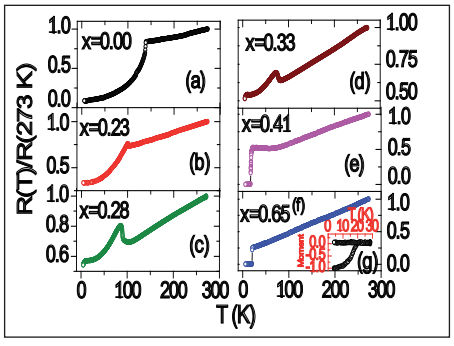

Fig. 2 *(a-f) Variation of resistivity as a function of temperature in $BaFe_{2-x}Ru_xAs_2$ (g) the diamagnetic signal corresponding to (f)*

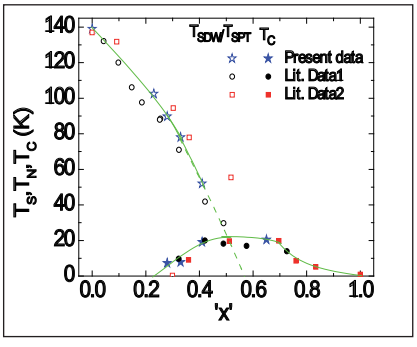

Fig. 3 *Phase diagram $BaFe_{2-x}Ru_xAs_2$; compiled from our work and from literature*

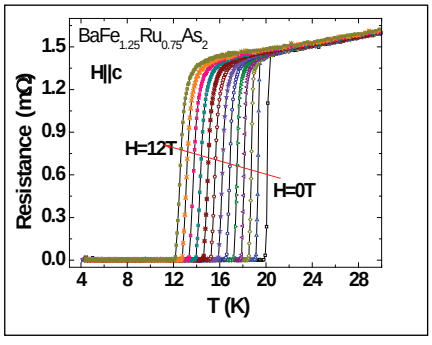

Fig. 4 *The superconducting transitions measured using resistivity as a function of magnetic field*

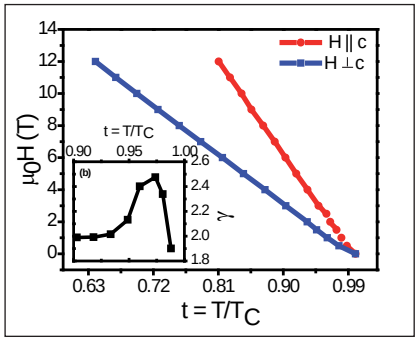

Fig. 5 *T_C onsets for H parallel and perpendicular to C obtained from magnetoresistance data shown in Figure 4*

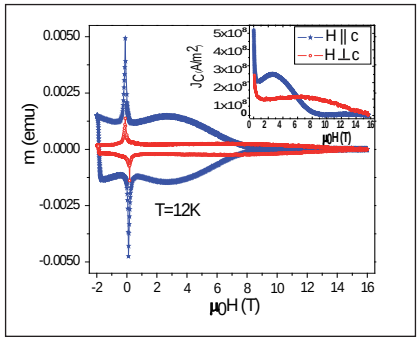

Fig. 6 *Magnetisation loops measured in a $BaFe_{2-x}Ru_xAs_2$ single crystal with x=0.75. The Inset shows the critical current density M versus H graphs*

the upper critical field for H parellel and perpendicular to c-axis was used to estimate the upper critical field anisotropy. A small anisotropy was measureable whose magnitude has a temperature dependence as shown in inset Figure 5. A small peak in the upper critical field is seen close to T_C. We also measured the anisotropy in the critical current density in the superconducting crystals using the magnetization technique. The measurements were carried out in a vibrating sample magneto-meter operating at 1.5 to 300 K range in magnetic fields up to 16 Tesla. A typical magnetization graph is shown in Figure 6 for magnetic field perpendicular and parallel to the c axis in one of the crystals. Large critical current density derived from the M versus H graphs are shown in the inset. A small anisotropy is seen in the critical current density as well.

V.4 TEM Studies of Refinement of Oxide Particle Size and Effect of Displacement Damage on Model Oxide Dispersion Strengthened Alloys

Nano structured ferritic alloys, which are produced by mechanical alloying of the elemental or pre-alloyed metallic powder with yttria oxide powder and consolidated by hot extrusion or hot isostatic pressing derive their strength from the dispersion of thermally stable oxide nanoparticles into the matrix and are enormously promising high temperature alloys for many applications including high energy neutron environment of advanced fission and especially fusion reactors. The nano structured ferritic alloy microstructures and nano structures are remarkably stable and these alloys are very resistant to radiation damage and manage helium by trapping in fine bubbles to suppress void swelling and to protect grain boundaries. There are several studies on oxide dispersion strengthened (ODS) alloys to investigate aspects related to the resultant nano oxide precipitates, their size, distribution, chemical composition etc., and their stability under irradiation conditions. There are no systematic studies on the role of titanium and the associated changes in the microstructure, and its eventual influence on the mechanical properties. In the present investigation, model ODS alloys (Fe-0.3Y_2O_3, Fe-0.3Y_2O_3-0.2Ti and Fe-14Cr-0.3Y_2O_3-0.2Ti) were prepared in the form of a rod by combination of ball milling and hot extrusion at high temperature for studying the effect of titanium and chromium on particle size distribution. Another model ODS alloy Fe + 0.3% yttria has been fabricated by powder metallurgy, including ball milling at 350 rpm for 20 hours in argon atmosphere and subsequent high temperature hipping at 1423 K for two hours.The resulting material, is in the form of

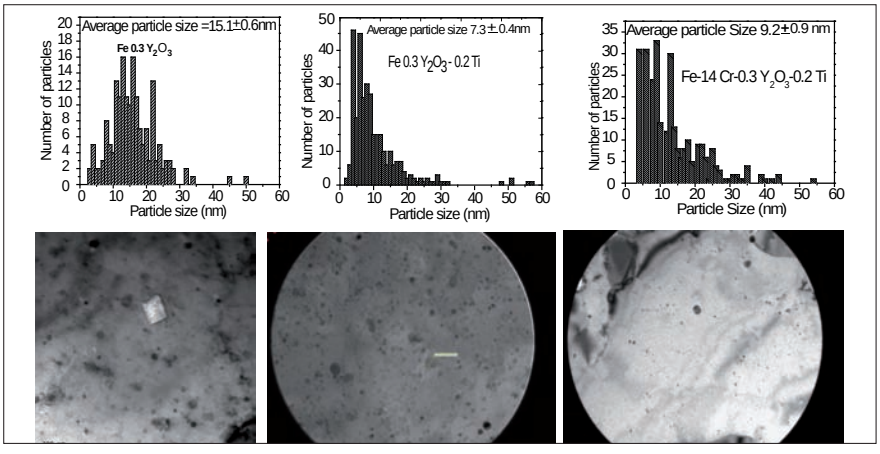

Fig. 1 *The typical microstructure of the as-prepared alloys and the particle size distribution*

a rod and has heterogeneous grain sizes (2 to 100 µm).

The TEM samples were prepared by mechanical thinning, polishing and electropolishing method. The HRTEM imaging was done using the LIBRA 200 electron microscope with the information limit of 0.13 nm. Figure 1 shows the typical microstructure and particle size distribution of alloys Fe-0.3 Y_2O_3, Fe-0.3 Y_2O_3-0.2Ti, and Fe-14Cr-0.3 Y_2O_3-0.2Ti. The average particle size was 15.1, 7.3 and 9.2 nm for alloys Fe-0.3Y_2O_3, Fe-0.3Y_2O_3-0.2Ti and Fe-14Cr-0.3Y_2O_3-0.2Ti respectively. In presence of titanium, a drastic reduction was found in particle size of ODS alloy and chromium addition did not show any significant effect on particle dispersion.

The HRTEM image of one such particle in model Fe-0.3Y_2O_3 alloy is shown in the Figure 2. From the observed d-spacing, the crystal structure of the particle is found to be body centered cubic (bcc). However, the particle is not coherent with iron matrix. The HRTEM imaging of a couple of particles in Fe-14Cr-0.3 Y_2O_3-0.2Ti, indicate the particles to be coherent (Figure 3). From Figure 3, one can observe that the particles are close to each other and they are coherent. The inverse FFT(IFFT) of spot 1 shows the d-spacing of 1.815 A° whereas IFFT of spot 2 shows a d-value of 2.183 A°. Also in

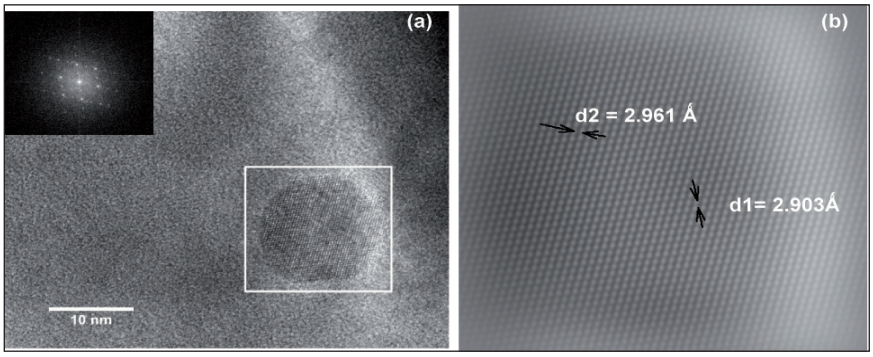

Fig. 2 *(a) The HRTEM image of the alloy iron 0.3 Y_2O_3 and FFT (inset) and (b) IFFT of the selected area of the image. The yttria particle shows bcc in nature*

IFFT (Figure 3), one can see misfit dislocations. When the particles are coherent with the matrix, a misfit strain is created at the interface. The particle seems to be the complex of Y-Ti-O structure.

Model ODS alloy Fe + 0.3% yttria fabricated by ball milling and hipping has been irradiated in the form of 3 mm discs in JANNUS facilities at CEA, Saclay, France using dual beams of 5 MeV Fe^+ and 1.5 MeV He^+ at 873 K. For helium implantation 3 and 3.8 micron thick aluminium degrader foils were used. The helium and iron doses are 2.6 x 10^{16} and 7.6 x 10^{16} ions/cm^2 respectively. In these conditions, from TRIM calculations, the peak damage corresponds to 100 dpa, localized to ~1 µm below the irradiated surface and the damage in the near surface region corresponds to 25 dpa. Pre-thinning from the irradiated surface followed by polishing from back side was used for preparing the TEM samples.The micrographs of as prepared and irradiated samples are given in Figure 4. The as prepared sample contains a majority of fine (3 nm) yttria particles, although larger (20 nm) particles are also found. Density of small particles seems to be independent of grain sizes. Observations of these foils also show that dislocation density is very low (< 10^{12} m^{-3}), both before and after ion irradiation.

From Figure 4 we observe that fine (3 nm) and large (20 nm) particles are stable under irradiation at 873 K upto 25 dpa. Further at 25 dpa, the big particles (>20 nm) were spherical in shape whereas at 80 dpa, big particles appeared as ellipsoidal or shapeless thus confirming the particle dissolution at 80 dpa. The TEM micrographs of the samples have been analyzed using ImageJ software to get the particle size distribution. The average yttria particle size is found to be 3.1, 3.5 and 9.7 nm respectively for the as prepared sample, samples under the irradiation condition of 25 and 80 dpa. From the histograms we see that at 80 dpa the size dispersion of particles is higher as compared to the

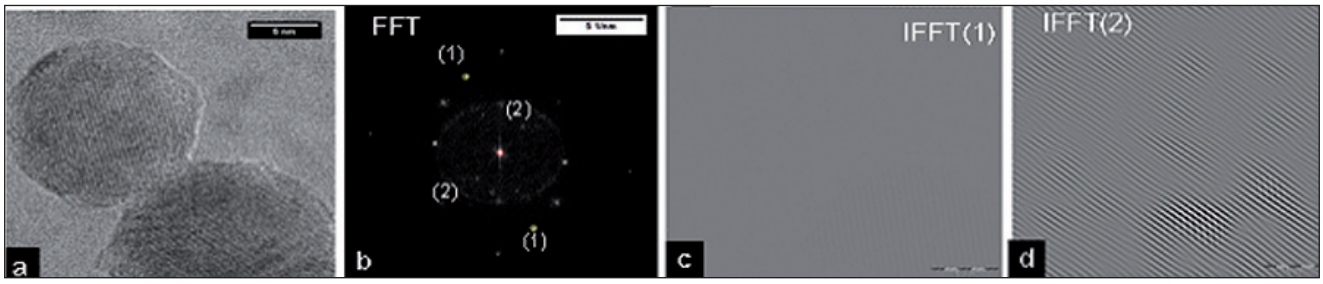

Fig. 3 *(a) HRTEM image of particles in alloy Fe-14Cr 0.3 Y_2O_3-0.2 Ti , (b) FFT from selected area, (c) FFT with filtered spots and (d) Inverse FFT image showing lattice coherency between particle and matrix*

particles present in as prepared and 25 dpa samples. This clearly indicated that yttria particles in our model ODS alloy are unstable and particle size increases with dose. However, in earlier reports, a decrease in particle size with dose has been observed at 873 K in a 9Cr–ODS steel. This contrasting behaviour could be due to (i) the larger partcle size of yttria (12 nm) and (ii) also the other alloying elements in the 9Cr-ODS steel .

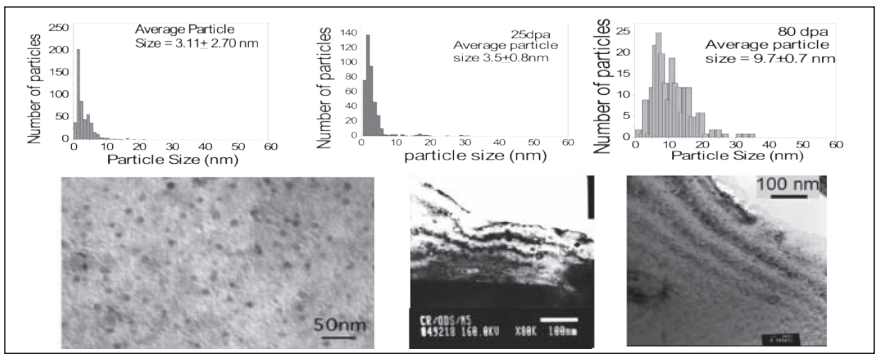

Fig. 4 The typical microstructure of the as-prepared model ODS alloy (Fe 0.3 Y_2O_3), sample irradiated upto 80 dpa and 25 dpa and their particle size distribution

V.5 Optimization of Yttria Content in 9Cr-ODS Steel Clad Tube for Enhanced Creep Rupture Strength

Yttria content plays an important role in the creep deformation and rupture behaviour of 9Cr-ODS steel. 9Cr-2W-Y_2O_3 ODS steel clad tubes of 6.6 mm outer diameter and 0.45 mm thickness having 0.27 and 0.34 wt.% yttria content have been produced. A complex powder metallurgy route followed by hot and cold mechanical processing was adopted to produce the clad tube. Pre-alloyed powders of the steel and yttria were mixed in a high energy simoloyer type of mill in argon atmosphere. The mixed powder was canned in mild steel can, degassed and sealed. The sealed cans were upset at high temperature to compact the powder into billet. The billet was hot extruded to produce rod. Mother tube was prepared by drilling the extruded rod. Clad tubes were produced by cold drawing (pilgering) the mother tube. The clad tubes were finally subjected to normalizing at 1338 K for two minutes and tempering at 1038 K for one hour heat treatments in inert atmosphere. Tensile tests have been carried on the steels over a wide temperature range at a nominal strain rate of $3x10^{-3}$ s^{-1}. Creep tests at 973 K and over a stress range of 100-175 MPa have been carried out on the steels. The addition of yttria increased the tensile strength of the ferritic steel significantly (Figure 1a). The increase in yttria content from 0.27 to 0.34 wt.% further increased the tensile strength. The creep deformation rate of the steel decreased by two order of magnitude with the increase in yttria content from 0.27 to 0.34 wt.%. Creep rupture strength of the steel improved significantly with the increase in yttria content (Figure 1b). Long-term creep rupture strength of the 9Cr-ODS clad tube having 0.34 wt.% of yttria is comparable to that of the alloy D9 clad tube.

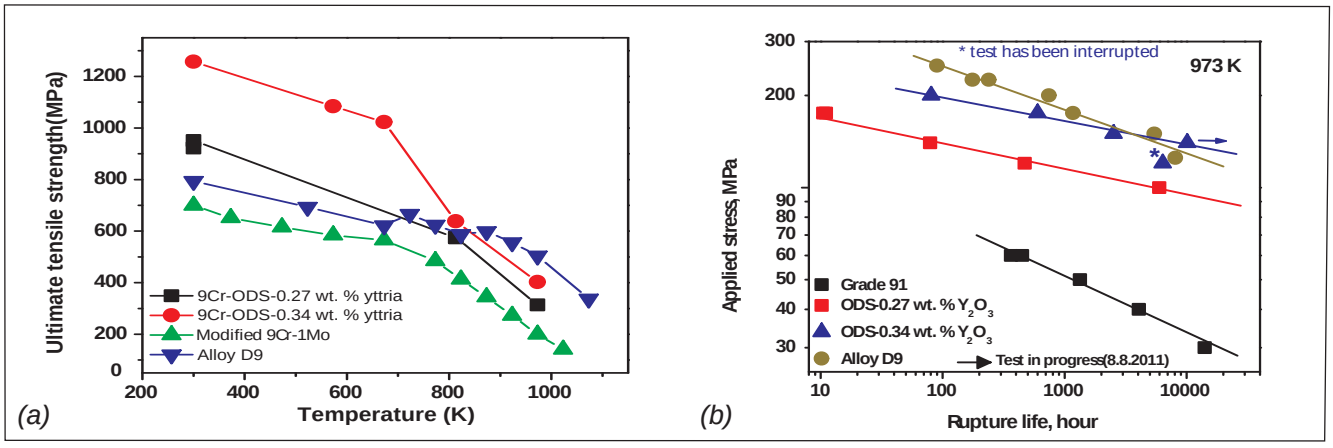

Fig. 1 (a) Effect of yttria on tensile strength of 9Cr-ODS steel at different temperature (b) Effect of yttria on creep rupture strength of 9Cr-ODS steel at different temperature

V.6 Role of Composition on Long Term Microstructures in 9Cr Reduced Activation Ferritic Martensitic Steel

Optimisation of chemical composition of reduced activation ferritic – martensitic steels (RAFM) is necessary for achieving the required strength and toughness. Accordingly, 9Cr-W-Ta-0.2V-0.1C steels, with W and Ta concentrations varying respectively from 1 to 2% and 0.06 to 0.14% have been produced for which detailed evaluation of various physical and mechanical properties and correlation to microstructural changes have been carried out.

The normalized and tempered steels consist of a tempered martensite microstructure, with a decoration of coarse interlath $M_{23}C_6$ and fine intralath MX precipitates. (Figure 1). Increase in W and Ta concentration resulted in a reduction of prior austenite grain size. This is attributed to the presence of undissolved primary carbides whose number density and size increased with W and Ta concentration. Also, W/Fe ratio of $M_{23}C_6$ carbides increased, with W concentration, but Cr/Fe ratio did not show a significant change, suggesting the substitution of Fe by W in $M_{23}C_6$.9Cr-1W-0.06Ta-0.1C steel subjected to long term aging in the temperature regime 773-873 K showed the following features.

- Retention of lath structure with no significant coarsening of precipitates at 773 K upto 5000 hours
- Partial recrystallisation of the lath structure beyond 2000 h at 823 and 873 K (Figure 2).
- Increase in Cr/Fe ratio of $M_{23}C_6$ precipitates with aging time and temperature, with slow coarsening kinetics due to the presence of W.
- Absence of the deleterious Laves phase at these temperatures suggesting its delayed kinetics due to the presence of W.

Increase in W from 1 to 1.4 or 2%, was beneficial to retain the lath structure for longer durations (Figure 2), and no significant coarsening of $M_{23}C_6$ or MX precipitates was observed.

However, creep exposures produced significant substructural changes, which were also dependant upon the W and Ta contents. Extensive subgrain formation (Figure 3) was observed and the subgrain size increased from 0.65 to 0.95 mm with increase in W from 1 to 1.4%, while it decreased to about 0.86 mm for 2W steel, due to the effective pinning of lath boundaries by $M_{23}C_6$ carbides and the slow recovery of martensitic substructure by the fine MX precipitates. This was also reflected in the higher rupture time of this steel. However, the effect of Ta on subgrain size was less pronounced. Increase in Ta to 0.14% resulted in a shorter rupture time, which is attributed to the presence of coarse primary carbides in the initial microstructure. The role of W and Ta on the microstructure can be summarised as follows:

- Increase in the number density of primary carbides.
- Reduction in the prior austenite grain size.
- Reduced coarsening kinetics of $M_{23}C_6$ carbides, which is accelerated by stress.
- Higher influence of W on subgrain evolution during creep deformation than Ta.

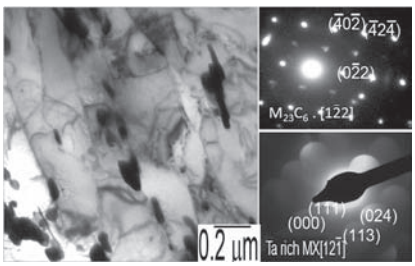

Fig. 1 *Tempered martensitic structure in normalized and tempered 9Cr-1.4W-0.06Ta RAFM steel with coarse interlath $M_{23}C_6$ (arrow marked) and fine intralath MX precipitates (circled)*

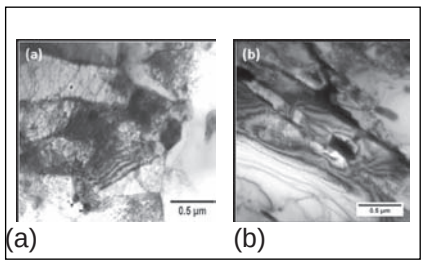

Fig. 2 *(a) Partial recrystallization in 1W-0.06Ta steel (b) retention of lath structure in 2W-0.06Ta steel at 823 K after 2000 and 5978 h respectively*

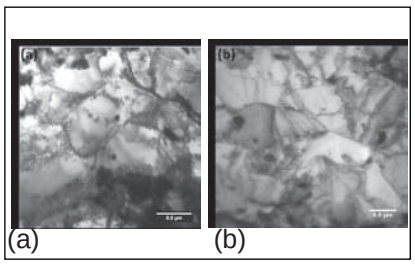

Fig. 3 *Extensive subgrain formation after creep testing at 823 K at 220 MPa in (a) 9Cr-2W-0.06Ta and (b) 9Cr-1W-0.14Ta steels*

V.7 Ferrofluid Seal Development for Sodium Pumps

The centrifugal sodium pumps of PFBR are sealed from the atmosphere by means of triple mechanical seals. These seals are cooled by circulating oil, which is pumped through the seals via dedicated oil circuits. There is some possibility of this oil getting leaked into the reactor and therefore from point of view of improved operation and also for removing fire hazard it is proposed to eliminate the oil circuit completely. One of the options to eliminate the oil based cooling is to deploy ferrofluid seals in combination with magnetic bearings. In view of this, development activities on ferrofluid seal have been initiated. Initially preliminary testing of ferrofluid seal was carried out with 8 mm diameter shaft which gave satisfactory results. Based on the experience in this testing a ferrofluid seal having 25 mm diameter shaft was fabricated. The test results for this seal are presented below.

Ferrofluid seal comprises of ferrofluid (colloidal solution of magnetically suspended particles) which is filled between a magnetically permeable shaft/shaft sleeve and stationary pole piece. Permanent magnets are used to create a magnetic field in this gap. This kind of arrangement forms a closed magnetic circuit with the magnetic force holding the ferrofluid in the gap and thus forming a liquid sealing ring that adheres to the pole pieces and the shaft surface.

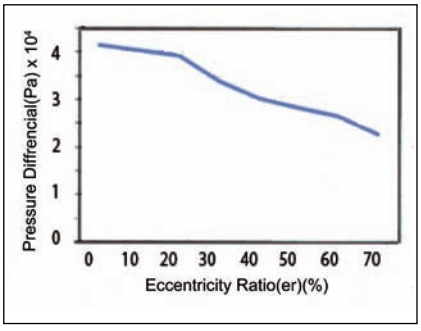

Fig. 2 *Effect of shaft eccentricity on burst pressure*

The experimental setup for testing ferrofluid seal with 25 mm diameter shaft as represented in Figure 1 consists of bearing housing, ferrofluid seal housing, motor with speed control system, vessel and argon gas header with pressure regulators and gauges (bourdon gauge manometer). Eleven ferrofluid seal samples have been tested so far and the ferrofluid with optimal performance in terms of best burst pressure and endurance has been chosen for further studies.

The burst pressure testing was carried out in static condition, and maximum burst pressure of around 500–600 mbar was observed. Pressure hold testing of seal over a month in static condition of shaft was carried out at a pressure of 220 mbar. The same seal was holding pressure at 220 mbar even under dynamic condition of shaft at 2500 rpm over a period of five months. Noticeably there was no pressure drop and ferrofluid seal did not lose its stability.

A 3-D finite element model of 25 mm diameter shaft ferrofluid seal (Figure 2) was modeled in COMSOL software, in order to calculate the burst pressure for a given configuration of ferrofluid seal. The burst pressure is determined by obtaining the gradient of magnetic field intensity

Fig. 1 *Test setup for 25 mm diameter shaft*

in the ferrofluid gap. The calculated value of burst pressure (618 mbar) is in close agreement with the experimentally observed value (600 mbar) of burst pressure.

Shaft eccentricity effect on burst pressure was studied using COMSOL software. Figure 2 shows the variation of burst pressure with eccentricity. It is observed that shaft eccentricity of 50% results in reduction of burst pressure by nearly 30% with that of concentric shaft. The effect of tooth orientation and taper angle of tooth on the burst pressure was also modeled in COMSOL. Experimental validation for the effect of tooth orientation and taper angle is in progress. Further works are being carried out towards testing of ferrofluid seal with shaft diameter 70 mm. After independent testing of the seal, integrated testing of seal by introducing it in small centrifugal pump and studying its performances is planned.

V.8 Thermal and Rheological Properties of Response Stimuli Nanofluids

Magnetic nanofluid is a unique material that exhibits both the liquid and magnetic properties. Since the properties and the location of these fluids are easily influenced by an external magnetic field, they have many scientific, industrial, and commercial applications. In an effort to develop magnetic nanofluid as a multifunctional smart material, we study both the thermal and rheological properties of magnetic nanofluids under different magnetic field strength and orientation with respect to the direction of heat flow. We have synthesized surfactant capped magnetite (Fe_3O_4) nanoparticles of different sizes and carried out systematic measurements of thermal conductivity in two different hydrocarbon based Fe_3O_4 nanofluids under varying magnetic field strengths and orientations. The average particle size of the particle used is ~9.0 nm. The thermo gravimetric studies confirm the presence of a monolayer of surfactant on nanoparticles that ensures steric stabilization. Stable magnetic nanofluids are prepared by dispersing the oleic acid coated Fe_3O_4 nanoparticles in kerosene and hexadecane. The dispersions showed excellent long term stability, as nanoparticles are not influenced by the gravitational force owing to their small size.

The percentage of enhancement in thermal conductivity as a function of volume fraction (ϕ) at different magnetic field strengths for kerosene based Fe_3O_4 nanofluids shows a moderate thermal conductivity enhancements within the predictions of Maxwell's effective medium theory (EMT) for zero field and a large enhancement in thermal conductivity at higher magnetic field.

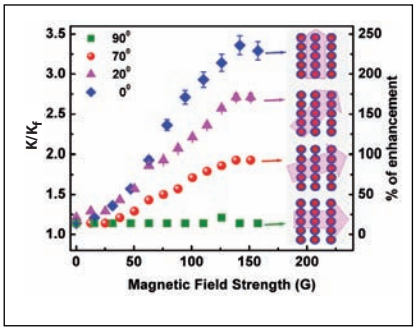

Fig. 1 *The thermal conductivity ratio (k/k_f) and the percentage of enhancement of k as a function of external magnetic field*

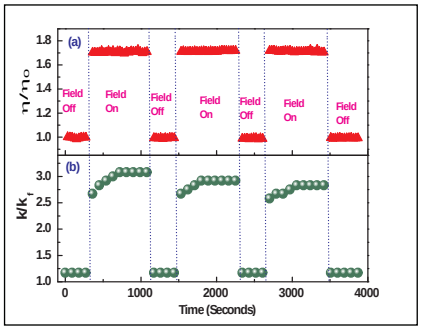

Fig. 2 *The variation of (a) k/k_f and (b) η/η_0 with time during field ON and field OFF condition*

The large enhancement in thermal conductivity in presence of magnetic field parallel to temperature gradient is attributed to the effective conduction of heat through the dipolar structures. The extent of chain formation in presence of an external magnetic field increases with increase in ϕ since the number of particles per unit volume increases with increase in ϕ. Figure 1 shows the variation of k/k_f with magnetic field strength for hexadecane based Fe_3O_4 nanofluids with ϕ=0.0608 under different field orientations of 0, 20, 70 and 90°. The maximum enhancement in thermal conductivity is observed when the field direction was exactly parallel to the thermal gradient whereas practically no enhancement is observed when field was perpendicular to thermal gradient. A gradual reduction in the thermal conductivity enhancement is observed as the field direction is shifted from parallel to perpendicular direction with respect to thermal gradient. Inset of Figure 1 shows the schematics of nanoparticle orientation with respect to thermal gradient when the magnetic field direction is varied from parallel to perpendicular direction. Application of magnetic field not only enhances the thermal conductivity of the fluid but also the rheological properties of the fluid. Such field induced enhancements in thermal conductivity and viscosity of ferrofluids can be exploited for a number of technological applications such as damping cum cooling. Figure 2 (a) and (b) shows the viscous and thermal conductivity change of hexadecane based Fe_3O_4 nanofluid with ϕ=0.067, where magnetic field strength is varied in steps. Both the k/k_f and η/η_0 measurements are carried out under on–off conditions at a magnetic field strength of 120 G (ON) and zero (OFF) respectively.

The shear rate for viscosity measurement is 50 s^{-1}. The steady viscosity with time for a given magnetic field indicates that the magnetic structures are not broken by shear under flow.

This offers interesting possibilities of using these fluids in microfluidic devices. Under the influence of an external magnetic field, the magnetic moment of the particle aligns in the field direction and the particle will rotate around the field direction. When the field is perpendicular to vorticity, the viscous friction tilts the magnetic moment against the field direction. The resulting finite angle between the magnetic moment and the field direction will give rise to a magnetic torque counteracting the viscous torque that tries to realign the moment along the field direction. Hindrances of the free rotation of the particles in the flow occur due to the counteraction of the torques. Further, it also increases the viscosity of the fluid. Though the equilibrium value of viscosity is achieved instantaneously, it is realized after ~400 seconds in the case of thermal conductivity. However, with increase in number of switching cycles, an equilibrium value is achieved faster. Upon turning off the magnetic field, both the k/k_f and h/h_0 values drops to zero immediately, which shows the perfect reversibility of the observed phenomena, which may have several interesting practical applications in smart devices. Our studies show that the thermal and rheology of the fluid is precisely tuned from low to very high values by varying the magnetic field strength and its orientation. The increase in k/k_f with particle size is attributed to enhanced dipolar interaction and aspect ratio of the chains. As the parallel mode has a geometric configuration that allows the most efficient means of heat propagation through nanoparticle paths, large thermal conductivity enhancement is achieved with parallel fields. As the thermal and rheological properties of these fluids are perfectly reversible, these magnetic fluids are ideal for applications in smart devices. As conventional nanofluids exhibit modest thermal conductivity enhancement, significantly large thermal conductivity enhancement observed in this response stimulus material makes them ideal candidate for applications in miniature devices.

V.9 Phase Diagram Studies on $CaBr_2$-$CaCl_2$, $CaBr_2$-LiBr and $CaBr_2$-CaHBr Systems

Understanding the phase diagrams of alkali and alkaline earth metal halides is important to develop hydride ion conducting electrolytes which can be used in electrochemical hydrogen sensors to monitor hydrogen concentration in ppb levels in sodium. These sensors are compact and can be used to detect steam leaks during the operation of fast reactors. The phase diagram of the pseudo-binary systems, $CaBr_2$-$CaCl_2$, $CaBr_2$-LiBr and $CaBr_2$-CaHBr have been investigated by DTA technique. The phase diagrams were established in the temperature range from room temperature to 1073 K. As the systems are moisture and air sensitive, the samples were sealed in tiny iron capsules and hermetically weld closed by pulsed arc welding inside dry argon atmosphere glove box before loading into the DTA equipment. From DTA results the contour of solidus and liquidus temperatures with composition are plotted and the phase diagrams were constructed.

$CaBr_2$-CaHBr system shows appreciable solid solution of CaHBr in $CaBr_2$ at high temperatures and it shows a eutectic reaction at 843 K and the eutectic composition is at ~73.4 mol% $CaBr_2$. LiBr-$CaBr_2$ system exhibits a complicated phase diagram. The phase diagram of LiBr-$CaBr_2$ system is found to have a compound $LiCaBr_3$, which showed a eutectic reaction at 805 K with a solid solution rich in LiCl at ~35 mol% $CaBr_2$. $CaBr_2$-$CaCl_2$ system exhibits continuous solid solution in the entire range of compositions from pure $CaCl_2$ to pure $CaBr_2$ with thermal minimum at 971 K and at 56.5 mol% $CaBr_2$. The experimentally determined phase diagram of $CaBr_2$-$CaCl_2$ system is shown in Figure 1 and has promising characteristics for identifying a ternary hydride ion conducting electrolyte that is more convenient than the binary $CaBr_2$-CaHBr system in assembling a hydrogen sensor for sodium.

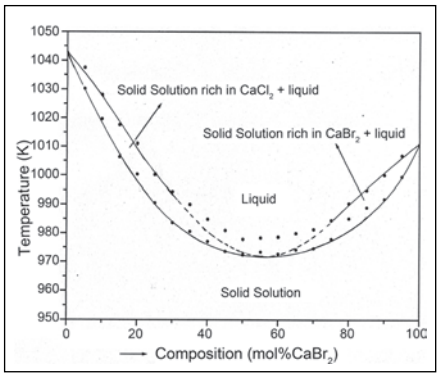

Fig. 1 *Phase diagram of $CaCl_2$-$CaBr_2$ system determined from DTA experiments*

V.10 Thermodynamic Studies on Compounds of Relevance to Nuclear Waste Forms

Study of vapourization of sodium metaborate by transpiration thermogravimetry and Knudsen effusion mass spectrometry

In continuation of a detailed vapourization study of boric acid by transpiration thermogravimetry (TTG) and Knudsen effusion mass spectrometry (KEMS), It was sought to undertake a similar study of another boron containing system, sodium metaborate, an important component of sodium borosilicate glasses, the industrial development of which is of practical interest for nuclear waste disposal. Additional motivating factors for starting the present study are: (1) no transpiration measurements exist on $NaBO_2$ (s) and (2) among the three previously reported KEMS studies on $NaBO_2$(s,l), the values of partial pressure of $NaBO_2$(g) obtained in the KEMS studies are not that well consistent.

The transpiration measurements, performed for the first time on $NaBO_2$(s), involved the use of argon as the carrier gas for vapour transport and derivation of vapour pressure of $NaBO_2$(g) (by assuming it as the sole vapour species) through many flow dependence runs (eleven) and temperature dependence runs (nine) in the temperature range 1075 to 1218 K. The KEMS measurements performed in the temperature range 1060 to 1185 K confirmed $NaBO_2$(g) as the principal vapour species over $NaBO_2$(s), in accord with the previously reported KEMS studies. The values of p($NaBO_2$) obtained by both TTG and KEMS are consistent within the uncertainties associated with each method and so are the second- and third-law values of

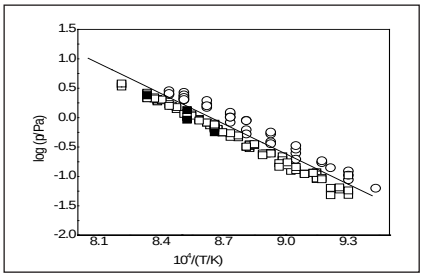

Fig. 1 *Results of TTG runs (□-temperature dependence ■-flow dependence and ○-KEMS runs)*

enthalpy of sublimation, the latter aspect consistently missing in all previous vapourization studies. Figure 1 shows the temperature dependence of p($NaBO_2$) obtained in TTG and KEMS studies. The results of both TTG and KEMS were combined to recommend the following thermodynamic parameters pertinent to the sublimation reaction, $NaBO_2$(s) = $NaBO_2$(g): $\log\{p(NaBO_2)/Pa\} = -(17056 \pm 441)/(T/K) + (14.73 \pm 0.35)$ for the temperature range 1060 to 1218 K; $\Delta_r H^o_m(298.15\ K) = (346.3 \pm 9.4)$ kJ.mol^{-1} and $\Delta_r S^o_m(298.15\ K) = (210.2 \pm 6.8)$ J.mol^{-1}.K^{-1}.

Thermodynamic properties of alkaline earth chloroapatites $M_{10}(PO_4)_6Cl_2$(M=Ba,Sr,Ca)

Apatites are a class of compounds having the general formula of $M_{10}(PO_4)_6(X)_2$, where M is a divalent metal cation (mainly Ca^{2+}, Sr^{2+}, Ba^{2+}, Cd^{2+} and Pb^{2+}) and X is a monovalent anion (OH^-, F^-, Cl^-, and Br^-). The hexagonal crystal structure of apatite (space group P63/m) permits a wide range of anions and cations to be accommodated in their crystal lattice by forming substitutional solid solutions. The attractive feature of the apatites for nuclear waste immobilization is the ease of preparation of waste forms at relatively low temperatures and

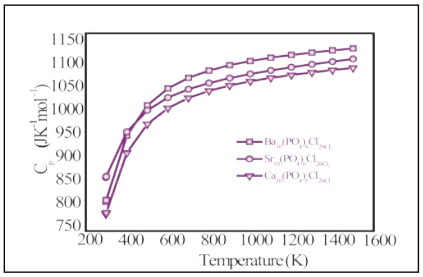

Fig. 2 *Heat capacity of alkaline earth chloroapatites*

at atmospheric pressure which is a pre-requisite to avoid loss of volatile fission products from the matrix during processing. The apatites show good performance on incorporation of highly radioactive and heat generating radioactive elements, Cs, Ba and Sr and can accommodate a variety of metal elements. These materials are considered to be suitable solid host matrices for immobilizing metal chloride wastes generated from pyrochemical reprocessing of metallic nuclear fuel as they contain 6.8 wt.% of chlorine in their lattice. Thermodynamic data of the apatites are of importance to optimize the process parameters for preparation to predict the stability of the host matrices and to understand their phase behaviour after immobilizing the chloride wastes of alkali, alkaline earth and rare earth fission products in the apatite structure. Enthalpy increment measurements were carried out on the single phase, pure $Ba_{10}(PO_4)_6Cl_2$, $Sr_{10}(PO_4)_6Cl_2$ and $Ca_{10}(PO_4)_6Cl_2$ by means of drop calorimetry in the temperature range 523 to 1423 K. Thermodynamic functions such as heat capacity (plotted in Figure 2) entropy and Gibbs energy functions were computed in the temperature range 298 to 1500 K from the measured enthalpy increments.

V.11 Studies on the Synthesis of Boron and Boron Carbide

Boron carbide enriched ^{10}B is used as a control rod material in PFBR. The boron carbide is fabricated by reacting boron with carbon. The elemental boron in turn is produced by electrowinning process.

The technology for the production of high-purity enriched elemental boron through high temperature (1073 K) electrolysis of a molten salt mixture of KCl (72.96 mol%), KBF_4 (11.04 mol%, boron enriched in ^{10}B isotope to an extent of ~ 65 at.%) and KF (16 mol%) was developed. In this process boron is electrodeposited on a mild-steel cathode and F_2 / Cl_2 are liberated at the anode which is a graphite crucible containing the molten salt mixture. The electrochemistry of the above melt system is of importance to optimize the parameters of the electrowinning process. To carry out this basic electrochemical studies, a Ag/AgCl reference electrode suitable for molten salt application was designed, developed and fabricated. The schematic of the reference electrode is given in Figure 1.

The suitability of this reference electrode for the intended end use was checked. Its stability and non-polarizability were tested and found to be satisfactory in the temperature range 1073–1123 sK. This electrode was used for studying the electrochemistry of the boron electrodeposition process.

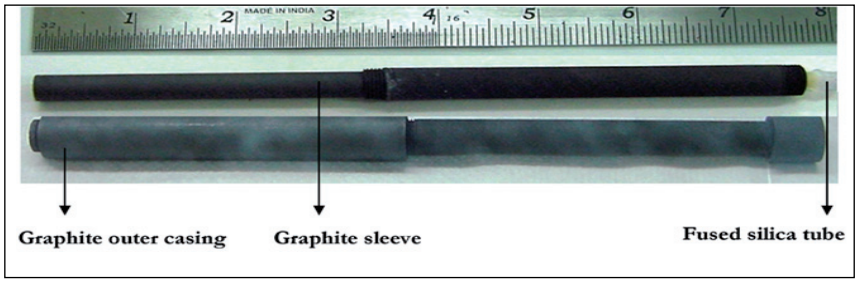

Fig. 1 *Ag/AgCl reference electrode*

Even though extensive research has been carried out on the electrolytic processes that employ a halide melt as a medium for electrolyzing a boron compound in the past, the electrochemistry and the mechanism of these processes are yet to be completely understood. In order to understand the basic electrochemistry behind this process, data on current, voltage and yield of boron were generated using an experimental cell. The progress of the electrowinning of boron from the melt (KCl + KF + KBF_4) was investigated by assaying the salt mixtures withdrawn from the melt at periodic intervals. Based on the experimental results, empirical reactions were formulated to arrive at the most probable reaction scheme in vogue during the course of the electrolysis. The probable electrochemical reactions taking place at the electrodes are given in Table 1.

These reactions were formulated based on the existence of various chloride - fluoride complexes derived from the fluoroborate anion. During electrolysis all these chloride - fluoride complex anions of boron would undergo decomposition. Experimentally it was concluded that during electrowinning, reactions 2 and 3 are followed.

Table 1: Electrochemical reactions

Sl.No.	Reaction
1	$KBF_4 + 0.5\ KCl \rightarrow B + 1.5\ KF + 0.25Cl_2 + 1.25\ F_2$
2	$KBF_4 + 1.25\ KCl \rightarrow B + 0.625Cl_2 + 2.25\ KF + 0.875\ F_2$
3	$KBF_4 + 2.3\ KCl \rightarrow B + 1.15\ Cl_2 + 3.3\ KF + 0.35\ F_2$
4	$KBF_4 + 3\ KCl \rightarrow B + 1.5\ Cl_2 + 4\ KF$

Thermodynamic analysis of carbothermic reduction of boric oxide

Commercially, boron carbide is produced by the carbothermic reduction of either boric oxide or boric acid. However, the loss of boron due to volatilization of its oxides during the reduction process is very significant. In order to understand the volatilization behaviour as well as to optimize the C/B_2O_3 mole ratio for the fabrication of B_4C with minimum loss of boron and minimum contamination by free carbon, a thermodynamic analysis of the carbothermic reduction was carried out. The equilibrium product composition in the carbothermic process was calculated by using equilibrium module of Fact sage 6.2. For these calculations, the following reaction conditions were assumed. (i) Possible reactants and products namely, $B_2O_3(s)$, C(s), B_4C (s), CO(g), B(s), B(l), $B_2O_3(g)$, B_2O_2 (g), $BO_2(g)$, $B_2O(g)$, B(g), $B_4C(l)$ (ii) temperature range 273-3573 K and (iii) Pressure – 0.98 bar. From the results of these calculations the stability boundaries of $B_2O_3(l)$, C (s), $B_4C(s)$, CO(g), B(s),

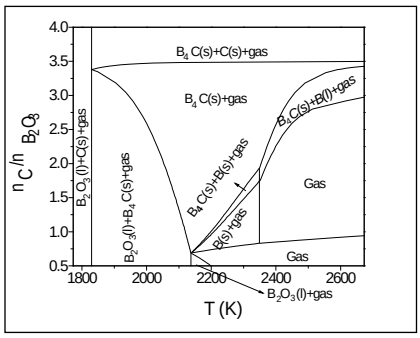

Fig. 2 Stability diagram of B-O-C system

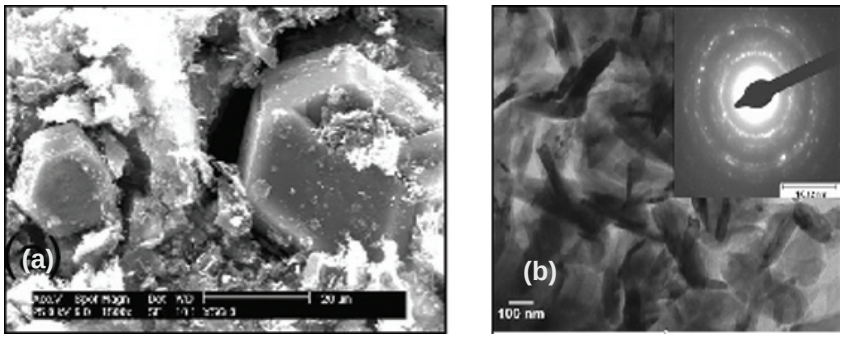

Fig. 3 (a) Scanning electron micrograph and (b) Transmission electron micrograph of boron carbide (The inset shows the SAED pattern of nanocrystalline boron carbide)

B_4C(l), B(l) at 0.98 bar pressure with varying initial mole ratios of C to B_2O_3 ($n_c / n_{B_2O_3}$) and temperature were established. These results are shown in Figure 2.

If the initial mole ratio ($n_c / n_{B_2O_3}$) is less than 0.69 and the temperature is above 2137 K, B_4C(s) is not formed as one of the condensed phases. However, below 2137 K, B_4C(s) is found in the condensed phase along with B_2O_3 (l). When the initial ratio is between 0.69 and 3.38, B_4C(s) is the most predominant and stable phase in the temperature range 2000 – 2300 K. Above 3.38, B_4C(s) is more predominant and stable species along with C(s) in the temperature range of 1830 - 2600 K. The presence of carbon is due to loss of B_2O_3 (l) as various gaseous oxides of boron. From this study, it is established that single phase B_4C can be prepared when carbothermic reduction is carried out in the temperature range 2000 – 2200 K at 0.98 bar pressure using B_2O_3 and C mixture in the mole ratio of 0.69 – 3.48. Several investigators have reported experimental studies on the carbothermic reduction by boric oxide. The results of these experimental studies are in agreement with the present calculations.

Novel route for the synthesis of boron carbide

The carbothermic reduction of boric anhydride by carbon in an electric arc furnace is an energy intensive process and involves loss of boron in the form of boron oxides. Further, the product obtained through this method is a coarse powder which is difficult to sinter without further grinding. To circumvent these problems, a novel method, based on the combustion of boric acid–sucrose xerogel was developed to synthesize boron carbide powder. Boric acid and sucrose were taken in the molar ratio of 1:0.145. The overall reaction between boric acid and sucrose could be represented by 48 H_3BO_3 + 7$C_{12}H_{22}O_{11}$ = 12 B_4C + 72 CO + 149 H_2O. The xerogel obtained from the above reaction was pyrolyzed at 1273 K. Boron carbide was obtained by heating this precursor at 1823 K. The yield of boron carbide was improved by the use of a novel graphite crucible (sample cell) designed for this purpose. By suitably tailoring the design of this sample cell, CO generated during the carbothermic reduction was effectively removed from the reaction site while the oxides of boron (mostly B_2O_3) were retained within the reaction zone. This resulted in the improved yield of boron carbide.

The xerogel and the precursor were characterized by using Fourier transform infrared spectroscopy (FTIR). FTIR results suggest that a complex is formed between boric acid and sucrose, which subsequently undergoes pyrolysis resulting in a precursor that yields boron carbide on further decomposition. The constituent phases were identified by X-ray diffraction while their elemental composition was established with the help of chemical assay. The microstructure of the final product is shown in Figure 3a. From this microstructure, it is evident that the crystallites of boron carbide formed during heat treatment agglomerate into irregular fine particles. Selective growth of crystallites of B_4C was also observed.

Transmission electron micrograph of the boron carbide synthesized by this route is shown in Figure 3b. The spotty ring pattern confirms the nanocrystallinity of randomly oriented boron carbide crystallites while the intensities of the diffraction pattern correspond to the hexagonal B_4C phase. In this study, it was demonstrated for the first time that boron carbide could be obtained by pyrolysing a xerogel precursor (derived from boric acid – sucrose) at 1823 K for 3 h under flowing argon. It was also shown that this synthesis could be accomplished at a relatively lower temperature (1823 K) compared to the conventional process (> 1973 K). A final product with relatively lesser free carbon (~ 6%) could be synthesized with the help of a novel high temperature sample container made out of graphite. The use of this innovative feature also helped in improving the yield of the final product to about 48% of the theoretical value.

V.12 Calorimetry Studies on Recrystallization Kinetics and Thermal Properties in IFAC-I

For sodium cooled fast breeder reactors, the selection of materials for clad and wrapper is mainly based on their resistance to irradiation induced void swelling and high temperature creep resistance, in order to achieve high burn-up of the fuel. In this regard, alloy D9 (14Cr-15Ni-Ti modified SS) has been chosen as the clad and wrapper material for prototype fast breeder reactor (PFBR). However, with a view to enhance the fuel burn-up, up to about 150 GWd/t**,** an improved version of D9 SS, known as IFAC-I has been developed by optimizing the amount of P, Si and Ti contents in the standard D9 alloy. In addition to such careful compositional tailoring, IFAC-I will be used in 20% cold worked condition for ensuring adequate swelling resistance. Due to the cold worked starting microstructure, IFAC I will undergo recovery, recrystallization and grain growth processes at high temperatures with attending changes in mechanical properties. In addition, reliable and critically assessed thermo-physical property data are essential from the point of view of enabling the knowledge-driven approach to alloy design and component fabrication practices. Having these twin objectives in mind, a comprehensive calorimetry and high temperature X-ray diffraction studies have been initiated to unravel the mechanistic and energetic aspects of recovery and recrystallization processes in addition to generating heat capacity and thermal expansivity data on IFAC I.

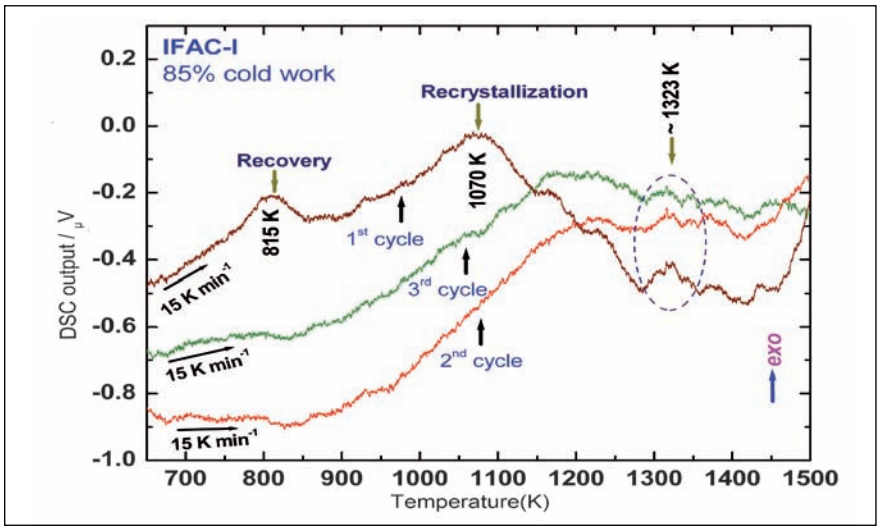

Fig. 1 Comparison of three successive heating DSC traces obtained on the same sample under identical experimental conditions

Recovery and recrystallization behavior in IFAC-I

In Figure 1, the on-heating differential scanning calorimetry (DSC) responses obtained at a heating rate of 15 K min^{-1} are compared for three successive heating cycles, carried out under identical experimental conditions on the IFAC-I sample cold work for 85%. The findings suggest that both recovery and recrystallization events are almost fully over in the first primary heating cycle itself. From the Figure 1 it is clear that both recovery and recrystallization occur at 815 and 1070 K respectively. However, the small post recrystallization exothermic humps seen at about 1321 K are still present, which suggests that the dissolution of carbide particles is not completed in the first heating cycle. It is in fact gradual and occurs over a period of time.

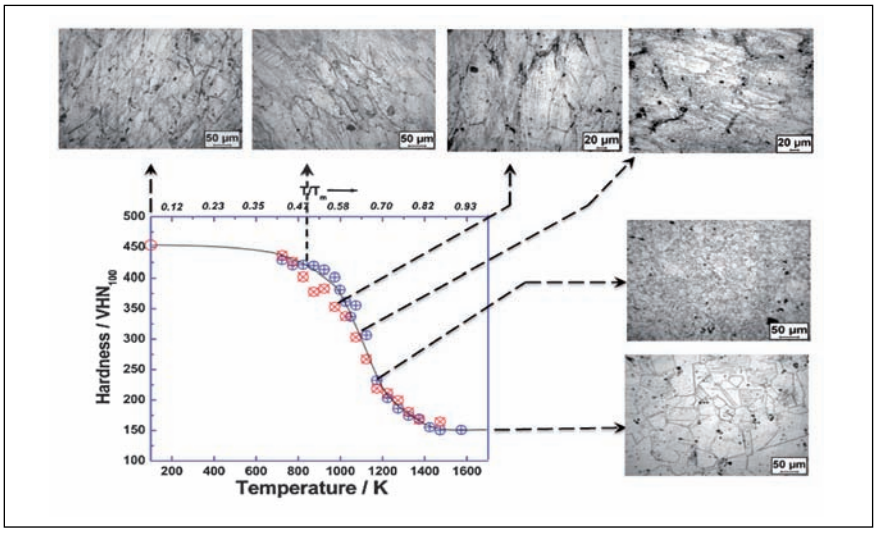

Fig. 2 Variation of microhardness with annealing temperature for 85% cold worked sample along with the corresponding microstructural change

Similar DSC experiments have been carried out for various heating rates in range from 5 to 40 K min^{1} and these data have been used to evaluate the kinetic parameters such as effective activation energy. The overall activation energies are found to be 198 and 335 kJ mol^{-1} for recovery and recrystallization processes respectively. These values suggest that the recovery is mainly mediated by grain boundary diffusion characteristics, while bulk recrystallization requiring long range interfacial movement is catalysed by volume diffusivity.

In Figure 2, the isochronal variation of hardness as a function of annealing temperature for both 15 and 30 minutes of annealing is presented for 85% cold worked sample, along with accompanying changes to the microstructure. From this figure, it emerges that the isochronal hardness variation with temperature is of inverse sigmoidal in character, which is typical of diffusional transformation. It is found that significant lattice softening sets in at about $0.5T/T_m$; however, its rate increases dramatically and reaches maximum at about $0.6T/T_m$ = 1150 K. Here, T_m is the melting temperature which is measured as 1838 K. This observation matches well with the peak temperature of the principal recrystallization event, as registered in the DSC trace (Figure 1). With further increase in temperature, the rate of hardness change is found to exhibits gradual decrease (Figure 2).

Heat capacity and thermal expansivity data for IFAC-I

In order to obtain high temperature thermal property data, the enthalpy increment ($H_T - H_{298.15}$) as a function of temperature (T) has been measured for the temperature range of 400 to 1473 K using inverse drop calorimeter. Besides, high temperature XRD is also carried out for obtaining lattice thermal expansivity up to 1200 K. The measured thermal property data have also been modelled through Debye-Gruneisen quasiharmonic formalism to obtain an integrated and self-consistent estimates of thermal properties in a comprehensive temperature domain ranging from, 0-1400 K.

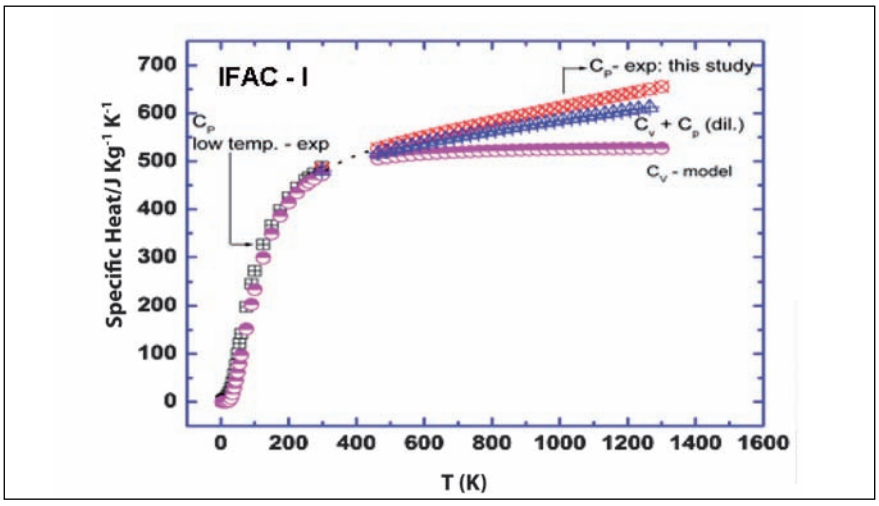

Fig. 3 *Debye-Gruneisen model estimates of C_p for IFAC-I are compared with experimental measurements*

In Figure 3, the calculated C_p curve for the overall temperature range, 0≤T≤1400 K is compared with present experimental data. The Debye-Gruneisen model slightly underestimates the high temperature experimental C_p by about 30 J kg^{-1} K^{-1} at high temperatures. This is less than the typical experimental uncertainty of the measured data. The room temperature C_p for IFAC-I is estimated to be 486 J kg^{-1} K^{-1}. In Figure 4, the estimated instantaneous and relative linear thermal expansivity data for IFAC-I are compared with literature data for some related stainless steels. As can be seen, the present data are in line with the expected trend for austenitic stainless steels. It may be mentioned that both thermal property data and recrystallization kinetics on IFAC I have been characterized using calorimetry for the first time in the present study.

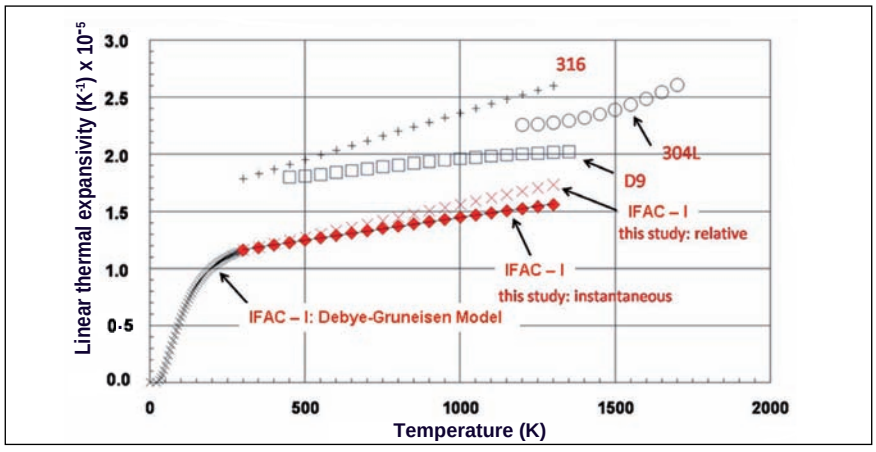

Fig. 4 *Comparison of measured linear thermal expansion coefficient for IFAC-I with literature data on related steels*

V.13 Development of Successful Weld Joints of IFAC-1 SS Tubes with SS 316 LN End Plugs

The swelling and irradiation creep resistance properties of Indian fast reactor advanced cladding-1 stainless steel (IFAC-1 SS) are better than that of alloy D9 that is presently being used as cladding material of PFBR. Higher swelling and irradiation creep resistance properties will enhance the allowable radiation damage level in the cladding and consequently the burn-up of the fuel pins. IFAC-1 SS clad tube with SS316LN end plug is proposed to be used in fabrication of future fuel pins of fast reactor. During welding of austenitic stainless steels such as IFAC-1 SS and SS316LN, depending on alloy composition, weld solidification cracking can occur, primarily due to low-melting liquid phases which allow boundaries to separate under the thermal and shrinkage stresses resulting from weld solidification and cooling. IFAC-1 SS which contains higher levels of low-melting eutectic phase forming elements such as phosphorous and silicon is particularly susceptible to solidification cracking.

Welds that solidify as primary austenite may be highly susceptible to solidification cracking. This susceptibility is increased by impurity elements such as sulphur and phosphorous and minor alloying elements such as boron, silicon, titanium and niobium that promote the formation of low-melting eutectics. Solidification-cracking susceptibility of austenitic stainless steels is described in the literature by plotting the Cr_{eq}/Ni_{eq} ratios against impurity content in terms of phosphorus plus sulphur, as shown in Figure 1. A dramatic transition in cracking susceptibility occurs at a Cr_{eq}/Ni_{eq} value of approximately 1.5, as shown in Figure 1. When Cr_{eq}/Ni_{eq} is less than 1.5, the weld is highly susceptible for cracking. This transition at Cr_{eq}/Ni_{eq} = 1.5 represents the shift in solidification behavior from primary austenite to primary ferrite mode. Using the Cr_{eq} and Ni_{eq} relations given in the literature, Cr_{eq}/ Ni_{eq} ratios of IFAC-1 SS and SS 316LN are calculated to be 1.128 and 1.512 respectively and these are marked in Figure 1. It can be seen that IFAC-1 SS with Cr_{eq}/Ni_{eq}=1.128 is highly susceptible for weld cracking and SS316LN with Cr_{eq}/Ni_{eq} = 1.512 is on the boundary line between cracking and no-cracking zones.

Extensive pulsed TIG welding trials with varied welding parameters have been carried out on the IFAC-1 SS tube - SS316LN end plug joints to find out the feasibility of obtaining weld free of solidification crack. Weld cracks of varied lengths and widths were observed during the initial trials as shown in Figure 2a. By systematically varying the welding and geometrical parameters during the trials, the number of cracks and their dimensions were gradually brought down and finally completely eliminated, as shown in Figure 2b. During welding, the weld torch was focussed slightly towards the end plug side so that the weld metal contained more of SS316LN, thereby enhancing the Cr_{eq}/Ni_{eq} ratio in the weld pool. Optimized weld parameters have been identified and defect-free weld joints qualified in leak testing and radiography have been obtained. This is a significant step in utilization of IFAC-1 SS as cladding material in future fast reactor cores.

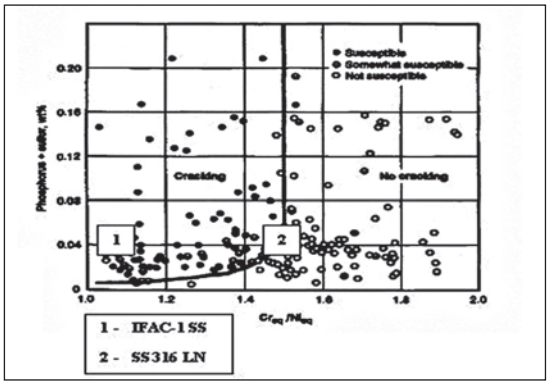

Fig. 1 Relationship between solidification cracking susceptibility and Cr_{eq}/Ni_{eq} ratio

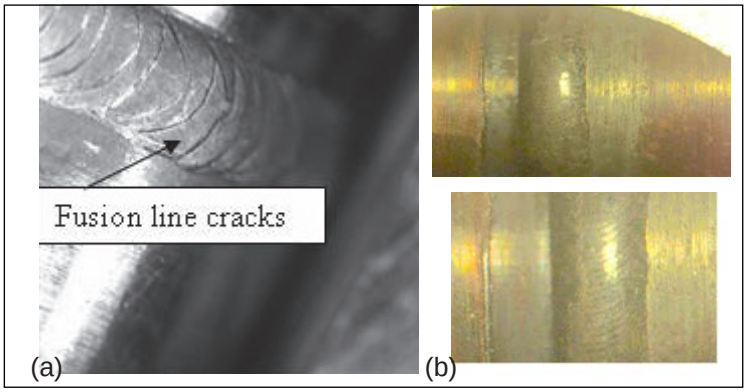

Fig. 2 Photograph of IFAC-1 SS316 LN welds (a) Initial trials and (b) Defect-free welds

V.14 Dislocation Density Evaluation in Cold Worked Austenitic Stainless Steel by XRD Line Profile Analysis

The study of line-broadening of X-ray reflections of deformed materials has been widely used to obtain dislocation densities. The dislocation density in cold worked type 316L stainless steel (SS) by X-ray diffraction Rietveld analysis is reported here because of the application of similar 20% cold worked stainless steel as structural materials in breeder reactors. In this study, the calculation of dislocation density in annealed and cold worked samples of the type 316L SS from parameters such as crystallite size and strain using Williamson–Smallman approach is presented.

XRD investigations showed an increase in the peak broadening of planes with increasing cold work due to increase in defect density and residual stress of the material. The crystallite size and the RMS strain as a function of cold work are shown in Figures 1(a) and 1(b), respectively. The crystallite size and strain parameters were extracted using Rietveld technique. It is noticed that the cold work reduces the crystallite size and increases the RMS strain in all the planes. The crystallite size decreases significantly from ~450 to ~40 nm even for cold work as low as 2%, while the strain increases steadily with the cold work for all the planes. Although both crystallite size and RMS strain show anisotropic behaviour, the variation in the strain versus crystallographic planes is more significant as a function of cold work.

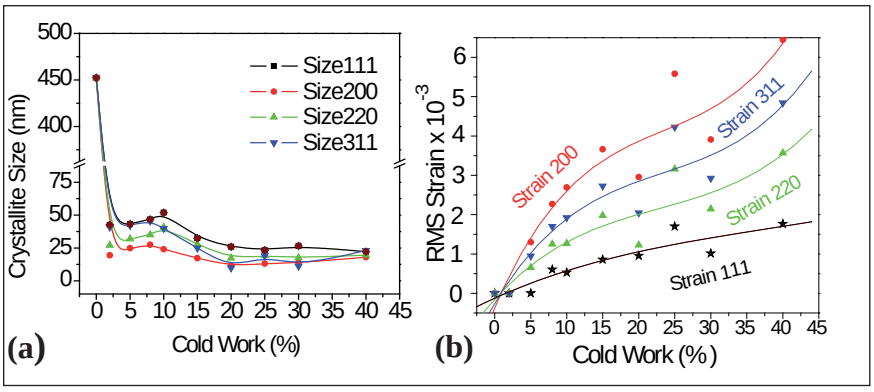

Fig. 1 *(a) Crystallite size and (b) RMS strain of the cold worked samples for several planes of type 316L stainless steel*

The dislocation density, ρ due to domain size (or crystallite size, $\rho_{D)}$ and strain ($\rho_{s)}$ in the material was calculated using the relation, $\rho=(\rho_D\rho_s)^{1/2}$. It is observed that the dislocation density and hardness of the material increase with increase in the cold work (Figure 2). The typical dislocation density of the annealed sample is found to be $1.8x10^{11}/m^2$ and for 20% and 40% cold worked type 316L SS are $3.6x10^{15}/m^2$ and $5.4x10^{15}/m^2$, respectively. It must be mentioned that there is a significant increase in the dislocation density up to 20% of cold work and thereafter, the increase in the dislocation density tends to slow down. This is understandable clearly from Figure 1(a), where the crystallite size has decreased significantly up to 20% cold work. On the other hand, the strain has been found to increase with increase of cold work. In summary, the present work describes X-ray diffraction analysis to study the effect of cold work on dislocation density in austenitic stainless steel.

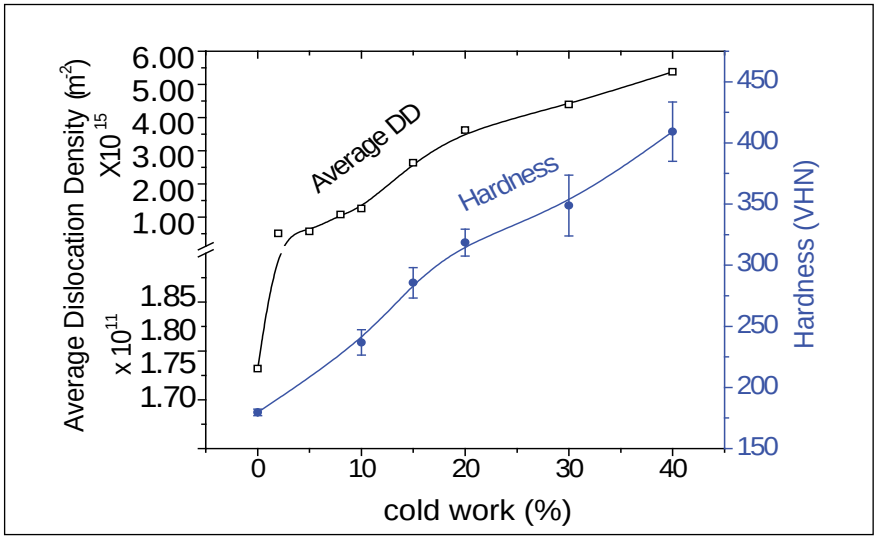

Fig. 2 *Average dislocation density and hardness of the cold worked samples*

V.15 Dislocation Driven Chromium Clustering in Fe-9Cr Alloy: Positron Annihilation Study

Having better void swelling resistance at elevated temperatures and irradiation conditions, Ferritic / martensitic steels are considered to be the candidate structural materials for future fission and fusion reactors. EUROFER-97 is one such examples with 9 (wt.%) chromium and 1 (wt.%) tungsten as major alloying elements. Chromium being major alloying element in these steels, the iron rich phase diagram of Fe-Cr binary alloy is much needed to be understood both in equilibrium and non-equilibrium conditions. There still exist open questions and differences between theoretical predictions and experimental observations. It is well known that decomposition of chromium in Fe-Cr binary alloy occurs for chromium concentrations higher than 19 wt.%. It was also found that even for alloys with low chromium concentration, precipitation occurs in non-equilibrium conditions, such as irradiation. For room temperature electron and neutron irradiations, chromium precipitation was found only above 8.4 wt.% chromium. For high temperature electron irradiation, precipitation was observed with chromium concentration even below 5 wt.%. On the other hand, ion irradiation causes precipitation in alloys with chromium as low as 2.6 wt.%. However, there were few reports of chromium precipitation induced by heat treatment alone for chromium concentration less than 19%.

The present work involves observation of fine chromium precipitates of size ~ 5 nm, in Fe-9% chromium high purity binary alloy with mere heat treatment

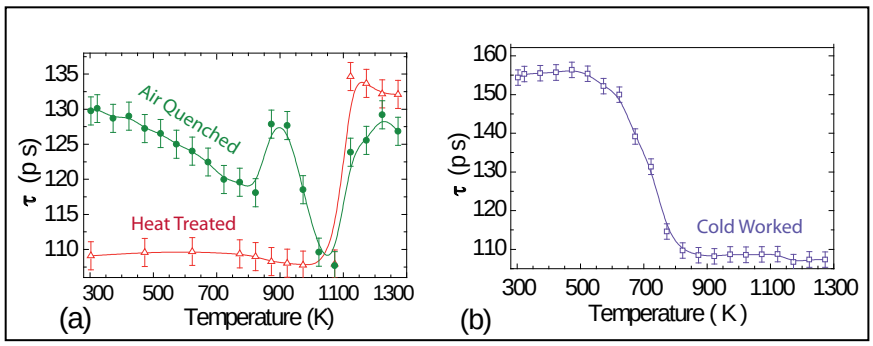

Fig.1 *Variation of mean positron lifetime in (a) Fe-9Cr alloys (air-quenched and heat treated) and (b) Cold worked pure iron as a function of annealing temperature*

and its dependence on initial state/microstructure. One set of normalized samples, air-quenched from 1313 K (inside γ-loop of Fe-Cr equilibrium phase diagram), and another set of samples heat treated for 2 hours at 1073 K (α-phase, just below γ-loop) were prepared. Air-quenched sample preparation is equivalent to normalization in ferritic steels. The similarity in initial microstructure is significant with respect to precipitation observed in this study. One set of annealed pure iron samples, cold worked to 20%, were also studied as a reference. Isochronal annealing was carried out on these samples from 300 to 1273 K with a holding time of one hour at each 50 K step in a vacuum of ~10^{-6} Torr. Positron lifetime measurements were carried out after each annealing step. TEM studies were carried out on air-quenched samples at representative temperatures. Figure 1 shows positron lifetime results of air-quenched, heat treated and cold worked samples. Air-quenched sample has initial microstructure with lath morphology (as shown in Figure 2 (a)) due to phase change during cooling process. The average lath size is around 0.1 μm and contains dense random dislocations within the laths. Heat treated sample will have well developed grain structure with grain size of order 20 μm and relatively negligible dislocations.

These differences in dislocation densities cause difference in positron lifetime in as-prepared conditions. The lifetime in initial condition of heat treated sample is equal to positron lifetime in annealed pure iron, indicating it is defect free. cold worked sample will have deformed grains with dislocations produced during cold working. As the heat treatment temperature increases the dislocations anneal out and consequently lifetime decreases. The observed decrease in lifetime until 823 K in AW and cold worked samples are consistent with this. As heat treated sample initially contains negligible dislocations, there are no noticeable changes during initial annealing temperature range.

As the annealing temperature is increased beyond 823 K, lifetime in cold worked sample reaches that of annealed iron value, indicating complete recrystallization. Increase in lifetime of air-quenched sample, beyond 823 K, indicates distinct

behavior compared to cold worked sample. This increase in positron lifetime could be due to precipitation, with interfaces of precipitates and matrix acting as positron trapping sites. Further TEM observations, of air quenched, 900 K annealed and 937 K annealed confirmed precipitation at 900 K. Also, TEM studies confirm well developed, precipitation free, grain structure at 937 K Interestingly, this stage is absent in HT sample which contains negligible dislocation concentration.

These observations are understood as follows. During their motion dislocations sweep chromium atoms and leave chromium rich local regions, as dislocations interact/anneal out during this temperature range. Further investigations using selected area diffraction and energy dispersive X-ray spectroscopy showed they are likely to be σ-phase of Fe-Cr.

This aspect is being further investigated. The increase in lifetime beyond 1023 K, both in air-quenched and heat treated samples, is due to the formation of microstructure similar to that of the initial state of air-quenched sample, as the temperature is inside γ-loop of phase diagram.

The equilibrium phase diagram along with irradiation induced precipitation and the results of the present study (dislocation driven precipitation) are

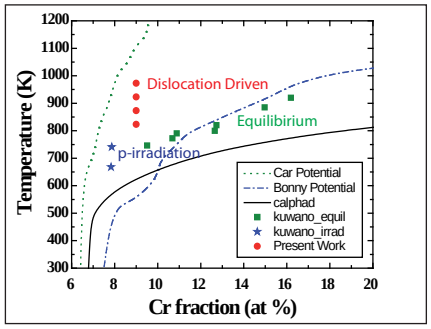

Fig. 2 *Iron rich side of phase diagram of Fe-Cr system. Calculated phase boundaries are shown as lines and data points corresponding to experimental observations*

shown in Figure 2. As a summary, the dislocations cause local enrichment of chromium, while they move and interact/annealed out. The localized chromium rich regions could turn into σ-phase at corresponding temperature.

V.16 Development and Characterisation of India Specific RAFM Steel for Test Blanket Module of Fusion Reactor ITER

Considerable progress has been made on indigenous development of reduced activation ferritic/martensitic (RAFM) steel for first wall and blanket applications in fusion reactors. As a part of first phase, efforts have been made to optimize the composition and processing route. As part of this programme, mechanical behaviour of the indigenously developed RAFM steel has been evaluated.

In the development of India specific RAFM steel for test blanket module (TBM) to be tested in ITER, the tungsten and tantalum contents have been optimized for better combination of impact, tensile, creep and fatigue properties. Four heats of the steel having tungsten in the range 1 – 2 wt.% and tantalum in the range 0.06 – 0.14 wt.% were melted. The steels were subjected to normalizing (1250 K for 30 minutes) and tempering (1033 K for 60 minutes) heat treatments and had tempered martensitic microstructure. Prior austenitic grain size was found to decrease with increase in tungsten and tantalum contents. Impact properties of the steel including ductile to brittle transition temperature (DBTT) were found to depend on tungsten and tantalum contents (Figure 1a). The upper-self energy as well as DBTT of the steel increased with both tungsten and tantalum content. Tensile strength of the steel was not influenced significantly by the increase in tungsten content, however decreased marginally with the increase in tantalum content at temperatures >723 K with the consequent

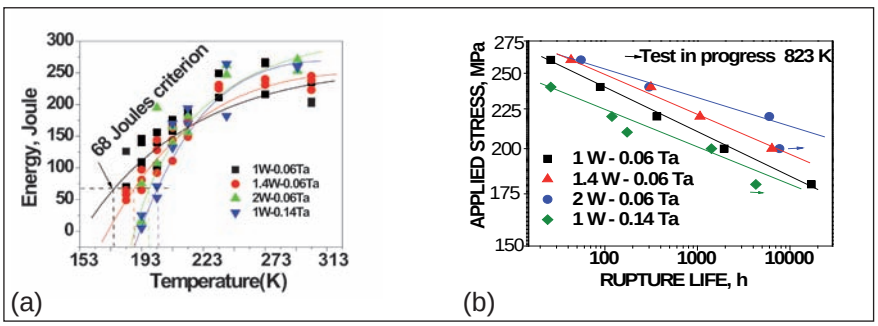

Fig. 1 *RAFM steel - effect of tungsten and tantalum on* (a) *Impact energy (b) Creep rupture life*

increase in ductility. Increase in tungsten content decreased the minimum creep rate and delayed the onset of tertiary stage of creep deformation in the steel and reverse was found with the increase in tantalum. Creep rupture strength of the steel was found to increase significantly with tungsten content whereas it decreased with the increase in tantalum content (Figure 1b). Cyclic stress response of the steels is shown in Figure 2. Fatigue life of the steel was found to increase with increase in tungsten and tantalum contents, however extensive cyclic softening was exhibited by the steel with a tungsten content greater than 1.4 wt.%. RAFM steel having 1.4 wt.% tungsten with 0.06 wt.% tantalum tends to have better combination of creep and fatigue strength, ductility and toughness and is decided as India-specific RAFM steel.

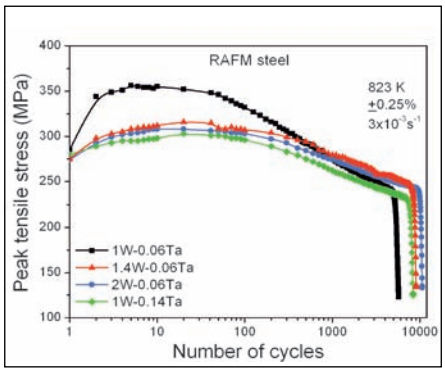

Fig. 2 Cyclic Stress Response of RAFM steel with various tungsten and tantalum contents

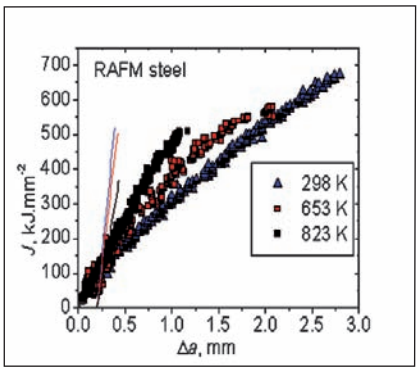

Fig. 3 J-R curves for RAFM steel

Having arrived at an India-specific version, further characterization to assess the performance of the steel with reference to fracture and fatigue crack growth was carried out. Elastic plastic fracture behaviour of RAFM steel was studied at ambient and elevated temperatures. The J resistance curves were established (Figure 3) and fracture toughness corresponding to 0.2 mm crack extension ($J_{0.2}$) has been evaluated as ~106, 131 and 160 kJ.m^{-2} respectively at 298, 653 and 823 K.

FCG behaviour of RAFM is evaluated at 300, 653 and 823 K in both Paris and threshold regimes. FCG results without and with crack closure corrections are presented in Figures 4(a-b). The threshold stress intensity factors for FCG (ΔK_{th}) of Indian RAFM steel and EUROFER 97 are presented in Table 1 for comparison. The effective thresholds ($\Delta K_{eff,th}$) of RAFM steel at R = 0.1 are compared with the ΔK_{th} of EUROFER 97 at R=0.5 as it can be considered to be free from crack closure effects. It can be seen that the FCG properties of the indigenous RAFM steel are meeting the EUROFER 97 at these test conditions.

Table 1: FCG Thresholds of RAFM and EUROFER 97

T(K)	Threshold stress intensity factor, MPa.m$^{1/2}$			
	RAFM (R=0.1)		EUROFER 97	
	ΔK_{th}	$\Delta K_{eff,th}$	ΔK_{th} (R=0.1)	ΔK_{th} (R=0.5)
300	7.80	5.65	9.02	4.73
653	5.56	5.36	--	--
823	7.02	5.24	6.98	5.21

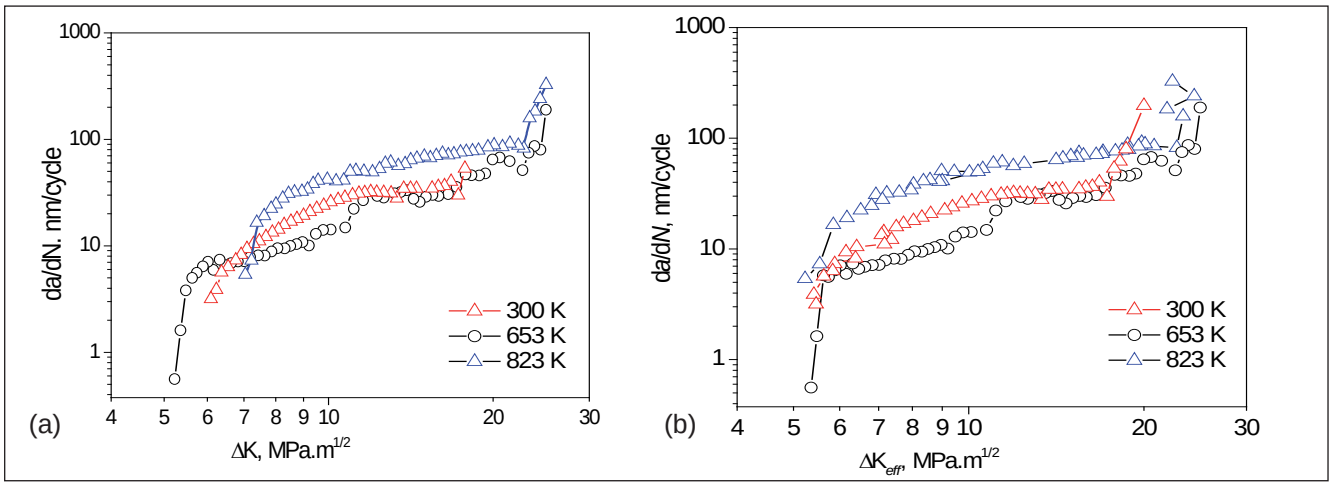

Fig. 4 Fatigue crack growth behaviour of RAFM steel with load ratio 0.1 and frequency 15 Hz at different temperatures (a) Without and (b) With crack closure correction

V.17 Development of Welding Procedure for A-TIG Welding of Type 304 L Stainless Steel Pipes

Major limitations of TIG welding of austenitic stainless steels are due to the limited thickness of material which can be welded in a single pass, poor tolerance to cast variations and low productivity. Thickness of austenitic stainless steel that can be welded in single pass is normally restricted to 3 mm with argon as shielding gas. Therefore, improvements in weld penetration have long been sought in austenitic stainless steel welds produced by TIG welding process because TIG welding results in high quality welds besides providing for precise control of heat input and low cost of the equipment. A novel variant of the TIG welding process called A-TIG or DEEPTIG is known to overcome the limitations. This process involves applying a thin coating of activated flux on the joint prior to welding. The specific activated flux has been developed in the present work for enhancing the penetration during autogenous TIG welding of type 304 LN and type SS316 LN. The use of activated flux produced a significant increase in penetration of 10–12 mm in single pass TIG welding of 304LN and 316 LN stainless steels. Significant improvement in penetration achieved using the activated flux developed in the present work was attributed to the constriction of the arc and as well as reversal of marangoni flow in the molten weld pool. The molten metal in the weld pool flow inwards as the temperature coefficient of surface tension becomes positive due to application of activated flux.

Hence, combined operation of the above two mechanisms only lead to increased penetration by as much as 300% in 304 LN and 316 LN stainless steels. This innovative technology allows faster welding speed, requires reduced joint preparation, consumes less filler wire and involves reduced residual stresses and distortion. Up to 10 mm depth of penetration could be achieved in single pass welding using A-TIG welding. The variable weld penetration i.e inconsistency in weld penetration with increasing welding current was observed when the 316 LN stainless steel welds were produced without flux due to low sulphur content below 50 ppm. A-TIG welding has been found to mitigate variable weld penetration in low sulphur austenitic stainless steels. Overcoming the variable weld penetration using activated flux during autogenous TIG welding of austenitic stainless steels is considered as significant achievement.

Significant improvement in Creep-rupture life and impact toughness (more than 40% increase) have been observed in austenitic stainless steel weld joints made by A-TIG welding process compared to that of the weld joints made by conventional multipass TIG weld joints.

The process has been optimized and the welding procedure has been qualified for fabrication of type SS304 L pipes. Plates of 4 mm thick were rolled into pipe of outer diameter 208 mm and cut to length of 250 mm size. Then A-TIG welding was carried out after the activated flux was applied on the joint area. A-TIG welding was carried out in 1G position at 115 A, and at 125 mm/min of torch speed. Argon was used as the shielding gas at 10 liter per minute. Figure 1 shows the L seam A-TIG weld of the pipe. There was no concavity observed. Figure 2a shows the root side of the L seam A-TIG weld on the pipe. There is complete penetration on the root side. Figure 2b shows the C seam of the A-TIG weld of the pipe. Both the L seam and C seam A-TIG 304 L stainless steel pipe welds passed radiographic examination as per ASME code requirements. The technology will find application in future FBRs.

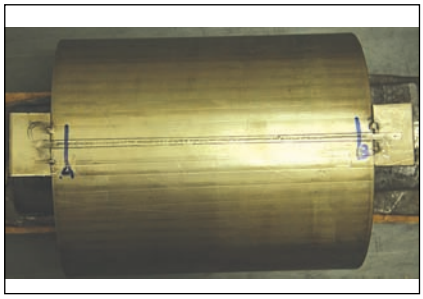

Fig. 1 *L seam A-TIG welding of 304 L stainless steel pipe*

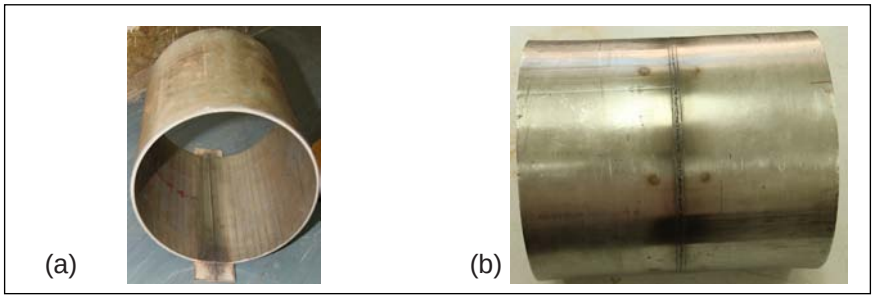

Fig. 2 *304 L stainless steel (a) Root side of the L seam welding (b) C seam A-TIG welding*

V.18 Characterisation of Microstructural Changes and Tensile Deformation of Steels Using Acoustic Emission and Non-Linear Ultrasonic Techniques

Non-destructive evaluation techniques are useful for characterization of microstructures, deformation and crack growth behaviour in metallic materials. The application of nonlinear ultrasonic and acoustic emission techniques during tensile deformation has been studied. In nonlinear ultrasonic technique, high amplitude ultrasonic waves of a particular frequency are made to propagate through the material. The harmonics generated due to interaction of ultrasonic waves with lattice defects, microstructural and substructural features, are detected and their amplitude is used for materials evaluation. In general, the ratio of amplitude of the second harmonic (A2) to that of square of the fundamental amplitude (A1), known as β parameter, is used. On the other hand, in acoustic emission technique, transient elastic waves generated during rapid release of energy from localized sources as a consequence of deformation and fracture processes are detected and dynamic changes occurring in the material are analyzed.

Acoustic emission technique has been explored to study the formation of Lüders bands in ferritic steel. The Lüders bands are localized bands of plastic deformation formed by pinning of dislocations at interstitial atoms. The formation of a Lüders band is preceded by a yield point and drop in the flow stress.

Medium carbon steel in water quenched (WQ, 1223 K for 1 h) and tempered (WQ+T, 923 K for 5 h and 25 h) conditions was studied. The specimens were tensile tested and the acoustic emission signals were recorded using resonant (150 kHz) and broadband (100 kHz – 1 MHz) sensors. Frequency analysis of the acoustic emission signals was carried out.

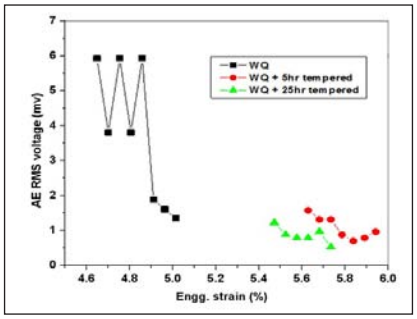

Fig. 1 Acoustic emission rms voltage with engineering strain during Lüders band formation for WQ, 5 h tempered and 25 h tempered specimen

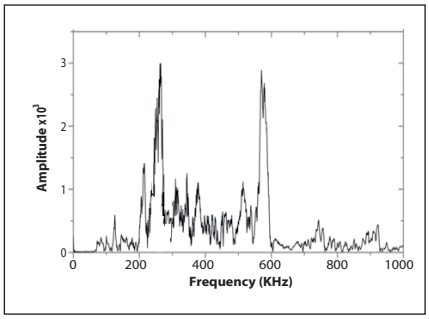

Fig. 2 Acoustic emission dominant frequencies generated during Lüders band region of WQ specimen

The variation of acoustic emission rms voltage with engineering. strain during Luders band region of different specimens is shown in Figure 1. The values of lower yield point and peak rms voltage during Lüders deformation for different specimens are given in Table 1. The results show that the yield stress and acoustic emission rms voltage during Luders band formation decrease for the WQ+T specimens as compared to WQ specimen. The observed results are explained by dissociation of martensite into ferrite and cementite and increase in ferrite size and coarsening of cementite with concomitant reduction in dislocations due to tempering.

Characteristic frequencies were observed in the frequency spectra of acoustic emission signals (Figure 2). The characteristics frequencies of 270 and 590 kHz observed in the water quenched specimen are related to the dislocation pile up breakaway and presence of higher amount of martensite. The frequencies of 100 and 270 kHz for the tempered specimens are related to the dislocation pile up breakaway caused by back stress at grain boundaries and bending stress. The studies establish that acoustic emission technique can be used to study the formation of Lueder bands during plastic deformation of quenched and tempered medium carbon steel.

Table 1: Lower yield point and peak RMS voltage for different specimens

Specimen	Lower Yield Stress (MPa)	AE rms Peak Voltage (mV)
Water Quenched (WQ)	635	5.9
WQ + Tempered for 5h	302	1.61
WQ + Tempered for 25h	288	1.2

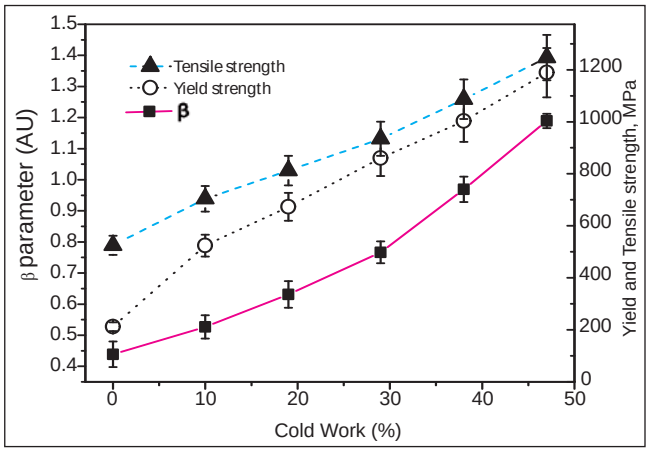

Fig. 3 Variation of β parameter, yield strength and tensile strength with cold work in AISI type 304 stainless steel

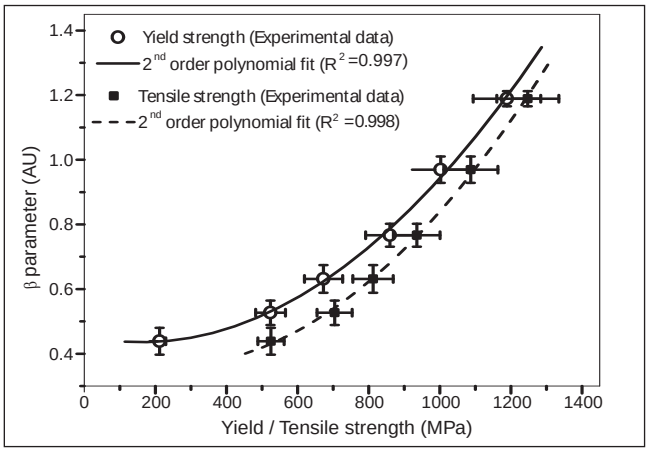

Fig. 4 Variation of β parameter with yield strength and tensile strength

Nonlinear ultrasonic technique has been used for assessment of tensile properties of AISI type 304 stainless steel. The mechanical properties of this type of steel are improved by either cold working or by addition of alloying elements. During cold work, the metastable austenitic stainless steel undergoes microstructural changes and results in increase in yield strength and tensile strength. Nonlinear ultrasonic technique has been explored for non-destructive assessment of tensile and yield strengths.

High amplitude ultrasonic waves with 5 MHz frequency were injected into the specimens and the amplitude of second harmonics generated (10 MHz) was measured. Figure 3 shows the variation of β parameter, yield strength and tensile strength with increasing cold work from 0 to 47%.

The β parameter is found to increase by 170% for a cold work of 47%. Figure 4 shows the variation of yield strength and tensile strength with β parameter. A quadratic relationship (correlation coefficient > 0.997) exists between the tensile strength and the β parameter. This relationship has been investigated by analyzing the microstructural changes. Figure 5 shows the bright field transmission electron microscopy images of solution annealed, 19% and 47% cold worked specimens.

Various changes observed in microstructure during cold work include (i) increase in dislocation density, (ii) dislocation substructural changes and (iii) formation of strain-induced α'-martensite. All these result in generation of higher order harmonics due to distortion which increase in β parameter, yield strength and tensile strength with increase in cold work.

The quadratic relationship between tensile properties and β parameter can be effectively used to quantify the cold work and also to assess yield strength and tensile strength of cold worked 304 stainless steel. It is possible that this type of approach can be directly applied on finished components.

Thus, studies on tempered carbon steel and cold worked stainless steel reveal that acoustic emission and nonlinear ultrasonic techniques can be used to study the changes during tensile deformation and to understand the interaction of changes in microstructures using suitable non-destructive evaluation parameters.

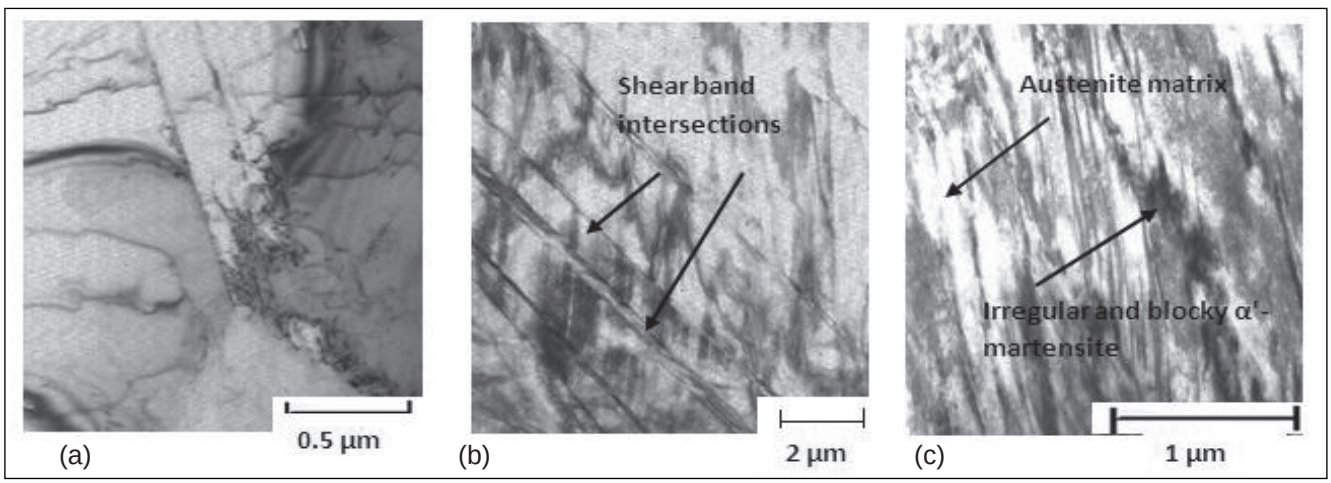

Fig. 5 Bright field images obtained using TEM for a) solution annealed, b) 19% cold worked and c) 47% cold worked specimen

V.19 Application of Resonant Nuclear Reaction for Studying the Minor Alloying Elements in Reactor Structural Materials

One of the main problems resulting from radiation damage of structural materials is the dimensional changes brought about by void swelling; leading to a decreased residence time of the fuel assemblies in the reactor core and lowering fuel burn-up. Among various means to mitigate this effect, addition of fast diffusing alloying elements viz., Ti, Si and P in order to suppress void nucleation has been reported. The fast diffusing species increases the effective vacancy diffusion coefficient and the consequent reduction in the void nucleation rates play a crucial role in imparting significant void swelling resistance to the alloy. There also exists an alternative supposition that the trapping of vacancies with interstitial impurity atoms enhances the probability of recombination hence aiding in reduction of void swelling. In order to model such complex irradiation effects, knowledge of the diffusion behavior of constituent species is essential due to their considerable redistribution during irradiation. Here, the behavior of implanted nitrogen (which is incorporated during processing) and diffusion of silicon (a solute additive) in titanium modified D9 steels as followed by Resonant Nuclear Reaction Analysis (RNRA) is presented.

D9 samples which are implanted with 30 keV nitrogen atoms to fluences of 1×10^{15} and 5×10^{15} nitrogen atoms per square centi meter are respectively designated as low fluence and high fluence samples. Depth profiling of N^{15} has been carried out using the 429 keV resonance of the $N^{15}(p,\alpha\gamma)C^{12}$ reaction. This reaction is ideally suited for obtaining quantitative depth profiles of nitrogen with superior depth resolution (~3 nm at the surface) and high sensitivity (~0.01 at %). The profiling experiments in general involve increasing incident proton energies beyond the resonance energy in 1 keV steps and collecting the gamma rays emitted in an energy window (3–5 MeV for nitrogen profiling) which encompass the photo peak along with the escape peaks. The gamma ray yield in the said energy interval which serves as the signal is proportional to the concentration of the element at depths described by the incident energy. The relationship between the incident energy and the depth at which the reaction is taking place can be established by taking into account the energy loss of protons in the alloy.

The experimental depth profiles of N^{15} in low fluence and high fluence samples obtained by RNRA are shown in Figure 1(b) and 1(c) respectively. The depth profiles in both samples exhibit an asymmetric Gaussian profile near the surface. The experimental data has been fitted into two Gaussians with a variance of 0.95. A simulation of 30 keV nitrogen ions incident on steel using SRIM software shows that the peak damage and the projected range are located around 20 and 40 nm respectively (Figure 1(a)). The peak positions of the fitted Gaussians coincide with the peak damage region and the projected range of implantation, as defined by the SRIM simulation. It is observed that a part of implanted nitrogen atoms is located around the peak damage region in addition to being present at the predicted range of implantation (Rp). A comparison of the relative intensities of nitrogen residing in the peak damage region and implanted regions of the samples show that in the higher nitrogen fluence implanted case, a greater fraction of nitrogen resides in the peak damage region as compared to its lower fluence implantation counterpart. Although several groups have observed similar bimodal distribution, they have ascribed such behavior to ion induced sputtering. An inquiry into this behavior by means of positron annihilation spectroscopy

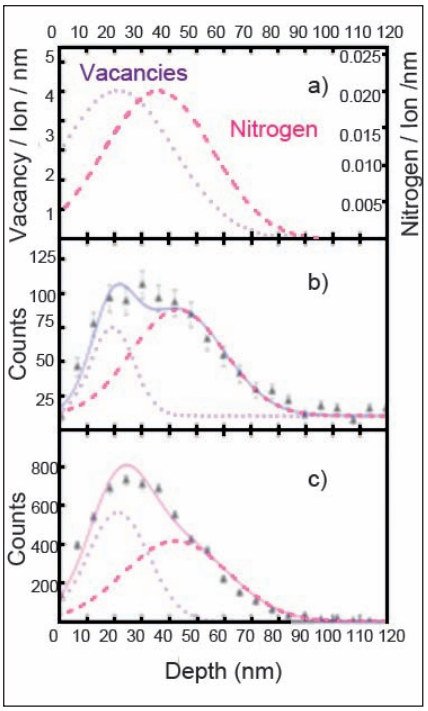

Fig. 1 *(a) Experimental depth profile of N^{15} implanted in steel to a fluence of (b) 1×10^{15} N/cm^2 and (c) 5×10^{15} N/cm^2 using RNRA*

(the details of this experiment is beyond the scope of this article) has revealed clear evidences of nitrogen trapping in vacancy-nitrogen complexes at depths corresponding to the peak damage. And these experiments have revealed that the formation of vacancy-nitrogen complexes could be a cause for the fluence dependent nitrogen redistribution.

As regards to studies on silicon diffusion, D9 samples which are solution annealed are implanted at room temperature with 200 keV ^{30}Si ions to a fluence of 3×10^{16} atoms cm^{-2} using a 1.7 MV Tandetron accelerator. The depth profiling of silicon in ^{30}Si implanted D9 samples was carried out using the 620 keV Yresonance ($\Gamma\sim$ 68eV) of the ^{30}Si (p,γ) ^{31}P nuclear reaction. The experimentally obtained depth distribution of the implanted silicon as illustrated in Figure 2a is a Gaussian profile with centre and full width at half-maximum (FWHM) as 120 and 95 nm respectively. This implanted silicon distribution serves as the marker layer and its broadening is used for following the diffusion behavior of silicon in D9 steel samples. The silicon implanted sample was annealed in steps of 50 K in vacuum for duration of 30 min at each step followed by RNRA experiments after each annealing. It is found that there is no significant change in the width of the implanted profile in the sample up to 873 K with the annealing time of half an hour. After prolonged annealing at 873 K for few hours followed by RNRA experiment at different increments of time, the implantation profile showed a discernible change after eleven hours (Figure 2a). Further, four Si implanted D9 samples were annealed independently at four different temperatures from 923 to 1073 K in steps of 50 K for different durations. Figures 2a & 2b show the diffusion profile of silicon in the temperature interval of 873 to 1073 K, and the annealing time for each temperature is indicated in the figures.

A model of an infinitely thin source diffusing into a semi-infinite system is considered and the profile broadening for each of the annealing temperatures T is used to deduce the diffusion co-efficient D(T). The Arrhenius plot is shown in Figure 3 and activation energy of 2.1 eV is obtained for the silicon diffusion in D9 steel. The activation energy deduced here for silicon diffusion is much greater than the experimentally determined effective vacancy migration energy (1.13 eV) in solution-annealed D9 steel. Hence, silicon diffusion in the solution annealed D9 steel is regarded as a vacancy-assisted mechanism.

The present value of activation energy for silicon diffusion is lower than a previously reported value of 2.43 eV for silicon diffusion in fcc Fe. Addition of fast diffusing solutes can increase the vacancy migration and in turn the diffusion of solvent atoms. Evidences exist in the literature with respect to the increase in the diffusivity of major alloying elements like Fe, Cr and Ni due to silicon additions. It should be noted that another fast diffusing species, namely titanium is present in D9 steel. Titanium being an oversized element in the D9 alloy would diffuse via vacancy mechanism. Hence, the the relatively lower activation energy obtained here for silicon diffusion in solution annealed D9 steel is ascribed to the increased vacancy migration due to the presence of both silicon and titanium in D9 steels. Therefore, the present observation strongly suggests that the synergetic effects due to the presence of various fast diffusing solutes contribute to enhanced vacancy mobility and the consequment void swelling suppression.

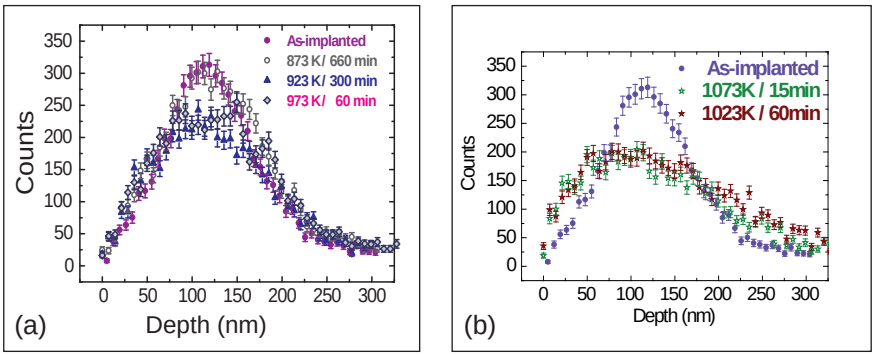

Fig. 2 *The depth profile of implanted ^{30}Si determined by RNRA measurements at different annealing temperatures. Different time duration of annealing as indicated in figure was followed in order to obtain a measurable broadening*

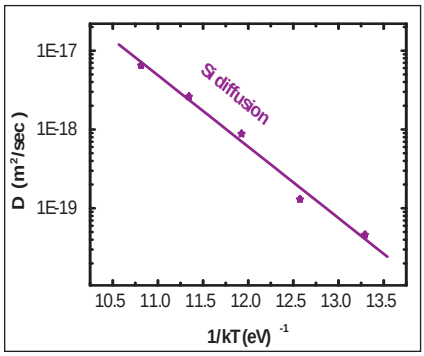

Fig. 3 *Arrhenius plot for the determination of activation energy for Si diffusion in D9 steel*

V.20 Characterisation of Magnetron Sputtered ZrN Coatings

Transition metal nitride coatings such as ZrN and TiN have been extensively studied for industrial applications, such as hard coatings, diffusion barriers in semiconductor technology, optical applications for heat mirrors and decorative coatings because of their outstanding properties. Thin films are deposited by various methods: evaporation, spray pyrolysis, chemical vapour deposition and sputtering. In the present work, microstructural characterization of ZrN films sputter deposited from a zirconium target in a mixture of Ar/N_2 using pulsed direct current magnetron sputtering is investigated as a function of nitrogen flow rate and substrate temperature. The pulsed magnetron sputtering is capable of reducing the arcing event, which results from charge accumulation on target surfaces. It consequently prevents the deterioration of film properties and maintains a stable deposition process.

A zirconium target of 76 mm diameter and 2 mm thickness and purity of of 99.9% was used to deposit zirconium nitride films of about 0.8 mm thickness at 873 K on to Si (100) substrates at different nitrogen flow rates. The flow rate of Ar (99.99%) was varied in the range of 50 to 35 standard cubic centimeter per minute (sccm) and flow rate of nitrogen was also varied using mass flow controller in the range of 0 to 15 centimeter per minute such that total flow of the gases inside the chamber was at 50 sccm during the sputtering.

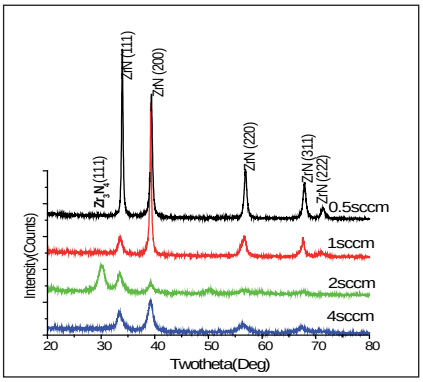

Fig. 1 *XRD patterns of ZrN thin films deposited on Si (100) substrate at 773 K and different N_2 flow rates*

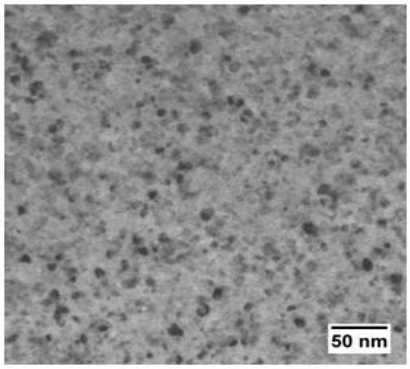

Fig. 2 *Bright field image of ZrN thin film on KCl crystal at 2 sccm of nitrogen flow rate showing nanocrystallites of size in the range 4 -9 nm*

The substrate temperature was varied from 300 to 873 K .

XRD patterns of the thin films deposited as a function of nitrogen flow rate at 873 K is shown in Figure 1. The figure shows that up to 1 sccm of nitrogen, only ZrN is present while films deposited with N_2 flow rates > 1 sccm show a mixture of phases such as ZrN and Zr_3N_4. At higher nitrogen flow rates (6 sccm), the films become amorphous. This can be explained by the absence of the stable phases in the nitrogen rich zone of Zr-N system. The crystallite size of the ZrN also decreases with increasing nitrogen flow rate. Increase of nitrogen partial pressure was accompanied by the decrease of the partial pressure of argon in order to keep the total flow rate constant. As a result, the overall sputtering yield of the target is found to decrease due to lower ionization of molecular nitrogen compared to argon, which causes a continuous decrease in the deposition rate of the films. The reduction in the crystallite size with increase in the nitrogen flow rate could be due to decrease in the film thickness for a constant time of deposition. ZrN films were also deposited in the temperature range 300-873 K and at constant N_2 flow rate of 1 sccm. The films are generally polycrystalline in nature and form with fcc-ZrN structure even at room temperature. The crystallite size calculated using (200) reflection was found to increase with increase in temperature up to 773 K due to increased ad-atom mobility at higher deposition temperatures. HREM studies showed that the films deposited in pure argon as the sputtering gas are nanostructured with nanocrystallites sizes in the range 40-70 nm and film contains hcp-Zr phase. The zirconium nitride films deposited ≥1 sccm flow rate of nitrogen show nanocrystallites in the range of 4-9 nm and the film contains fcc-ZrN and o-Zr_3N_4 phase(Figure 2). The study illustrates the tunability of the microstructure of the Zr-N films, especially the crystallite size and phase formation as a function of nitrogen flow rate and substrate temperature.

V.21 Enhancing Corrosion and Biofouling Resistances Through Superhydrophobic Surface Modification

The lotus leaf is a famous example of a naturally occurring superhydrophobic surface, where water droplets falling on them bead up and roll off due to 'lotus effect'. Because of their interesting properties, basic research and industrial applications for superhydrophobic surfaces have attracted significant attention. When a liquid droplet contacts a solid substrate, it either remains as a droplet or spreads out on the surface to form a thin liquid film, a property normally characterized using contact angle measurements. A solid substrate is called superhydrophobic when the contact angle of water on it is larger than 150°; water drops just bounce-off the surface. On the other hand, when the WCA on a surface is almost 0°, it is called superhydrophilic. Although, the lotus leaf appears to have a smooth surface, it consists of micro-nano epidermal structures. Moreover, they are often covered with tiny wax crystals of a few hundred nanometers size. This combination of micro-nanostructures, with a hydrophobic chemistry, generates the phenomenon of superhydrophobicity in lotus leaf with water-droplets on surfaces exhibiting contact angle above 150°.

The biomimetic superhydrophobic surfaces due to several potential industrial applications such as corrosion protection coatings, anti-snow sticking and monument protection have invoked much interest in recent times. A simple and novel approach for generating superhydrophobic

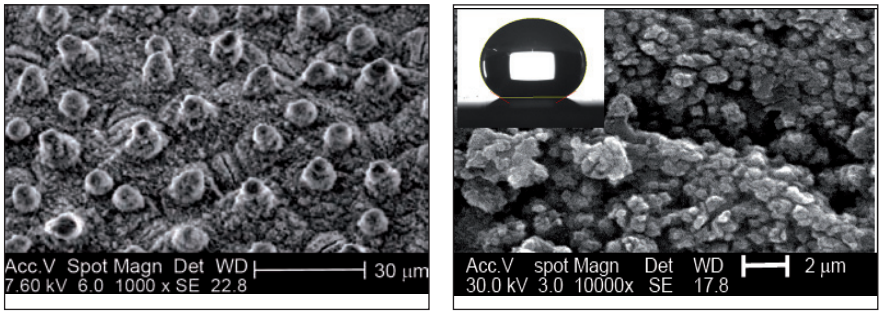

Fig. 1 *SEM images of (a) lotus leaf showing micro-nano scale papillae (b) superhydrophobic titanium surface; inset shows the contact angle 157±2°*

surface modification of titanium and 9Cr-1Mo steel has been developed. The modified surfaces showed enhanced corrosion and bio-fouling resistance. Titanium, used in condenser in nuclear power plants and dissolver vessels in spent nuclear fuel reprocessing plants face an unresolved problem of corrosion and biofouling due to its high biocompatibility and surface hydrophilicity. 9Cr-1Mo steel a structural material in power plants, easily forms rust layers during fabrication, storage and service conditions. By suitable modification of the surfaces, corrosion initiation could be avoided or delayed as the modified surfaces do not provide conditions conducive for corrosion attack. Thus, generating superhydrophobic surface with water repellency is an attractive option to prevent and delay the onset of corrosion processes on engineering components in natural atmosphere.

A close microscopic examination of the lotus leaves using AFM and SEM, revealed micro nano-structures, with papillose epidermal cells and an additional layer of epicuticular waxes that provide the water repellency as shown in Figure 1(a). As air is trapped between the micro-nano features, the water drops rest only on the tip of the surface microstructures, thereby minimizing the interfacial area between the surface and the water drop. Having studied the lotus leaf structure in detail, attempts were made to fabricate superhydrophobic titanium. In order to achieve the required surface roughness, a prerequisite for better adhesion of the coating as well as requirement for a surface to exhibit superhydrophobicity, four different types of surface finishes were prepared:

- type 1-anodised,
- type 2-anodised and pickled for 2 minutes,
- type 3-polished and subjected to extended pickling for 10 minutes and
- type 4-as polished specimen.

Anodisation was carried on the titanium coupon at 30 V for a duration of 1 h using cylindrical titanium cathode and a mixture of 1 M H_2SO_4 and 0.16 M HF as electrolyte. The four samples with different surface finishes were

dipped in 0.5 M myristic acid/ stearic acid and kept for 10 days at 310 K. After 10 days, the samples were taken out and baked at 403 K in order to stabilize the coating.

SEM image of myristic acid coated type 1 titanium surface (Figure 1b) shows rough surface with bunch like projections which increase the effective surface area and enable the titanium surface to give high contact angle of water. It is believed that the gaps between the projections act as valleys where air gets trapped so that water minimizes its contact area with the surface leading to an increase in the contact angle of water.

The "tail" of the fatty acid is a long hydrocarbon chain, making it hydrophobic and the "head" of the molecule is a carboxyl group which is hydrophilic. While coating the fatty acid on the surface, the head (hydrophilic end) gets adhered to the surface leaving the tail (hydrophobic end) upwards, making the coated surface hydrophobic. The measured contact angle of the surfaces indicated that precoating treatment by anodisation followed by dip coating in myristic acid/ stearic acid led to the development of superhydrophobic surfaces with a contact angle of 157°±2°. Hydrophobic surface modification of 9Cr-1Mo steel involved two steps: (i) pretreatment to modify the surface roughness by polishing the coupons and etching in ethanol: nitric acid mixture in the ratio of 9:1 and (ii) dip coating in 0.5 M myristic acid, followed by baking at 383 K for 1 h. A thick and uniform hydrophobic coating was obtained in 9Cr-1Mo when the sample was immersed in myristic acid for 24 hour (contact angle of water 107±2°), as shown in Figure 2.

The stability of the superhydrophobic coating in seawater and nitric acid medium (0.1 N, 0.5 N and 1 N) was studied using electrochemical impedance spectroscopy (EIS). Variation in open circuit potential (OCP) with time was observed for coated and polished titanium specimens in 0.5 N and 1 N nitric acid showed nearly noble and steady state. It is evident from Figure 3 that the shifting of OCP towards the noble direction indicated greater passivity of the protecting layer on the surface. Nyquist plot showed that there was noticeable increase in diameter of the semicircle for coated titanium surface compared to the polished surface. The increase in semicircle radius normally showed an increase in stability of the passive film; also, the increase in charge transfer resistance which is inversely proportional to the corrosion rate of the system.

The 9Cr-1Mo steel also showed a similar behavior. The corrosion properties of the coated surfaces were tested by keeping the uncoated and coated 9Cr-1Mo steel samples in seawater for about 24 h. The results showed that the surface of uncoated steel corroded with visible accumulation of rust while the coated 9Cr-1Mo steel surface did not show any sign of corrosion. Therefore, it could be inferred that the hydrophobic coating acts as a physical barrier between the metal and environment leading to increased corrosion resistance.

Superhydrophobic titanium samples were surface sterilized and exposed to seawater for about 24 h. The samples were then rinsed, air dried and flooded using acridine orange - a fluorescent dye. The stained samples observed under an epifluorescence microscope revealed their ability to resist microbial attachment. The present study showed that the superhydrophobic titanium surfaces had less microbial attachment in contrast to significant biofilm formation in control sample which is superhydrophilic in nature.

The present study confirmed that the surface modification of titanium by anodization and 9Cr-1Mo steel by etching and then coating with a low surface energy material lead to the formation of superhydrophobic and hydrophobic surfaces respectively with good resistance to biofouling and corrosion. Extensive studies are under progress in this direction to study the practical feasibility of implementing this coating technology for real life applications.

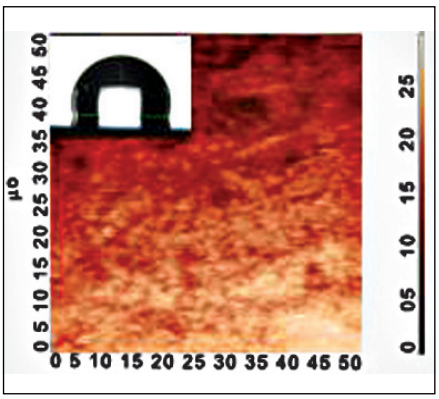

Fig. 2 *AFM image of hydrophobic 9Cr-1Mo steel. Inset shows the contact angle 107±2°*

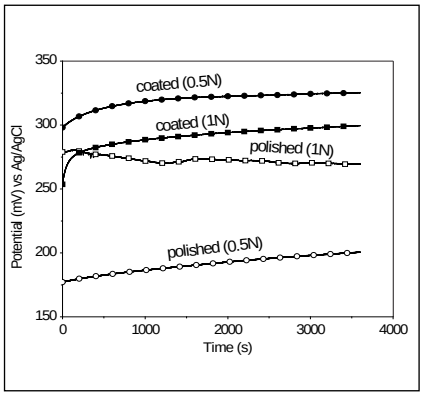

Fig. 3 *Open Circuit Potential-time measurements for polished and superhydrophobic surfaces in 0.5N and 1N nitric acid*

V.22 Calculation of Thermo- Physical Properties of UO_2 Using ab-initio and Molecular Dynamics Simulations

Continuous production of defects and fission products due to exposure to high temperature and pressure prevailing in the reactor causes complex microstructural changes in the fuel material. These changes occurring across a range of time and length scales need multi scale modeling for the description. Our approach will be to first calculate properties for the perfect system and then subsequently add the defects and other complexities to address the issues associated with the real material. In this study we have investigated UO_2 as commonly used fuel material. Simple density functional theory based calculations shows UO_2 to be metallic but experimentally it is an insulator. Incorporating an appropriate on site coulomb repulsion of U_{eff} = 4 eV for the strongly correlated 5f electrons of uranium in the DFT+U formalism reproduces the correct anti ferromagnetic (AFM) insulating ground state of UO_2. As DFT can give only the properties at 0 K, for temperature higher than 0 K Quasi Harmonic Approximation along with density functional perturbation theory (DFPT) calculations is being used. The instability of oxygen sub lattice in UO_2 at temperatures above 2300 K limits the applicability of QHA based approach. So to predict the high temperature behavior, we have used molecular dynamics simulations. In QHA, the anharmonicity of the atomic interactions is included in an approximate way whereas molecular dynamics automatically considers full anharmonicity of the atomic interactions. We have used two of the available potentials for UO_2-Y Amada and Basak potentials.

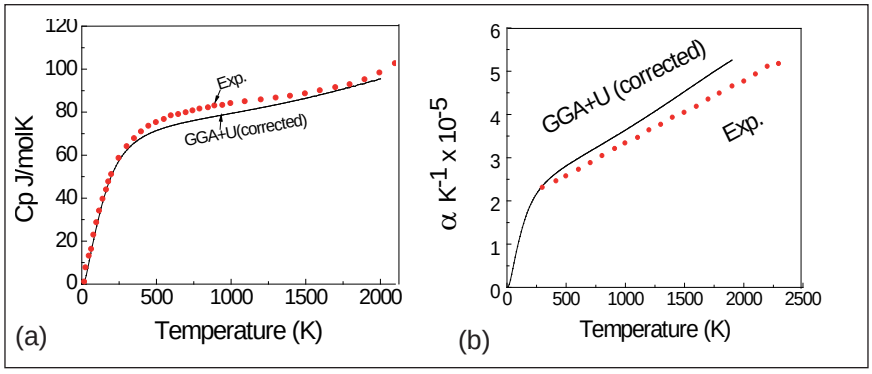

Fig. 1 *(a) Calculated specific heat at constant volume (GGA+U) with pressure correction and experimental values as a function of Temperature (b) Calculated and experimental thermal expansion coefficient vs temperature*

Density functional theory calculations are done with a PAW-PBE pseudo potential and Generalized Gradient Approximation for exchange correlation functional using Vienna ab-initio Simulation Package (VASP). The strength of onsite Coulomb repulsions (U_{eff}) for 5f electrons of uranium is taken to be 4 eV which gives the correct insulating AFM ground state of UO_2 with a band gap of 2 eV. But this approach over-predicts the lattice parameter which implies an under binding of the system. It is observed that applying a pressure of 7 GPa reproduces the lattice parameter and bulk modulus close to experimental values.

The pressure corrected AFM insulating ground state is used for all further calculations of thermal properties. A 48 atom supercell with a 4x4x3 Monkhorst-Pack grid for k-point sampling is used. The force constants are calculated using density functional perturbation theory (DFPT) for seven different volumes and phonon frequencies are obtained for each of these volumes. These phonon frequencies are used to calculate free energy which on minimization with respect to volume for different temperatures will give equilibrium volume and bulk modulus at the corresponding temperatures. The lattice contribution to specific heat is also calculated using the phonon frequencies for corresponding temperatures.

The calculated specific heat (Figure 1(a)) matches almost exactly with experimental values at lower temperatures and fairly well at higher temperatures less than or equal to 1900 K. This shows that up to this temperature the contribution from electrons and defects is small. The computed variation of thermal expansion coefficient (Figure1(b)) also closely matches the trend of experimental values. In this system, above 1900 K the anharmonicity becomes too large and some of the phonon modes become unstable signaling the impending instability of oxygen sub lattice. As a consequence QHA cannot be

used above this temperature. For calculating thermal conductivity, phonon life time is required which QHA does not readily give. Phonon life times can be obtained from molecular dynamics simulations.

To study high temperature properties we have done classical molecular dynamics simulation by using Yamada and Basak potential. The optimized simulation cell is 10 x 10 x 10 of conventional unit cell which contains 12000 atoms. The coulomb interactions between the atoms are computed by using Ewald summation method. The thermo physical properties which include thermal conductivity, specific heat, mean square displacement, and radial distribution function are calculated from 300 - 3000 K.

The temperature dependence of the thermal conductivity of single crystal UO_2 is computed by Green-Kubo formalism using fluctuation dissipation theorem. By using the optimized cell size several simulations were done for different temperature (300 -2000 K) for 4ns with a time step of 1fs. Since the present calculations give only the lattice contribution to the thermal conductivity, at higher temperature we added the electronic contribution. At high temperature the calculated values are in good agreement with experiment, at low temperature the discrepancy between the experimental and calculated values

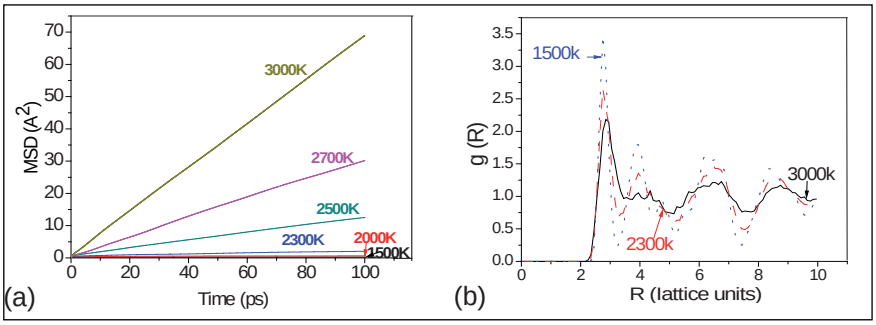

Fig. 2 *(a) Mean square displacement of oxygen as a function of time for various temperatures and (b) Radial distribution function of oxygen atom for various temperatures*

can be due to inadequacy of the inter atomic potential or due to the quantum effects, which become important at low temperatures and are beyond the scope of classical molecular dynamics.

The structural aspects of UO_2 at high temperatures are investigated by calculating the radial distribution function and mean square displacement. The above calculations show the super ionic diffusion of oxygen atom from the oxygen sub lattice. The oxygen sub lattice is fairly stable up to 2300 K; above 2300 K the oxygen sub lattice become unstable and oxygen atoms start diffusing; this is clearly visible in mean square displacement, which remains constant up to 2300 K and increases linearly with time beyond this temperature (Figure 2(a)). The oxygen-oxygen correlation at three different temperatures is shown in the Figure 2(b). Above 2300 K there is a decrease in the sharpness of the peaks; some peaks have disappeared or broadened, which is a signature of loss of correlation between the oxygen-oxygen atoms which confirms the diffuse transition of UO_2 above 2300 K. This diffuse transition is also visible in specific heat calculations as a peak at 2300 K.

From the above study it is clear that DFT calculations along with QHA is able to give specific heat and thermal expansion at low and intermediate temperatures but it does not give clear information about the diffuse transition occurring at high temperature except for some signature in terms of softening of some phonon modes. On the other hand, molecular dynamics has given higher temperature properties correctly and predicted the diffuse phase transition at 2300 K, which is clear from mean square displacement and radial distribution plots. Thermal conductivity calculated from molecular dynamics simulations also shows a good agreement at high temperatures.

V.23 Scanning Tunneling Microscopy Studies Unveiling the Mechanisms of Electron Field Emission in UNCD and Diamond Nanowires on Si

Scanning tunneling microscopy has been used to study the mechanisms of electron field emission in smooth ultra nanocrystalline diamond (UNCD) and diamond nanowire thin films grown by microwave plasma enhanced chemical vapour deposition. CH_4 (1%)/Ar (99%) plasma is used for growing UNCD film without any intentional heating of Si substrate. Plasma with CH_4

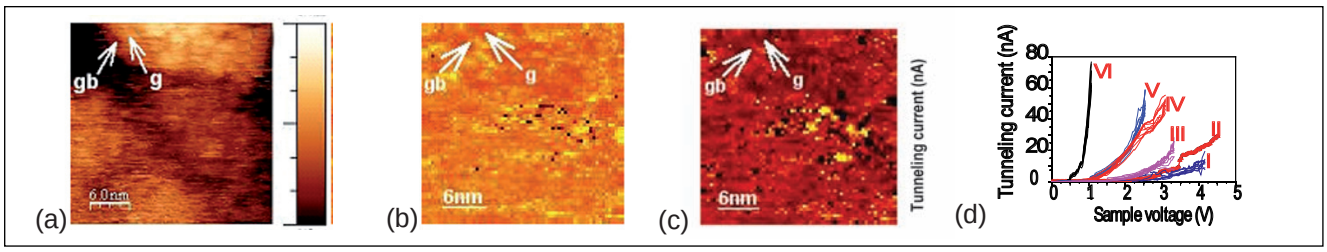

Fig. 1 *(a) STM image from N-implanted UNCD (b) CITS current map (c) CITS conductivity map (d) STS from as-prepared (I,II), N-implanted (III,IV) and post-annealed (V,VI) UNCD*

(6%) and N_2 (94%) is used for growing diamond nanowire film on Si substrate at 1023 K.

Ultra-nanocrystalline diamond (UNCD) films contain diamond grains of (~5 nm) size with graphitic (sp^2) grain boundaries (~1 nm) between them (STM not shown). These grain boundaries behave as field emission sites and the smooth UNCD films show good electron field emission (EFE) characteristics without the need for complicated process of fabrication of an array of sharp tips and has applications in flat panel displays, high frequency electronic devices, etc. Field emission properties of UNCD get enhanced upon nitrogen doping, as measured from a home made set up in tunable parallel plate capacitor configuration. Energetically N favours to occupy the grain boundaries, since the grains of ultra nanocrystalline diamond are extremely small and does not favour the substitutional incorporation of the N species into the grains. Presumably, there are two possible mechanisms by which the incorporated nitrogen residing at the grain boundaries can enhance the EFE properties of the films, namely (i) the conducting-channel process, which is the formation of a conducting path and emission along the grain boundaries and (ii) the transfer-doping process, which is the STM has been used to study the mechanisms of electron field emission in smooth ultra nanocrystalline diamond and diamond nanowire thin films grown by microwave plasma enhanced chemical vapour deposition. CH_4 (1%)/Ar (99%) plasma is used for growing UNCD film without any intentional heating of Si substrate. CH_4 (1%)/Ar (89%)/ N_2 (10%) plasma is used for growing diamond nanowire film on Si substrate at 1023 K. Ultra nanocrystalline diamond films are doped with nitrogen by implanting with 75 keV nitrogen ions at a fluence of 5×10^{15} ions/cm^2 and postannealing at 873 K. STM and CITS images of N-implanted UNCD is shown in Figure 1. Diamond grain size has reduced to 3 nm as seen in Figure 1(a) and grain boundary width has increased compared to as-prepared UNCD, implying that there is increase in sp^2 content upon implantation. Figure 1(b) and 1(c) are CITS images taken at a substrate bias of -3.255 V showing current mapping and conductivity (dI/dV) mapping respectively. These images show that grain boundaries are the prominent electron emitters and their conductivity is larger than that of the grains, implying that conducting-channel process is responsible for field emission. STS spectra (I-V) from different positions on diamond grains and graphitic grain boundaries in as-prepared (I, II), N-implanted (III, IV) and post-annealed (V, VI) samples are shown in Figure 1(d). In each pair, the steeper curve corresponds to grain boundary. It shows significantly that local electron emission is better from the grain boundaries. Also local electron emission is higher in N-implanted sample and gets further enhanced upon post-annealing. The bandgap is measured to be 4.8 eV at the grain and 3.8 eV at the grain boundary for as prepared UNCD. Reduction in the bandgap of the grain is consistent with theoretical predictions of 25% reduction in bandgap of nanodiamond upon N doping and also the introduction of density of states in the bandgap, caused by increase in sp^2 content

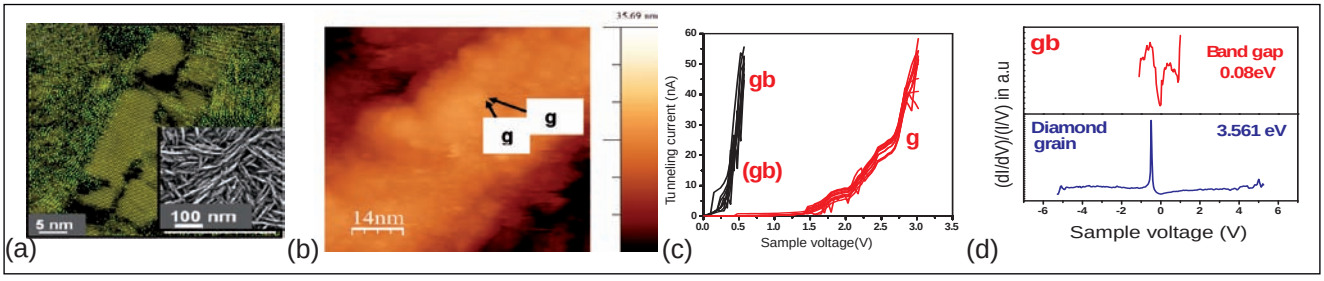

Fig. 2 *(a) DF HRTEM of DNW film showing diamond nanowire (yellow) and graphitic (green) sheath around it. SEM image is in the inset; (b) STM image from part of a DNW; (c) STS spectra from grain and grain boundary; (d) Variation of normalized conductance versus Voltage*

and new bonds at the diamond grains.

Diamond nanowire films also show better field emission properties compared to as-prepared UNCD and XPS measurements show nitrogen bonding with carbon in this film. Inset of Figure 2(a) shows SEM image of diamond nanowire films and diamond nanowires of 30 nm diameter and 150 nm length are seen. Figure 2(a) shows dark field HRTEM revealing that diamond nanowire is only of 5 nm diameter and there is a sheath around it which is composed of graphite and diamond grains of diameter 2-5 nm. Figure 2(b) is the STM image taken on part of a DNW surface which reveals diamond grains and graphitic grain boundaries in the sheath of the nanowire. CITS images (not shown) show that graphitic grain boundaries within the sheath are the prominent electron emitters and have higher conductivity. It is also obvious from the STS spectra (Figure 2(c)) where grain boundary shows better local electron emission. Like in UNCD, the conducting-channel process is the mechanism responsible for the field emission. From the variation of normalized conductance $\frac{dI/dV}{I/V}$ versus voltage (Figure 2(d)), band gap is measured to be 3.56 eV, implying N-doping and grain boundaries show nearly metallic behaviour. Lower bandgap of the grains and high density of grain boundaries within the nanowire is responsible for the enhanced field emission properties of diamond nanowire film.

V.24 Decorated Carbon Nanotubes Hybrids for Gas Sensor Applications

Carbon nanotubes are generally grown by chemical vapor deposition on well dispersed, nanosized transition metal catalysts like Fe, Co, Ni etc., and using a carbon containing source. While the physical deposition of these catalysts and subsequent thermal treatments offer the possibility of generating such catalyst particles, holding the catalyst nanoparticles in thermally stable porous templates is a simpler alternative and it also overcomes the agglomeration of catalyst particles at high temperature. Depending upon the catalyst support interaction, the carbon nanotubes growth can be tip growth or base growth as depicted in Figure 1a. The as grown carbon nanotubes generally contain catalyst material, support material and other forms of carbon called soot and thus need to be purified.

We have synthesized few walled-carbon nanotubes by thermal chemical vapor deposition (TCVD) at 1173 K using Fe and Mo as catalyst loaded on to porous MgO support and using methane as the carbon source. The as grown few walled carbon nanotubes were subjected to mild and multistep purification process to get high pure few walled carbon nanotubes. Further, surface was functionalized with OH and COOH groups to make them wettable by SnO_2 molecules and provide sites for nucleation and growth for SnO_2 nanoparticles. The procedure involved vigorous sonication of five milli gram of functionalized few walled carbon nanotubes in DM water and then slow addition of one gram of $SnCl_2$. This results in a colloidal solution due to hydrolysis of $SnCl_2$ in to $Sn_4(OH)_6Cl_2$. To this colloidal solution 5 M HCl was added drop by drop till the solution becomes clear. The precipitate was washed thoroughly and then dried overnight at 393 K. The morphology and uniformity of SnO_2 decoration on few walled carbon nanotube were investigated using a FEG SEM. Further, the spatial isolation of these attached SnO_2 and their crystalline orientation were investigated by HRTEM. In addition, crystalline phase of the SnO_2 and

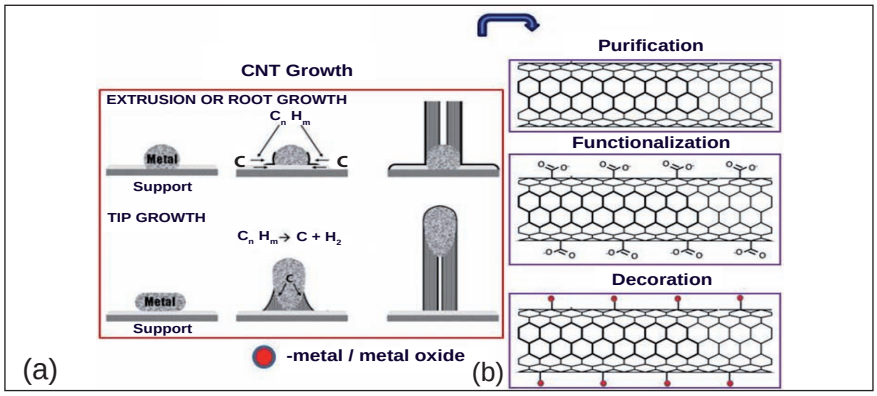

Fig. 1 *(a) Carbon nanotube growth mechanism on supported catalyst and (b) The steps involved to get decorated carbon nanotube like : purification, functionalization and decoration*

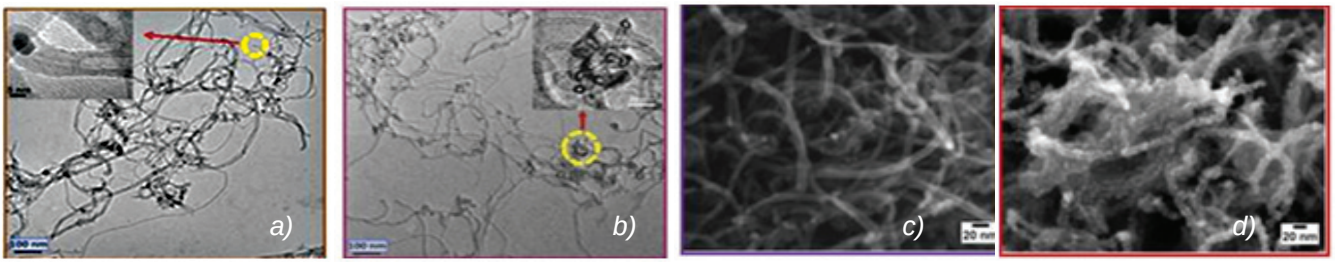

Fig. 2 *(a) First step - removes support, (b) 2nd step - removes trapped catalyst, (c) High pure few walled carbon nanotube and (d) SnO_2 decorated carbon nanotubes*

the few walled carbon nanotube were studied by XRD. Finally, the SnO_2 decorated few walled carbon nanotubes were dispersed in isopropyl alcohol and spin coated on an interdigitated electrode patterned on an alumina substrate. This configuration acts as a device consisting of random networks of SnO_2 decorated few walled carbon nanotubes between the electrodes. The gas sensing characteristics of this device towards ammonia gas and ethanol vapor was investigated.

The electrical conductivity measurements of the sensor were carried out in argon atmosphere. The resistance of the few walled carbon nanotube and few walled carbon nanotube/SnO_2 random networks at room temperature is 1.55 MΩ and 1.01 kΩ, respectively. Electrical conductivity in the present system can be visualized as the flow of current through the highly conducting carbon nanotube modulated by the decorated semiconducting nano-particles and thereby makes its conductivity to fall between highly conducting carbon nanotube and highly insulating SnO_2.

It is well known that SnO_2 is a wide band gap semiconductor with very high resistivity and does not show any reaction with the analyte at room temperature. Inherent oxygen vacancy and interstitial Sn in the SnO_2 makes it to behave like an n-type semiconductor at temperatures above 473 K. When SnO_2 is exposed to analyte, it adsorbs the vapor and catalytically decomposes it and injects the electrons to enhance the conductivity. On the other hand, the conduction in the carbon nanotube is ballistic at room temperature. However, it behaves like p-type semiconductor due to surface adsorbed O^{2-}. Increase of electron concentration at elevated temperatures in SnO_2 reduces the hole current in the carbon nanotube, which makes the Fermi level in carbon nanotube move near to the band center and hence any small disturbance can make it to drift towards conduction band (n-type) or valence band (p-type). Hence, the electron or hole current depends on the reaction of the analyte with SnO_2 and few walled carbon nanotube.

This property of the few walled carbon nanotube and SnO_2 is effectively utilized to get selective gas sensor material. The present study has shown the different response of the decorated few walled carbon nanotubes towards ethanol and ammonia. Here, both the analytes are electron donors. Hence, the p-type few walled carbon nanotube shows the increase in resistance irrespective of temperature. Whereas, the few walled carbon nanotube-SnO_2 hybrid sensor shows a temperature dependent behavior for these analytes (Figure 2a to 2d).

As a result of above studies we get conclusive evidence on switching of the conduction mechanism between 'n' & 'p' type dictated by temperature and nature of the analyte gas. This new observation can be potentially exploited for the development of a new family of gas sensors with both high sensitivity and selectivity. The selectivity is achieved by the virtue of the narrow band gap of few walled carbon nanotube which aids significant changes in the resistance values in combination with SnO_2, whose conductivity is influenced by the analyte gases.

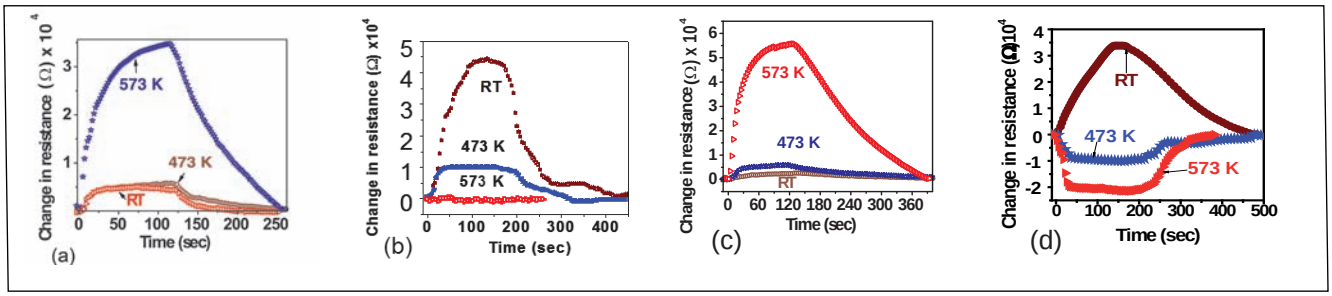

Fig. 3 *Gas sensing response at two temperatures for ammonia and ethanol in few walled carbon nanotube (a) Ammonia (b) SnO_2 – Ammonia (c) Ethanol and (d)SnO_2 – Ethanol*

V.25 Micro Raman Studies on Silicon Microcantilevers

A micro cantilever (MC) is a micro meter sized fixed free beam structure and can act as a physical, chemical or biological sensor by detecting change in its bending (static mode) or vibration frequency (dynamic mode). When used in atomic force microscopy (AFM), a thin layer of aluminum or gold is deposited onto the MC (bimaterial) to enhance the surface reflectivity for optical detection. However, mismatch in the coefficient of thermal expansion between two materials bonded in bimetallic AFM tip results in thermal bending related deformation. Interestingly this property can be used to detect an external stimulus of temperature change and absorbed power using these bimaterial cantilevers.

Knowledge of the temperature distribution and mechanical stress on the bimaterial cantilever is critical and depends on various mechanisms. Micro Raman spectroscopy is an interesting technique to study thermometry and stress distribution in micro systems. The combination of Raman spectroscopy with optical microscope systems enables the incident beam to be focused to a spot with a diameter of 1 μm. Thus, it is capable of analyzing the local temperature and stress on a micrometer scale. It is a non-destructive, fast and accurate technique.

Raman spectra can be used to estimate the temperature information of the sample in three different ways viz., the ratio of anti-Strokes to Strokes intensities, Raman shift and Raman width broadening due to rise in temperature.

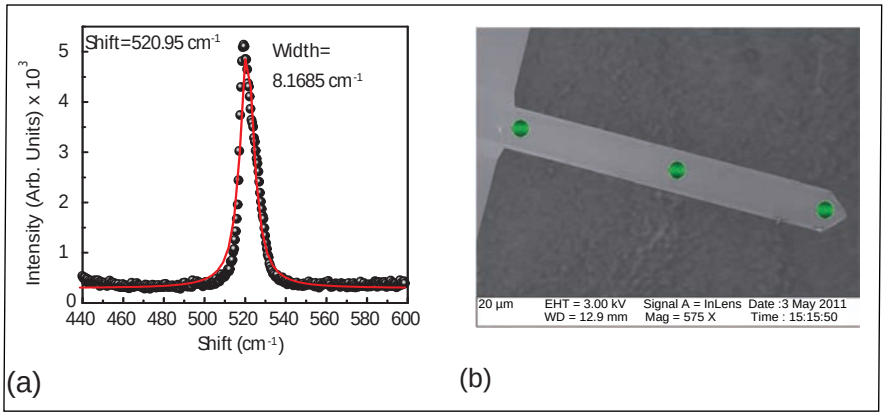

Fig. 1 *(a) Raman shift at room temperature on the substrate of the cantilever with Lorentzian fit (b) Three different positions on microcantilever where Raman spectra was recorded*

Mechanical stress may also affect the frequencies of the Raman modes. Stress or strain in Raman measurements can be obtained via so-called phonon deformation potentials, which are linear coefficients linking the change in the phonon frequency and the strain or stress in the material. Using the phonon deformation potentials, the stress (σ) can be estimated as $\sigma = -518\,\Delta\omega$, where $\Delta\omega$ is difference between Raman shift measured with and without stress and expressed in cm^{-1} and σ is expressed in MPa.

Thermometry of commercially available tip less microcantilevers are studied (Figure 1(a)) using Renishaw (inVia) micro-Raman spectrometer. MC is made of single crystal n-type Si and is coated with Al. The dimensions of the cantilever are 450 μm long, 40 μm wide and 2.5 μm thick. Al coating thickness is 30 nm. All spectra were excited with visible (514.5 nm; power 40 mW) laser light and collected in the backscattering configuration.

First the experiment was performed on the substrate of the cantilever at room temperature and the observed Raman shift and width are 520.95 and 8.16 cm^{-1}, respectively which are close to ideal value (Figure 1(a)). Then the experiment was repeated at three different positions on the cantilever namely fixed, middle and free ends of the cantilever (shown in Figure 1(b)) and by varying the temperature of the MC from -83 to 573 K in steps of 25 K using the cold-hot cell. At every step, Raman data was recorded at three positions of MC. Figure 2(a) shows the variation of Raman Shift with temperature at three different positions of cantilever. The graphs are linearly fitted. Raman shift changes with a rate of -0.021, -0.026 and -0.031 cm^{-1}/K at fixed, middle and free ends of the cantilever respectively. From this figure it is clear that as temperature increases, the Raman shift decreases irrespective of the position on MC. But shift at free end with respect to fixed end is always higher. It is also observed that the difference between the shifts at three positions of MC is seemed to merge at low temperatures. Figure 2(b) shows the variation of Raman width (RW) with temperature. The data is fitted to a parabola. As temperature increases Raman width increases indicating the rise in temperature. For a given

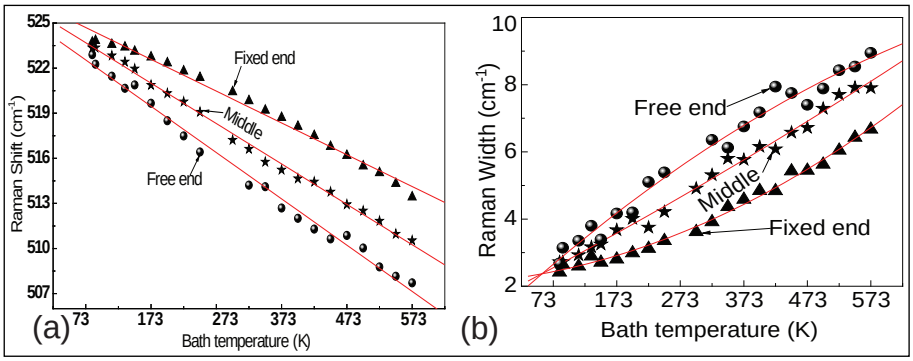

Fig. 2 *Variation of (a) Raman shift and (b) Raman width with temperature at three different positions (shown in figure 1) of the microcantilever*

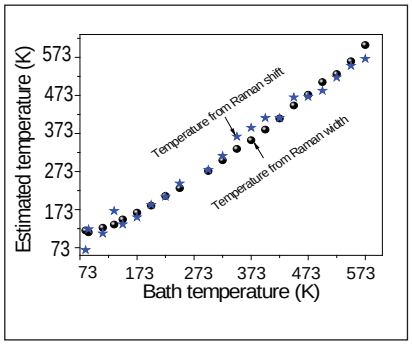

Fig. 3 *Variation of estimated temperature from Raman Shift and Raman width at fixed end of the cantilever*

temperature Raman width at free end is higher than fixed end. Now, the temperature at every data point is calculated from both Raman shift (T_{RS}) and Raman width (T_{RW}) by fitting the data in Figure 2(a) and 2(b) using the equations,

$$T_{RS} = T_o + \frac{\Delta\omega}{A} \qquad (1)$$

$$T_{RW} = \sqrt{\frac{\Gamma - D}{B}} - C \qquad (2)$$

Where, T_o is room temperature and $\Delta\omega$ is difference between Raman shift measured at room temperature and at higher temperature. Γ is Raman width at high temperature and A, B, C, D are calibration constants estimated from Figure 2.

Figure 3 shows the variation of estimated T_{RS} and T_{RW} with increasing bath temperature at the fixed end of the cantilever and is almost linear. This result indicates that both Raman shift and Raman width can be used to estimate the temperature on the micro cantilever. It is interesting to note that thermo mechanical stress induced in the micro cantilever cannot be estimated from Raman shift alone.

V.26 ZnO and GaN Nanostructures for Gas and Humidity Sensor Applications

The objective of this study is to correlate the effect of synthesis and operating temperatures on morphology, crystal structure in gas sensing properties of nanostructured ZnO film. We also report response of nanoprotruded GaN microbelts for the detection of humidity using Kelvin probe force microscopy (KPFM). In Kelvin probe force microscopy mode, simultaneous acquisition of topography and surface potential (SP) are imaged, SP=$\Delta\phi$/e. Here, $\Delta\phi$ is the difference between tip and sample work functions.

ZnO nanostructured thin films were grown by spray pyrolysis using Zn-acetate as precursor on alumina substrate pre-patterned with gold interdigitated electrodes at different substrate temperatures (T_S=623 K, 673 K and 723 K). NH_3 and NO_2 sensing experiments were then performed in the in-house designed exposure facility for gas sensing at different operating temperatures. The gas sensing response was evaluated with respect to microstructure for different synthesis and operating temperatures. The morphologies of ZnO nanostructures show mostly L-shaped nano-wall structures of 120° bends corresponding to truncated edge in the hexagonal structure in sample grown up to 673 K (Figures 1a and 1b). Sharp nano-cone like structures are observed for 723 K grown sample (Figure 1c). This is a consequence of the nucleation of c-axis oriented grains that grew geometrically and impinge laterally.

The growth of GaN belts with nanoprotrusions was performed

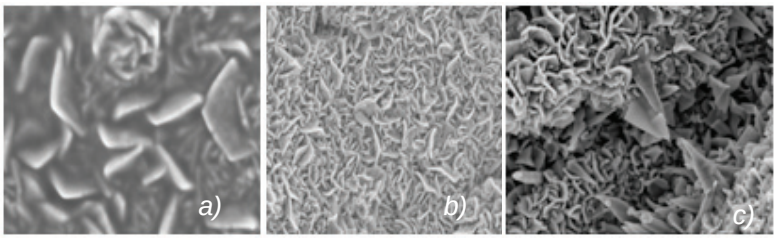

Fig. 1 *Morphologies of ZnO nanostructures at (a) 623 K (b) 673 K and (c) 723 K*

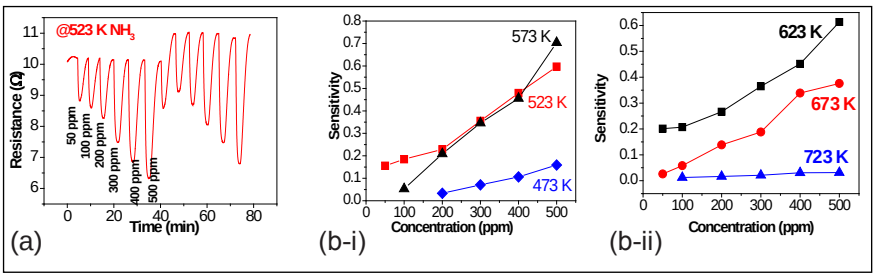

Fig. 2 (a) NH_3 sensing and (b) Sensitivity plots for (i) Various operating temperatures at Ts =623 K and (ii) Various Ts at constant operating temperature

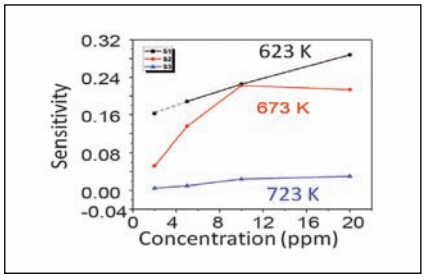

Fig. 3 NO_2 sensing and sensitivity plots

using conventional chemical vapor deposition (CVD) techniques. Growth was carried out at 1223 K for 5 hours. A large quantity of free standing belt-like microstructures of GaN was found on highly pure alumina (99.95%) boat without catalyst in the vapor-solid (VS) process (Figure 2a). The total belt thickness was found to be 10-15 µm with 1 µm GaN rich layer covering the top surface.

For the SP measurement, the GaN belts were transferred to clean Cu substrates which were electrically grounded. Commercially available metallorganic CVD grown GaN films (6-7 µm thick) on sapphire were electrically contacted through the top layer to avoid capacitance effects. Topography and SP images were acquired simultaneously using an Agilent 5500 with a three-lock-in amplifier in the amplitude modulation Kelvin probe force microscopy. For the measurements, VAC bias at frequencies in the range 10-15 kHz plus a DC bias, VDC, were applied between tip and sample. The Kelvin probe force microscopy measurements were carried out in an environmental chamber where humidity levels in the atmosphere could be controlled by injecting pure N_2 flow. Dry atmosphere refers to humidity levels below 15%.

Figure 2 shows the NH_3 sensing response of sample grown at 623 K at an operating temperature of 523 K with minimum detection at 50 ppm. The sensitivity, defined as the ratio of change in resistance due to introduction of gas to the resistance in air, versus concentration plot are shown in Figures 2. Similar observation was made for NO_2 down to 2 ppm at an operating temperature of 573 K for sample grown at 673 K. A typical NO_2 sensing and sensitivity plot at various operating temperature is shown in Figure 3.

When exposed to air, O_2 molecules are adsorbed on the surface of the ZnO film and capture electrons to form chemisorbed oxygen species (O^-). Oxygen vacancy in ZnO nanostructures donate electron to O_2 molecules to form O^- species.

$$2NH_3+3O^-_{(ads)} \rightarrow N_2+3H_2O + 3e^-$$
$$2NO_2+3O^-_{(ads)} \rightarrow NO(gas)+O_2+e^- \cdots$$

When a gas such as NH_3 comes into contact with the sensor, it undergoes oxidation by hole transfer from the surface state to the gas thereby decreasing the resistance of the sensor. Higher the oxygen vacancy, higher is the sensitivity. Hence it can be concluded that NH_3 or NO_2 sensing is better at higher temperatures. However, sensitivities decrease with increase in growth temperature which favors nano-cone morphology Hence it is found that nano-wall like structures are more suitable for ammonia detection than nano-cone type structures.

Enhanced sensitivity to humidity is reported for the GaN microbelts as compared to GaN thin films. Oxide and oxinitride phases, as well as native defect complexes comprising Ga vacancies and oxygen antisite (Figure 4), are assumed to be responsible for the surface charge accumulation leading to enhanced response for the surface potential variation as a measure of humidity. We could report a linear variation up to 50% humidity. A reaction mechanism for the dissociation of H_2O on GaN surface at specific defects has been predicted.

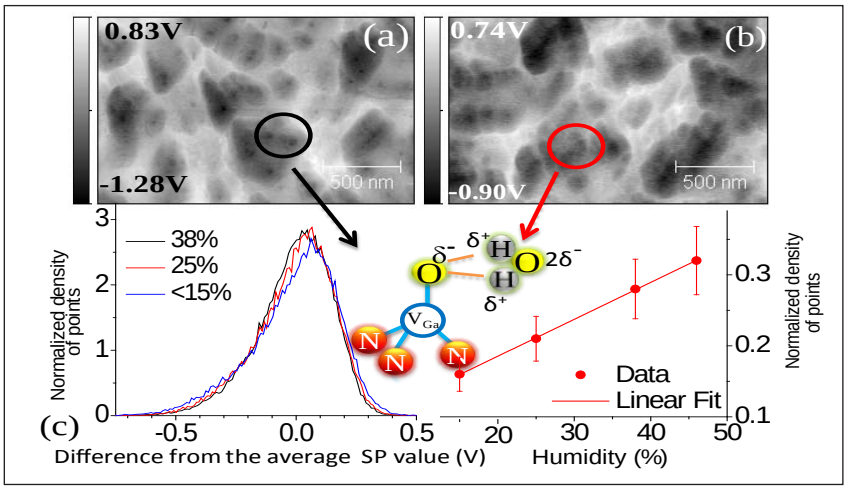

Fig. 4 SP surface profiles at a) dry atmosphere b) 20% humidity level c) The normalized density of SP points in each image and its linear dependence on humidity. The inset in (c) water adsorption on GaN screening the electrical features of original surface

V.27 Tribological Properties of Reactor Grade NiCr-B Coating

To improve the surface properties of high temperature structural materials used in fast breeder reactor (FBR), nickel base NiCr-B hardfacing alloys have been developed to replace traditionally used cobalt base alloys. This coating is also used in primary pumps, grid plates, sleeves and several rotating components where sliding between contacting surfaces occurs.

ERNiCr-B hardfacing alloys were deposited on 25 mm thick SS 316 LN steel plates using the gas tungsten arc welding (GTAW) process. The diameter of the hardfacing rod was 4.0 mm and final thickness of the coating was 10 mm. The dimension of the test specimen was 12 × 12 × 16 mm including substrate. The specimen was polished up to 0.25 μm surface finish. Chemical composition of the hardfaced deposit was analyzed using optical emission spectroscopy and inductively coupled plasma mass spectrometry (ICP-MS). The linear reciprocating mode of a ball on disk tribometer was used to carry out tribological tests on NiCr-B deposit. A spherical steel ball (100 Cr6 SS) of ø 6 mm was used as a sliding body to measure the coefficient of friction (CoF). The tests were performed at ambient (dry and unlubricated) conditions with a relative humidity of 62%. The tribo-test was interrupted at various sliding distances. The constant normal load, sliding speeds and stroke length were 1 N, 1 cm/s and 3 mm, respectively.

The low friction regime (region I) in Figure 1 is observed at sliding distance up to 2 meter. The progressive nature of friction is

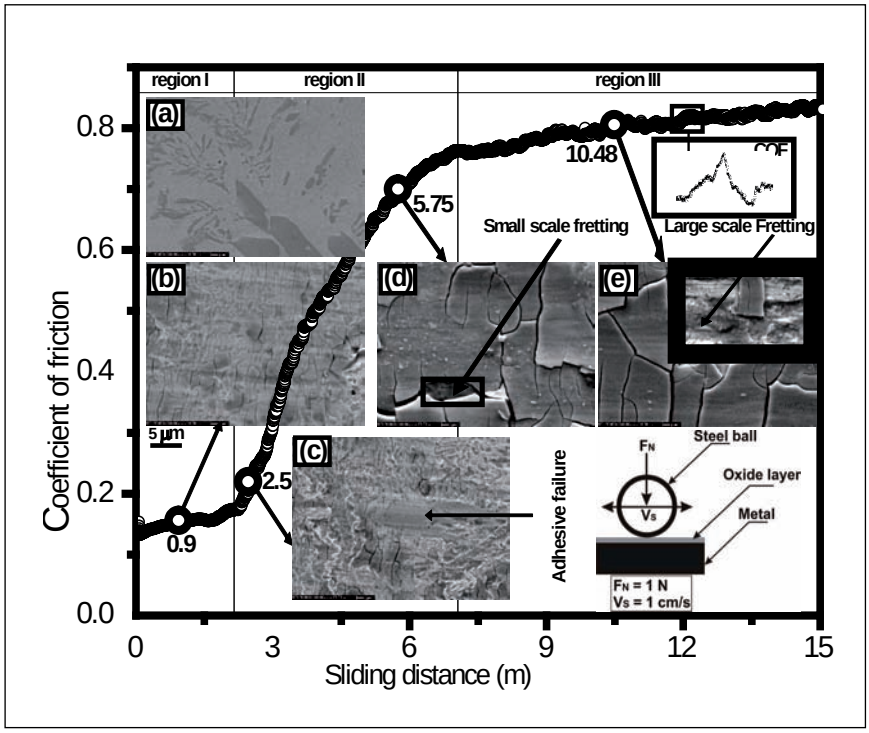

Fig. 1 *Coefficient of friction as a function of sliding distance with change in wear scars morphology*

observed between 2 to 7 m (region II). In the third regime (region III), coefficient of friction stabilizes towards a steady value. This occurs between 7 to 15 m. In the inset (a) of figure, the micrograph of the surface of the specimen near the interface is shown. Typically after 0.9 m of sliding distance where the coefficient of friction is low (0.15), the uniform micro cracking of the oxide layer occurs. This is shown in the inset of micrograph (b). With an increase in sliding distance to 2.5 m, the CoF increases to a value 0.2. This is concomitant with cracking of oxide scales. The wear scars are also found to be relatively larger as shown in inset of micrograph (c). The extent of cracking observed in micrograph (b) was less compared to micrograph (c). At sliding distance of 5.75 and 10.48 m, the coefficient of friction is found to be 0.7 and 0.8, respectively. This is where the severe fretting fatigue of the oxide layer is observed as depicted in inset (d) and (e) of the figure. In the inset (e) of the micrograph, the magnitude of fretting wear of oxide scales is high. This periodic fretting is clearly revealed in the region III. The periodic behavior of coefficient of friction during fatigue induced fretting is shown typically in the inset mentioned as coefficient of friction in Figure 1.

The evolution of oxide scale during sliding process is confirmed with Raman spectroscopy. The micro Raman spectra are obtained from the surface and wear scars formed during sliding. The micro Raman results are presented in Figure 2 (a - e). These are taken from the wear scars presented in insets (a) to (e) of Figure 1. The intensity

of Raman peak corresponding to phase evolution is relatively weak as seen in Figure 2 (a). It corresponds to inset (a) of Figure 2. In Figure 2 (b-e), two Raman peaks at 560 cm^{-1} and 692 cm^{-1} could be assigned as α–Fe_2O_3 and Fe_3O_4. The remaining third peak at higher wave number 928 cm^{-1} is also assigned to Fe_3O_4. It is also observed that the peak appearing at 560 cm^{-1} has higher intensity corresponding to α–Fe_2O_3 as seen in Figure 2 (e). The peak at 1363 cm^{-1} corresponds to $FeCr_2O_4$. The band formed at 1590 cm^{-1} results from the vibrational stretch of atmospheric O_2 molecules. It can be seen that these peaks have higher intensities compared to (b) and (c).

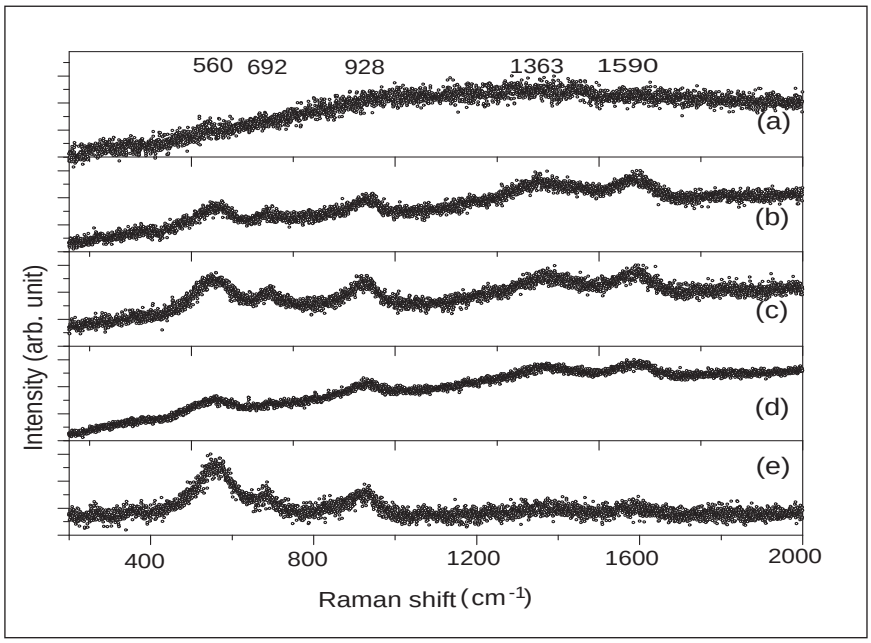

Fig. 2 *Micro Raman at (a) surface of coating and (b-e) Raman in wear scars*

The lower value of coefficient of friction is basically due to lower adhesive strength prevailing between the contact of oxide/oxide surface or metal/oxide surface. The adhesion can be weakened due to rise in local temperature with sliding. The mechanism for weak adhesion is related to thermal expansion of oxide scales. The surface roughness of oxides is found to be low at lower sliding distances. This is accompanied with low wear depth of 142 µm at the terminal step of 2.15 meter sliding. Consequently, in this region, the value of CoF is found to have a lower value of 0.14. These can be discussed with respect to the absence of adhesive failure and plastic deformation on the oxide scales. With increase in sliding distance to 2.5 meter, the wear depth is found to increase where the transition from low to high value of coefficient of friction is observed. This is accompanied with randomly distributed micro-cracks on the oxide scales and the presence of adhesive failure. Transfer of oxide layer causes severe fretting fatigue wear in the region II. The growth of this oxide continues with increase in temperature till a critical thickness is reached and then the film detaches itself due to fatigue wear. After the detachment of oxide scale, the growth of new layers occur due to chemical reaction on the virgin surface. In the Raman spectra, higher intensity of first order TO modes of α–Fe_2O_3 and Fe_3O_4 at wave numbers 560 cm^{-1}, 692 cm^{-1} could be assigned. These correspond to lower shear resistance. The band at 928 cm^{-1} is also assigned to Fe_3O_4 which indicates thickening of this phase with increase in spectral intensity. This phase causes higher shear resistance during sliding which brings in higher value of coefficient of friction. At initial passes, oxides of α–Fe_2O_3 is formed on the wear track of steel surface. This can make transition to Fe_3O_4 at higher temperature. The Cr_2O_3 phase is also formed at high temperature. The α–Fe_2O_3, Fe_3O_4 and Cr_2O_3 act as oxide lubricants due to their weak adhesive strength. The Raman peak at 1363 cm^{-1} corresponds to the formation of $FeCr_2O_4$ phase. This phase is known to be a good solid lubricant. The intensity of this phase decreases after lapse of longer sliding distances as shown in Figure 2 (d) and (e) where coefficient of friction has higher value. The remaining peak at 1590 cm^{-1} corresponds to vibrational stretch of O_2 molecule. It is observed that with increasing sliding distance, the intensities of both these peaks decrease. There is also a possibility to dissolve the solid solution of oxide due to this continuing cyclic shearing process. This implies that the fretting action induced is unique to the transformation in oxide structure. For pure iron, it would be α–Fe_2O_3→Fe_3O_4 transformation caused due to complex stress-strain response of the interface under loadings and rise in local temperature. At sliding induced local temperature of 473 K, a thermodynamically stable inverse spinel phase of Fe_3O_4 forms. Transformation of rhombohedral Fe_2O_3 phase to Fe_3O_4 also brings down wear rate.

V.28 Hexagonal to Orthorhombic Transformation in $LaGa_2$ at 12 GPa

Systematic studies on rare earth and actinide based intermetallics are interesting as well as important. It is found that the dialuminides stabilizing in cubic $MgCu_2$ type structure are found to be stable over a wide range of pressures. We have studied $LaAl_2$, $CeAl_2$ and $GdAl_2$ under high pressure up to ~35, 23, 16 GPa, respectively. All were found to be stable in cubic structure up to the maximum pressure investigated. Further, the rare-earth digallide systems mostly realise AlB_2 type structure at normal temperature and pressure but, under high pressure, a structural transformation to AlB_2 variant structures (with reduced *c/a* ratio) have been observed. For example, $CeGa_2$, it transforms to an AlB_2 variant structure type with reduced c/a ratio at 16 GPa. However, the actinide digallides seem to follow a different structural sequence with pressure as compared to the rare-earth digallides. In our high pressure studies carried out on $ThGa_2$ and UGa_2, different structural trends have been observed under high pressure. While $ThGa_2$ was found to be stable in its $ThSi_2$ type tetragonal structure up to 62 GPa, UGa_2 (AlB_2-hexagonal at normal temperature and pressure) transformed to a tetragonal phase at 16 GPa. As a continuation of our systematic studies on digallides, a high pressure structural stability study on $LaGa_2$ was carried out. $LaGa_2$ with AlB_2 hexagonal structure is a typical anisotropic ferromagnet like $CeGa_2$ and is a superconductor below a transition temperature of 1.15 K $LaGa_2$ was prepared by arc-melting stoichiometric quantities of La (99.99%) and Ga (99.9%) in helium atmosphere. The arc melted sample was annealed and the powdered sample was characterized by X- ray diffraction (XRD) using a Guinier diffractometer having an overall resolution of $\Delta d/d \approx 0.0001$. The sample was found to be of good quality, and single phase, AlB_2 type hexagonal structure having lattice parameters a = 4.308±0.001 A° and c = 4.418±0.005 A°. Our XRD data on $LaGa_2$ have been accepted as PDF in release of ICDD 2002.

High pressure X-ray diffraction (HPXRD) studies on $LaGa_2$ were carried out with a Mao-Bell type diamond anvil cell (DAC) in angle- dispersive mode using the Guinier geometry. The Huber-Guinier diffractometer is in vertical configuration (in symmetric transmission mode) with a Seeman-Bohlin focusing circle of diameter 114.6 mm. It consists of a curved quartz crystal monochromator and a flat position sensitive detector (PSD) of length 50 mm. The Mao- Bell type DAC is fitted to the diffractometer such that the position of the sample inside the DAC lies exactly on the Seeman- Bohlin focusing circle. The incident Mo X-ray is obtained from a Rigaku 18 kW rotating anode X-ray generator. This diffractometer system gives an almost truly $K\alpha_1$ molybdenum radiation (λ =0.70926 A°). The overall resolution is $\Delta d/d \approx 0.01$. A mixture of methanol, ethanol and water (MEW) in the volume ratio 16:3:1 was used as pressure transmitting medium.

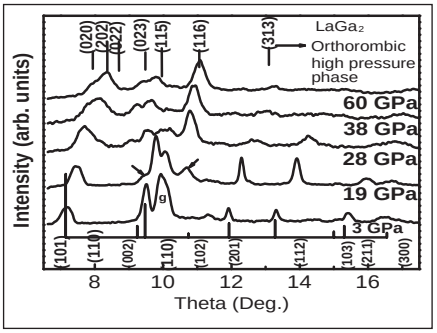

Fig. 1 *HPXRD patterns of $LaGa_2$ upto 60 GPa. g is the gasket peak. The arrows on the 19 GPa pattern indicate appearance of a new peaks*

The HPXRD experiments on $LaGa_2$ were conducted at pressures up to ~60 GPa and two sets of experiments were carried out; one with Ag as the pressure marker (up to ~33 GPa) and the other with out pressure marker. The runs with out pressure marker was carried out to obtain a clear pattern for the purpose of structural analysis. The HPXRD patterns at various pressures are depicted in Figure 1. The structure was found to be stable up to ~12 GPa. Around this pressure, several new peaks started to appear, the predominant one next to the gasket peak at θ =10º, as indicated by the arrow in Figure 1. The intensities of the diffraction peaks (110), (201), (112) and (211) came down drastically with pressure and eventually disappeared at a pressure of ~28 GPa. Additionally, another important observation was that the 100% sample peak at θ = 7.2º broadened out significantly and split into three new peaks. The parent and daughter phase coexisted between 12 and 28 GPa. The hydrostatic limit of our experiment is ~20 GPa and the large width of the transition can not be attributed to the non-hydrostatic

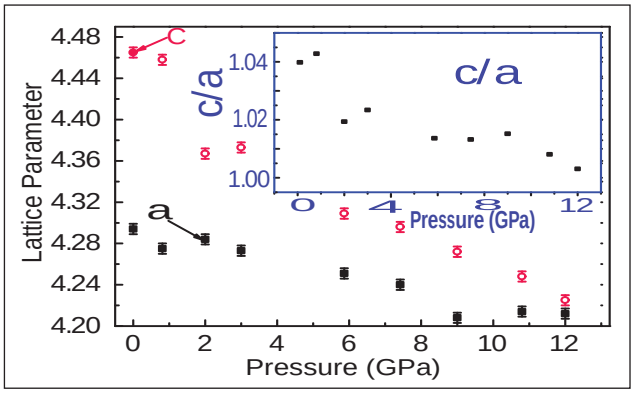

Fig. 2 Variation of lattice parameters a and c of the parent phase with respect to pressure up to ~12 GPa. The inset is the variation of c/a ratio up to 12 GPa

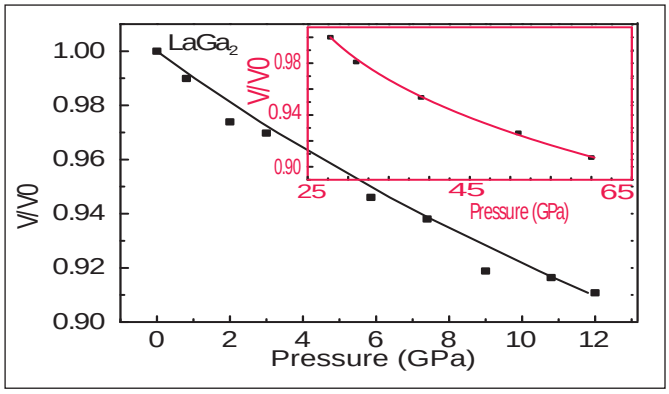

Fig. 3 The P-V data for the parent AlB_2 phase up to 12 GPa. The solid line is the Birch Murnaghan EOS fit. The inset shows the P-V data for the high pressure phase

pressure medium; it may be due to the inherent sluggish nature of the transition. The daughter phase was found to exist up to ~60 GPa.

In the above series of experiments, up to ~33 GPa, Ag was used as the pressure marker. New Bragg peaks belonging to the daughter phase started appearing above ~12 GPa and coexisted with the parent phase up to ~28 GPa. We have used a couple of Bragg peaks belonging to the daughter phase for calibration against Ag equation of state. Further, this calibration was extrapolated to make a conservative estimation of pressure in the experiments carried out without Ag. Thereby the highest pressure was estimated to be ~60 GPa. Figure 2 shows the variation of lattice parameters *a* and *c* of the parent phase with pressure up to 12GPa. It is clear from the figure that the rate of decrease in *c* with pressure is more compared to that of *a*. The inset shows the variation of *c/a* ratio with respect to pressure before transition.The P-V data up to 12 GPa is shown in Figure 3. The fitting was carried out using Birch Murnaghan equation of state. The bulk modulus B_0 and its derivative B_o' were found to be 100±16GPa and 5±4 respectively and are similar to the reported values for most of the rare-earth digallide systems.

The 60 GPa pattern was considered for structural analysis of the high-pressure phase. Totally six peaks were considered for the analysis. Determination of the high pressure phase is a non- trivial task and one looks for systematics observed in similar compounds for clues. First, we consider the hexagonal lattice itself with a smaller c/a ratio, as is seen in other rare-earth digallide systems. However, a least-squares analysis of the XRD data resulted in a very poor figure of merit, implying that the high- pressure phase is probably not hexagonal. This result is interesting as it behaves differently from other rare-earth digallide systems.

Next, we sought the help of structural stability maps, according to which the following structural sequence has been predicted: AlB_2 (Hex) → $ThSi_2$ (Tet) → $ZrSi_2$ (ortho) → $SmSb_2$ (Ortho) → Cu_2Sb (Tet). Moreover, high pressure HPXRD study on $LaCu_2$ shows a structural transition from AlB_2 (hex) → $CeCu_2$ (Ortho) structure at ~5.6 GPa. Using the above clues, we carried out the analysis to look for a tetragonal lattice similar to $ThSi_2$. However it was observed that the most intense peak of the high- pressure phase at $\theta = 11.05^0$ was left unindexed. Next, we searched for an orthorhombic lattice similar to either $ZrSi_2$ or $SmSb_2$. Interestingly, we were able to get a very good figure of merit for an orthorhombic lattice with lattice parameters: *a*=12.79 , *b*=5.09 and *c*=5.28 A°. However, the generated X-ray diffraction patterns for the $ZrSi_2$, $SmSb_2$, Cu_2Sb, CeCu, type structures did not match with the observed pattern at 60 GPa. It appears that $LaGa_2$ adopts some other type of orthorhombic structure at high-pressure.

The inset in Figure 3 is the P- V data for the high pressure phase fitted with Birch-Murnaghan equation of state in the modified form P= Pr + f(V/Vr). Here, V and Vr are the volumes at pressures P and Pr, respectively. For calculating the bulk modulus of the high pressure phase Pr was fixed at ~28 GPa, since between ~12 to 27 GPa it was a mixed phases of hexagonal and orthorhombic lattices. The bulk modulus B_r and its derivative B_r' were found to be 166± 18 GPa and 17 ± 4 respectively.

In summary, the HPXRD studies have been carried out on $LaGa_2$ up to a pressure of ~60 GPa. A phase transition from AlB_2 (hexagonal) to orthorhombic phase was initated at ~12 GPa and was completed at ~28 GPa. The orthorhombic structure was stable up to ~60 GPa. The bulk modulus and its derivative were estimated using Birch-Murnaghan EOS and its modified form for high-pressure phase.

V.29 Deployment of an In-House Developed Conductometric Measurement System for Assay of Boron in Water and Heavy Water at Trace Level

A high resolution conductometric titration technique using a new class of sensor viz. pulsating sensor developed in-house has been deployed for the determination of boron in light water and heavy water down to 100 µg/l level. This is to have a simple and rapid analytical technique for assay of boron in heavy water moderator system of a pressurised heavy water reactor (PHWR).

The method involves conversion of trace quantity of extremely poor conducting boric acid present in the sample matrix to a relatively better conducting complexing species, using a polyhydroxyl alcohol viz. mannitol as reactant. Boron-mannitol complex, thus formed, is titrated against standard NaOH solution using a high resolution conductometric titration device. Due to complexation, though the ionic conducting power of the solution increases to some extent, at boron concentrations of a few mg/l or µg/l levels the change in conductivity is too small to be detected by conventional conductivity meters. The newly designed pulsating conductivity meter could easily measure such a small change in conductivity with high precision in measurement (RSD: < 2% at 100 µg/l B level) due to some of the salient features such as (i) high resolution (ii) high precision and excellent sensitivity in measurement (iii) rapid response (iv) extremely immunity from back ground noise etc.

Non-reactive specimens (specimens which do not react with the titrant, here NaOH), if present in sample, do not interfere in quantitative analysis of boric acid during titration. The influence of some of the common interfering specimens such as NaCl, KCl, LiCl and NaF on assay of boron has been investigated. It was found that these impurities even present upto 500 µg/mL level in 1 µg/mL boron did not cause any interference. Any acidic impurities even present at trace levels could be easily identified from the online titration plot which provided quantitative information of impurities present in the sample (Figure 1). The entire titration process including offline analysis of data to get quantitative information of sample was completed within a couple of minutes. Thus besides chemical analysis at trace level chemical speciation could be performed in much simpler way.

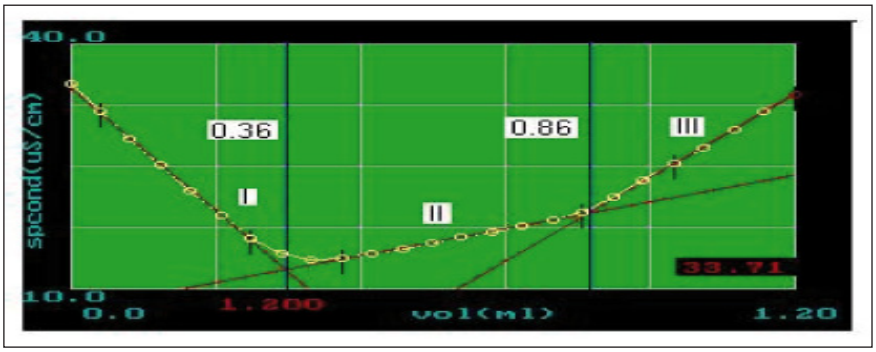

Fig. 1 *A typical online titration plot of boron at trace level in presence of acidic impurities*

Besides conductometric titration technique, we also demonstrated a high resolution conductivity monitoring technique for quick assay of boron down to 20 µg/L boron level (Precision in measurement 0.82 (n=10), RSD: 4.1%,) in solution where boron was present in relatively pure form and it was possible to have a blank sample of equivalent purity. In the former measurement approach both dissociated and undissociated specimens are associated, whereas in the latter only a small fraction of undissociated ions are involved in conductivity measurement. This rapid conductometric technique (either titration or direct conductivity measurement approach depending upon the nature of sample matrix) can be easily adopted for quick offline analysis of heavy water in moderator system in PHWRs.

The influence of isotopic effect on sensitivity of measurements has also been studied in the determination of boric acid present in light water and heavy water matrixes. The significant difference in conductivity shift in both matrixes (about 2.6 to 2.8 times higher in light water matrix than heavy water matrix) is attributed due to less ionic mobility of deuterium ion than that of hydrogen ion. There is further scope of applying this technique for assay of boron in steam distillates collected from nuclear fuel samples where boron is present at trace levels.

V.30 Round Robin Exercise on Atmospheric Flowfield Modeling at Kalpakkam

Atmospheric dispersion of radioactive effluent releases is determined by the flow field and turbulence. Hence, accurate simulation of flowfield is necessary to obtain realistic radiological impact assessment for a given site. Atmospheric flowfield consists of different scales of circulations such as micro (~2 km), local (up to 10 km) and mesoscale (~100 km) which influences the plume dispersion in the respective distance ranges. Hence, suitable models need to be applied to provide meteorological input to dispersion estimation in the respective distance ranges. In this context, a round robin exercise sponsored by BRNS is conducted in collaboration with 13 institutions (EAD-BARC, NARL, IITM, TIFR-CAM, IIT-Kharagpur, Andhra Univ., Jadavpur Univ., SRI-AERB, SRM Univ., Annamalai Univ., Satyabama Univ and CFD companies Fluidyne, ACRi). The objective of round robin exercise is to evaluate various meteorological wind field models and to converge to best acceptable methodology for dispersion simulation in the three spatial scales.

The round robin exercise study programme is grouped into observational, modeling and theoretical studies. As part of round robin exercise, extensive observational data was collected in the Kalpakkam coastal region during August 2010 -February 2011 for intensive model validations. The observation network consisted 5 multi-level Meteorological Towers, 35 Automated Weather Stations, 4 portable masts equipped with UltraSonic Anemometers, a GPS Radiosonde, shortwave/long wave radiation sensors, Doppler Lower atmospheric wind profiler (LAWP), soil moisture and temperature sensors collectively deployed by the collaborating institutes and distributed in respective modeling domains. LAWP and GPS sonde were used to collect vertical atmospheric profiles in the intensive observation period (IOP) at the site. The meteorological measurements included surface wind, temperature, humidity at forty locations, micrometeorological observations at five locations, turbulent components (u',v',w',q') at four locations, vertical profiles of winds, temperature and humidity at two locations, short-wave/long-wave, soil temperature and moisture data at one location with relatively high density of measurement in the local (20 km) and micro scales (2 km).

Observations at Kalpakkam during the intensive observation period indicated prevalence of a wide range of atmospheric conditions, the significant features being mesoscale sea breeze circulation development across the coast on days with strong insolation, spatio-temporal variation in daytime boundary layer structure, mixing height and atmospheric stability in the monsoon and post-monsoon conditions. High resolution GPS sonde vertical profiles during intensive observation period indicated formation of deep mixed layers up to 1350 meter at the local noon time on most days and shallow convective mixed layers (of 300 to 600 meter height) on the days with sea breeze development (Figure 1). Smallscale convective turbulence and boundary layer

Fig. 1 *Observational system at Kalpakkam with Met Towers, Wind Profiler, GPS radiosonde*

cloud activity was noticed during some days of intensive observation period in September 10. Tower observations indicated vertical variation (gradients) in surface layer parameters characterizing various atmospheric conditions. The LAWP backscatter echograms indicated significant convective activity in the daytime (00-16 IST) with regions of enhanced radar reflectivity marking mixed layer developments up to 1 km in the afternoon on many days during intensive observation period (Figure 2). Sonic anemometer observations during intensive observation period indicated stable morning conditions, neutral conditions up till noon, highly unstable conditions in the afternoon (after 1300 IST) and relatively higher turbulence in the daytime between 1000-1600 IST. A sudden drop in the gradually growing heat flux was also observed during the daytime after the onset of sea breeze between 1100-1600 IST on various days.

Wind field simulations and validations were made by IITM, NARL, Andhra University, Jadavpur Univ., BARC and IGCAR with high resolution mesoscale models MM5,

ARW, RAMS adopting multi-scale nesting approach. IITM used six boundary layer parameterizations in ARW model and showed simulated wind field has positive bias in daytime and negative bias during night time with all schemes (Figure 3). PBL scheme based on dissipation rate performed better than others in reproducing vertical variations in observed parameters. Results from both IITM and Andhra University showed the Hong-Pan non-local diffusion scheme produced better simulations for surface level winds, mixing height. (Figure 4). Both IITM, Andhra University (AU) reported less errors for simulation of various lower atmospheric parameters with the use of non-local PBL diffusion schemes. Simulations with RAMS model by Jadapur Univ., indicated positive bias in wind filed though sea breeze circulation is simulated. The wind flow strength and TIBL development are found stronger with local PBL schemes based on TKE closure relative to non-local diffusion schemes. AU assimilated experimental observations using 3DVAR in ARW model and showed improvement in simulations of wind flow, boundary layer structure with less error metrics. A linear model relevant for the Kalpakkam region was derived by TIFR by including Coriolis force and non-zero background wind in a linear hydrostatic Boussinesq system of

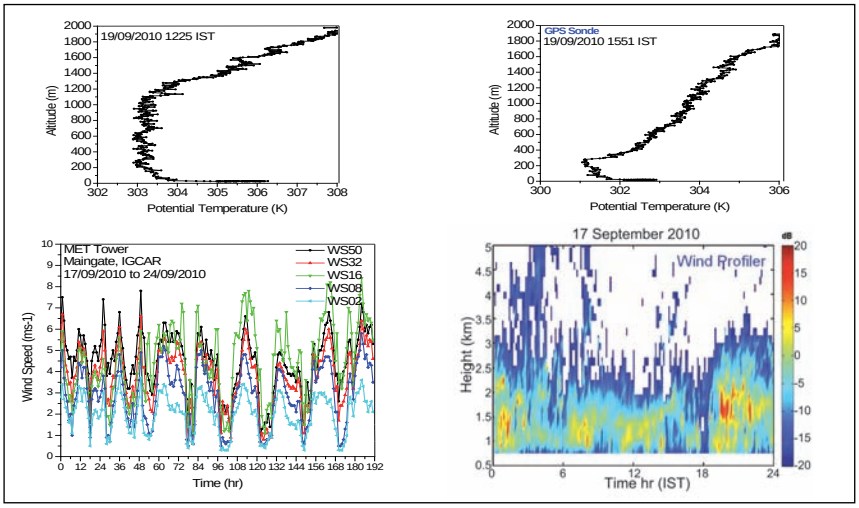

Fig. 2 *Observations during intensive observation period from GPS sonde, MET Tower and Wind Profiler at Kalpakkam site*

equations and its solutions obtained using Fourier transform technique. Observations from round robin exercise experiments were used as input through the standard Kalman filter technique. Fluidyne, Banglore used the MM5 model derived mesoscale meteorological fields and generated the mass-consistent wind-field as input to their CFD atmospheric dispersion model Panache. Simulated wind field for 15 to 21st September 2010 were compared with experimental data which indicated slight overestimation of winds. However the microscale simulations gave better comparisons with sonic anemometer data. ACRi generated a mesoscale wind field around Kalpakkam with MM5 prognostic model which was downscaled to a 20 km domain using a diagnostic model CALMET. ANSWER CFD code was used for a full 3D simulation of flow field around the medium 20 km domain. The CFD simulations showed advantages over local and micro scales through representing the fine variations in the flow and dispersion patterns. The IIT-Kharagpur analysed the measured turbulence data from Sonic Anemmometer at Kalpakkam and derived new empirical diffusion formulae based on surface layer similarity theory for use in the lagrangian particle dispersion model (Flexpart). The formulations are applicable in other dispersion models too.

Round robin exercise Winfield modeling studies are being continued in different phases up to a period of 3 years till reasonable accuracy of results is obtained.

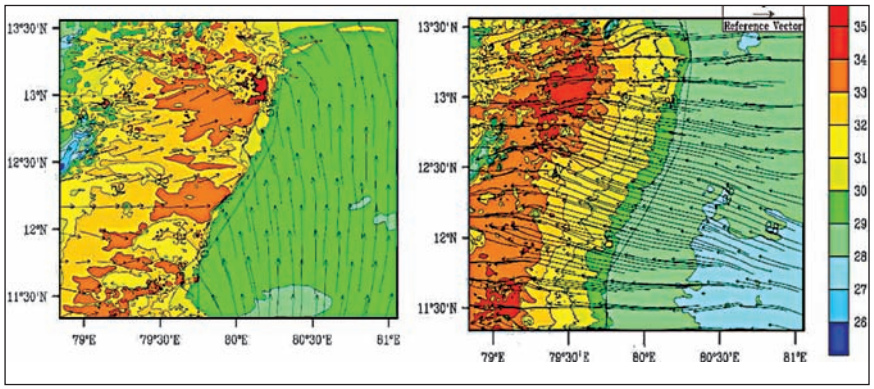

Fig. 3 *Simulated 2m level temperature, wind field at Kalpakkam for the cases of off-shore (left panel) and onshore (right panel) synoptic wind system*

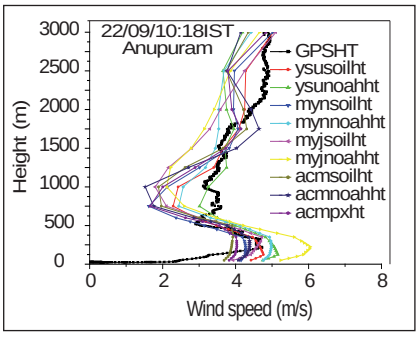

Fig. 4 *Comparison of vertical profiles of wind speed with GPS observations for 22/9/2010 10:06 Indian standard time*

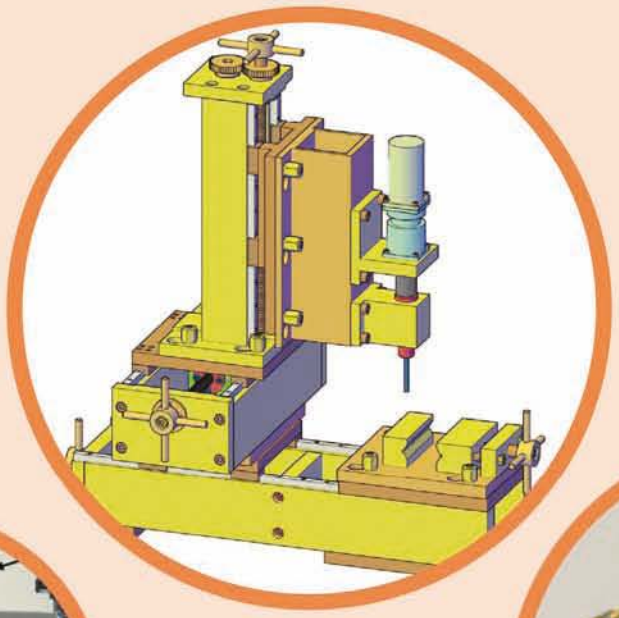

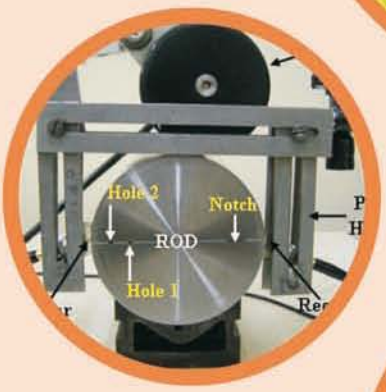

CHAPTER - VI

Infrastructure Facilities

VI.1 Supercomputing Facility at IGCAR

A multi-purpose parallel 134-noded high-performance computing cluster with 1608 processor cores and 6.4 TB memory delivering a sustained numerical performance of 16.7 Teraflops based on latest 6-core Intel Xeon Nehalem Processors has been installed and commissioned to solve compute intensive Fast Breeder design challenges like Fluid Structure interaction, Multi-phase phenomena, Chemical-Thermal-Mechanical studies, Reactor physics, Molten fuel coolant interactions, Gas Entrainment, etc.

The Cluster System has two master/login nodes in high-availability configuration and 134 compute nodes interconnected by 40 Gbps InfiniBand network. Four of the compute nodes are Fat nodes with higher clock rates to cater the sequential codes run on the cluster. Also a cluster storage system with 24 TB of disk capacity and LTO-4 Tape library has been configured to meet the storage and backup requirements of users.

Cluster Configuration

The master node is the head node of the cluster which is used for cluster administration and provides user interface for job submission and management. This node is configured in high-availability mode to increase availability of the cluster. The compute nodes are the cluster nodes where the users' jobs actually run. They are highly optimized to execute the parallel codes of the users. In addition, a console server is configured for hardware management of all compute nodes.

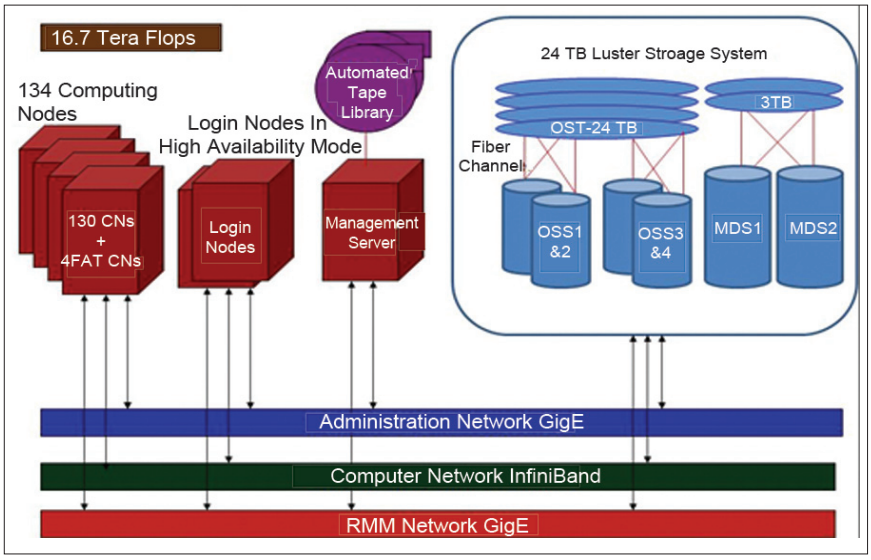

Fig. 1 *Supercomputing cluster at IGCAR*

Interconnect Networks

To exploit the full potential of the high performance computing cluster with increased processor speeds, it is essential to have high-performance interconnects between cluster nodes. InfiniBand Architecture is an industry standard, channel-based, switched fabric, interconnect architecture for servers. It provides very high bandwidth and low latency for communication and better scalability to large number of nodes. It uses low-level Remote Direct Memory Access (RDMA) protocol to reduce the application latency and processor overhead.

This cluster system has three interconnect networks. The primary network meant for inter-processor communication (IPC) is based on the InfiniBand architecture. The InfiniBand switch supports upto 216 QDR 4X ports each with speed of 40 Gbps. The Administration network meant for cluster management and monitoring is based on 1 Gbps Gigabit Ethernet. The Management network meant for hardware remote management and console access of nodes using remote management module is based on Gigabit Ethernet and provides remote access, monitoring, and control functions for hardware without using KVM switches and complex wiring.

Storage System

Lustre storage architecture for clusters and an open source shared file system, is configured to address the I/O needs of the cluster. The storage architecture consists of two metadata servers which manage the names and directories in the file system and four object storage servers which provide file I/O service. Lustre metadata servers are configured as an active/passive pair, while object storage servers are deployed in an active/active mode. This configuration provides redundancy without extra overhead improves file system performance, enhances file system recoverability and availability. The Lustre recovery feature allows servers to be upgraded without the need to take

the system down. The disk drives use RAID 6 configurations, enabling file system operations to continue in the event of a double disk failure.

Automated tape library

To meet the large data backup requirements of the cluster storage, an automated Tape Library with eight LTO-4 HH Drives and 77 media slots to backup up to 61.6 TB of data using 800/1600 GB LTO-4 Tapes is used. A backup server is setup and programmed to take periodic backups of user data.

Software

Advanced cluster distribution software high performance computing suite is used for building and managing this high-performance computing cluster. The cluster nodes run on Red Hat Enterprise Linux 5.5 64-bit Operating System and installed with Intel C/C++ & Fortran compilers (ver. 12), Lahey/Fujitsu Linux64 Fortran Compiler (Release L8.10b) with all relevant scientific & mathematical libraries and special-purpose CAE applications. Open source cluster tools Sun Grid Engine for Resource and Job Management and Ganglia for Distributed Cluster Monitoring are configured for smooth functioning of the cluster.

Performance Benchmarking

The performance of the cluster is measured in terms of number of Floating-point Operations per Second (GigaFLOPS/TeraFLOPS). The industry-standard High-Performance Linpack (HPL) is used to evaluate the parallel cluster performance. It gives the sustained performance of 16.7 TFLOPS during initial runs (Figure 1). The maximal sustained performance can be achieved after fine tuning various system factors and benchmarking parameters. Currently this system is the fastest cluster supercomputer available in DAE. Based on the sustained performance ratings, this cluster may be rated in the top ten supercomputers in India.

The twin-noded cluster systems in 1U form factor are compactly housed in seven 42U racks with efficient cooling arrangement made through 30 Tons chilled water based Precision Air-Conditioning system.

Applications

This parallel supercomputing cluster is designed to meet the large-scale numerical computing requirements of IGCAR Scientists and Engineers. Highly compute-intensive scientific applications in the areas of Computational Molecular Dynamics, Material design with desirable properties, Reactor Core calculations, Multiscale modeling of radiation damage, Quantum Monte Carlo investigation of materials, Computational modeling and Simulations of Plutonium recovery, Weather modeling and Engineering applications in the area of Finite Element Analysis, Computational Fluid Dynamics can effectively make use of the cluster to vastly reduce their run times.

VI.2 Development of Autonomous Gamma Dose Logger for Environmental Monitoring

Environmental Radiation level monitoring is mandatory in and around all nuclear facilities to ensure that public exposure is well within the limits prescribed by the International Commission for Radiation Protection (ICRP). As Kalpakkam is growing into a multi functional nuclear facility, both offline and online environmental radiation monitors are necessary for the acquisition of baseline data. Imported GammaTRACERs are being used for this purpose for more than a decade. Hence, a portable autonomous gamma dose logger is indigenously designed and developed for environmental radiation monitoring and recording. The response of the system is compared with the GammaTRACER (Genitron Instruments GmbH, Germany, Model No.G121) to evaluate its performance. The autonomous gamma dose logger has added features like LCD display for instantaneous dose rate with date and time stamps and standard deviation of measured dose as compared to GammaTRACER.

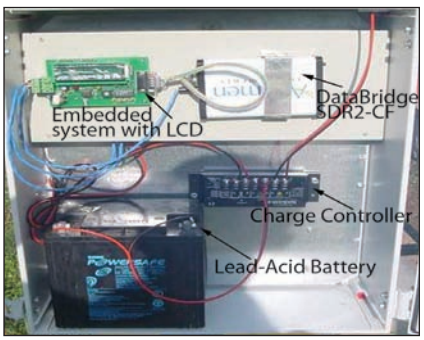

Fig. 1 *Autonomous gamma dose logger*

The autonomous gamma dose logger is a microcontroller based system it continuously monitor and store environmental gamma dose rate with preset time intervals. Photograph of autonomous gamma dose logger is shown in Figure 1. Autonomous gamma dose logger uses energy compensated halogen quenched Geiger Muller tube (LND 7807) with energy response of ± 20% in the range 50 keV to 2 MeV. The system hardware comprises of high voltage module, signal conditioning electronics, micro-controller (AT89S52) which handles data acquisition and archival, real time clock to maintain real time, LCD for display of instantaneous dose rate and a DataBridge serial data recorder for permanent storage of archived data. The system works on 12 V battery with solar power back up. The GM pulses are fed to signal conditioning circuit to convert them into TTL pulses. Unlike most commonly used hardware based counting; autonomous gamma dose logger employs software counting technique to count the TTL pulses from GM detector. This is achieved by configuring one of the timers in the microcontroller as an event counter which records the incoming TTL pulses. An optimal pulse width of 500 µs is used for accurate counting. Autonomous gamma dose logger uses sixteen-character two-line LCD module for displaying instantaneous dose rate ($nSvh^{-1}$) along with date and time stamps and is updated at the rate of 0.1 Hz. The application software is developed in Keil C and it performs initial configuration setting of autonomous gamma dose logger, data acquisition with sampling time of 10 seconds, calculates counts per second, applies calibration factor and calculates average and standard deviation at the end of every 10 minutes and sends the data to the DataBridge serial data recorder along with time and date stamps for permanent storage. The Autonomous Gamma Dose Logger has dedicated file management system and registered data can be easily retrieved at any time for analysis and documentation as they are recorded in a removable compact flash card. Maximum data file size per day is 10 KB. This implies that a flash card of 512 MB would lead the system to operate for months together without being replaced.

The system is calibrated using ^{60}Co standard source (8.1 MBq) at various source to detector distances using free field calibration technique to account for scattered components. The system showed fine linearity from low to high dose rates (20 $nSvh^{-1}$ to 30 μSvh^{-1}). The sensitivity of the system was calculated as 0.018 cps/ $nSvh^{-1}$. Performance evaluation of AGDL system has been carried out with internationally acclaimed GammaTRACER by keeping both the systems in known radiation field from a standard source (^{60}Co of 8.1 MBq) and readings were taken for different source to detector distances. The dose responses of both the systems are in good agreement.

Field response evaluation of autonomous gamma dose logger and GammaTRACER are carried out by deploying both systems in the field. Base line data recorded in both the systems are found to be in good agreement (Figure 2). The peaks ranging from 200 to 575 $nSvh^{-1}$ with corresponding standard deviation from 26 to 80 $nSvh^{-1}$ against the general background standard deviation of 10 $nSvh^{-1}$ indicate the increase in radiation level above background radiation level which may be due to the presence of argon plume released from MAPS during normal operation. If standard deviation is low enough, it is assumed that the measured dose represents background alone. From Figure 3, it is seen that there is no significant standard deviation peak in the absence of ^{41}Ar. The sharp increase in standard deviation for a period of time infers that the increase in background is contributed by the presence of ^{41}Ar plume. Thus standard deviation analysis method has shown to be accurate in identifying ^{41}Ar peaks.

In addition to baseline data collection, autonomous gamma dose logger with wireless technologies provides online facilities and has wide applications. A networking of such systems installed at different predefined locations in the site would provide radiological status of the site in real time. This type of system would help to take faster decision support actions in case of inadvertent incidents.

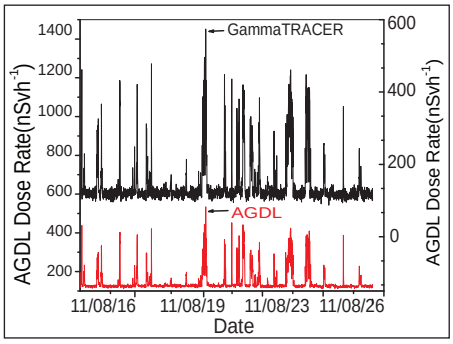

Fig. 2 Dose response of autonomous gamma dose logger and Gamma TRACER in the field

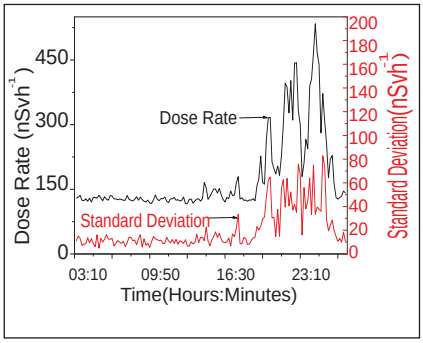

Fig. 3 Standard deviation with dose rate of autonomous gamma dose logger

VI.3 Development of High Field SQUID Magnetometer for Magnetization Measurements

Measurement of magnetization of a specimen as a function of applied magnetic field and temperature is an important experimental technique for the characterization of magnetic materials. Popular techniques for accurate measurement of the magnetization of materials are Vibrating Sample Magnetometer (VSM) and SQUID Magnetometer. Since SQUID (Superconducting Quantum Interference Device) is the most sensitive device available today for measuring extremely small changes in magnetic flux with a magnitude much less than a flux quantum Φ_0 (= 2.07×10^{-15} Wb), magnetometers employing SQUID as a detector can be designed to achieve very high sensitivity. Here we describe the design and fabrication of a high field SQUID magnetometer developed for magnetization measurements by using a home built SQUID sensor and its associated readout electronics.

The design is modular and all the sub-systems have been fabricated in the form of separate modules in order to simplify the assembly and to facilitate maintenance. The system consists of four major modules : (i) sample chamber with variable temperature regulator for varying the sample temperature from one value to another with uniform rates of heating and cooling and for maintaining the temperature of the sample constant with a high stability, (ii) superconducting shield chamber for maintaining stable magnetic field across the superconducting gradiometric pickup loop, (iii) SQUID sensor and its input circuit in the form of second order gradiometer and (iv) stepper motor driven sample transport assembly for oscillating the sample across the pickup loop to record the SQUID output signal with respect to the positional coordinates of the sample. In this setup, several novel features have been incorporated such as an impedance chamber based variable temperature regulator for achieving uniform rates of cooling and heating and for maintaining the sample temperature constant with a high stability, whenever desired, and the use of two different SQUID sensors with different strengths of input signal coupling in order to improve the overall dynamic range

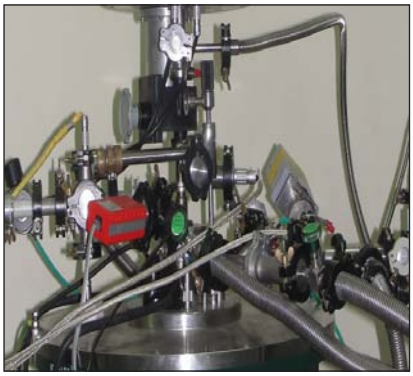

Fig. 1 *The high field SQUID magnetometer set-up*

of the system. The photograph of the high field SQUID magnetometer set up is shown in Figure 1. The SQUID magnetometer comprises of a liquid helium cryostat with a capacity of 43 litres and a

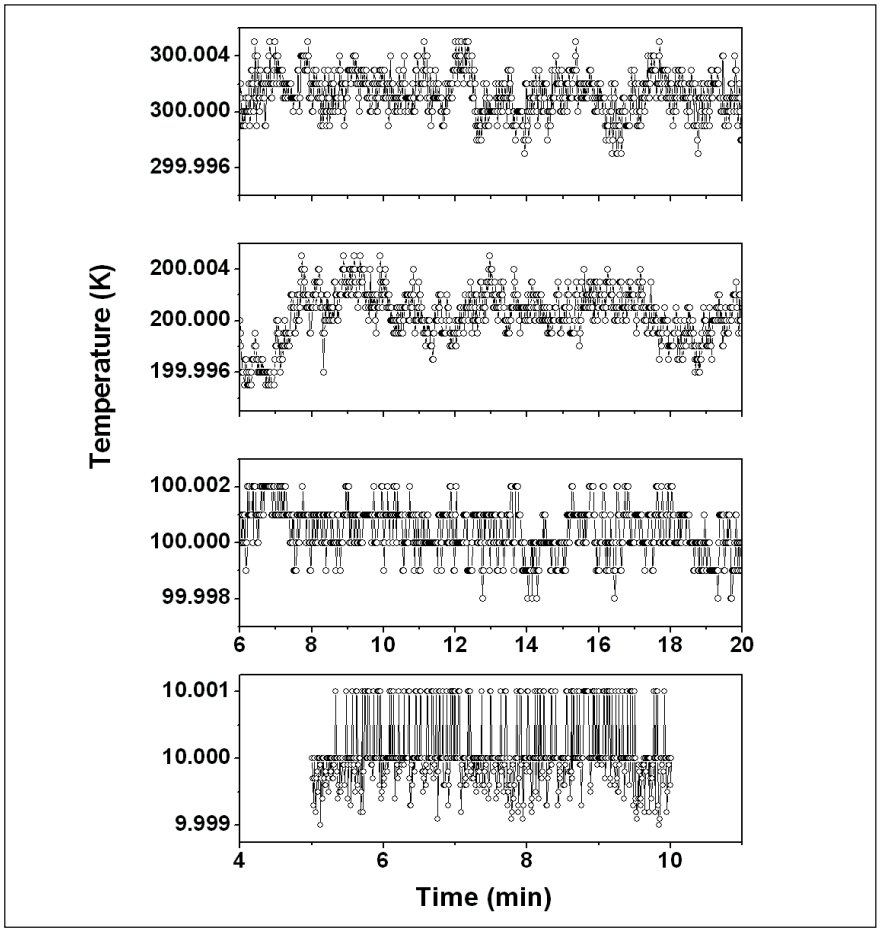

Fig. 2 *Temperature stabilities recorded experimentally while maintaining a constant temperature of 10, 100, 200 and 300 K in the vicinity of the sample region*

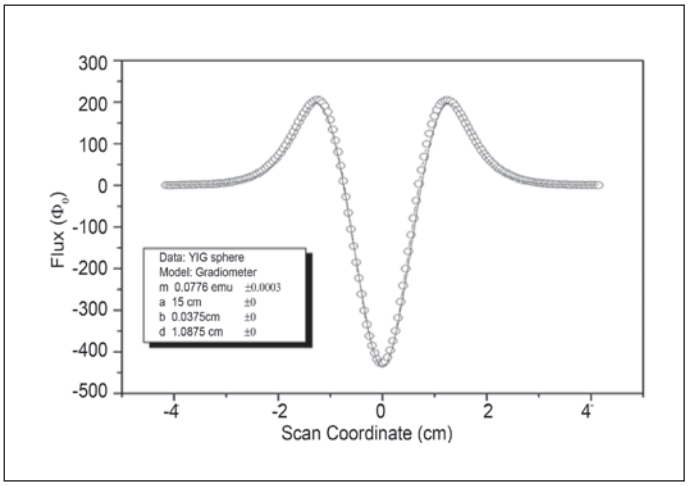

Fig. 3 Recorded SQUID output data for the yttrium iron garnet sphere is fitted to its magnetic moment to infer the calibration factor of the SQUID magnetometer

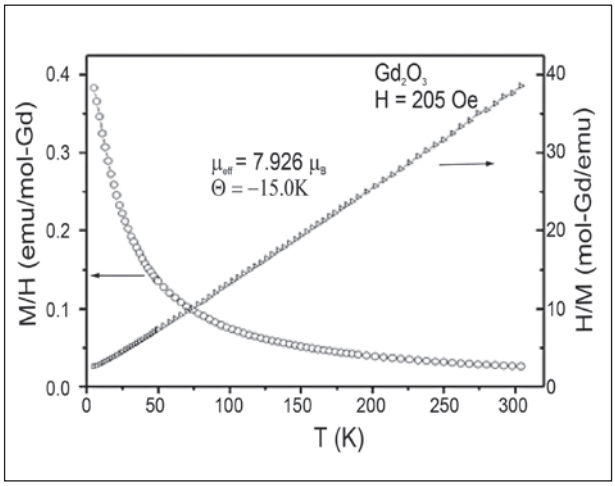

Fig. 4 Temperature dependent susceptibility (M/H) and inverse susceptibility (H/M) of Gd_2O_3 sample plotted as a function of temperature

superconducting magnet with a clear bore diameter of 52 mm capable of producing a maximum magnetic field of about 7 T.

The impedance chamber shown on the right side in Figure 1 comprises of a capillary, just 200 µm in diameter, which can be heated to a user desired temperature to regulate the flow rate of cold helium gas in the sample chamber. The heated capillary acts as an electronically controlled valve which precisely controls the flow of cold helium gas drawn to cool the sample region. The desired flow rate can easily be achieved by controlling both the heater current in the impedance chamber and the pressure in the variable temperature regulator chamber. The temperature stabilities typically achieved while maintaining the sample region at different constant temperatures have been shown in Figure 2.

In this system, a novel input circuit has been incorporated to enable a user selectable trade-off between high resolution measurements with a lower dynamic range and low resolution measurements with a higher dynamic range in order to permit the use of the system to measure magnetization of samples with low as well as high values of magnetic moment. For this, two different SQUID sensors have been used for sensing the magnetization of the sample. One sensor is connected to a highly sensitive input coil system to sense relatively weak magnetic signals with high resolution and the other one is connected to an input coil system of lower sensitivity to sense strong magnetic signals without allowing the system to reach saturation.

The measurement process has been fully automated using custom designed software developed on a LABVIEW platform. The personal computer monitors and controls the electronic instruments as well as various modules of the SQUID magnetometer to perform the magnetization measurements either at constant magnetic field as a function of temperature (M vs T at constant H) or at constant temperature as a function of magnetic field (M vs H at constant T).

The SQUID magnetometer has been calibrated with yttrium iron garnet sphere, which is a standard reference material. The calibration factor was determined by fitting the measured flux profile of the yttrium iron garnet sphere to that expected for a point dipole. The flux profile of the yttrium iron garnet sphere is fitted to the expected flux profile by using standard least square fitting procedures as shown in Figure 3, and the calibration factor is obtained from this fitting. Gd_2O_3 was also used as another reference material for the calibration and the effective magnetic moment of the Gd^{3+} could be evaluated from the temperature dependent magnetization measurements. The temperature dependent measurements of magnetization of Gd_2O_3 carried out using the present system show a very clear Curie-Weiss like behavior (Figure 4). Based on a fit to the linear dependence of the inverse susceptibility χ^{-1} on the temperature, the effective magnetic moment of Gd^{3+} was estimated to be μ_{eff} = 7.92 ± 0.02 μ_B, close to the theoretical value of 7.94 μ_B for Gd^{3+}, with a Curie-Weiss temperature of θ = -15.0 K which agrees well with the values reported in the literature. The sensitivity of the system has been estimated to be about 10^{-7}emu at low magnetic fields and about10^{-5} emu at high magnetic fields ~7 T.

VI.4 Establishment of a 37 Channel Magnetocardiography System for Measurement of Cardiac Magnetic Fields

The strength of the magnetic field generated by the electrophysiology of human heart on the anterior thoracic surface is only about 50 pico-Tesla, more than a million times weaker than the earth's magnetic field and requires the use of Superconducting Quantum Interference Devices (SQUIDs) for their measurement and characterization. The first facilities in India for the SQUID based measurement of extremely weak magnetic fields associated with the physiological activities of the human brain (magnetoencephalography or MEG) and human heart (magnetocardiography or MCG), have been established at IGCAR. The MEG / MCG techniques allow a non-contact and non-invasive characterization of the underlying electrophysiology and offer several distinct advantages compared to the other techniques available for the study of human heart / human brain.

A multichannel MCG system enables a comprehensive study of the electrophysiology of the heart from measurements of magnetic field carried out simultaneously at multiple locations on the chest paving way for the reconstruction of sources responsible for the observed distribution of the magnetic fields. The MCG system developed has been progressively upgraded from a single channel to thirteen channels over an year ago; however these systems enabled measurements to be carried out simultaneously only over a limited area on the chest and often required sequential measurements to be carried out in several overlapping configurations on the chest to provide complete information related to the spatial distribution of cardiac magnetic field. This limitation has now been overcome with the assembly of a 37 SQUID channel MCG system which is currently operational (Figure 1).

The new system extends the probed area on the chest to about 350 cm^2, which is considered to be adequate for uncovering the complete electrophysiology of the heart with a temporal resolution of one millisecond. The measurement is quick and is completed in a five minute easy scan over the chest of the subject with practically no preparation of the subject. The flat bottom liquid helium cryostat has a capacity of 20 litres of liquid helium that can last for 4 days before it needs to be refilled again. The thirty seven sensors are arranged in a hexagonal array (with an inter-sensor spacing of about 28 mm) inside a circular area of 210 mm diameter. The sensors are located in recesses in the bottom plate of the liquid helium vessel of the cryostat which are 20 mm in diameter and 8 mm in depth, and reduce the warm-to-cold distance of the cryostat to only 12 mm; this is important to enhance the signal-to-noise ratio. The software integrated with the data acquisition system allows multi-channel display of data (Figure 2) and incorporates modules such as filtering the data to user selectable bandwidth, epoching and averaging the data for the suppression of uncorrelated

Fig. 1 *37 channel cryostat positioned over the chest of a subject for Magnetocardiography*

noise etc. The data can be presented in the form of iso-field contour lines on the Magnetic Field Map (MFM) at each instant of time during the cardiac cycle (Figure 3) to provide a visual aid to the clinician and also enables the evaluation of the parameters which characterize the electrical activity of the heart. The sources can often be modeled as either single or a small number of equivalent current dipoles (ECD), whose location, orientation and strength can be determined at each instant of cardiac cycle by an analysis of the recorded data. Using the MCG data recorded, it has been possible to generate MFM at several instants of cardiac cycle and present it as a video to illustrate the changes in the orientation of the dipole as the cardiac cycle proceeds. The

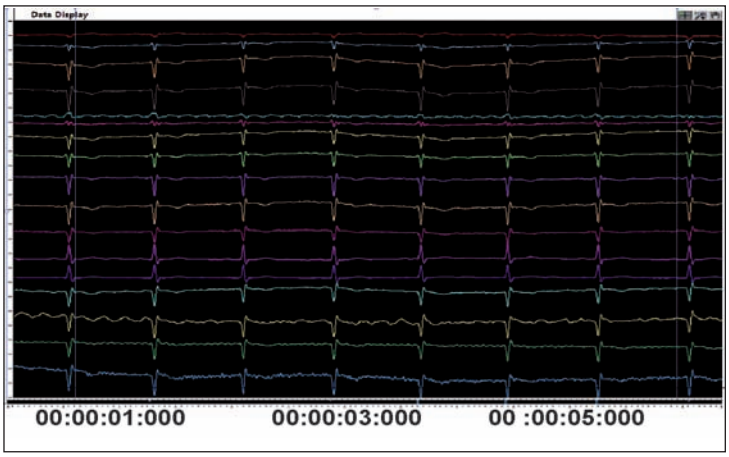

Fig. 2 Screen traces of MCG signals (magnetic field vs time) recorded with the 37 channel MCG system (only 17 channels shown for illustration)

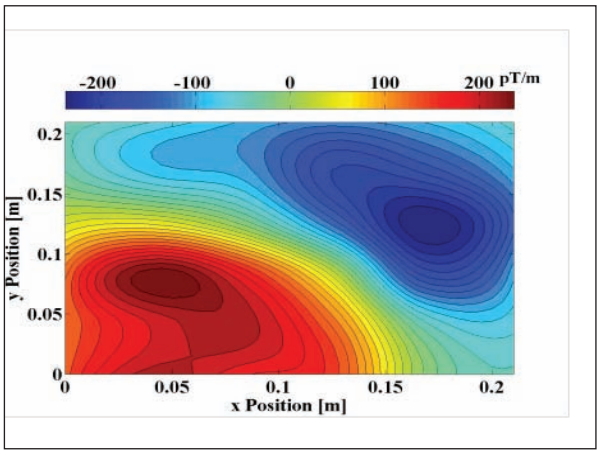

Fig. 3 Magnetic Field Map (MFM) at the instant of R wave peak in the cardiac cycle of a healthy subject

mathematical method used to infer the ECD has been validated by using both simulated as well as experimentally measured data. The method has been applied to the measured MCG of several normal subjects to localize the ECD at several instants of cardiac cycle.

Signal averaging methodology has been used to suppress uncorrelated random noise with a view to extract clinically significant signals which are extremely weak, and hence, difficult to detect. By averaging more than 100 cardiac cycles aligned with respect to a fiducial reference, it was possible to non-invasively track the activity associated with an anatomical structure in the conduction system of the heart known as His bundle, which requires the use of invasive catheter based electrodes in the current clinical practice; indeed, detection of His bundle activity is considered to be important in the context of management of arrhythmia. During the course of these studies, it became apparent that the conventional use of the R wave peak as a fiducial reference for averaging was possibly responsible for the poor success achieved by other research groups in the past in extracting the His bundle activity. In view of this, a novel Q onset based averaging has been proposed which exploits the relative constancy of the interval between the activation of His bundle and the activation of the ventricles, despite the inevitable small, yet significant, variation in the heart rate on account of the intrinsic autonomic control.

Several investigations relating to different types of cardiac anomalies in subjects referred to the facility by the DAE Hospital, Kalpakkam have been successfully carried out. Several researchers have shown the MCG to be useful in the investigation of ischemic heart disease, for locating the arrythmogenic foci in the electrical conduction pathway etc. and to be distinctly superior to ECG, which is often non-diagnostic or non-specific. Even the rest MCG has been shown to have a high predictive value for Obstructive Coronary Artery Disease, without requiring the use of stress provocation.

Several leading cardiologists have shown active interest in evaluating the use of MCG for clinical research in areas that may bring out the specific advantages of the MCG technique. Based on the successful demonstration of the non-invasive tracking of His bundle activity, clinicians have proposed a study to investigate the possible use of MCG to non invasively identify ventricular late potentials (VLP) in the S-T segment of the cardiac cycle, which are attributed to the existence of abnormal conduction channels in an otherwise scarred tissue. VLPs are often precursors to uncontrolled arrhythmia, which, if untreated, can develop into life threatening ventricular fibrillation. Invasive procedures are often necessary in the current clinical practice to detect and localize these arrhythmogenic substrates for ablation; development of a non-invasive technique such as MCG to probe the VLP is considered to be clinically important.

While the existing 37 channel system in the flat bottom liquid helium cryostat has also been used for MEG investigations over a limited cortical area, there is an ongoing effort to establish a whole head 86 channel MEG system inside a concave bottom helmet shaped cryostat to facilitate simultaneous measurements over the whole head.

VI.5 A High Resolution Reagent Dispenser Using Pulsating Position Sensor for Rapid Automated Titrations

A personnel computer based rapid titration facility using in-house built pulsating sensors developed in this Centre has become a work horse for many miscellaneous chemical analyses including chemical assay at ppm/ sub-ppm levels. An attractive feature of this titration technique is to derive quantitative information of chemical specimens present in a composite system. Besides discrete type conductance based reagent dispenser using a disposable medical syringe and continuous type capacitance based reagent dispenser being used in this titration device, another innovative inductance based reagent dispenser has been introduced recently in the titration device in order to conduct titrations with high resolution reagent volume dispension.

The concept of sensing minor shift in position with high precision and reproducibility in measurement using a specially designed pulsating position sensor is employed in developing this innovative approach of designing such reagent dispenser for high resolution rapid PC based titration. The reagent dispensing device consists of a disposable medical syringe with a specially made ferrite piston which moves inside the syringe for continuous delivery of reagent to the titration vessel. The syringe with piston is placed in a typical inductor. The inductor is placed in the timing circuit of a specially designed RCL (R: resistance, C: capacitance, L: inductance) type logic gate oscillator. R and C in the logic gate oscillator are fixed where as L changes with the change in reagent volume in the syringe. The output of logic gate oscillator is digital pulse frequency. The reagent volume in the syringe changes with the change in the position of the ferrite piston moving inside the inductor. This results change in inductance which in turn causes a shift in pulse frequency. Hence shift in pulse frequency is a function of volume of reagent delivered during titration.

The inductor which is a major component of reagent dispensing device consists of a PTFE bobbin wound with copper wire which is enclosed with a PTFE cover. This inductor is the inductance component of the logic gate oscillator which is powered by 5 V DC. The ferrite piston is constructed by placing a ferrite rod inside a PTFE enclosure. Using this piston a fixed volume of reagent is withdrawn from the reagent vessel to the syringe during titration. The syringe with piston is placed inside the inductor. The piston is driven by a DC pump in order to deliver reagent to the titration vessel during titration. Before onset of the titration the reagent in the dispenser is maintained at a constant volume in order to give a fixed frequency value (f_R). During titration with the change in reagent volume the frequency value shifts from the reference frequency. The real time shift in frequency ($\Delta f = f_R - f$) is monitored online in a separate channel. The relation between Δf and volume of reagent is obtained by appropriate calibration before titration. The

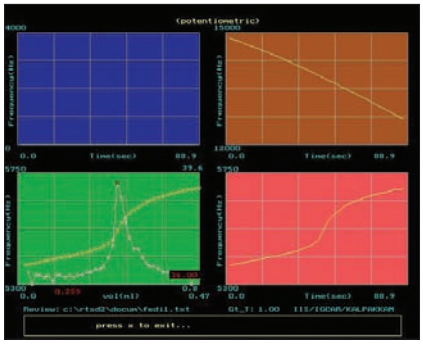

Fig. 1 *Screen capture view of an online potentiometric titration plot (Fe^{2+}-dichromate REDOX system)*

reagent dispenser with respective logic gate oscillator is connected to second channel of a three-channel system. The titration process is similar to earlier titrations reported using drop type dispenser. In the present case with this new reagent dispenser, channel 2 provides information of volume dispensed with respect to time. Immediately after completion of titration offline processing of data generates titration plot in volume domain in a separate channel from which the end point is determined. There is provision for generating first derivative plot in redox titration. The entire operations which include (i) start up of titration, (ii) volume dispension, (iii) real time data acquisition, (iv) end of titration and plotting in volume domain are governed by an indigenously developed user friendly software package. The performance of the device was tested in several conductometric and potentiometric titrations. Figure 1 shows redox titration plot for Fe^{2+}-$Cr_2O_7^{2-}$ system. The introduction of this newly developed dispenser to the titration facility has made the device more user friendly.

VI.6 Ultrasonic Time of Flight Diffraction Technique for Accurate Determination of Cracks inside Metallic Rods

Conventionally ultrasonic pulse echo technique is widely used for the qualification of solid metallic rods. This method, being based on reflection of high frequency sound waves (ultrasound), is highly dependent on the orientation of the defects. Defects, especially crack tips, will not always be favorable to reflection and hence error in sizing and positioning is likely to be higher. Time of flight diffraction technique, which works on the principle of diffraction of ultrasonic waves from the extremities of the discontinuities, is one of the best methods for detecting and sizing cracks accurately. Hitherto, this technique has been applied only for examination of welds of simple planar geometry. Time of flight diffraction technique has been extended for the detection of discontinuities such as cracks in the extruded metallic rods.

For the initial studies, this technique has been attempted on a calibration rod of length 170 mm and diameter 90 mm on which a total of two notches and eight holes were made for calibration purpose. One notch and two side drilled holes were made on face A of the rod, one notch and one hole on face B and five holes at different depths on the cylindrical surface. The positions and separations between the notches and holes were well maintained in order to evaluate the technical feasibility of defect detection at various depths and positions and to find out the percentage error as a function of depth. The notches were of depth 0.5 mm and length and depth 10 mm. All the holes were of 2 mm diameter. The experimental set-up for time of flight diffraction scanning of the 90 mm diameter reference rod is shown in Figure 1. Transmitter and receiver probes were placed diametrically opposite using a special probe holder with provisions for adjusting the encoder for axial and circumferential scanning and tilting the probes for proper contact with the material. Ultrasonic probes of 6 mm crystal diameter and 5 MHz frequency attached to 45º longitudinal wedges were used. The transducers were coupled to the material by industrial standard grease.

The axial and circumferential scanning with this probe

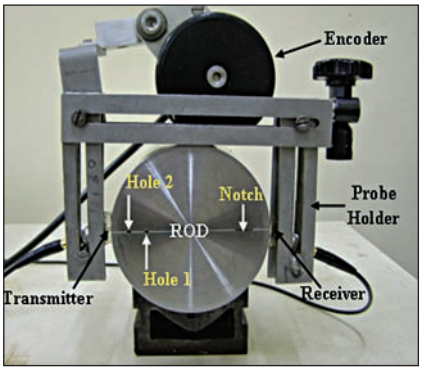

Fig. 1 *Experimental set–up for time of flight diffraction*

configuration provides full volume coverage of the rod. The number of scans depends on the diameter of the rod and the beam spread. The orientation and location of the defect could exactly be determined from the B-scan images. Figure 2 shows the time of flight diffraction B-scan images of the holes and notch on the reference rod at face A. This image is a result of circumferential scanning of the rod for 360° by the arrangement as shown in Figure 1 and hence the length of the image is 314 mm (2πr). It is possible to measure the location of the holes and notch from this image by measuring the distance from the back wall echo corresponding to the surface and

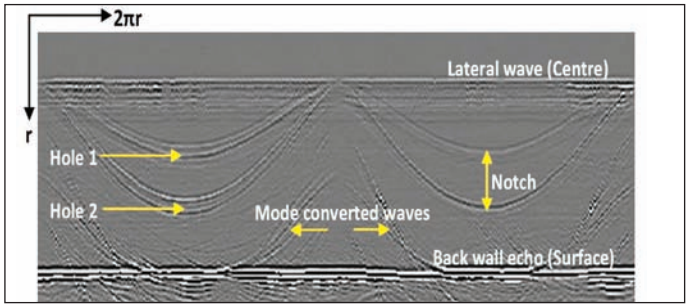

Fig. 2 *Time of flight diffraction image of the circumferential scan on the reference rod at face A. The notches and the holes are clearly revealed. shows two holes and the notch*

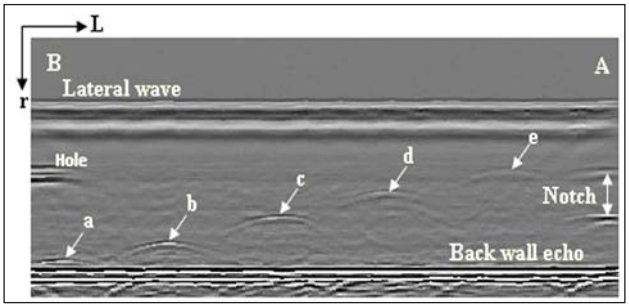

Fig. 3 *Time of flight diffraction image of the axial scan of the reference rod*

the lateral wave corresponding to the centre of the rod.

Figure 3 shows the Time of flight diffraction image obtained by axial scanning of the rod, starting from the B end. This scan could detect all the holes made on the cylindrical surface along with the hole at face B and notch at face A. Comparison of the depth measurements with standard techniques indicated that the errors are within 2%.

This technique was attempted on a stainless steel rod of 100 mm diameter with a crack inside propagating to a length of 1.5 m. In such rounded specimens, pulse echo, being a reflection technique, is not adequate to give exact location of the narrow crack tips.

Circumferential time of flight diffraction images of this defective rod at four locations with 50 mm interval are shown in Figure 4. Length of each image is same as the circumference of the rod which is equal to 314 mm. The exact location of the crack tips can be determined from these images. It is clear that the extension of the crack towards the surface is varying as it propagates along the length of the rod. Also from the B-scan images it is clear that the crack tip is branched.

It is estimated from the B-scan images that the Tip-1 of the crack is laying between 85º to 107º as the crack Propagates along the rod for a length of 250 mm and tip-2 was from 223º to 241º with respect to a reference line drawn on the surface. Crack profile constructed from the B – scan images is shown in Figure 5.

For the complete coverage of the 100 mm diameter rod by a 10 mm diameter ultrasonic normal beam

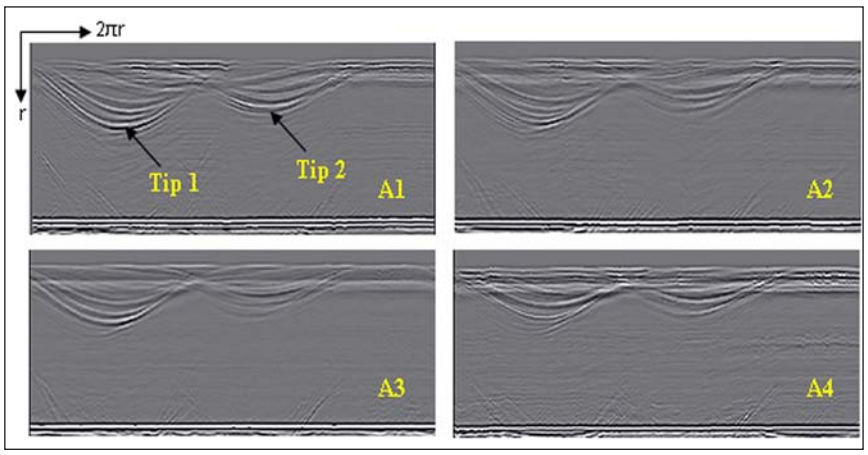

Fig. 4 *Circumferential scan of the 100 mm rod having crack*

transducer by pulse echo (PE) method, 35 axial scans are required. But with the new methodology proposed, total of eight scans along the length is quite adequate. This number would however vary depending on the diameter of the rod. The scanning times are also much lesser and more accurate. For the defective rod of diameter 100 mm and length 2 m, pulse echo examination with a 10 mm diameter normal beam transducer has taken 2.15 hrs including the defect's depth measurement and analysis. But with time of flight diffraction axial scanning, it has taken only 45 minutes including defect's depth measurement from the B-scan images and analysis.

In conclusion, apart from the established fact that time of flight diffraction provides a faster inspection, the main advantage is the superior profiling of the crack tips along the length of the rod in 3D which can clearly indicate the zone of the defect to be removed. Imaging the orientation of the crack plane is an additional possibility by this method, which is not possible in conventional pulse – echo method. The technique is thus a value addition to the industrial quality assurance and amenable for automation. It can be applied for the inspection or as part of industrial quality control of rods used in manufacturing industries where metallic rods are being used for, fabrication of hollow cylinders, pipes, nozzles etc. This method may also be applied for in-service inspection or condition management of such metallic or non metallic rods that form part of the equipment or components or assemblies in all the above mentioned industries including areas under pressure, radiation and high temperature.

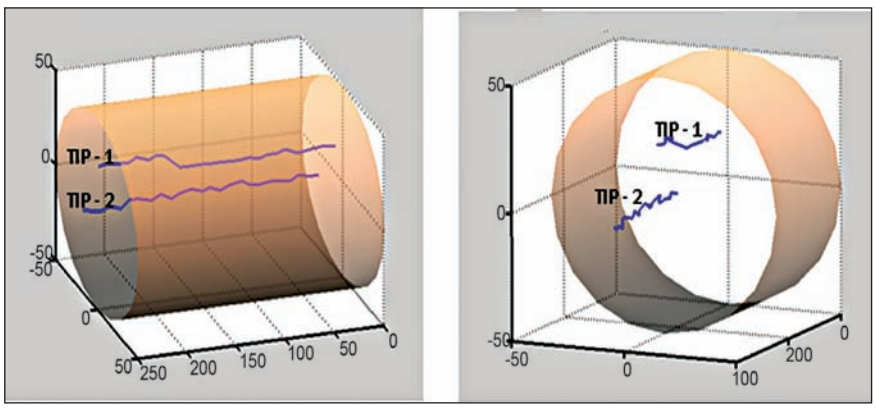

Fig. 5 *Profile of the crack tips along the length of the rod*

VI.7 Wireless Hand Held RFID Reader for ID Card Photo Verification

It is vital to identify the authentication of the employees entering the main / KKM gate of the DAE complex at Kalpakkam. All the employees were issued Radio Frequency Identification (RFID) based Smart Card with the necessary data programmed to the card. The photo with other details of the employees is printed on the card. The disadvantage of this type card is that the outer design of the card can be duplicated and thus it will not be possible for the security to detect whether the person is carrying the genuine card or not. At the main gate all the personnel entering the DAE complex need to go through the RFID based Access Control System with full height turnstiles. Thus the credentials of the employees and contractor personnel are thoroughly verified by the access control system. However the employees and contractor personnel who are allowed via two / four wheelers do not validate their entry through the RFID based Access Control System with full height turnstiles. Thus it is necessary to verify the credentials of the ID card being carried by the personnel being traveled by the vehicles. In view of this, a wireless Hand Held RFID reader is developed.

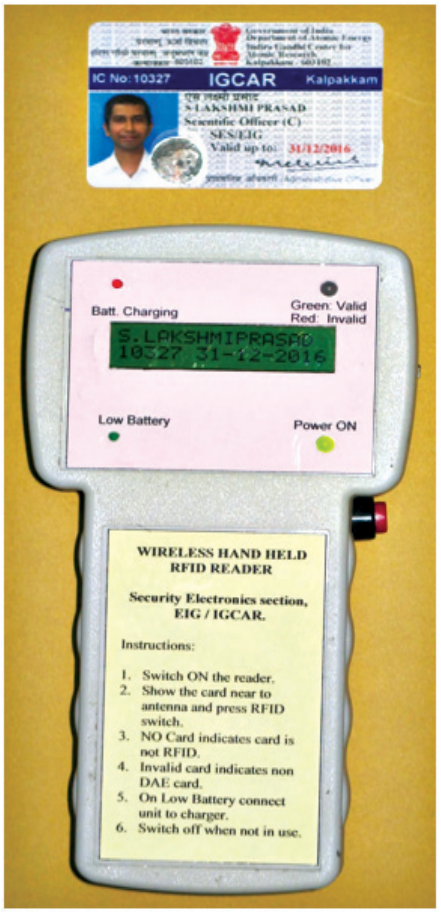

Fig. 1 *Hand held RFID reader*

System description

The hand held reader authenticates the identity card and reads the details of employee. It displays the name of the employee, IC No. and date of validity of the card on a LCD display and the same details are sent to a PC placed within 50 meters through wireless. The PC receives all these details of the employee from Hand Held Reader via wireless ZIGBEE protocol and displays on a 42" monitor along with the photo of the employee picked from the employee database available in the PC. Thus, the wireless Hand Held RFID reader developed enhances the screening of all the employees entering by two / four wheelers passing through the main gate and KKM gate, so that nobody enters with a proxy or fake ID card.

Hand Held Mifare® Smart Card Reader has been designed with ARM7 (Advanced RISC Machine) and CLRC632 IC (Integrated Circuit) for ISO14443A for RFID protocol implementation. The board has LEDs (Light Emitting Diode) and Buzzer for indication, 2x16 LCD for displaying personal information of card holder like IC No, name and the card validity. It has RS232 serial interface with the PC for the programming of the card and changing the settings of the reader. The board has on board memory which can be used for storing the details of the cards read if required. The board has an in-built charging circuit for charging a 3.7 V, 1800 mAh Lithium Ion battery which is used as the power supply to the system.

VI.8 Retrofitting of Differential Scanning Calorimeter with Contemporary Instrumentation

The practice of retrofitting of analytical instruments for the sake of corrective maintenance, feature enhancements, import substitute of components, enhanced user friendly operations is in vogue. Retrofitting of vintage instruments like mass spectrometers, spectrophotometers and calorimeters are some exemplifying cases. In this series, presently the retrofitting of SETARAM make Differential Scanning Calorimeter DSC-111 is completed.

DSC is a thermal analysis instrument where energy changes in a sample are investigated with temperature. The temperature of a sample is raised in increments via a temperature program, while a reference substance is heated at the same rate. The heat flow to or from the sample from or to the reference is monitored as a function of temperature or time. Such measurement provides qualitative and quantitative information about physical and chemical changes that involve endothermic and exothermic processes, or changes in heat capacity, i.e. thermal transitions.

The thirty year old DSC-111 was a heat flux calorimeter. The instrumentation had been built around DOS, Z80 processor, TTL digital, and then old analog ICs for the operation and measurement of the calorimeter signals. It exhibited inconsistency in thermal programming and reproducible heat flux measurements. On exhaustive analysis of the system hardware and the schematic it emerged that the current measurement techniques and processing software methods can be adapted to the original calorimeter assembly so that contemporary version of the DSC can be constructed.

The original calorimeter heater and linear power driver, the thermopile sensor and thermocouple were retained. The calorimeter heater temperature programming and control, sensor signal conditioners and signal measurement were developed and adapted to the calorimeter components. A comprehensive user friendly operational procedure and GUI in LabVIEW were developed, optimized and integrated with the system successfully.

There is a heater embedded in a silver block with a provision for loading the sample and reference materials. The sample and reference pans are placed over the thermopile and the thermopile output directly represents the heat flow signal between the sample and the reference. There are a couple of type K thermocouples located in the assembly to measure the sample temperature and heater temperature respectively. A suitable commercial temperature programmer and controller are adapted to program the thermal profile of the heater. A signal conditioner block is designed for the thermopile and the sample thermocouple signals. A local cold junction measurement channel is also included to calculate the sample temperature accurately. The signals are digitized and optically coupled to the crown regions that have been made of mild steel to demonstrate the capability and understanding of the manufacturer's comprehension.

A high temperature (423 K) test chamber was fabricated which will be used to validate the device assembly and the choice of its subsystems for high temperature operation. High temperature standalone tests of the traction motor and the steering motor (with compressed air cooling) were successful, thus justifying the selection of the motors.

Customized slip-skid sensors have been successfully developed and tested and are ready for integration with the main ISI device. It is also imperative to optimize the pneumatic tubing and electrical/ electronic wiring and plan the routing accordingly. A customized heat exchanger has been fabricated for cooling the nitrogen which is used for cooling the cameras and motors on board the ISI device. Software for the operation of the ISI devices is under development. Prototyping experience has provided lot of inputs while formulating the architecture of the software.

Visual examination camera has been customized and tested at room temperature with satisfactory results. High temperature tests are due once the heat exchanger is operational.

The trials and experimentation at the manufacturing site has revealed quality information for ensuring the development of a robust system. High temperature test and validation of the integrated system will be taken up shortly followed by comprehensive testing and validation in the mock-up test facility. The benchmark trials will be finally conducted in the reactor.

VI.9 Development of Compact CNC Machine for Remote Tensile Specimen Preparation

A remotely operated tensile specimen preparation machine has been designed, developed and commissioned inside the hot cells of Radiometallurgy laboratory. This machine is used to prepare uni-axial tensile test specimens from highly radio-active hexagonal sheaths of fuel subassemblies irradiated in FBTR. The evaluation of residual ductility of the irradiated hexagonal sheath material is very essential since exhaustion of ductility is one of the factors that limits the burn-up of fuel subassemblies in fast reactors.

The machine (Figure 1) consisting of a mechanical system and the motion control system was designed for remote installation, operation and maintenance inside the hot cells, using the in-cell handling devices such as master-slave manipulators, power manipulator and in-cell crane. Modular construction is adopted in the design to meet this objective. The size of individual modules is such that they can be posted in or out of the hot cells through the cell transfer ports, and their weights are designed within the lifting capacities of the handling equipments. Materials that can withstand upto 10^8 Rads have been used for the construction of the machine to the extent possible. However some essential components that do not meet this criterion and whose service life is limited have been included as easily replaceable modules.

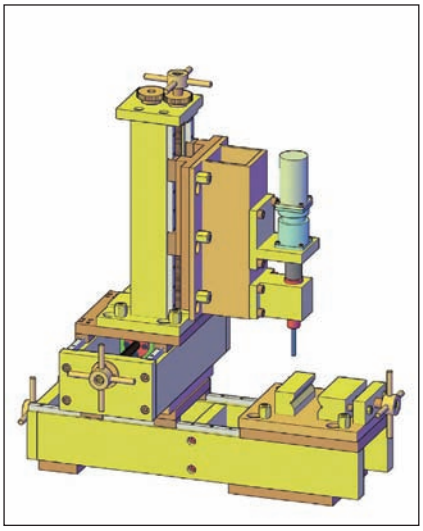

Fig. 1 *Mechanical system of the CNC machine*

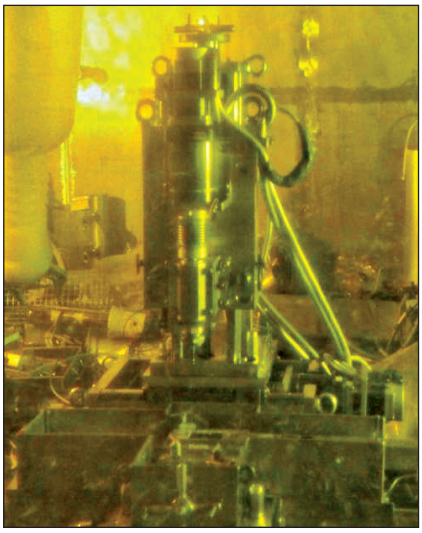

Fig. 2 *Machine in hot cell*

The mechanical system consists of a motorized spindle with milling cutter module mounted on a motorized X-Y-Z stage and a vice module to rigidly clamp the hexagonal wrapper during milling. The motion control system contains four geared servo motors with resolvers, 4-axis CNC controller, electronic linear displacement scales and limit switches. The contour of the specimens to be machined is traced by the end mill cutter through programming to mill the specimen from the hexagonal wrapper. Dry cutting at slow speed is employed due to restrictions in the hot cell. A special fixture ensures that the specimen is rigidly held in position until the specimen gets fully detached from the wrapper. Dimensional verification of the machined specimen is carried out in a special measurement device with a measurement accuracy of ±10 µm.

After the completion of mock-up trials in shop floor to ensure that the machined specimen meets all requirements, trials were carried out in the mockup cell, to qualify the machine for remote operation and maintenance in the hot cells. During these qualification trials, the machine has undergone extensive modifications and improvements to ensure that the modules are amenable for remote handling, assembly and disassembly. Various modules of the machine were transferred to hot cells through the transfer ports by following approved safety procedures and guidelines. The signal and power cables were installed using leak-tight service penetrations specially designed and installed in the hot cell wall. The mechanical modules were remotely assembled and installation of the machine was completed (Figure 2) by interfacing them with the control panel installed in the operating area. Tensile specimens were machined from unirradiated hexagonal sheath to demonstrate procedures and to arrive at the accuracies.

This machine has been successfully used for the preparation of tensile test specimens from the FBTR fuel subassembly (155 GWd/t burn-up FBTR fuel subassembly).

Specimens extracted from various locations of the subassembly corresponding to different levels of displacement damages (dpa) were tested (Figure 3) to generate tensile properties of 20% cold worked AISI 316 L hexagonal sheath material at ambient and elevated temperatures.

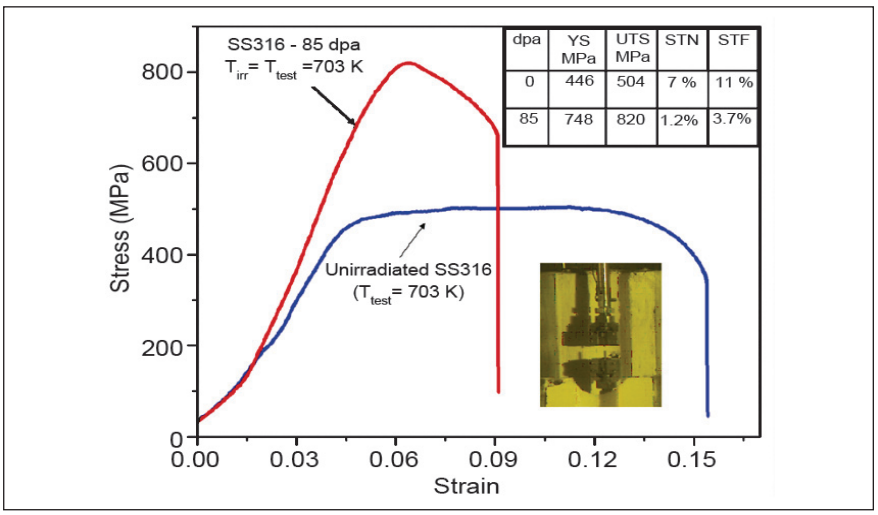

Fig. 3 *Ambient and high temperature tensile property of 20% cold worked AISI 316 L hexagonal sheath material STN- Strain to Necking calculated as strain from yield stress to point of neck initiation STF- Strain to Fracture calculated as strain from yield stress to point of failure*

VI.10 Unique Experience in Establishing the Third Power Source from PFBR Switchyard

The electrical power distribution system at IGCAR, Kalpakkam was established in 1977. The maximum power demand in 1977 was only 1.5 MVA and it has progressively increased to Maximum Demand of 24 MVA. When the Electrical system was designed, importance to reliability & power quality was considered and hence redundancy was built in. The system design was based on single failure criteria. Two independent incomers from MAPS, namely IGCAR Feeder no. I & II were introduced in the system. The system reliability was kept high by following proper operation and maintenance practices.

The load growth was closely monitored and it was observed that the maximum demand was approaching very close to system design capacity. A detailed load growth study indicated a load growth of about 50 MVA by the end of 12th plan period. Based on the projected load, a decision was taken to augment the system by providing third power source/ incomer to IGCAR. After evaluating different configurations, it was decided to introduce third incomer feeder from PFBR switch yard. The third feeder was designed for 50 MVA capacity which is capable of feeding 25 MVA power at 33 kV level and 25 MVA capacity at 11 kV level. This will ensure adequate & reliable power to various new DAE facilities at IGCAR such as 2 MGD desalination plant, Hall IV, Hall V, DFRP, SM Lab and various other facilities under BARC (NRGPK new projects), FRFCF (30 MVA) and Townships.

Details of augmentation

33 kV central switching station was fed by two Nos. of 25 MVA feeders coming from MAPS switch yard, functioning with one working and one as a standby. Augmentation of 33 kV central switching station was completed to receive the third feeder from BHAVINI by the addition of one more 33 kV bus. With the introduction of third feeder, the configuration at central switching station is as follows.

- Feeder-1 (33 kV Cable) is in service since 1980
- Feeder-2 (33 kV OH Line) is in service since 1991
- Feeder-3 (33 kV cable) was commissioned in 2010. With the introduction of third feeder the operating philosophy have been changed to two out of three configuration.

Introduction of 33 kV new central switching station (NCSS-2)

To meet the requirements of optimum distribution of additional

power received from BHAVINI a new 33 kV indoor substation was built in the year 2009 near NCSS-1 which is opposite to NDDP site. The 33 kV bus at NCSS has independent bus sections to receive 25 MVA power from PFBR switch yard and from MAPS switch yard. The power received is getting distributed to FRFCF, 2MGD desalination plant and IGCAR loads through central switching station.

Implementation of unique and innovative design features in the new system

A unique feature could be implemented with the help of numerical relays to identify the faulty zone and to clear the fault within 100 ms, which is very less compared to the fault clearing time of about 1500 ms in the existing system by conventional electromagnetic relays. This drastic reduction in fault clearing time will reduce the dynamic forces seen by all the equipment like cable, cable joints, transformers and switchgear and hence to get enhanced life for all of the above equipment. This intelligent protection system has the added advantage of discriminating the faulty zone and to prevent the tripping of healthy zone.

Improved human safety

New design features are introduced in the system to improve the human safety. Interlocks have been introduced to prevent the accidental opening of live panel. The backside cover is fastened by Solenoid interlocking levers/ locks which prevent the opening of backside cover when the panel is live. Interlock is provided for the front door also to enhance operator safety

Commissioning experience

The entire system was installed and tested to verify system integrity and have been cleared by CEA.

VI.11 Automation of HVAC Equipment using Microprocessor Controlled Building Management System at IGCAR

Central water chilling plant (CWCP) was established for the purpose of providing uninterrupted and reliable air-conditioning & ventilation services to the centre. CWCP caters to the air-conditioning & ventilation demands of various radioactive laboratories, FBTR, computer centre and other buildings. The HVAC system is energy intensive and consumes about 55% of total energy consumption of IGCAR. Operation of centrifugal chillers and associated condenser cooling pumps, chilled water pumps, cooling towers, booster pumps and air handling units is an essential feature. Operation and maintenance of CWCP and associated equipments of various laboratories distributed over two square kilometers area at IGCAR is a challenging task. In order to manage the system efficiently, automation of operation of these equipments was envisaged and an intelligent state-of-the-art microprocessor controlled Building Management System [BMS] through LAN is successfully installed and commissioned. The objectives of automation of HVAC equipments are as follows:

- Total automation and optimum utilization of available resources
- Centralized monitoring and control via LAN
- Effective fault diagnosis and analysis

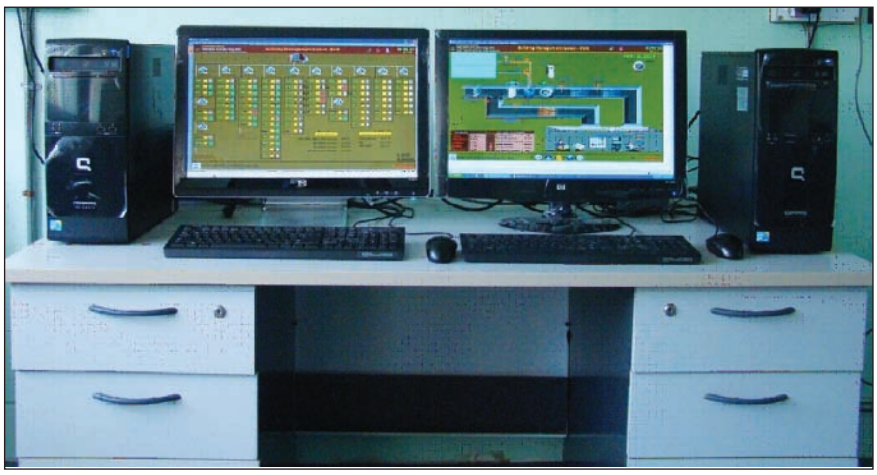

Fig. 1 *Central monitoring station at CWCP*

- Improved system reliability, control and management
- Energy saving.

The automation system consists of central monitoring station-supervisory control and data acquisition system (SCADA), direct digital controllers, Variable frequency drives, system integrator and process instruments.

The air-conditioning equipments such as air handling units, booster pumps, cooling towers etc. are controlled & monitored by a dedicated direct digital controller. The BACnet over IP enabled direct digital controllers are in turn connected to the central monitoring station at CWCP through existing high speed 100 Mbps LAN. The direct digital controller receives input process parameters from field instruments/sensors and controls the equipment using control software as per assigned program. The central workstation is a SCADA system which serves as master and communicates with all the networked direct digital controllers and represents the process parameters/data in an easily understandable manner.

The features of the automation system are remote monitoring, data logging and trending of process parameters, alarm & event management, scheduling & sequencing, energy management, multi level user access protection and enhanced fire safety. The photograph of central monitoring station at CWCP indicating chiller and air handling unit graphics is shown in Figure 1.

The successful installation and commissioning of HVAC automation has enhanced the system reliability, precise control and monitoring of various parameters and precise scheduling of AC equipment based on seasonal conditions. Energy saving of about 7 to 8% has been achieved.

VI.12 Monitoring of Coastal Ecology in the Inner Shelf Region of Bay of Bengal (Off Kalpakkam Coast)

Monitoring of the coastal milieu at Kalpakkam, up to 5 km from shore and about 15 km along the shore in a north-south transect, has been in progress since 2006 which covers physical, chemical and biological aspects of the nearshore water. Recently the monitoring was extended up to 50 km from coast covering the inner shelf region from Chennai to Pondicherry (Figure 1) to meet Ministry of Environment & Forest guidelines. Sampling was carried out on board coastal research vessel Sagar Paschimi provided by MoES.

A strong stratification was evident from the temperature and salinity data with high saline and cold bottom water. Weaker winds over the Bay, unable to erode the strongly stratified surface layer thereby restricting the turbulent wind driven vertical mixing only to a shallow

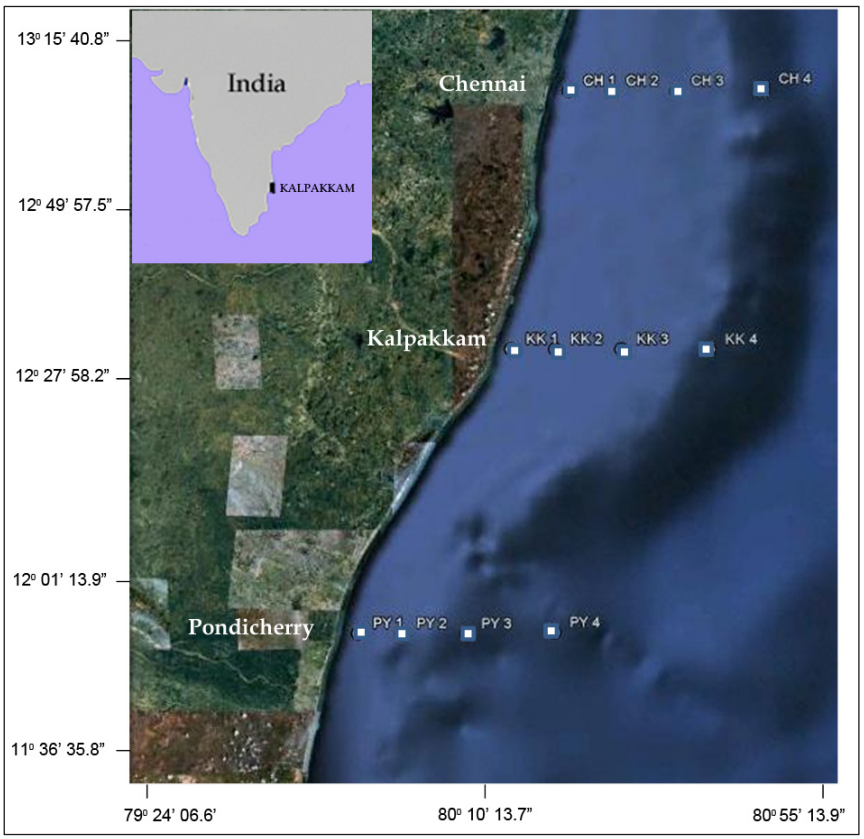

Fig. 1 *Sampling locations/transects covering shelf and slope region of Southwest Bay of Bengal investigated during September 2010*

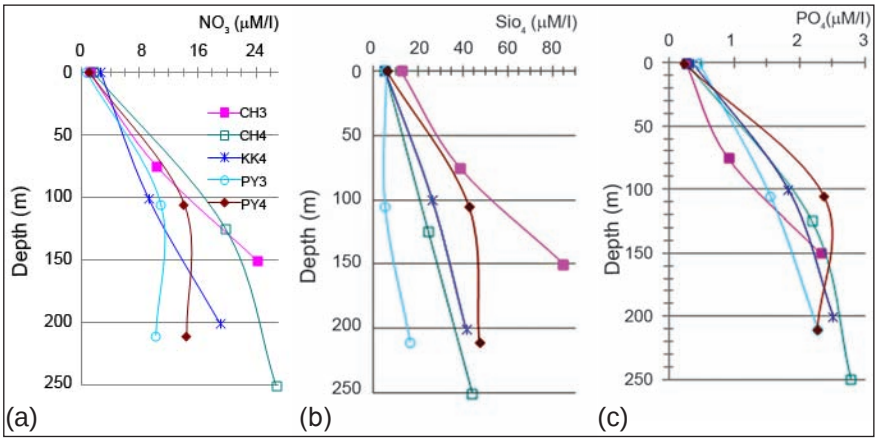

Fig. 2 *Dissolved inorganic nutrient profile in the continental shelf and slope region of Southwest Bay of Bengal during Sept 2010 (CH –Chennai, KK-Kalpakkam, PY-Pondicherry (a) NO_3 (b) SiO_4 and (c) PO_4*

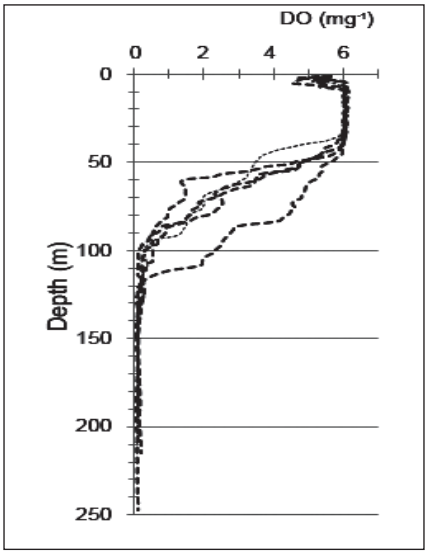

Fig. 3 *Vertical distribution of oxygen indicating hypoxic and anoxic conditions in the South western Bay of Bengal during September 2010*

depth of <20 m. The stratified water column is more visible at a water depth of ~40 m and the halocline persists up to ~80 m down the surface (from ~40 m). In a similar approach the water temperature also declines drastically within the depth range of ~40 to ~100 m (ΔT = 10 degrees). This is indicative of a cooler (12-15 degrees) and more saline (35 psu) bottom water mass, that probably intruded to the southern Bay of Bengal by the West Australian Current. Usually the dissolved nutrient concentrations in the near shore surface waters were found to be relatively high as compared to that of the offshore water. Whereas, in the offshore region, sinking of organic matter that remineralize to nutrients, contribute to the nutrient budget in the bottom water. A significant difference in nutrient concentration was observed between the shallow and deeper waters. Inorganic nitrogen, phosphate and silicate concentrations were relatively high in the intermediate and bottom waters of the western Bay of Bengal during the current observation (Figure 2). Inorganic nitrate, phosphate and silicate values were significantly high during this observation as compared to the earlier records.

Interestingly the upper 40 m of this region of investigation was reported to be devoid of nitrate & phosphate and silicate hovered around 2 $\mu moll^{-1}$ during the southwest monsoon (July-September) of 2001. However, surprisingly the present results not only indicated their presence but also it pointed to a level indicative of anthropogenic influence particularly close to Chennai region (13^o N). Similarly, among the three transects (Chennai, Kalpakkam and Pondicherry), coastal waters off Kalpakkam was found to be least polluted with nutrients. This is indicative of the actuality of terrestrial input due to intense urbanization in the Chennai metropolitan city which could have detrimental effects on the marine ecosystem. Relatively low nutrient concentrations off Kalpakkam coast as compared to 60 km north and south gradient, point towards minimal human induced impact on the functioning of this marine ecosystem.

The community structure as well as the standing stock of plankton showed a remarkable difference spatially. In total, 82 phytoplankton and 75 zooplankton species were identified in the offshore region. Phytoplankton community was dominated by diatoms with 53 species. Copepods formed the dominant component of the zooplankton community with 52 species. A comparison of offshore and coastal waters showed that coastal water is rich in plankton diversity (phytoplankton 385 species and zooplankton 120 species).

One of the most important observations of this study was the presence of hypoxic and anoxic conditions (Figure 3) in the bottom water of the shelf region which has got significant ecological implications. We measured a vertical expansion of hypoxic conditions ($0.14 < O_2 \leq 2$ mg/l) at a minimum depth of 59 m and further anoxia ($O_2 = 0$mg/l) at a depth of ~98 m within 30 km offshore. The onset of shallow water (59 m) hypoxia within the oxygen minimum zone was associated with a sporadic event of inner shelf hypoxia (24 m) in a broad section of the southern Indian east coast (Figure 3). However, earlier reports only explained about the hypoxia and further oxygen minimum zone at the lowest depth of 91 meters in

the continental slope and ridge. In the present investigation, hypoxia prevailed in several places across the area extending between 11° to 13°N and 79° to 80°E spreading from shelf break to the inner shelf encompassing ~8000 sq. km. Irrespective of a seasonal prototype emergence of hypoxia and anoxia in the Arabian Sea, Bay of Bengal witnessed year-round hypoxic and anoxic zones in 2010 which is the first observations of hypoxia extending on to shallow continental shelf (24-59 m deep) of this region. It is worthwhile to mention that hypoxia and/or anoxia was observed at 30 km away from the shore off Chennai and Pondicherry whereas off Kalpakkam it was evident at a distance of 50 km ashore.

VI.13 Knowledge Management Activities at IGCAR

Knowledge management maturity model

Maturity models describe the development of an entity over time. The entity can be anything of interest. It can be a human being, an organization, a technology, a product, a process etc. In the current context, the entity of interest is knowledge management knowledge management maturity models (KMMM) are driven by the necessity to have a clear cut road map for any organization that is embarking on knowledge management implementation. It provides the clear vision with a description of the path ahead. KMMM can be considered as an application of structured approach to knowledge management implementation. In other words development of a KMMM is nothing but engineering of KM. Hence Knowledge Management Maturity Model can be defined as the “application of systematic, disciplined, quantifiable approach-that is an engineering approach to development, implementation and successive progression to attain maturity in knowledge management”. Maturity models are basically application of life cycle approach. The entity develops through the levels, until the highest level, which is the level of perfection.

A Knowledge Management Maturity Model was developed at IGCAR. It has six maturity levels (level 0 to level 5). The maturity levels are named as ‘Default’, ‘Initial’, ‘Qualitative Development’, ‘Quantitative Development’, ‘Maturity’ and ‘Extended-Organizational Maturity’. The model identifies five Key Areas(KA) viz People, Process, Technology, Knowledge and Return On Investment (ROI). It also identifies 20 parameters(Key Parameters) for all the Key Areas (People-6, Process-4, Technology-6, Knowledge-3, ROI-1). The parameters for People KA are Awareness, Participation, Reward and Recognition Scheme, KM roles, Communities of Practice, Mentoring and Succession Planning. The parameters for Process KA are KM Policy, KM Strategy, KM Processes, and Process Integration. The parameters for Technology KA are Network, Data and Information management, Explicit Knowledge Management, Tacit Knowledge Management, Artificial Intelligence (AI) and Knowledge Engineering (KE) techniques, Technology Integration. The parameters for Knowledge KA are Knowledge Classification Knowledge Capability Areas, and Knowledge Organization. Employee Satisfaction is the only parameter for ROI.

The parameters can have different values called Key Values, which can be either qualitative values (Low, Medium and High) or quantitative values (0-100%). The value ‘Nil’ the indicates that, either parameter is not applicable, or it is not assessed or the value is negligible. Each maturity level is identified by a group of Key Maturity Indicators (KMI), which is a combination of Key Areas, Key Parameters and Key Values.

For an organization to be in a specific maturity level all the KMIs pertaining to that level and all preceding levels need to be satisfied. No levels can be skipped. If an organization satisfies all the KMIs pertaining to one level say level 1 and at least one KMI pertaining to the next level for each KA, then the organization can be considered to be in a level 1+. Similarly if the organization satisfies at least 50% of the KMIs pertaining to level 2 for each KA, then that organization can be considered to be in a level of 1++. Also if the organization satisfies all KMIs of level 1 and satisfies at least one KMI or at least 50 % of the KMIs of level 2 in one or more specific KAs alone, then the organization is considered to be in level 1 in the over all maturity and 1+ or 1++ in the specific KAs alone. The Maturity Levels and Key Maturity Indicators are shown in Figure 1.

The maturity levels of IGCAR and various groups were assessed based on the above model. Recommendation for improving the maturity level is being prepared.

Tacit knowledge elicitation

Tacit knowledge of senior officers was elicited through video / audio recordings and documents. The elicited knowledge modules were made available in the IGCIMS server with necessary metadata at http://igcims/tacit/tacit.htm

Taxonomy development

A taxonomy pertaining to the domain knowledge of Computer Division was developed and implemented. The knowledge is classified into nine categories viz Advanced Visualization, Application Software, Computational Intelligence, Knowledge Management, Networking & Communication, Scientific Computing, Simulation & Modeling, Wireless Sensor Networking and General. Under each domain the knowledge documents are classified into publications, presentations, design reports, elicited knowledge, frequently asked questions, tech bits and general.

Knowledge management portal

A knowledge management portal was developed for Computer Division using share point services. It has facilities for submission and viewing of knowledge documents, based on the taxonomy and meta-data. The portal is being improved with facilities for, knowledge quality rating for documents and knowledge sharing rating for knowledge workers. Also implementation of domain specific discussion forum, creation of database for frequently asked questions etc. are planned.

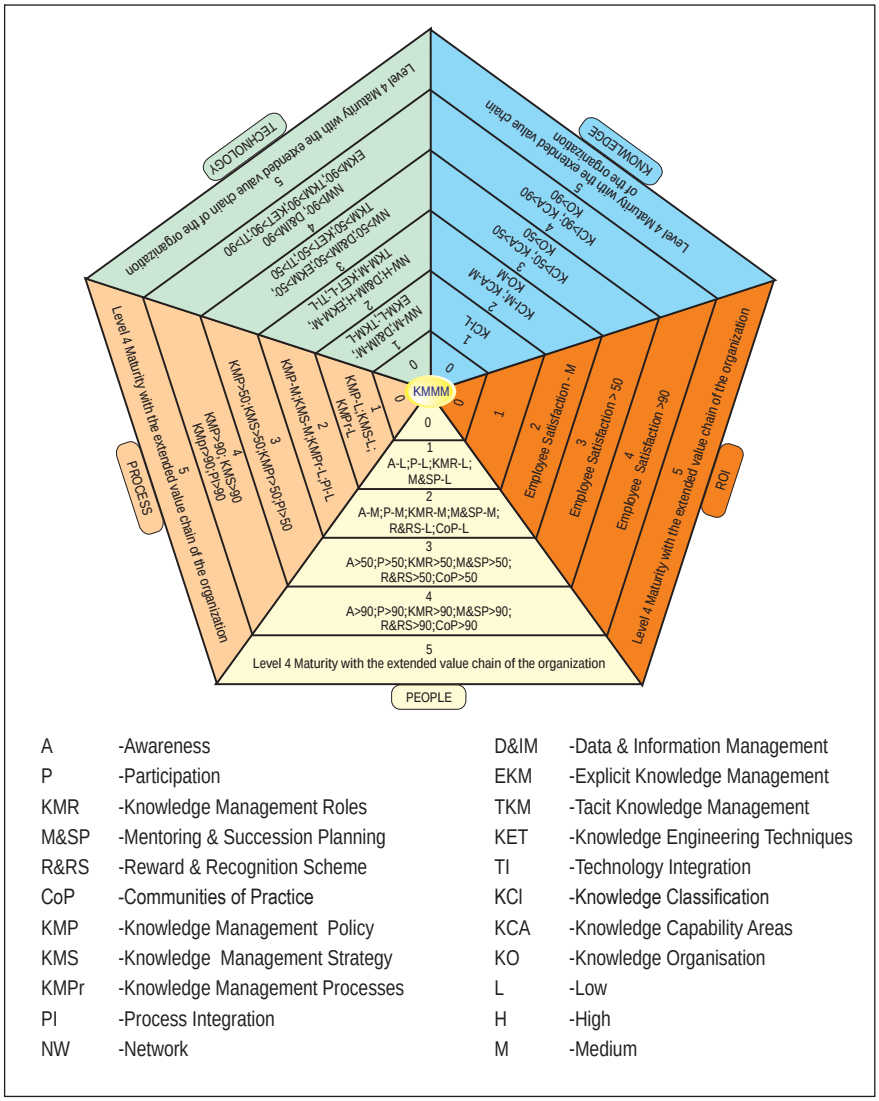

A	-Awareness	D&IM	-Data & Information Management
P	-Participation	EKM	-Explicit Knowledge Management
KMR	-Knowledge Management Roles	TKM	-Tacit Knowledge Management
M&SP	-Mentoring & Succession Planning	KET	-Knowledge Engineering Techniques
R&RS	-Reward & Recognition Scheme	TI	-Technology Integration
CoP	-Communities of Practice	KCl	-Knowledge Classification
KMP	-Knowledge Management Policy	KCA	-Knowledge Capability Areas
KMS	-Knowledge Management Strategy	KO	-Knowledge Organisation
KMPr	-Knowledge Management Processes	L	-Low
PI	-Process Integration	H	-High
NW	-Network	M	-Medium

***Fig. 1** Maturity levels and key maturity indicators*

Knowledge management awareness

In order to improve awareness of KM among the employees, KM awareness seminars were conducted in various groups of IGCAR. The discussions during the awareness seminar were audio recorded and made available at : http://igcims/kmawareness.htm.

Also feedbacks were collected from 245 participants. The analysis of the feedbacks indicates that there are many inhibiting factors to improve the current KM practices. Among them, the most predominant inhibiting factors are 'lack of user friendly technology infrastructure', 'lack of integration of the process of contribution with day to day work', 'lack of awareness of knowledge requirements', 'lack of awareness on the significance of the contribution to the organization', 'lack of feedback' and 'lack of awareness of the process of contribution'. Follow up actions on eliminating the inhibiting factors and further improvement of the KM practices is being planned.

The success of knowledge management depends on the active participation of all employees. In order improve the participation, several measures such as public recognition, annual KM Day etc. are planned.

VI.14 Enhanced Information Services at SIRD

Scientific information resource division continues to enhance the information services and infrastructure in order to satisfy the information needs of the patrons with the perfect combination of emerging technologies. During this year, the major e-resources such as IEEE journals and e-books, Nature archive, ASM Handbook, Nature Materials, Alloy phase diagram data sets, etc were added to the collection. Twenty thin client systems (Figure 1) were added with modular workstation tables for users to access information at SIRD.

Journal back volumes which consume much of physical space area have been arranged into five units of optimizers (compact shelves modules) as shown in Figure 2. This has reduced about 60% of total space and also made a systematic way of archiving the journal back volumes with controlled access. Simultaneously, to accommodate hard copy technical reports two units of optimizers were procured and installed.

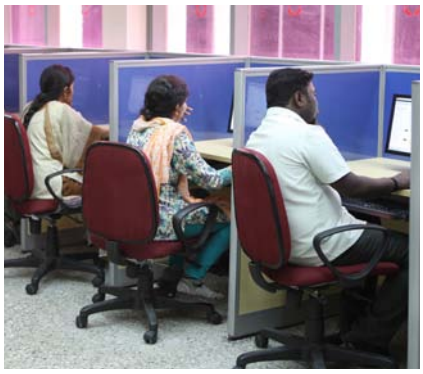

Fig. 1 *Thin client workstations at SIRD*

Library management software (LibSys) has been upgraded to the latest web centric version (LibSys 7) with more enhanced features including automatic integration of table of contents and other relevant information from the world wide web. Radio frequency identification (RFID) based infrastructure (Figure 3) has also been enhanced with more additional features such as people counter, wi-fi-inventory reader, shelving automation, automatic book drop,etc.

Fig. 2 *Compact shelving*

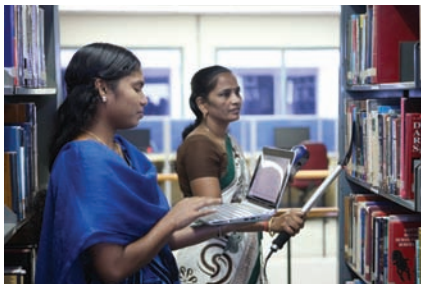

Fig. 3 *Shelf rectification using RFID systems*

VI.15 Human Resource Initiatives at IGCAR

IGCAR has developed the expertise and built comprehensive facilities to realize the mission programmes of the Department. The efforts are directed towards meeting the expectation and aspiration of the nation for ensuring energy security. Taking into consideration the enhanced role FBRs are likely to play in contributing to the nuclear power component of the nation, there is a need to augment skilled manpower for the critical assignments to take up challenges in the design of plant, development of equipment and processes. Thus human resource development has been one of the areas of emphasis in the management philosophy of the Centre. Initiating the Training School programme at Kalpakkam towards orienting the young talents by way of transfer of tacit and implicit knowledge of peers, identifying research scholars to take up the problems in interface areas or “Gap Areas” for achieving breakthroughs, attracting young people and empowering them has been some of the human resource initiatives of the Centre. Multilevel mentoring process has been built-in to cherish and orient the young talent and mould them to take up the challenges.

BARC Training School at IGCAR

The Training School at IGCAR, which is affiliated to the BARC Training School, Mumbai, made a humble

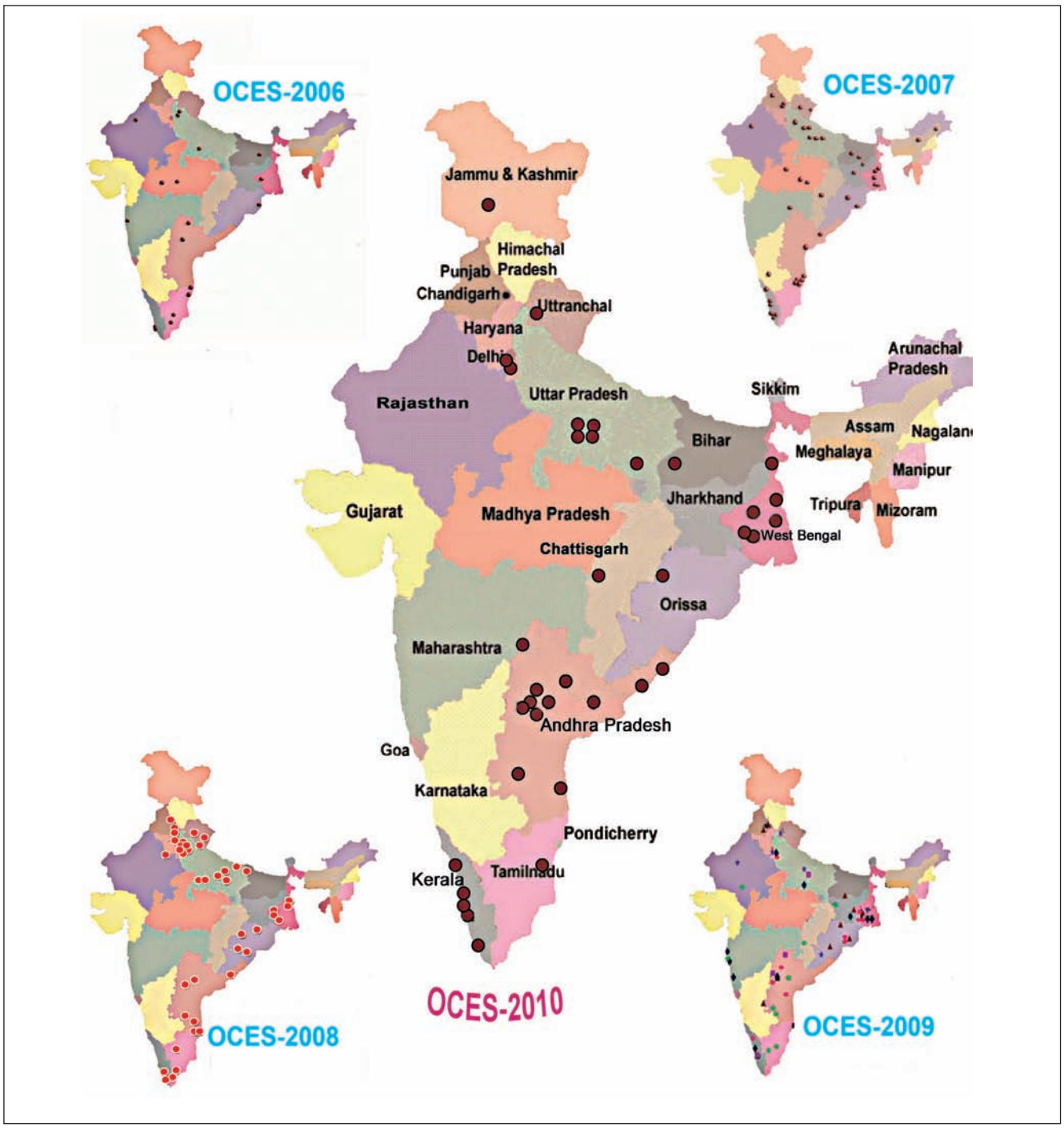

Fig. 1 *Batch-wise distribution of Trainee Scientific Officers*

beginning with twenty trainees in September, 2006. To start with, the training programme for the 1st batch was conducted in three engineering disciplines (viz.) Mechanical, Electronics & Instrumentation and Chemical engineering. Keeping in mind the emphasis on challenging issues related to Reactor Physics, Safety, Processing of nuclear materials including reprocessing two additional disciplines namely Nuclear Reactor Physics and Nuclear Fuel Cycle Chemistry

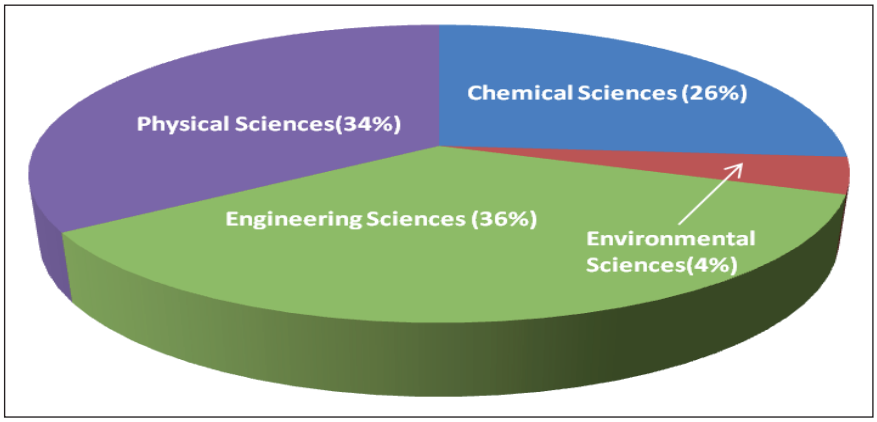

Fig. 2 *Discipline-wise distribution of research scholars at IGCAR*

Table 1: Batch-wise and Discipline-wise distribution of Trainee Scientific Officers undergoing training at BARC-TS at IGCAR

Discipline	OCES-2006	OCES-2007	OCES-2008	OCES-2009	OCES-2010	OCES-2011	Total
Mechanical	14	11	9	9	5	5	53
Chemical	1	6	5	4	3	5	24
Electronics & Instrumentation	5	9	5	10	6	2	37
Nuclear Reactor Physics	-	9	11	6	6	7	39
Nuclear Fuel Cycle Chemistry	-	10	9	9	7	11	46
Materials Science	-	-	4	10	9	5	28
Total	20	45	43	48	36	35	227

commenced in the year 2007 for the second batch of graduates. In order to take up the R&D challenges in Materials Science, a new discipline of training was initiated from the year 2008 onwards. The Training School has also imparted training to BHAVINI trainees with special orientation to operation and maintenance of Fast Breeder Reactors. The best of the experts from the Department of Atomic Energy have been roped in for the tutelage, majority of them coming from IGCAR. We have also utilised the expertise available in reputed academic institutions nearby like Indian Institute of Technology and Anna University, Chennai. Special lectures and visits to the laboratories has been the part of the curriculum for the trainees. Evening lectures and interaction sessions at the Training School hostel with eminent personalities in various fields form a part of the continuous mentoring exercise. In the current academic year, thirty five of the 6th batch of OCES Trainee Scientific Officers are undergoing training in the six disciplines (Table 1). The Trainee Scientific Officers, on successful completion of training, have been placed in various units of DAE. Giving a true national flavour, the trainees have come from all parts (Figure 1) of the country: Some of them left their lucrative jobs in other industries to pursue their passion in R&D in DAE.

One of the special features of the training programme is the provision to acquire an M.Tech. or M.Phil. degree from Homi Bhabha National Institute after successful completion of the orientation course and the project work. All the Trainee Scientific Officers graduated from the 1st and 2nd batch from IGCAR and pursuing their careers at our Centre, have completed their project work thereby fulfilling the academic requirements to getting the M.Tech. degree from HBNI and the officers from the 3rd batch would be soon completing their project work.

Research scholors

Towards making significant technological advancements, scientific challenges in R&D related to FBRs operating on advanced fuel with inherent safety and economy have to be addressed. Working with technology that has firm foundations in Physical, Chemical and Engineering Sciences is the approach to solving most of the challenges. This approach would enable to achieve breakthroughs, and also provide for an adequate resilience in front line technologies. In order to realize these goals, young research scholars have been inducted into vibrant R&D programmes. The strength of the research scholars in the Centre has been constantly increasing from fifteen about five years ago to a present sanctioned strength of two hundred for the current academic year. Problems in areas which have a direct bearing on the mission related activities of the Centre that include Fast Reactor Physics and engineering, Chemistry and Chemical Engineering, Computer Science, Electronics and Control Instrumentation, Materials Science and Reactor Safety have been identified to be taken up by the research scholars. Research scholars will be pursuing research in interdisciplinary fields that links basic sciences with engineering, such as Physics and Reactor Engineering, Chemistry and Chemical Engineering etc. and also in the exotic “gap areas”(Very relevant but has not been explored thus far). This will promote the involvement of basic sciences in challenging mission programmes of the Centre and also provide opportunities for original research and potential for breakthroughs. The present strength of the research scholars in the Centre is 126 and their discipline wise distribution is given in Figure 2.

“Excellence with Relevance and with Human Touch” is the motto practiced in organising the human resources towards taking up the mission oriented challenges of the Centre.

VI.16 Implementation of Workflow Management System

As part of e-governance initiative in IGCAR, the project of Workflow Management System has been taken up. The objective of this project is to automate and integrate the functions of Administration, Accounts, Stores and Purchase. Automation in these areas provides an efficient, transparent and effective system to the employees and is envisaged to lead to a paper-less office in the future.

This automation and integration activity was taken up as part of XI plan projects. It is an online, role based and workflow based system. The term "Workflow" can be defined as a series of actions performed by various people in order to complete a process. In this system employees are granted various roles according to their organizational responsibilities and the system takes care of moving the process in the workflow, based on the role matrix defined in the system.

Since this system covers wide areas of Administration, Accounts, Stores and Purchase activities, various domain experts from these areas were identified to provide the input to the development team during the requirement collection phase. The same teams were involved in the user acceptance testing also.

This project was executed using agile software methodology. Agile methodology is an iterative and evolutionary software development cycle. In this process the development team presents shippable increment of work (known as sprints) to end-user for testing and feedback on regular intervals of two to three weeks. It is in contrast to Waterfall / traditional sequential software development where the end-user tests the developed work only at the end of development phase and the requirements are frozen before the development begins.

Workflow management system is implemented as a portal on which various modules are deployed as portlets. A portal is a container that contains various portlets which process requests and generate dynamic contents. Open source infrastructure like Java, MySQL and Ajax has been used in the development of this system.

About 150 processes have been developed as part of this project. This system is available in the Local Area Network of IGCAR and caters to about 2500 employees. Provisions for various management information reports and automated e-mail alerts have been made. This system has also introduced 'paper-less' operations for material arrival notice, functional test report, official lunch booking request, meeting room booking, leave request and transport requisition.

The workflow management system aims at becoming a single window interface between employees of IGCAR, Administration, Accounts, Stores and Purchase.

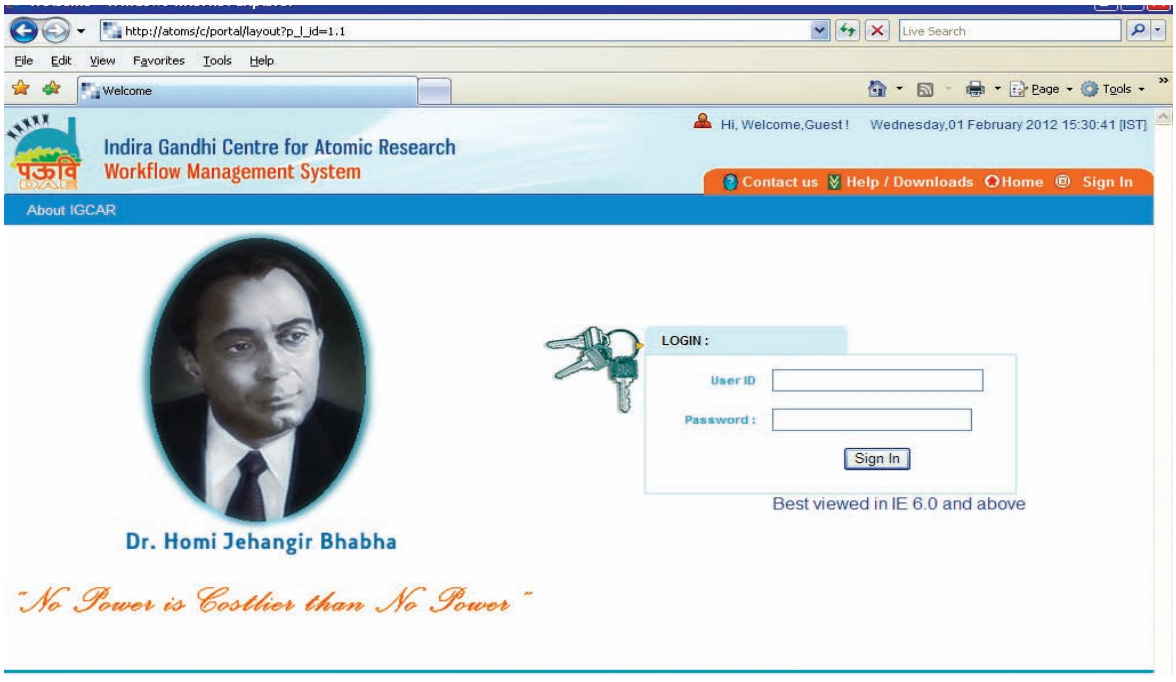

Fig. 1 Screen shot of webpage of workflow management system

CHAPTER - VII

Awards / Publications / News & Events / Organisation

AWARDS & HONOURS

Dr. Baldev Raj, former Director, IGCAR is the recipient of Indian National Science Academy Prize for Materials Science, from Indian National Science Academy (2010), for his contributions to nuclear materials, technologies, cultural heritage and mentoring of generations of students and colleagues.

He delivered the Prof. N.P. Gandhi Memorial Lecture, organised by The Indian Institute of Metals (2011).

He has delivered the Portevin Lecture of International Institute of Welding (2011) for his contributions valued for sustained excellence in welding science and technology.

He has delivered the First Annual Materials Lecture of International Centre for Materials Science in June 2011.

He was awarded 16th M.N. Saha Memorial Lecture Award, from Indian Science New Association, Kolkata (2011).

He was honoured with 6th Raja Ramanna Memorial Lecture award by VECC, Kolkata during June 2011.

He has been elected as:

- Member of the Tamil Nadu State Council for Science & Technology (2010-2013)
- Honorary Member of the Association of Scientists, Developers and Facilities (2011)
- Honorary Professor of Sichuan University, Chengdu, China
- Member, Editorial Board, Nano Trends
- President, Indian National Academy of Engineering (INAE 2011)

Dr. P.R. Vasudeva Rao, Director, Chemistry Group, was selected for award of Silver Medal by the Chemical Research Society of India in 2011.

He has also awarded the MRSI-ICSC Superconductivity and Materials Science Senior Award-2011 by Materials Research Society of India.

Dr. B.V.R. Tata, CMPD, MSG has been recognised as "ERUDITE Visiting Professor" at the School of Chemical Sciences, Mahatma Gandhi University, Kottayam, Kerala.

Dr. S. Venugopal, GRIP, MMG has been elected as a "Fellow of American Society of Materials (ASM)" for his significant contributions in the area of "Deformation processing of materials".

Dr. John Philip, NDED, MMG was awarded the MRSI Medal-2011 by Materials Research Society of India and he has been given Membership in the American Nano Society.

Dr. A.K. Tyagi, SND, MSG has been awarded "Award of Excellence" by Sathyabama University, Chennai in the area of Nanoscience and Nanotechnology.

Dr. Sumantra Mandal, MTD, MMG has been awarded the "Sudharshan Bhat Memorial Prize" for best Ph.D thesis in Metallurgical and Materials Engineering from IIT-Madras, Chennai.

He has also been selected for the "IEI Young Engineers Award 2011-2012" in Metallurgical and Materials Engineering discipline.

Dr. Vaidehi Ganesan, MMG has been awarded with "Marie Curie Mahila Vijnana Puraskara" during the fourth National Women's Science Congress held at Bengaluru during November 7-9, 2011.

Dr. B.P.C. Rao, Shri S. Thirunavukkarasu, Dr. T. Jayakumar, Dr. Baldev Raj, Shri Aravinda Pal, Shri T.K. Mitra and Shri Pandurang Jadhav of MMG have been adjudged the winner of "Weldman Award-2011" for the best

Technical paper on "A new Methodology for Qualification of Welding Procedure for circumferential shell welds of steam generators of PFBR" presented during National Welding Seminar -2010.

Shri Girish Kumar Padhy, Research Scholar, MTD, MMG has been adjudged the winner of "ESAB India Award-2011" for his paper on "Diffusible Hydrogen Measurement in Steel Welds using an Electrochemical Hydrogen Sensor" for the best Technical paper across all categories.

Shri M. Santhanam, Shri V. Venkatachalapathy, Shri C. Sivathanupillai and Shri R. Gettu got "Corps of Engineers Prize" from The Institution of Engineers (India) for their paper on "Mechanical properties of High Density Concrete used in Fast Reactors for Structural and Shielding Purposes" published in the Journal of the Institution during 2010-2011.

Shri M. Kasinathan, Ms. S. Sosamma, Dr. C. Babu Rao, Shri N. Murali and Dr. T. Jayakumar received the Best Poster Award for paper titled "Liquid level measurement using Raman Distributed Temperature Sensor" at International conference on Specialty Glass & Optical Fiber: Materials, Technology & Devices (ICGF-2011), Kolkata, August 2011.

Ms. S. Ramya, Shri C. Arunchandran, Dr. R.P. George and Dr. U. Kamachi Mudali, received the Best Oral Presentation Award for "Studies on Passive Films of Type 316LN Stainless Steels using Micro Laser Raman Analysis and Imaging", at National Symposium on Electrochemical Science and Technology (NSEST-2011), Indian Institute of Science, Bangalore, India, August 2011.

Shri Jagadeesh Sure, Shri A. Ravi Shankar and Dr. U. Kamachi Mudali, received the Best Poster Presentation award for "Laser Surface Melting of Plasma Sprayed Alumina-Titania Coating on High Density Graphite", International Conference on Advanced Materials (ICAM 2011), PSG College of Technology, Coimbatore, India, December 2011.

Shri Ashish Jain, Shri S. Kandasamy and Dr. K.K. Satpathy received 2nd prize for poster presentation on "Construction site monitoring through a systematic Safety observation methodology in IGCAR" during 28th DAE Safety & Occupational Health Professionals Meet-2011.

DAE AWARDS

Department of Atomic Energy has instituted annual awards for excellence in Science, Engineering and Technology in order to identify best performers in the area of Research, Technology Development and Engineering in the constituent units (other than Public Sector Undertakings and Aided Institutions). The Young Scientist, Young Engineer, Young Technologist, Homi Bhabha Science and Technology Award and Scientific and Technical Excellence Award fall under this category. Group Achievement awards for recognition of major achievements by groups have also been instituted. Life time Achievement Award is awarded to one who has made significant impact on the DAE's programme. They are the icons for young scientists and engineers to emulate. The awards consist of a memento, citation and cash prize.

The recipients of the Awards from IGCAR for the year 2011 are:

Homi Bhabha Science & Technology Award	:Shri A. Ravisankar, RpG
Scientific & Technical Excellence Award	:Shri U. Partha Sarathy, REG and Shri S. Raghupathy, NSEG
Young Applied Scientist & Technologist Award	:Shri V. Rakesh, MMG and Shri Abhishek Mitra, NSEG
Meritorius Award	:Shri A. Govindarajan and Shri T. Logaiyan, FRTG Shri B. Syed Ali and Shri K. Ganesan, ROMG Shri T.G. Swaminathan, ESG and Shri K. Dasarathan, MSG
Young Engineer Award	:Shri G.V. Prasad Reddy, MMG and Shri E. Hemanth Rao, NSEG

Group Achievement Award:

Design and development of roof slab for Prototype Fast Breeder Reactor

Dr. P. Chellapandi, NSEG, Group Leader
Shri Sriramachandra Aithal, Shri S. Raghupathy, Shri P. Puthiya Vinayagam, Shri V. Balasubramaniyan, Shri V. Rajan Babu, Shri P. Selvaraj, Dr. K. Velusamy, Shri S. Jalaldeen, Shri R. Gajapathy, Shri A. Biswas, Shri T. Selvaraj, Shri K. Natesan, Shri C. Raghavendran, Shri R. Suresh Kumar, Shri S.D. Sajish, Shri Bhuwan Chandra Sati, Shri Abhishek Mitra, Shri Gagan Gupta, Shri Arul Bhaskar, Shri Ramkumar Maity, Shri S. Saravanan, Shri G. Venkataiah, Shri S.K. Rajesh, Shri M. Babu Rao, Shri R. Manu, Ms. P. Swetha, and Shri V. Devaraj from NSEG, Dr. Arun Kumar Bhaduri, Shri V. Ramasubbu, Shri M. Arul, and Dr. Shaju K. Albert from MMG, Dr. R.S. Keshavamurthy, Dr. B. Venkatraman, Shri R.J. Paul Surendranath, Shri Abdul Gani H I, Shri V. Venkatachalapathy, Shri C. Sivathanu Pillai and Shri C. Hari Kumar from CEG, Shri P. Ramesh, Shri D. Sunil Kumar, Shri G. Radhakrishnan and Shri R. Mathiarasu from REG.

Design and development of Dual Phosphor Hand Monitor

Shri P. Vijayasekaran, RpG, Group Leader
Shri A. Dhanasekaran from REG, Shri K.P. Desheeb, Shri S. Manickam, Shri P.C. Sandeep and Shri P. Anbazhagan from RpG.

In-Sodium Materials Testing Faciility

Dr. M. D. Mathew, MMG, Group Leader
Dr. S. Venugopal, Dr. K. Laha, Dr. R. Sandhya, Shri S. Ravi, Shri R. Kannan, Shri K. Mariappan, Shri G. Sukumaran, Shri V. Ganesan, Shri P.C. Gopi and Shri S. Sakthy from MMG, Shri M. Shanmugavel, Shri M. Shanmugasundaram, Shri S. Vijayaraghavan, Shri P. Rajasundaram, Smt. Sundari Madasamy, Shri T. Chandran, Shri J. Vincent, Shri M. Mani, Shri K.K. Rajan, Shri T. Ramalingam, Shri R. Kamaraj, Shri V. Tharmaraj, Shri R. Sabari Kumar, Shri S. Rangasamy, Shri K. Narasimha and Shri V. Suresh from FRTG.

Steam Generator Test Facility

Shri I. B. Noushad, FRTG, Group Leader
Shri V.A. Suresh Kumar, Shri B.K. Sreedhar, Smt. J.I. Sylvia, Shri G. Madhusoodhanan, Shri V.S.P. Babu, Shri V. Vinod, Shri N. Nagarajan, Shri K. Thanigairaj, Shri A. Ashokkumar, Shri S. Kishore, Shri L.S. Sivakumar, Shri Rakesh Kumar Mourya, Shri M. Ravishankar, Shri K. Jayagopi, Shri S.P. Pathak, Shri Vishal D Paunikar, Shri M. Anandraj, Shri T.V. Maran, Shri Shiv Prakash Ruhela, Shri D. Laxman, Shri V. S. Krishnaraj, Shri Gautam Anand, Shri Y. Suresh, Shri R. Kannan, Shri P. Sivasubramaniapillai, Shri Ramesh Kumar Sharma, Shri Chaitlal Thakur, Shri P. Anupkumar, Shri P. Mohanraj, Shri V. Elumalai, Shri P. Narayana Rao, Shri K. Selvaraj, Shri K. V.S.S.N. Murthy, Shri V. Saravanan, Shri Sukanta Kumar Roy, Shri K.G. Radhakrishnan Unni, Shri G. Anandan, Shri T. Solaiappan, Shri M. Sankaran, Shri K. Radhakannan, Shri S. Shanmugham, Shri Vijay Tirkey, Shri A. Kolanjiappan, Shri R. Kuppuswamy, Shri A. Kumaraswamy, Shri M. Muralidharan, Shri M.P. Sunny, Shri N. Premanand, Shri K. Sekar, Shri E.G. Prabhakaran, Shri K. Sadiq Batcha, Shri C. Pavaderadjane, Shri A. Saravanan, Shri G. Rathnachalam, Shri P. Hrishikesh, Shri J. Jaikanth, Shri S. Kannan, Shri J. Prem, Shri H. Rafiq Batcha, Shri M. Munikumar, Shri S. Saravanan, Shri K. Arulselvam, Shri S. Ponthilagar, Shri L. Muthu, Smt. Indra G Ramdoss and Shri A. Elumalai from FRTG.

Design, Manufacture and Testing Challenges of Prototype Fast Breeder Reactor Secondary Sodium Pump

Shri K.V. Sreedharan, REG, Group Leader
Shri A.S.L.K. Rao from ESG, Shri V. Balasubramaniyan, Shri S. Athmalingam, Shri Bhagwana Ram, Shri S. Chandrasekar, Shri S. Satheesh Kumar, Shri K. Madhusoodhanan, Shri S.L.N. Swamy and

Shri M. Sakthivel from REG, Shri K. Velusamy, Shri S. Jalaldeen, Shri K. Natesan, Shri Bhuwan Chandra Sati and Shri P. Jayaraj from NSEG, Shri B.K. Sreedhar from FRTG

Setting up, Commissioning and Operating the SAMRAT Model Test Facility for Conducting Experiments in Water to Validate the Thermal Hydraulic Design of Prototype Fast Breeder Reactor

Shri G. Padmakumar, FRTG, Group Leader
Shri N. Murali, Ms. P. Parimalam and Shri A. Shanmugam from EIG, Shri V. Prakash and Shri G. Madhusoodanan, Shri Indranil Banerjee, Shri D. Ramadasu, Shri N.S. Shivakumar, Shri Gautam Kumar Pandey, Shri S. Ajesh Kumar, Shri Viajunath Mente, Shri Piyush Kumar Aggarwal, Shri M. Thirumalai, Shri M. Anandaraj, Shri P. Anup Kumar and Shri J. Saravanan, Shri R. Rajendra Prasad, Shri Gautam Anand, Shri D. Laxman, Shri K. Jayagopi, Shri P. Adhithan, Shri R. Raghuraman, Shri K.H. Anub, Shri K. Srinivasa Rao, Shri N. Mariappan, Shri S. Rajkamal Singh, Shri J. Jaikanth, Shri A. Kanakaraj, Shri K. Tamil Selvan, Shri R. Iyyapan, Shri T. Soliappan, Shri V. Veeraraghavan, Shri R. Kuppuswamy, Shri V. Gunasekaran, Shri M. Kathiravan, Shri R. Rajendran, Shri C.N. Sridhar and Shri Hadibandu Singh from FRTG.

Setting up and Engineering Scale Facility for Pyroprocess studies and demonstration of Electrofining of Uranium

Dr. K. Nagarajan, CG, Group Leader
Shri G. Ravisankar, Dr. B. Prabhakara Reddy, Shri V. Sureshkumar, Shri P. Venkatesh, Shri T. Subramanian, Shri G. Seenivasan, Shri Suddhasattwa Ghosh, Smt. S. Vandarkuzhali, Dr. Manish Chandra, Smt. Nibedita Gogoi, Shri R. Sridhar, Shri A. Ananthakumar, Shri G. Rajendra Prasad, Ms. B. Suhasini, Shri N. Ravi, Shri E. Mohanraj, Shri K. Satya Govinda Raju, Shri M. Ganapathy, Shri S. Vannia Perumal, Shri S. Nedumaran, Ms. S. Suganthi, Shri M. Kakkum Perumal, Smt. K. Suriyakumari, Shri S. Mariyappan, Shri A. S. Ganapathi, Ms. S. Raja Rajeswari, Shri V. Arunkumar, Shri V. Yuvaraj, Shri N. Vinodkumar, Shri M. Saravanan, Shri P. Marimuthu, Shri P. Jagannathan, Shri K. Logannathan, Shri R. Rajaram, Shri N. Eswaran, Shri E. Nagappan, Shri K. Dayalan, Shri N. Radhakrishnan, Shri N. Nagarajan, Shri G. Raman, Shri K. Ganesan, Shri V. Balagopalan, Shri S. Rajendran and Shri D. Kothandan from CG, Shri S.P. Ruhela from FRTG, Dr. U. Kamachi Mudali, Shri G. Senthil Kumaran, Shri S. Sakthivel, Shri R. Ravikumar, Shri K. V. Kasi Viswanathan and Shri D. Jagadisan from MMG, Shri Vijayan Varier, Shri P. Jagannathan, and Shri K. Logannathan from REG.

Nitric Acid Loop for Long-Term Corrosion Studies

Dr. U. Kamachi Mudali, MMG, Group Leader
Shri Ravikumar Sole, Shri K. Kamalanathan, Shri A. Ramakrishnan, Shri T. Nandakumar, Shri R. Thiruvalluvan and Shri R. Rajendran from MMG. Shri R. Rajeev, Shri T. Selvan, Shri Geo Mathews and Shri A. Sriramamurthy from RpG.

QUALITY CIRCLE AWARDS

PLUTONIUM Quality Circle of Chemistry Group, IGCAR with members Shri E. Mohanraj, Shri B. Vijayavelu, Shri N. Ravi, Shri N. Radhakrishnan, Shri R. Padmanabhan, Shri K. Satya Govinda Raju and Shri V. Suresh Kumar has won GOLD AWARD in the Chennai Chapter Quality Circle Convention (CCQCC-2011) held at Puducherry during September 3-4, 2011

STAR Quality Circle of Central Work Shop Division, ESG, IGCAR with members Shri R. Tamilamuthan, Shri K.M. Natarajan, Shri G. Narendar Reddy, Shri V. Kodiarasan, Shri A. Padmanaban, Shri B. Thiruvengadam, Shri R. Murugupandian, Shri J. Abilash, Shri E. Venkatesh, Shri S. Sateesh Kumar has won SILVER AWARD in the Chennai Chapter Quality Circle Convention (CCQCC-2011) held at Puducherry during September 3-4, 2011

RAHFA Quality Circle of Hospital, GSO with members Ms. M. Suganthi Robert, Ms. V. Vanasundari, Shri S. Rajagopal, Shri P. Selvamani, Ms. P. Jansileema, Ms. P. Sumathi, Shri G. Mahalingam, Shri M.K.Mohammed Razeek has won GOLD AWARD in the Chennai Chapter Quality Circle Convention (CCQCC-2011) held at Puducherry during September 3-4, 2011

IGCAR Publications during the year 2011

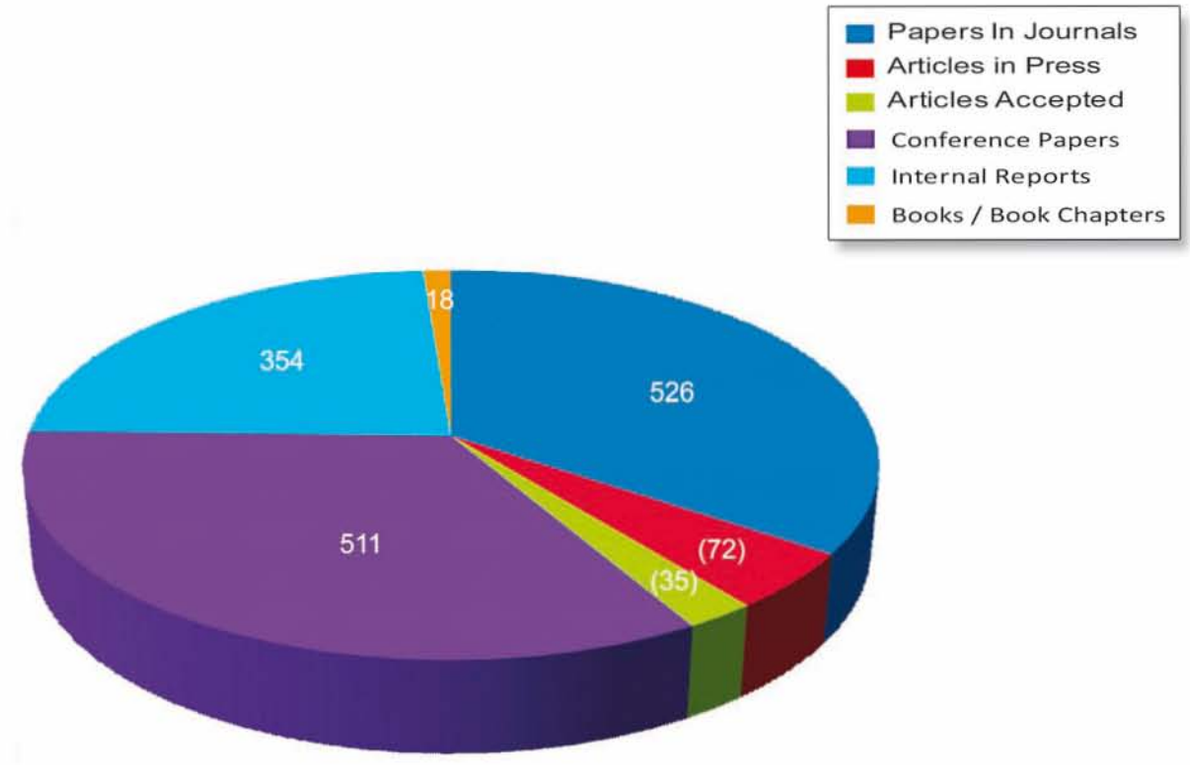

Special Lectures and Colloquia Series

1. "Medical Education and research in independent India", Vikram Sarabhai Memorial Lecture by Dr. C. V. Krishnaswami, Honorary Consultant and Head of the Diabetes Department, Voluntary Health Services, Chennai on February 11, 2011.
2. "Historical Development on Present Status of Forensic Activation Analysis" by Prof. Krishnan, Professor (Retd.) University of Toronto, Canada on February 18, 2011.
3. "Ethical issues related to advances in science and technology" by Dr. Vasantha Muthusamy on March 28, 2011.
4. "Magic and Science: Art of doing Research" by Dr. Anil Kumar, IIT, Bombay on April 21, 2011.
5. "Fukushmia-Regulator perspective", IGC colloquium on by Shri S. S. Bajaj, Chairman, Atomic Energy Regulatory Board on May 13, 2011.
6. "Safety Aspects of Radiochemical and Fuel Cycle Plants", IIChE colloquium invited talk on by Shri A. R. Sundararajan, Former Director, AERB on August 2011.
7. "A New Heavy Water Production in India", IIChE colloquium invited talk on by Shri S.C Hiremath, Former Director, HWB, August 26, 2011.
8. "Modelling the Thermodynamics and Kinetics of Oxidation of Multiphase Multicomponent Alloys", Placid Rodriguez Memorial Lecture by Dr. S. Srikanth, NML, Jamshedpur on October 5, 2011.
9. "Radiation and Human Health: Perceptional Divide", Curie Memorial Lecture by Shri L.V. Krishnan, Former Director, SR&HPG, IGCAR on November 21, 2011.

Seminars, Workshops and Meetings

1. Inauguration of "International year Chemistry", January 7, 2011.
2. Seminar on "Welding of Austenitic Stainless Steels", February 19, 2011.
3. 16th International Workshop on "Electromagnetic Non-Destructive Evaluation (ENDE-2011)", March 10-12, 2011.
4. Theme Meeting on "Alloy Design", March 11, 2011.
5. Theme Meeting on "Advances in Electronics Instrumentation and Information Technology", March 24, 2011.
6. 7th CEA-IGCAR Annual Seminar on "Liquid Metal Fast Reactors Safety", April 13-21, 2011.
7. Theme meeting on "Challenges in the Performance Assessment of Fast Reactor Components", May 27, 2011.
8. Seminar on "Waste management", June 8, 2011.
9. Natural Disaster Management Programme, July 11-12, 2011.
10. Theme Meeting on "Manufacturing Simplifications for Commercial Fast Breeder Reactor Core Sub-Assemblies", September 10, 2011.
11. Theme meeting on "Reactor Physics; Current Status and Future Directions", September 23, 2011
12. International Conference on "Vistas in Chemistry 2011", October 11-13, 2011.
13. Theme meeting on "Characterization of Fuel and Structural Materials", October 17, 2011.
14. "Vigilance Seminar", November 3, 2011.
15. SMiRT Post Conference Seminars on "Innovative Fast Reactor Design and High Temperature Design", November 6-11, 2011.
16. IAEA Technical Meeting (TM-41429) on "Fast Reactor Physics and Technology", November 14-18, 2011.
17. Structure and Thermodynamics of Emerging Materials (STEM-2011), with the theme of "Diffusion, Mass Transfer and its Consequences in Materials", November 24-26, 2011.
18. Seminar on "Clinic on Failure Analysis", December 22-24, 2011.
19. Conference on "Recent Advances in Information Technology (READIT 2011)", December 28-29, 2011.

Nurturing Activities

1. "Work Flow Management Training Programme" on January 5, 2011.
2. One day Hindi Workshop on March 11, 2011.
4. "Being a Women in Today's World" by Dr. Gita Arjun on March 16, 2011.
5. "Role of Women and Science on Society & Human Development Index" on March 27, 2011.
6. "Gender Issues and Women Empowerment" by Dr. Kaiser Jamil, Head of Genetic Department, Bhagwan Mahavir Medical Research Centre, Hyderabad on April 21, 2011.
8. Technical talk in Hindi on "Reprocessing of Spent Fuel from Fast Breeder Test Reactor" by Shekhar Kumar, RpG, IGCAR on May 27, 2011.
9. "Summer Training programme in Physics and Chemistry (STIPAC 2011)" during May 23 – July 1, 2011.
10. "International year of Chemistry Programme" on July 14 -15, 2011.
11. "Quality Circles meet for GSO employees"July 20, 2011.
12. "Conditions & Management of LD/Autism/ADHD", July 28, 2011.
14. One day Hindi workshop on August 2, 2011.
16. "QCAM 2011 Annual Meet" on August 25, 2011.
17. "Environment, Science-interlinks and Impacts", by Dr. Ramanujam, IMSc, Chennai, on September 3, 2011.
18. "Hindi week celebration" program organized by Hindi Cell during September 14-21, 2011.
20. Invited talk on "Group Career Counselling", by Smt. Kalavathi Amarchelvam, Bodhi, Chennai, October 20, 2011.
21. "Quiz, Lecture and Chemistry Demonstration for Surrounding Tamil medium School" during December 2-3, 2011.
22. "Elimination of Violence Against Women", Smt. Vijayadharani, MLA, Vilavancode on December 14, 2011.
23. Lecture on "PRIS & APAR" December 29, 2011.

News and Events

IGCAR Transfers Flux based TIG Process to Industry

April 28, 2011

Dr. Baldev Raj, the then Director, IGCAR, Shri Raman Kumar, Managing Director and Shri R. Ravi, M/s. ADOR Welding Ltd. and Dr. U. Kamachi Mudali, Head, Technology Transfer Cell during the signing of MoU with M/s. ADOR Welding Ltd.

Indira Gandhi Centre for Atomic Research, Kalpakkam has entered into a memorandum of agreement with M/s. ADOR Welding Limited, Mumbai for the transfer of an international patented process “Penetration Enhancing Activated Flux for TIG Welding of Austenitic Stainless Steels”.

Activated Tungsten Inert Gas process involves the development of formulation and technology for using a specially designed flux that can enhance the penetration, depth and quality of austenitic stainless steel welds. The flux thus developed can be used for deep penetration welding of Stainless Steel plates of 10 mm thickness for one meter length with one gram of the flux. The process was demonstrated to the industry for transferring to the same for a period of three years on an non-exclusive basis. In an exclusive function at IGCAR, the memorandum of agreement between IGCAR and M/s. ADOR Welding Ltd., Mumbai was signed by Dr. Baldev Raj, the then Director, IGCAR and Shri Raman Kumar, Managing Director, M/s. ADOR Welding Ltd. for the transfer of Activated Flux based TIG Process. During the occasion Dr. Baldev Raj, the then Director IGCAR addressed the importance of technology transfer and explained how this would enhance the strength of Indian industry with indigenous technologies. He also explained the importance of pooling the technological resources in the country and effectively utilising the same for demanding applications. Shri Raman Kumar thanked IGCAR for providing valuable technologies for the benefit of Indian industry and assured the utilisation of the technology transferred.

Inauguration of UGC-DAE CSR, Kalpakkam Node

April 28-29, 2011

UGC-DAE CSR, Kalpakkam Node building was inaugurated by Dr. S. Banerjee, Chairman, AEC & Secretary, DAE on April 28, 2011 in the presence of Dr. Baldev Raj, the then Director, IGCAR and Prof. Ajay Gupta, Centre Director, UGC-DAE CSR, Indore Centre. Senior scientists from IGCAR as well as research scholars participated in the inaugural function. The construction of the building had commenced in April 2009 and was completed within two years. Advanced experimental facilities have been installed in physical and engineering science wings and collaborations with various academic institutes and universities have been initiated using these facilities.

Dr. S. Banerjee, Chairman, AEC & Secretary, DAE, Dr. Baldev Raj, the then Director, IGCAR, Prof. Ajay Gupta, Centre Director, UGC-DAE CSR, Indore Centre, Dr. G. Amarendra, Scientist In-Charge, UGC-DAE CSR, Kalpakkam Node during inauguration of Kalpakkam Node

Signing of MoU with Stella Maris College, Chennai

April 29, 2011

A Memorandum of Understanding (MoU) for academic and neighbourhood development was signed between IGCAR and Stella Maris College, Chennai on April 29, 2011. A team from Stella Maris College led by Dr. Sr. Jasintha Quadras, FMM, Principal, Shri S. C. Chetal, Director, IGCAR, Dr. Baldev Raj, the then Director, IGCAR and Senior Colleagues of the Centre were present during the signing of MoU.

Dr. Baldev Raj, the then Director, IGCAR, Shri S.C.Chetal, Director, IGCAR and senior colleagues of the Centre with Dr. Sr. Jasintha Quadras, FMM Principal and colleagues from Stella Maris College

Annual Meet of Quality Circles– 2011

August 25, 2011

Quality circle is a volunteer group of workers (or even students), usually under the leadership of their supervisor (but they can elect a team leader), who are trained to identify, analyze and solve work-related problems and present their solutions to management in order to improve the performance of the organization and motivate and enrich the work of employees. When matured, true quality circles become self-managing having gained the confidence of management.

In IGCAR, Quality Circles Annual Meet (QCAM) is conducted to provide a common platform to all the employees to present the QC case studies. This year, QCAM was conducted on August 25, 2011. Welcome address was given by Dr. C. Anand Babu, Associate Director, Component Development Group. The presidential address was delivered by Shri G. Srinivasan, Director, Reactor Operations & Maintenance Group.

Dr. R. Srinivasan, Director, Chennai Manufacturing Services & Chairman, NIQR, Chennai Branch delivered the key note address. Vote of thanks was proposed by Shri V. Praveenkumar, Member, Organising committee.

Totally, eighteen Quality Circles (about two hundred members) from IGCAR presented their QC case-studies in a wide Spectrum of topics covering Technical, Research & Development and Services. Three Quality Circles of GSO QCAM-2011 with top scores were invited as guest presenters to present their QC case studies. Professional judges from Quality Circle Forum of India, Chennai chapter had assessed the QC case-study presentations held at Sarabhai Auditorium MOON QC and EXCEL QC bagged Dr. Placid Rodriguez Trophy and Shri M. K. Ramamurthy Trophy in 'Mechanical and Manufacturing' and 'Plant Operation and Services' respectively.

During valedictory function, the events were summed up by Shri G. Kempulraj, Superintendent, Central Work Shop. The programme was concluded with the valedictory address and Prize distribution by Shri S.A.V. Satya Murty, Director, Electronic & Instrumentation Group. Vote of thanks was proposed by Shri S. Suresh, Member, Organising committee.

MOON QC receiving Dr. Placid Rodriguez Trophy (Mechanical and Manufacturing Category) from Shri S.A.V. Satya Murty, Director, EIG

EXCEL QC receiving Shri M.K. Ramamurthy Trophy (Plant Operation & Services Category) from Shri S.A.V. Satya Murty, Director, EIG

Graduation Function of the fifth batch of Trainee Scientific Officers of Training School at IGCAR

August 26, 2011

Dr. S. Banerjee, Chairman, AEC and Secretary, DAE, addressing the gathering during the graduation function. Prof. G.D. Yadav, Director (Vice-Chancellor), Institute of Chemical Technology, Mumbai, Shri S.C.Chetal, Director, IGCAR, Dr. M. Sai Baba, Associate Director, RMG and Shri R.V. Subba Rao, Head, OCES –TS, RMG are seated on the dais

The fifth batch of thirty six TSOs from the BARC Training School at IGCAR have successfully completed their training and the graduation function was held on August 26, 2011 at the Sarabhai Auditorium, Homi Bhabha Building, IGCAR. Prof. G.D. Yadav, Director (Vice- Chancellor), Institute of Chemical Technology, Mumbai graced the occasion as the Chief Guest. Dr. S. Banerjee, Chairman, AEC and Secretary, DAE, presided over the function. Dr. M. Sai Baba, Associate Director, Resources Management Group welcomed the gathering. Shri S.C. Chetal, Director, IGCAR, gave an enlightening address enumerating some recipes for success. Dr. S. Banerjee released the souvenir featuring the training school programme of the academic year that passed by and Prof. G.D. Yadav received the first copy. In his presidential address Dr. S. Banerjee gave a very motivational and thought provoking lecture to the graduates passing out. Prof. G.D. Yadav gave away the prestigious 'Homi Bhabha Prize' comprising of a medallion and books worth Rs.5000 to the meritorious toppers of all the disciplines. He also gave away the course completion certificates to all the graduates passing out. A few of the Trainee Scientific Officers passing out shared their experiences and gave a feedback on the academic programme and their stay at hostel. Prof. G.D. Yadav gave a very inspiring lecture to the students. Shri R.V. Subba Rao, Head, OCES–TS, RMG proposed the vote of thanks.

Fifth Batch of Graduates of BARC Training School at IGCAR with Prof. G.D. Yadav, Director (Vice-Chancellor), Institute of Chemical Technology, Mumbai, Dr. S. Banerjee, Chairman, AEC & Secretary, DAE, Shri S.C. Chetal, Director, IGCAR and senior colleagues of the Department

Conference/Meeting Highlights

Theme Meeting on "Alloy Design"

March 11, 2011

Dr. Baldev Raj, the then Director, IGCAR while delivering his address, also seen are Prof. Markus O. Speidel, Swiss Materials Science Academy, Prof. Jacques Foct, Universitie Lille and Dr. U. Kamachi Mudali, Chairman, IIM-Kalpakkam Chapter & Head, CSTD seated on the dias

IGCAR and the Indian Institute of Metals, Kalpakkam Chapter organised a theme Meeting on "Alloy Design" on March 11, 2011 at IGCAR, Kalpakkam coinciding with the visit of two eminent professors to IGCAR, viz. Prof. Markus O. Speidel of Swiss Materials Science Academy, Switzerland and Prof. Jacques Foct of Universitie Lille, France. The theme meeting started with a welcome address by Dr. U. Kamachi Mudali, Chairman IIM- Kalpakkam Chapter & Head, CSTD who mentioned the necessity for organising such theme meetings. In his opening remarks, Dr. Baldev Raj, Distinguished Scientist and the then Director, IGCAR highlighted the need for designing suitable alloys which can withstand severe environments like high radiation field as in the case of FBRs or fusion reactors, and the elevated temperatures and pressures as anticipated in ultra supercritical power plants. He also emphasised the need to address global problems like climate change and green house effect when choosing materials for meeting the requirements.

The theme meeting consisted of three talks with the first talk delivered by Prof. M.O. Speidel who covered at length various aspects of alloy design at length in terms of his experiences with nitrogen added steels. Prof. J. Foct introduced the audience about the basic mechanisms behind designing interstitial alloys, functionally gradient alloys, thermodynamically forbidden alloys etc. and highlighted a few in terms of their unique properties and low cost, refractoriness etc. The third lecture was delivered by Dr. M. Vijayalakshmi, Head, Physical Metallurgy Division, MMG who discussed about the alloy design for avoiding sensitisation of stainless steel, preparing dissimilar weld joints without soft zones through suitable filler materials etc. Dr. P. Parameswaran, Convener of the meeting proposed the vote of thanks. The meeting was well attended by the scientific community at Kalpakkam with good interaction and wide ranging discussions.

16th International Workshop on Electromagnetic Non-destructive Evaluation (ENDE-2011)

March 10-12, 2011

Dr. Baldev Raj, the then Director, IGCAR releasing the souvenir of ENDE-2011 workshop during the inaugural function held on March 10, 2011 Prof. M.S. Ananth (second left), Prof. Fumio Kojima, Prof. Krishnan Balasubramaniam and Dr. B.P.C. Rao at the inauguration

Indira Gandhi Centre for Atomic Research, Kalpakkam and Indian Institute of Technology Madras, Chennai jointly organised the 16th International Workshop on Electromagnetic Non-destructive Evaluation (ENDE-2011) during March 10-12, 2011 at IC&SR Auditorium, IIT Madras, Chennai. One hundred and fifity delegates from fifteen countries took part in the workshop, organised for the first time in India. The objective of ENDE-2011 is to bring together the scientists and engineers to discuss the recent advances in electromagnetic NDE techniques including eddy currents, magnetic flux leakage, micro-magnetics, Barkhausen emission, potential drop and microwave, by giving special emphasis to innovative applications, modeling, novel sensors, signal & image processing techniques, material characterisation, quality assurance, in-service inspection and automation. The workshop was inaugurated by Dr. Baldev Raj, the then Director, IGCAR. During the inaugural address, Dr. Baldev Raj recalled how a variety of electromagnetic nondestructive evaluation techniques were developed for the Indian nuclear power programme and highlighted the future role to be played by these techniques for enhanced quality and safety of engineering components through early detection of defects and microstructure degradations. Prof. Fumio Kojima, Chairman, ENDE Standing Committee, Kobe University, Japan gave a brief account of the ENDE workshop series. Dr. B.P.C. Rao, Convener, ENDE-2011 and Head, Electromagnetic Modelling Sensors & Imaging Section, NDED, MMG, IGCAR gave the details of the structure of the technical sessions of ENDE-2011.

Theme Meeting on "Advances in Electronics, Instrumentation and Information Technology"

March 24, 2011

A Theme Meeting on "Advances in Electronics, Instrumentation and Information Technology" was organised by Electronics and Instrumentation Group, IGCAR on March 24, 2011 at Sarabhai Auditorium. Shri S.A.V. Satya Murty, Associate Director, EIG welcomed the participants and gave the genesis of the theme meeting. Shri S. C. Chetal, Director, REG, delivered the inaugural address with an appreciation for progresses made in Instrumentation and Control Systems for PFBR compared to FBTR. He highlighted the use of advanced electronics towards enhanced reliability and safety of the reactor and simulator for operator training. He also stressed the importance of conducting a thorough and independent verification and validation of I&C systems before implementation in the plant. He emphasised the need for R&D efforts towards the improved control room configuration and layout for better information management and avoid operator overload. Dr. P. Swaminathan, the then Director, EIG presented the reminiscences of his experiences in the Centre. Dr. M. Sai Baba, Head, SIRD, proposed the vote of thanks. Invited lectures were delivered by the system experts in each field covering, various topics - Security concerns in Wireless Sensor Networking, R&D activities of Real Time Systems Division and open platform for leveraging collective wisdom, Good Practices for Grounding of instrumentation and control systems, Design experiences of instrumentation and control for PFBR, Digital Library at IGCAR, Vital signs of Identity–Radio Frequency Identification and Biometrics, Challenges in neutronics instrumentation, Evolution of real time computers for reactor control and Development of Time domain electromagnetic system for exploration of Conductive deposits. About 200 officers of IGCAR working in the field of Electronics, Instrumentation & Control systems and Information Technology attended the theme meeting. The technical talks were very informative and were well received. The theme meeting was followed by a felicitation function to Dr. P. Swaminathan, the then Director, EIG.

Dr. P. Swaminathan, Director, EIG delivering the address during the theme meeting. Shri S.C. Chetal, Director, REG, Shri S.A.V. Satya Murty, Director, EIG and Dr. M. Sai Baba, Head SIRD are seated on the dais

Report on the 7th CEA-IGCAR Annual Seminar on Liquid Metal Fast Reactors Safety

April 13-21, 2011

Delegation from CEA and participants from IGCAR with Shri S.C. Chetal, Director, IGCAR during the meeting

A series of four specialists meetings with different themes under the aegis of the 7th CEA-IGCAR Annual Seminar on Liquid Metal Fast Reactors Safety was organized at IGCAR during April 13-21, 2011. Meetings were conducted on the following themes:

(1) Atmospheric dispersion & Aerosol studies
(3) R&D needs of sodium fast reactors
(2) Instrumentation for measurements in sodium
(4) Severe accidents R&D needs for sodium fast reactors.

The Specialist meeting on "Atmospheric Dispersion and Aerosol Release" was held on April 13, 2011. Welcoming the CEA delegates, Shri S.C. Chetal, Director, REG, IGCAR, in his introductory remarks, briefly outlined the genesis of the CEA-IGCAR collaborations. Dr. C. Latge, thanked IGCAR for organizing this meeting and briefly outlined the status of the various on-going collaborative projects. After a brief introduction of all the participants, presentations were made by Shri P.T. Rakesh on implementing agreement on mesoscale and microscale atmospheric dispersion for impact studies on nuclear sites, Dr. V. Subramanian on "Status of Sodium Aerosol Carbonation Studies at IGCAR" and Shri Amit Kumar on the activities on "Sodium Aerosol Studies in Cover Gas Region at IGCAR". Dr. C. Latge made presentations on behalf of CEA highlighting the activities and the salient results on all the above mentioned topics. The technical meeting was followed by a visit to the

Delegates from CEA holding discussions with Shri S.C. Chetal, Director, IGCAR and participants from IGCAR during the meeting “Instrumentation for Measurements in Sodium”

Shri S.C. Chetal, Director, IGCAR and senior colleagues of the Centre during discussions with the members of CEA delegation during the meeting on "R&D Needs of Sodium Fast Reactor"

sodium aerosol facilities and atmospheric dispersion facilities and a demonstrative experiment was carried out in the presence of the visitors in order to show the possibilities for future experiments.

The second meeting on the theme "Instrumentation for Measurements in Sodium" was conducted during April 14-15, 2011. The meeting started with the introductory remarks by Shri P. Kalyanasundaram, then Director, FRTG followed by Dr. C. Latge of CEA, France. Presentations were made on various topics including core monitoring, detection sensors and in-service inspection by delegates from IGCAR and CEA. A discussion on the potential areas of future collaborations also took place.

The third meeting on April 18, 2011 was conducted on the theme "R&D needs of Sodium Fast Reactors". The meeting had presentations on overviews of ongoing R&D for Sodium Fast Reactors, R&D need for CFBR, R&D facilities at CEA and experimental facilities at IGCAR. The team then visited Steam generator test facility, Large component test rig, In-Sodium testing, Sodium water reaction test rig and SAMRAT facilities.

The fourth and final meeting was on "Severe accidents R&D needs for Sodium Fast Reactor" during April 19-21, 2011. Dr. P. Chellapandi, Director, NSEG presented an overview on severe accident studies at IGCAR and the CEA gave an overview of the R&D programme in severe accidents. A number of speakers presented on safety aspects, studies on accidents, fuel coolant interaction, sodium fire, qualification of fire resistant cables, tiles and extinguishers and imaging sodium fires.

The concluding session on April 21, 2011 reviewed the "Status on sodium cooled fast reactors, current and potential collaborations". The summary of the Technical meetings were also presented in the concluding session.

Participants from the CEA Delegation with Dr. Baldev Raj, the then Director, IGCAR, during the concluding session on April 21, 2011

Theme Meeting on Manufacturing Simplifications for Commercial Fast Breeder Reactor Core Sub-Assemblies

September 10, 2011

One day theme meeting was organised to deliberate on the experience and to identify from the feedback towards simple and improved design facilitating cost effective manufacture. The meeting was attended by designers, material specialists, fuel chemistry experts, PIE experts from IGCAR, fabricators from NFC, Hyderabad, AFFF, Tarapur and Quality inspection agencies particularly in Non-destructive evaluation. Concerned Unit Heads, senior officials along with young engineers participated in the meeting. The topics covered were international perspectives, design improvements, advanced quality analysis techniques and manufacturing aspects. The major highlights of the presentations, deliberations, summary of observations and road map for implementation are discussed in this report.

The approach adopted and the current evolution of core design in Russia, Japan, China and France were focussed since these countries are embarking with design of future fast reactors.

he approach adopted in IGCAR for improving the fuel performance were presented and the results of the important studies carried out such as acceptable defects, influence of fabrication parameters on linear power from the point of view of higher production recovery were impressed upon. The design features which are retained for future FBRs are reactor power, pin diameter and sub-assembly size. Several design features were identified for optimization, simplification, standardization, relaxation of inspection requirements and performance improvement. Ferro-boron is envisaged to be an alternative bulk shielding material which would reduce the thickness by one row. Optimization of sub-assembly height, simple end plug weld, shifting the auto orientation feature to fuel handling machine and removal of bottom labyrinth are some of the features identified for further work. Hard facing of sleeves in the grid plate is a potential area for research which has to be re-looked since it is a costlier and lengthier process. Development of alternative hard materials is an option.

The following points have been identified for further consolidation and implementation

- Need to review the specification and tolerances of the different core sub-assemblies as they belong to different safety classes
- Identification and incorporation of design changes to facilitate automation in machining and assembly
- Rationale document for chemical specification giving the effect of variation of each element on the performance and manufacturing aspects
- Implementation of advanced NDE techniques with focus on reduced time and reliable detection leading to faster manufacture
- Optimization of blanket pin design taking into account breading, reactor engineering and reprocessing aspects
- Weldability studies with D9I, 9Cr-1Mo ferritic steels
- Road map and a detailed report with identification of design features for standardization and rationalization based on the rich experience from PFBR core sub-assembly manufacture would be jointly prepared by IGCAR, NFC, AFFF and BHAVINI comprising experts from different fields by March 2012.

It was decided to continue the consultations and discussions among the concerned units on a regular basis paving the way for cost effective manufacture of core sub-assemblies for future cores of PFBR and CFBR.

Shri S.C. Chetal, Director, IGCAR and senior colleagues of the Centre and the Department during the theme meeting

SMiRT Post Conference Seminars on Innovative Fast Reactor Design and High Temperature Design

November 14-15, 2011

Delegates of the SMiRT Post Conference on Innovative Fast Reactor Design

Structural Mechanics in Reactor Technology (SMiRT) is an international conference being organised once in every two years. Two of the Post Conference Seminars (PCS) on "Innovative Fast Reactor Design" and "High Temperature Design" were held concurrently at IGCAR, Kalpakkam during November 14-15, 2011. The objective of both the seminars was to provide a global platform for in-depth discussions and deliberations on the roadmap, R&D being carried out, results obtained so far within the various fast reactor development programmes and high temperature design issues. The seminar on Innovative Fast Reactor Design focused on the themes such as technological concepts covering fuel, operating experience, numerical and experimental studies on PFBR systems and sodium technology. The themes were chosen to avoid any overlap with the physics and advanced reactor concepts themes of the IAEA technical meeting which were held concurrently. There were 42 participants including 6 from Japan, Netherlands, Ukraine and Belgium. Experts from academic institutes also presented their research results. There were a total of 35 technical presentations in seven technical sessions in the topics of Reactor Physics and Fuel, Advanced Reactor Concepts, Advanced Materials, Experience in Manufacture and Reactor Operation, Reactor Systems Optimization, Sodium Technology and Testing. The major feedback from the seminar are (i) co-operation among fast reactor countries should be on a larger framework (ii) academic institutes should get involved on a much larger scale (iii) more experimental programmes need to be undertaken. The seminar on high temperature design was to cover all the technical and professional practice issues in the concerned area of nuclear power plant components, to discuss about the high temperature failure modes like creep, fatigue and their interactions, the codes and standards, materials and piping analytical methodology at high temperature. There were twenty nine IAEA participants including seven from France, Japan and Russia. There were a total of twenty technical presentations in five technical sessions in the topics like high temperature codes and standards, materials, piping, etc. The major feedback emerged from the seminar is that there should be many such international seminars arranged in future on this topic which is crucial for the fast reactor technology. There were also participants from BARC, NFC and IPR, Gandhi Nagar. An important highlight was that an 'Young Engineer Session' in each Post Conference Seminar was conducted in which many young engineers presented their technical study results, which was well appreciated. Young engineers presented their work on advanced high temperature design and innovative design concepts for the advanced fast reactor systems. This event would help in establishing collaborations with participating countries apart from strengthening the existing technical collaborations towards developing science & technology of Sodium Cooled Fast Reactors.

IAEA Technical Meeting (TM-41429) on Fast Reactor Physics and Technology

November 14-18, 2011

Shri S.C.Chetal, Director, IGCAR addressing the gathering during the inaugural session. Seated in the dais are Dr. Andrej Zeman, Scientific Secretary of the meeting, Dr. P. Chellapandi, Director, NSEG, IGCAR and Dr. Stefano Monti, Head, TWGFR, IAEA

A five day Technical Meeting on "Fast Reactor Physics and Technology" was held at IGCAR under the auspices of IAEA during November 14-18, 2011. The objective of the meeting was to bring together the experts to discuss the state of the art reactor designs and in particular, recent innovative reactor concepts, novel core structural materials and to evolve designs with improved reliability & cost effectiveness for future FBRs. Seventy delegates including twenty-nine international participants from fifteen countries and forty one national participants from BARC, BHAVINI, SRI, NPCIL and IGCAR attended the meeting. Dr. P. Chellapandi welcomed the delegates and highlighted the significance of organizing the meeting in the current Indian context. Shri S. C. Chetal, Director, IGCAR gave an inspiring inaugural address and brought out the multi-disciplinary capability of IGCAR towards scientific research, advanced engineering of fast reactors and its associated fuel cycle. He gave a comprehensive view of various activities of IGCAR and the current status of fast reactors worldwide. Dr. Andrej Zeman presented an overview of the activities of IAEA including the various co-ordinated research projects and training programmes. This was followed by an overview of fast reactor activities being carried out under TWGFR by Dr. Stefano Monti. Forty six presentations were made in seven technical sessions including seventeen by international delegates. The main focus of the meeting deliberations was on the current status of fast reactor activities in fifteen countries, innovative fast reactor designs to improve safety, economy, strategy & key results of R&D carried out in various countries including India. The meeting brought out the current international re-look on various load combinations including design extension conditions and the comprehensive approach to address the safety issues post Fukushima accident. Alternative coolant technologies like Lead and Lead-Bismuth were also discussed. Concepts of development of core structural materials to improve burn-up, advanced fast reactor thermal hydraulics and safety were discussed in-depth. The presentation on PFBR construction experience, design approach for CFBR, various R&D and technological activities at IGCAR were well appreciated. Though many countries do not have an active fast reactor programme, they showed a keen interest to work with India and collaborate on various R&D activities. The technical sessions were very lively with active participation from the delegates. They evoked great interest and motivation among the younger colleagues currently involved in the design and development activities of future FBRs. Overall, the technical meeting evoked a positive response from various countries to interact more effectively and to provide a basic platform for more active joint co-operative efforts to sustain and improve the economy and safety of fast breeder reactors. It also gave a valuable opportunity to the Indian delegates to interact with renowned experts and to present their current work to the international community.

Theme Meeting on Structure and Thermodynamics of Emerging Materials (STEM-2011)

November 24-26, 2011

Prof. Ajay Gupta, Director, UGC - DAE consortium for Scientific Research, Indore Centre delivering the plenary lecture during STEM-2011

The BRNS sponsored theme meeting, 'STEM-2011' focusing on "Diffusion, Mass Transfer and its Consequences in Materials" was organized jointly by Indira Gandhi Centre for Atomic Research and The Indian Institute of Metals – Kalpakkam Chapter during November 24-26, 2011 at Convention Centre, Anupuram. Dr. M. Vijayalakshmi, Associate Director, PMG welcomed the participants and highlighted the wide spread application of diffusion in various fields. She emphasized the necessity to explore the possibility of extending the diffusion based concepts to new and advanced materials and processes. Dr. S. Saroja, Convener, STEM-2011 briefed upon the genesis of the STEM annual meetings on a focused theme to foster professional knowledge. Professor Ajay Gupta, Director, UGC-DAE Consortium for Scientific Research, Indore Centre delivered the plenary lecture on "Nanoscale Atomic Diffusion in Thin Films and Multilayers Studies using X-ray Techniques" and provided an excellent insight into the basic difference between diffusion in bulk, thin films and various experimental techniques used to measure the diffusion parameters in multilayer thin films. The vote of thanks was proposed by Smt. C. Sudha, Secretary STEM-2011. On the first day, lectures were delivered by eminent scientists from leading national R&D institutions and academia covering aspects related to mass transport in materials of importance to the power generation industry, diffusion bonding of dissimilar materials, diffusion studies with respect to materials used in the back end of the fuel cycle and the Kirkendall effect in solid state interdiffusion. On the second day tutorial lectures and practical demonstrations were held on the application of Monte Carlo and molecular dynamic simulation techniques to study the diffusion of atoms. On the third day the participants were taken for field visit to MAPS and to the Laboratories in the Physical Metallurgy Group. About 120 specialists, delegates and students from various acadamic institutes such as IISc, IITs, NIT, IPR, Anna University, Bengal Engineering College, Sandvik and DAE units of BARC, NFC and IGCAR and participated in the deliberations. The technical programme was appreciated by the participants and valuable inputs for future theme meetings were provided during the feedback session at the end of the theme meeting.

Participants of STEM-2011

8th Biennial National Conference on Recent Advances in Information Technology (READIT)

December 28-29, 2011

Dr. M. Sai Baba, Convener, READIT addressing during the panel discussion chaired by Dr. Sandhya Shekhar CEO, IITM research park, Chennai and other eminent panelist

The 8th Biennial National Conference on Recent Advances in Information Technology (READIT) was organized by Scientific Information Resource Division of IGCAR in association with the Kalpakkam Chapter of Madras Library Association (MALA) during December 28-29, 2011. The theme of the Conference was "Knowledge Sharing with Semantic Grids". More than 200 delegates including information technology professionals, librarians, students and academicians attended the conference. The sub themes of the conference were Advanced Digital Library Infrastructure, Grid Computing and Semantic Web Technologies, Content Organizing and Knowledge Management, Collaboration and Connecting Libraries. The format of conference included invited talks by eminent experts, oral/poster presentations by research scholars/participants. The conference was preceded by a one day Tutorial Session on the theme "Preservation Technique for Archives and Access Management" on December 27, 2011. The conference was inaugurated on December 28, 2011 by Prof. R. Balasubramanian, Director, Institute of Mathematical Sciences, Chennai. The function was presided over by Shri S.A.V. Satya Murty, Director, EIG, IGCAR & Chairman Library and Information Services Committee. Dr. M. Sai Baba, Convener, READIT, AD, RMG & Head, SIRD welcomed the gathering. Prof. R. Balasubramanian released the Souvenir and Shri S.A.V. Satya Murty inaugurated the exhibition. Shri E. Soundararajan, SIRD delivered the vote of thanks. Intensive technical discussions on various aspects of Semantic Grids, Digital Library Infrastructure, Knowledge Management and implications for the Libraries were presented during the confrence. The conference concluded in the evening of December 29, 2011 with a panel discussion on the topic "Emerging Trends in Digital Technologies and Implications for Information Access". This panel discussion was chaired by Dr. Sandhya Shekhar, Chief Executive Officer, IITM Research Park, Chennai and was moderated by Dr. M. Sai Baba. The panelist were Shri Umesh Chandra, Senior Executive Director, Safety and Knowledge Management, NPCIL, Mumbai, Prof.C.K. Ramaiah, Head, DLIS, Pondicherry University, Dr. S. Venkadesan, Director, Learning Resource Centre, ISB, Hyderabad, Dr. J. K. Suresh, Vice President, Knowledge Management, Infosys Technologies Ltd, Bengaluru Shri Vikram Pothnis, Product Manager, Wipro Infotech Ltd, Bengaluru, and Shri Prashant Gangwal, Key Account Manager, Elsevier. Interesting and inspiring discussions were made by the delegates and students during the panel discussion. At the end, the summary of technical sessions was presented by Dr. M. Sai Baba.

Dr. M. Sai Baba, Convener, READIT & AD, RMG, Dr. Balasubramanian, Director, IMSc, Shri S.A.V. Satya Murty, Director, EIG and Shri E. Soundararajan, SIRD during the release of souvenir at the inaugural function of READIT

Eminent Visitors To IGCAR

Dr. Yukiya Amano, Director-General, IAEA with Mr. Rafael Crossi, Chief De Cabinet, IAEA with Dr. Baldev Raj, the then Director, IGCAR and other senior colleagues of the Centre and the Department

Dr. Yukiya Amano, Director-General, **Mr. Rafael Crossi,** Chief De Cabinet and **Mr. S. Akbaruddin,** Director, Office of the external relations and policy creation, IAEA visited the Centre on January 18, 2011. After meeting the Director and the members of DAC, they visited Fast Breeder Test Reactor, Hot Cells and Non-Destructive Evaluation Division, Sodium Fire Facility in Nuclear and Safety Engineering Group, Atmospheric Aerosol Dispersion Facility in Reactor Engineering Group, Magnetoencephalography studies laboratory at Materials Science Group, Safety Research Institute of Atomic Energy Regulatory Board and construction site of PFBR.

Dr. C.V. Krishnaswami delivering the Vikram Sarabhai Memorial Lecture

Dr. C.V. Krishnaswami, Honorary Consultant and Head of the Diabetes Department, Voluntary Health Services, Chennai, (Formerly) Honorary Clinical Professor & Honorary Physician, Government Stanley Hospital, Chennai, Chairman, Healthtrack Info Solutions Private Limited, Chennai visited the Centre during February 11-12, 2011 along with his wife, **Dr. (Mrs.) Prema Krishnaswami,** renowned Obstetrician and Gynaecologist, Chennai to deliver the 7th Vikram Sarabhai Memorial Lecture on the topic, "Medical Education and Research in Independent India". **Dr. Krishnaswami** visited the Fast Breeder Test Reactor, Magnetoencephalography studies laboratory at Materials Science Group and construction site of PFBR. The dignitaries also interacted with the medical fraternity and the students from the schools at Kalpakkam.

Delegation from Idaho National Laboratory led by Mr. John Grossenbacher with Dr. Baldev Raj, the then Director, IGCAR and other senior colleagues of the Centre

A delegation from Idaho National Laboratory, USA led by its Director, **Mr. John Grossenbacher,** along with **Dr. Harold McFarlane,** Deputy Associate Laboratory, Director and Technical Director of Generation-IV International Forum, **Dr. Satish Kulkarni,** INL Consultant and **Dr. Hamilton Maxwell Janek,** Political/ Economic Officer, American Consulate, Chennai visited the Centre on February 16, 2011. After a meeting with **Dr. Baldev Raj,** the then Director, IGCAR and a meeting with the DAC members. The team visited Fast Breeder Test Reactor, Large Component test facility and Steam Generator Test facility facilities at Fast Reactor Technology Group, Magnetoencephalography studies laboratory at Materials Science Group, Sodium fire test facility at Nuclear and Safety Engineering and the construction site of PFBR at BHAVINI.

Team from Institute of Defence Studies and Analyses and Indian Pugwash Society, led by its convenor, Dr. Arvind Gupta with Shri S.C. Chetal, Director, REG and senior colleagues of the Centre

A team from Institute of Defence Studies and Analyses and Indian Pugwash Society, led by its convener, **Dr. Arvind Gupta,** Additional Secretary, Ministry of External Affairs & **Lal Bahadur Shastri** Chair, Institute of Defence Studies and Analyses along with **Mrs. Purnima Gupta,** Economic Advisor, Tariffs Commission, Government of India, **Prof. K.D. Kapur,** Consultant, Indian Pugwash Society, **Dr. Ch.V. Sastry,** Research Fellow, Institute of Defence Studies and Analyses, **Shri P. K. Sundaram,** Senior Research Fellow, Indian Pugwash Society and **Shri Kapil Patil,** Intern, Indian Pugwash Society visited the Centre during February 25-26, 2011. The team had discussions with **Dr. Baldev Raj,** the then Director, IGCAR and DAC members and visited Fast Breeder Test Reactor, Hot Cells and Non-destructive Evaluation Division, Development of sodium testing of components and magnetic bearings with ferrofluid seals in the Fast Reactor Technology Group, Sodium Fire Facility in Nuclear and Safety Engineering Group, Aerosol and Atmospheric Dispersion studies at Reactor Engineering Group and the construction site of PFBR at BHAVINI.

Delegation from Engineering and Physical Sciences Research Council, UK with Shri S.C. Chetal, Director, REG and other senior colleagues of the Centre

A delegation from the Engineering and Physical Sciences Research Council, UK under the leadership of **Dr. Jason Green,** visited the Centre on March 8, 2011. The delegation held discussions with senior colleagues of the Centre on possible avenues of collaboration. The team later visited Fast Breeder Test Reactor, Accelerator studies facility at Materials Science Group, Facilities for newer welding methodologies at the Metallurgy and Materials Group and the construction site of PFBR at BHAVINI.

Shri S.S. Bajaj, Chairman, AERB Delivering the IGC colloquium on “Fukushima-Regulator Perspective“

Shri S.S. Bajaj, Chairman, Atomic Energy Regulatory Board during his visit to the Centre on May 13, 2011 delivered the “IGC Colloquium” on “Fukushima – Regulator Perspective ”.

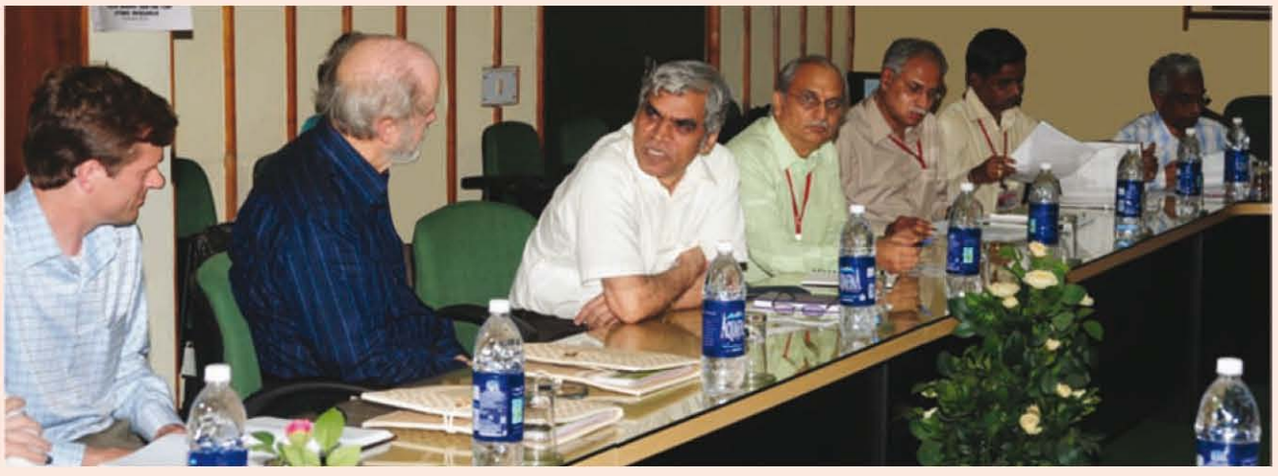

Delegation from M/s. Terrapower, USA with Shri S.C.Chetal, Director, IGCAR and senior colleagues of the Centre

A delegation from **M/s. Terrapower,** USA, led by its executive vice president **Mr. David McAlees,** along with **Shri Ashok Misra,** Chairman-India, Head of Global Alliances visited the Centre on May 20, 2011. The team had discussions with **Shri S.C. Chetal**, Director, IGCAR, and senior colleagues of the Centre on possible avenues of collaboration.

Shri T.K.A. Nair, Principal Secretary to the Prime Minister with Shri S.C. Chetal, Director, IGCAR and senior colleagues of the Department

Shri T.K.A. Nair, Principal Secretary to the Prime Minister visited the Centre on July 9, 2011. During the meeting he was briefed about the Research and Development activities at Indira Gandhi Centre for Atomic Research by **Shri S.C. Chetal,** Director, IGCAR and on the status of Prototype Fast Breeder Reactor by **Dr. Prabhat Kumar,** Project Director, BHAVINI. **Shri T.K.A. Nair** visited the Fast Breeder Test Reactor, Magnetoencephalography facility and construction site of PFBR.

Dr. R. Chidambaram, Principal Scientific Advisor to Government of India, Dr. Baldev Raj, President, PSG Institutions, Coimbatore and Shri Neeraj Sinha, Senior Director, Office of Principal Scientific Advisor to Government of India with Shri S.C. Chetal, Director, IGCAR and senior colleagues of the Centre during their visit to Chemistry Group

Dr. R. Chidambaram, Principal Scientific Advisor to Government of India, Dr. Baldev Raj, President, PSG Institutions, Coimbatore and Shri Neeraj Sinha, Senior Director, Office of Principal Scientific Advisor to Government of India, visited the Centre on August 10, 2011. The team visited the Chemistry Group, Materials Science Group, UGC-DAE-CSR complex and construction site of PFBR.

Delegation from American Nuclear Society, USA with senior colleagues of the Centre

A delegation from the American Nuclear Society, USA, led by **Dr. Eric Paul Loewen,** visited the Centre on September 27, 2011. After a meeting with senior colleagues, the delegation visited the Fast Breeder Test Reactor and facilities in Nuclear and Safety Engineering, Reactor Engineering and Materials Science Groups.

Delegation from United States Nuclear Regulatory Commission led by Dr. Gregory B. Jaczko, with Shri S.C. Chetal, Director, IGCAR and senior colleagues of the Centre

Delegation from the United States Nuclear Regulatory Commission led by **Dr. Gregory B. Jaczko,** chairman, visited the Centre during November 16-18, 2011. After meeting the Director and senior colleagues of the centre, the delegation visited the Fast Breeder Test Reactor, Hot Cells and Non-Destructive Evaluation Division, Facilities in Fast Reactor Technology Group, Sodium Fire Facility in Nuclear and Safety Engineering Group, Structural Mechanics Laboratory, construction site of Prototype Fast Breeder Reactor and Madras Atomic Power Station.

IGC COUNCIL

Chairman

Shri S.C. Chetal graduated in Mechanical Engineering from Delhi college of Engineering in 1970. After graduating from the 14th Batch of BARC Training School, he joined in IGCAR in 1971. Since, then, he has been engaged in the field of Fast Reactor Engineering. At present, he is Distinguished Scientist & Director, IGCAR and Director Reactor Engineering Group. He has made contributions towards design of FBTR sodium systems and components. He is the principal design engineer of PFBR. He has made outstanding contributions towards the material selection, manufacturing technology, R & D design and construction of 500 MWe Prototype Fast Breeder Reactor. He has enhanced the capabilities of the Indian industries to manufacture nuclear components with stringent tolerances. His contributions include the design and manufacturing of high temperature reduction retorts for zirconium and titanium sponge, design and technical specifications for the manufacture of the large size cryostat for ITER, and materials development for advanced ultra supercritical plants. He is member of many professional institutions and fellow of Indian National Academy of Engineering. He is a recipient of Indian Nuclear Society INS Award 2003 for contributions towards nuclear related high technology, National Design Award-2007 by Institution of Engineers, 2003 VASVIK Award, Agni Award for Excellence in self-reliance by DRDO for titanium sponge production, and Certification of Appreciation by IAEA towards fast reactor technology. His interests include pressure vessel and materials technology. He is on the Board of BHAVINI.

He is also Director, General Services Organisation, managing the two townships with associated facilities of schools, hospitals, entertainments and sports and unique facility of zero solid waste in ensuring quality living.

Members

Dr. Ratan Kumar Sinha graduated in Mechanical Engineering from Patna University in 1972, standing first in the University. After completing the one year Course of BARC Training School he joined Reactor Engineering Division of BARC in the year 1973. Before his appointment as Director, BARC, he served as Director, Reactor Design & Development Group and, Director Design, Manufacturing & Automation Group, BARC. Dr. Sinha has been guiding the programmes for new advanced reactors under design and development at BARC to utilise thorium. These include, the Advanced Heavy Water Reactor (AHWR), which produces most of its power from thorium, and has several innovative passive safety systems. The reactor has been designed to be robust against equipment malfunction, human errors and even insider's malevolent acts. Dr. Sinha, thus, guided the development of technologies that should enable, in a large scale deployment scenario, the siting of advanced nuclear power plants close to population centers. Most of the technological innovations in the design of AHWR have been validated under his guidance, in large experimental facilities. Dr. Sinha initiated the design and development of a Compact High Temperature Reactor (CHTR), with its first objective to demonstrate generation of process heat at nearly 1273 K, as needed for efficient thermo-chemical splitting of water for producing hydrogen, and the second objective to demonstrate technologies needed for transportable nuclear power packs capable of being deployed in remote areas, with practically no need for skilled operation, and no need to refuel for 15 years. He and his team are developing a first-of-a-kind design to meet these objectives by introducing thorium based coated particle type nuclear fuel, a reactor physics design to achieve inherently safe neutronic characteristics, use of molten lead-bismuth as coolant driven by natural circulation, passive emergency cooling systems that deliver core heat to atmosphere, passive shutdown device, and passive control devices capable of operation at very high temperatures. These innovative features are unparalleled in any other reactor in the world. Dr. Sinha carried out extensive work to assess the residual service life and determine the fitness-for-service criteria for these channels. Dr. Sinha and his team developed several indigenous technologies for the timely repair and maintenance of reactor systems.

Dr.P. Chellapandi is an Outstanding Scientist and Director, Nuclear & Safety Engineering Group, IGCAR, Kalpakkam. He is from 22nd batch of BARC training school with first rank and joined IGCAR in 1979. He is responsible for the design and development of fast reactor components including core and shutdown systems. He is one of the key persons who have involved in the design and development activities of 500 MWe Prototype Fast Breeder Reactor (PFBR) since its inception. He has contributed significantly for PFBR over a wide spectrum of design, viz., conceptualization, consolidation of failure modes, development of sophisticated computer codes and analysis methodologies, detailed analysis, design confirmation and validation of components, preparation of preliminary safety analysis reports, execution of R&D activities involving national academic institutions and R&D establishments in the country towards ensuring the robustness of design. His current activities focus on the development of innovative design features for the future fast breeder reactors beyond PFBR, planned by the Department. He has established two dedicated and unique laboratories at IGCAR: one for structural mechanics studies and another for safety engineering studies for the design validations. He has formulated many national collaboration with various reputed institutes and particularly played a key role for establishing MoUs with IIT Madras, IIT Kanpur and IISc Bangalore. As a member of Technical Working Group on Fast Reactor under IAEA, he has been responsible for formulating and coordinating many technical meetings and collaborating research projects with international experts.He has outstanding academic record in Mechanical Engineering and Gold Medal with perfect grade point average of 10 in his Master's Degree in field of applied mechanics, from IIT Madras. He is a Professor of Homi Bhabha National Institute. He has guided more than 120 MTech projects and more than 300 B.E. Projects, all relevant to fast reactor design. He has a very impressive record of publications (540) to his credit out of which 80 are journals. He is a Fellow of Indian National Academy of Engineering. He has received the Homi Bhabha Science and Technology Award for the year 1997, Indian Nuclear Society Award and National Design Award in Mechanical Engineering in 2006, Agni Award for Excellence in Self-reliance – DRDO-2007, DAE Group Achievement Awards in 2006, 2007, 2008, 2009 and 2010 for Design, manufacture and Erection of PFBR reactor assembly components, for which he is the convener of the task force.He is been bestowed upon Distinguished Alumnus Award of the IIT Madras in 2010.

Dr. A.K. Ghosh, joined the Bhabha Atomic Research Centre in 1971 after graduating in Mechanical Engineering from Indian Institute of Technology, Kharagpur, India. He obtained his Ph.D from Indian Institute of Technology, Bombay. Currently, he is the Director, Health, Safety and Environment Group of BARC. Dr. Ghosh has been carrying out R&D work in the field of reactor safety and his area of work includes both thermal-hydraulic safety and structural safety. He has carried out some pioneering work on the hazards due to earthquakes and tsunamis. Presently, he is also associated with various programmes on radiation safety. He has published more than 100 papers in International Journals and Conferences. He is a Chairman/Member of various Safety Committees of BARC and Atomic Energy Regulatory Board (AERB) for Siting and Design Safety Review and has made significant contribution in the preparation of various Safety Codes and Guides on these subjects.

Dr. P.D. Gupta, Distinguished Scientist is Director, Raja Ramanna Centre for Advanced Technology, Indore. Dr. Gupta is an internationally known laser-plasma physicist who has made pioneering research contributions to this area. He passed M.Sc. Hons (Physics) from Panjab University in 1972 and joined Bhabha Atomic Research Centre after a brilliant academic record. He is a recepient of four gold medals for securing first rank in various university examinations. He joined BARC in August 1973 after passing out from 16th batch (1972-73) of Training School and was awarded Homi Bhabha Medal and Prize. He received his Ph.D from Bombay University in 1984, did his Post-doctoral work at the Department Of Electrical Engineering, University of Alberta, Canada during 1984-86. He is recepient of Young Scientist Award of Indian

National Science Academy (1984), Young Associateship of Indian Academy of Sciences (1986-91) and became Fellow of the National Academy of Sciences, India, in 2004. As Director, Dr. Gupta is steering many R&D programmes in frontline areas of accelerators and lasers at RRCAT. These include synchrotron radiation sources and their utilization, development of superconducting radio-frequency cavities for high energy accelerators, proton linac spallation neutron source, cryogenics and magnet technology, ultra-intense laser-plasma interaction, and lasers in research and industry. He on NAT projects, and a member of the Core Group on Asian Intense Laser Network. Dr. Gupta is a Senior Professor of Homi Bhabha National Institute (HBNI), Mumbai and a member of its Academic Council. He has guided many young researchers for the award of Ph.D / M. Tech / M. Sc degrees. He has made ~ 350 research contributions of which 160 are published in international journals.

Dr. T. Jayakumar, B.Tech. (Metallurgy, REC Warangal), M.S (Metallurgy, IIT Madras), Ph.D (Engineering, University of Saarland, Germany) is currently an Outstanding Scientist & the Director, Metallurgy and Materials Group at IGCAR. Since 1978, he has been engaged in the field of Non-Destructive Evaluation. Over the years he has carried out and steered innovative research and development programmes in the areas of Non-Destructive Evolution, Failure Analysis and Structural integrity of Nuclear Components specifically for the Fast Breeder Reactor. For the last few years he is actively coordinating and guiding research activities related to development of materials and manufacturing technologies for sodium cooled fast reactors, associated fuel cycle and Indian fusion programme. He is a Fellow of the Indian National Academy of Engineering. He has been a recipient of several awards such as National NDT Award from ISNT, Metallurgist of the Year award from IIM, Homi Bhabha Science and Technology Award from DAE, Outstanding Services Award from INS. He has co-authored 3 books, co-edited 4 books and has published over 270 papers in International Journals. He also has 6 patents to his credit.

Shri P.V. Kumar joined the Training School of BARC in 1971 after graduation in mechanical engineering. He was involved in design, construction and commissioning of the Radiometallurgy Laboratory at IGCAR, Kalpakkam. He was a member of the KAMINI Reactor Commissioning Authority. He is presently Project Director of the Fast Reactor Fuel Cycle Facility that is planned to be established at Kalpakkam to close the fuel cycle of PFBR. He is a fellow of The Institution of Engineers (I) and Indian Institute of Welding.

Shri R.N. Jayaraj, presently the Chairman & Chief Executive of Nuclear Fuel Complex (NFC), Hyderabad, is a Mechanical Engineer from Osmania University, Hyderabad. Shri Jayaraj, after obtaining the Bachelors Degree in Mechanical Engineering in the year 1973, joined the 17th batch of BARC Training School, Mumbai, India for one-year orientation course in Nuclear Engineering. At BARC, he has carried out development and manufacturing of metallic fuels for thermal research reactors. Shri Jayaraj joined NFC in 1978 and was responsible for establishing a facility for the fabrication of core sub-assemblies for the Fast Breeder Test Reactor (FBTR). After successful completion of the first core requirement, he was assigned the responsibility of fabricating fuels for all the Power Reactors in India. Shri Jayaraj has played a pioneering role in standardizing the processes and manufacturing fuel bundles required for 540 MWe Pressurized Heavy Water Reactors (PHWRs) for the first time in the country. Presently he is engaged in the expansion activities of fuel fabrication capacities to meet the enhanced fuel demands. Shri Jayaraj has received many prestigious awards including the Indian Nuclear Society (INS) Award, DAE Group Achievement Award and The Indian Institute of Metals (IIM) and SMS-Damag Excellence Award-2009. He is a Fellow of Indian National Academy of Engineering (INAE), Fellow of Andhra Pradesh Akademi of Sciences (APAS) and Honorary Fellow of Indian Institute of Chemical Engineers (IIChE). Shri Jayaraj, besides being a Member of IGC Council, is on the Board of Directors of Uranium Corporation of India Limited (UCIL) and Indian Rare Earths Limited (IREL). He is also the Council Member of Indian Institute of Metals (IIM), Kolkata and the Chairman of Indian Nuclear Society, Hyderabad Chapter.

Shri Y.C. Manjunatha, Director, Engineering Services Group of Indira Gandhi Centre for Atomic Research, Kalpakkam, is an M.Tech. in Electrical Engineering from IIT, Madras and graduated from the 16th batch of BARC Training School. He steers one of the largest multidisciplinary groups in the Centre which focuses on providing reliable and robust services through cutting edge technologies and methodologies. The Group comprises of AC&VSD, CWD, CED, ESD and infrastructural divisions of GSO. Some of his major contributions are development and sustenance of infrastructural works of IGCAR & GSO involving civil, electrical, air conditioning, ventilation, communication and workshop activities. He has published more than twelve papers. He has nurtured and mentored the quality circle activities of the Group. He has played a significant role in making the project site and townships more greener and presentable. Introduction of a systematic domestic solid waste management system at GSO is being appreciated by all. The present focus is on establishment of 2 MGD desalination plant, water treatment plants and provision of common services features to FRFCF. Earlier, he has also played active role in establishment of infrastructural facilities for other Units like RMP Mysore, PRP, NDDP, IMSC-Chennai and PFBR (Pre-project activities). He is a fellow of Institution of Engineers, patron of ISHRAE and Chairman of Kalpakkam Chapter of Indian Society of Non-Destructive Testing.

Shri S.D. Misra is a Graduate in Electrical and Mechanical Engineering. He joined BARC in the year 1970 after completion of 13th batch of Orientation Programme of BARC Training School. Since then, he has been involved in the back-end activities of nuclear fuel cycle. He was a Member of the team that pioneered setting up of the first vitrification plant for management of high level radioactive liquid waste in the country. He was responsible for design & construction of vitrification plants at Trombay and Kalpakkam. Shri Misra has participated in a number of international technical meetings on radioactive waste management. He has also served as an expert on various technical committees of International Atomic Energy Agency (IAEA). Presently, he is a Member of the International Radioactive Waste Technical Committee (WATEC) of IAEA. He also served as Director, Purchase & Stores, Department of Atomic Energy. In this capacity, he has successfully overcome the problems of technology control regime and made available some of the critical stores for the programmes of the Department of Atomic Energy. Presently, as Director, Nuclear Recycle Group, BARC, he is holding the responsibility of setting up and operation of Reprocessing and Waste Management Plants at various sites in the country.

Shri R. Natarajan, a Chemical Engineer is from the 19th batch of BARC Training School and joined the Department of Atomic Energy in 1975. He is presently the Director of Reprocessing Group in IGCAR. Under his leadership, the CORAL facility, for establishing the process technology for the reprocessing of fast reactor fuels was designed, erected and commissioned. He led the team which has successfully completed the reprocessing of fast reactor spent fuel, with a burn-up of as high as 155 GWd/t of a plutonium rich fuel, which is an international benchmark. He is also responsible for the R&D activities of fast reactor fuel reprocessing and setting up of demonstration as well as the commercial PFBR fuel reprocessing plants. His specialization is in the design, development of process flow sheets and plant design. He has also experience in the design and operation of equipment for Thorium-Uranium cycles. He has participated in the irradiated thorium fuel reprocessing campaigns at the Reprocessing Development Laboratory and the U recovered is used as fuel for the reactor KAMINI. He has interest in solvent extraction process modeling, extraction equipment design, design of feed clarification systems of high active solutions, acid recovery systems, system designs of radioactive off-gas circuits and ventilation design of radioactive plants. He has over hundred technical presentations and publications to his credit. He has won the prestigious NOCIL Award for Excellence in Design and Development of Process Plant and Equipment for the year 2005 for his contribution in the development of fast reactor fuel reprocessing. He is also the recipient of Indian Nuclear Society's INS award for the year 2006 for his contributions to Nuclear Fuel Cycle technologies. He is a Fellow of the Indian National Academy of Engineering and Indian Institute of Chemical Engineers.

Dr. G.J. Prasad, Director, Nuclear Fuels Group, BARC graduated from BARC Training School in the 14th Batch (Metallurgy) after graduating in Metallurgical Engineering from NIT Rourkela and received PhD (Technology) from University of Mumbai. His main area of work is in the development and fabrication of research and test reactor fuels and alloy fuels. He was responsible for the development and fabrication of U^{233} plate fuels for the KAMINI Reactor and currently LEU plate fuel for the modified core of APSARA reactor. His area of interest also includes fuels for thermal and fast reactors for generation of nuclear power. He is a designated Senior Professor of HBNI in Engineering Science. He has received the Prime Minister's Award in 1998, MRSI Medal in 2001 and DAE Special Contribution Award in 2006.

Dr. Prabhat Kumar, Distinguished Scientist and Project Director, BHAVINI is responsible for construction and commissioning of India's first Prototype Fast Breeder Reactor which has been designed indigenously and launched as a precursor to commercial exploitation on a large scale. This advanced technology reactor requires understanding of various disciplines of science, multidisciplinary capability of engineering and management skills to achieve the success. In his career, he has worked on nuclear system and component design, indigenisation of critical nuclear equipment, participated in erection of the equipment and their commissioning. He has headed Quality Assurance Group of Kudankulam project during its formative years, later he worked for Coolant Channel Life Management, Remote Tooling for reactor inspection, maintenance and started the R&D centre for NPCIL. He has steered many programmes of vital importance for Indian nuclear power plants and has broad vision of the issues involved. With a large exposure on Pressurized Heavy Water Reactor and Pressurized Water Reactor technologies, he has been chosen to construct India's prestigious Prototype Fast Breeder Reactor, PFBR. He has lead multi disciplinary team from NPCIL, IGCAR and direct towards ensuring a robust construction of PFBR.

Shri K.K. Rajan is from 24th batch of BARC Training School and he joined Indira Gandhi Centre for Atomic Research, Kalpakkam in 1981. He is an electrical engineer from NIT Calicut. His initial contributions were purification, transportation and charging of sodium required for FBTR, Calibration of FBTR sodium flowmeters and other sodium experiments in support of FBTR. He has been steering a multidisciplinary program in the area of Sodium Technology. He has made substantial contributions towards the construction, commissioning and sustained operation of SGTF. He has made significant contributions towards design, construction commissioning of LEENA facility for evaluation of the PFBR secondary system wire type leak detector and in setting up the 1/22 scale mode SADHANA loop, of PFBR Safety Grade Decay Heat Removal system to experimentally demonstrate the feasibility of passive decay heat removal. He has played a key role in operating sodium systems in FRTG safely without any incidents, over the years. He is a member of Indian Nuclear Society and a fellow of Institution of Engineers (India). He has more than 80 publications in both national and international journals to his credit. He is presently Outstanding Scientist and Director of the Fast Reactor Technology Group.

Shri Rajnish Prakash has been appointed as Chairman and Chief Executive, Heavy Water Board, Department of Atomic Energy and has assumed charge w.e.f. 1st April 2011. Shri R. Prakash graduated in Chemical Engineering from University of Roorkee(presently I.I.T. Roorkee) in 1974. He has done post graduate course DIIT in Chemical Reaction Engineering from I.I.T. Delhi. Shri Prakash has worked in most of the Heavy Water Plants in various capacities. Shri Prakash played an important role in setting up and commissioning of India 's first Ammonia based Heavy Water Plant at Baroda and later in new generation plants. He also worked in the area for process development of Ammonia-Water exchange process which included pilot plant studies and development of efficient column internals. He is credited with indigenous development of catalyst for Ammonia based Heavy Water Plants. Shri Prakash has been instrumental in process development for production of various stable isotopes like Oxygen 18 and is instrumental in promoting the non nuclear applications of Deuterium in the country through collaboration with academics and industry. Shri Prakash was also involved in design and implementation of various modifications and ENCON Schemes at the plants which resulted in substantial saving of energy and reduction in cost of production. Shri Prakash was elevated to the post of Associate Director (Operation) at Heavy Water Board (Corporate Office) in April 2005. Later he was elevated to the post of Director (Technical) in January 2008. He was also working as Technical Advisor to Chief Executive, HWB, looking after Corporate / Strategic Planning, Diversification & growth strategies, export of heavy water and alternate applications of Heavy Water.Shri Prakash coordinated the first export of Heavy Water to South Korea; a proud moment for DAE and the country. Later his efforts led to further export of Heavy Water to South Korea , China and USA .Besides being technocrat par excellence, he has been a good sportsman and has represented his College in many events. Even today, he is a good swimmer and good player of badminton/Table Tennis/Chess, etc. Shri Prakash is recipient of many awards including Group Achievement Award of DAE for the year 2010 for his excellent contribution in "Indigenous Development of 2nd Stage Cylinder Body of High Pressure Synthesis Gas Compressor at HWP (Baroda)".

Smt. Revathy Iyer, is from the Indian Audit & Accounts Services of the 1980 batch. She is a Post Graduate in Chemistry from Delhi University. After joining the Services, initially she was posted to Office of AG, Maharashtra, Mumbai. She has worked in various capacities in Audit offices in Hyderabad, New Delhi and Bhopal. During May 1990 to May 1994, she was on deputation to Department of Personnel & Training, New Delhi. From April 2003 to March 2005, she was posted as Principal Director of Audit in High Commission of India, London, UK and thereafter in 2005-2007 as Principal Director of Commercial Audit & ex-officio Member Audit Board, Mumbai auditing Public Sector Units in oil & aviation sector. From October 2007, she is on Central deputation to Department of Atomic Energy as Joint Secretary in-charge of Industrial units, Public Sector Undertakings, IR&W matters, training activities, etc. From July 2010, she has taken over charge of R&D wing of DAE which deals with units like BARC, IGCAR, RRCAT, VECC and all Aided Institutions under DAE.

Dr. K.L. Ramakumar obtained his post graduation from Sri Venkateswara University, Tirupati and joined Bhabha Atomic Research centre (BARC), Mumbai in 1975 after successfully completing one year orientation course in Chemistry discipline from 18th batch of BARC Training School. He is Outstanding Scientist and is currently Director, Radiochemistry & Isotope Group, BARC. He is a specialist in Analytical Chemistry, trace elemental analysis employing mass spectrometry, chromatography and optical spectrometry. He has been peer reviewer for International Science Foundation, USA for financial grant to Russian scientists. Dr. Ramakumar was also on expert assignment to the IAEA for mass spectrometry measurements. Dr. Ramakumar was a member of Indian negotiating team for concluding (i) civil nuclear cooperation agreements with the USA and France, (ii) India's safeguards agreement and additional protocol with the IAEA, and (iii) agreement with the USA on arrangements and procedures for reprocessing of safeguarded spent fuel. He has also vast experience in nuclear safeguards and nuclear material accounting and control. He was one of the coauthors of NUMAC Manual for Indian nuclear facilities. He is also actively involved in the preparation of standard analytical methodology for chemical quality control measurements. Dr. Ramakumar is a recognised Ph.D. guide for Mumbai University and HBNI for Chemistry and also strategic studies (HBNI). Dr. Ramakumar has more than 300 publications.

Shri S.A.V. Satya Murty did his B.Tech. from Jawaharlal Nehru Technological University in 1977. He was a University Gold Medalist in his B.Tech. Later, he joined one year orientation course in Nuclear Science & Engineering (21st Batch) at BARC. He was awarded Homi Bhabha prize for getting 1st rank. In the initial years, he was working in the Central Data Processing System Section of FBTR. In 1981, he joined Computer Division and played a key role in the establishment of Mainframe Computer System for IGCAR. He is instrumental in establishing internet and E-Mail facilities, Network Security Systems, IGCAR Campus network etc. He also played an important role in the installation and development of High Performance Computing Facility, Intra DAE VSAT Network (Anunet), Grid Computing facility, PFBR Simulator, Advanced Visualization Centre, Wireless Sensor Networks lab etc., He has more than 110 Journal Publications / Conference Papers and edited two International Conference Proceedings. Currently he is the Director of Electronics & Instrumentation Group and is responsible for the development of robust I&C systems for PFBR.

Shri G. Srinivasan is a mechanical engineer from the 18th batch of BARC Training School. He joined FBTR project as a designer in 1975, and participated in the design, fabrication and installation of Reactor Assembly Components. He moved over to O&M in 1983. After holding the positions of Senior Engineer (Planning) & Senior Engineer (Technical), he took over as Technical Services Superintendent and later as AD (O&M). He is Director, ROMG since September 2008.

Dr. C.S. Sundar, obtained his Masters degree in Physics from the University of Delhi in 1973, and a Ph.D in Physics from the University of Madras in 1983. He heads the Materials Science Group at IGCAR with a comprehensive research programme on basic research in materials science. He is also a Professor at the Homi Bhabha National Institute, Mumbai. Dr. Sundar's research contributions, spanning over three decades, has been on the investigation structure, defects and phase transitions in novel materials that include high temperature superconductors, fullerenes, strongly correlated systems and colossal magnetoresistive manganites using the techniques of positron annihilation and infrared spectroscopy, and has over 100 journal publications. He is a recipient of the Materials Research Society of India Medal, 1994 , the Young Research award, IUMRS, ICA the MRSI-ICSC superconductivity and Materials Research Annual Prize 2007 and the Tamil Nadu Scientist (TANSA) award, 2008. He is a Fellow of the Indian Academy of Sciences, Bengaluru and the National Academy of Sciences, Allahabad. Dr. Sundar is a member of the DST-Programme Advisory Committee on Condensed Matter Physics and Materials Science and the Nano Science Advisory Group of Department of Science and Technology. He is on the Editorial Board of Solid State Communications, and is an Associate Editor, Bulletin of Materials Science.

Shri Umesh Chandra is Senior Executive Director, Safety and Knowledge Management in Nuclear Power Corporation of India Ltd. His areas of responsibilities include Reactor Safety & Analysis of Design, Health, Safety & Environment of nuclear power plants in operation and construction, Software Quality Assurance of C&I Systems, Training Simulators and Knowledge Management. Before joining NPCIL in 2001, he worked in Reactor Control Division, BARC for 30 years. At BARC, his major contributions were towards creation of teams and fostering of technology for development of computer based Control and Monitoring Systems for nuclear power plants. These systems are operating in 14 Nuclear Power Plants (NPP). At NPCIL, he has established R&D activities and infrastructure including an R&D Centre at Tarapur Site and a digital C&I systems lab at Mumbai. He has been responsible for design and engineering of Control and Instrumentation systems of 540 MWe PHWRs, TAPS-3&4 at Tarapur. He has also been responsible for establishment of qualification methodology and safety guide for Digital I&C Systems in NPPs. He has contributed in preparation of C&I related safety guides for Atomic Energy Regulatory Board (AERB). He is also a part-time Director on the Board of ECIL, Hyderabad. Shri Umesh Chandra is a Distinguished Scientist and is a graduate in Electrical Engineering from IIT, Kanpur.

Dr. P.R. Vasudeva Rao, is a Distinguished Scientist and presently Director of Chemistry Group in IGCAR. He obtained his Doctorate degree in Inorganic Chemistry from Bombay University in 1979. He has played an active role in shaping the Radiochemistry Programme of IGCAR to its current status. His research interests cover a wide range of areas such as development of alternate extractants and resins for actinide recovery, solvent extraction, third phase formation, thermodynamics, applications of ionic liquids and supercritical fluid extraction in actinide separations, development of pyrochemical and other non-aqueous processes for recovery of actinides and rare earths, thermochemical studies on nuclear materials, fuel behaviour in reactors and high performance liquid chromatography. He has published more than 200 papers in reputed international journals apart from guiding several research scholars for their doctorate degrees. He is also a Fellow of Tamil Nadu Academy of Sciences. He was awarded the MRSI Medal in 1998 and the INS award for the year 2007. He was also selected for the Chemical Research Society of India Silver medal - 2011 and MRSI-ICSC Superconductivity and Materials Science Senior Award - 2011.

Members of IGCSC and Activities of Various Groups

Chairman

Shri S.C. Chetal
Director, IGCAR

Chemistry Group

Dr. P.R. Vasudeva Rao
Director, CG

Dr. T. Gnanasekaran
AD, CG & Head, LM&SCD

Dr. V. Ganesan
Head, MCD

Dr. K. Nagarajan
Head, FChD

Shri G. Ravishankar
Head, CFD

The Chemistry Group is responsible for carrying out R&D to provide inputs with respect to all the chemistry aspects of the fast reactor and its fuel cycle. Besides the R&D activities, the Chemistry Group also provides extensive analytical support using a wide range of analytical techniques to all the programmes at Kalpakkam. The areas of R&D in Chemistry Group include sodium chemistry, chemistry of un-irradiated as well as irradiated fuel materials, development of fuel cycle, high temperature chemistry, analytical chemistry, spectroscopy and boron chemistry. Chemistry Group also has been developing instrumentation and facilities in support of the R&D programme. Development of sensors for PFBR and sensors for environmental applications, development of radionuclide traps for PFBR, development of cleaning and decontamination techniques for fast reactor components, development of techniques for on-line monitoring of plutonium streams in reprocessing plants, development of technology for production of plutonium rich fuels and minor actinide containing fuels through sol-gel route, development of sodium bonding for metallic fuels and pyroprocessing are some of the R&D programmes on the anvil. Recent achievements include the fabrication of the sodium bonded U-Zr pins for irradiation in FBTR, mixer-settler demonstration of the extraction of Pu and U using Tri-iso-amyl Phosphate (TiAP) and separation of strontium-89 from yttrium irradiated in FBTR in the hot cell.

Electronics and Instrumentation Group

Shri S.A.V. Satya Murty
Director, EIG & Head, CD

Shri B. Krishnakumar
Head, EID

Shri N. Murali
Head, RTSD

Dr. S. Bagavathy Murugan
MS(Surgical)

Dr. K.S.R. Murthy
MS (Medical)

The Electronics & Instrumentation Group is actively involved in the development of Instrumentation & Control for the 500 MWe Prototype Fast Breeder Reactor. Towards this the I&C systems are designed with safety and availability of the reactor as the guiding requirements through redundant systems and also keeping in mind the simplicity of design and maintainability. A judicious combination of hardwired and computer based I&C systems, state-of-the-art design, manufacturing processes and testing were employed in the design of I&C systems. The systems developed include Safety Critical, Safety Related and Non Safety I&C Systems. The Prototype systems were qualified after rigorous environmental, EMI/EMC and seismic testing. The application software developed was subjected to thorough Verification & Validation procedures. The Group is also developing a Full Scope Replica type Operator Training Simulator for PFBR. An advanced visualization centre was established and various PFBR systems are modeled for visualization in 3D and walkthrough. R&D activities in the areas of innovative instrumentation using pulsating sensors, Wireless Sensor Networks for use in future reactors, Computational Intelligence, Knowledge Management etc. are in progress. State-of-the-art Computational facilities with a total processing power of about 30 Tera FLOPS and Data Communication facilities are being provided. To take care of the security challenges the security electronics systems are constantly deployed and upgraded. The group is also responsible for providing health services to about 30000 beneficiaries.

Engineering Services Group

The Engineering Services Group is responsible for providing quality services pertaining to Civil engineering, Electrical Engineering, Voice Communication Systems, Air-conditioning & Ventilation Systems, Material Handling Equipments, Central Workshop activities. The group also coordinates the telecommunication requirements of the Centre. The group has a mandate to establish additional infrastructure requirements so as to meet Design, R&D and operational objectives of IGCAR. The group has expert teams with capability to design, engineer and execute systems under their jurisdiction. Electricity, water, quality-air and other services including services from Central Workshop are being extended to other units of DAE located at Kalpakkam. The nature of work involves interaction with several State Government and Central Government Organisations.

Shri Y.C. Manjunatha
Director, ESG

Shri C. Sivathanu Pillai
AD, CEG

Shri C. Chandran
Head, AC & VSD

Shri A. Jyothish Kumar
Head, ESD

Shri K. Manoharan
Dy. Director & HEAD, CED, GSO

Fast Reactor Technology Group

Shri K.K. Rajan
Director, FRTG

Dr. C. Anand Babu
AD, CDG

Shri B. Babu
Head, IDSD

Shri B.K. Nashine
Head, DDRSD

Shri G. Padmakumar
Head, SE&HD

Shri V. Prakash
Head, VDD

The Fast Reactor Technology Group is responsible for development and testing of FBR components, design validation through experiments in sodium, air and water, design, development and manufacture of sodium sensors, process development for enrichment of boron and separation technologies. The group has developed expertise in sodium handling and in the design, construction, commissioning and operation of high temperature sodium systems. FRTG has set up major sodium facilities such as 5.5 MWt Steam Generator Test Facility, the Large Component Test Rig, INSOT facilities for creep and fatigue studies, SOWART facilities for studies on effect of water leak in sodium heated steam generator and SADHANA loop for experimentally demonstrating natural convection in safety grade decay heat removal system. Some of the important assignments for PFBR

that were completed by FRTG were the qualification of all the shutdown mechanisms by conducting tests in air, sodium calibration of all the Eddy Current Flowmeters for the primary sodium pump, demonstration of the utilization of the side viewing transducers for Under Sodium Ultra Sonic scanner and successful completion of the air testing of the PR&PTM of IFTM. The other facilities available in the group are the SAMRAT model and the Sub assembly test rig for thermal hydraulic studies in water, the Cover gas Purification system (CGPS) and the Boron Enrichment Plant (BEP). Development of sodium purification systems, discrete and continuous sodium level sensors, sodium flow measuring sensors and different types sodium leak detectors are some of the recent achievements. In short, the Group is working on all Engineering development aspects of FBRs.

Materials Science Group

Dr. C.S. Sundar
Director, MSG

Dr. A.K. Arora
Head, CMPD

Dr. A.K. Tyagi
Head, SND

Shri M.C. Valsakumar
Head, MPD

Dr. G. Amarendra
Head, MPS

Shri M.P. Janawadkar
Head, SQUIDS

The Materials Science Group, comprising of three Divisions, has the mandate of pursuing high quality basic research on topical problems in Materials Science, to work towards ion beam and computer simulation of radiation damage and to pursue research on innovative sensors accruing from basic research in superconductivity and nanomaterials. The Condensed Matter Physics Division focuses on the investigation of physical properties of novel materials under temperature, pressure and magnetic fields. Active research programs on Raman spectroscopy studies of vibrational properties, Dynamic light scattering and Confocal Microscopy studies of soft condensed matter, Laser heated diamond anvil cell facility for synthesis and study of materials under high pressure and high temperature and investigation of material properties at low temperatures under high magnetic fields and pressures are being pursued. The indigenously built SQUID sensors and control electronics have been translated into SQUID based measuring systems such as a high field magnetometer, a SQUID based set-up for Non-Destructive Evaluation (NDE), and SQUID based Magnetoencephalography (MEG). The activities of Materials Physics Division pertain to studies on Ion beam simulation of radiation damage using a 1.7 MV tandem accelerator; in depth studies on defects using Positron Annihilation Spectroscopy and Computer simulation of material properties. The Surface and Nanoscience Division focuses on studies on thin films using a variety of techniques such as Secondary Ion Mass Spectrometry and Scanning Probe Microscopy. Studies on controlled growth of nanometric multi-layer films for increased hardness and exploration of nanomaterials micromachined cantilevers and MEMS as sensors are being actively pursued.

Metallurgy and Materials Group

Dr. T. Jayakumar
Director, MMG & Head, NDED

Dr. A.K. Bhaduri
AD, MDTG

Dr. U. Kamachi Mudali
AD, CSTG

Dr. S. Venugopal
AD, GRIP & Head, RIRD

Dr. M. Vijayalakshmi
AD, PMG

Shri Jojo Joseph
Head, PIED

Dr. M.D. Mathew
Head, MMD

Dr. Shaju K. Albert
HEAD, MTD

The Metallurgy and Materials Group pursues a wide range of Research Programmes of the Centre that encompass both basic and applied aspects of the structural materials development for fast breeder reactors and associated fuel cycle facilities. The key areas of research and development include 1. Materials Design and Manufacturing Technology, 2. Materials Mechanics and Properties, 3. Physical Metallurgy and Characterisation, 4. Nondestructive Evaluation and In Service Inspection, 5. Irradiation Experiments and Post-Irradiation Examination, 6. Robotics, Innovative design, Engineering and Synthesis and 7. Corrosion Science and Technology. The current activities of importance being pursued are: development of special materials like Oxide Dispersion Strengthened (ODS) Ferritic Steels and Reduced Activation Ferritic - Martensitic (RAFM) Steels, IFAC-1 (D9I) SS, development of welding consumables, optimisation of thermo mechanical treatments and other fabrication processes, characterisation of microstructures and mechanical properties and their interrelationship, modeling of microstructural stability and phase evolution, corrosion and biofouling studies, development and application of specialised NDE techniques and advanced mechanical property measurement techniques like impression creep testing and ball indentation testing, irradiation experiments, post-irradiation examination, and development of technologies for robotics and remote handling. The group also has several novel technology development missions for meeting the requirements of future FBRs such as the development of hard facing procedures for critical components, studies on leak detection in sodium circuits using Raman distributed optical fiber sensor, development of ferro fluid based seals for sodium pump applications and development of advanced shielding materials, advanced materials and coatings for pyrochemical reprocessing of spent fuels. The Group has also started development of materials and manufacturing technology towards the National mission programme on advanced ultra supercritical thermal plants.

Nuclear & Safety Engineering Group

Dr. P. Chellapandi
Director, NSEG

Shri B.K. Nashine
Head, SED

Shri P. Puthiyavinayagam
Head, RCD

Shri S. Raghupathy
Head, CH & MD

Shri P. Selvaraj
Head, MHD

Nuclear Safety Engineering Group is responsible for the design and development of reactor assembly components including core, shutdown and handling mechanisms for the sodium cooled fast reactors (SFR) and getting safety clearance from Atomic Energy Regulatory Board (AERB). The group also executes R&D in the domain of structural mechanics, thermal hydraulics and safety engineering, involving national and international institutions. It provides design support to the construction and commissioning of 500 MWe Prototype Fast Breeder Reactor (PFBR), which is under construction at Kalpakkam. It also provides analytical support to other groups in the Centre including Fast Breeder Test Reactor (FBTR) as well as for other strategic and high end technologies in the country. The responsibility of group includes developing high quality human resource for the design and analysis of SFRs in the country. It is currently engaged in conceptualizing as well as detailing the innovative reactor components for the reactor assembly of future SFRs. The group has about 100 scientists and engineers, who are relatively younger. They are organized under four divisions viz. Reactor Components Division (RCD), Component Handling and Mechanism Division (CHMD), Mechanics and Hydraulics Division (MHD) and Safety Engineering Division (SED). These apart, it has a modern design office with many advanced modeling and analysis softwares, Structural Mechanics Laboratory (SML) having state-of-the-art facilities for carrying out tests on large components, high temperature structural integrity and seismic tests with large size shake tables and safety engineering laboratory for carrying out tests in the domain of severe accidents and to study the science & technology of sodium fires and fire extinguishers. This group has high quality expertise in the domain of design of mechanisms operating in sodium, mechanical design and analysis of components as per the American (ASME) and French (RCC-MR) design codes, thermal hydraulics of liquid metal, plant dynamics, etc.

Reactor Engineering Group

Shri S.C. Chetal
Director, REG

Shri C. Sivathanu Pillai
AD, CEG

Dr. B. Venkatraman
AD, RSEG & Head, RSD

Shri B. Ananthapadmanaban
Head, QAD

Shri V. Balasubramaniyan
Head, HTSD & Head SRI, AERB

Dr. K. Devan
Head, RND

Dr. R.S. Keshavamurthy
Head, RSDD

Shri K. Madhusoodanan
Head, PPCD

Dr. K.K. Satpathy
Head, E&SD

Shri N. Vijayan Varier
Head, TC&QCD

The Reactor Engineering Group (REG) comprising of Reactor Shielding and Data Division, Reactor Neutronics Division, Heat Transport Systems Division, Power Plant Control Division, Technical Coordination & Quality Control Division, Civil Engineering Design Division and Radiological Safety and Environmental Group which has Radiological Safety Division Environmental & Industrial Safety Division & Quality Assurance Division. The group activities includes fast reactor physics, heat transport system, plant layout, steam water system, instrumentation & control systems and civil structures of fast reactors. It has carried out the design of above systems for 500 MWe Prototype Fast Breeder Reactor (PFBR) and has obtained the statutory / regulatory clearances from AERB. Along with BHAVINI, REG engineers are responsible for getting the heat transport, instrumentation & control system components of PFBR manufactured by the Indian industries. REG also provides necessary design support to FBTR. REG is presently engaged in design of above stated disciplines for future 500 MWe FBRs to provide enhanced safety and improved economics. As a spin off, the expertise acquired in mechanical design is being provided to a number of organizations for non-reactor activities. The Group is also responsible for providing quality assurance / quality control services for all the major projects being undertaken by IGCAR through the ISO 9001-2008 certified Quality Assurance Division. The Radiological Safety Division of the Group is responsible for R&D activities in the areas of radioactivity transport and improving the radiation detection and measurements through advanced techniques. This Division provides health physics and radiation safety services for the radioactive facilities in IGCAR. Environmental and Industrial Safety Division provides industrial safety services to all the facilities at IGCAR. This Division also carries out R&D in the domain of aquatic and terrestrial biodiversity and sediment characterization. The Group organizes public awareness programs on radiation safety and nuclear energy in addition to training and awareness programs on industrial, radiation and fire safety to occupational workers.

Reactor Operations and Maintenance Group

Shri G. Srinivasan
Director, ROMG

Shri B. Ananthapadmanaban
Head, RMD

Shri N. Kasinathan
Head, RAD

Shri K.V. Suresh Kumar
Head, ROD

Shri P.R. Swaminathan
Head, PPD

Ms. S. Usha
Head, TSD

ROMG is responsible for safe operation of Fast Breeder Test Reactor (FBTR) and KAMINI reactor within the limits given in technical specification documents. The group also takes part in the operational safety review of PFBR Project documents. The Training section of the group is also responsible for training the O&M staff of PFBR and future FBR's besides training O&M staff of FBTR and KAMINI. Progressive modifications in FBTR to increase its availability and for gaining newer experience in operation, utilizing the reactor for irradiation of advanced fuels and materials for fast reactors and conducting safety related experiments form a major part of ROMG's activities.

Reprocessing Group

Shri R. Natarajan
Director, RpG

Dr. U. Kamachi Mudali
Head, RRDD

Shri P. Ramkumar
Head, RPSD

Shri A. Ravishankar
Head, RPDD

Shri V. Sundararaman
Head, FRPD

Shri M. Venkataraman
Head, RPOD

The success of Indian Fast Breeder Reactor (FBR) programme depends on the closing the fuel cycle within a short period so that the inventory of fissile material outside the reactor can be as small as possible. The Reprocessing Group (RpG) of IGCAR is responsible for achieving this objective. Various activities with regard to

the fast reactor fuel reprocessing technology such as the design, construction and operation of the reprocessing plants are being undertaken by this group. There are facilities at the Reprocessing Development Laboratory (RDL), where extensive engineering scale testing of equipment and systems are carried out before installation in radioactive hot cells. Chopper, dissolver, feed clarification equipment, centrifugal extractors and different types of pulse columns are a few important equipment that are being developed at RDL for deployment in fast reactor fuel reprocessing plants. Apart from equipment development, research is undertaken for understanding and solving various process, chemistry and analytical problems of fast reactor fuel reprocessing such as, process flow sheet studies to improve the plant performance for higher recoveries and reduced waste generation, mathematical modeling of solvent extraction of the complex U-Pu system, solvent management, development of alternate solvent-diluent systems, development of online monitoring of Pu for process control, liquid flow metering in high radioactive fields, development of material handling equipment inside the hot cells, etc. In one of the hot cell facilities at RDL, U was recovered from irradiated thorium rods using THOREX process which is used as fuel in KAMINI reactor and in FBTR (as PFBR test fuel). The other hot cell facility, called CORAL(Compact facility for Reprocessing Advanced fuels in Lead cells) commissioned in 2003, is being deployed as a versatile test bed for validating the process flow sheet and scaling up of equipment designs for fast reactor fuel reprocessing, by processing the FBTR spent fuel. This experimental facility has been used for reprocessing several batches of mixed carbide fuels irradiated in FBTR with 25, 50, 100 and 155 GWd/t burn-ups. This has provided valuable experience to the design of Demonstration Fast Reactor Fuel Reprocessing Plant (DFRP) in which all the types of FBTR fuels, such as the mixed carbide and oxide of different compositions, will be reprocessed on a regular basis. DFRP is also designed to reprocess PFBR fuel subassemblies also for demonstrating the reprocessing of irradiated PFBR oxide fuels. In addition to these activities, RpG is also carrying out the design of the reprocessing plant, FRP for reprocessing spent fuels of PFBR on commercial basis.

Fast Reactor Fuel Cycle Facility

Shri P.V. Kumar
Project Director

Fast Reactor Fuel Cycle Facility Project Group is entrusted with the work of planning, designing and constructing the Fast Reactor Fuel Cycle Facility (FRFCF) to close the fuel cycle of PFBR. FRFCF is a multi unit project involving BARC, IGCAR, and NFC. IGCAR is piloting the work on the project. The Project Group interacts with the participating groups from different units of DAE . Preparation of the detailed project report, processing for obtaining financial sanction, development of infrastructure at the project site, and obtaining regulatory and other statutory clearances is the mandate of this group.

Resources Management Group

Dr. M. Sai Baba
AD, RMG

Resources Management Group (RMG) comprises of the Scientific Information Resource Division, Strategic Planning and Human Resources Development Division and OCES-Training Section. The mandate of the Group is towards planning and management of resources like financial (budget), human and scientific information resources in the Centre. The significant activities of the Group include: Strategic planning and human resource management, Conducting the academic programmes of BARC Training school at IGCAR, Formulating and monitoring Capital projects towards budget planning and management including providing necessary reports and proposals to DAE, Automation and integration of activities pertaining to administration,

accounts, stores, budget and procurement on a single platform, Coordinating the visits of important dignitaries and delegations to the Centre, Formulating and facilitating collaborations and MoU, Providing technical coordination with various agencies and conducting public awareness programmes for the benefit of public and media, Providing information resources through conventional library and the library on the desktop by digital networking with special emphasis to cater to the needs of students and young scholars and publishing important documents of the Centre like IGC Newsletter, Annual Report, Benchmarks, preparation of annual reports and plan related documents.

Madras Regional Purchase Unit

Shri A.S.L.K. Rao
RD, MRPU

Material Management activities for IGCAR and General Services Organisation are taken care by Madras Regional Purchase Unit which comes under Directorate of Purchase & Stores of Department of Atomic Energy. Procurement and payment to suppliers are carried out at Chennai and inventory and accounting are carried out by Central Stores at Kalpakkam. E-Tendering was implemented successfully and more than 200 files were processed by E-Tendering mode. Total expenditure for purchase of material and equipment in the calendar year 2010 has crossed 180 crores. Some of the major equipment for which orders have been placed are Laser Raman Spectrometer, Digital Holographic Microscope, XRD with High Temperature attachments, HPC Cluster System, Tri-Junction Forged Rings and Neutronic Channels. Timely action taken by MRPU has resulted in excellent compliance of expenditure budget targets.

Administration and Accounts

Shri O.K. SATHIAN
Chief Administrative Officer

Shri C.G.S. Nair
Joint Controller (Finance & Accounts)

Smt. Saroja Gopal
AO(R&SR) & Secretary, IGCSC

General Services Organisation

Shri K. Padamanabhan
Chief Administrative Officer

LIST OF IMPORTANT ABBREVIATIONS

AC&VSD	Air Conditioning and Ventilation System Division
AERB	Atomic Energy Regulatory Board
BARC	Bhabha Atomic Research Centre
BARCF	Bhabha Atomic Research Centre Facilities
BHAVINI	Bharatiya Nabhikiya Vidyut Nigam Limited
CD	Computer Division
CEG	Civil Engineering Group
CERMON	Continuous Environmental Radiation Monitoring Network
CFD	Chemical Facilities Division
CG	Chemistry Group
CDG	Components Development Group
CH&MD	Components Handling & Mechanism Division
CMPD	Condensed Matter Physics Division
CORAL	Compact facility for Reprocessing Advanced fuels in Lead cell
CSTG	Corrosion Science & Technology Group
CT&VDD	Chemical Technology and Vibration Diagnostics Division
CWD	Central Workshop Division
DDRSD	Device Development and Rig Services Division
EID	Electronics and Instrumentation Division
EIG	Electronics and Instrumentation Group
E&SD	Environmental & Safety Division
ESD	Electrical Services Division
ESG	Engineering Services Group
FBR	Fast Breeder Reactor
FBTR	Fast Breeder Test Reactor
FChD	Fuel Chemistry Division
FRFCF	Fast Reactor Fuel Cycle Facility
FRPD	Fuel Reprocessing Process Division
FRTG	Fast Reactor Technology Group
GRIP	Group for Remote Handling, Robotics, Irradiation Experiments and PIE
GSO	General Services Organisation
HTSD	Heat Transport Systems Division
IAEA	International Atomic Energy Agency
IIT	Indian Institute of Technology
ID&SD	Instrumentation Development & Services Division
IMSc	Institute of Mathematical Sciences
LMFBR	Liquid Metal Cooled Fast Breeder Reactor
LM&SCD	Liquid Metals and Structural Chemistry Division
MAPS	Madras Atomic Power Station
MCD	Materials Chemistry Division
MDTG	Materials Development and Technology Group
MHD	Mechanics & Hydraulics Division
MMD	Mechanical and Metallurgy Division
MMG	Metallurgy and Materials Group
MPD	Metal Physics Division
MRPU	Madras Regional Purchase Unit
MSG	Materials Science Group
MTD	Materials Technology Division
NDED	Non-Destructive Evaluation Division
NFC	Nuclear Fuel Complex
NICB	Nuclear Island Connected Building
NPC	Nuclear Power Corporation
NSEG	Nuclear and Safety Engineering Group
PDCG	Process Design & Commissioning Group
PFBR	Prototype Fast Breeder Reactor
PHWR	Pressurized Heavy Water Reactor
PIED	Post Irradiation Examination Division
PMG	Physical Metallurgy Group
PPCD	Power Plant Control Division
PPD	Project Planning Division
QAD	Quality Assurance Division
RAD	Reactor Analysis Division
RCD	Reactor Components Division
REG	Reactor Engineering Group
RIRD	Remote Handling, Irradiation Experiments and Robotics Division
RMD	Reactor Maintenance Division
RMG	Resources Management Group
RND	Reactor Neutronics Division
ROD	Reactor Operation Division
ROMG	Reactor Operation and Maintenance Group
RPDD	Reprocessing Plant Design Division
RpG	Reprocessing Group
RPOD	Reprocessing Plant Operations Division
RPOG	Reprocessing Projects & Operation Group
RRDD	Reprocessing Research and Development Division
RSD	Radiological Safety Division
RSDD	Reactor Shielding and Data Division
RSEG	Radiological Safety & Environmental Group
RTSD	Real Time Systems Division
SED	Safety Engineering Division
SE&HD	Sodium Experiments & Hydraulics Division
SIRD	Scientific Information Resource Division
SND	Surface and Nanoscience Division
SOWART	Sodium Water Reaction Test facility
SP&HRDD	Strategic Planning & Human Resource Development Division
TC&QCD	Technical Coordination & Quality Control Division
TSD	Technical Services Division
VDD	Vibration Diagnostics Division

LIST OF IMPORTANT ABBREVIATIONS

AC&VSD	Air Conditioning and Ventilation System Division
AERB	Atomic Energy Regulatory Board
BARC	Bhabha Atomic Research Centre
BARCF	Bhabha Atomic Research Centre Facilities
BHAVINI	Bharatiya Nabhikiya Vidyut Nigam Limited
CD	Computer Division
CEG	Civil Engineering Group
CERMON	Continuous Environmental Radiation Monitoring Network
CFD	Chemical Facilities Division
CG	Chemistry Group
CDG	Components Development Group
CH&MD	Components Handling & Mechanism Division
CMPD	Condensed Matter Physics Division
CORAL	Compact facility for Reprocessing Advanced fuels in Lead cell
CSTG	Corrosion Science & Technology Group
CT&VDD	Chemical Technology and Vibration Diagnostics Division
CWD	Central Workshop Division
DDRSD	Device Development and Rig Services Division
EID	Electronics and Instrumentation Division
EIG	Electronics and Instrumentation Group
E&SD	Environmental & Safety Division
ESD	Electrical Services Division
ESG	Engineering Services Group
FBR	Fast Breeder Reactor
FBTR	Fast Breeder Test Reactor
FChD	Fuel Chemistry Division
FRFCF	Fast Reactor Fuel Cycle Facility
FRPD	Fuel Reprocessing Process Division
FRTG	Fast Reactor Technology Group
GRIP	Group for Remote Handling, Robotics, Irradiation Experiments and PIE
GSO	General Services Organisation
HTSD	Heat Transport Systems Division
IAEA	International Atomic Energy Agency
IIT	Indian Institute of Technology
ID&SD	Instrumentation Development & Services Division
IMSc	Institute of Mathematical Sciences
LMFBR	Liquid Metal Cooled Fast Breeder Reactor
LM&SCD	Liquid Metals and Structural Chemistry Division
MAPS	Madras Atomic Power Station
MCD	Materials Chemistry Division
MDTG	Materials Development and Technology Group
MHD	Mechanics & Hydraulics Division
MMD	Mechanical and Metallurgy Division
MMG	Metallurgy and Materials Group
MPD	Metal Physics Division
MRPU	Madras Regional Purchase Unit
MSG	Materials Science Group
MTD	Materials Technology Division
NDED	Non-Destructive Evaluation Division
NFC	Nuclear Fuel Complex
NICB	Nuclear Island Connected Building
NPC	Nuclear Power Corporation
NSEG	Nuclear and Safety Engineering Group
PDCG	Process Design & Commissioning Group
PFBR	Prototype Fast Breeder Reactor
PHWR	Pressurized Heavy Water Reactor
PIED	Post Irradiation Examination Division
PMG	Physical Metallurgy Group
PPCD	Power Plant Control Division
PPD	Project Planning Division
QAD	Quality Assurance Division
RAD	Reactor Analysis Division
RCD	Reactor Components Division
REG	Reactor Engineering Group
RIRD	Remote Handling, Irradiation Experiments and Robotics Division
RMD	Reactor Maintenance Division
RMG	Resources Management Group
RND	Reactor Neutronics Division
ROD	Reactor Operation Division
ROMG	Reactor Operation and Maintenance Group
RPDD	Reprocessing Plant Design Division
RpG	Reprocessing Group
RPOD	Reprocessing Plant Operations Division
RPOG	Reprocessing Projects & Operation Group
RRDD	Reprocessing Research and Development Division
RSD	Radiological Safety Division
RSDD	Reactor Shielding and Data Division
RSEG	Radiological Safety & Environmental Group
RTSD	Real Time Systems Division
SED	Safety Engineering Division
SE&HD	Sodium Experiments & Hydraulics Division
SIRD	Scientific Information Resource Division
SND	Surface and Nanoscience Division
SOWART	Sodium Water Reaction Test facility
SP&HRDD	Strategic Planning & Human Resource Development Division
TC&QCD	Technical Coordination & Quality Control Division
TSD	Technical Services Division
VDD	Vibration Diagnostics Division

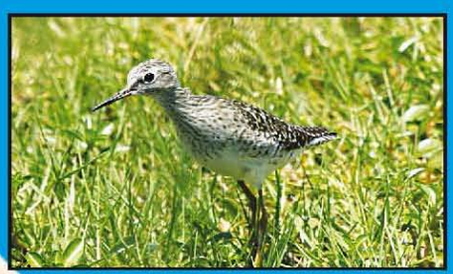

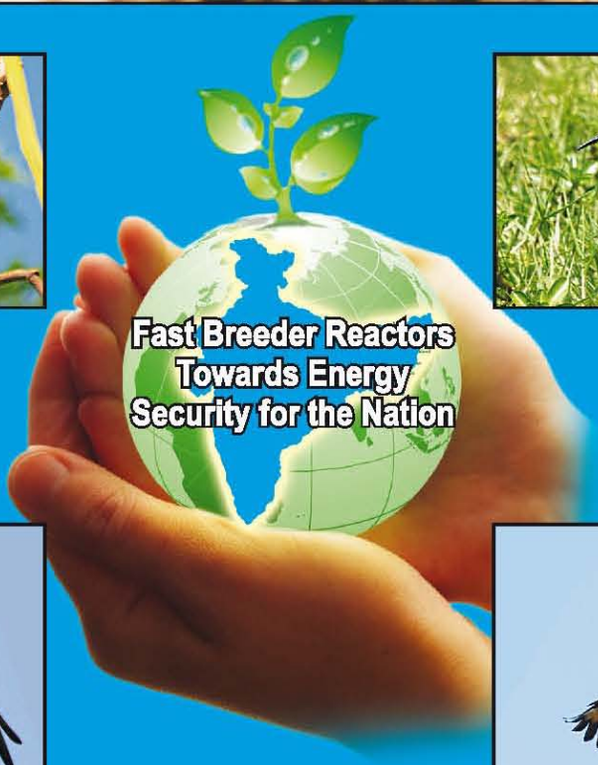

Fast Breeder Reactors Towards Energy Security for the Nation